Computational drug design based in natural leads to overcome drug resistance in targeted and pan-cancer therapy

Inaugural-Dissertation

zur Erlangung des Doktorgrades
der Mathematisch-Naturwissenschaftlichen Fakultät
der Heinrich-Heine-Universität Düsseldorf

vorgelegt von

David Bickel
aus Mühlhausen (Thür.)

Düsseldorf, September 2021

aus dem Institut für Pharmazeutische und Medizinische Chemie
der Heinrich-Heine-Universität Düsseldorf

Gedruckt mit der Genehmigung der Mathematisch-Naturwissenschaftlichen Fakultät
der Heinrich-Heine-Universität Düsseldorf

Berichterstatter:

1. Prof. Dr. Holger Gohlke

2. Prof. Dr. Thomas Kurz

Tag der mündlichen Prüfung: 8.12.2021

Erklärung

Ich versichere an Eides Statt, dass die Dissertation von mir selbständig und ohne unzulässige fremde Hilfe unter Beachtung der "Grundsätze zur Sicherung guter wissenschaftlicher Praxis an der Heinrich-Heine-Universität Düsseldorf" erstellt worden ist.

Diese Dissertation wurde in der vorgelegten oder in ähnlicher Form noch bei keiner anderen Institution eingereicht. Ich habe bisher keinen erfolglosen Promotionsversuch unternommen.

Brüssel, den 20.09.2021   _____

David Bickel

The presence of those seeking the truth is infinitely to be preferred to the presence of those who think they've found it.

Terry Pratchett

Table of contents

Abstract

Cancer is a leading cause of death world-wide. Though remarkable progress has been made in the development of chemotherapeutics, therapy resistance in tumors still occurs on a regular basis, leading to relapses and death. Thus, there is a need for novel anti-cancer drugs to overcome therapy resistance and reduce adverse effects in patients. To rationally design and improve lead compounds for anti-cancer therapy, it is pivotal to understand the molecular interactions that drive the anti-cancer effect. Therefore, in this thesis computational and experimental work is combined to provide insights on the molecular mode of action of the investigated compounds.

In a first study, the natural product phomoxanthone A is investigated as a prospective anti-cancer drug. It exhibits a strong apoptotic effect by depolarizing the mitochondrial membrane. In umbrella sampling simulations, the energy barrier for PXA passing through the inner mitochondrial membrane is computed, and rate constants are derived, which suggest that the compound may act as a protonophoric decoupler.

In a second project, an inhibitor of the C-terminal dimerization of heat shock protein 90 (HSP90) is studied with respect to its binding site. HSP90 functions as a dimer and promotes proliferation in various cancer types. By unbiased ligand diffusion molecular dynamics (MD) simulations, we could show that the compound binds to the dimer interface and might thus interfere with the HSP90 function by preventing the homodimerization.

Finally, a small molecule modulator of RUNX1-ETO that binds to the NHR2 domain is studied by unbiased MD simulations. The RUNX1-ETO fusion protein is associated with the onset of a subtype of acute myeloid leukemia. By the simulations, a first binding model of the compound to the NHR2 domain could be obtained. Moreover, a virtual screening was performed, identifying structural analogues of the compound, enabling the deduction of first structure-activity relations.

Taken together, these studies advance their respective projects by providing structural insights on the molecular level on the mode of action of the investigated compounds.

Zusammenfassung

Krebs ist ein der führenden Todesursachen weltweit. Trotz zahlreicher Fortschritte in der Behandlung mit Chemotherapeutika, ist Therapieresistenz bei Tumoren nach wie vor ein häufiges Problem, dass zu Rückfällen und zum Tod führen kann. Daher ist es wichtig, weiter neue Chemotherapeutika zu entwickeln, um auch therapierefraktäre Tumore behandeln zu können. Um rational neue Wirkstoff für die Krebstherapie zu entwickeln, ist es entscheidend die molekularen Interaktionen zu verstehen, auf denen der therapeutische Effekt beruht. Zu diesem Zweck wurden in dieser Arbeit computergestützte und experimentelle Studien zusammengeführt, um Einblicke in die molekulare Wirkweise der untersuchten Verbindungen zu geben.

In einer ersten Studie wurde die Verbindung Phomoxanthon A (PXA) als potentielles Chemotherapeutikum untersucht. Die Verbindung übt einen starken apoptotischen Effekt durch Depolarisierung der mitochondriellen Membran aus. Über Molekulardynamiksimulationen wurde die Energiebarriere der Passage von PXA durch die innere mitochondriale Membran berechnet. Davon abgeleitete Geschwindingkeitskonstanten unterstützen die These, dass PXA als Protonophore das Membranpotential entkoppelt.

In einem weiteren Projekt wurde der Bindungsmodus eines C-terminalen Inhibitors des Hitzeschockproteins 90 (HSP90) untersucht. HSP90 liegt als funktionales Dimer vor und unterstützt die Proliferation verschiedener Tumore. In Simulationen der freien Diffusion des Inhibitors konnten wir zeigen, wie dieser im C-terminalen Dimerisierungsinterface bindet und so die Dimerisierung von HSP90 beeinträchtigen könnte.

Schließlich wird ein niedermolekularer Modulator von RUNX1-ETO, der an die NHR2-Domäne bindet, durch MD-Simulationen untersucht. Das RUNX1-ETO-Fusionsprotein ist mit dem Auftreten eines Subtyps der akuten myeloischen Leukämie verbunden. In den Simulationen konnte ein erstes Bindungsmodell der Verbindung an der NHR2-Domäne erhalten werden. Darüber hinaus wurde ein virtuelles Screening durchgeführt, bei dem strukturelle Analoga der Verbindung identifiziert wurden, um die ersten Struktur-Aktivitäts-beziehungen abzuleiten.

Zusammengenommen bringen diese Studien ihre jeweiligen Projekte voran, indem sie strukturelle Einblicke auf molekularer Ebene in die Wirkungsweise der untersuchten Verbindungen liefern.

List of publications

This thesis is based on the following articles:

I. Bickel, D., and Gohlke, H.

C-terminal modulators of heat shock protein of 90 kDa (HSP90): State of development and modes of action

Bioorganic & Medicinal Chemistry 2019; **27**(21): 115080.

II. Wang, C., Engelke, L., Bickel, D., Hamacher, A., Frank, M., Proksch, P., Gohlke, H., and Kassack, M.U.

The tetrahydroxanthone-dimer phomoxanthone A is a strong inducer of apoptosis in cisplatin-resistant solid cancer cells

Bioorganic & Medicinal Chemistry 2019; **27**(19): 115044.

III. Bhatia, S., Spanier, L., Bickel, D., Dienstbier, N., Woloschin, V., Vogt, M., Pols, H., Lungerich, B., Reiners, J., Aghaallaei, N., Diedrich, D., Frieg, B., Schliehe-Diecks, J., Bopp, B., Lang, F., Gopalswamy, M., Loschwitz, J., Bajohgli, B., Skokowa, J., Borkhardt, A., Hauer, J., Hansen, F.K., Smits, S., Jose, J., Gohlke, H., and Kurz, T.

Development of a first-in-class small molecule inhibitor of the C-terminal HSP90 dimerization

ChemRxiv 2021; 10.26434/chemrxiv-2021-qwxbh.

IV. Gopalswamy, M., Kröger, T., Bickel, D., Frieg, B., Akter, S., Schott-Verdugo, S., Viegas, A., Pauly, T., Mayer, M., Przibilla, J., Reiners, J., Nagel-Steger, L., Smits, S., Groth, G., Etzkorn, M., and Gohlke, H.

Biophysical and pharmacokinetic characterization of a small-molecule inhibitor of RUNX1/ETO tetramerization with anti-leukemic effects

bioRxiv 2021; 10.1101/2021.12.22.473911.

Publications not included in this thesis:

V. Bovdilova, A., Alexandre, B.M., Höppner, A., Luís, I.M., Alvarez, C.E., Bickel, D., Gohlke, H., Decker, C., Nagel-Steger, L., Alseekh, S., Fernie, A.R., Drincovich, M.F., Abreu, I.A., and Maurino, V.G.

Posttranslational modification of the NADP-malic enzyme involved in C4 photosynthesis modulates the enzymatic activity during the day

The Plant Cell 2019; **31**(10): 2525-39.

VI. Hüdig, M., Tronconi, M.A., Zubimendi, J.P., Sage, T.L., Poschmann, G., Bickel, D., Gohlke, H., and Maurino, V.G.

Respiratory and C_4-photosynthetic NAD-malic enzyme coexist in bundle sheath cells mitochondria and evolved via association of differentially adapted subunits

The Plant Cell 2021; 10.1093/plcell/koab265.

Abbreviations

ABL1	Abelson murine leukemia viral oncogene homolog 1
ADP	Adenosine diphosphate
AML	Acute myeloid leukemia
ATP	Adenosine triphosphate
CCCP	Carbonyl cyanide *m*-chlorophenyl hydrazone
CDC37	Cell division cycle 37 protein
CML	Chronic myeloid leukemia
CPS1	Carbamoyl-phosphate synthase 1
CTD	C-terminal domain
DARTS	Drug affinity responsive target stability
DHFR	Dihydrofolate reductase
DNA	Desoxyribonucleic acid
DOPC	1,2-Dioleoyl-*sn*-glycero-3-phosphatidylcholine
DOPE	1,2-Dioleoyl-*sn*-glycero-3-phosphtadylethanolamine
DOPG	1,2-Dioleoyl-*sn*-glycero-3-phosphatidylglycerol
EMA	European medicines agency
ER	Endoplasmic reticulum
FDA	U.S. Food and drug administration
GRP94	Glucose-regulated protein 94
HOP	HSP70/HSP90 organizing protein
HSF-1	Heat shock factor-1
HSP(s)	Heat shock protein(s)
HSP90	Heat shock protein of 90 kDa
HSR	Heat shock response
IMM	Inner mitochondrial membrane

MD	Molecular dynamics
MiD	Middle domain
NHR[1-4]	Nervy homology region [1-4]
NMR	Nuclear magnetic resonance
NTD	N-terminal domain
PMF	Potential of mean force
PPI	Protein-protein interaction
PXA	Phomoxanthone A
RHD	Runt homology domain
SAR	Structure-activity relationship
STD-NMR	Saturation transfer distance nuclear magnetic resonance
TPR	Tetratricopeptide repeat
TRAP1	Tumor necrosis factor receptor-associated protein 1
WHAM	Weighted histogram analysis method
WHO	World health organization

1 Introduction

Cancer is a group term for diseases that involve unchecked proliferation of aberrant cells [1]. The term originates back to the Greek word *καρκίνος* that was firstly used in the *Corpus Hippocraticum* attributed to the Ancient Greek physician HIPPOKRATES [2,3]. However, cancerous lesions were already described long before that, for instance in the Ebers Papyrus [3,4]. In our industrialized society cancer has risen to be a leading cause of death. This increase in cancer incidence and mortality is caused by several factors. For one, due to the overall increase in life expectancy, people are more likely to reach older ages when cancer is more likely to occur [1]. Into this category also falls the progress in medical development that allows for better control of other diseases like infectious diseases and cardiovascular diseases [1,5,6]. Finally, changes in lifestyle (e.g., diet, smoking, obesity) may also contribute to the increases in cancer incidence [1]. For 2020, it was estimated that there were more than 19 million new cases and about 10 million deaths due to cancer worldwide [7,8]. This amounts to one in six people dying from cancer [9], and these numbers are still believed to rise over the next decade due to improved life expectancy and changes in demographics [9-11]. Therefore, the World Health Organization (WHO) adopted the improvement of cancer treatment and reduction of "premature death" (deaths between the ages of 30 and 69) as Sustainable Development Goal target 3.4 [9].

The manifestation of cancer varies widely, depending on which tissue is affected and if there is a solid tumor or diffuse proliferations (e.g., in leukemia) [9,12]. All cancer cells, however, share common biological traits that enable tumor growth and metastatic dissemination: sustaining proliferative signaling, insensitivity to growth suppression, evasion of apoptosis, limitless replicative potential, sustained angiogenesis, and tissue invasion [13]. Furthermore, cancer cells need to avoid immune destruction and to restructure their energy metabolism to maintain the sustained proliferation [14]. When Hanahan & Weinberg proposed these "Hallmarks of cancer" they deliberately limited their description to functional characteristic, leaving open how these capabilities may be achieved [13]. In fact, different types of tumors may develop these traits via distinct mechanisms and to varying degrees [13,14]. During the transformation of normal cells towards malignancies each of these hallmarks represents a barrier the cell needs to overcome to become cancerous [13,14]. Therefore, a certain degree of genomic instability is necessary, so that the cell accumulates random mutations that, driven by selection, may eventually lead to unlocking these capabilities [13,14].

For the longest time in history, surgery was the only effective treatment option for cancerous growths, joined by radiotherapy in the 1960s [15-17]. However, both these treatment options
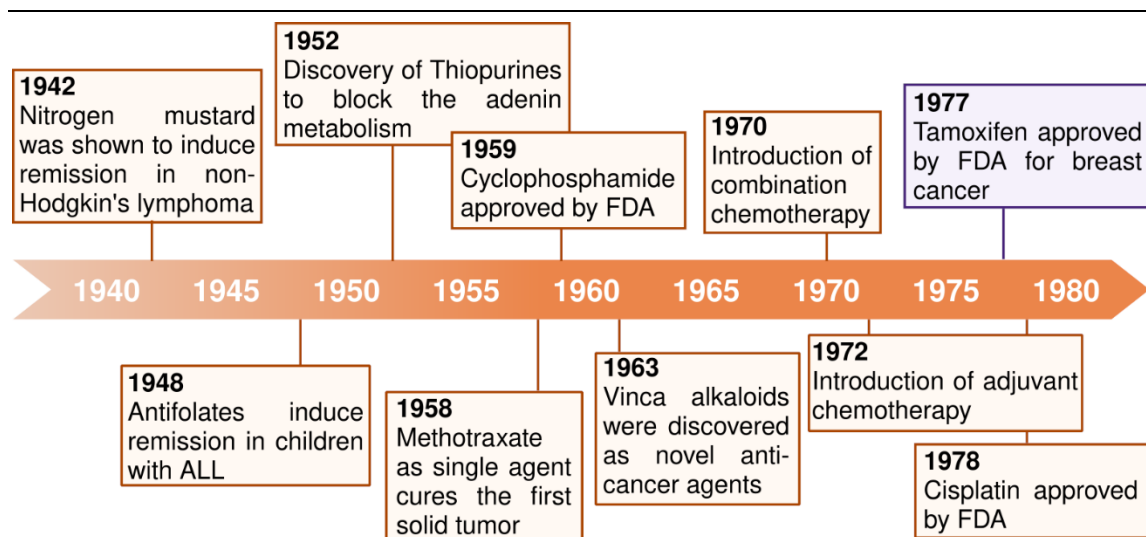
Figure 1. Timeline of key developments in cancer therapy. The timeline shows key advances in the pharmacological treatment of cancer. Classical chemotherapeutics and related advances are marked in orange, the first hormonal agent is shown in violet, targeted therapies and related discoveries are shown in green, and recent advances in immunotherapy are shown in blue. Figure is based on REFS [16-19].

cannot treat metastatic disseminations, limiting their success rates [17]. Starting in the mid-20th century massive effort was undertaken to discover drugs to treat cancer (Figure 1). In 1942, nitrogen mustard was discovered as a first compound that induces remission in tumors [17,20]. This provided a first proof-of-principle that cancer could be treated with chemical compounds and ultimately led to the wide variety of cancer chemotherapeutics available today.

Nowadays, **chemotherapeutic agents** are typically compounds that prevent the cancer from further proliferation, either by damaging the DNA directly, or blocking cell reduplication (i.e., mitosis). The modes of action of these compounds include among others alkylation of the nucleobases forming intra- (e.g., cisplatin [21]) and inter-strand (e.g., cyclophosphamide [22,23]) crosslinks, inhibition of DNA (e.g., cytarabine [24]) and nucleobase synthesis (e.g., methotrexate [25]), and by modulating the mitotic spindle apparatus (e.g., paclitaxel [26], vincristine [27]). All have in common that these compounds target cell components like the DNA or microtubule apparatus, which are present in all living cells. This leads to toxic effects on physiologically fast proliferating tissues (e.g., bone marrow or gastrointestinal epithelia), substantially limiting the therapeutic window for these compounds [28].

Some cancers are dependent on certain hormones to grow. These cancers typically exploit the pathways of nuclear hormone receptors to sustain their growth. The aim of **hormonal oncotherapy** is to deprive these tumors from their growth signals by either blocking the hormone receptors (e.g., tamoxifen [29]) or reducing the hormone secretion (e.g., letrozole [30]). In comparison to the chemotherapeutics discussed above, hormonal drug therapy is less toxic.
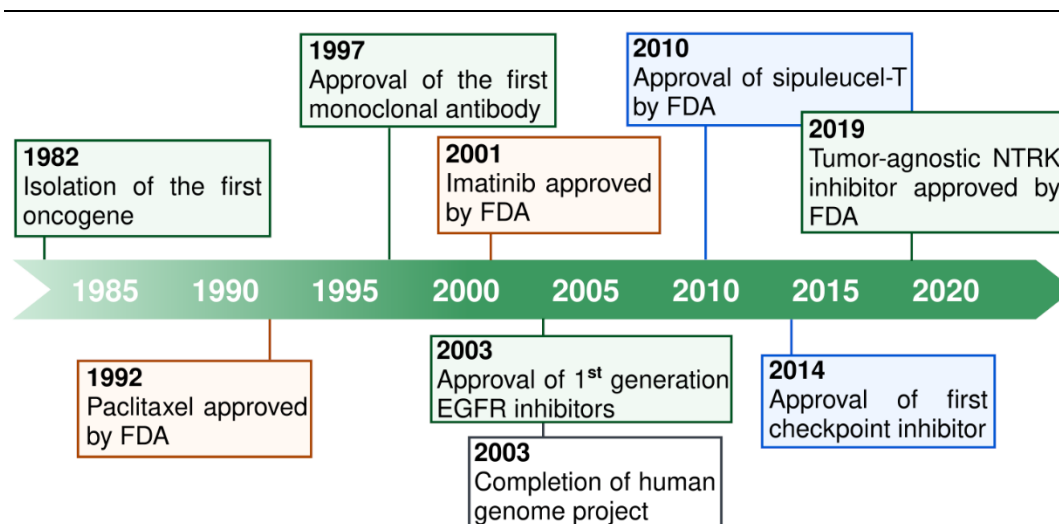
Figure 1. continued

However, the systemic alteration of hormone levels leads to adverse effects related to the hormone system that is targeted [31]. Still, hormonal oncotherapy provided a first way to target specific proliferative pathways in tumors.

Building further on that concept in conjunction with the discovery of oncogenes, tumor suppressor genes and overall molecular markers of cancer, **targeted therapies** were developed with the focus on targeting specifically molecular targets unique to cancer cells, minimizing toxic effects in healthy tissues [32,33]. To this end, several strategies are employed including targeted delivery systems, monoclonal antibodies, as well as small molecules [32,33]. In the following, I want to focus on small molecules which have been specifically designed to act on targets in the proliferative pathways of tumors. A primary example for this group is the tyrosine kinase inhibitor imatinib. This compound competitively inhibits the ATP binding site of the kinase BCR-ABL [34]. This kinase is a fusion protein caused by the t(9;22) translocation, also known as Philadelphia chromosome, which is found in roughly 90% of patients with chronic myeloid leukemia [34,35]. Although, imatinib also inhibits its target kinases[*] in non-cancer cells, most cells can cope with this, while Philadelphia chromosome-positive cancer cells are highly susceptible to imatinib treatment [35-37]. Overall, imatinib did largely improve the clinical outcome of Philadelphia chromosome-positive chronic myeloid leukemia [38,39].

In other types of cancer, targeted therapies have not fulfilled the initial high expectations. In many cases, mechanism-targeting drugs only show weak and transient responses before tumors

---

[*] Next to BCR-ABL, imatinib also blocks the non-fusion protein ABL1 kinase, as well as receptor tyrosine kinases c-KIT and platelet-derived growth factor receptor α (PDGFRα). The latter two allowed for its successful application in gastrointestinal stromal tumors.

become resistant [12,40,41]. There are many ways for tumors to become resistant against compounds. Typical modes of resistance include mutations in the target-site (e.g., acquired imatinib-resistance in CML), activation of "parallel" pathways to replace a blocked mechanism, but also changes and heterogenicity of the cellular environment throughout the cancerous tissue [12,35,40,42]. Thus, despite the great advances in cancer therapy over the last decades, our limited understanding of the molecular changes that drive development of cancers as well as the emergence of drug resistance limits the success of pharmacological cancer therapies. Thus, there is a need for novel compounds that circumvent drug resistance by having novel modes of action.

In this thesis, three independent projects that aim to develop anti-cancer drugs for the treatment of therapy-resistant tumors will be presented. In all these projects, molecular simulation techniques are applied to gain mechanistic insights on the mode of action of the investigated compounds. In **Publication II** phomoxanthone A (PXA), a natural product with promising anti-proliferative properties is studied, with respect to its ability to permeate through the inner mitochondrial membrane. In **Publication III** a small molecule inhibitor of the C-terminal dimerization of heat shock protein of 90 kDa (HSP90) is presented. Molecular dynamics (MD) simulations are applied to study the association of the compound to the target protein, revealing the preferred binding of the compound in the dimerization interface. Finally, inhibitors that target the NHR2 domain of the AML1-ETO fusion protein are studied. In **Publication IV**, 7.44, a compound binding to the NHR2 domain, is investigated regarding its biophysical properties. Finally, structural analogues of 7.44 with improved activities against cells *ex vivo* are identified.

1.1 Drug design inspired by nature

In rational drug discovery the first steps are understanding the disease and its pathophysiology on the level of biochemical pathways, genetics, and structural biology. This allows for the selection of a target to focus the drug design on. The next step is to identify a preliminary lead structure that elicits to some extend the desired effect on the target [43].

Natural products, i.e., secondary metabolites [*] extracted from plants, bacteria, or fungi, comprise a primary source for bioactive lead compounds. Being produced by living organism, these compounds "evolved" to exhibit relevant pharmacophores to trigger biological effects to grant the producer an evolutionary advantage[44,45]. Therefore, it is not surprising, that many blockbuster drugs can be traced back to natural product leads. In fact, out of 136 small-

---

[*] Compounds that do not have an explicit function in the cellular economy of the organism producing it.

molecules approved for the treatment of cancer during 1981 and 2014, 113 were natural products or compounds mimicking natural products in the broadest sense [46].

The chemical space covered by natural products is vast, and distinct from molecule libraries based on building block assembly *via* combinatorial synthesis. They differ in the average number of stereocenters, number of sp^3-hybridized carbons, and content of heteroatoms [47,48], resulting in different outcomes in screening campaigns [49,50]. Moreover, some natural products have been categorized into the "dark chemical matter" , comprised of compounds for which no bioactivity of any sort has been discovered yet, making them a promising screening set as highly selective compounds for future targets [51,52]. Thus, natural products represent a promising subset of the chemical space, that has been guiding drug discovery in the past and is likely to continue to do so in the future.

In **section 3** the natural product PXA, which was extracted from the endophytic fungus *Phomopsis longicolla*, is discussed [53]. The compound exhibits promising activity against solid and humoral tumors; however, its molecular mechanism of action is not fully understood [53-55]. To gain further knowledge about how the compound elicits its apoptotic effect, in **section 3.2** (**Publication II**) a computational study is presented, in which the potential of PXA as a protonophoric decoupler of the mitochondrial membrane potential is explored.

1.2 Drugs that modulate protein-protein interactions

Non-covalent associations of proteins, known as protein-protein interactions (PPI), are fundamental to a multitude of physiological processes. Many signaling pathways and regulatory processes in the cell depend on the formation of protein-protein complexes [56,57]. Being essential to the regulation of the cellular function, PPIs are also involved in various diseases involving various types of cancer [58-60]. Thus, in the past decade increasing efforts were undertaken to target PPIs. The development of drug-like molecules that can inhibit a PPI is considered a challenging task, though. This is mainly due to the distinct structural characteristics that set protein-protein interfaces apart from "classical" drug binding sites [56,57,61].

Unlike classical receptor-ligand interactions, which typically take place in a moderately sized (less than 1,000 Å^2) and well-defined binding cavity, PPI interfaces tend to be larger and relatively shallow (1,000 – 3,000 Å^2 or even larger) [56,57,62,63]. Thus, when designing a small-molecule PPI modulator, a challenge is to form enough interactions such that the ligand's binding free energy ($\Delta G_{bind.}$) is competitive with the $\Delta G_{bind.}$ of the interacting proteins [57]. Key to making this possible at all was the finding that the binding affinity between the interaction

partners in not distributed evenly across the interaction interface. Rather, few residues (known as hot spots) contribute the bulk part of the $\Delta G_{bind.}$ [64-66]. Typically, such a hotspot is defined by a change in binding energy of $\Delta\Delta G_{bind.} \geq 2$ kcal mol^{-1} upon mutation to alanine, and are enriched in tryptophane, tyrosine, and arginine, while leucine, serine, and valine are disfavored [67]. This demonstrates that PPIs do not rely purely on hydrophobic contacts, opening the possibility for the development of selective small molecule inhibitors.

1.3 The heat shock protein of 90 kDa

This chapter is in most parts taken from **P**ublication I (see page 71):

C-terminal modulators of heat shock protein of 90 kDa (HSP90): State of development and modes of action

Bickel, D. [a], and Gohlke, H. [a,b]

[a] Institute for Pharmaceutical and Medicinal Chemistry, Heinrich Heine University Düsseldorf, Düsseldorf, Germany

[b] John von Neumann Institute for Computing (NIC), Jülich Supercomputing Centre (JSC), Institute of Biological Information Processing (IBI-7: Structural Biochemistry) & Institute of Bio- and Geosciences (IBG-4: Bioinformatics), Forschungszentrum Jülich GmbH, Jülich, Germany

To survive cells must cope with challenging environmental conditions [68,69]. In the 1960's RITOSSA first observed an overexpression of certain genes in *Drosophila melanogaster* after exposure to elevated temperatures [70,71]. This observed response to heat stress (heat shock response, HSR) includes the synthesis of highly conserved proteins, called heat shock proteins (HSPs) [72-74]. These HSPs assist cells in maintaining their living function in the presence of proteotoxic stressors (e.g., hyperthermia, heavy metals, acidosis, and hypoxia) [75,76]. Thus, HSPs were mostly recognized as a family of molecular chaperones [77,78]. However, they were also found to be involved in a wide variety of cellular functions under normal conditions, including the promotion of proper protein folding [78,79], signal transduction [80-83], and cellular translocation processes [84,85]. The heat shock proteins are a structurally very diverse set of proteins [73,74,86]. Based on their molecular weights they are categorized into six families: small HSPs, HSP40, HSP60, HSP70, HSP90, and large HSPs [86,87].

The heat shock protein of 90 kDa (HSP90) is the most abundant of the HSPs, constituting 1-2% of the total cellular protein, which is increased to 3-5% upon exposure to external stressors [88,89]. In eukaryotes, it forms the heart of a complex machinery involving multiple cofactors and cochaperones [90,91]. This "modular design" enables the HSP90 chaperoning complex to interact with a wide variety of client proteins along important cellular signaling pathways, such as steroid hormone receptors or protein kinases [81].

1.3.1 Structure of HSP90 and function

In the cell, HSP90 exists as a homodimer [92,93]. Each monomer consists of three domains: a N-terminal domain (NTD), followed by a middle (MiD) and C-terminal domain (CTD) (Figure 2A) [94]. The NTD is the main ATPase domain of HSP90 and belongs to the GHKL superfamily; it shares high structural similarity to histidine kinases, gyrases, and topoisomerases (Figure 2B) [95,96]. A highly charged linker region that varies in length and composition between species and isoforms connects it to the MiD [97-99], which appears to play an important role in the ATP hydrolysis and client recognition [99,100]. The C-terminal domain forms the main dimerization interface of HSP90 (Figure 2C) [101,102]. The C-terminus also contains the MEEVD motif, which is an important interaction site for a subset of co-chaperons containing tetratricopeptide repeat (TPR) domains [103].

During the chaperone cycle, periodically transient interactions occur via the respective N- and C-terminal domains of the dimer [104]. The two monomers thus interact in a flexible clamp-like way (Figure 3). The opening and closing are associated to the hydrolysis of ATP and occurs at slow time scales of 0.1 ATP min^{-1} in humans [90,105].
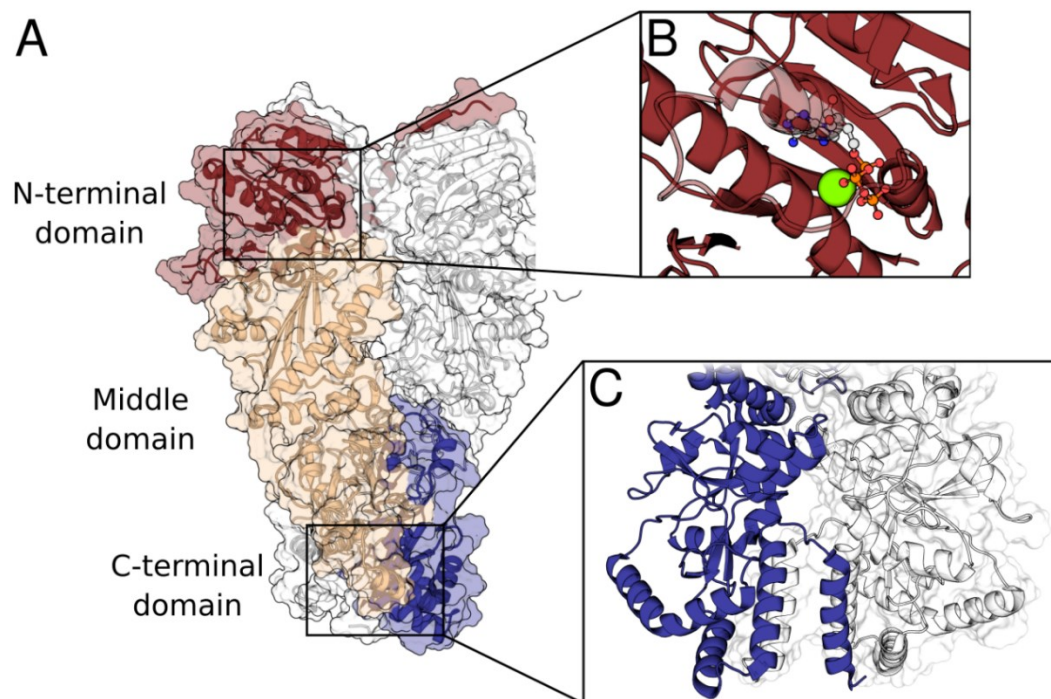
Figure 2. Surface representation of human HSP90β as resolved from cryo-electron microscopy (PDB ID: 5fwk). A. For monomer A the N-terminal domain is represented in red, the middle domain in beige, and the C-terminal domain in blue. The monomer B is shown in light grey. The charged linker region and the C-terminal fragment that interacts with TPR domains are not resolved, and therefore not shown in the graphic. **B.** Blow-up of the ATP binding site in the N-terminal domain with bound Mg^{2+}-ATP. **C.** Blow-up of the C-terminal domains of monomer A (blue) and monomer B (light). The helix-bundle in the center formed by the C-terminal helices 4, 4', 5, and 5'constitutes the primary dimerization interface in the C-terminal domain.

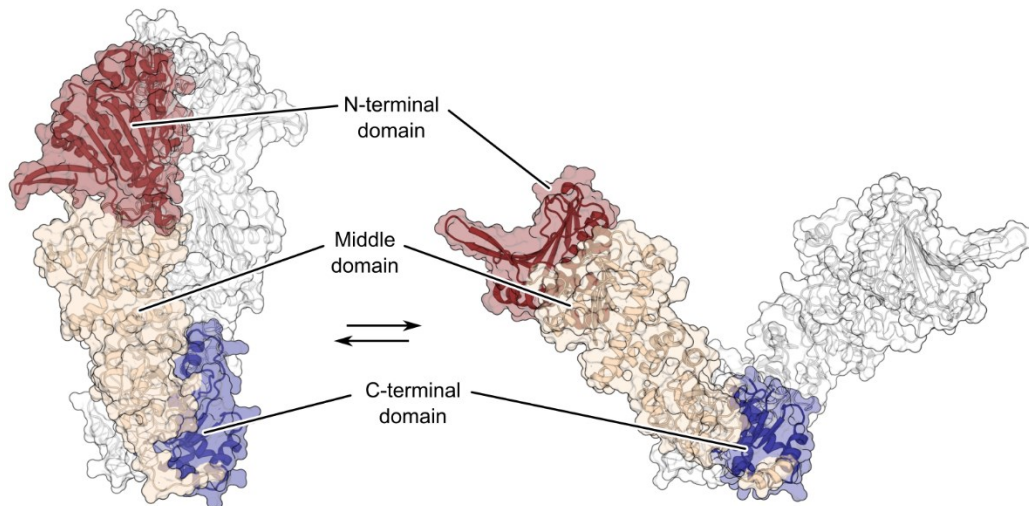**Figure 3. Opening and closing of *E. coli* HSP90-orthologue.** The *E. coli* orthologue of HSP90, high temperature protein G (HtpG), in its closed (PDB ID: 2iop) and open (PDB ID: 2ioq) conformation. The N-terminal domain is represented in red, the middle domain in beige, and the C-terminal domain in blue.

1.3.2 HSP90 isoforms

Higher eucaryotes generally have two cytoplasmic isoforms of HSP90: HSP90α which is inducible by heat stress, and HSP90β which is constitutively expressed. In addition, there are HSP90 homologues present in the mitochondria, chloroplasts, and endoplasmic reticula (ER). In humans these would be the tumor necrosis factor receptor-associated protein 1 (TRAP1) in mitochondria, and glucose-regulated protein 94 (GRP94) in the ER [88,106]. All isoforms share a conserved structure, consisting of a N-terminal ATPase domain, the MiD and the CTD. However, TRAP1 is lacking the charged linker region between NTD and MiD; and both GRP94 and TRAP1 are missing the C-terminal MEEVD motif [107]. The two major cytoplasmic isoforms have a sequence identity of 86% [108], yet vary in their expression. HSP90β is constitutively expressed at higher levels than HSP90α [88,106]. The expression of HSP90α is highly stress-inducible, though [88,106]. Differences in regulation as well as isoform specificity observed for some client proteins and co-chaperones suggest distinct cellular function between the two isoforms [109-112]. Despite this fact, most of the functional assays are performed on cytoplasmic HSP90 (i.e., mixtures of HSP90 α and β). Therefore, except for a few cases, there is no information on isoform selectivity.

In this thesis, I will focus entirely on the cytoplasmic HSP90 isoforms in humans. So, HSP90 in general refers to the cytosolic isoforms, while HSP90α and HSP90β will only be used, when isoform specific experiments were performed.

1.3.3 HSP90 in cancer

While basal levels of HSP90 are needed for maintaining protein homeostasis under physiological conditions, the HSP90 machinery can be exploited by cancer cells to cope with proteotoxic stressors, such as a high mutation burden, hypoxia, and acidosis that are frequently found in the tumor microenvironment [113-115]. Accordingly, elevated levels of HSP90 are observed in various types of malignancies [114,116,117], and correlate with poor prognosis in breast cancer [118,119], gastric cancer [120], and acute myeloid leukemia [121]. However, HSP90 is not frequently found as a driver of cancerous transformation and aberrant proliferation, but as enabling factor for a subset of the hallmarks of cancer [14,114,115,122]. For instance, the secretion of HSP90α into the extracellular space was shown to promote tumor invasiveness [123,124]. Consequently, the last decades have seen increasing efforts to develop drug-like HSP90 inhibitors for clinical use.

1.3.4 N-terminal inhibitors of HSP90

In 1994, the ansamycin antibiotic geldanamycin (**1**, Figure 4) was reported to elicit antiproliferative effects by inhibiting HSP90, which subsequently led to depletion of tyrosine kinases and cell death in cancer cell lines [125,126]. In the following years, the natural product radicicol (**2**, Figure 4) was shown to have the same effect but higher potency [127,128]. Both compounds bind to the ATP binding site in the N-terminal domain of HSP90 [129,130]. Subsequent structure-activity relationship (SAR) studies in concert with the resolution of co-crystal structures of ADP [95], geldanamycin [130], and radicicol [129] with HSP90 led to the development of a set of drug candidates with improved pharmacodynamic and pharmacokinetic properties compared to the original natural products. For geldanamycin, particularly the semi-synthetic modification of the 17-methoxy group was found to lead to active compounds with reduced toxicity with respect to the natural compound [131-133], leading to the four ansamycins that entered clinical trials so far (https://clinicaltrials.gov, accessed February 2019) (Figure 4).

Structure-based drug design, based on the unconventional conformation that ATP adopts in GHKL-ATP binding sites, has furthermore led to the development of fully synthetic purine analogues as inhibitors of HSP90 ATPase activity [134-137], which could be administered orally [134,136,138]. Of these, six entered clinical trials (Figure 4). In a high throughput screening against yeast HSP90 ATPase activity, the substituted resorcinols were found to inhibit HSP90, of which five entered clinical trials in the following years (Figure 4) [139-142]. Finally, a rather diverse class of HSP90 inhibitors entered clinical trials, where all compounds feature a substituted benzamide substructure (Figure 4). All compounds share a similar binding mode in the ATP binding site [143-145].
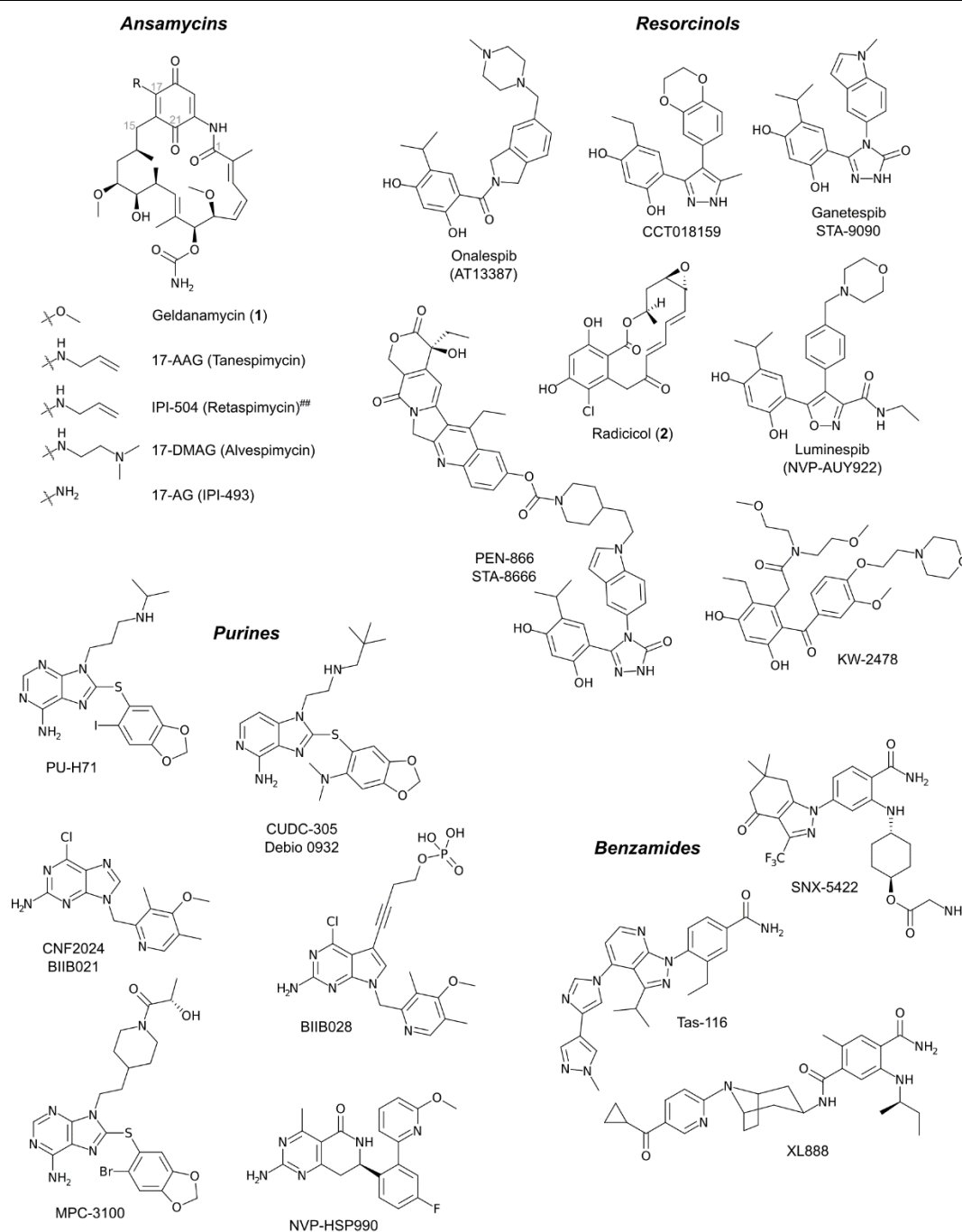
Figure 4. N-terminal HSP90 inhibitors that entered clinical trials. For the natural compound-derived classes, we also show their predecessors (**1**, **2**). Ansamycins: Four compounds derived from geldanamycin (**1**) entered clinical trials so far ([##] the quinone moiety in retaspimycin is reduced to a dihydroquinone moiety). Resorcinols: Five structurally distinct resorcinols derived from radicicol (**2**) entered clinical trials. The compound PEN-866 is a special case because it is a drug conjugate of the HSP90 inhibitor STA-9090 and an irinotecan metabolite that inhibits topoisomerase I. Purines: Six purine and purine analogues entered clinical trials. These compounds share similar binding modes mimicking the bend conformation of ATP in the N-terminal ATP binding site. Benzamides: Three compounds entered clinical trials. Despite their structural diversity, they exhibit similar binding modes with a conserved placement of the benzamide motif in the ATP binding site.

In summary, 19 structurally distinct HSP90 inhibitors that exert their activity by targeting the N-terminal HSP90 binding site have entered in clinical trials (https://clinicaltrials.gov, accessed February 2019) (Figure 4). Altogether, none of the classical HSP90 inhibitors was approved by the FDA for therapeutic use yet. One reason is the induction of the heat shock response (HSR), a well-known side effect of this class of inhibitors [114,146-151], which was already described for geldanamycin. According to a current model of HSR mechanism, the binding of N-terminal HSP90 inhibitors releases heat shock factor-1 (HSF-1) [152,153]. The transcription factor becomes phosphorylated, trimerizes, and translocates to the nucleus, leading to overexpression of multiple heat shock proteins, including HSP70, HSP40, and HSP27 [76,154]. As HSR is a pro-survival mechanism, it can be detrimental in an anti-cancer therapy [114,155,156]. In addition, other severe adverse effects, such as hepatotoxicity found for ansamycins [133,157-159] and ocular toxicity [150,157,160], have been hampering the clinical success of HSP90 inhibitors until now.

1.3.5 Non-N-terminal inhibitors of HSP90

In the meantime, many groups have started investigating alternative strategies to inhibit HSP90 without inducing HSR and/or ocular toxicity. The first compound to reach this goal was the coumarin antibiotic novobiocin, an inhibitor binding to the CTD of HSP90 (Figure 5) [161,162]. A first phase I clinical trial of a C-terminal HSP90 inhibitor (RTA 901) has been performed on non-cancer patients (https://clinicaltrials.gov, identifier: NCT02666963). This compound has been reported to be based on novobiocin [147], although the structure has not been released yet. Similar to the molecular origins of N-terminal inhibitors, many of the non-N-terminal inhibitors are natural products. In the context of this introduction, only a quick overview of the classes and different modes of action shall be given. For a more in-depth discussion of these inhibitors, please refer to the original publication (see page 71).

One of the primary molecular modes of action, proposed for various C-terminal HSP90 inhibitors, is the binding to the C-terminal ATP binding site. It was discovered when investigating novobiocin (3, Figure 4), previously shown to interfere with nucleotide binding in bacterial gyrase B. Yet, in HSP90, no binding to the NTD was observed, and pull-down assays suggested a binding mode different from geldanamycin [161,162]. Further studies revealed a second ATP binding site in the CTD [162-164]. This binding site is only accessible when the N-terminal ATP binding site is occupied [163]. Furthermore, the C-terminal binding site is able to bind purine as well as pyrimidine nucleotides, while the NTD is rather specific for adenine [165]. Up to this point, there is no experimentally validated crystal structure of a compound binding to this binding site. Yet, there have been several approaches to predict the C-terminal ATP
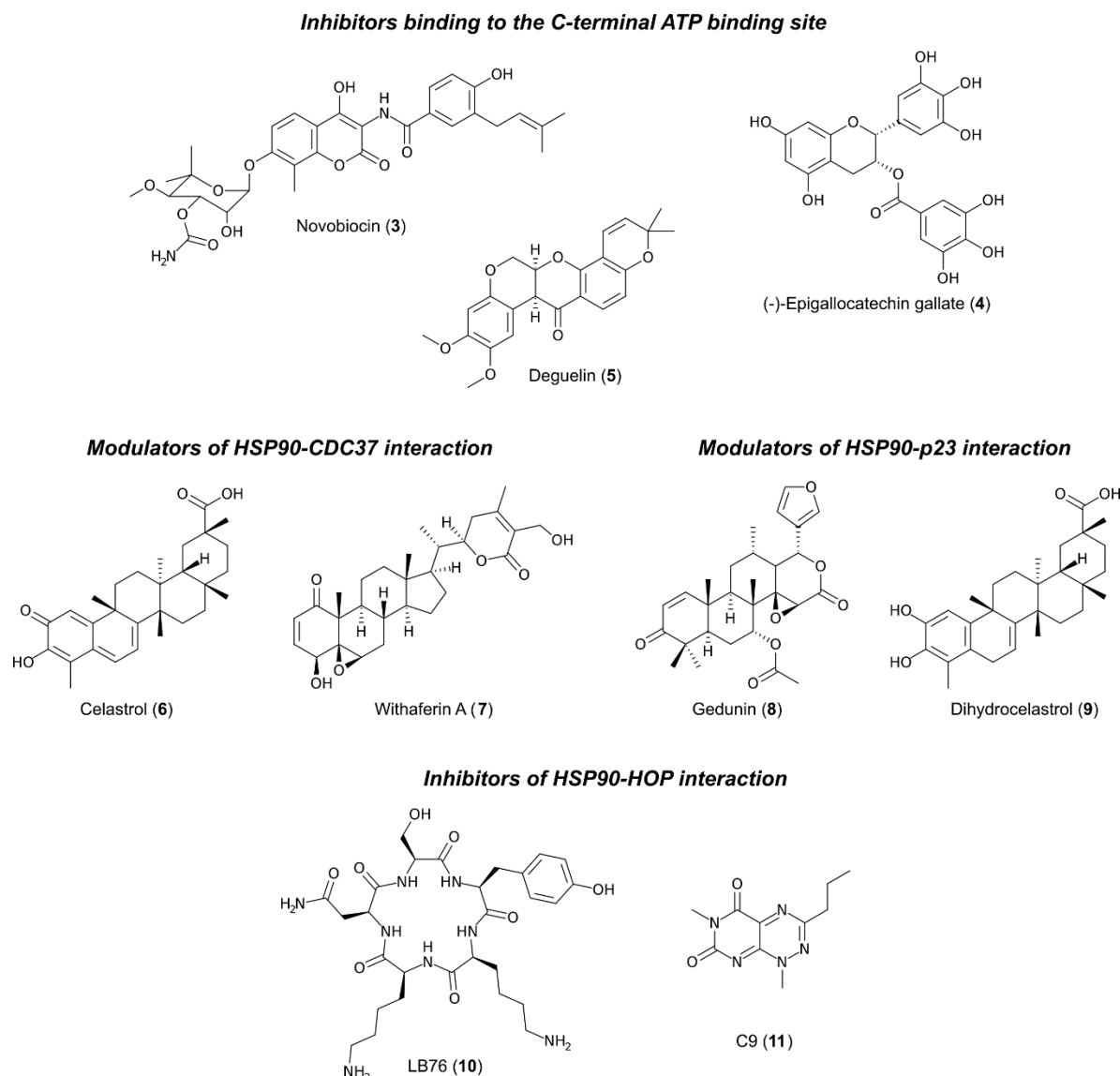
Figure 5. Non-N-terminal inhibitors of HSP90. On top, selected inhibitors the are proposed to bind to the C-terminal ATP binding site of HSP90 are depicted: novobiocin (**3**), (-)-epigallocatechin gallate (**4**), and deguelin (**5**). Below on the left side, two modulators of the HSP90-CDC37 interaction are depicted: celastrol (**6**) and withaferin A (**7**). On the right gedunin (**8**) and dihydrocelastrol (**9**) are depicted as modulators of the HSP90-p23 interaction. On the bottom modulators of the interactions mediated by the C-terminal MEEVD motif are depicted: LB76 (**10**) and C9 (**11**).

binding site using molecular modelling (Figure 6) [166-169]. Further compounds which are described to be binding to that binding site, are the catechin (-)-epigallocatechin-3-gallate (**4**, Figure 5) [170-172], and deguelin (**5**, Figure 5) [173,174] as well as derived compounds.

Other compounds were proposed to modulate the interaction between HSP90 and the cell division cycle 37 protein (CDC37). The latter is a co-chaperone primarily associated with the chaperoning of protein kinases and is essential for the stabilization of HSP90-kinase complexes [109,175]. CDC37 interacts with HSP90 via a large interaction surface, wrapping itself around the
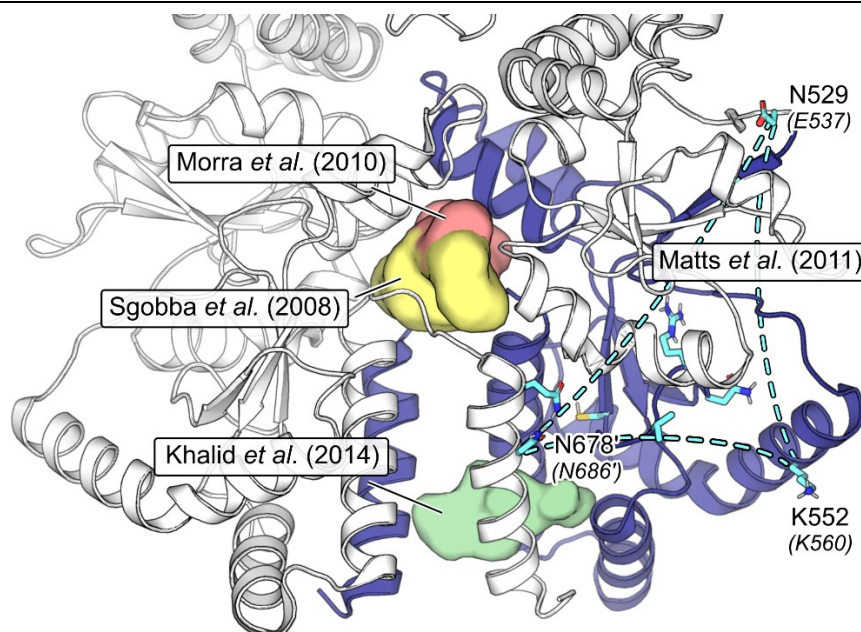
Figure 6. Overview over approaches to identify the C-terminal ATP binding site in HSP. The results were mapped on the structure of human HSP90β. Corresponding residue numbers in human HSP90α are given in brackets. The part of the C-terminal domain that was shown by Marcu et al. to contain the ATP-binding motif is colored in blue [162]. Sgobba et al. performed molecular simulations on a homology model of human HSP90α and used binding site prediction tools to predict the C-terminal ATP binding site [169]. Morra et al. used molecular dynamics simulations and signal propagation analysis to identify allosteric binding sites on the structure of yeast HSP90 and molecular docking to obtain binding poses of novobiocin and analogues [168]. Matts et al. used an azide-analogue of novobiocin as a probe to identify the C-terminal ATP binding site. They found that this probe binds covalently to K560 (HSP90α) and built an putative open-conformation HSP90 model based on SAXS data that showed direct interactions of novobiocin with K560, E537, and N686 [167]. Khalid et al. used webserver-based tools to predict the C-terminal HSP90 binding site [166].

NTD and middle domain [99], which prevents the hydrolysis of ATP [176]. CDC37 knockout was shown to sensitize HSP90 for other inhibitors [177,178]. Thus, inhibiting the interaction between HSP90 and CDC37 might lead to kinase-specific HSP90 inhibitors and could provide a synergistic approach for combination with other inhibitors. Compounds belonging to this category are the triterpenoid celastrol (**6**, Figure 5) [179,180] and the steroidal lactone Withaferin A (**7**, Figure 5) [181].

The small acidic protein p23 interacts with HSP90 via the NTD and MiD. This interaction halts the HSP90 ATPase cycle and appears to facilitate HSP90 binding to client proteins [182]. While not essential for the maturation of HSP90 kinase clients, such as Cdk4 and Akt, p23 is necessary for the stabilization of steroid hormone receptors. The compounds gedunin (**8**, Figure 5) and dihydrocelastrol (**9**, Figure 5) have been shown to disrupt the interaction between HSP90 and its co-chaperone p23 [183]. Even though it was shown that gedunin binds to p23, the disruption of

this interaction halts the HSP90 machinery, leading to typical effects of HSP90 inhibitors, like the degradation of steroid hormone receptors [183].

The HSP90 C-terminal domain ends in a most likely unstructured loop that contains the highly conserved MEEVD motif [184]. This motif forms the key interaction with tetratricopeptide repeat domains, which are present in various HSP90 co-chaperones [90]. One of these is the HSP70/HSP90-organizing protein (HOP), which mediates the interaction between the HSP70-HSP40 complex and HSP90 [185]. HOP contains three TPR domains, of which the domains TPR2A and TPR2B bind to the MEEVD motifs in HSP90 and HSP70, respectively [186]. Based on the fungal depsipetide Sansalvamide A, McAlpine and co-workers developed LB76 (**10**, Figure 5) which blocks interactions between HSP90 and TPR domain-containing co-chaperones [187-190]. A second compound, C9 (**11**, Figure 5) binds to the TPR2A domain of HOP preventing the interaction with HSP90 on the co-chaperone site [191,192].

1.3.6 Conclusion

HSP90 has been a major target for drug discovery in academia and pharmaceutical industry for several decades, and many inhibitors have been published and patented. Most of these inhibitors target the N-terminal ATP binding site, and – except for RTA 901 – only compounds of this class have undergone clinical trials so far. However, a major drawback of this compound class is the induction of pro-survival HSR, which limits the compounds' efficacy and/or may lead to adverse effects. Inhibiting HSP90 via allosteric binding sites, including the secondary ATP binding site in the CTD, or inhibiting PPIs between HSP90 monomers, or between HSP90 and other interacting proteins essential for the function of the HSP90 machinery, are notable alternatives. Novobiocin was the first compound reported to inhibit HSP90 by an alternative mechanism, and by now a wide variety of compounds have been shown to elicit HSP90 inhibitory effects that way. Many of these newly identified compounds are natural products that show activity in the micromolar range. However, as a result of the complexity of the HSP90 machinery, only few details are known about the molecular mode of action of these compounds.

For the further development and optimization of these compounds, understanding the molecular mechanism behind their inhibitory effect will be essential. For many of the compounds, the inhibition of interactions between HSP90 and co-chaperones are assumed to be the mode of action. However, it is often not clear whether these compounds bind to HSP90 or to the respective co-chaperone. Furthermore, due to the flexible nature of HSP90, ligands could bind allosterically to the protein, thereby disrupting the co-chaperone interaction by imposing a certain conformation on HSP90 without binding to the protein-protein interface itself.

Resolving complex structures of HSP90 and the ligands would be the optimal way to obtain structural information about the binding of such inhibitors. Alternatively, molecular modeling techniques such as molecular docking and molecular dynamics simulations of free ligand diffusion can provide valuable insights.

However, only few approaches have been presented, where structure-based *de novo* design was applied to specifically induce particular effects on the HSP90 machinery. In **section 4.1**, I will discuss one such approach which lead to the development of aminoxyrone, a peptidomimetic inhibitor of the C-terminal dimerization of HSP90 [193]. This further led to the development of a small molecule compound, LSK82, which is then further characterized with respect to its binding properties towards HSP90 in **section 4.2** (**Publication III**).

1.4 The RUNX1-ETO fusion protein

The t(8;21) translocation is one of the most frequent chromosomal alterations found in acute myeloid leukemia (AML) [194]. It results in the RUNX1-ETO fusion protein which then suppresses the hematopoietic differentiation mediated by native RUNX1, leading to a pre-leukemic condition [195,196]. In the following sections, the structural characteristics of the RUNX1-ETO fusion protein as well as its role in the emergence of leukemia will be discussed.

1.4.1 Structure of the RUNX1-ETO fusion protein

The t(8;21)(q22;q22) translocation fuses the *RUNX1* gene (Runt-related transcription factor-1, also referred to as *AML1*) on chromosome 21 and the *ETO* gene (eight twenty-one, also referred to as myeloid translocation gene on 8 (*MTG8*), or *RUNX1T1*) on chromosome 8. In *RUNX1* the breakpoints cluster in intron 5, while for *ETO* two breakpoint cluster regions in the introns 1a and 1b are described (Figure 7) [197-199]. Regardless of the location of the breakpoints, they lead to the same gene transcript [200]. The translated fusion protein contains 177 N-terminal residues of RUNX1 and 575 residues of ETO [197].

Wild-type RUNX1 is a transcription factor in the core binding factor α protein family. It is involved in cell cycle regulation and was found to be essential for hematopoietic differentiation [196,201,202]. The protein contains a conserved DNA binding Runt homology domain (RHD, named after *Drosophila* Runt protein). The RHD specifically recognizes 5'-YGPYGGTY-3' (where Y is C or T) [201,202]. Inhibitory domains N- and C-terminal of the RHD prevent direct DNA interactions in the apo state though [203,204]. To restore DNA binding RUNX1 requires the formation of a heterodimer with the non-DNA binding core binding factor β (CBF) [203-206]. In addition to the RHD, RUNX1 contains a transactivation domain, a matrix attachment signal, and an inhibitory domains [202]. However, only the N-terminal RHD is transferred to the fusion protein, while the functionalities of the remaining domains are replaced by ETO [195].

The ETO protein has been discovered as the fusion partner of RUNX1 in t(8;21) translocation [198]. It is mainly responsible for the gene-repressive activity of RUNX1-ETO, by recruiting transcriptional repressor proteins, like mSin3A, a silencing mediator for retinoid and thyroid hormone receptor (SMRT), nuclear receptor co-repressor (NCOR), and histone deacetylases (HDACs) 1-3 [207-209]. It contains three proline/serine/threonine-rich regions and four highly conserved nervy homology domains (NHR1 to NHR4, named for homology to *Drosophila* nervy protein) [197,209]. In particular, the NHR2 domain (Figure 8) was shown to contribute many of the biochemical properties of ETO. It mediates PPIs with co-repressors as well as homo-
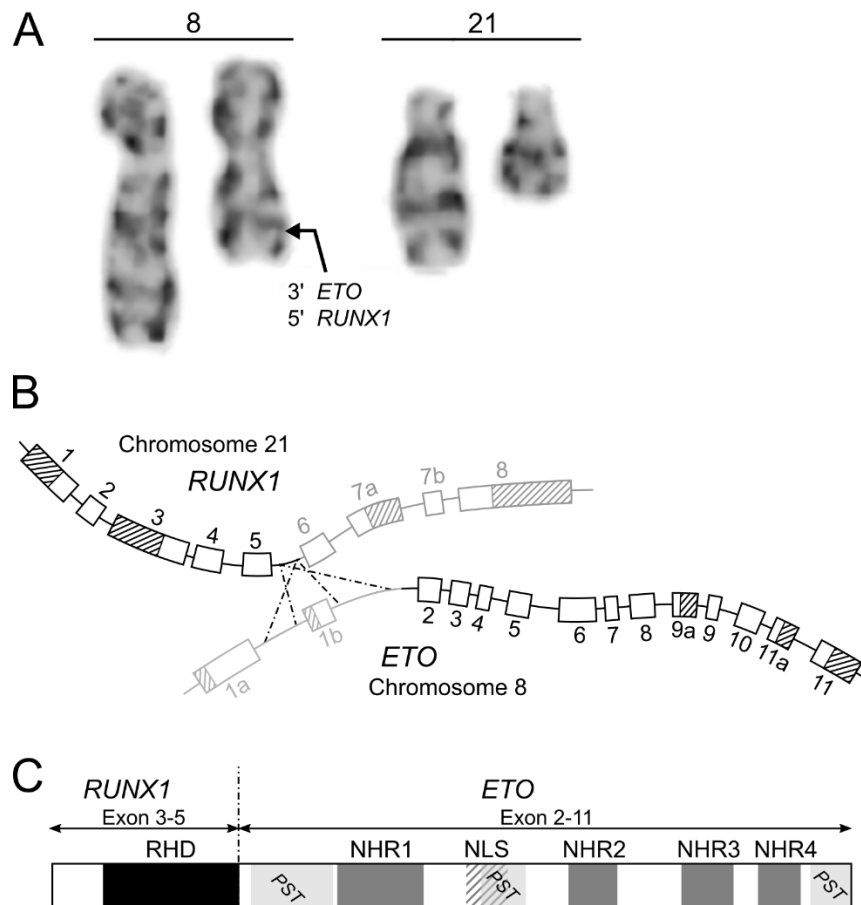
Figure 7. The t(8;21)(q22;q22) translocation. A. Partial karyotype of t(8;21)(q22;q22) showing chromosome pairs 8 and 21. The derivative chromosomes are on the left in each pair. The position of the *RUNX1-ETO* fusion gene is indicated by a black arrow. **B.** Schematic representation of the genomic structure of t(8;21). Translated and untranslated sequences of the exons are represented by white and shaded boxes, respectively. The breakpoint cluster regions are denoted by crossing lines. Thus, the fusion gene may include the *ETO* exon 1b. Still, all breakpoints result in the same gene transcript as exon 1b does not contain a splice acceptor site. **C.** Schematic representation of full-length RUNX1-ETO with the DNA-binding Runt homology domain (RHD), and the nervy homology domains (NHR) 1-4. PST indicates the proline/serine/threonine-rich regions [197]. Overlapping with second PST is the nuclear localization signal (NLS) [210]. (A. taken from *Atlas of Hematological Cytology*. Masaryk University, University Hospital Brno, http://www.leukemia-cell.org/atlas; B and C. adapted from Refs [195,200])

oligomerization [211,212]. This oligomerization was shown to be crucial for the malignant transformation [213-215].

Next to full-length RUNX1-ETO described above, alternative splicing can lead to two further gene transcripts. The exons 9a and 11a in the *ETO* part of the gene provide stop codons, leading to the C-terminally truncated isoforms RUNX1-ETO [216,217]. The *RUNX1-ETO9a* transcript is lacking the NHR3 and NHR4 domain and was shown to have reduced repressive activity on the translational gene activation mediated by RUNX1 than the full-length fusion protein. However,
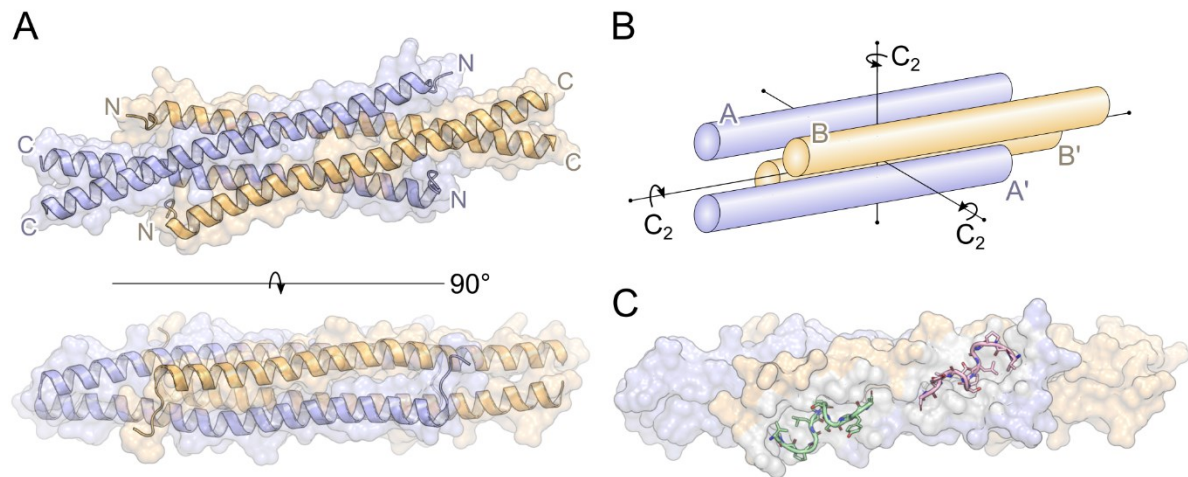
Figure 8. The NHR2 domain forms a homo-tetramer complex. A. The NHR2 domain consists of an amphiphilic α-helix (PDB ID: 1wq6). Two of the helices associate to form an anti-parallel dimer (A/B), which can further associate with another dimer to form the tetramer (A/B//A'/B'). Parallel helices (e.g., A/A') of the dimers are depicted in matching colors. On top the dimer-interface (A/B) is shown in plane, with the opposing dimer below (A'/B'). On the bottom, the tetramer-interface (B/A') is depicted. **B.** Schematic representation of the NHR2 domain as a dimer of dimers. The composition of this homo-tetramer leads to a highly symmetric complex. For any binding epitope formed by two anti-parallel helices (A$^{(')}$/B$^{(')}$), three congruent epitopes exist. The congruent binding epitopes can be transformed into one another through rotation around three orthogonal C_2 axes. **C.** The tetrameric NHR2 interacting with two identical fragments of transcription factor 12 (green and pink) (PDB ID: 4ojl). The interface lies on the surface formed by A/B'. Thus, tetramer formation is required for the interaction interface to form. Two more identical interface would be available on the opposing side of the complex (A'/B).

mice transfected with the *RUNX1-ETO9a* showed rapid development of leukemia, in fact stronger than for the fusion protein. [218] The transcript of *RUNX1-ETO11a* only lacks the NHR4 domain. It was shown as well to exhibit a lower repressive activity against native RUNX1 gene transactivation [217]. Though both isoforms were found in patient samples with RUNX1-ETO-positive leukemia, their influence on the onset and progression of leukemia in humans remains unclear [195,219].

1.4.2 *RUNX1-ETO fusion protein in leukemogenesis*

The role of RUNX1-ETO in the emergence of leukemia is not fully understood. There are a variety of different mechanisms discussed. The most prevalent one is the suppression of the function of wild-type RUNX1 [200]. Physiologically, RUNX1 acts as key regulator of hematopoietic differentiation. After association with CBFβ it binds to DNA through the RHD and activates its target genes [203]. As RUNX1-ETO inherits the DNA-binding RHD from RUNX1 the two proteins share 60-80% of their binding sites [195]. Thus, a first proposed mechanism of action for the fusion protein was that it represses transactivation of RUNX1 target genes by the co-repressors recruited by the ETO domains [208,220]. However, RUNX1-ETO does

not always act as a transcription repressor but can occasionally induce transcription of target genes through epigenetic mechanisms [221]. Also, studies showed that in patients with RUNX1-ETO-positive leukemia no inactivating mutations occur in the native *RUNX1* gene [222]. This hints towards, that the cancer cells still depend on the function of wild-type RUNX1 and thus, the relationship between RUNX1 and RUNX1-ETO is likely more complex than initially assumed [195,223].

Still, the epigenetic alterations induced by co-repressors recruited by the ETO part of the fusion protein appear to be pivotal in the leukemogenesis [224]. The recruitment of co-repressors is mostly mediated *via* the NHR1 and NHR2 domain [195,208,209,225]. The NHR2 domain, which mediates the homo-oligomerization, was shown to represent an important interface for PPIs (Figure 8C) [211]. Several groups found that abrogation of the associations mediated by NHR2 lead to reduction in the leukemic phenotypes [213-215].

1.4.3 Therapeutic strategies

Among AML, the t(8;21) leukemia is considered a rather favorable subtype, due to its low rate of primary drug resistance and increased overall survival [226,227]. The current therapeutic intervention consists in anthracycline- and cytarabine-based induction chemotherapy. This leads to complete remission in ~90% of the patients [228]. Half of the patients will experience relapses though within 36 months [229], and the median overall survival is less than five years [230]. Post-remission high dose cytarabine treatment was shown to increase the disease-free and overall survival. However, the continued chemotherapeutic cycles are associated with considerable toxicities. Thus, older patients and patients with compromised health status may not tolerate the intensive treatment [228].

Targeted therapeutics, with a decreased overall toxicity would present a promising treatment approach for t(8;21) leukemia. A first approach in this direction is gemtuzumab ozogamizin, an antibody directed against the CD33 antigen and coupled to the cytotoxic calicheamicin. In 2000, drug was given accelerated approval by the FDA for patients > 60 years, who were not eligible for standard chemotherapy. After a preliminary withdrawal from the market in 2010 [231], the drug was re-approved by the FDA and approved by the EMA. The admission is as an addition to the established anthracycline- and cytarabine-based induction chemotherapy, though, as gemtuzumab ozogamizin could not replace it.

1.4.4 Conclusion

As the t(8;21) leukemia is dependent on the RUNX1-ETO, the fusion protein would represent a prime target for a targeted therapy approach. This would limit any drug effects to the cancer

cells, reducing the toxic side effects on other cells. The RUNX1-ETO fusion protein acts principally as a repressor of wild-type RUNX1 with which it shares the DNA-binding RHD. Thus, inhibiting DNA-binding through the RHD would likely cause off-target effects on wild-type RUNX1. However, the transforming ability of RUNX1-ETO was shown to depend on the oligomerization of the NHR2 domain of ETO. Thus, disrupting the protein interactions formed by the ETO part of the fusion protein, or interfere with the NHR2-mediated homo-tetramerization appears to be a viable approach.

In **section 5**, I will discuss 7.44, a compound that was specifically designed to interfere with the oligomerization of the NHR2 domain of RUNX1-ETO. The associated **Publication IV** aims to further characterize the biophysical properties of 7.44 on the NHR2 domain. In supporting simulation studies, we could identify preferred binding epitopes of the compound in the tetramer. Furthermore, in **section 6**, a virtual screening approach and molecular dynamics simulations will be presented, which lead to analogues of 7.44 with stronger antiproliferative properties than the original compound.

1.5 Scope of the thesis

Throughout the previous chapters the importance of the development of novel compounds to treat cancer was demonstrated. We explored two approaches, how structures already present in nature can be used to guide the drug design. In **section 1.1** we discussed, how natural compounds can serve as leads in drug design. In **section 1.2** we explored how protein-protein interaction modulators can serve as anti-cancer drugs, and how the structures of the protein-protein interface can serve as a template for the design of small molecule inhibitors. Furthermore, we introduced two potential molecular targets in cancer therapy. In **section 1.3** HSP90 was presented as a promotor of cell survival and facilitator of genetic alterations in a variety of tumors, thus representing a promising target in pan-cancer therapy. In contrast, in **section 1.4** the RUNX1-ETO fusion protein was presented, which is specifically associated with a single type of AML induced by the t(8;21) translocation.

This thesis aims to explore novel approaches to overcome drug resistance in cancer. To this end, computational methods in the field of molecular simulations are employed to provide insights in the mechanism of action of the investigated compounds on the molecular level.

In the past, the development of anti-cancer drugs has benefitted enormously from natural product leads (**section 1.1**). A potential future lead, phomoxanthone A (PXA), was shown to selectively induce apoptosis in cancer cells. In **Publication II** the efficacy of PXA on cisplatin resistant solid tumors was assessed. We further hypothesized, that the apoptotic effect of PXA might in part be elicited by the decoupling of the proton gradient of the inner mitochondrial membrane (IMM). To check this hypothesis, the energy barrier for different protonation states of PXA is computed by umbrella sampling simulations (**section 2.2**). The calculations revealed significant differences in the membrane partition of the PXA protomers. Overall, the energy barriers suggest, that at least two of the investigated protonation states of PXA can permeate through the membrane at biological relevant time scales. Though this does not explain the full spectrum of effects PXA elicits in cells, it corroborates a first hypothesis on the action of PXA on the mitochondrial membrane.

In the past decades, there has been an increased interest in the rational design of compounds that target protein-protein interactions (PPIs) (**section 1.2**). PPIs are pivotal to many physiological and pathophysiological cellular processes, including malignant transformation and cancer. A popular anti-cancer target is the heat shock protein 90 (HSP90) which is involved in a multitude of cellular signaling pathways and represents a hub for PPIs (**section 1.3**). Thus, inhibitors of HSP90 have the potential to elicit anti-proliferative and anti-invasive effects in a

wide variety of cancers. Based on prior studies providing a proof of concept, in **Publication III**, LSK82 is presented as a first-of-class small molecule inhibitor of HSP90. We performed large-scale ligand diffusion simulations with LSK82 diffusing around HSP90α and HSP90β. These simulations suggest a preferred binding to the C-terminal dimerization interface of HSP90. Moreover, for both isoforms very similar distributions were obtained, suggesting that the novel compound does not exhibit specificity for either isoform over the other.

In contrast to HSP90, which promotes proliferation in many cancers but is not intrinsically oncogenic, some cancer types are directly linked to a single genomic alteration and the associated gene transcripts. Such a case is the t(8;21) AML, whose etiology is directly associated with the RUNX1-ETO fusion protein (**section 1.4**). Essential to the transformative function of the fusion protein is the NHR2 domain in the ETO part. By self-oligomerization, this domain forms an interaction interface for transcriptional co-repressors, which alter the transcription profile of the affected cell. Interfering with this self-organization would provide a novel way to interfere with t(8;21)-related cancer genesis. With the compound 7.44 a first inhibitor of the oligomerization of the NHR2 domain was identified. In **Publication IV** we subjected this inhibitor to biophysical and simulation studies. By free ligand diffusion simulations, preferred binding epitopes on the NHR2 tetramer as well as a preferred binding mode for the encounter of 7.44 with the NHR2 tetramer is identified. This provided first insights on the molecular level into the specific interactions formed between 7.44 and NHR2. Finally, in **section 6** close and remote structural analogues of 7.44 were identified, which showed increased antiproliferative effects against RUNX1-ETO-positive leukemia cells. Unbiased diffusion simulations of a selected subset of the compounds showed preferred binding areas. However, the binding distributions of the compounds across the protein suggest different binding classes.

In summary, the publications in this work represent different approaches in modern drug design. The work regarding PXA represents a lead-based drug design, where a natural product serves as an active lead, without having the molecular mode of action completely understood. In contrast, in the HSP90- and RUNX1-ETO-related projects, a rational drug design approach was applied to develop targeted drugs. In the case of compounds targeting HSP90, these could be of therapeutic benefit against a wide variety of tumor types, while the ones targeting the RUNX1-ETO fusion protein would likely be limited to t(8;21) leukemia. In the following sections, the computational work that was contributed to these studies and the new information gained thereby will be presented.

2 Methods

2.1 Molecular dynamics simulations

Molecular dynamics (MD) simulation is a technique to sample motions of atomistic systems over time. In this method, the atomic interactions are described using mechanical potentials (see chapter 2.1.1), which in their simplest form represent atoms and their covalent interactions as masses connected by springs. In that way, even large biological systems (e.g., proteins) that cannot be handled using quantum mechanics can be simulated [232,233]. In MD simulations, a successive series of conformations of a system are calculated to generate a trajectory. Such a trajectory and the motion of the conforming atoms are obtained by integrating equation 1 over a given time step [233].

$$\frac{d^2 x_i}{dt^2} = \frac{F_{x_i}}{m_i} \tag{1}$$

Here, the motion of particle i along coordinate x_i is described in dependence of the force (F_{x_i}) acting on the particle of mass m_i along the coordinate [233]. During one integration time step dt the forces on a particle are not getting updated. Thus, choosing too large time-steps may lead to high-energetic artifacts and instabilities during the simulation. On the other hand, reducing the time step size increases the computational cost for obtaining comparable configurational samplings and simulation lengths. As a rule, the integration time step has to be about one order of magnitude smaller than the period of the highest-frequency motion [233]. These are typically the translational vibrations of hydrogen-heavy atom bonds, which are in the range of $1 \cdot 10^{14}$ s^{-1} ($\lambda = 10$ fs), hence limiting the simulation time steps to ~1 fs [233]. As these high-frequency internal vibrations are usually decoupled from the conformational changes of a system, algorithms like SHAKE [234], SETTLE [235], and hydrogen mass repartitioning have been introduced that constrain or slow these vibrations [236], so that the time step can be increased.

The use of mechanical potentials in molecular dynamics allows for fast and efficient calculation of the energy terms. However, for a mechanical potential to model processes that are described at the quantum theory level (e.g., molecular bond stretching), it needs to be parametrized to accurately represent (free) energy profiles from quantum mechanical calculations. This parametrization is typically performed for sets of similar molecules (e.g., amino acids, nucleic

acids). However, also more general force fields exist. Some exemplary force fields used in the works in this thesis are listed below with their application:

- ff14SB for proteins [237]
- GAFF and GAFF2 for organic small molecules [238,239]
- LIPID17 for phospholipids in biological membranes (updated version of LIPID14 [ref 240])
- TIP3P, three-point water model [241]

The potentials used in the AMBER force fields are shown in equation 2. Harmonic potentials are used to describe the stretching of bonds between two atoms, as well as the bending of angles between three bonded atoms. A cosine term is used to add torsion barriers to the rotation around rotatable bonds. The same term is also used for out-of-plane bending potentials, referred to as "improper dihedrals". Finally, non-bonded interactions are represented by a 12-6 Leonnard-Jones-Potential to describe van-der-Waals interactions and a Coulomb potential for electrostatic interactions [239,242,243].

$$
\begin{aligned}
E_{total} = &\sum_{bonds} k_b (r - r_0)^2 \\
&+ \sum_{angles} k_\theta (\theta - \theta_0)^2 \\
&+ \sum_{dihedrals} V_n [1 + \cos(n\phi - \gamma)] \\
&+ \sum_{i=1}^{N-1} \sum_{j=i+1}^{N} \left[\frac{A_{ij}}{R_{ij}^{12}} - \frac{B_{ij}}{R_{ij}^{6}} + \frac{q_i q_j}{\varepsilon R_{ij}} \right]
\end{aligned}
\tag{2}
$$

2.2 Free energy calculations using umbrella sampling

The goal of sampling in MD simulations is to reach independence of the distribution of observed properties from the initial configuration of the system. At this point the probability densities of individual states follow the Boltzmann distribution [233]. Thus, the distribution of states along a given reaction coordinate can be used to calculate free energy differences [244]. In unbiased molecular dynamics simulations, however, the low energy regions close to the initial configuration will be explored, while the regions behind large energy barriers (i.e., larger than multiple $k_B T$) will be likely undersampled. Moreover, for deriving the magnitude of the energy barrier, high-energy transition states need to be sampled. Thus, unachievable long simulation times would be required to obtain sufficient sampling for accurate free energy predictions [245].

This can be countered by applying a biasing potential, that confines the sampling to a given region or "window" along the reaction coordinate. Commonly, simple harmonic potentials are used. By placing multiple overlapping sampling windows along the whole reaction coordinate, individual states can be sampled more efficiently. Finally, these individual window samplings can be recombined yielding an accurate sampling along the full reaction coordinate. However, to calculate free energies along the pathway, it is necessary to account for the biasing potentials applied during the sampling [245,246].

The weighted histogram analysis method (WHAM) is an algorithm specifically designed to unbias sampling data obtained from biased simulations [247,248]. This method determines a weight functional that minimizes the statistical error for the weighted sum of the data from all simulations [246,248].

An application of the umbrella sampling method in the field of biomedical research is determining the membrane permeability for small molecules. Here, umbrella sampling is used to sample a compound's passage through the membrane [249,250]. This was applied to estimate the membrane permeability of phomoxanthone A (see **section 3**, **Publication II**).

3 Simulation studies on the permeation of Phomoxanthone A through the inner mitochondrial membrane

Most parts of this chapter are taken from **Publication II** (see page 83):

The tetrahydroxanthone-dimer phomoxanthone A is a strong inducer of apoptosis in cisplatin-resistant solid cancer cells

Wang, C. [a], Engelke, L. [a], <u>Bickel, D. [a]</u>, Hamacher, A. [a], Frank, M. [b], Proksch, P. [b], Gohlke, H. [a,c], and Kassack, M.U. [a]

[a] Institute for Pharmaceutical and Medicinal Chemistry, Heinrich Heine University Düsseldorf, Düsseldorf, Germany

[b] Institute of Pharmaceutical Biology and Biotechnology, Heinrich Heine Universität Düsseldorf, Düsseldorf, Germany

[c] John von Neumann Institute for Computing (NIC), Jülich Supercomputing Centre (JSC), Institute of Biological Information Processing (IBI-7: Structural Biochemistry) & Institute of Bio- and Geosciences (IBG-4: Bioinformatics), Forschungszentrum Jülich GmbH, Jülich, Germany

3.1 Background

Natural products have a long and ongoing history in drug discovery (see **section 1.1**) [45,46]. In the case of the dimeric tetrahydroxanthone phomoxanthone A (PXA), it was isolated from the endophytic fungus *Phomopsis longicolla*, which lives in mangrove plants. Here, it is exposed to challenging environmental conditions, like periodic changes in tidal submergence, water salinity, and temperature. Such conditions have been suggested to promote the activation of novel biosynthetic pathways that produce bioactive secondary metabolites [53,55,251]. PXA is a symmetric tetrahydroxanthone-dimer with a 4,4'-biaryl linkage and bulky substituents in positions 5, 5', 10a, and 10a' (Figure 9). This results in atropisomerism between the two tetrahydroxanthone moieties.

In prior studies the compound showed promising anti-proliferative effects on native and cisplatin-resistant cancer cell lines. Interestingly, this effect was selective for cancer cells over non-cancer cells (peripheral blood mononuclear cells) by two orders of magnitude [53,55], making PXA a promising natural lead for the further development of anticancer drugs.
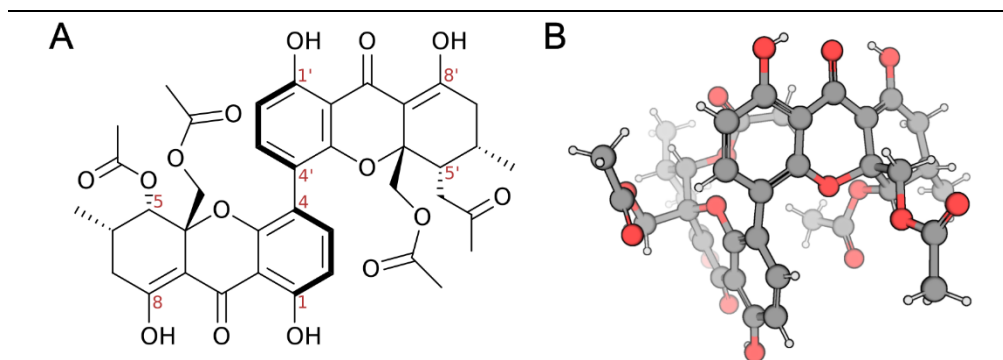
Figure 9. Structure of PXA. The absolute configuration of PXA was determined by X-ray analysis as *aR*, 5*S*, 6*S*, 10a*S*, 5'*S*, 6'*S*, 10a'*S* [55]. **A.** Schematic representation of the structure of PXA. **B.** X-ray crystal structure of PXA where the 4,4'-biaryl axis is rotated by ~92°.

It has been shown, that in the cell, PXA induces fission in the mitochondrial network [54]. This effect is typically associated with compounds that deplete the membrane potential ($\Delta\Psi_m$) of the inner mitochondrial membrane (IMM), like the protonophore carbonyl cyanide *m*-chlorophenyl hydrazone (CCCP) [54,252]. The membrane potential of the IMM is mostly maintained by the proton gradient between the cytoplasm and the mitochondrial matrix, leading to the hypothesis that PXA may act as a protonophoric decoupler similar to CCCP.

As described in **section 2.2**, energy barriers for molecular processes that would normally not be observable with unbiased sampling can be obtained by applying umbrella sampling. With this technique, we obtained potentials of mean force for the passive permeation of PXA in various protonation states through the IMM. The obtained PMFs allow for a general estimation of membrane partition of PXA, as well as for the time scales on which membrane permeation may take place.

3.2 Potential of mean force calculation to estimate the membrane permeability of phomoxanthone A

For PXA to act as a proton shuttle and deplete the proton gradient across the IMM, the compound would need to satisfy two conditions: I) being able to exist in at least two protonation states under physiological pH, and II) being able to permeate the IMM in those two protonation states at timescales relevant for biological processes.

As for PXA, no experimental pK_a values have been reported yet, sequential pK_a values for PXA in aqueous environment were computed using EPIK [253,254]. The computations indicate that the hydroxyl groups in 8- and 8'-position are the most acidic functional groups with pK_a = 5.1 ± 1.1 in both cases. Thus, the computations do not reveal a mutual influence due to deprotonation of

one hydroxyl group onto the pK_a value of the other group, which may be explained by the large separation between the two groups. Therefore, the doubly deprotonated species of PXA is predicted to be the predominant species under physiological conditions in aqueous solution. However, in a low dielectric medium such as a lipid bilayer membrane, pK_a values are known to increase [255], which would shift the (de)protonation equilibrium to the side of the less charged species.

To address the question if differently charged PXA species (PXA^0, PXA^{1-}, and PXA^{2-}) can permeate the IMM, I calculated a potential of mean force (PMF) for the transition of PXA through the membrane by the means of umbrella sampling MD simulations and WHAM. The lipid composition of the membrane in the simulations aimed to resemble the IMM *in vivo* [256]. However, an overly realistic representation of the physiological system would increase the complexity of the simulation, requiring exhaustive sampling times to reach convergence [257]. Therefore, the IMM composition was simplified to DOPC, DOPE and DOPG* in the ratios of 40:34:18. The umbrella sampling reference points along the membrane normal were generated by steered MD simulations, dragging the PXA species along the membrane normal (z, Figure 10A). The starting point was located at the membrane center and the end point in the solvent phase at 35 Å (Figure 10B). To exclude any influence of the potential applied during the steered MD, all umbrella windows were simulated for 50 ns and only then sampling for further 50 ns was started. The umbrella windows display considerable overlap regarding the frequency distribution of values for the reaction coordinate (Figure 10C). Furthermore, computing the PMFs with increasing sampling intervals showed that the PMFs appear converged after 30-40 ns of sampling per window (Figure 10D). Accordingly, the statistical error was estimated by computing individual PMFs for equally sized chunks of the sampled data. That way a standard error of the mean of < 0.4 kcal mol^{-1} along the PMFs was obtained.

For both PXA^0 and PXA^{1-}, the global minima of the PMFs are located at $z = 13$ Å with ~-2.8 kcal mol^{-1} (Figure 11A), revealing that a partially immersed state (state I) of PXA within the membrane (Figure 11B) is thermodynamically more favorable than a fully solvent-exposed state. In this state, the hydrophobic part of PXA is located towards the interior of the membrane, whereas the polar part is located close to the head group region, solvated by a shell of water molecules. Performing unbiased MD simulations of 500 ns lengths as controls starting from

---

* The neutral lipid DOPG serves as a surrogate for the cardiolipins present in the mitochondrial membrane, as at the time of this study no validated cardiolipin parameters were available for the Amber membrane force fields.
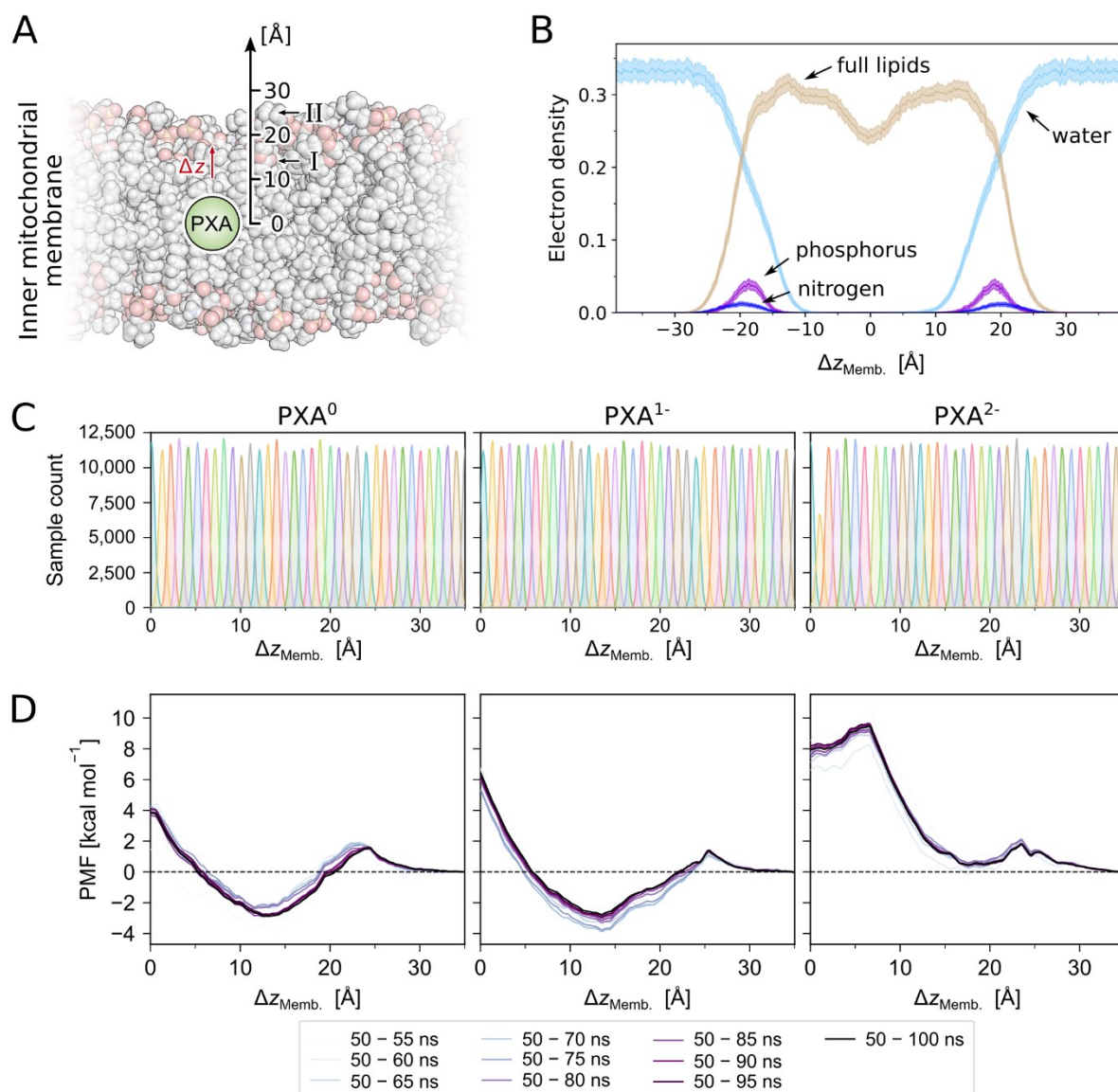
Figure 10. PMF computation for the permeation of PXA through the IMM. A. Simulation setup for the generation of the umbrella windows. The PMFs were calculated from the membrane center ($\Delta z = 0$ Å) to a fully solvent exposed state ($|\Delta z| = 35$ Å). **B.** Normalized electron density distribution of an unperturbed membrane used in the MD simulations, which shows the average location of the hydrophilic and hydrophobic components. The polar headgroups are located at $|\Delta z| = 19$ Å. **C.** The distribution of values along the reaction coordinate obtained from the umbrella sampling. All windows show good overlap to their adjacent windows. **D.** Convergence of the computed PMFs over the sampling time. The PMFs appear to converge after 30-40 ns of sampling per window.

PXA located at the membrane center confirms this finding in that the most frequently sampled distance of PXA from the center is at $z = 12.5$-13.0 Å. A small energy barrier of ~1.5 kcal mol^{-1} is observed at $z = 25$ Å (state II), separating the semi-immersed state from the solvent-exposed one. Here, PXA is in proximity to the polar head groups of the lipids (Figure 11C), which form a polar barrier before more favorable hydrophobic interactions can be formed. The height of the energy barrier to pass the membrane is 3.8 and 6.4 kcal mol^{-1} with respect to the fully
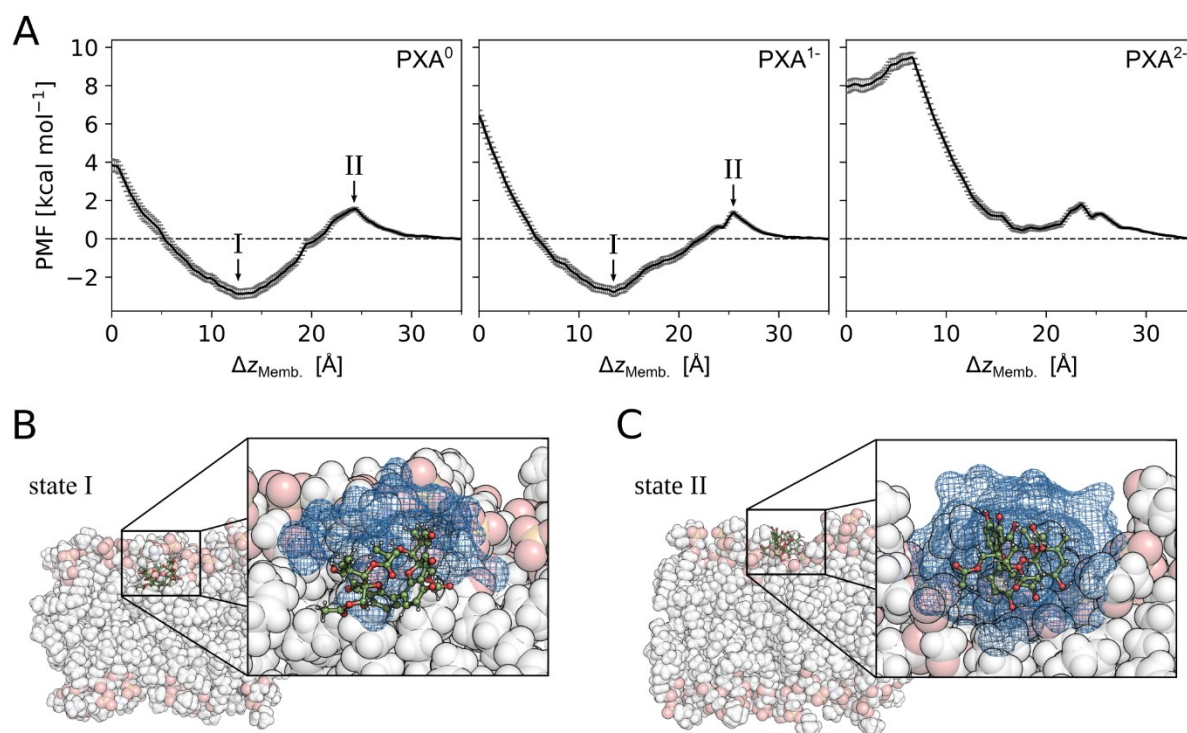
Figure 11. The energy profile of the permeation of PXA through the IMM. A. The computed PMFs for transition of the uncharged, singly charged, and doubly deprotonated species of PXA from the membrane center to solvent. All values are normalized with respect to the bulk solvent. The error bars indicate the SEM at the respective positions. Interesting states in the potentials are marked with I and II. **B.** The thermodynamically favorable state I (see panel A). Here, PXA is partially desolvated, allowing for the hydrophobic 4,4'-biaryl-linkage to interact with the membrane lipids, while the polar substituents are still solvated. **C.** State II indicates the transition of PXA from a fully solvent-exposed state to a partial membrane immersion.

solvent-exposed state for PXA^0 and PXA^{1-}, respectively, and 6.7 and 9.2 kcal mol^{-1} with respect to state I, respectively. These barrier heights are markedly lower than those found for protein-free phosphatidylcholine, -ethanol, and -glycin lipid flip-flop in respective membranes [258]. Employing Eyring theory [259] at $T = 300$ K, kinetic rates of $1.37\cdot10^8$ to $9.88\cdot10^9$ s^{-1} are obtained, although obtaining a barrier height pertinent to kinetics via a PMF has been debated [260]. By contrast, the doubly charged species is most favorable in water, and the barrier height with respect to the fully solvent-exposed state for passage through the membrane is 9.5 kcal mol^{-1}, which would result in a kinetic rate slower by ~2 orders of magnitude.

Taken together, the simulation results indicate that both the PXA^0 and PXA^{1-} species, but less so PXA^{2-}, show membrane partitioning and can penetrate the inner mitochondrial membrane with a high rate, similar to what can be estimated from permeabilities for non-electrolyte compounds like benzoic acid and codeine [249]. This would indicate, that PXA can act as a protonophore across the IMM. In our simulations, the membrane potential was not considered,

which would drive the passage of negatively charged deprotonated PXA towards the intermembrane space, where they can take up a proton and penetrate back as neutral PXA across the membrane. Overall, these processes might allow PXA to act as a proton shuttle and dissipate the proton gradient along the IMM.

3.3 Conclusion and significance

The natural product PXA is a very potent inhibitor of cell proliferation and inducer of apoptosis in cancer cells. In previous studies the effect of PXA on mitochondria, i.e., the depolarization of the mitochondrial membrane potential, was described. Thus, we hypothesized, that PXA depolarizes the membrane by depleting the proton gradient between the cytoplasm and the mitochondrial matrix. In the context of this thesis, the ability of PXA to shuttle protons through the IMM was assessed by computational methods.

The computation of pK_a values identified the hydroxy groups in 8 and 8'-positon as the most acidic functional groups in PXA, forming a vinylogous acid with the carbonyls in 9 and 9'-position respectively. Moreover, the values show that in aqueous solution the double deprotonated species of PXA is prevalent. Still, the computed p$K_a = 5.1 \pm 1.1$ allows for a fraction of PXA to exist in singly deprotonated, and neutral states.

The energy profiles for the membrane passage through the IMM of the three protomers of PXA were computed based on umbrella sampling MD simulations. For the neutral, singly, and doubly deprotonated species, barrier heights of 3.8 kcal mol^{-1}, 6.4 kcal mol^{-1}, and 9.5 kcal mol^{-1} were obtained with respect to the fully solvent-exposed state, respectively. Moreover, for both the neutral and the singly deprotonated protomers a thermodynamically favorable state was found along the membrane passage.

In conclusion the simulations indicate that the neutral and singly protonated state of PXA can permeate through the IMM. This would allow PXA to act as a proton shuttle and depolarize the membrane potential of mitochondria, corroborating the initial hypothesis. However, at this point no experimental evidence for this mode of action of PXA is available. Also, unlike the established protonophoric decoupler CCCP, PXA does not responsively increase cellular respiration [54]. That indicates, that in any case the effect of PXA on the mitochondria is not exclusively triggered by protonophoric decoupling. In a recent study employing the drug affinity responsive target stability (DARTS) approach the mitochondrial carbamoyl-phosphate synthase 1 (CPS1) was identified as a protein target of PXA [261]. According to the study, high micromolar concentrations of PXA increase CPS1 activity in a concentration-dependent

manner. Although this provides an alternative mode of action of PXA targeting an enzyme, the observed increase in CPS1 activity *in vitro* does not explain the depolarization of the IMM. Likely, PXA is pleiotropic eliciting its unique effect on the mitochondria through multiple pathways.

4 Full-atomistic simulations to predict binding epitopes of a novel C-terminal HSP90 inhibitor

Most parts of this chapter are taken from **Publication III** (see page 99):

Development of a first-in-class small molecule inhibitor of the C-terminal HSP90 dimerization

Bhatia, S. [a], Spanier, L. [b], Bickel, D. [b], Dienstbier, N. [a], Woloschin, V. [b], Vogt, M. [a], Pols, H. [b], Lungerich, B. [b], Reiners, J. [c], Aghaallaei, N. [d], Diedrich, D. [b], Frieg, B. [b,e], Schliehe-Diecks, J. [a], Bopp, B. [f], Lang, F. [a], Gopalswamy, M. [b], Loschwitz, J. [b], Bajohgli, B. [d], Skokowa, J. [d], Borkhardt, A. [a], Hauer, J. [g,h], Hansen, F.K. [i], Smits, S. [c,j], Jose, J. [f], Gohlke, H. [b,e], and Kurz, T. [b]

[a] Department of Pediatric Oncology, Hematology and Clinical Immunology, Medical Faculty, Heinrich Heine University Düsseldorf, Düsseldorf, Germany

[b] Institute for Pharmaceutical and Medicinal Chemistry, Heinrich Heine University Düsseldorf, Düsseldorf, Germany

[c] Center for Structural Studies, Heinrich Heine University Düsseldorf, Düsseldorf, Germany

[d] Department of Hematology, Oncology, Clinical Immunology and Rheumatology, University Hospital Tübingen, Germany

[e] John von Neumann Institute for Computing (NIC), Jülich Supercomputing Centre (JSC), Institute of Biological Information Processing (IBI-7: Structural Biochemistry) & Institute of Bio- and Geosciences (IBG-4: Bioinformatics), Forschungszentrum Jülich GmbH, Jülich, Germany

[f] Institute for Pharmaceutical and Medicinal Chemistry, PharmaCampus, Westphalian Wilhelms University, Münster, Germany

[g] Department of Pediatrics, Pediatric Hematology and Oncology, University Hospital Carl Gustav Carus, Dresden, Germany

[h] National Center for Tumor Diseases (NCT), Partner Site Dresden, Dresden, Germany

[i] Pharmaceutical and Cell Biological Chemistry, Pharmaceutical Institute University of Bonn, Bonn, Germany

[j] Institute of Biochemistry, Heinrich Heine University Düsseldorf, Düsseldorf, Germany

4.1 Background

The heat shock protein 90 (HSP90) is known to promote cancer cell survival and proliferation. The physiological function of HSP90 is to protect cells against proteotoxic stressors, like elevated temperatures, hypoxia, and acidosis, but also high mutation burden can be exploited by tumor cells to survive their tumor microenvironment [114,115,122,262] (see **section 1.3.3**). Thus,

many groups explore HSP90 inhibitors for the prospective use in cancer therapy. While the main focus of the clinical development of HSP90 inhibitors has been focused on the N-terminal ATP binding site (see **section 1.3.4**) [158], in recent years an increased interest in C-terminal HSP90 inhibitors has been reported (see **section 1.3.5**) [68,149].

As HSP90 functions as a dimer, the inhibition of its dimerization provides a novel way to inhibit this chaperone. Initially the dimerization interface in the CTD was believed to be in a permanent dimerized state and thus inaccessible. FRET studies, however, revealed that the CTD undergoes cycles of dissociation and association in a similar fashion as the NTD in the second time scale [104]. In a study by Gohlke and co-workers, hot spot residues (**section 1.2**) in the HSP90 dimerization interface were identified, applying molecular dynamics and free energy calculations [263]. These hotspots are clustered in the interfacial helices H4 and H5. Peptides designed on the basis of these helices were shown to bind to the CTD of HSP90 with apparent K_d values around 1 μM [264], and inhibit dimerization in an autodisplay assay [264,265]. Thus, these peptides represented the first inhibitors of the C-terminal dimerization of HSP90 [68].

Based on these results and the hotspot analysis, the peptidomimetic compound aminoxyrone (Figure 12A) was designed, which binds to the CTD with a K_d of 27.4 μM [193,266]. The compound induces cell cycle arrest and growth inhibition in various leukemia cells cell lines, without inducing the HSR typically associated with clinical inhibitors of HSP90 (**section 1.3.4**) [68,193]. Therefore, the compound is an attractive lead for further drug optimization.
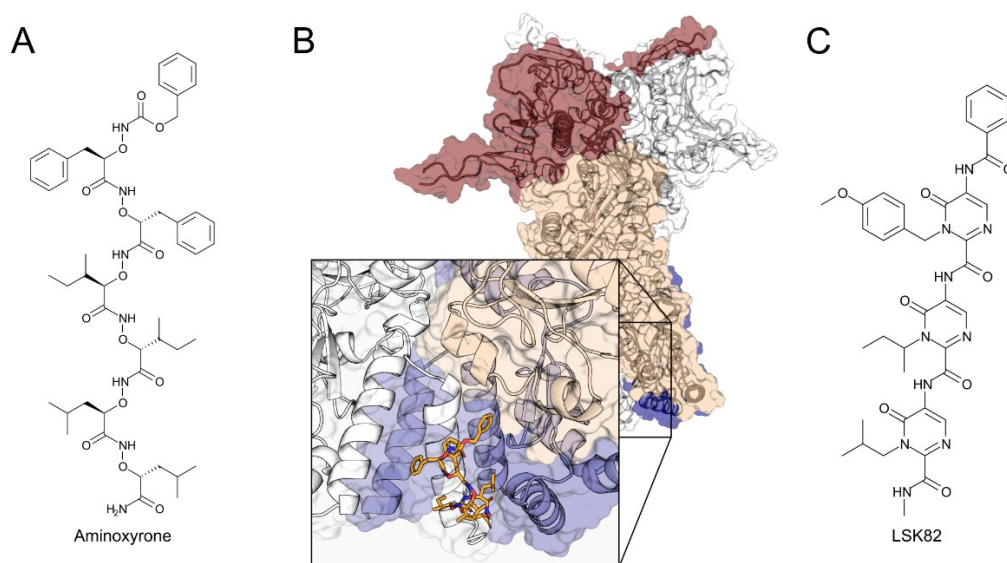

Figure 12. Aminoxyrone, a peptidomimetic inhibitor of the HSP90 dimerization. A. The α-aminoxy peptide-based inhibitor aminoxyrone of HSP90. In solution this compound adopts a conformation mimicking an α-helix. **B.** Binding-mode of aminoxyrone predicted by MD simulations [193]. The compound binds to the C-terminal dimerization interface of HSP90, mimicking helix H5. **C.** The novel α-helix mimetic inhibitor LSK82, based on a pyrimidoneamide backbone.

In this study, we replaced the α-aminoxypeptide backbone of aminoxyrone by pyrimidoneamides, which were shown before to function as α-helix mimetics, too [267]. This yielded a set of compounds, of which LSK82 (Figure 12C) is the most potent inhibitor of the HSP90 function. By unbiased molecular dynamics simulations, the binding of LSK82 to HSP90α was simulated to identify the most probable binding epitopes. Furthermore, the binding of LSK82 to the cytosolic HSP90α and HSP90β was compared, to investigate on the structural level, if the compound exhibits isoform specificity.

4.2 Unbiased ligand diffusion simulations

To provide structural insights into the binding of LSK82 to the CTD of HSP90, we performed 40 independent MD simulations[*] of free diffusion of LSK82 in the presence of truncated monomeric HSP90α (residues 294-699) and HSP90β (residues 286-691). In order to accurately represent the α-helix mimetic properties of the trispyrimidoneamides, the modified GAFF parameters were used [267]. The initial configurations of the simulation systems were generated such that the ligand is at least at 10 Å distance from the protein. To counteract the high flexibility particularly of the C-terminal helix interface, we introduced positional restraints on the backbone atoms, adjusting the reference coordinates every 100 ns to allow for moderate protein movements. Simulations of 500 ns length in total were performed, leading to 20 μs cumulative simulation time for each of the isoforms.

To analyze binding epitopes of LSK82, a criterium needs to be established, how binding can be detected during the simulation. Based on the premise, that a stably bound ligand is restrained in its movement with respect to the target protein, we defined the ligand as bound, if its displacement with respect to the protein between two subsequent frames is ≤ 1.5 Å[†]. Mapping the probability density of occurrence of LSK82 onto the surface of Hsp90 revealed two main binding regions of LSK82: one in the C-terminal helix interface (Figure 13A, green), where binding occurred in 10 out of the 40 replicas, and another in a cleft between the CTD and MiD (Figure 13A, blue), where binding occurred in 6 out of 40 replicas. In the latter case, an area of high density with the shape of LSK82 is observed (Figure 13A, light blue), resulting from a single trajectory. This indicates that the ligand was kinetically trapped in this one case, although the position is thermodynamically unfavorable. By contrast, the densities in the C-terminal

---

[*] The MD simulations on HSP90α were set up by Dr. Benedikt Frieg.

[†] This was calculated as the no-fit RMSD of LSK82 towards the previous frame after superimposing on the protein.
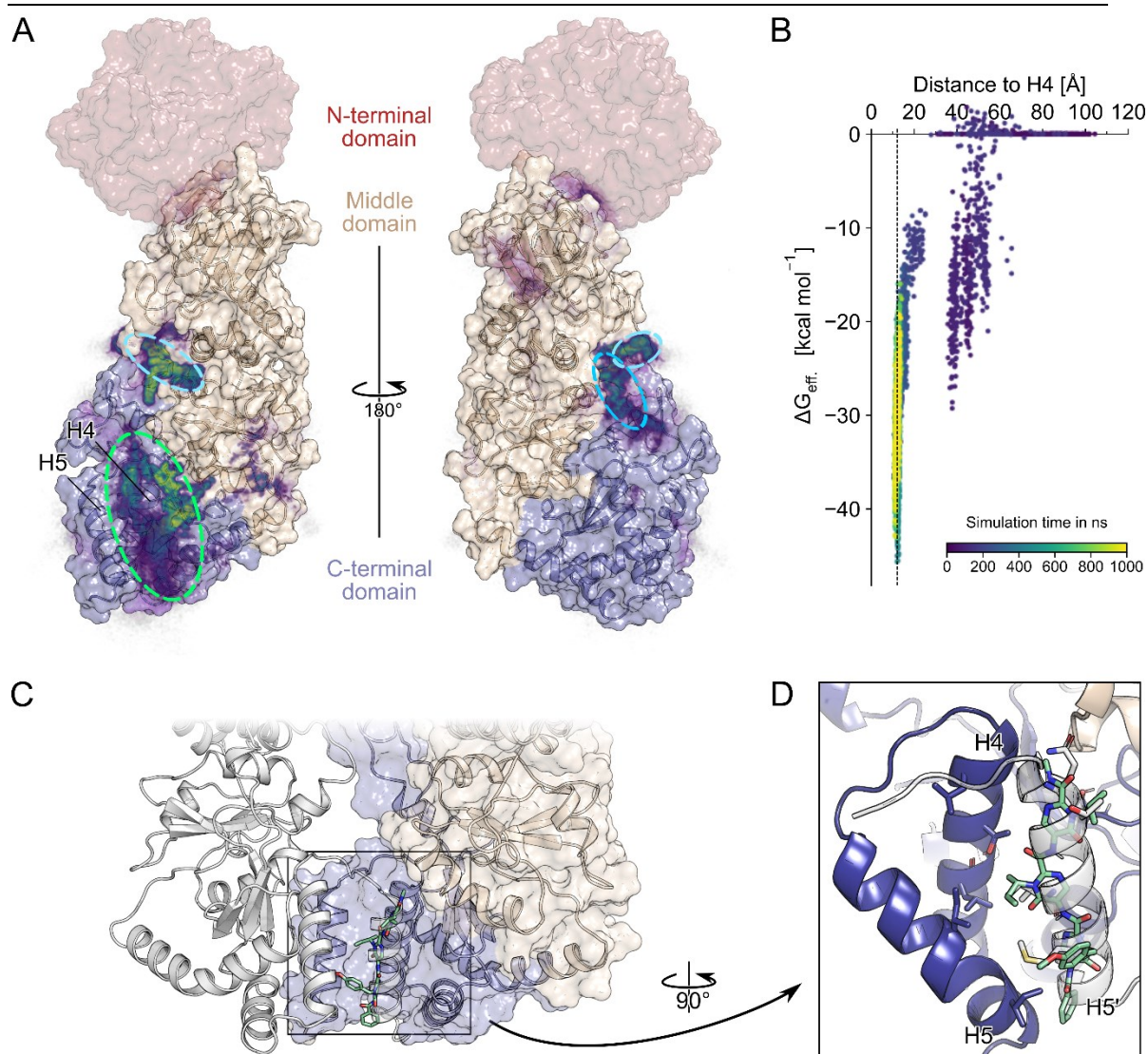
Figure 13. MD simulations of LSK82 binding to HSP90α. A. The relative densities of the bound poses of LSK82 after 500 ns are mapped on the HSP90α monomer fragment used in the simulations (PDB ID: 3q6m). The missing NTD is shown in red, based on the HSP90β structure (PDB ID: 5fwk). Particularly high densities are observed in the region between H4 and H5 (green circle). A second, less preferred site is in the cleft between the CTD and middle domain (blue circles). **B.** Effective energy calculations over a single trajectory that resulted in LSK82 binding in the C-terminal helix interface as a function of the center-of-mass distance between LSK82 and H4 and the simulation time (see color scale). The dashed line at 12.1 Å corresponds to the H4-H5' distance in the crystal structure of PDB ID 3q6m. **C.** Possible binding mode of LSK82 in the helix interface, where LSK82 mimics H5'. **D.** Blow-up of the possible binding mode of LSK82 showing how its sidechains mimic side chains of H5'.

interface are more ambiguously shaped, indicating that, while binding there is favorable, the ligand can still explore multiple binding modes, which are also seen to interchange.

To further study these binding modes, we clustered the bound frames of LSK82 mapped on the protein surface with respect to their RMSD after superimposing HSP90. Among the clustered binding modes were several that form interactions to the C-terminal helix interface, with LSK82 positioned such that it mimics interactions formed by H5' in the dimer (Figure 13C and D). To

37

corroborate that this binding mode is favorable, we computed the effective binding free energies by the MM-GB/SA approach for the trajectory that led to it. Already first transient interactions with the protein resulted in effective energies down to ~-30 kcal mol^{-1}. The effective energies decreased further to ~-45 kcal mol^{-1} once the ligand bound to the C-terminal interface, thereby forming interactions with Hsp90 that remained stable even when the trajectory was extended to 1 µs, indicating that such poses are particularly favorable (Figure 13B). With respect to the magnitude of the effective energies, it is important to note that configurational entropy contributions were not considered, since estimating such contributions by normal mode analysis may introduce additional uncertainties [268,269].

Overall, regarding the probability density of bound LSK82 poses, the proportion of replicas, and the results of the MM-GB/SA computations indicates that LSK82 preferentially binds to the C-terminal helix interface, where it can adopt poses that mimic H5'.

We then set out to study if LSK82 exhibits isoform specific binding. The dimerization interface between the cytosolic α- and β-isoform differ in three positions: S641 / P633, S658 / A650, and A685 / S677 (Figure 14A). Using the same setup as before, we performed MD simulations of
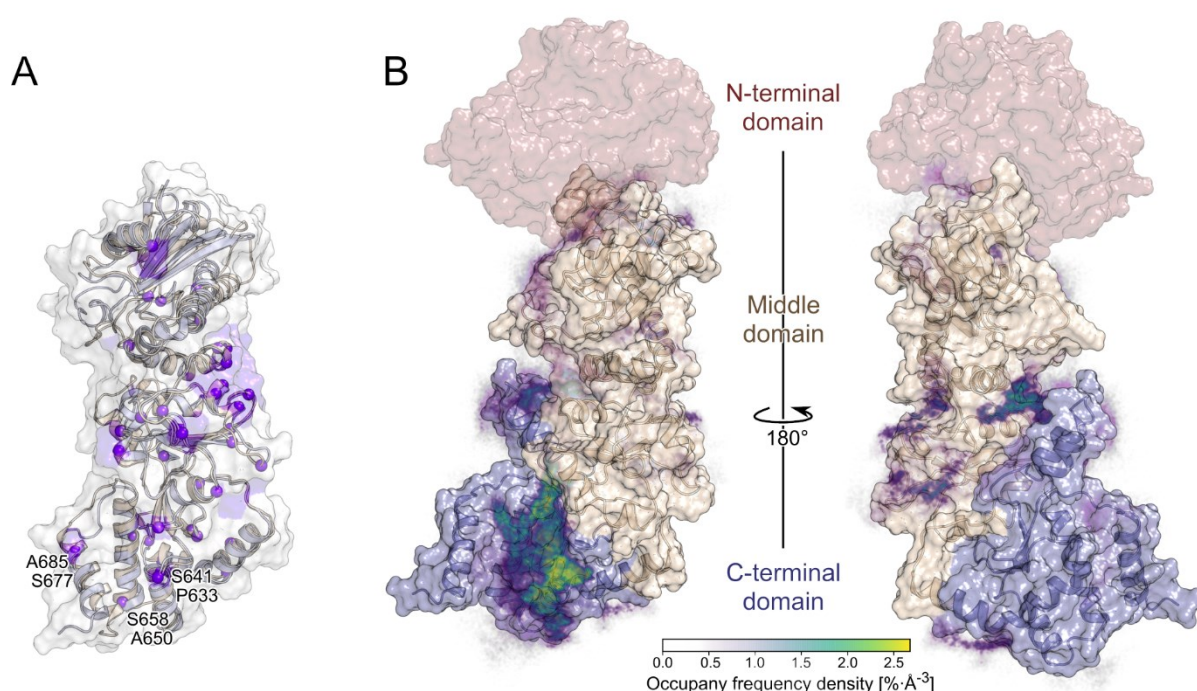

Figure 14. MD simulations of LSK82 binding to HSP90β. A. The structure shows an overlay of the MiD and CTD of HSP90α (light orange, PDB ID: 3q6m) and HSP90β (light blue, PDB ID: 5fwk). Substitutions are highlighted by purple spheres. The three substitutions in the C-terminal dimerization interface are labeled with residue and sequence-position (HSP90α on top; HSP90β below). **B.** The relative densities of the bound poses of LSK82 after 500 ns are mapped on the HSP90β monomer fragment used in the simulations (PDB ID: 5fwk). The missing NTD is shown in red. The epitopes exhibiting high densities correspond to the areas observed in HSP90α (see Figure 13)

free ligand diffusion around HSP90β. The probability density of bound LSK82 revealed that the C-terminal helix interface is the most preferred region, followed by the cleft between the CTD and middle domain (Figure 14B). Notably, no high density in this cleft was found now, in contrast to HSP90α, confirming that the observation there resulted from kinetic trapping. Hence, despite the few sequence variations in the C-terminal helix interface between HSP90α and HSP90β, the same preferred binding region of LSK82 was found.

4.3 Conclusion and significance

In this study, we present the HSP90 inhibitor LSK82, which is the first compound of a novel class of C-terminal HSP90 inhibitors that does not induce the heat shock response. To study the binding of the compound to the molecular chaperone, we performed extensive MD simulations of the compound freely diffusing around the MiD-CTD of the cytosolic isoforms of HSP90. Notably, over the course of these simulations after binding no complete dissociation was observed. This limits the amount of sampling that could be obtained, so that no quantitative estimates on the binding affinities to either side can be made.

In the binding simulations on HSP90α the compound was observed to preferably bind in the area that comprises the dimerization interface of HSP90α. A second less populated area was detected in a cleft between the MiD and CTD. This indicates that LSK82 preferably binds to the C-terminal dimerization interface.

In the simulations performed on HSP90β very similar results to the simulations on HSP90α were obtained. This aligns well with the overall high sequence identity between the two isoforms. It further corroborates the conclusion that LSK82 preferably binds to the C-terminal dimerization interface. Moreover, it indicates that LSK82 binds equally to both isoforms.

In conclusion though no quantitative estimates about the binding affinities could be obtained, the simulations indicate, that the C-terminal dimerization interface is a preferred binding epitope. Moreover, LSK82 appears to bind equally to both isoforms.

5 Characterization of an inhibitor targeting the NHR2 domain of the RUNX1-ETO fusion protein

Most parts of this chapter are taken from **Publication IV** (see page 191):

Biophysical and pharmacokinetic characterization of a small-molecule inhibitor of RUNX1/ETO tetramerization with anti-leukemic effects

Gopalswamy, M. [a], Kröger, T. [a], Bickel, D. [a], Frieg, B. [b], Akter, S. [a], Schott-Verdugo, S. [a,b,c], Viegas, A. [d], Pauly, T. [b,d], Mayer, M. [e], Przibilla, J. [e], Reiners, J. [f], Nagel-Steger, L. [d], Smits, S. [f], Groth, G. [g], Etzkorn, M. [d], and Gohlke, H. [a,b,c]

[a] Institute for Pharmaceutical and Medicinal Chemistry, Heinrich Heine University Düsseldorf, Düsseldorf, Germany

[b] Institute of Biological Information Processing (IBI-7: Structural Biochemistry), Forschungszentrum Jülich GmbH, Jülich, Germany

[c] John von Neumann Institute for Computing (NIC), Jülich Supercomputing Centre (JSC), and Institute of Bio- and Geosciences (IBG-4: Bioinformatics), Jülich, Germany

[d] Institute for Physical Biology, Heinrich Heine University Düsseldorf, Düsseldorf, Germany

[e] Pharmacelsus GmbH, Saarbrücken, Germany

[f] Institute of Biochemistry, Heinrich Heine University Düsseldorf, Düsseldorf, Germany

[g] Institute of Biochemical Plant Physiology, Heinrich Heine University Düsseldorf, Düsseldorf, Germany

5.1 Background

The RUNX1-ETO fusion protein is the gene transcript associated with t(8;21) leukemia, found in patients with acute myeloid leukemia (AML). The fusion protein is comprised by the DNA-binding Runt homology domain (RHD) encoded in the *RUNX1* gene and four nervy homology regions (NHR1-4) encoded in *ETO*. Particularly, the NHR2 domain contributes to various of the biochemical properties of the RUNX1-ETO fusion protein. It mediates its self-association to dimers and tetramers, which in turn forms the interaction sites for transcriptional co-repressors (**section 1.4.1**). Therefore, the NHR2 domain is essential for the function of the RUNX1-ETO fusion protein in leukemogenesis, and preventing the homo-oligomerization of the NHR2 domain would represent a promising approach to treat RUNX1-ETO-positive leukemia.

In prior studies the tetramerization of the NHR2 domain was shown to be crucial for the development of leukemic phenotypes and proliferation [213]. Moreover, it was shown that the homo-tetramerization can be inhibited by peptides mimicking the NHR2 domain which provides a conceptual basis, that the homo-oligomerization of the NHR2 domain can be competitively inhibited [214]. With the release of the crystal structure of the tetrameric NHR2 complex [212], structural approaches became possible and lead to the identification of five hot spot residues in the tetramerization interface [215]: W498, W502, D533, E536, and W540 (Figure 15; sequence numbering according to the *RUNX1-ETO* gene sequence [197]).

Based on these hot spot residues, a virtual screening for putative oligomerization inhibitors was performed, yielding the compounds 7.18 and 7.44 which selectively inhibit tetramer-dependent DNA binding of a RUNX1-NHR2 construct [270] (Figure 15) and reduce the tumor burden in a xenograft mouse model [271]. In the present study we further characterize the binding of 7.44 to the isolated NHR2 domain. By saturation transfer distance NMR (STD-NMR) and multidimensional NMR the binding of 7.44 to the NHR2 domain has been confirmed. Furthermore, MD simulations of the tetrameric NHR2 domain and the compound 7.44 were conducted and provide structural insight into the compound's binding in context of the quaternary structure.
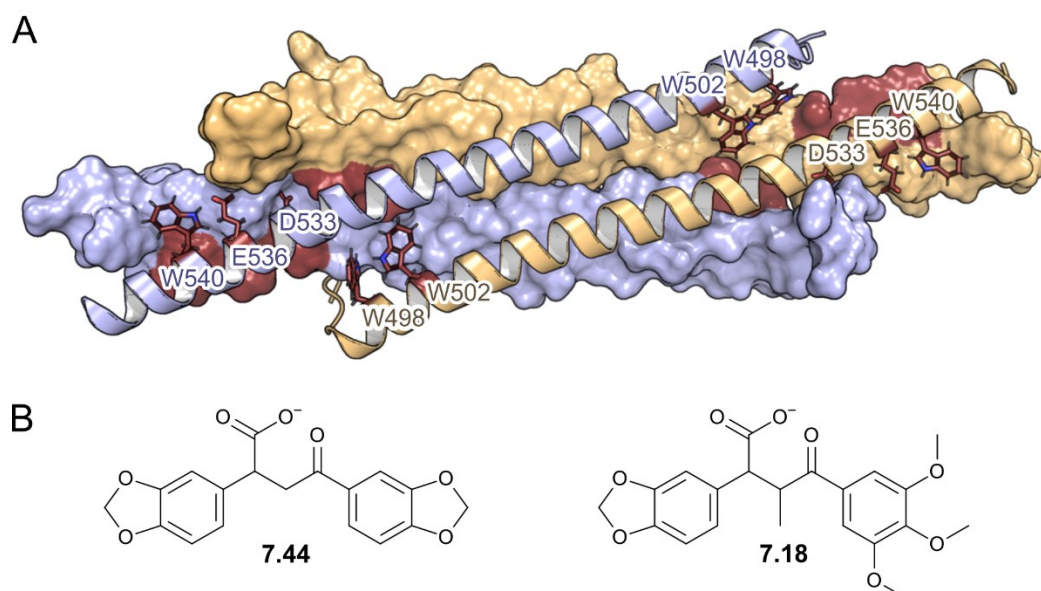

Figure 15. The tetrameric NHR2 domain (PDB ID: 1wq6). A. The homo-tetramer is a dimer of dimers. One dimer is shown in surface representation, while for the other the helices are shown. The monomers of the same color are in parallel. The hot spot residues are shown in red sticks and labeled. **B.** The compounds 7.44 and 7.18 which were screened to mimic the hotspot residues in the tetramerization interface of NHR2.

5.2 Interactions of 7.44 with tetrameric NHR2

To study how 7.44 elicits its effect on the tetrameric NHR2 domain on a structural level, we performed MD simulations of the tetrameric NHR2 domain (PDB ID: 1wq6) in the presence of 7.44 [*]. Overall, 35 replicate simulations of 1 μs length were performed leading to a cumulative simulation time of 35 μs. In these simulations, no biasing force was applied to any of the molecules. In all trajectories multiple events of 7.44 binding and unbinding were observed.

For a first inspection, we defined binding as the distance between any heavy atom of NHR2 and any heavy atom of 7.44 being less than 4 Å. For those "bound poses" we then calculated their respective occupancy, highlighting preferred binding epitopes of 7.44 on the NHR2 tetramer. In total, five densities > 0.5 % Å^{-3} are observed (Figure 16). Considering the rotational symmetry of the NHR2 tetramer these correspond to three distinct binding epitopes. The most densely populated binding epitope (**I**) is formed between W502 on A and R528 on B[†], and
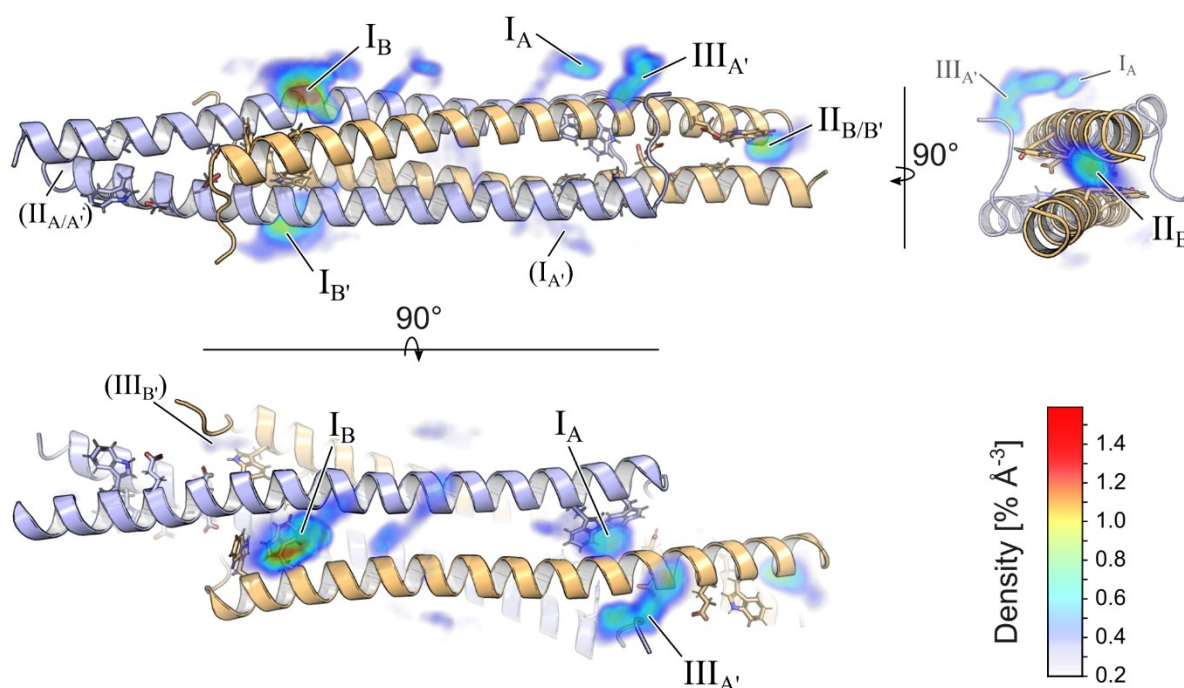

Figure 16. Grid densities of 7.44 interacting with tetrameric NHR2. The three distinct binding epitopes are labeled as **I**, **II**, and **III**. The indices are used to distinguish congruent epitopes and refer to the main monomer, the epitope is associated with (*vide infra*). For epitopes where the labels are written in parentheses, only low occupancy densities of < 0.5 % Å^{-3} are observed.

---

[*] The simulations were set up and performed by Dr. Benedikt Frieg.

[†] To refer to the monomers of the NHR2 tetramer and their relative location to each other, the nomenclature introduced in section 1.4.1 is used. Accordingly, A/B and A'/B' refer to the antiparallel monomers that form the dimers. The tetramer is then formed by the primed and unprimed dimer A/B//B'/A', where the same letters denote monomers that are in parallel to each other.

7.44 binding to this epitope is observed in all four of its congruent areas, though the grid densities differ. The second binding epitope (**II**) is formed by the C-termini of the two parallel monomers A and A'. Here, binding is observed for the identical site on B and B' as well, though the grid occupancy densities also differ between the two sites. Finally, a third epitope (**III**) is observed between the unstructured N-terminus of a monomer A and the central part of monomer B'. However, since the N-terminus is not completely resolved in the crystal structure [212], it is unlikely that this interface would form and be accessible in the full-length fusion protein *in vivo*. Thus, we further focused on studying the binding mode of 7.44 to the epitopes **I** and **II**.

To further characterize the binding mode of 7.44 to these epitopes binary interaction fingerprints were calculated for each frame of the MD trajectories (Figure 17). These fingerprints indicate which residues of NHR2 the compound forms contacts with (here again an interaction was defined as heavy atom-heavy atom distance < 4.0 Å between NHR2 and 7.44, respectively). We excluded all frames where 7.44 interacts with less than five different residues of NHR2, as those are likely unbound or transiently bound states. To account for the internal symmetry of NHR2, the fingerprints were then transformed to a canonical orientation such that monomer A always forms the most N-terminal contact(s) (Figure 17B). Finally, the resulting symmetry-normalized interaction fingerprints were clustered using a hierarchical clustering algorithm and a Jaccard distance-cutoff of 0.35. The two largest clusters directly correspond to the binding epitopes **I** and **II** containing 12,395 and 8,513 frames, respectively.

For each of the clusters, representative binding modes can be extracted, showing how 7.44 interacts with the NHR2 tetramer (e.g., Figure 17D-E). Interestingly, for both epitopes **I** and **II**, the compound forms interactions with a hot spot tryptophane residue (**I**: W502; **II**: W540). These interactions are primarily mediated by one of the 1,3-benzodioxole moieties, which intercalates between the monomers A/B (**I**) and monomers A/A' (**II**), respectively.

Still, the epitopes **I** and **II** differ considerably from the original model, 7.44 was screened on [270]. This is mostly due to the fact, that the model was generated under the assumption of a complete dissociation of the tetramer, which was not observed during the simulations. Considering the experimentally determined K_D of the NHR2 tetramer of 11.3 ±1.81 μM [272] and assuming an association rate constant (k_{on}) in the range 10^5 to 10^7 $M^{-1} s^{-1}$ [273], the dissociation rate constant (k_{off}) for the tetramer would lie in the range of 1 to 100 s^{-1}, which is at least four orders of magnitude higher than the length of the performed simulations. However, the interaction of 7.44 and W540 observed in epitope **II** is similar to the interaction proposed by the original
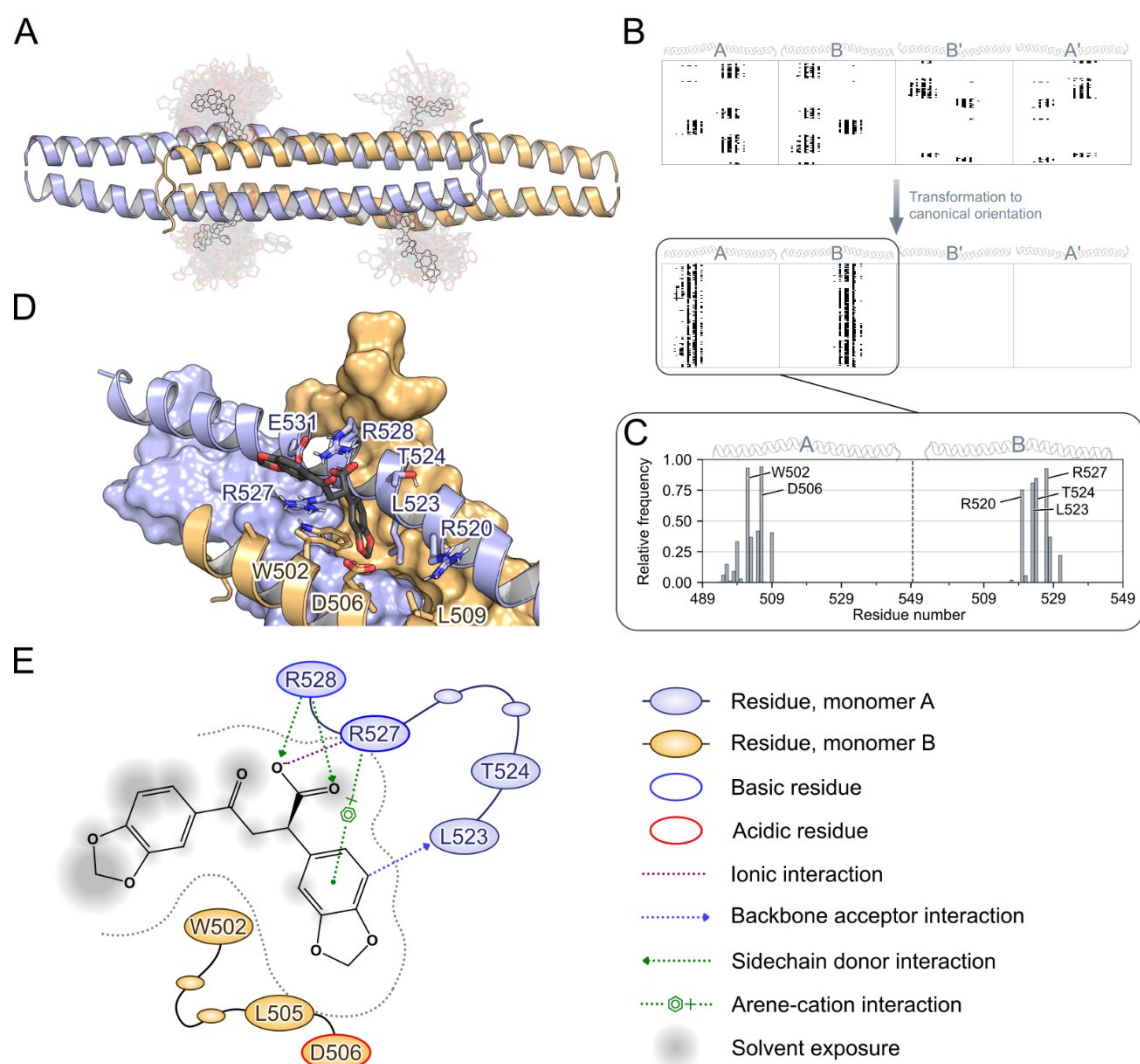
Figure 17. Clustering of the interaction fingerprints performed on the cluster corresponding to the binding epitope I. A. Due to the rotational symmetry of NHR2 the four binding sites shown, constitute identical binding epitopes. For each site a representative binding pose (outline) and a set of individual binding poses is shown. **B.** On top the binary contact fingerprints are depicted for all frames of the cluster. Each line represents a single frame with black dots showing single-residue interactions. Note, that those frames are not necessarily consecutive. By transforming the fingerprints to a canonical representation (i.e., the complex will be "rotated" such that the most N-terminal contact is formed to helix A) the similarities within the cluster become apparent. **C.** By averaging over the symmetry-normalized fingerprints, the frequency of individual interactions in the cluster can be identified. **D.** A representative binding pose for cluster 1, extracted from the most populated of the four congruent epitopes. The 1,3-benzodioxole moiety enters in a hydrophobic grove formed by W502, L505, L509, and L523'. At the same time, the carboxyl group interacts with R527 and R528. **E.** 2-dimensional representation of the binding pose shown in D. The graphic was generated with MOE [274] and modified to match the color scheme of the monomers throughout this chapter.

model. Thus, this state could represent an intermediary pose towards the originally proposed pose, which can only be assumed following a spontaneous dissociation of the tetramer.

5.3 Conclusion and significance

In this study, the compound 7.44 was characterized by biophysical assays with respect to its effect on the NHR2 domain. Furthermore, we studied the binding of 7.44 to NHR2 tetramer by large-scale unbiased ligand diffusion simulations.

By mapping occupancy densities of 7.44 on the NHR2 tetramer, preferred binding epitopes were identified. Two of the three discussed epitopes are likely accessible in the full-length RUNX1-ETO fusion protein, making them probable interaction sites for 7.44.

To further analyze the binding of 7.44 to NHR2, an algorithmic approach to cluster the bound poses of 7.44 based on binary interaction fingerprints was developed and implemented. The use of interaction fingerprints allowed us to account for the symmetry of NHR2. Thus, in the established clustering approach identical interaction patters in congruent epitopes will be identified and clustered together, regardless of in which congruent epitope the interact was recorded.

This approach was applied to identify clusters, corresponding to the regions of high occupancy density. For those regions, representative binding modes were extracted from the clusters. Those binding modes suggested that the interactions between 7.44 and NHR2 are driven by interaction between arginines and the compound's carboxyl group, as well as between tryptophanes and the 1,3-benzodioxole group.

Following the characterization of 7.44 we continued to search for structural analogues with potentially improved biological properties. The results of this and a characterization of selected hits is described in the following **section 6**.

6 Identification and characterization of improved inhibitors of RUNX1-ETO

6.1 Background

In the prior studies, the small molecule inhibitor 7.44 was identified as a PPI inhibitor that targets the NHR2 domain of the RUNX1-ETO fusion protein [270]. In **Publication IV** we additionally characterized the compound with respect to its binding properties to the NHR2 domain. Based on these results we further set out to explore the chemical space around 7.44. The MD simulations suggested a binding model in which the 1,3-benzodioxoles interact with tryptophane residues and the carboxylic acid forms interactions with arginine residues.

To further our understanding of the importance of structural features, we performed a virtual screening for structural analogues, exploring the chemical space around 7.44. These compounds were further evaluated, by biophysical and biological assays, as well as simulation studies.

6.2 Identification and characterization of new compounds

To identify analogues of 7.44, we built a query from 7.44 in the conformation that was originally overlayed with the hot spot residues in the NHR2 tetramerization interface [270]. Based on this query we screened a prepared version of the drug-like subset of ZINC15 with ROCS [275], and ordered a manually selected subset of the top ranking compounds[*].

The ordered compounds were subsequently screened for interactions with the isolated NHR2 domain by STD-NMR experiments[†] (Table 1). As the virtual screening is limited to commercially available compounds, the purchased and tested compounds in general differ from 7.44 in multiple positions. Thus, the changes in the binding affinity observed in the STD-NMR can often not be linked to a single alteration. Still, by grouping compounds with common structural features (Figure 18), even from the multivariate data presented here, a few SAR claims can be deduced. The carboxyl group is not essential for binding and can be replaced by small aliphatic substituents (e.g., M18, M22, M23). In the aliphatic linker, the CH_2 adjacent to the 4-ketone group can be replaced by a nitrogen atom, forming an amide (e.g., M22, M23). This may lead to a loss of affinity though, if combined with a carbonyl in 1-position, probably

---

[*] The virtual screening was performed by Dr. Mohanraj Gopalswamy. The preparation of the ZINC15 database and the implementation of the scripts was done by David Bickel. The screening software ROCS was kindly provided free of charge for academic use from OpenEye.

[†] The STD-NMR experiments were performed by Dr. Mohanraj Gopalswamy.

Table 1. Compounds ordered from the virtual screening and evaluated by STD-NMR. The structures are shown in a 2D representation. Since the purchased compounds were racemic, the stereocenters in the structures are not defined. The qualitative labels in the STD-NMR column refer to the intensity changes of the [1]H-signals of the compounds. Thus, "strong" changes indicate that the compound is binding to NHR2, while compounds that do not show any changes in the signal intensity ("none") are likely not binding to NHR2. These experiments were performed by Dr. Mohanraj Gopalswamy. Due to low solubility, no values for M26 could be obtained. The compounds labeled with # are further studied by MD simulations.
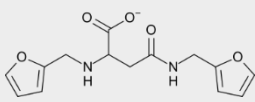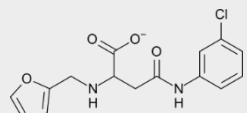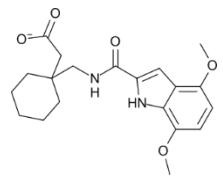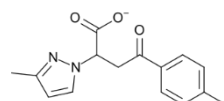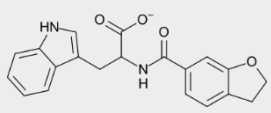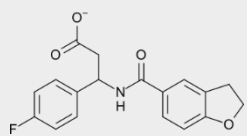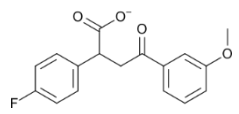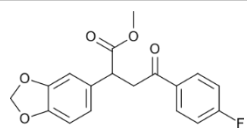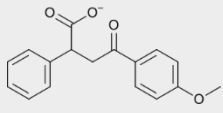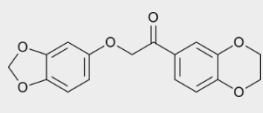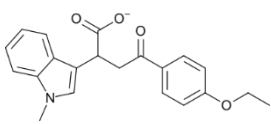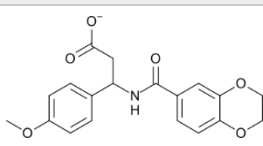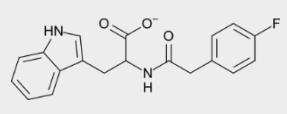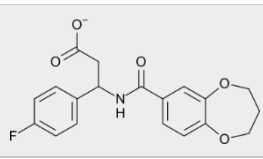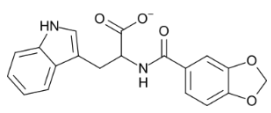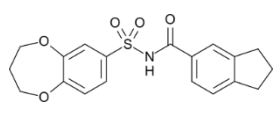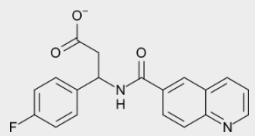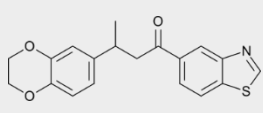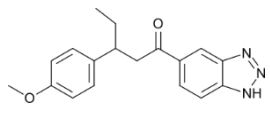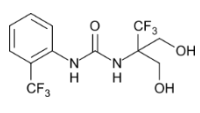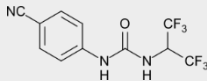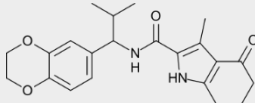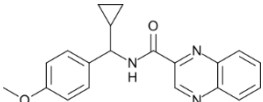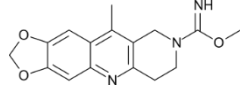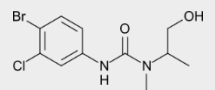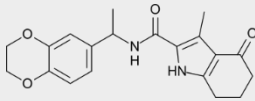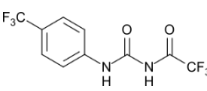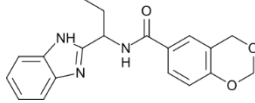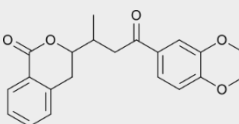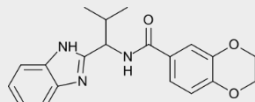
Compounds		STD-NMR signal	Compounds		STD-NMR signal
M1		none	**M2**		none
M3		strong	**M4**		none
M5		weak	**M6**		none
M7#		strong	**M8**#		strong
M9#		weak	**M10**#		strong
M11#		strong	**M12**		none
M13		weak	**M14**		none
M15		weak	**M16**		weak
M17		none	**M18**		strong
M19		strong	**M20**		strong

Table 1. continued

	Compounds	STD-NMR signal		Compounds	STD-NMR signal
M21		none	**M22**		strong
M23#		strong	**M24**		none
M25		weak	**M26**		n.d.
M27#		strong	**M28**		none
M29		strong	**M30**		none

due to the formation of an intramolecular hydrogen bond that stabilizes a conformation that is unfavorable for binding (e.g., M5, M13, M15). Between the 2- and 4-aryl substituents, no clear distinguishing traits could be identified, suggesting that the compounds can bind in two mirrored poses where the 2-aryl replaces the 4-aryl and vice versa. Still, one of the aryls should be electron-rich (e.g., M11, M18, M19) or at least have a +M substituent like an alkoxy group (e.g., M7, M10).

To study, if the compounds form similar interactions to the tetrameric NHR2 as compared to 7.44, unbiased ligand diffusion simulations were performed on seven compounds: M7, M8, M9, and M11 which show high structural analogy to 7.44; M10 and M23 which are lacking the carboxyl group; and M27 which represents a novel urea-based scaffold. The MD simulations were performed in analogy to the simulations on 7.44, presented in **section 5** (**Publication IV**). For each of the compounds twenty independent starting conformations were simulated for 1 μs, accumulating 20 μs of MD simulations per compound (140 μs in total).

For all compounds, their bound states were mapped on the NHR2 tetramer, and the relative occupancy was calculated (Figure 19A-G). Overall, the same binding epitopes – **I**, **II**, and **III** – as for 7.44 were detected. To quantify the binding to these areas, the fingerprint-based clustering approach described before (**section 5.2**) was used. This showed that the negatively charged compounds M7, M9, M11, and M27 preferably encounter the NHR2 tetramer in

Figure 18. Systematic overview of the modifications in the screened analogues of 7.44. The intensity change observed in the STD-NMR experiments are labeled strong/weak/none. The group R refers to aliphatic substituents for the carboxylic acid moiety, including methyl, ethyl, *i*-propyl, and cyclopropyl.

49
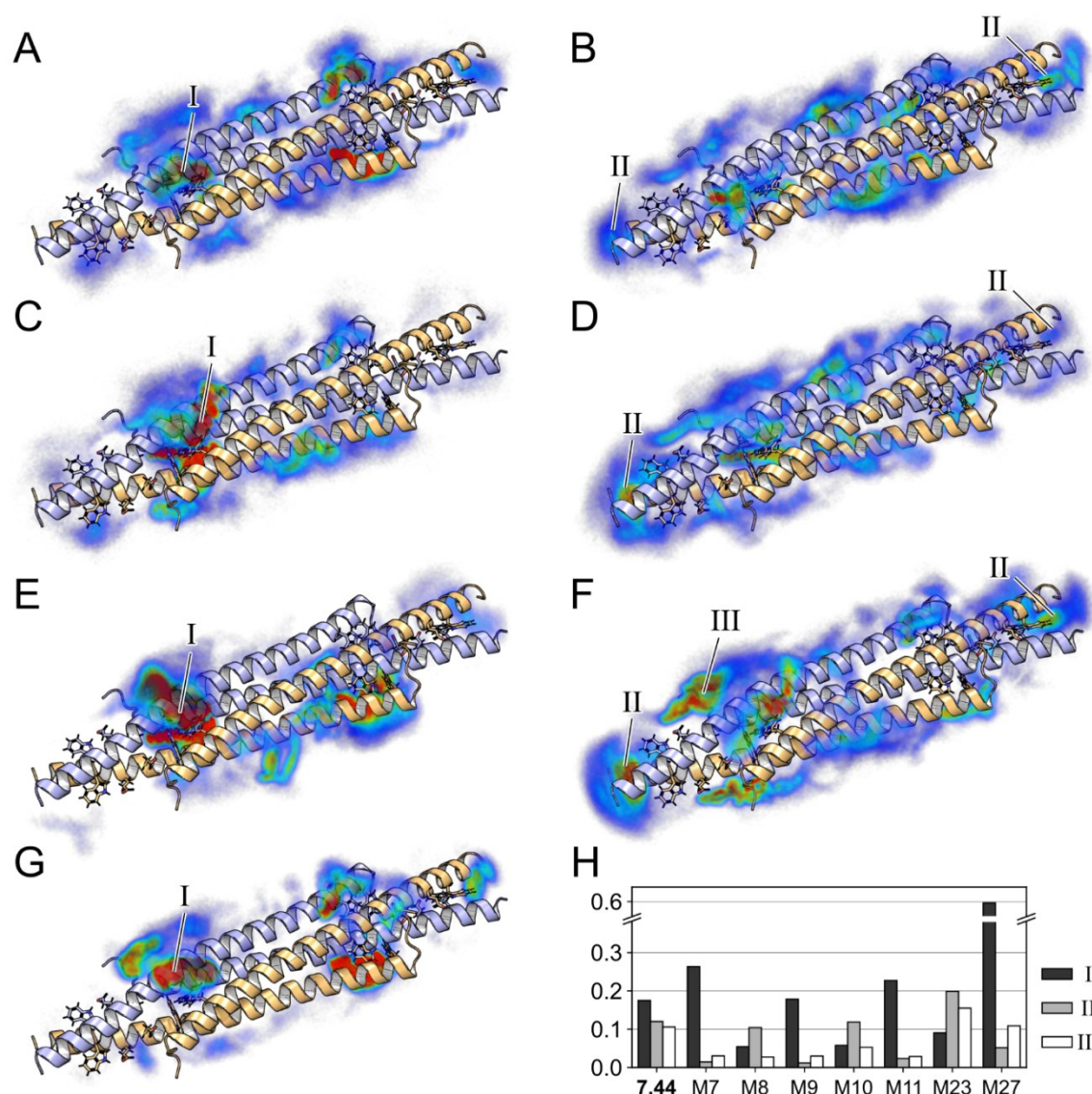
Figure 19. Grid density and clustering analysis of the compounds M7, M8, M9, M10, M11, M23, and M27. Grid densities mapped on the structure of the tetrameric NHR2 domain (PDB ID: 1wq6). The most prominent epitopes are indicated and labeled. **A.** M7. **B.** M8. **C.** M9. **D.** M10. **E.** M11. **F.** M23. **G.** M27. **H.** The graphic shows the relative frequency of the largest cluster corresponding to the epitopes **I**, **II**, and **III**, respectively. Results for 7.44 are taken from the simulations in **section 5**.

epitope **I**, where the compounds can form interactions with R527 and R528. In contrast, for the neutral compounds M8, M10 and M23 the ratios between the epitopes **I**, **II**, and **III** are more even, with **II** being the most frequented binding epitope. This suggests that negatively charged and neutral compounds interact with the NHR2 domain differently, and thus, might elicit different effects in the cell or differ in their potency.

Finally, we tested the compounds that showed strong signals in the STD-NMR in a cell-based proliferation assay [*]. The compounds M5 and M6 were included as negative controls. The compounds were tested in three cell lines of which two cell lines express the *RUNX1-ETO* fusion gene (Kasumi and SKNO-1), and one is a BCR-ABL-positive leukemia cell line (K562). All compounds that were tested, except for the negative controls M5 and M6 showed higher antiproliferative effects than 7.44 (Figure 20). Interestingly, the neutral compounds M23 and M10 are the most potent compounds, while still having some selectivity for the RUNX1-ETO-positive cells. This might indicate that compounds binding in epitope **II** elicit a higher antiproliferative effect, than compounds that preferably bind to epitope **I**.

6.3 Conclusion and significance

In prior studies the compound 7.44 was shown to interact with the NHR2 domain of the RUNX1-ETO fusion protein, and interfere with its (**section 5**, **Publication IV**) oncogenic effect [270,271]. To further our understanding about which structural features of 7.44 enable this effect, we started a virtual screening campaign.

On basis of a shape-based virtual screening, we identified a set of 30 analogues of 7.44. Among these are compounds that share high structural analogy with 7.44, and compounds which can assume a 7.44-like conformation and mimic its interactions, but do not share a common molecular scaffold.
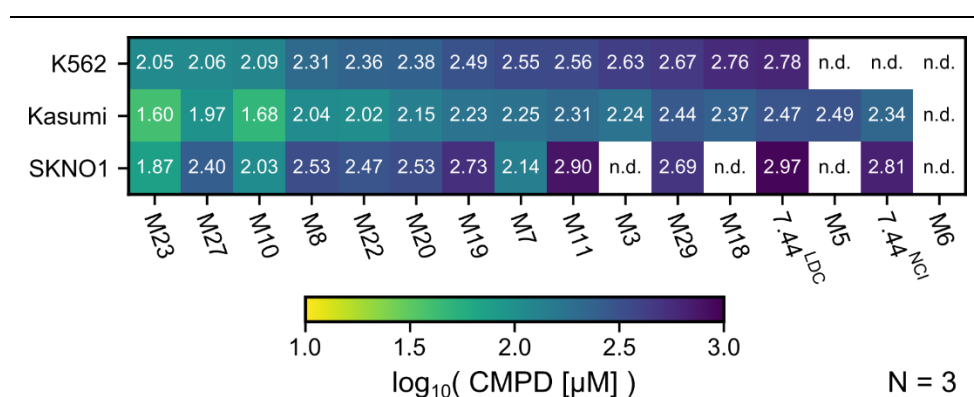
Figure 20. Cell toxicity assay. K562 is a BCR-ABL-positive leukemia cell line, while Kasumi and SKNO-1 are RUNX1-ETO-positive. The values correspond to the decadic logarithm of the IC_{50} in µM. For the compounds labeled n.d., the IC_{50} is > 1,000 µM. For 7.44, two sources of compound were used.

---

[*] The CellTiter-Glo® experiments were performed by Niklas Dienstbier and Jia-Wey Tu in the research group of Dr. Sanil Bhatia.

In STD-NMR experiments 12 (18) of the 30 screened compounds show strong (strong or weak) intensity shifts, indicating that these compounds bind to the NHR2 domain. This constitutes a hit rate of 40% (60%) for the first batch of tested compounds. Based on the STD-NMR results, a preliminary SAR study was performed. Though, this study is limited by the commercial availability very close analogues of 7.44, still, structural determinants of the action of 7.44-like compounds could be deduced and are to be tested by further studies.

In MD simulations of the unbiased diffusion, two distinct interaction patterns could be identified. Negatively charged compounds preferably interact with the NHR2 tetramer in a site formed by R527, R528, and W502. In contrast, the uncharged compounds we simulated intercalated in the C-termini of the NHR2 monomers, forming interactions with W540.

Finally, the screening hits were evaluated for their anti-proliferative properties in a cell viability assay. Here, for all screened compounds an improvement over the template compound 7.44 was seen. The uncharged compounds M23 and M10 showed very promising antiproliferative effects, while still maintaining moderate selectivity for RUNX1-ETO-positive cells.

7 Summary and perspectives

Over the course of this thesis, studies to three independent projects were performed. The common objective was to explore novel mechanisms of action to counter therapy resistance in solid and humoral tumors. The first project was centered around the lead compound PXA, while the other two projects were target-centered, focusing on HSP90, which is a promoter of proliferation in many cancers, and the RUNX1-ETO fusion protein, which is directly linked to the etiology of a subset of AML.

The natural product PXA was described before to induce apoptosis in various cancer cells. This was shown to be associated with the depolarization of the mitochondrial membrane potential which in turn lead to fission of the mitochondrial network [54,276]. Here, the hypothesis of PXA acting as protonophoric decoupler across the IMM is explored. The computations suggest that the natural product can cross the membrane in the neutral and singly deprotonated state, carrying protons along the concentration gradient into the mitochondrial matrix (**Publication II**). Thus, our calculations align with the hypothesis of PXA acting as a protonophore across the IMM, though experimental evidence is yet to be provided. In a recent publication, the mitochondrial enzyme CPS1 was identified as a target of PXA [261]. This provides an alternative mode of action for the natural product. However, the demonstrated effect on the CPS1 does not explain the observed depletion of the mitochondrial membrane potential [54,276]. Thus, PXA likely acts on multiple sites in the cell, leading to its unique activity. To further the development of PXA or its derivatives as a new anticancer drug, its primary mode of action as well as off-targets need to be elucidated.

The molecular chaperone HSP90 promotes proliferation and cell survival in cancer cells. Thus, it was targeted by researchers in an attempt to develop new targeted anti-cancer drugs. However, at this point virtually all clinical studies on HSP90 inhibitors have been performed on competitive inhibitors of the N-terminal ATP binding site, which are potent anti-cancer drugs, but elicit dose-limiting toxicities. Consequently, no HSP90 inhibitors have been approved by the FDA or EMA so far. We reviewed the state of the art of HSP90 inhibitor development, focusing on non-N-terminally acting compounds (**Publication I**). We further studied LSK82 on a molecular level. The compound is a novel, first-of-class C-terminal HSP90 inhibitor, which was designed to mimic the helix 5 in the C-terminal dimerization interface. In the simulations LSK82 exhibited a preference for binding in the C-terminal dimerization interface. Moreover, from the simulations a binding mode could be extracted, where LSK82 binds in a fashion similar to the helix 5 of the second dimer (**Publication III**). LSK82 however

is still characterized by a poor solubility. Thus, further studies are being performed to explore chemical scaffolds that can form identical interactions to LSK82, while exhibiting more favorable physicochemical properties. Moreover, the bound pose of LSK82 will be used in a virtual screening to identify new scaffolds that could replace the bulky trispyrimidone.

While an upregulation of HSP90 is found in many types of cancer as a mechanism that promotes cancer proliferation, the RUNX1-ETO fusion protein is only found in a subset of AML associated with the t(8;21) translocation. The compound 7.44 was identified as a modulator of NHR2-mediated tetramerization of the RUNX1-ETO fusion protein. In **Publication IV**, we further characterized the interaction of 7.44 with NHR2 by biophysical studies and MD simulations. In the MD simulations, two likely binding epitopes of 7.44 were identified. We further performed a template-based virtual screening to explore the chemical space around 7.44. This yielded a set of analogous structures, which were screened by STD-NMR with respect to their binding to NHR2. About half of the screened compounds were confirmed binders and were further analyzed with respect to their antiproliferative properties. This yielded compounds with significantly improved anti-proliferative properties in comparison to 7.44. Furthermore, in MD simulations, the compounds were shown to occupy similar binding epitopes. Moreover, a preliminary SAR study gave first insights into structural features of 7.44 that are crucial to its modulation of the NHR2. In the next steps, 7.44 will be replaced as a lead compound by one of its more active derivatives. For this compound, it would be highly desirable to obtain experimental structural information to validate the binding mode obtained from the MD simulations. In addition, the established SAR will guide the screening for novel inhibitors of the RUNX1-ETO fusion protein, while being iteratively expanded.

8 Acknowledgements

9 Literature

1. National cancer control programmes: Policies and managerial guidelines: World Health Organization; 2002.

2. Salaverry O. La etimología del cáncer y su curioso curso histórico. *Rev Peru Med Exp Salud Publica* 2013; **30**(1): 137-41.

3. Karpozilos A, Pavlidis N. The treatment of cancer in Greek antiquity. *Eur J Cancer* 2004; **40**(14): 2033-40.

4. Hajdu SI. A note from history: Landmarks in history of cancer, part 1. *Cancer* 2011; **117**(5): 1097-102.

5. Omram AR. The epidemiologic transition: A theory of the epidemiology of population change. *Bull World Health Organ* 2001; **79**: 161-70.

6. Mackenbach JP. The epidemiologic transition theory. *J Epidemiol Community Health* 1994; **48**(4): 329.

7. Sung H, Ferlay J, Siegel RL*, et al.* Global cancer statistics 2020: GLOBOCAN estimates of incidence and mortality worldwide for 36 cancers in 185 countries. *CA: Cancer J Clin* 2021.

8. Ferlay J, Ervik M, Lam F*, et al.* Global cancer observatory: Cancer today. 2020. https://gco.iarc.fr/today (accessed 19 Jan 2021).

9. WHO report on cancer: setting priorities, investing wisely and providing care for all. Geneva: World Health Organization; 2020.

10. Arnold M, Karim-Kos HE, Coebergh JW*, et al.* Recent trends in incidence of five common cancers in 26 European countries since 1988: Analysis of the European Cancer Observatory. *Eur J Cancer* 2015; **51**(9): 1164-87.

11. Ferlay J, Ervik M, Lam F*, et al.* Global cancer observatory: Cancer tomorrow. 2020. https://gco.iarc.fr/tomorrow (accessed 19 Jan 2021).

12. De Palma M, Hanahan D. The biology of personalized cancer medicine: facing individual complexities underlying hallmark capabilities. *Mol Oncol* 2012; **6**(2): 111-27.

13. Hanahan D, Weinberg RA. The hallmarks of cancer. *Cell* 2000; **100**(1): 57-70.

14. Hanahan D, Weinberg RA. Hallmarks of cancer: The next generation. *Cell* 2011; **144**(5): 646-74.

15. Morrison W. Cancer chemotherapy: An annotated history. *J Vet Intern Med* 2010; **24**(6): 1249-62.

16. DeVita VT, Jr., Chu E. A history of cancer chemotherapy. *Cancer Res* 2008; **68**(21): 8643-53.

17. Chabner BA, Roberts TG. Chemotherapy and the war on cancer. *Nat Rev Cancer* 2005; **5**(1): 65-72.

18. Colomer R, Mondejar R, Romero-Laorden N, Alfranca A, Sanchez-Madrid F, Quintela-Fandino M. When should we order a next generation sequencing test in a patient with cancer? *EClinicalMedicine* 2020; **25**.

19. Dobosz P, Dzieciątkowski T. The Intriguing History of Cancer Immunotherapy. *Front Immunol* 2019; **10**: 2965-.

20. Gilman A. The initial clinical trial of nitrogen mustard. *Am J Surg* 1963; **105**: 574-8.

21. Siddik ZH. Cisplatin: Mode of cytotoxic action and molecular basis of resistance. *Oncogene* 2003; **22**(47): 7265-79.

22. Emadi A, Jones RJ, Brodsky RA. Cyclophosphamide and cancer: Golden anniversary. *Nat Rev Clin Oncol* 2009; **6**(11): 638.

23. Dong Q, Barsky D, Colvin ME*, et al.* A structural basis for a phosphoramide mustard-induced DNA interstrand cross-link at 5'-d(GAC). *Proc Natl Acad Sci USA* 1995; **92**(26): 12170.

24. Hamada A, Kawaguchi T, Nakano M. Clinical pharmacokinetics of cytarabine formulations. *Clin Pharmacokinet* 2002; **41**(10): 705-18.

25. Allegra CJ, Hoang K, Yeh GC, Drake JC, Baram J. Evidence for direct inhibition of de novo purine synthesis in human MCF-7 breast cells as a principal mode of metabolic inhibition by methotrexate. *J Biol Chem* 1987; **262**(28): 13520-6.

26. Rowinsky M, Eric K. The development and clinical utility of the taxane class of antimicrotubule chemotherapy agents. *Annu Rev Med* 1997; **48**(1): 353-74.

27. Jordan MA, Himes RH, Wilson L. Comparison of the effects of vinblastine, vincristine, vindesine, and vinepidine on microtubule dynamics and cell proliferation in vitro. *Cancer Res* 1985; **45**(6): 2741.

28. Xu G, McLeod HL. Strategies for enzyme/prodrug cancer therapy. *Clin Cancer Res* 2001; **7**(11): 3314.

29. Ring A, Dowsett M. Mechanisms of tamoxifen resistance. *Endocr-Relat Cancer* 2004; **11**(4): 643-58.

30. Miller WR. Aromatase inhibitors: Mechanism of action and role in the treatment of breast cancer. *Semin Oncol* 2003; **30**(4 Suppl 14): 3-11.

31. Chabner BA, Longo DL. Cancer chemotherapy and biotherapy: Principles and practice. Sixth edition ed: Wolters Kluwer; 2019.

32. Padma VV. An overview of targeted cancer therapy. *Biomedicine (Taipei)* 2015; **5**(4): 1-6.

33. Lee YT, Tan YJ, Oon CE. Molecular targeted therapy: Treating cancer with specificity. *Eur J Pharmacol* 2018; **834**: 188-96.

34. Deininger MWN, Druker BJ. Specific targeted therapy of chronic myelogenous leukemia with imatinib. *Pharmacol Rev* 2003; **55**(3): 401.

35. Galmarini D, Galmarini CM, Galmarini FC. Cancer chemotherapy: A critical analysis of its 60 years of history. *Crit Rev Oncol Hematol* 2012; **84**(2): 181-99.

36. Dasgupta Y, Koptyra M, Hoser G*, et al.* Normal ABL1 is a tumor suppressor and therapeutic target in human and mouse leukemias expressing oncogenic ABL1 kinases. *Blood* 2016; **127**(17): 2131-43.

37. Hantschel O, Rix U, Superti-Furga G. Target spectrum of the BCR-ABL inhibitors imatinib, nilotinib and dasatinib. *Leuk Lymphoma* 2008; **49**(4): 615-9.

38. Kalmanti L, Saussele S, Lauseker M*, et al.* Safety and efficacy of imatinib in CML over a period of 10 years: Data from the randomized CML-study IV. *Leukemia* 2015; **29**(5): 1123-32.

39. Druker BJ, Guilhot F, O'Brien SG*, et al.* Five-year follow-up of patients receiving imatinib for chronic myeloid leukemia. *N Engl J Med* 2006; **355**(23): 2408-17.

40. Hanahan D. Rethinking the war on cancer. *Lancet* 2014; **383**(9916): 558-63.

41. Haber DA, Gray NS, Baselga J. The evolving war on cancer. *Cell* 2011; **145**(1): 19-24.

42. Mansoori B, Mohammadi A, Davudian S, Shirjang S, Baradaran B. The different mechanisms of cancer drug resistance: A brief review. *Adv Pharm Bull* 2017; **7**(3): 339-48.

43. Singh IP, Ahmad F, Chatterjee D, Bajpai R, Sengar N. Natural products: Drug discovery and development. In: Poduri R, ed. Drug discovery and development: From targets and molecules to medicines; 2021: 11-65.

44. Stone MJ, Williams DH. On the evolution of functional secondary metabolites (natural products). *Mol Microbiol* 1992; **6**(1): 29-34.

45. Rodrigues T, Reker D, Schneider P, Schneider G. Counting on natural products for drug design. *Nat Chem* 2016; **8**(6): 531-41.

46. Newman DJ, Cragg GM. Natural products as sources of new drugs from 1981 to 2014. *J Nat Prod* 2016; **79**(3): 629-61.

47. Lachance H, Wetzel S, Kumar K, Waldmann H. Charting, navigating, and populating natural product chemical space for drug discovery. *J Med Chem* 2012; **55**(13): 5989-6001.

48. Morrison KC, Hergenrother PJ. Natural products as starting points for the synthesis of complex and diverse compounds. *Nat Prod Rep* 2014; **31**(1): 6-14.

49. Hann MM, Leach AR, Harper G. Molecular complexity and its impact on the probability of finding leads for drug discovery. *J Chem Inf Comp Sci* 2001; **41**(3): 856-64.

50. Shelat AA, Guy RK. Scaffold composition and biological relevance of screening libraries. *Nat Chem Biol* 2007; **3**(8): 442-6.

51. Macarron R. How dark is HTS dark matter? *Nat Chem Biol* 2015; **11**(12): 904-5.

52. Wassermann AM, Lounkine E, Hoepfner D*, et al.* Dark chemical matter as a promising starting point for drug lead discovery. *Nat Chem Biol* 2015; **11**(12): 958.

53. Frank M, Niemann H, Bohler P*, et al.* Phomoxanthone A - From mangrove forests to anticancer therapy. *Curr Med Chem* 2015; **22**(30): 3523-32.

54. Böhler P, Stuhldreier F, Anand R*, et al.* The mycotoxin phomoxanthone A disturbs the form and function of the inner mitochondrial membrane. *Cell Death Dis* 2018; **9**(3): 286.

55. Rönsberg D, Debbab A, Mandi A*, et al.* Pro-apoptotic and immunostimulatory tetrahydroxanthone dimers from the endophytic fungus Phomopsis longicolla. *J Org Chem* 2013; **78**(24): 12409-25.

56. Metz A, Ciglia E, Gohlke H. Modulating protein-protein interactions: from structural determinants of binding to druggability prediction to application. *Curr Pharm Des* 2012; **18**(30): 4630-47.

57. Smith MC, Gestwicki JE. Features of protein-protein interactions that translate into potent inhibitors: topology, surface area and affinity. *Expert Rev Mol Med* 2012; **14**: e16.

58. Vidal M, Cusick Michael E, Barabási A-L. Interactome networks and human disease. *Cell* 2011; **144**(6): 986-98.

59. Kar G, Gursoy A, Keskin O. Human cancer protein-protein interaction network: a structural persAective. *PLoS Comput Biol* 2009; **5**(12): e1000601.

60. Jonsson PF, Bates PA. Global topological features of cancer proteins in the human interactome. *Bioinformatics* 2006; **22**(18): 2291-7.

61. Scott DE, Bayly AR, Abell C, Skidmore J. Small molecules, big targets: drug discovery faces the protein–protein interaction challenge. *Nat Rev Drug Discov* 2016; **15**(8): 533-50.

62. Conte LL, Chothia C, Janin J. The atomic structure of protein-protein recognition sites. *J Mol Biol* 1999; **285**(5): 2177-98.

63. Jones S, Thornton JM. Principles of protein-protein interactions. *Proc Natl Acad Sci USA* 1996; **93**(1): 13-20.

64. DeLano WL. Unraveling hot spots in binding interfaces: Progress and challenges. *Curr Opin Struct Biol* 2002; **12**(1): 14-20.

65. Moreira IS, Fernandes PA, Ramos MJ. Hot spots—A review of the protein–protein interface determinant amino-acid residues. *Proteins* 2007; **68**(4): 803-12.

66. Clackson T, Wells JA. A hot spot of binding energy in a hormone-receptor interface. *Science* 1995; **267**(5196): 383-6.

67. Bogan AA, Thorn KS. Anatomy of hot spots in protein interfaces. *J Mol Biol* 1998; **280**(1): 1-9.

68. Bickel D, Gohlke H. C-terminal modulators of heat shock protein of 90 kDa (HSP90): State of development and modes of action. *Bioorg Med Chem* 2019; **27**(21): 115080.

69. Schopf FH, Biebl MM, Buchner J. The HSP90 chaperone machinery. *Nat Rev Mol Cell Biol* 2017; **18**(6): 345.

70. Ritossa F. Discovery of the heat shock response. *Cell Stress Chaperones* 1996; **1**(2): 97-8.

71. Ritossa F. A new puffing pattern induced by temperature shock and DNP in Drosophila. *Experientia* 1962; **18**(12): 571-3.

72. Lindquist S. The heat-shock response. *Annu Rev Biochem* 1986; **55**: 1151-91.

73. Schlesinger MJ. Heat-shock proteins. *J Biol Chem* 1990; **265**(21): 12111-4.

74. Lindquist S, Craig EA. The heat-shock proteins. *Annu Rev Genet* 1988; **22**: 631-77.

75. Wu J, Liu T, Rios Z, Mei Q, Lin X, Cao S. Heat shock proteins and cancer. *Trends Pharmacol Sci* 2017; **38**(3): 226-56.

76. Whitesell L, Bagatell R, Falsey R. The stress response: Implications for the clinical development of Hsp90 inhibitors. *Curr Cancer Drug Targets* 2003; **3**(5): 349-58.

77. Ellis J. Proteins as molecular chaperones. *Nature* 1987; **328**(6129): 378-9.

78. Hartl FU. Molecular chaperones in cellular protein folding. *Nature* 1996; **381**(6583): 571-80.

79. Hartl FU, Bracher A, Hayer-Hartl M. Molecular chaperones in protein folding and proteostasis. *Nature* 2011; **475**(7356): 324-32.

80. Streicher JM. The role of heat shock proteins in regulating receptor signal transduction. *Mol Pharmacol* 2019; **95**(5): 468.

81. Richter K, Buchner J. Hsp90: Chaperoning signal transduction. *J Cell Physiol* 2001; **188**(3): 281-90.

82. Dittmar KD, Demady DR, Stancato LF, Krishna P, Pratt WB. Folding of the glucocorticoid receptor by the heat shock protein (hsp) 90-based chaperone machinery: The role of p23 is to stabilize receptor·hsp90 heterocomplexes formed by hsp90·p60·hsp70. *J Biol Chem* 1997; **272**(34): 21213-20.

83. Nathan DF, Lindquist S. Mutational analysis of Hsp90 function: interactions with a steroid receptor and a protein kinase. *Mol Cell Biol* 1995; **15**(7): 3917-25.

84. Yang Z, Sun W, Hu K. Molecular mechanism underlying adenosine receptor-mediated mitochondrial targeting of protein kinase C. *Biochim Biophys Acta - Mol Cell Res* 2012; **1823**(4): 950-8.

85. Young JC, Hoogenraad NJ, Hartl FU. Molecular chaperones Hsp90 and Hsp70 deliver preproteins to the mitochondrial import receptor Tom70. *Cell* 2003; **112**(1): 41-50.

86. Pirkkala L, Sistonen L. Heat shock proteins (HSPs): Structure, function and genetics. *e LS* 2001.

87. Chatterjee S, Burns TF. Targeting heat shock proteins in cancer: A promising therapeutic approach. *Int J Mol Sci* 2017; **18**(9): 1978.

88. Csermely P, Schnaider T, Söti C, Prohászka Z, Nardai G. The 90-kDa molecular chaperone family: Structure, function, and clinical applications. A comprehensive review. *Pharmacol Ther* 1998; **79**(2): 129-68.

89. Welch WJ, Feramisco JR. Purification of the major mammalian heat shock proteins. *J Biol Chem* 1982; **257**(24): 14949-59.

90. Schopf FH, Biebl MM, Buchner J. The HSP90 chaperone machinery. *Nat Rev Mol Cell Biol* 2017; **18**(6): 345-60.

91. Taipale M, Jarosz DF, Lindquist S. HSP90 at the hub of protein homeostasis: emerging mechanistic insights. *Nat Rev Mol Cell Biol* 2010; **11**(7): 515-28.

92. Wayne N, Bolon DN. Dimerization of Hsp90 is required for in vivo function. Design and analysis of monomers and dimers. *J Biol Chem* 2007; **282**(48): 35386-95.

93. Minami Y, Kawasaki H, Miyata Y, Suzuki K, Yahara I. Analysis of native forms and isoform compositions of the mouse 90-kDa heat shock protein, HSP90. *J Biol Chem* 1991; **266**(16): 10099-103.

94. Ali MMU, Roe SM, Vaughan CK, *et al.* Crystal structure of an Hsp90–nucleotide–p23/Sba1 closed chaperone complex. *Nature* 2006; **440**(7087): 1013-7.

95. Prodromou C, Roe SM, O'Brien R, Ladbury JE, Piper PW, Pearl LH. Identification and structural characterization of the ATP/ADP-binding site in the Hsp90 molecular chaperone. *Cell* 1997; **90**(1): 65-75.

96. Dutta R, Inouye M. GHKL, an emergent ATPase/kinase superfamily. *Trends Biochem Sci* 2000; **25**(1): 24-8.

97. Jahn M, Rehn A, Pelz B, *et al.* The charged linker of the molecular chaperone Hsp90 modulates domain contacts and biological function. *Proc Natl Acad Sci USA* 2014; **111**(50): 17881.

98. Tsutsumi S, Mollapour M, Prodromou C, *et al.* Charged linker sequence modulates eukaryotic heat shock protein 90 (Hsp90) chaperone activity. *Proc Natl Acad Sci USA* 2012; **109**(8): 2937.

99. Verba KA, Wang RY, Arakawa A, *et al.* Atomic structure of Hsp90-Cdc37-Cdk4 reveals that Hsp90 traps and stabilizes an unfolded kinase. *Science* 2016; **352**(6293): 1542-7.

100. Meyer P, Prodromou C, Hu B, *et al.* Structural and functional analysis of the middle segment of Hsp90: implications for ATP hydrolysis and client protein and cochaperone interactions. *Mol Cell* 2003; **11**(3): 647-58.

101. Minami Y, Kimura Y, Kawasaki H, Suzuki K, Yahara I. The carboxy-terminal region of mammalian HSP90 is required for its dimerization and function in vivo. *Mol Cell Biol* 1994; **14**(2): 1459.

102. Harris SF, Shiau AK, Agard DA. The crystal structure of the carboxy-terminal dimerization domain of htpG, the Escherichia coli Hsp90, reveals a potential substrate binding site. *Structure* 2004; **12**(6): 1087-97.

103. Young JC, Obermann WM, Hartl FU. Specific binding of tetratricopeptide repeat proteins to the C-terminal 12-kDa domain of hsp90. *J Biol Chem* 1998; **273**(29): 18007-10.

104. Ratzke C, Mickler M, Hellenkamp B, Buchner J, Hugel T. Dynamics of heat shock protein 90 C-terminal dimerization is an important part of its conformational cycle. *Proc Natl Acad Sci USA* 2010; **107**(37): 16101-6.

105. Prodromou C, Panaretou B, Chohan S, *et al.* The ATPase cycle of Hsp90 drives a molecular 'clamp' via transient dimerization of the N-terminal domains. *EMBO J* 2000; **19**(16): 4383.

106. Sreedhar AS, Kalmar E, Csermely P, Shen YF. Hsp90 isoforms: functions, expression and clinical importance. *FEBS Lett* 2004; **562**(1-3): 11-5.

107. Chen B, Piel WH, Gui L, Bruford E, Monteiro A. The HSP90 family of genes in the human genome: Insights into their divergence and evolution. *Genomics* 2005; **86**(6): 627-37.

108. Gupta RS. Phylogenetic analysis of the 90 kD heat shock family of protein sequences and an examination of the relationship among animals, plants, and fungi species. *Mol Biol Evol* 1995; **12**(6): 1063-73.

109. Taipale M, Tucker G, Peng J, *et al.* A quantitative chaperone interaction network reveals the architecture of cellular protein homeostasis pathways. *Cell* 2014; **158**(2): 434-48.

110. Taherian A, Krone PH, Ovsenek N. A comparison of Hsp90α and Hsp90β interactions with cochaperones and substrates. *Biochem Cell Biol* 2008; **86**(1): 37-45.

111. Chadli A, Felts SJ, Toft DO. GCUNC45 is the first Hsp90 co-chaperone to show α/β isoform specificity. *J Biol Chem* 2008; **283**(15): 9509-12.

112. Millson SH, Truman AW, Rácz A, *et al.* Expressed as the sole Hsp90 of yeast, the α and β isoforms of human Hsp90 differ with regard to their capacities for activation of certain client proteins, whereas only Hsp90β generates sensitivity to the Hsp90 inhibitor radicicol. *FEBS J* 2007; **274**(17): 4453-63.

113. Workman P, Burrows F, Neckers L, Rosen N. Drugging the cancer chaperone HSP90: Combinatorial therapeutic exploitation of oncogene addiction and tumor stress. *Ann N Y Acad Sci* 2007; **1113**: 202-16.

114. Whitesell L, Lindquist SL. HSP90 and the chaperoning of cancer. *Nat Rev Cancer* 2005; **5**(10): 761-72.

115. Jaeger AM, Whitesell L. HSP90: Enabler of cancer adaptation. *Annu Rev Cancer Biol* 2019; **3**(1): 275-97.

116. Lianos GD, Alexiou GA, Mangano A, *et al.* The role of heat shock proteins in cancer. *Cancer Lett* 2015; **360**(2): 114-8.

117. Mahalingam D, Swords R, Carew JS, Nawrocki ST, Bhalla K, Giles FJ. Targeting HSP90 for cancer therapy. *Br J Cancer* 2009; **100**(10): 1523-9.

118. Pick E, Kluger Y, Giltnane JM, *et al.* High HSP90 expression is associated with decreased survival in breast cancer. *Cancer Res* 2007; **67**(7): 2932.

119. Ciocca DR, Calderwood SK. Heat shock proteins in cancer: Diagnostic, prognostic, predictive, and treatment implications. *Cell Stress Chaperones* 2005; **10**(2): 86-103.

120. Wang J, Cui S, Zhang X, Wu Y, Tang H. High expression of heat shock protein 90 is associated with tumor aggressiveness and poor prognosis in patients with advanced gastric cancer. *PLoS One* 2013; **8**(4): e62876.

121. Thomas X, Campos L, Mounier C, *et al.* Expression of heat-shock proteins is associated with major adverse prognostic factors in acute myeloid leukemia. *Leuk Res* 2005; **29**(9): 1049-58.

122. Isaacs JS. Hsp90 as a "chaperone" of the epigenome: Insights and opportunities for cancer therapy. *Adv Cancer Res* 2016; **129**: 107-40.

123. Wang X, Song X, Zhuo W, *et al.* The regulatory mechanism of Hsp90α secretion and its function in tumor malignancy. *Proc Natl Acad Sci USA* 2009; **106**(50): 21288.

124. Eustace BK, Sakurai T, Stewart JK, *et al.* Functional proteomic screens reveal an essential extracellular role for hsp90α in cancer cell invasiveness. *Nat Cell Biol* 2004; **6**(6): 507-14.

125. Whitesell L, Mimnaugh EG, De Costa B, Myers CE, Neckers LM. Inhibition of heat shock protein HSP90-pp60v-src heteroprotein complex formation by benzoquinone ansamycins: essential role for stress proteins in oncogenic transformation. *Proc Natl Acad Sci USA* 1994; **91**(18): 8324-8.

126. Whitesell L, Shifrin SD, Schwab G, Neckers LM. Benzoquinonoid ansamycins possess selective tumoricidal activity unrelated to src kinase inhibition. *Cancer Res* 1992; **52**(7): 1721-8.

127. Sharma SV, Agatsuma T, Nakano H. Targeting of the protein chaperone, HSP90, by the transformation suppressing agent, radicicol. *Oncogene* 1998; **16**(20): 2639-45.

128. Schulte TW, Akinaga S, Soga S, *et al.* Antibiotic radicicol binds to the N-terminal domain of Hsp90 and shares important biologic activities with geldanamycin. *Cell Stress Chaperones* 1998; **3**(2): 100-8.

129. Roe SM, Prodromou C, O'Brien R, Ladbury JE, Piper PW, Pearl LH. Structural basis for inhibition of the Hsp90 molecular chaperone by the antitumor antibiotics radicicol and geldanamycin. *J Med Chem* 1999; **42**(2): 260-6.

130. Stebbins CE, Russo AA, Schneider C, Rosen N, Hartl FU, Pavletich NP. Crystal structure of an Hsp90-geldanamycin complex: Targeting of a protein chaperone by an antitumor agent. *Cell* 1997; **89**(2): 239-50.

131. Tian ZQ, Liu Y, Zhang D, *et al.* Synthesis and biological activities of novel 17-aminogeldanamycin derivatives. *Bioorg Med Chem* 2004; **12**(20): 5317-29.

132. Le Brazidec J-Y, Kamal A, Busch D, *et al.* Synthesis and biological evaluation of a new class of geldanamycin derivatives as potent inhibitors of Hsp90. *J Med Chem* 2004; **47**(15): 3865-73.

133. Supko JG, Hickman RL, Grever MR, Malspeis L. Preclinical pharmacologic evaluation of geldanamycin as an antitumor agent. *Cancer Chemother Pharmacol* 1995; **36**(4): 305-15.

134. Menezes D, Taverna P, Jensen MR, *et al.* The novel oral HSP90 inhibitor NVP-HSP990 exhibits potent and broad-spectrum anti-tumor activities in vitro and in vivo. *Mol Cancer Ther* 2012; **11**(3): 730-9.

135. Zhang H, Neely L, Lundgren K, *et al.* BIIB021, a synthetic Hsp90 inhibitor, has broad application against tumors with acquired multidrug resistance. *Int J Cancer* 2010; **126**(5): 1226-34.

136. Chiosis G, Kang Y, Sun W. Discovery and development of purine-scaffold Hsp90 inhibitors. *Expert Opin Drug Discov* 2008; **3**(1): 99-114.

137. Chiosis G, Timaul MN, Lucas B, *et al.* A small molecule designed to bind to the adenine nucleotide pocket of Hsp90 causes Her2 degradation and the growth arrest and differentiation of breast cancer cells. *Chem Biol* 2001; **8**(3): 289-99.

138. Biamonte MA, Shi J, Hong K, *et al.* Orally active purine-based inhibitors of the heat shock protein 90. *J Med Chem* 2006; **49**(2): 817-28.

139. Woodhead AJ, Angove H, Carr MG, *et al.* Discovery of (2,4-dihydroxy-5-isopropylphenyl)-[5-(4-methylpiperazin-1-ylmethyl)-1,3-dihydroisoindol-2-yl]methanone (AT13387), a novel inhibitor of the molecular chaperone Hsp90 by fragment based drug design. *J Med Chem* 2010; **53**(16): 5956-69.

140. Nakashima T, Ishii T, Tagaya H, *et al.* New molecular and biological mechanism of antitumor activities of KW-2478, a novel nonansamycin heat shock protein 90 inhibitor, in multiple myeloma cells. *Clin Cancer Res* 2010; **16**(10): 2792.

141. Lin T-Y, Bear M, Du Z, *et al.* The novel HSP90 inhibitor STA-9090 exhibits activity against Kit-dependent and -independent malignant mast cell tumors. *Exp Hematol* 2008; **36**(10): 1266-77.

142. Eccles SA, Massey A, Raynaud FI, *et al.* NVP-AUY922: A novel heat shock protein 90 inhibitor active against xenograft tumor growth, angiogenesis, and metastasis. *Cancer Res* 2008; **68**(8): 2850-60.

143. Whitesell L, Robbins N, Huang DS, *et al.* Structural basis for species-selective targeting of Hsp90 in a pathogenic fungus. *Nat Commun* 2019; **10**(1): 402.

144. Uno T, Kawai Y, Yamashita S, *et al.* Discovery of 3-ethyl-4-(3-isopropyl-4-(4-(1-methyl-1 H-pyrazol-4-yl)-1 H-imidazol-1-yl)-1 H-pyrazolo[3,4- b]pyridin-1-yl)benzamide (TAS-116) as a potent, selective, and orally available HSP90 inhibitor. *J Med Chem* 2018.

145. Bussenius J, Blazey CM, Aay N, *et al.* Discovery of XL888: A novel tropane-derived small molecule inhibitor of HSP90. *Bioorg Med Chem Lett* 2012; **22**(17): 5396-404.

146. Ferraro M, D'Annessa I, Moroni E, *et al.* Allosteric modulators of HSP90 and HSP70: Dynamics meets function through structure-based drug design. *J Med Chem* 2019; **62**(1): 60-87.

147. Neckers L, Blagg B, Haystead T, Trepel JB, Whitesell L, Picard D. Methods to validate Hsp90 inhibitor specificity, to identify off-target effects, and to rethink approaches for further clinical development. *Cell Stress Chaperones* 2018; **23**(4): 467-82.

148. Shrestha L, Bolaender A, Patel HJ, Taldone T. Heat shock protein (HSP) drug discovery and development: Targeting heat shock proteins in disease. *Curr Top Med Chem* 2016; **16**(25): 2753-64.

149. Garg G, Khandelwal A, Blagg BS. Anticancer inhibitors of Hsp90 function: Beyond the usual suspects. *Adv Cancer Res* 2016; **129**: 51-88.

150. Hall JA, Forsberg LK, Blagg BSJ. Alternative approaches to Hsp90 modulation for the treatment of cancer. *Future Med Chem* 2014; **6**(14): 1587-605.

151. Matts RL, Brandt GEL, Lu Y, *et al.* A systematic protocol for the characterization of Hsp90 modulators. *Bioorg Med Chem* 2011; **19**(1): 684-92.

152. Bagatell R, Paine-Murrieta GD, Taylor CW, *et al.* Induction of a heat shock factor 1-dependent stress response alters the cytotoxic activity of Hsp90-binding agents. *Clin Cancer Res* 2000; **6**(8): 3312-8.

153. Zou J, Guo Y, Guettouche T, Smith DF, Voellmy R. Repression of heat shock transcription factor HSF1 activation by HSP90 (HSP90 complex) that forms a stress-sensitive complex with HSF1. *Cell* 1998; **94**(4): 471-80.

154. Voellmy R, Boellmann F. Chaperone regulation of the heat shock protein response. *Adv Exp Med Biol* 2007; **594**: 89-99.

155. Jolly C, Morimoto RI. Role of the heat shock response and molecular chaperones in oncogenesis and cell death. *J Natl Cancer I* 2000; **92**(19): 1564-72.

156. Leppa S, Sistonen L. Heat shock response - Pathophysiological implications. *Ann Med* 1997; **29**(1): 73-8.

157. Jhaveri K, Ochiana SO, Dunphy MPS, *et al.* Heat shock protein 90 inhibitors in the treatment of cancer: Current status and future directions. *Expert Opin Investig Drugs* 2014; **23**(5): 611-28.

158. Avsar E. Chapter 13: Hsp90 inhibitors in clinic. In: Machajewski TD, Gao Z, eds. Inhibitors of molecular chaperones as therapeutic agents: The Royal Society of Chemistry; 2014: 336-78.

159. Neckers L, Workman P. Hsp90 molecular chaperone inhibitors: Are we there yet? *Clin Cancer Res* 2012; **18**(1): 64-76.

160. Zhou D, Liu Y, Ye J, *et al.* A rat retinal damage model predicts for potential clinical visual disturbances induced by Hsp90 inhibitors. *Toxicol Appl Pharmacol* 2013; **273**(2): 401-9.

161. Marcu MG, Schulte TW, Neckers L. Novobiocin and related coumarins and depletion of heat shock protein 90-dependent signaling proteins. *J Natl Cancer Inst* 2000; **92**(3): 242-8.

162. Marcu MG, Chadli A, Bouhouche I, Catelli M, Neckers LM. The heat shock protein 90 antagonist novobiocin interacts with a previously unrecognized ATP-binding domain in the carboxyl terminus of the chaperone. *J Biol Chem* 2000; **275**(47): 37181-6.

163. Söti C, Rácz A, Csermely P. A Nucleotide-dependent molecular switch controls ATP binding at the C-terminal domain of Hsp90. N-terminal nucleotide binding unmasks a C-terminal binding pocket. *J Biol Chem* 2002; **277**(9): 7066-75.

164. Garnier C, Lafitte D, Tsvetkov PO, *et al.* Binding of ATP to heat shock protein 90 - Evidence for an ATP-binding site in the C-terminal domain. *J Biol Chem* 2002; **277**(14): 12208-14.

165. Söti C, Vermes Á, Haystead TAJ, Csermely P. Comparative analysis of the ATP-binding sites of Hsp90 by nucleotide affinity cleavage: A distinct nucleotide specificity of the C-terminal ATP-binding site. *Eur J Biochem* 2003; **270**(11): 2421-8.

166. Khalid S, Paul S. Identifying a C-terminal ATP binding sites-based novel Hsp90-inhibitor in silico: a plausible therapeutic approach in Alzheimer's disease. *Med Hypotheses* 2014; **83**(1): 39-46.

167. Matts RL, Dixit A, Peterson LB, *et al.* Elucidation of the Hsp90 C-terminal inhibitor binding site. *ACS Chem Biol* 2011; **6**(8): 800-7.

168. Morra G, Neves MAC, Plescia CJ, *et al.* Dynamics-based discovery of allosteric inhibitors: Selection of new ligands for the C-terminal domain of Hsp90. *J Chem Theory Comput* 2010; **6**(9): 2978-89.

169. Sgobba M, Degliesposti G, Ferrari AM, Rastelli G. Structural models and binding site prediction of the C-terminal domain of human Hsp90: A new target for anticancer drugs. *Chem Biol Drug Des* 2008; **71**(5): 420-33.

170. Bhat R, Adam AT, Lee JJ, Gasiewicz TA, Henry EC, Rotella DP. Towards the discovery of drug-like epigallocatechin gallate analogs as Hsp90 inhibitors. *Bioorg Med Chem Lett* 2014; **24**(10): 2263-6.

171. Bhat R, Adam AT, Lee JJ, *et al.* Structure–activity studies of (−)-epigallocatechin gallate derivatives as HCV entry inhibitors. *Bioorg Med Chem Lett* 2014; **24**(17): 4162-5.

172. Yin Z, Henry EC, Gasiewicz TA. (-)-Epigallocatechin-3-gallate is a novel Hsp90 inhibitor. *Biochemistry* 2009; **48**(2): 336-45.

173. Lee S-C, Min H-Y, Choi H, *et al.* Synthesis and evaluation of a novel deguelin derivative, L80, which disrupts ATP binding to the C-terminal domain of heat shock protein 90. *Mol Pharmacol* 2015: mol.114.096883.

174. Oh SH, Woo JK, Yazici YD, *et al.* Structural basis for depletion of heat shock protein 90 client proteins by deguelin. *J Natl Cancer Inst* 2007; **99**(12): 949-61.

175. Roe SM, Ali MM, Meyer P, *et al.* The mechanism of Hsp90 regulation by the protein kinase-specific cochaperone p50(cdc37). *Cell* 2004; **116**(1): 87-98.

176. Siligardi G, Hu B, Panaretou B, Piper PW, Pearl LH, Prodromou C. Co-chaperone regulation of conformational switching in the Hsp90 ATPase cycle. *J Biol Chem* 2004; **279**(50): 51989-98.

177. Gray Jr PJ, Prince T, Cheng J, Stevenson MA, Calderwood SK. Targeting the oncogene and kinome chaperone CDC37. *Nat Rev Cancer* 2008; **8**: 491.

178. Gray PJ, Stevenson MA, Calderwood SK. Targeting Cdc37 inhibits multiple signaling pathways and induces growth arrest in prostate cancer cells. *Cancer Res* 2007; **67**(24): 11942.

179. Sreeramulu S, Gande SL, Göbel M, Schwalbe H. Molecular mechanism of inhibition of the human protein complex Hsp90–Cdc37, a kinome chaperone–cochaperone, by triterpene celastrol. *Angew Chem Int Ed* 2009; **48**(32): 5853-5.

180. Zhang T, Li YY, Yu YK, Zou P, Jiang YQ, Sun DX. Characterization of celastrol to inhibit Hsp90 and Cdc37 interaction. *J Biol Chem* 2009; **284**(51): 35381-9.

181. Grover A, Shandilya A, Agrawal V, *et al.* Hsp90/Cdc37 Chaperone/co-chaperone complex, a novel junction anticancer target elucidated by the mode of action of herbal drug Withaferin A. *BMC Bioinform* 2011; **12**(1): S30.

182. Felts SJ, Toft DO. p23, a simple protein with complex activities. *Cell Stress Chaperones* 2003; **8**(2): 108-13.

183. Patwardhan CA, Fauq A, Peterson LB, Miller C, Blagg BS, Chadli A. Gedunin inactivates the co-chaperone p23 protein causing cancer cell death by apoptosis. *J Biol Chem* 2013; **288**(10): 7313-25.

184. Pearl LH, Prodromou C. Structure and mechanism of the Hsp90 molecular chaperone machinery. *Annu Rev Biochem* 2006; **75**(1): 271-94.

185. Wegele H, Wandinger SK, Schmid AB, Reinstein J, Buchner J. Substrate transfer from the chaperone Hsp70 to Hsp90. *J Mol Biol* 2006; **356**(3): 802-11.

186. Nelson GM, Huffman H, Smith DF. Comparison of the carboxy-terminal DP-repeat region in the co-chaperones Hop and Hip. *Cell Stress Chaperones* 2003; **8**(2): 125-33.

187. Horibe T, Torisawa A, Kohno M, Kawakami K. Molecular mechanism of cytotoxicity induced by Hsp90-targeted Antp-TPR hybrid peptide in glioblastoma cells. *Mol Cancer* 2012; **11**(1): 59.

188. Horibe T, Kohno M, Haramoto M, Ohara K, Kawakami K. Designed hybrid TPR peptide targeting Hsp90 as a novel anticancer agent. *J Transl Med* 2011; **9**(1): 8.

189. Rahimi MN, McAlpine SR. Protein-protein inhibitor designed de novo to target the MEEVD region on the C-terminus of Hsp90 and block co-chaperone activity. *Chem Commun (Camb)* 2019; **55**(6): 846-9.

190. Buckton LK, Wahyudi H, McAlpine SR. The first report of direct inhibitors that target the C-terminal MEEVD region on heat shock protein 90. *Chem Commun (Camb)* 2016; **52**(3): 501-4.

191. Pimienta G, Herbert KM, Regan L. A compound that inhibits the HOP–Hsp90 complex formation and has unique killing effects in breast cancer cell lines. *Mol Pharm* 2011; **8**(6): 2252-61.

192. Yi F, Regan L. A novel class of small molecule inhibitors of Hsp90. *ACS Chem Biol* 2008; **3**(10): 645-54.

193. Bhatia S, Diedrich D, Frieg B*, et al.* Targeting HSP90 dimerization via the C terminus is effective in imatinib-resistant CML and lacks the heat shock response. *Blood* 2018; **132**(3): 307-20.

194. Krauter J, Wattjes MP, Nagel S*, et al.* Real-time RT-PCR for the detection and quantification of AML1/MTG8 fusion transcripts in t(8;21)-positive AML patients. *British Journal of Haematology* 1999; **107**(1): 80-5.

195. Lin S, Mulloy JC, Goyama S. RUNX1-ETO Leukemia. In: Groner Y, Ito Y, Liu P, Neil JC, Speck NA, van Wijnen AJ, eds. RUNX proteins in development and cancer: Springer; 2017: 151-73.

196. Okuda T, Nishimura M, Nakao M, Fujita Y. RUNX1/AML1: A central player in hematopoiesis. *Int J Hematol* 2001; **74**(3): 252-7.

197. Miyoshi H, Kozu T, Shimizu K*, et al.* The t (8; 21) translocation in acute myeloid leukemia results in production of an AML1-MTG8 fusion transcript. *EMBO J* 1993; **12**(7): 2715-21.

198. Erickson P, Gao J, Chang KS*, et al.* Identification of breakpoints in t(8;21) acute myelogenous leukemia and isolation of a fusion transcript, AML1/ETO, with similarity to drosophila segmentation gene, . *Blood* 1992; **80**(7): 1825-31.

199. Miyoshi H, Shimizu K, Kozu T, Maseki N, Kaneko Y, Ohki M. t(8;21) breakpoints on chromosome 21 in acute myeloid leukemia are clustered within a limited region of a single gene, AML1. *Proc Natl Acad Sci USA* 1991; **88**(23): 10431-4.

200. Peterson LF, Zhang D-E. The 8;21 translocation in leukemogenesis. *Oncogene* 2004; **23**(24): 4255-62.

201. Sood R, Kamikubo Y, Liu P. Role of RUNX1 in hematological malignancies. *Blood* 2017; **129**(15): 2070-82.

202. Chuang LS, Ito K, Ito Y. RUNX family: Regulation and diversification of roles through interacting proteins. *Int J Cancer* 2013; **132**(6): 1260-71.

203. Lam K, Zhang D-E. RUNX1 and RUNX1-ETO: Roles in hematopoiesis and leukemogenesis. *Front Biosci (Landmark Ed)* 2012; **17**: 1120-39.

204. Kanno T, Kanno Y, Chen L-F, Ogawa E, Kim W-Y, Ito Y. Intrinsic transcriptional activation-inhibition domains of the polyomavirus enhancer binding protein 2/core binding factor α subunit revealed in the presence of the β subunit. *Mol Cell Biol* 1998; **18**(5): 2444-54.

205. Wang S, Wang Q, Crute BE, Melnikova IN, Keller SR, Speck NA. Cloning and characterization of subunits of the T-cell receptor and murine leukemia virus enhancer core-binding factor. *Mol Cell Biol* 1993; **13**(6): 3324-39.

206. Ogawa E, Maruyama M, Kagoshima H*, et al.* PEBP2/PEA2 represents a family of transcription factors homologous to the products of the Drosophila runt gene and the human AML1 gene. *Proc Natl Acad Sci USA* 1993; **90**(14): 6859-63.

207. Hildebrand D, Tiefenbach J, Heinzel T, Grez M, Maurer AB. Multiple regions of ETO cooperate in transcriptional repression. *J Biol Chem* 2001; **276**(13): 9889-95.

208. Lutterbach B, Westendorf JJ, Linggi B*, et al.* ETO, a target of t(8;21) in acute leukemia, interacts with the N-CoR and mSin3 corepressors. *Mol Cell Biol* 1998; **18**(12): 7176-84.

209. Lutterbach B, Sun D, Schuetz J, Hiebert SW. The MYND motif is required for repression of basal transcription from the multidrug resistance 1 promoter by the t(8;21) fusion protein. *Mol Cell Biol* 1998; **18**(6): 3604-11.

210. Odaka Y, Mally A, Elliott LT, Meyers S. Nuclear import and subnuclear localization of the proto-oncoprotein ETO (MTG8). *Oncogene* 2000; **19**(32): 3584-97.

211. Sun X-J, Wang Z, Wang L*, et al.* A stable transcription factor complex nucleated by oligomeric AML1–ETO controls leukaemogenesis. *Nature* 2013; **500**(7460): 93-7.

212. Liu Y, Cheney MD, Gaudet JJ*, et al.* The tetramer structure of the nervy homology two domain, NHR2, is critical for AML1/ETO's activity. *Cancer cell* 2006; **9**(4): 249-60.

213. Kwok C, Zeisig BB, Qiu J, Dong S, So CWE. Transforming activity of AML1-ETO is independent of CBFβ and ETO interaction but requires formation of homo-oligomeric complexes. *Proc Natl Acad Sci USA* 2009; **106**(8): 2853-8.

214. Wichmann C, Chen L, Heinrich M*, et al.* Targeting the oligomerization domain of ETO interferes with RUNX1/ETO oncogenic activity in t(8;21)-positive leukemic cells. *Cancer Res* 2007; **67**(5): 2280-9.

215. Wichmann C, Becker Y, Chen-Wichmann L*, et al.* Dimer-tetramer transition controls RUNX1/ETO leukemogenic activity. *Blood* 2010; **116**(4): 603-13.

216. Wolford JK, Prochazka M. Structure and expression of the human MTG8/ETO gene. *Gene* 1998; **212**(1): 103-9.

217. Kozu T, Fukuyama T, Yamami T, Akagi K, Kaneko Y. MYND-less splice variants of AML1-MTG8 (RUNX1-CBFA2T1) are expressed in leukemia with t(8;21). *Genes Chromosom Cancer* 2005; **43**(1): 45-53.

218. Yan M, Kanbe E, Peterson LF*, et al.* A previously unidentified alternatively spliced isoform of t(8;21) transcript promotes leukemogenesis. *Nat Med* 2006; **12**(8): 945-9.

219. Peterson LF, Boyapati A, Ahn E-Y*, et al.* Acute myeloid leukemia with the 8q22;21q22 translocation: Secondary mutational events and alternative t(8;21) transcripts. *Blood* 2007; **110**(3): 799-805.

220. Ptasinska A, Assi SA, Mannari D*, et al.* Depletion of RUNX1/ETO in t(8;21) AML cells leads to genome-wide changes in chromatin structure and transcription factor binding. *Leukemia* 2012; **26**(8): 1829-41.

221. Wang L, Gural A, Sun XJ*, et al.* The leukemogenicity of AML1-ETO is dependent on site-specific lysine acetylation. *Science* 2011; **333**(6043): 765-9.

222. Goyama S, Mulloy JC. Molecular pathogenesis of core binding factor leukemia: Current knowledge and future prospects. *Int J Hematol* 2011; **94**(2): 126-33.

223. Li Y, Wang H, Wang X*, et al.* Genome-wide studies identify a novel interplay between AML1 and AML1/ETO in t(8;21) acute myeloid leukemia. *Blood* 2016; **127**(2): 233-42.

224. van der Kouwe E, Staber PB. RUNX1-ETO: Attacking the epigenome for genomic instable leukemia. *Int J Mol Sci* 2019; **20**(2): 350.

225. Wei Y, Liu S, Lausen J*, et al.* A TAF4-homology domain from the corepressor ETO is a docking platform for positive and negative regulators of transcription. *Nat Struct Mol Biol* 2007; **14**(7): 653-61.

226. Hospital MA, Prebet T, Bertoli S*, et al.* Core-binding factor acute myeloid leukemia in first relapse: A retrospective study from the French AML intergroup. *Blood* 2014; **124**(8): 1312-9.

227. Döhner H, Estey E, Grimwade D*, et al.* Diagnosis and management of AML in adults: 2017 ELN recommendations from an international expert panel. *Blood* 2017; **129**(4): 424-47.

228. Paschka P, Döhner K. Core-binding factor acute myeloid leukemia: Can we improve on HiDAC consolidation? *Hematology Am Soc Hematol Educ Program* 2013; **2013**: 209-19.

229. Schlenk RF, Benner A, Krauter J, *et al.* Individual patient data-based meta-analysis of patients aged 16 to 60 years with core binding factor acute myeloid leukemia: A survey of the German acute myeloid leukemia intergroup. *J Clin Oncol* 2004; **22**(18): 3741-50.

230. Marcucci G, Mrózek K, Ruppert AS, *et al.* Prognostic factors and outcome of core binding factor acute myeloid leukemia patients with t(8;21) differ from those of patients with inv(16): A cancer and leukemia group B study. *J Clin Oncol* 2005; **23**(24): 5705-17.

231. Laszlo GS, Estey EH, Walter RB. The past and future of CD33 as therapeutic target in acute myeloid leukemia. *Blood Rev* 2014; **28**(4): 143-53.

232. Cramer CJ. Essentials of computational chemistry: Theories and models: John Wiley & Sons; 2013.

233. Leach AR. Molecular modelling: Principles and applications. Harlow, England; New York: Prentice Hall; 2001.

234. Ryckaert JP, Ciccotti G, Berendsen HJC. Numerical-integration of cartesian equations of motion of a system with constraints: Molecular dynamics of *n*-Alkanes. *J Comput Phys* 1977; **23**(3): 327-41.

235. Miyamoto S, Kollman PA. Settle: An analytical version of the SHAKE and RATTLE algorithm for rigid water models. *J Comput Chem* 1992; **13**(8): 952-62.

236. Hopkins CW, Le Grand S, Walker RC, Roitberg AE. Long-time-step molecular dynamics through hydrogen mass repartitioning. *J Chem Theory Comput* 2015; **11**(4): 1864-74.

237. Maier JA, Martinez C, Kasavajhala K, Wickstrom L, Hauser KE, Simmerling C. ff14SB: Improving the accuracy of protein side chain and backbone parameters from ff99SB. *J Chem Theory Comput* 2015; **11**(8): 3696-713.

238. Wang JM, Wang W, Kollman PA, Case DA. Automatic atom type and bond type perception in molecular mechanical calculations. *J Mol Graph Model* 2006; **25**(2): 247-60.

239. Wang JM, Wolf RM, Caldwell JW, Kollman PA, Case DA. Development and testing of a general amber force field. *J Comput Chem* 2004; **25**(9): 1157-74.

240. Dickson CJ, Madej BD, Skjevik ÅA, *et al.* Lipid14: the amber lipid force field. *J Chem Theory Comput* 2014; **10**(2): 865-79.

241. Jorgensen WL, Chandrasekhar J, Madura JD, Impey RW, Klein ML. Comparison of simple potential functions for simulating liquid water. *J Chem Phys* 1983; **79**(2): 926-35.

242. Case DA, Belfon K, Ben-Shalom IY, *et al.* AMBER 2020. University of California, San Francisco; 2020.

243. Case DA, Cheatham III TE, Darden T, *et al.* The Amber biomolecular simulation programs. *J Comput Chem* 2005; **26**(16): 1668-88.

244. Shell MS, Panagiotopoulos A, Pohorille A. Methods Based on Probability Distributions and Histograms. In: Chipot C, Pohorille A, eds. Free energy calculations: Theory and applications in chemistry and biology. Berlin, Heidelberg: Springer Berlin Heidelberg; 2007: 77-118.

245. Kästner J. Umbrella sampling. *Wiley Interdiscip Rev Comput Mol Sci* 2011; **1**(6): 932-42.

246. Roux B. The calculation of the potential of mean force using computer simulations. *Comput Phys Commun* 1995; **91**(1-3): 275-82.

247. Grossfield A. WHAM: an implementation of the weighted histogram analysis method. http://membrane.urmc.rochester.edu/content/wham/; version 2.0.9.1.

248. Kumar S, Rosenberg JM, Bouzida D, Swendsen RH, Kollman PA. The weighted histogram analysis method for free-energy calculations on biomolecules. I. The method. *J Comput Chem* 1992; **13**(8): 1011-21.

249. Lee CT, Comer J, Herndon C*, et al.* Simulation-based approaches for determining membrane permeability of small compounds. *J Chem Inf Model* 2016; **56**(4): 721-33.

250. Chipot C, Comer J. Subdiffusion in membrane permeation of small molecules. *Sci Rep* 2016; **6**: 35913.

251. Kusari S, Hertweck C, Spiteller M. Chemical ecology of endophytic fungi: Origins of secondary metabolites. *Chem Biol* 2012; **19**(7): 792-8.

252. van der Bliek AM, Shen Q, Kawajiri S. Mechanisms of mitochondrial fission and fusion. *Cold Spring Harb Perspect Biol* 2013; **5**(6): a011072.

253. Shelley JC, Cholleti A, Frye LL, Greenwood JR, Timlin MR, Uchimaya M. Epik: A software program for pKa prediction and protonation state generation for drug-like molecules. *J Comput Aid Mol Des* 2007; **21**(12): 681-91.

254. Schrödinger Release 2018-1: Epik. New York, NY: Schrödinger, LLC; 2018.

255. Sarmini K, Kenndler E. Ionization constants of weak acids and bases in organic solvents. *J Biochem Bioph Methods* 1999; **38**(2): 123-37.

256. Horvath SE, Daum G. Lipids of mitochondria. *Prog Lipid Res* 2013; **52**(4): 590-614.

257. Marrink SJ, Corradi V, Souza PCT, Ingólfsson HI, Tieleman DP, Sansom MSP. Computational modeling of realistic cell membranes. *Chem Rev* 2019; **119**(9): 6184-226.

258. Allhusen JS, Conboy JC. The ins and outs of lipid flip-flop. *Accounts Chem Res* 2017; **50**(1): 58-65.

259. Anglin TC, Cooper MP, Li H, Chandler K, Conboy JC. Free energy and entropy of activation for phospholipid flip-flop in planar supported lipid bilayers. *J Phys Chem B* 2010; **114**(5): 1903-14.

260. Dellago C, Bolhuis PG, Csajka FS, Chandler D. Transition path sampling and the calculation of rate constants. *J Chem Phys* 1998; **108**(5): 1964-77.

261. Ceccacci S, Deitersen J, Mozzicafreddo M*, et al.* Carbamoyl-phosphate synthase 1 as a novel target of phomoxanthone A, a bioactive fungal metabolite. *Biomolecules* 2020; **10**(6): 846.

262. Neckers L. Heat shock protein 90: The cancer chaperone. *J Biosci* 2007; **32**(3): 517-30.

263. Ciglia E, Vergin J, Reimann S*, et al.* Resolving hot spots in the C-terminal dimerization domain that determine the stability of the molecular chaperone Hsp90. *PLoS One* 2014; **9**(4): e96031.

264. Bopp B, Ciglia E, Ouald-Chaib A, Groth G, Gohlke H, Jose J. Design and biological testing of peptidic dimerization inhibitors of human Hsp90 that target the C-terminal domain. *Biochim Biophys Acta* 2016; **1860**(6): 1043-55.

265. Jose J, Meyer TF. The autodisplay story, from discovery to biotechnical and biomedical applications. *Microbiol Mol Biol Rev* 2007; **71**(4): 600-19.

266. Diedrich D, Moita AJR, Rüther A*, et al.* α-Aminoxy oligopeptides: Synthesis, secondary structure, and cytotoxicity of a new class of anticancer foldamers. *Chem Eur J* 2016; **22**(49): 17600-11.

267. Spanier L, Ciglia E, Hansen FK*, et al.* Design, synthesis, and conformational analysis of trispyrimidonamides as alpha-helix mimetics. *J Org Chem* 2014; **79**(4): 1582-93.

268. Sun H, Duan L, Chen F, *et al.* Assessing the performance of MM/PBSA and MM/GBSA methods. 7. Entropy effects on the performance of end-point binding free energy calculation approaches. *Phys Chem Chem Phys* 2018; **20**(21): 14450-60.

269. Gohlke H, Case DA. Converging free energy estimates: MM-PB(GB)SA studies on the protein-protein complex Ras-Raf. *J Comput Chem* 2004; **25**(2): 238-50.

270. Metz A, Schanda J, Grez M, Wichmann C, Gohlke H. From determinants of RUNX1/ETO tetramerization to small-molecule protein–protein interaction inhibitors targeting acute myeloid leukemia. *J Chem Inf Model* 2013; **53**(9): 2197-202.

271. Schanda J, Lee C-W, Wohlan K, *et al.* Suppression of RUNX1/ETO oncogenic activity by a small molecule inhibitor of tetramerization. *Haematologica* 2017; **102**(5): e170.

272. Kröger T. Assay development and optimization for the validation and quantification of NHR2 tetramerization inhibitors and prediction of the binding mode [Dissertation]. Düsseldorf: Heinrich Heine University, Düsseldorf; 2018.

273. Veselovsky AV, Ivanov YD, Ivanov AS, Archakov AI, Lewi P, Janssen P. Protein-protein interactions: mechanisms and modification by drugs. *J Mol Recognit* 2002; **15**(6): 405-22.

274. Molecular Operating Environment (MOE). 2019.01. 1010 Sherbooke St. West, Suite #910, Montreal, QC, Canada, H3A 2R7: Chemical Computing Group ULC; 2019.

275. Hawkins PC, Skillman AG, Nicholls A. Comparison of shape-matching and docking as virtual screening tools. *J Med Chem* 2007; **50**(1): 74-82.

276. Wang C, Engelke L, Bickel D, *et al.* The tetrahydroxanthone-dimer phomoxanthone A is a strong inducer of apoptosis in cisplatin-resistant solid cancer cells. *Bioorg Med Chem* 2019; **27**(19): 115044.

Appendix

Publication I

C-terminal modulators of heat shock protein of 90 kDa (HSP90): State of development and modes of action

Bickel, D. [a], and Gohlke, H. [a,b]

[a] Institute of Pharmaceutical and Medicinal Chemistry, Heinrich Heine University Düsseldorf, Düsseldorf, Germany

[b] John von Neumann Institute for Computing (NIC), Jülich Supercomputing Centre (JSC), Institute of Biological Information Processing (IBI-7: Structural Biochemistry) & Institute of Bio- and Geosciences (IBG-4: Bioinformatics), Forschungszentrum Jülich GmbH, Jülich, Germany

C-terminal modulators of heat shock protein of 90 kDa (HSP90): State of development and modes of action

David Bickel[a,1], Holger Gohlke[a,b,*,2,3]

[a] Institute for Pharmaceutical and Medicinal Chemistry, Heinrich Heine University Düsseldorf, Düsseldorf, Germany
[b] John von Neumann Institute for Computing (NIC), Jülich Supercomputing Centre (JSC) & Institute for Complex Systems – Structural Biochemistry (ICS 6), Forschungszentrum Jülich GmbH, Jülich, Germany

ABSTRACT

Cells constantly need to adopt to changing environmental conditions, maintaining homeostasis and proteostasis. Heat shock proteins are a diverse class of molecular chaperones that assist proteins in folding to prevent stress-induced misfolding and aggregation. The heat shock protein of 90 kDa (HSP90) is the most abundant heat shock protein. While basal expression of HSP90 is essential for cell survival, in many tumors elevated HSP90 levels are found, which is often associated with bad prognosis. Therefore, HSP90 has emerged as a major target in tumor therapy. The HSP90 machinery is very complex in that it involves large conformational changes during the chaperoning cycle and a variety of co-chaperones. At the same time, this complexity offers a plethora of possibilities to interfere with HSP90 function. The best characterized class of HSP90 modulators are competitive inhibitors targeting the N-terminal ATP-binding pocket. Nineteen compounds of this class entered clinical trials. However, due to severe adverse effects, including induction of the heat shock response, no N-terminal inhibitor has been approved by the FDA so far. As alternatives, compounds commonly referred to as "C-terminal inhibitors" have been developed, either as natural product-based analogues or by rational design, which employ multiple mechanisms to modulate HSP90 function, including modulation of the interaction with co-chaperones, induction of conformational changes that influence the chaperoning cycle, or inhibition of C-terminal dimerization. In this review, we summarize the current development state of characteristic C-terminal inhibitors, with an emphasis on their (proposed) molecular modes of action and binding sites.

1. Introduction

Cells constantly need to adopt to changing environmental conditions, maintaining homeostasis. The heat shock proteins are a diverse class of molecular chaperones that serve this purpose. Originally discovered, and named, with respect to their elevated expression upon cell exposure to heat, they were also found to assist cellular function under basal conditions.[1–3] The heat shock protein of 90 kDa (HSP90) is the most abundant heat shock protein, constituting 1–2% of the total cellular protein, which is increased to 3–5% upon exposure to external stressors.[4,5] In eukaryotes, it forms the heart of a complex machinery involving multiple cofactors and cochaperones.[1,6] This "modular design" enables the HSP90 chaperoning complex to interact with a wide variety of client proteins along important cellular signaling pathways, such as steroid hormone receptors or protein kinases.[7]

1.1. HSP90 structure

In the cell, HSP90 exists as a homodimer.[8,9] Each monomer consists of three domains: a N-terminal domain (NTD), followed by a middle (MD) and C-terminal domain (CTD)[10] (Fig. 1). The NTD is the main ATPase domain of HSP90 and belongs to the GHKL superfamily; it shares high structural similarity to histidine kinases, gyrases, and topoisomerases.[11,12] A highly charged linker region that varies in length and composition between species and isoforms connects it to the middle domain (MD),[13–15] which appears to play an important role in the ATP hydrolysis and client recognition.[15,16] The C-terminal domain forms the main dimerization interface of HSP90.[17,18] The C-terminus also contains the MEEVD motif, which is an important interaction site for a subset of co-chaperones containing tetratricopeptide repeat (TPR) domains.[19]
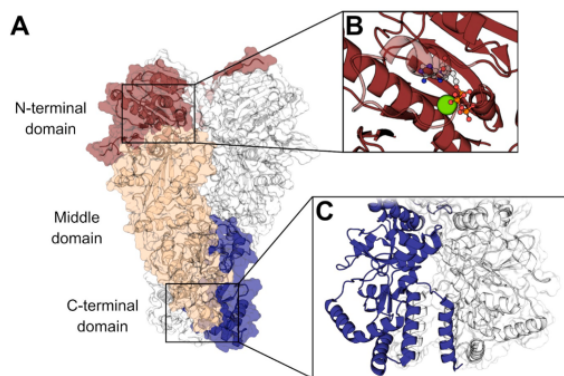

Fig. 1. Surface representation of human HSP90β as resolved from cryo-electron microscopy (PDB ID: 5FWK). (A) For monomer A the N-terminal domain is represented in red, the middle domain in beige, and the C-terminal domain in blue. The monomer B is shown in light grey. The charged linker region and the C-terminal fragment that interacts with TPR domains are not resolved, and therefore not shown in the graphic. (B) Blow-up of the ATP binding site in the N-terminal domain with bound Mg^{2+}-ATP. (C) Blow-up of the C-terminal domains of monomer A (blue) and monomer B (light). The helix-bundle in the center formed by the C-terminal helices 4, 4′, 5, and 5′ constitutes the primary dimerization interface in the C-terminal domain.

During the chaperone cycle, periodically transient interactions occur via the respective N- and C-terminal domains of the dimer.[20] The two monomers thus interact in a flexible clamp-like way, which is essential for the ATP hydrolysis.[1,21]

1.2. HSP90 isoforms

In humans four isoforms of HSP90 have been identified: cytosolic HSP90α and HSP90β, mitochondrial TRAP1 (tumor necrosis factor-associated protein 1), and GRP94 (94 kDa glucose-related protein) in the endoplasmic reticulum.[4,22] All isoforms share a conserved structure, consisting of a N-terminal ATPase domain (NTD), the MD, and the CTD. However, TRAP1 is lacking the charged linker region between NTD and MD, and both GRP94 and TRAP1 are missing the C-terminal MEEVD motif.[23] A fifth isoform – HSP90N (HSP89αΔN) – lacking the N-terminal ATP binding site was reported to be associated with tumor formation.[24,25] However, subsequent studies concluded that this isoform is most likely a chimeric translocation product of the *HSP90AA1* gene, limited to very few cancer cell strains.[23,26]

The two major cytoplasmic isoforms have a sequence identity of 86%[27] but vary in their expression. HSP90β is constitutively expressed at higher levels than HSP90α.[4,22] Yet, the expression of HSP90α is highly stress-inducible.[4,22] Differences in regulation as well as isoform specificity observed for some client proteins and co-chaperones suggest distinct cellular functions of the two isoforms.[28–31] Despite this fact, most of the functional assays are performed on cytoplasmic HSP90 (i.e., mixtures of HSP90α and β). Therefore, except in a few cases, there is no information on isoform selectivity of HSP90 modulators.

1.3. HSP90 in cancer

While basal levels of HSP90 are needed for maintaining protein homeostasis under physiological conditions, the HSP90 machinery can be exploited by cancer cells to cope with proteotoxic stressors, such as a high mutation burden, hypoxia, and acidosis that are frequently found in the tumor microenvironment.[32,33] Accordingly, elevated levels of HSP90 are observed in various types of malignancies[33–35] and correlate with poor prognosis in breast cancer,[36,37] gastric cancer,[38] and acute myeloid leukemia.[39] Furthermore, secretion of HSP90α into the

extracellular space was shown to promote tumor invasiveness.[40,41] As a consequence, the last decades have seen increasing efforts to develop drug-like HSP90 inhibitors for clinical use.

1.4. Inhibitors of HSP90 in clinical trials

In 1994, the ansamycin antibiotic geldanamycin (**1** (Arabic numbers in bold are only assigned to "first-in-class" molecules in this review), Fig. 2) was reported to elicit antiproliferative effects by inhibiting HSP90, which subsequently led to depletion of tyrosine kinases and cell death in cancer cell lines.[42,43] In the following years, the natural product radicicol (**2**, Fig. 2) was shown to have the same effect but higher potency.[44,45] Both compounds bind to the ATP-binding site in the N-terminal domain of HSP90.[46,47] Subsequent structure-activity relationship (SAR) studies in concert with the resolution of co-crystal structures of ADP,[11] geldanamycin,[47] and radicicol[46] with HSP90 led to the development of a set of drug candidates with improved pharmacodynamic and pharmacokinetic properties compared to the original natural products. For geldanamycin, particularly the semi-synthetic modification of the 17-methoxy group was found to lead to active compounds that exhibited less toxicity with respect to the natural compound,[48–50] leading to the four ansamycins that entered clinical trials so far (https://clinicaltrials.gov, accessed Feb 2019) (Fig. 2).

Structure-based drug design, based on the unconventional conformation that ATP adopts in GHKL-ATP binding sites, led to the development of fully synthetic purine analogues[51–54] as inhibitors of HSP90 ATPase activity, which could be administered orally.[51,53,55] Of these, six entered clinical trials (Fig. 2). In a high throughput screening against yeast HSP90 ATPase activity, the first synthetic resorcinolic HSP90 inhibitors were identified.[56] Since then, a set of diversely substituted resorcinols was found to inhibit HSP90,[57–60] of which five entered clinical trials in the following years (Fig. 2). Finally, a rather diverse class of HSP90 inhibitors entered clinical trials, where all compounds feature a substituted benzamide substructure (Fig. 2). All compounds share a similar binding mode in the ATP binding site.[61–63]

In summary, nineteen structurally distinct HSP90 inhibitors that exert their activity by targeting the N-terminal HSP90 binding site have entered in clinical trials (https://clinicaltrials.gov, accessed Feb 2019) (Fig. 2). Another putative *N*-terminal HSP90 inhibitor (DS-2248, Daiichi Sankyo, structure undisclosed) was registered for phase I clinical trial, but discontinued (https://clinicaltrials.gov, identifier: NCT01288430). Altogether, none of the classical HSP90 inhibitors was approved by the FDA for therapeutic use as yet. One reason is the induction of the heat shock response (HSR), a well-known side effect of this class of inhibitors,[33,64–69] which was already described for geldanamycin. According to current model of HSR mechanism, the binding of N-terminal HSP90 inhibitors releases heat shock factor-1 (HSF-1).[70,71] The transcription factor becomes phosphorylated, trimerizes, and translocates to the nucleus, leading to overexpression of multiple heat shock proteins, including HSP70, HSP40, and HSP27.[72,73] As HSR is a prosurvival mechanism, it can be detrimental in an anti-cancer therapy.[74] In addition, other severe adverse effects, such as hepatotoxicity found for ansamycins[50,75–77] and ocular toxicity,[68,75,78] have been hampering the clinical success of HSP90 inhibitors until now. Further information on the clinical development of N-terminal HSP90 inhibitors can be found in excellent reviews by Neckers and Workman,[77] Avsar,[76] and Jhaveri et al.[75,79]

In the meantime, many groups have started investigating alternative strategies to inhibit HSP90 without inducing HSR and/or ocular toxicity. The first compound to reach that goal was novobiocin, an inhibitor binding to the CTD of HSP90 (see also Chapter 2.1.1).[80,81] A first phase I clinical trial of a C-terminal HSP90 inhibitor (RTA 901) has been performed on non-cancer patients (https://clinicaltrials.gov, identifier: NCT02666963). This compound has been reported to be based on novobiocin,[65] although the structure has not been released yet (see Chapter 2.1.1 for further details). Similar to the molecular origins of *N*-

Fig. 2. N-terminal HSP90 inhibitors that entered clinical trials. For the natural compound-derived classes, we also show their predecessors (**1**, **2**). Ansamycins: Four compounds derived from geldanamycin (**1**) entered clinical trials so far (** the quinone moiety in retaspimycin is reduced to a dihydroquinone moiety). Resorcinols: Five structurally distinct resorcinols derived from radicicol (**2**) entered clinical trials. The compound PEN-866 is a special case because it is a drug conjugate of the HSP90 inhibitor STA-9090 and an irinotecan metabolite that inhibits topoisomerase I. Purines: Six purine and purine analogues entered clinical trials. These compounds share similar binding modes mimicking the bend conformation of ATP in the *N*-terminal ATP-binding site. Benzamides: Three compounds entered clinical trials. Despite their structural diversity, they exhibit similar binding modes with a conserved placement of the benzamide motif in the ATP binding site.

terminal inhibitors, many of the non-*N*-terminal inhibitors are natural products. In the following, we review some of the successes in the discovery and development of non-N-terminal HSP90 inhibitors. In doing so, we categorize the compounds according to their (proposed) binding site and molecular mode of action.

2. Non-N-terminal inhibitors of HSP90

2.1. Inhibitors binding to the C-terminal nucleotide binding site

The discovery of the C-terminal ATP binding site is tightly linked to the evaluation of novobiocin (**3**) as a HSP90 inhibitor. The coumarin antibiotic was previously shown to interfere with nucleotide binding in

3
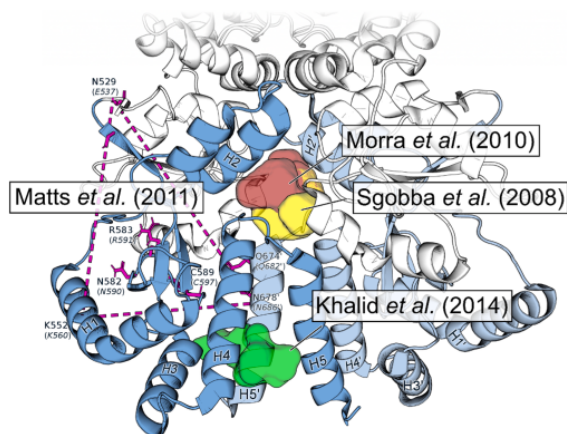
Fig. 3. Overview over approaches to identify the C-terminal ATP binding site in HSP90. The results were mapped on the structure of human HSP90β. Corresponding residue numbers in human HSP90α are given in brackets. The part of the C-terminal domain that was shown by Marcu et al. to contain the ATP-binding motif is colored in blue.[81] Sgobba et al. performed molecular simulations on a homology model of human HSP90α and used binding site prediction tools to predict the C-terminal ATP binding site.[88] Morra et al. used MD simulations and signal propagation analysis to identify allosteric binding sites on the structure of yeast HSP90 and molecular docking to obtain binding poses of novobiocin and analogues.[87] Matts et al. used an azide-analogue of novobiocin as a probe to identify the C-terminal ATP binding site. They found that this probe binds covalently to K560 (HSP90α) and built an putative open-conformation HSP90 model based on SAXS data that showed direct interactions of novobiocin with K560, E537, and N686.[86] Khalid et al. used web-server based tools to predict the C-terminal HSP90 binding site.[85]

bacterial gyrase B. Yet, in HSP90, no binding to the NTD was observed, and pull-down assays suggested a binding mode different from geldanamycin.[80,81] Further studies revealed a second ATP binding site in the CTD.[81–83] This binding site is only accessible when the N-terminal ATP-binding site is occupied.[82] Furthermore, the C-terminal binding site is able to bind purine as well as pyrimidine nucleotides, while the NTD is rather specific for adenine.[84]

To our knowledge, to date, no experimentally validated structure of an inhibitor binding to this site has been released. Yet, there have been several approaches to predict the C-terminal ATP binding site using molecular modeling (Fig. 3).[85–88] In the following, we will discuss HSP90 inhibitors that are considered to bind to the C-terminal ATP binding site.

2.1.1. Novobiocin and derivatives

The amino-coumarine novobiocin (**3**, Fig. 4) and the closely related compounds chlorobiocin and coumermycin A1 were the first C-terminal HSP90 inhibitors to be reported. Like geldanamycin, novobiocin leads to a depletion of HSP90 clients such as Raf-1 and HER2,[80,81] although in rather high concentrations compared to N-terminal inhibitors. Co-immunoprecipitation assays further revealed that novobiocin interferes with the formation of HSP90-HSC70, HSP90-p23, and HSP90-CDC37 complexes.[81,89]

In order to gain derivatives with improved activities, a series of SAR studies were performed,[90–93] where cytotoxicity and depletion of HSP90 client proteins served as optimization criteria. Further efforts were made to expand the chemical space by replacing the central coumarine moiety,[94–97] e.g., by biphenyls or stilbenes. Several analogues with improved activities were obtained, with some analogues exhibiting a more than 1000-fold increase in cytotoxicity against the human breast cancer cell line SkBr3. Interestingly, also compounds that induce HSR were identified in these SAR studies, i.e., A4[93] and KU-32.[98]

As the upregulation of heat shock proteins associated with the HSR might prevent protein aggregation and promote cell survival, the application of HSR-inducing HSP90 inhibitors in neurodegenerative diseases was investigated.[74,99,100] The first C-terminal HSP90 inhibitor RTA 901 that has been evaluated in a phase I clinical trial was described as an analogue of KU-32 and showed neuroprotective activity in preclinical tests.[65]

No crystallographic complex structure is available for any of the non-N-terminal inhibitors of HSP90. A cross-coupling experiment with novobiocin-azide derivatives revealed the formation of a covalent bond with K560 in the CTD.[86] Since in the closed state crystal structure of HSP90 no binding site is visible that would be able to accommodate novobiocin in this position, the authors used SAXS data to generate a putative open state model with bound novobiocin. Other groups used computational methods, including binding site detection algorithms, molecular dynamics simulations, and molecular docking to elucidate the binding site of novobiocin.[85–88] In Fig. 3, we depict the corresponding results on closed-state human HSP90β.

2.1.2. Epigallocatechin gallate

The antiproliferative effect of the green tea catechin (−)-epigallocatechin-3-gallate (**4**, EGCG, Fig. 4) is well described.[101,102] This activity was suggested to be due to direct inhibition of AKT and ERK1/2. By proteolytic footprints and pull-down assays with EGCG-conjugated sepharose beads, EGCG was found to bind to a C-terminal fragment of HSP90.[101,103,104] Furthermore, EGCG inhibits luciferase refolding and leads to dose-dependent depletion of HSP90 client proteins ErbB2, Raf-1, and pAkt, which suggests that EGCG acts as a HSP90 inhibitor.[103] However, in pull-down assays also binding of EGCG to HSP70 was detected.[101] A set of SAR studies were performed leading to EGCG derivatives with enhanced antiproliferative activity.[105–107]

To further specify the binding site of EGCG, pull-down assays with ATP-agarose were performed. EGCG inhibited the binding of CTD-HSP90 to ATP.[101,103] In turn, free ATP was able to compete with the binding of HSP90 and HSP70 to EGCG-coupled sepharose.[101] These findings strongly indicate that the binding site of EGCG may overlap with the CTD ATP binding site.

In total, these results indicate that EGCG inhibits HSP90 in a similar way as novobiocin. The inhibition of HSP90 and subsequent depletion of client kinases could also account for the activity of ECGC on various tumor pathways.[67] Still, for the further development of EGCG derivatives, a potential promiscuity with respect to kinases and transcription factors[108,109] needs to be addressed.

2.1.3. Deguelin

The flavonoid deguelin (**5**, Fig. 4) exhibits potent antiproliferative and antiangiogenic properties in various cancer cell lines, as well as in xenograft mouse models.[110] Oh and co-workers found that deguelin downregulates the expression of hypoxia-inducible factor 1α. Subsequent experiments showed that this is caused by an inhibition of HSP90 via an ATP binding pocket.[111] In rats, however, deguelin was shown to induce a Parkinson's disease-like syndrome.[112] In order to overcome this potential adverse effect, structural analogues of deguelin were designed and tested. This resulted in the compound L80, which induces apoptosis in cancer cells and leads to reduced phosphorylation and degradation of HSP90 client proteins.[113,114]

The binding site of L80 was further characterized by a pull-down assay with ATP-agarose, where L80 was shown to inhibit the adsorption of the CTD and, partially, full-length HSP90, but not of the NTD.[114] This result suggests that L80 binds to a region overlapping the C-terminal ATP binding site. A molecular docking study based on the results from Sgobba et al.[88] further suggested a binding mode in between the homodimers, forming key interactions with K615, S677, and S677′.

2.1.4. Dihydropyridines

Dihydropridines have demonstrated neuroprotective properties. As
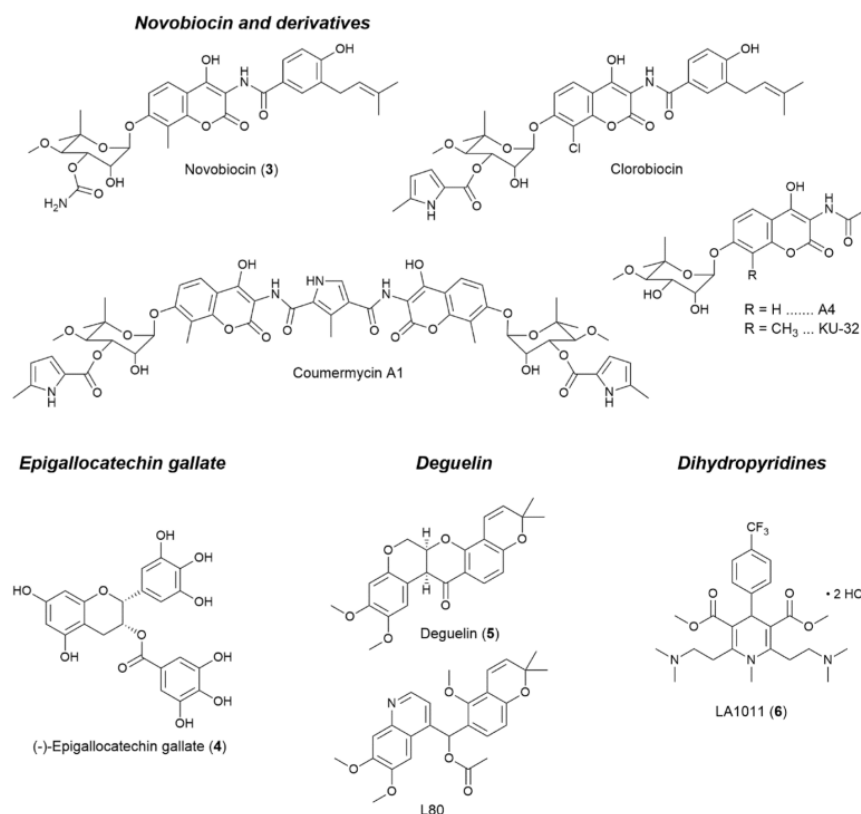
Fig. 4. Inhibitors considered to bind to the C-terminal ATP-binding site of HSP90.
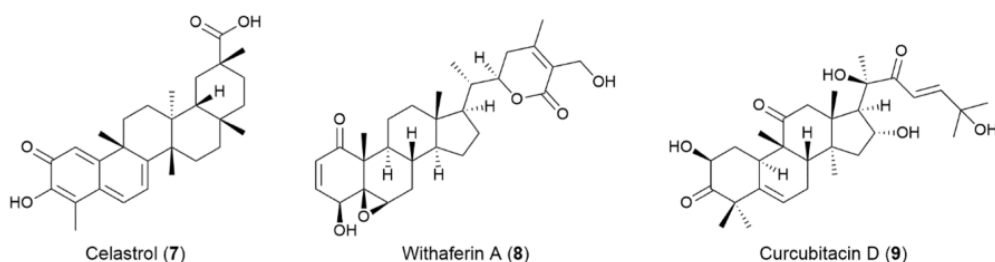
Fig. 5. Compounds considered to inhibit the HSP90-CDC37 interaction.

a possible mode of action, the upregulation of the expression of HSP27, HSP40, and HSP70 upon heat shock in comparison to untreated control was proposed.[115] In a subsequent study, the dihydropyridin LA1011 (6, Fig. 4) was shown to bind to HSP90 and, at millimolar concentrations, prevent refolding of thermally denatured luciferase. Unlike most other inhibitors of HSP90, no inhibition of HSP90 ATPase activity was observed, but an activation.[116]

Using isothermal titration calorimetry, LA1011 was demonstrated to bind to the HSP90 CTD. By molecular docking experiments and molecular dynamics simulations followed by sidechain substitutions, the authors suggested a binding site in between the C-terminal domains that roughly overlays with the location of the C-terminal ATP-binding site proposed independently by Sgobba et al.[88] and Morra et al.[87] for ATP and novobiocin.[116] However, to our knowledge, there is no experimental evidence that demonstrates that LA1011 inhibits the ATP binding to the C-terminal domain. Thus, investigations in that direction might be very interesting.

2.2. Modulators of HSP90-CDC37 interaction

CDC37 (cell division cycle 37 protein) is a co-chaperone primarily associated with the chaperoning of protein kinases. It is essential for the stabilization of HSP90-kinase complexes.[117,118] The protein interacts with HSP90 via a large interaction surface, wrapping itself around the NTD and MD,[15] which prevents the hydrolysis of ATP.[119] CDC37 knockout was shown to sensitize HSP90 for other inhibitors.[120] Thus, inhibiting the interaction between HSP90 and CDC37 might lead to kinase-specific HSP90 inhibitors and could provide a synergistic approach for the combination with other inhibitors.

2.2.1. Celastrol

Already in 2004 an activation of HSF-1 by the triterpenoid celastrol (7, Fig. 5) was reported, leading to the expression of heat shock proteins, including HSP70, HSP40, and HSP27.[121] Later, Hieronymus and co-workers demonstrated properties of celastrol as an HSP90

5

inhibitor in a gene expression signature-based screening.[122] Co-immunoprecipitation assays and HSQC NMR studies revealed that celastrol prevents the interaction of HSP90 with its co-chaperone CDC37, leading to degradation of client kinases such as Akt and Cdk4.[123,124] Another study showed that celastrol is also able to disrupt the interaction of HSP90 and p23, leading to the selective degradation of client steroid receptors.[125]

Celastrol prevents proteolytic degradation of the CTD by trypsin, suggesting a binding site in the CTD.[123] Likewise, in DSF and DSC measurements, the stabilizing effect of celastrol on the CTD was confirmed.[126] By mass-spectrometric analysis of CDC37 after incubation with celastrol, it was shown that the compound forms covalent Michael adducts to CDC37-cysteins, which lead to the disruption of HSP90-CDC37 interaction.[124]

2.2.2. Withaferin A

The steroidal lactone withaferin A (**8**, Fig. 5) possesses antiproliferative and antiangiogenic activity,[127,128] which at least partially is due to an inhibition of HSP90.[129] In cells, the natural product leads to degradation of client proteins (i.e., Akt, CDK4, and GR) in a dose-dependent manner via the proteasome-dependent pathway. In a pull-down assay with biotinylated withaferin A, binding to the C-terminal domain of HSP90 was confirmed.[129] Since withaferin A was only able to bind to the CTD when cysteine residues are present, the interaction of withaferin A with HSP90 is most likely of covalent nature. Furthermore, adding acetylcystein to the reaction buffer prevented client degradation completely.[129]

A pull-down assay with ATP-sepharose revealed that withaferin A does not inhibit ATP binding,[129] indicating a binding site different from the ATP binding sites. In a co-immunoprecipitation assay, the compound was shown to block the HSP90-CDC37 interaction. Two molecular docking studies performed by Grover et al. explored possible binding modes of withaferin A in the HSP90-CDC37 interface,[130,131] though in these studies the possible covalent binding via a cysteine was not addressed. The most likely covalent binding of withaferin A to its target proteins might compromise its selectivity.

2.2.3. Curcubitacin D

The triterpenoid curcubitacin D (**9**, Fig. 5) has been known for its antiproliferative properties since the 1960s and inhibits several cancer cell lines at submicromolar concentrations.[132–135] These cytotoxic properties can at least partially be attributed to an inhibition of HSP90. Curcubitacin D prevents the interaction of HSP90 and its co-chaperones CDC37 and p23, which leads to degradation of the HSP90 clients Her2, Raf, Cdk6, and pAkt in a concentration-dependent manner.[136] Inhibition of the chaperone activity does not lead to increased levels of HSP27 expression.[136] This indicates that curcubitacin D is able to inhibit HSP90 chaperone activity without inducing HSR.

However, the molecular mode of action of this compound remains unknown. As such, it is not known yet whether the compound binds to HSP90 or the co-chaperones in order to prevent their interaction. Both CDC37 and p23 bind to the NTD and MD of HSP90, which might indicate that curcubitacin D binds there as well. However, also compounds binding to the CTD, such as novobiocin, inhibit interactions between p23 or CDC37 with HSP90.[81,89]

2.3. Modulators of HSP90-p23 interaction

The small acidic protein p23 interacts with HSP90 via the NTD and MD. The interaction halts the HSP90 ATPase cycle and appears to facilitate HSP90 binding to client proteins.[137] While not essential for the maturation of HSP90 kinase clients, such as Cdk4 and Akt, p23 is necessary for the stabilization of steroid hormone receptors.

2.3.1. Gedunin

Gedunin (**10**, Fig. 6) was first identified as an inhibitor of HSP90 by
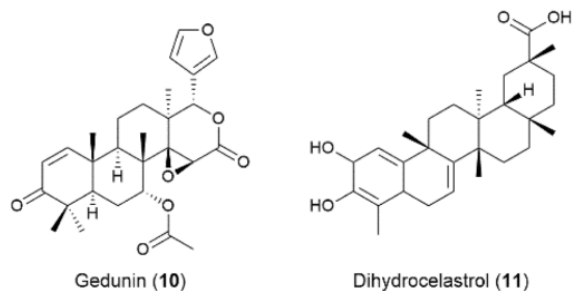
Fig. 6. Compounds that modulate the HSP90-p23 interaction.

a connectivity map approach using gene expression patterns to identify targets of compounds with unknown mode of action.[122,138] The compound was shown to elicit insecticidal,[139] antimalarial,[140] and antiproliferative effects against cancer cell lines.[141–143] In early studies, degradation of HSP90 clients Raf and HER2 under gedunin treatment were observed.[144] Yet, a later study suggested that this degradation is mostly specific for steroid hormone receptors, while changes in HSP90 client kinase levels are insignificant.[145]

In pull-down and co-immunoprecipitation assays with biotinylated gedunin, it was shown that the compound binds to p23 and disrupts the interaction between HSP90 and this co-chaperone. Since p23 is an essential component of the HSP90 complex responsible for stabilization of steroid hormone receptors, these results align very well with the selective degradation of the stereoid hormone receptors. Interestingly, free dihydrocelastrol (**11**, Fig. 6) inhibited the pull-down of p23 with gedunin, which might be an indication for similar binding sites.[145]

Like celastrol, gedunin has the potential to act as a Michael acceptor via the α,β-unsaturated ketone. However, SAR studies revealed that this is not the primary mode of action of the compound, although chemical modifications of the olefin generally resulted in less active derivatives.[144]

2.4. Inhibitors of HSP90-HOP interaction

The HSP90 C-terminal domain ends in a most likely unstructured loop that contains the highly conserved MEEVD motif.[146] This motif forms the key interaction with tetratricopeptide repeat (TPR) domains, which are present in various HSP90 co-chaperones.[1] One of these is the HSP70/HSP90-organizing protein (HOP), which mediates the interaction between the HSP70-HSP40 complex and HSP90.[147] HOP contains three TPR domains, of which the domains TPR2A and TPR2B bind to the MEEVD motifs in HSP90 and HSP70, respectively.[148]

2.4.1. Sansalvamide A-amide and derivatives

The fungal depsipeptide sansalvamide A (**12**, Fig. 7) and its derivatives have been investigated for their anticancer activity in various types of cancer.[149] A first mechanistic study performed with the amide analogue sansalvamide A-amide attributed the cytotoxic properties to the inhibition of the protein-protein interaction between HSP90 and its co-chaperone FKBP52 as well as its client IP6K2,[150] which are both associated to apoptotic pathways.[151,152] In a pull-down assay, sansalvamide A-amide was able to bind a NTD-MD construct lacking the CTD. In contrast, it showed only marginal affinity towards the individual domains and the CTD. This indicates that sansalvamide A-amide binds to the intersecting region between NTD and MD.[150] Since both FKBP52 and IP6K2 bind to the HSP90-CTD, McAlpine and co-workers suggested an allosteric mechanism for the modulation of this interaction.[150] Further studies investigating the properties of sansalvamide A-amide revealed that this compound and analogues induce the expression of HSP70 in a similar fashion as the N-terminal inhibitor 17-AAG.[153] However, other similar compounds
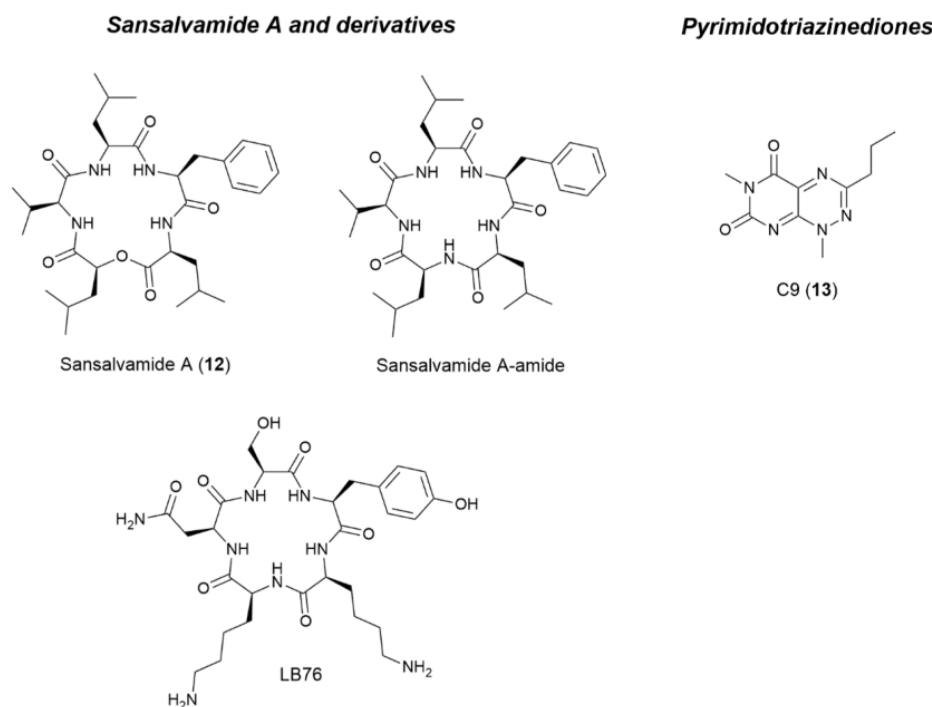
Fig. 7. Inhibitors of the HSP90-HOP interaction.

were reported, where no induction of HSR was observed.[154,155]

Kawakami and co-workers further designed peptides based on the TPR sequence, to directly inhibit interactions of HSP90 via the MEEVD motif.[156,157] These peptides showed antiproliferative *in vitro* and in a xenograft mouse model.[157] McAlpine and co-workers combined this approach with the macrocyclic peptide scaffold of the sansalvamides.[158] This effort led to the recently published compound LB76,[159] which was shown to bind to the CTD of HSP90 in a pull-down assay and inhibit the interactions of HSP90 with HOP, Cyp40, and, with lower potency, FKBP38 and FKBP51. Since HOP and Cyp40 bind to HSP90 via the MEEVD motif, while the interactions with the FKBPs are formed via a larger surface, the authors interpreted their findings as an indication for the specific binding of LB76 to the MEEVD motif.

2.4.2. Pyrimidotriazinediones

Regan and co-workers developed a high-throughput screening assay based on Amplified Luminescence Proximity Homogeneous Assay (AlphaScreen™) technology to identify small molecules that are able to inhibit the HSP90-TPR interactions.[160] They used this assay to identify a set of compounds featuring a common pyrimido[5,4-*e*][1,2,4]triazine-5,7-dione scaffold including the compound C9 (**13**, Fig. 7). Subsequently, they showed that these compounds are able to decrease the levels of the HSP90 client HER2. Cytotoxicity of the compound was observed in various breast cancer cell lines. No overexpression of HSP70 was observed upon treatment with C9.[161] Combinational treatment with inhibitors of the N-terminal ATP-binding site 17-AAG or AUY922 (resorcinole class) reduced the lethal-IC50 of C9 with respect to the individually applied compound, and the HSR induced by the N-terminal inhibitors was dampened by C9.[162]

Using ITC measurements C9 was identified to bind directly to the TPR2A domain, while no interaction to a C-terminal HSP90-peptide was observed.[161] Thus, C9 elicits its inhibitory effect on the HSP90 machinery by binding to HOP and supposedly preventing the formation of the HSP90 supercomplex, rather than directly binding and inhibiting HSP90.

2.5. Inhibitors of the C-terminal dimerization of HSP90

2.5.1. Aminoxyrone

The C-terminal domain of HSP90 is known to constitute the primary dimerization interface of HSP90, and HSP90 dimerization is essential for its chaperoning function.[17] Initially believed to be very stable, the interaction between the CTDs was later shown to exhibit a dynamic equilibrium of fast association and dissociation.[20] This finding offered the opportunity for small molecule compounds to bind to the dimerization interface.

In order to rationally design inhibitors targeting this interface, Gohlke and co-workers identified key residues ("hot spots") in the dimerization interface of HSP90, using a combination of molecular dynamics simulations and free energy calculations.[163] The hot spots were mostly located on helices H4 and H5 of the CTD, and substituting these residues with alanine led to reduced thermostability of the protein with respect to the wild type.[163] Peptides resembling the sequences of H4 (aa 656–675) and a combined H4-H5 construct (aa 656–697) were shown to bind to the CTD of HSP90 with apparent K_d values of 1.02 μM and 1.46 μM, respectively. Furthermore, the peptides were analyzed by an Autodisplay assay,[164] where HSP90 was displayed on the surface of *E. coli*, forms dimers there, and is able to bind FITC-labelled p53. The peptides interfered with HSP90's capability to bind p53, most likely by inhibiting HSP90's dimerization.[165] Hence, these peptides were the first inhibitors of HSP90 C-terminal dimerization shown to bind to the CTD.

Based on these findings, α-aminoxy peptide-based inhibitors were designed exploiting the knowledge of the orientation and type of the hot spot residues.[163] α-Aminoxy peptides are a class of peptidomimetics that form stable 2_8-helical structures and are able to mimic certain side chain orientations of α-helical peptides.[166] The resulting hexamer aminoxyrone (**14**, Fig. 8) mimics the key interactions of H5 in the C-terminal dimerization interface. To prove the ability of this compound to functionally inhibit HSP90, a luciferase refolding assay[167] was performed, where aminoxyrone inhibited refolding of firefly luciferase in a
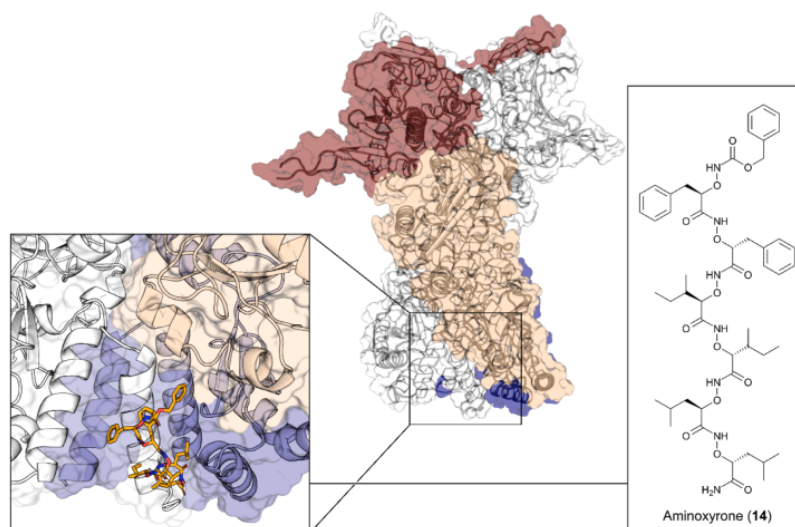
Fig. 8. Peptidomimetic dimerization inhibitor aminoxyrone. The blow-up on the left side shows aminoxyrone in its bound pose as predicted by molecular dynamics simulations of free ligand diffusion.[168] The compound mimics helix 5 in the dimerization interface.

dose-dependent manner. Using microscale thermophoresis, the binding of aminoxyrone to the CTD was shown (K_d = 27.4 μM).[168] The compound showed antiproliferative activity against various cancer cell lines *in vitro* as well as in a chronic myeloid leukemia xenograft mouse model.[168] The low toxicity profile and lack of HSR[168] make his compound an attractive lead for further drug optimization.

3. Conclusion

HSP90 has been a major target for drug discovery in academia and pharmaceutical industry for several decades, and many inhibitors have been published and patented. Most of these inhibitors target the N-terminal ATP binding site, and – except for RTA 901 – only compounds of this class have underwent clinical trials so far. However, a major drawback of this compound class is the induction of prosurvival HSR, which limits the compounds' efficacy and/or may lead to adverse effects.

Inhibiting HSP90 via allosteric binding sites, including the secondary ATP binding site in the CTD, or inhibiting protein-protein interactions between HSP90 domains, or HSP90 and interacting proteins essential for the function of the HSP90 machinery, are notable alternatives. Novobiocin was the first compound reported to inhibit HSP90 by an alternative mechanism, and by now a wide variety of compounds have been shown to elicit HSP90 inhibitory effects that way. Many of these newly identified compounds are natural products that show activity in the micromolar range. However, as a result of the complexity of the HSP90 machinery, only few details are known about the molecular mode of action of these compounds.

For the further development and optimization of these compounds, understanding the molecular mechanism behind their inhibitory effect will be essential. Given the complexity of the HSP90 chaperoning system, multivalent systems may be used to simultaneously target multiple binding epitopes.[169,170] In particular, since for many of the compounds, the inhibition of interactions between HSP90 and co-chaperones are assumed to be the mode of action. However, often it is not clear whether these compounds bind to HSP90 or to the respective co-chaperone. Furthermore, due to the flexible nature of HSP90, ligands could bind allosterically to the protein disrupting the co-chaperone interaction by imposing a certain conformation on HSP90 without binding to the protein-protein interface itself. Resolving complex structures of HSP90 and the ligands would be the optimal way to obtain structural information about the binding of such inhibitors. Alternatively, molecular modeling techniques such as molecular docking and molecular dynamics simulations of free ligand diffusion can provide valuable insights. In fact, for many C-terminal HSP90 inhibitors presented here, computational approaches have been successfully employed to guide ligand optimization.

A few approaches have been presented, where structure-based *de novo* design was applied to specifically induce particular effects on the HSP90 machinery. As such, LB76 is a rationally designed peptide-mimetic to inhibit interactions of HSP90 with HOP via the MEEVD motif, and aminoxyrone was developed as a peptidomimetic C-terminal HSP90 dimerization inhibitor. Although further optimization is required for both compounds to become potential drug candidates, they already now show that much can be gained by pursuing new routes towards HSP90 inhibition.

Declaration of Competing Interest

The authors declare that they have no known competing financial interests or personal relationships that could have appeared to influence the work reported in this paper.

Author contribution

HG conceived and supervised the study; DB and HG wrote the manuscript.

References

1. Schopf FH, Biebl MM, Buchner J. The HSP90 chaperone machinery. *Nat Rev Mol Cell Biol.* 2017;18:345–360.
2. Schlesinger MJ. Heat-shock proteins. *J Biol Chem.* 1990;265:12111–12114.
3. Lindquist S. The heat-shock response. *Annu Rev Biochem.* 1986;55:1151–1191.
4. Csermely P, Schnaider T, Söti C, Prohászka Z, Nardai G. The 90-kDa molecular

chaperone family: structure, function, and clinical applications. A comprehensive review. *Pharmacol Ther.* 1998;79:129–168.

5. Welch WJ, Feramisco JR. Purification of the major mammalian heat shock proteins. *J Biol Chem.* 1982;257:14949–14959.

6. Taipale M, Jarosz DF, Lindquist S. HSP90 at the hub of protein homeostasis: emerging mechanistic insights. *Nat Rev Mol Cell Biol.* 2010;11:515–528.

7. Richter K, Buchner J. Hsp90: chaperoning signal transduction. *J Cell Physiol.* 2001;188:281–290.

8. Wayne N, Bolon DN. Dimerization of Hsp90 is required for in vivo function. Design and analysis of monomers and dimers. *J Biol Chem.* 2007;282:35386–35395.

9. Minami Y, Kawasaki H, Miyata Y, Suzuki K, Yahara I. Analysis of native forms and isoform compositions of the mouse 90-kDa heat shock protein, HSP90. *J Biol Chem.* 1991;266:10099–10103.

10. Ali MMU, Roe SM, Vaughan CK, et al. Crystal structure of an Hsp90–nucleotide–p23/Sba1 closed chaperone complex. *Nature.* 2006;440:1013–1017.

11. Prodromou C, Roe SM, O'Brien R, Ladbury JE, Piper PW, Pearl LH. Identification and structural characterization of the ATP/ADP-binding site in the Hsp90 molecular chaperone. *Cell.* 1997;90:65–75.

12. Dutta R, Inouye M. GHKL, an emergent ATPase/kinase superfamily. *Trends Biochem Sci.* 2000;25:24–28.

13. Jahn M, Rehn A, Pelz B, et al. The charged linker of the molecular chaperone Hsp90 modulates domain contacts and biological function. *Proc Natl Acad Sci USA.* 2014;111:17881.

14. Tsutsumi S, Mollapour M, Prodromou C, et al. Charged linker sequence modulates eukaryotic heat shock protein 90 (Hsp90) chaperone activity. *Proc Natl Acad Sci USA.* 2012;109:2937.

15. Verba KA, Wang RY, Arakawa A, et al. Atomic structure of Hsp90-Cdc37-Cdk4 reveals that Hsp90 traps and stabilizes an unfolded kinase. *Science.* 2016;352:1542–1547.

16. Meyer P, Prodromou C, Hu B, et al. Structural and functional analysis of the middle segment of hsp90: implications for ATP hydrolysis and client protein and cochaperone interactions. *Mol Cell.* 2003;11:647–658.

17. Minami Y, Kimura Y, Kawasaki H, Suzuki K, Yahara I. The carboxy-terminal region of mammalian HSP90 is required for its dimerization and function in vivo. *Mol Cell Biol.* 1994;14:1459.

18. Harris SF, Shiau AK, Agard DA. The crystal structure of the carboxy-terminal dimerization domain of htpG, the Escherichia coli Hsp90, reveals a potential substrate binding site. *Structure.* 2004;12:1087–1097.

19. Young JC, Obermann WM, Hartl FU. Specific binding of tetratricopeptide repeat proteins to the C-terminal 12-kDa domain of hsp90. *J Biol Chem.* 1998;273:18007–18010.

20. Ratzke C, Mickler M, Hellenkamp B, Buchner J, Hugel T. Dynamics of heat shock protein 90 C-terminal dimerization is an important part of its conformational cycle. *Proc Natl Acad Sci USA.* 2010;107:16101–16106.

21. Prodromou C, Panaretou B, Chohan S, et al. The ATPase cycle of Hsp90 drives a molecular 'clamp' via transient dimerization of the N-terminal domains. *EMBO J.* 2000;19:4383.

22. Sreedhar AS, Kalmar E, Csermely P, Shen YF. Hsp90 isoforms: functions, expression and clinical importance. *FEBS Lett.* 2004;562:11–15.

23. Chen B, Piel WH, Gui L, Bruford E, Monteiro A. The HSP90 family of genes in the human genome: insights into their divergence and evolution. *Genomics.* 2005;86:627–637.

24. Grammatikakis N, Vultur A, Ramana CV, et al. The role of Hsp90N, a new member of the Hsp90 family, in signal transduction and neoplastic transformation. *J Biol Chem.* 2002;277:8312–8320.

25. Schweinfest CW, Graber MW, Henderson KW, Papas TS, Baron PL, Watson DK. Cloning and sequence analysis of Hsp89αΔN, a new member of the Hsp90 gene family. *Biochim Biophys Acta.* 1998;1398:18–24.

26. Zurawska A, Urbanski J, Bieganowski P. Hsp90n – an accidental product of a fortuitous chromosomal translocation rather than a regular Hsp90 family member of human proteome. *Biochim Biophys Acta.* 2008;1784:1844–1846.

27. Gupta RS. Phylogenetic analysis of the 90 kD heat shock family of protein sequences and an examination of the relationship among animals, plants, and fungi species. *Mol Biol Evol.* 1995;12:1063–1073.

28. Taipale M, Tucker G, Peng J, et al. A quantitative chaperone interaction network reveals the architecture of cellular protein homeostasis pathways. *Cell.* 2014;158:434–448.

29. Taherian A, Krone PH, Ovsenek N. A comparison of Hsp90α and Hsp90β interactions with cochaperones and substrates. *Biochem Cell Biol.* 2008;86:37–45.

30. Chadli A, Felts SJ, Toft DO. GCUNC45 is the first Hsp90 co-chaperone to show α/β isoform specificity. *J Biol Chem.* 2008;283:9509–9512.

31. Millson SH, Truman AW, Rácz A, et al. Expressed as the sole Hsp90 of yeast, the α and β isoforms of human Hsp90 differ with regard to their capacities for activation of certain client proteins, whereas only Hsp90β generates sensitivity to the Hsp90 inhibitor radicicol. *FEBS J.* 2007;274:4453–4463.

32. Workman P, Burrows F, Neckers L, Rosen N. Drugging the cancer chaperone HSP90: combinatorial therapeutic exploitation of oncogene addiction and tumor stress. *Ann NY Acad Sci.* 2007;1113:202–216.

33. Whitesell L, Lindquist SL. HSP90 and the chaperoning of cancer. *Nat Rev Cancer.* 2005;5:761–772.

34. Lianos GD, Alexiou GA, Mangano A, et al. The role of heat shock proteins in cancer. *Cancer Lett.* 2015;360:114–118.

35. Mahalingam D, Swords R, Carew JS, Nawrocki ST, Bhalla K, Giles FJ. Targeting HSP90 for cancer therapy. *Br J Cancer.* 2009;100:1523–1529.

36. Pick E, Kluger Y, Giltnane JM, et al. High HSP90 expression is associated with

decreased survival in breast cancer. *Cancer Res.* 2007;67:2932.

37. Ciocca DR, Calderwood SK. Heat shock proteins in cancer: diagnostic, prognostic, predictive, and treatment implications. *Cell Stress Chaperones.* 2005;10:86–103.

38. Wang J, Cui S, Zhang X, Wu Y, Tang H. High expression of heat shock protein 90 is associated with tumor aggressiveness and poor prognosis in patients with advanced gastric cancer. *PLoS One.* 2013;8:e62876.

39. Thomas X, Campos L, Mounier C, et al. Expression of heat-shock proteins is associated with major adverse prognostic factors in acute myeloid leukemia. *Leukemia Res.* 2005;29:1049–1058.

40. Wang X, Song X, Zhuo W, et al. The regulatory mechanism of Hsp90α secretion and its function in tumor malignancy. *Proc Natl Acad Sci USA.* 2009;106:21288.

41. Eustace BK, Sakurai T, Stewart JK, et al. Functional proteomic screens reveal an essential extracellular role for hsp90α in cancer cell invasiveness. *Nat Cell Biol.* 2004;6:507–514.

42. Whitesell L, Mimnaugh EG, De Costa B, Myers CE, Neckers LM. Inhibition of heat shock protein HSP90-pp60v-src heteroprotein complex formation by benzoquinone ansamycins: essential role for stress proteins in oncogenic transformation. *Proc Natl Acad Sci USA.* 1994;91:8324–8328.

43. Whitesell L, Shifrin SD, Schwab G, Neckers LM. Benzoquinonoid ansamycins possess selective tumoricidal activity unrelated to src kinase inhibition. *Cancer Res.* 1992;52:1721–1728.

44. Sharma SV, Agatsuma T, Nakano H. Targeting of the protein chaperone, HSP90, by the transformation suppressing agent, radicicol. *Oncogene.* 1998;16:2639–2645.

45. Schulte TW, Akinaga S, Soga S, et al. Antibiotic radicicol binds to the N-terminal domain of Hsp90 and shares important biologic activities with geldanamycin. *Cell Stress Chaperones.* 1998;3:100–108.

46. Roe SM, Prodromou C, O'Brien R, Ladbury JE, Piper PW, Pearl LH. Structural basis for inhibition of the Hsp90 molecular chaperone by the antitumor antibiotics radicicol and geldanamycin. *J Med Chem.* 1999;42:260–266.

47. Stebbins CE, Russo AA, Schneider C, Rosen N, Hartl FU, Pavletich NP. Crystal structure of an Hsp90-geldanamycin complex: targeting of a protein chaperone by an antitumor agent. *Cell.* 1997;89:239–250.

48. Tian ZQ, Liu Y, Zhang D, et al. Synthesis and biological activities of novel 17-aminogeldanamycin derivatives. *Bioorg Med Chem.* 2004;12:5317–5329.

49. Le Brazidec J-Y, Kamal A, Busch D, et al. Synthesis and biological evaluation of a new class of geldanamycin derivatives as potent inhibitors of Hsp90. *J Med Chem.* 2004;47:3865–3873.

50. Supko JG, Hickman RL, Grever MR, Malspeis L. Preclinical pharmacologic evaluation of geldanamycin as an antitumor agent. *Cancer Chemother Pharmacol.* 1995;36:305–315.

51. Menezes D, Taverna P, Jensen MR, et al. The novel oral HSP90 inhibitor NVP-HSP990 exhibits potent and broad-spectrum anti-tumor activities in vitro and in vivo. *Mol Cancer Ther.* 2012;11:730–739.

52. Zhang H, Neely L, Lundgren K, et al. BIIB021, a synthetic Hsp90 inhibitor, has broad application against tumors with acquired multidrug resistance. *Int J Cancer.* 2010;126:1226–1234.

53. Chiosis G, Kang Y, Sun W. Discovery and development of purine-scaffold Hsp90 inhibitors. *Expert Opin Drug Discov.* 2008;3:99–114.

54. Chiosis G, Timaul MN, Lucas B, et al. A small molecule designed to bind to the adenine nucleotide pocket of Hsp90 causes Her2 degradation and the growth arrest and differentiation of breast cancer cells. *Chem Biol.* 2001;8:289–299.

55. Biamonte MA, Shi J, Hong K, et al. Orally active purine-based inhibitors of the heat shock protein 90. *J Med Chem.* 2006;49:817–828.

56. Cheung KM, Matthews TP, James K, et al. The identification, synthesis, protein crystal structure and in vitro biochemical evaluation of a new 3,4-diarylpyrazole class of Hsp90 inhibitors. *Bioorg Med Chem Lett.* 2005;15:3338–3343.

57. Woodhead AJ, Angove H, Carr MG, et al. Discovery of (2,4-dihydroxy-5-iso-propylphenyl)-[5-(4-methylpiperazin-1-ylmethyl)-1,3-dihydrois oindol-2-yl]metha-none (AT13387), a novel inhibitor of the molecular chaperone Hsp90 by fragment based drug design. *J Med Chem.* 2010;53:5956–5969.

58. Nakashima T, Ishii T, Tagaya H, et al. New molecular and biological mechanism of antitumor activities of KW-2478, a novel nonansamycin heat shock protein 90 inhibitor, in multiple myeloma cells. *Clin Cancer Res.* 2010;16:2792.

59. Lin T-Y, Bear M, Du Z, et al. The novel HSP90 inhibitor STA-9090 exhibits activity against Kit-dependent and -independent malignant mast cell tumors. *Exp Hematol.* 2008;36:1266–1277.

60. Eccles SA, Massey A, Raynaud FI, et al. NVP-AUY922: a novel heat shock protein 90 inhibitor active against xenograft tumor growth, angiogenesis, and metastasis. *Cancer Res.* 2008;68:2850–2860.

61. Whitesell L, Robbins N, Huang DS, et al. Structural basis for species-selective targeting of Hsp90 in a pathogenic fungus. *Nat Commun.* 2019;10:402.

62. Uno T, Kawai Y, Yamashita S, et al. Discovery of 3-ethyl-4-(3-isopropyl-4-(4-(1-methyl-1H-pyrazol-4-yl)-1H-imidazol-1-yl)-1H-pyrazolo[3,4-b]pyridin-1-yl)benza-mide (TAS-116) as a potent, selective, and orally available HSP90 inhibitor. *J Med Chem.* 2018.

63. Bussenius J, Blazey CM, Aay N, et al. Discovery of XL888: a novel tropane-derived small molecule inhibitor of HSP90. *Bioorg Med Chem Lett.* 2012;22:5396–5404.

64. Ferraro M, D'Annessa I, Moroni E, et al. Allosteric modulators of HSP90 and HSP70: dynamics meets function through structure-based drug design. *J Med Chem.* 2019;62:60–87.

65. Neckers L, Blagg B, Haystead T, Trepel JB, Whitesell L, Picard D. Methods to validate Hsp90 inhibitor specificity, to identify off-target effects, and to rethink approaches for clinical development. *Cell Stress Chaperones.* 2018;23:467–482.

66. Shrestha L, Bolaender A, Patel HJ, Taldone T. Heat shock protein (HSP) drug discovery and development: targeting heat shock proteins in disease. *Curr Top Med Chem.* 2016;16:2753–2764.

67. Garg G, Khandelwal A, Blagg BS. Anticancer inhibitors of Hsp90 function: Beyond the usual suspects. *Adv Cancer Res.* 2016;129:51–88.

68. Hall JA, Forsberg LK, Blagg BSJ. Alternative approaches to Hsp90 modulation for the treatment of cancer. *Future Med Chem.* 2014;6:1587–1605.

69. Matts RL, Brandt GEL, Lu Y, et al. A systematic protocol for the characterization of Hsp90 modulators. *Biorg Med Chem.* 2011;19:684–692.

70. Bagatell R, Paine-Murrieta GD, Taylor CW, et al. Induction of a heat shock factor 1-dependent stress response alters the cytotoxic activity of Hsp90-binding agents. *Clin Cancer Res.* 2000;6:3312–3318.

71. Zou J, Guo Y, Guettouche T, Smith DF, Voellmy R. Repression of heat shock transcription factor HSF1 activation by HSP90 (HSP90 complex) that forms a stress-sensitive complex with HSF1. *Cell.* 1998;94:471–480.

72. Whitesell L, Bagatell R, Falsey R. The stress response: implications for the clinical development of Hsp90 inhibitors. *Curr Cancer Drug Targets.* 2003;3:349–358.

73. Voellmy R, Boellmann F. Chaperone regulation of the heat shock protein response. *Adv Exp Med Biol.* 2007;594:89–99.

74. Zhao H, Blagg BSJ. Chapter 10: Inhibitors of the Hsp90 C-terminus. In: Machajewski TD, Gao Z, eds. *Inhibitors of Molecular Chaperones as Therapeutic Agents.* The Royal Society of Chemistry; 2014:259–301.

75. Jhaveri K, Ochiana SO, Dunphy MPS, et al. Heat shock protein 90 inhibitors in the treatment of cancer: current status and future directions. *Expert Opin Investig Drugs.* 2014;23:611–628.

76. Avsar E. Chapter 13: Hsp90 Inhibitors in Clinic. In: Machajewski TD, Gao Z, eds. *Inhibitors of Molecular Chaperones as Therapeutic Agents.* The Royal Society of Chemistry; 2014:336–378.

77. Neckers L, Workman P. Hsp90 molecular chaperone inhibitors: are we there yet? *Clin Cancer Res.* 2012;18:64–76.

78. Zhou D, Liu Y, Ye J, et al. A rat retinal damage model predicts for potential clinical visual disturbances induced by Hsp90 inhibitors. *Toxicol Appl Pharmacol.* 2013;273:401–409.

79. Jhaveri K, Taldone T, Modi S, Chiosis G. Advances in the clinical development of heat shock protein 90 (Hsp90) inhibitors in cancers. *Biochim Biophys Acta.* 1823;2012:742–755.

80. Marcu MG, Schulte TW, Neckers L. Novobiocin and related coumarins and depletion of heat shock protein 90-dependent signaling proteins. *J Natl Cancer Inst.* 2000;92:242–248.

81. Marcu MG, Chadli A, Bouhouche I, Catelli M, Neckers LM. The heat shock protein 90 antagonist novobiocin interacts with a previously unrecognized ATP-binding domain in the carboxyl terminus of the chaperone. *J Biol Chem.* 2000;275:37181–37186.

82. Sôti C, Rácz A, Csermely P. A nucleotide-dependent molecular switch controls ATP binding at the C-terminal domain of Hsp90. N-terminal nucleotide binding unmasks a C-terminal binding pocket. *J Biol Chem.* 2002;277:7066–7075.

83. Garnier C, Lafitte D, Tsvetkov PO, et al. Binding of ATP to heat shock protein 90 – evidence for an ATP-binding site in the C-terminal domain. *J Biol Chem.* 2002;277:12208–12214.

84. Sôti C, Vermes Á, Haystead TAJ, Csermely P. Comparative analysis of the ATP-binding sites of Hsp90 by nucleotide affinity cleavage: a distinct nucleotide specificity of the C-terminal ATP-binding site. *Eur J Biochem.* 2003;270:2421–2428.

85. Khalid S, Paul S. Identifying a C-terminal ATP binding sites-based novel Hsp90-Inhibitor in silico: a plausible therapeutic approach in Alzheimer's disease. *Med Hypotheses.* 2014;83:39–46.

86. Matts RL, Dixit A, Peterson LB, et al. Elucidation of the Hsp90 C-terminal inhibitor binding site. *ACS Chem Biol.* 2011;6:800–807.

87. Morra G, Neves MAC, Plescia CJ, et al. Dynamics-based discovery of allosteric inhibitors: selection of new ligands for the C-terminal domain of Hsp90. *J Chem Theory Comput.* 2010;6:2978–2989.

88. Sgobba M, Degliesposti G, Ferrari AM, Rastelli G. Structural models and binding site prediction of the C-terminal domain of human Hsp90: a new target for anticancer drugs. *Chem Biol Drug Des.* 2008;71:420–433.

89. Allan RK, Mok D, Ward BK, Ratajczak T. Modulation of chaperone function and cochaperone interaction by novobiocin in the C-terminal domain of Hsp90: evidence that coumarin antibiotics disrupt Hsp90 dimerization. *J Biol Chem.* 2006;281:7161–7171.

90. Zhao H, Donnelly AC, Kusuma BR, et al. Engineering an antibiotic to fight cancer: optimization of the novobiocin scaffold to produce anti-proliferative agents. *J Med Chem.* 2011;54:3839–3853.

91. Donnelly AC, Mays JR, Burlison JA, et al. The design, synthesis, and evaluation of coumarin ring derivatives of the novobiocin scaffold that exhibit antiproliferative activity. *J Org Chem.* 2008;73:8901–8920.

92. Burlison JA, Neckers L, Smith AB, Maxwell A, Blagg BSJ. Novobiocin: redesigning a DNA gyrase inhibitor for selective inhibition of Hsp90. *J Am Chem Soc.* 2006;128:15529–15536.

93. Yu XM, Shen G, Neckers L, et al. Hsp90 inhibitors identified from a library of novobiocin analogues. *J Am Chem Soc.* 2005;127:12778–12779.

94. Byrd KM, Kent CN, Blagg BSJ. Synthesis and biological evaluation of stilbene analogues as Hsp90 C-terminal inhibitors. *ChemMedChem.* 2017;12:2022–2029.

95. Ghosh S, Liu Y, Garg G, et al. Diverging novobiocin anti-cancer activity from neuroprotective activity through modification of the amide tail. *ACS Med Chem Lett.* 2016;7:813–818.

96. Anyika M, McMullen M, Forsberg LK, Dobrowsky RT, Blagg BS. Development of noviomimetics as C-terminal Hsp90 inhibitors. *ACS Med Chem Lett.* 2016;7:67–71.

97. Zhao H, Garg G, Zhao J, et al. Design, synthesis and biological evaluation of biphenylamide derivatives as Hsp90 C-terminal inhibitors. *Eur J Med Chem.* 2015;89:442–466.

98. Kusuma BR, Zhang L, Sundstrom T, Peterson LB, Dobrowsky RT, Blagg BSJ. Synthesis and evaluation of novologues as c-terminal HSP90 inhibitors with cytoprotective activity against sensory neuron glucotoxicity. *J Med Chem.* 2012;55:5797–5812.

99. Ma J, Farmer KL, Pan P, et al. Heat shock protein 70 is necessary to improve mitochondrial bioenergetics and reverse diabetic sensory neuropathy following KU-32 therapy. *J Pharmacol Exp Ther.* 2014;348:281.

100. Urban MJ, Pan P, Farmer KL, Zhao H, Blagg BSJ, Dobrowsky RT. Modulating molecular chaperones improves sensory fiber recovery and mitochondrial function in diabetic peripheral neuropathy. *Exp Neurol.* 2012;235:388–396.

101. Tran PL, Kim SA, Choi HS, Yoon JH, Ahn SG. Epigallocatechin-3-gallate suppresses the expression of HSP70 and HSP90 and exhibits anti-tumor activity in vitro and in vivo. *BMC Cancer.* 2010;10:276.

102. Asano Y, Okamura S, Ogo T, Eto T, Otsuka T, Niho Y. Effect of (−)-epigallocatechin gallate on leukemic blast cells from patients with acute myeloblastic leukemia. *Life Sci.* 1996;60:135–142.

103. Yin Z, Henry EC, Gasiewicz TA. (−)-Epigallocatechin-3-gallate is a novel Hsp90 inhibitor. *Biochemistry.* 2009;48:336–345.

104. Palermo CM, Westlake CA, Gasiewicz TA. Epigallocatechin gallate inhibits aryl hydrocarbon receptor gene transcription through an indirect mechanism involving binding to a 90 kDa heat shock protein. *Biochemistry.* 2005;44:5041–5052.

105. Bhat R, Adam AT, Lee JJ, Gasiewicz TA, Henry EC, Rotella DP. Towards the discovery of drug-like epigallocatechin gallate analogs as Hsp90 inhibitors. *Bioorg Med Chem Lett.* 2014;24:2263–2266.

106. Bhat R, Adam AT, Lee JJ, et al. Structure–activity studies of (−)-epigallocatechin gallate derivatives as HCV entry inhibitors. *Bioorg Med Chem Lett.* 2014;24:4162–4165.

107. Khandelwal A, Hall JA, Blagg BSJ. Synthesis and structure–activity relationships of EGCG analogues, a recently identified Hsp90 inhibitor. *J Org Chem.* 2013;78:7859–7884.

108. Na HK, Surh YJ. Intracellular signaling network as a prime chemopreventive target of (−)-epigallocatechin gallate. *Mol Nutr Food Res.* 2006;50:152–159.

109. Tachibana H, Koga K, Fujimura Y, Yamada K. A receptor for green tea polyphenol EGCG. *Nat Struct Mol Biol.* 2004;11:380–381.

110. Oh S-H, Woo JK, Jin Q, et al. Identification of novel antiangiogenic anticancer activities of deguelin targeting hypoxia-inducible factor-1 alpha. *Int J Cancer.* 2008;122:5–14.

111. Oh SH, Woo JK, Yazici YD, et al. Structural basis for depletion of heat shock protein 90 client proteins by deguelin. *J Natl Cancer Inst.* 2007;99:949–961.

112. Caboni P, Sherer TB, Zhang N, et al. Rotenone, deguelin, their metabolites, and the rat model of Parkinson's disease. *Chem Res Toxicol.* 2004;17:1540–1548.

113. Cho T-M, Kim JY, Kim Y-J, et al. C-terminal HSP90 inhibitor L80 elicits anti-metastatic effects in triple-negative breast cancer via STAT3 inhibition. *Cancer Lett.* 2019.

114. Lee S-C, Min H-Y, Choi H, et al. Synthesis and evaluation of a novel deguelin derivative, L80, which disrupts ATP binding to the C-terminal domain of heat shock protein 90. *Mol Pharmacol.* 2015 mol.114.096883.

115. Kasza A, Hunya A, Frank Z, et al. Dihydropyridine derivatives modulate heat shock responses and have a neuroprotective. Effect in a transgenic mouse model of alzheimer's disease. *J Alzheimers Dis.* 2016;53:557–571.

116. Roe MS, Wahab B, Török Z, Horváth I, Vigh L, Prodromou C. Dihydropyridines allosterically modulate Hsp90 providing a novel mechanism for heat shock protein co-induction and neuroprotection. *Front Mol Biosci.* 2018;5.

117. Taipale M, Krykbaeva I, Koeva M, et al. Quantitative analysis of HSP90-client interactions reveals principles of substrate recognition. *Cell.* 2012;150:987–1001.

118. Roe SM, Ali MM, Meyer P, et al. The mechanism of Hsp90 regulation by the protein kinase-specific cochaperone p50(cdc37). *Cell.* 2004;116:87–98.

119. Siligardi G, Hu B, Panaretou B, Piper PW, Pearl LH, Prodromou C. Co-chaperone regulation of conformational switching in the Hsp90 ATPase cycle. *J Biol Chem.* 2004;279:51989–51998.

120. Gray PJ, Stevenson MA, Calderwood SK. Targeting Cdc37 inhibits multiple signaling pathways and induces growth arrest in prostate cancer cells. *Cancer Res.* 2007;67:11942.

121. Westerheide SD, Bosman JD, Mbadugha BN, et al. Celastrols as inducers of the heat shock response and cytoprotection. *J Biol Chem.* 2004;279:56053–56060.

122. Hieronymus H, Lamb J, Ross KN, et al. Gene expression signature-based chemical genomic prediction identifies a novel class of HSP90 pathway modulators. *Cancer Cell.* 2006;10:321–330.

123. Zhang T, Li YY, Yu YK, Zou P, Jiang YQ, Sun DX. Characterization of celastrol to inhibit Hsp90 and Cdc37 interaction. *J Biol Chem.* 2009;284:35381–35389.

124. Sreeramulu S, Gande SL, Göbel M, Schwalbe H. Molecular mechanism of inhibition of the human protein complex Hsp90–Cdc37, a kinome chaperonecCochaperone, by triterpene celastrol. *Angew Chem Int Ed.* 2009;48:5853–5855.

125. Chadli A, Felts SJ, Wang Q, et al. Celastrol inhibits Hsp90 chaperoning of steroid receptors by inducing fibrillization of the Co-chaperone p23. *J Biol Chem.* 2010;285:4224–4231.

126. Zanphorlin LM, Alves FR, Ramos CHI. The effect of celastrol, a triterpene with antitumorigenic activity, on conformational and functional aspects of the human 90kDa heat shock protein Hsp90α, a chaperone implicated in the stabilization of the tumor phenotype. *Biochim Biophys Acta.* 1840;2014:3145–3152.

127. Mohan R, Hammers H, Bargagna-mohan P, et al. Withaferin A is a potent inhibitor of angiogenesis. *Angiogenesis.* 2004;7:115–122.

128. Yu Y, Katiyar SP, Sundar D, et al. Withaferin-A kills cancer cells with and without telomerase: chemical, computational and experimental evidences. *Cell Death Dis.* 2017;8:e2755.

129. Yu Y, Hamza A, Zhang T, et al. Withaferin A targets heat shock protein 90 in pancreatic cancer cells. *Biochem Pharmacol.* 2010;79:542–551.

130. Grover A, Shandilya A, Agrawal V, et al. Hsp90/Cdc37 chaperone/co-chaperone complex, a novel junction anticancer target elucidated by the mode of action of herbal drug Withaferin A. *BMC Bioinf.* 2011;12:S30.
131. Grover A, Shandilya A, Agrawal V, et al. Blocking the chaperone kinome pathway: mechanistic insights into a novel dual inhibition approach for supra-additive suppression of malignant tumors. *Biochem Biophys Res Commun.* 2011;404:498–503.
132. Ateba SB, Mvondo MA, Ngeu ST, et al. Natural terpenoids against female breast cancer: a 5-year recent research. *Curr Med Chem.* 2018;25:3162–3213.
133. Rodriguez N, Vasquez Y, Hussein AA, Coley PD, Solis PN, Gupta MP. Cytotoxic cucurbitacin constituents from Sloanea zuliaensis. *J Nat Prod.* 2003;66:1515–1516.
134. Kim DK, Choi SH, Lee JO, et al. Cytotoxic constituents of Sorbaria sorbifolia var. stellipila. *Arch Pharmacal Res.* 1997;20:85.
135. Geissman TA. New substances of plant origin. *Annu Rev Pharmacol Toxicol.* 1964;4:305–1000.
136. Hall JA, Seedarala S, Rice N, Kopel L, Halaweish F, Blagg BS. Cucurbitacin D is a disruptor of the HSP90 chaperone machinery. *J Nat Prod.* 2015;78:873–879.
137. Felts SJ, Toft DO. p23, a simple protein with complex activities. *Cell Stress Chaperones.* 2003;8:108–113.
138. Lamb J, Crawford ED, Peck D, et al. The connectivity map: using gene-expression signatures to connect small molecules, genes, and disease. *Science.* 2006;313:1929.
139. Calderón José S, Céspedes Carlos L, Rosas R, et al. Acetylcholinesterase and insect growth inhibitory activities of Gutierrezia microcephala on fall army worm Spodoptera frugiperda J.E. Smith. *Z Naturforsch C.* 2001;56:382.
140. Omar S, Godard K, Ingham A, et al. Antimalarial activities of gedunin and 7-methoxygedunin and synergistic activity with dillapiol. *Ann Appl Biol.* 2003;143:135–141.
141. Subramani R, Gonzalez E, Nandy SB, et al. Gedunin inhibits pancreatic cancer by altering sonic hedgehog signaling pathway. *Oncotarget.* 2016;8:10891–10904.
142. Kamath SG, Chen N, Xiong Y, et al. Gedunin, a novel natural substance, inhibits ovarian cancer cell proliferation. *Int J Gynecol Cancer.* 2009;19:1564–1569.
143. Uddin SJ, Nahar L, Shilpi JA, et al. Gedunin, a limonoid from Xylocarpus granatum, inhibits the growth of CaCo-2 colon cancer cell line In Vitro. *Phytother Res.* 2007;21:757–761.
144. Brandt GEL, Schmidt MD, Prisinzano TE, Blagg BSJ. Gedunin, a novel Hsp90 inhibitor: semisynthesis of derivatives and preliminary structure–activity relationships. *J Med Chem.* 2008;51:6495–6502.
145. Patwardhan CA, Fauq A, Peterson LB, Miller C, Blagg BS, Chadli A. Gedunin inactivates the co-chaperone p23 protein causing cancer cell death by apoptosis. *J Biol Chem.* 2013;288:7313–7325.
146. Pearl LH, Prodromou C. Structure and mechanism of the Hsp90 molecular chaperone machinery. *Annu Rev Biochem.* 2006;75:271–294.
147. Wegele H, Wandinger SK, Schmid AB, Reinstein J, Buchner J. Substrate transfer from the chaperone Hsp70 to Hsp90. *J Mol Biol.* 2006;356:802–811.
148. Nelson GM, Huffman H, Smith DF. Comparison of the carboxy-terminal DP-repeat region in the co-chaperones Hop and Hip. *Cell Stress Chaperones.* 2003;8:125–133.
149. Belofsky GN, Jensen PR, Fenical W. Sansalvamide: a new cytotoxic cyclic depsipeptide produced by a marine fungus of the genus Fusarium. *Tetrahedron Lett.* 1999;40:2913–2916.
150. Vasko RC, Rodriguez RA, Cunningham CN, Ardi VC, Agard DA, McAlpine SR. Mechanistic studies of sansalvamide A-amide: an allosteric modulator of Hsp90. *ACS Med Chem Lett.* 2010;1:4–8.
151. Chakraborty A, Koldobskiy MA, Sixt KM, et al. HSP90 regulates cell survival via inositol hexakisphosphate kinase-2. *Proc Natl Acad Sci USA.* 2008;105:1134–1139.
152. Chen S, Sullivan WP, Toft DO, Smith DF. Differential interactions of p23 and the TPR-containing proteins Hop, Cyp40, FKBP52 and FKBP51 with Hsp90 mutants. *Cell Stress Chaperones.* 1998;3:118–129.
153. Ardi VC, Alexander LD, Johnson VA, McAlpine SR. Macrocycles that inhibit the binding between heat shock protein 90 and TPR-containing proteins. *ACS Chem Biol.* 2011;6:1357–1366.
154. McConnell JR, Alexander LA, McAlpine SR. A heat shock protein 90 inhibitor that modulates the immunophilins and regulates hormone receptors without inducing the heat shock response. *Bioorg Med Chem Lett.* 2014;24:661–666.
155. Koay YC, McConnell JR, Wang Y, et al. Chemically accessible Hsp90 inhibitor that does not induce a heat shock response. *ACS Med Chem Lett.* 2014;5:771–776.
156. Horibe T, Torisawa A, Kohno M, Kawakami K. Molecular mechanism of cytotoxicity induced by Hsp90-targeted Antp-TPR hybrid peptide in glioblastoma cells. *Mol Cancer.* 2012;11:59.
157. Horibe T, Kohno M, Haramoto M, Ohara K, Kawakami K. Designed hybrid TPR peptide targeting Hsp90 as a novel anticancer agent. *J Transl Med.* 2011;9:8.
158. Buckton LK, Wahyudi H, McAlpine SR. The first report of direct inhibitors that target the C-terminal MEEVD region on heat shock protein 90. *Chem Commun (Camb).* 2016;52:501–504.
159. Rahimi MN, McAlpine SR. Protein-protein inhibitor designed de novo to target the MEEVD region on the C-terminus of Hsp90 and block co-chaperone activity. *Chem Commun (Camb).* 2019;55:846–849.
160. Yi F, Pingjun Z, Southall N, et al. An AlphaScreen(TM)-based high-throughput screen to identify inhibitors of Hsp90-cochaperone interaction. *J Biomol Screen.* 2009;14:273–281.
161. Yi F, Regan L. A novel class of small molecule inhibitors of Hsp90. *ACS Chem Biol.* 2008;3:645–654.
162. Pimienta G, Herbert KM, Regan L. A compound that inhibits the HOP–Hsp90 complex formation and has unique killing effects in breast cancer cell lines. *Mol Pharm.* 2011;8:2252–2261.
163. Ciglia E, Vergin J, Reimann S, et al. Resolving hot spots in the C-terminal dimerization domain that determine the stability of the molecular chaperone Hsp90. *PLoS One.* 2014;9:e96031.
164. Jose J, Meyer TF. The autodisplay story, from discovery to biotechnical and biomedical applications. *Microbiol Mol Biol Rev.* 2007;71:600–619.
165. Bopp B, Ciglia E, Ouald-Chaib A, Groth G, Gohlke H, Jose J. Design and biological testing of peptidic dimerization inhibitors of human Hsp90 that target the C-terminal domain. *Biochim Biophys Acta.* 1860;2016:1043–1055.
166. Diedrich D, Moita AJR, Rüther A, et al. α-Aminoxy oligopeptides: synthesis, secondary structure, and cytotoxicity of a new class of anticancer foldamers. *Chem Eur J.* 2016;22:17600–17611.
167. Galam L, Hadden MK, Ma Z, et al. High-throughput assay for the identification of Hsp90 inhibitors based on Hsp90-dependent refolding of firefly luciferase. *Bioorg Med Chem.* 2007;15:1939–1946.
168. Bhatia S, Diedrich D, Frieg B, et al. Targeting HSP90 dimerization via the C terminus is effective in imatinib-resistant CML and lacks the heat shock response. *Blood.* 2018;132:307–320.
169. Ferraro M, Colombo G. Targeting difficult protein-protein interactions with plain and general computational approaches. *Molecules.* 2018;23.
170. Legnani L, Compostella F, Sansone F, Toma L. Cone calix[4]arenes with orientable glycosylthioureido groups at the upper Rim: An in-depth analysis of their symmetry properties. *J Org Chem.* 2015;80:7412–7418.

Holger Gohlke is Professor of Pharmaceutical and Medicinal Chemistry at Heinrich Heine University Düsseldorf and head of the NIC research group "Computational Biophysical Chemistry" at Forschungszentrum Jülich. He obtained his diploma in chemistry from the Technical University of Darmstadt and his PhD from Philipps-University, Marburg. He then did postdoctoral research at The Scripps Research Institute, La Jolla, USA. After appointments as Assistant Professor in Frankfurt and Professor in Kiel, he moved to Düsseldorf in 2009 and was appointed in Jülich in 2017. He was awarded the "Innovationspreis in Medizinischer und Pharmazeutischer Chemie" from the GDCh and the DPhG, the Hansch Award of the Cheminformatics and QSAR Society, and the Novartis Chemistry Lectureship. His current research focuses on the understanding, prediction, and modulation of interactions involving biological macromolecules from a computational perspective. His group applies and develops techniques grounded in computational pharmaceutical chemistry, computational biophysical chemistry, and molecular bioinformatics.

David Bickel has been a graduate student in the research group of Holger Gohlke at Heinrich Heine University Düsseldorf since 2017. He received his degree in Pharmacy from Leipzig University in 2015 and did his diploma thesis at the Fraunhofer Institute for Cell Therapy and Immunology IZI (Halle (Saale)) in the Department of Drug Design and Target Validation. His current research focuses on the modulation of protein-protein interactions by small molecules, employing molecular modeling and simulation techniques.

82

Appendix

Publication II

The tetrahydroxanthone-dimer phomoxanthone A is a strong inducer of apoptosis in cisplatin-resistant solid cancer cells

Wang, C. [a], Engelke, L. [a], Bickel, D. [a], Hamacher, A. [a], Frank, M. [b], Proksch, P. [b], Gohlke, H. [a,c], and Kassack, M.U. [a]

[a] Institute of Pharmaceutical and Medicinal Chemistry, Heinrich Heine University Düsseldorf, Düsseldorf, Germany

[b] Institute of Pharmaceutical Biology and Biotechnology, Heinrich Heine Universität Düsseldorf, Düsseldorf, Germany

[c] John von Neumann Institute for Computing (NIC), Jülich Supercomputing Centre (JSC), Institute of Biological Information Processing (IBI-7: Structural Biochemistry) & Institute of Bio- and Geosciences (IBG-4: Bioinformatics), Forschungszentrum Jülich GmbH, Jülich, Germany

The tetrahydroxanthone-dimer phomoxanthone A is a strong inducer of apoptosis in cisplatin-resistant solid cancer cells

Chenyin Wang[a], Laura Engelke[a], David Bickel[a], Alexandra Hamacher[a], Marian Frank[b], Peter Proksch[b], Holger Gohlke[a,c], Matthias U. Kassack[a,*]

[a] Institute of Pharmaceutical and Medicinal Chemistry, Heinrich Heine University Düsseldorf, 40225 Düsseldorf, Germany
[b] Institute of Pharmaceutical Biology and Biotechnology, Heinrich Heine Universität Düsseldorf, 40225 Düsseldorf, Germany
[c] John von Neumann Institute for Computing (NIC), Jülich Supercomputing Centre (JSC) & Institute for Complex Systems – Structural Biochemistry (ICS 6), Forschungszentrum Jülich GmbH, 52425 Jülich, Germany

ABSTRACT

Platinum compounds are the first-line therapy for many types of cancer. However, drug resistance has frequently been reported for and is a major limitation of platinum-based chemotherapy in the clinic. In the current study, we examined the anti-tumor activity of phomoxanthone A (PXA), a tetrahydroxanthone dimer isolated from the endophytic fungus *Phomopsis longicolla*, in several solid cancer cell lines and their cisplatin-resistant sub-cell lines. PXA showed strong cytotoxic effects with IC_{50} values in the high nanomolar or low micromolar range in MTT assays. IC_{50} values of PXA were lower than those of cisplatin. Remarkably, equipotent anti-cancer activity was found in cisplatin-sensitive and respective cisplatin-resistant cells. Anticancer effects of PXA were studied in further detail in ovarian cancer (A2780) and bladder cancer (J82) cell pairs. PXA led to rapid depolarization of the mitochondrial membrane potential and strong activation of caspase 3 and 7, eventually resulting in strong induction of apoptosis. These effects occurred again both in sensitive and resistant cell lines. IC_{50} values of PXA from MTT and mitochondrial membrane depolarization assays were in good agreement. Configurational free energy computations indicate that both the neutral and singly negatively charged PXA show membrane partitioning and can penetrate the inner mitochondrial membrane. PXA treatment did not damage the plasma membranes of cancer cells, thus excluding unspecific membrane effects. Further, PXA had neither an effect on intracellular ROS nor on reduction of ROS after hydrogen peroxide treatment. In conclusion, our studies present PXA as a natural compound with strong apoptotic anticancer effects against platinum-resistant solid cancers. This may open new treatment options in clinically resistant malignancies.

1. Introduction

Cancer is one of the major leading causes of death worldwide. It is predicted that there are approximately 1.7 million new cases of cancer and about 600,000 deaths from cancer are projected to occur in the US in 2018. The treatment options of cancer generally include surgery, radiation therapy, and chemotherapy. Cis- or carboplatin are among the most potent chemotherapeutic drugs and used to treat many types of cancers including ovarian, bladder, and head and neck cancers.[1] The cytotoxicity of platinum compounds is mediated by the formation of DNA adducts leading to apoptosis and cell cycle arrest.[2] The sensitivity or resistance of cancer cells against cisplatin is an important factor for treatment options.[3–4] Acquisition of cisplatin resistance in patients has been observed for many years. Generally, development of platinum

resistance is multifactorial, including pre-target mechanisms leading to the reduction in intracellular drug accumulation, on-target mechanisms increasing the rate of DNA damage repair, and post-target effects leading to defects in apoptotic signal transduction pathways which are normally activated in response to DNA damage. These processes will then inhibit apoptosis and subsequently lead to drug resistance.[5] Apoptosis is a vital component for many processes including embryonic development and tissue homoeostasis.[6] Apoptosis mainly proceeds through the activation of intrinsic and/or extrinsic signal transduction pathways. The major characteristic features of apoptosis include cell shrinkage, condensation of chromatin, and DNA fragmentation.[7] The extrinsic apoptosis pathway is triggered by activation of death receptors with recruitment of cytoplasmic adapter proteins followed by activation of caspase-8 and finally activating caspase 3.[8] The intrinsic or
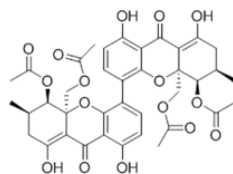

Figure 1. Structure of the mycotoxin phomoxanthone A (PXA) isolated from the fungus *Phomopsis longicola*.

mitochondrial pathway is initiated by a diverse array of stimuli causing reduction in the mitochondrial membrane potential and eventually leading to cellular apoptosis.[9] However, unlike healthy cells, the down regulation or mutation of pro-apoptotic genes are associated with dysregulation of apoptosis in cancer and leads to uncontrolled cell proliferation.[10] Therefore, promoting apoptosis is an important strategy for novel anti-cancer drug discovery.

Natural products have been a great source for anti-cancer drugs. For instance, paclitaxel, a plant-derived diterpenoid interacting with β-tubulin, thus inhibiting the degradation of microtubules and inducing apoptosis, is commonly used for the treatment of many types of cancer.[11] Phomoxanthone A (PXA), a tetrahydroxanthone dimer derived from the mangrove-associated fungus *Phomopsis longicola*, was previously shown by our groups to exhibit potent cytotoxic and antibiotic activity (Figure 1).[12] A review on the source, stereochemistry, biosynthesis, structure–activity relationships, and anticancer activities of PXA were summarized by Frank et al.[13] PXA demonstrates low micromolar or even 3-digit nanomolar IC_{50} values (MTT assay) in solid and lymphoma cancer cell lines, respectively. Interestingly, PXA retains high selectivity (> 100) for cancer over non-cancer cells as estimated in peripheral blood mononuclear cells (PBMCs).[13] A recent report provided further insight into the mechanism of PXA in lymphoma cells.[4] PXA leads to a rapid depolarization of the mitochondrial potential and disruption of the inner mitochondrial membrane. The molecular target however, is still unknown.[4]

Considering the severity of platinum resistance in clinical patient cases, the findings about PXA encouraged us to study the effects of PXA in models of cisplatin-sensitive and –resistant human cancers. Here, the ovarian cancer cell line A2780 as well as the urinary bladder cancer cell line J82 and their cisplatin resistant sublines were used. Clinically relevant cisplatin resistance was induced by intermittent treatment with cisplatin over several weeks to mimic clinical treatment cycles. Resistance developed after approximately 8 to 14 weeks.[14,15] In contrast to cisplatin which gave clinically relevant resistance factors between sensitive and resistant cell lines of 2 to 4, the potency of PXA was similar in sensitive and resistant cell lines. Furthermore, PXA turned out as a strong depolarizer of mitochondrial membrane potential and strong inductor of apoptosis with similar potency in cisplatin-sensitive and –resistant cell lines whereas cisplatin was much less potent in apoptosis induction in resistant cancer cell lines. PXA may thus serve as a new natural compound to overcome the clinically highly relevant problem of platinum resistance in cancer patients.

2. Results and discussion

2.1 Determination of the cytotoxic potential of PXA

The cytotoxic activity of PXA was tested against a panel of human solid cancer cell lines and their cisplatin resistant sublines using the MTT assay. Results from earlier tests and from this study are summarized in Table 1. PXA showed potent cytotoxicity in all cell lines. IC_{50} values of PXA were 2 to 10-fold lower than IC_{50} values of cisplatin except for the bladder cancer cell line J82. Figure 2 compares the cytotoxicity of cisplatin and PXA in the various cell lines. The ratio of the IC_{50} values of cisplatin and PXA is 2 to 10 (except for J82).

Table 1
Antiproliferative effects of PXA in different human cancer cell lines.

Cell line	IC_{50} [μM]	
	Cisplatin	PXA
A2780*	3.98	0.58
A2780CisR*	12.6	1.38
MDA-MB-231	24.5	3.7
MDA-MB-231CisR	44.7	4.37
Cal27*	10.2	5.25
Cal27CisR*	38.0	5.62
Kyse510*	2.51	0.76
Kyse510CisR*	8.51	0.79
J82	2.29	3.23
J82CisR	7.76	2.04
K562	9.55	1.86
HCT116	16.2	1.82

Values are the mean of three independent experiments each carried out in triplicates. *IC_{50} values were reported previously.[12]
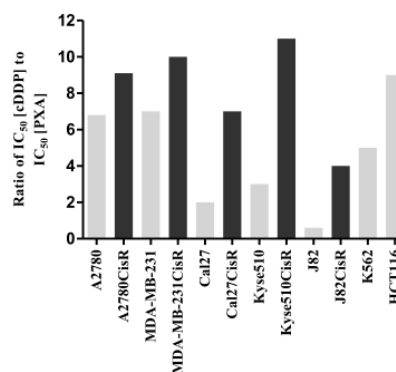
Figure 2. Ratios of IC_{50} values of cisplatin and PXA in different cell lines.

Interestingly, in all resistant cell lines (termed …CisR), the ratio of IC_{50} values increases (e.g. J82, Kyse510). This indicates that PXA is acting equipotent at cisplatin-resistant and cisplatin-sensitive cell lines and may thus serve as a suitable cytotoxic agent to address cisplatin-resistant cancers. In A2780 and A2780CisR cells, IC_{50} values of PXA were 7-fold and 9-fold lower compared to cisplatin, respectively (Table 1). The IC_{50} value of cisplatin was increased 4 times in the esophageal cell line Kyse510CisR cells compared to Kyse510. However, PXA exhibited similar cytotoxic effects in Kyse510 and Kyse510CisR cell lines (approx. 0.8 μM). Furthermore, the cytotoxicity of PXA was also investigated in the chronic myelogenous leukemia cell line K562 displaying an IC_{50} value of 1.86 μM which is 5 times lower than cisplatin (Table 1). PXA exhibited equipotent cytotoxicity against several other pairs of cisplatin-sensitive and cisplatin-resistant cell lines, such as the triple-negative breast cancer cell pair MDA-MB-231 and oral squamous cell carcinoma cell line Cal27. Even though PXA is slightly less potent in J82 cells (human bladder cancer) compared to cisplatin, the IC_{50} value of PXA is still in the low micromolar range and more importantly, PXA showed an even lower IC_{50} value in J82CisR cells.

Since PXA had the highest potency in A2780 cells (0.58 μM) and PXA was even more potent (1.6-fold) in J82CisR compared to J82, further studies on anticancer effects were carried out in these two pairs of cell lines. Remarkably, PXA has a rapid onset of its cytotoxic effect compared to cisplatin. Figure 3 shows the time-dependent concentration-effect curves of PXA and cisplatin in A2780 and A2780CisR. Whereas PXA showed only 2.5-fold (A2780) or 1.4-fold (A2780CisR) differences in IC_{50} values between 24 h and 72 h incubation time (MTT assay), cisplatin gave differences of 10.4-fold (A2780) and 6.9-fold (A2780CisR). These data demonstrate a fast cytotoxic effect of PXA.
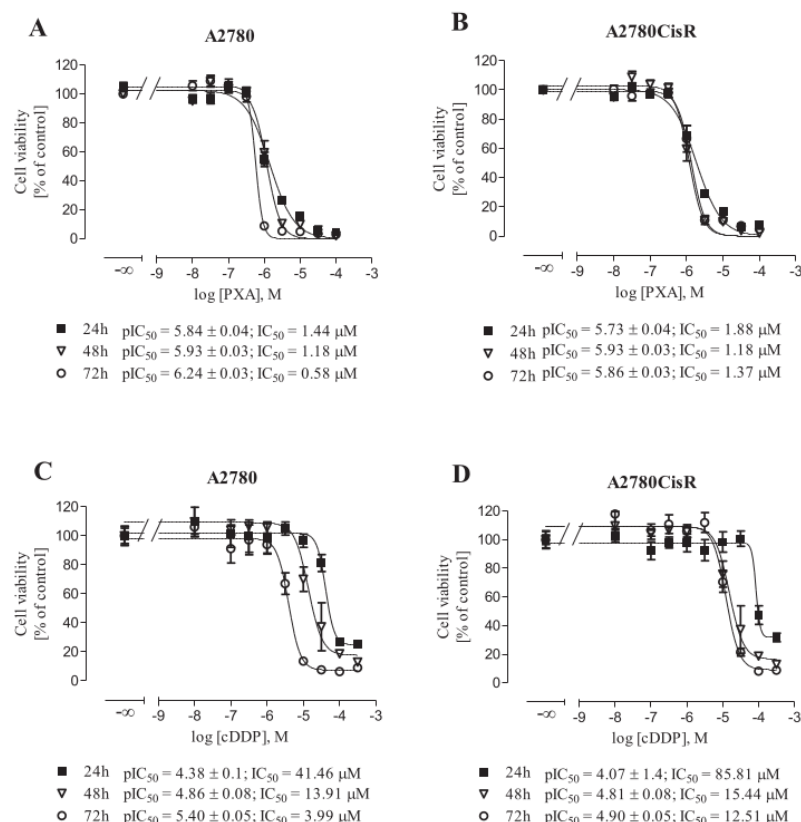
Figure 3. Time-dependent concentration-effect-curves of PXA and cisplatin. A2780 and A2780CisR cells were treated with PXA (A, B) or cisplatin (C, D) for different times. Data shown are average ± SEM of at least three independent experiments.

2.2 PXA induces G1 cell cycle arrest in A2780 and A2780CisR

MTT assays demonstrated a strong inhibition of cell proliferation upon PXA treatment. This prompted us to study cell cycle arrest after PXA treatment. The cell cycle profiles of A2780/A2780CisR and J82/J82CisR after PXA treatment are displayed in Figure 4. In A2780 and A2780CisR, the fraction of cells in G1 phase significantly increased in a dose-dependent manner after 24 h PXA treatment from 61.8% to 78.9% (A2780) and 68.7% to 81.1% (A2780CisR). In J82 and J82CisR cells however, no significant changes occurred in the cell cycle phases upon PXA treatment. These data suggest that the G1 phase cell cycle arrest induced by PXA is a cell type- and concentration-dependent effect.

2.3 PXA is a strong inducer of apoptosis in sensitive and cisplatin-resistant A2780 and J82 cell lines

PXA was further investigated for its effects on induction of apoptosis. Apoptosis induces several morphological changes including membrane blebbing, DNA degradation, and the formation of the apoptosome. Among these events, degradation of DNA characterized by an increased fraction of sub-G1 cells is a good marker for the detection of apoptosis. Figure 5 displays the effects of 24 h PXA treatment on apoptosis. In A2780, sub-G1 fraction increased (from 10% untreated control) dose-dependently up to almost 70%. Approx. 2x IC_{50} of PXA (1 μM) resulted already in 42% sub-G1 whereas 5x IC_{50} of cisplatin (20 μM) was needed to obtain a similar sub-G1 rate (47%), demonstrating the superior potency of PXA over cisplatin to induce apoptosis. In A2780CisR, PXA was even more potent: 0.7x IC_{50} of PXA (1 μM)

induced already almost 70% sub-G1 whereas 20 μM cisplatin (approx. 2x IC_{50}) did not significantly increase sub-G1 over untreated control. J82 cells gave a similar result: 1.6x IC_{50} PXA (5 μM) resulted in a similar amount of apoptotic cells (53%) as 8.7x IC_{50} cisplatin (20 μM). J82CisR cells seemed to be slightly more resistant to undergo apoptosis: 2.5x IC_{50} PXA (5 μM) or 2.5x IC_{50} cisplatin (20 μM) resulted in approx. 35% sub-G1 cells. Yet, considering 72 h MTT assay data (Table 1), it is clear that PXA is almost 4-fold more potent than cisplatin in J82CisR.

2.4 PXA treatment leads to rapid depolarization of the mitochondrial membrane potential

Mitochondria are cellular key players in the synthesis of ATP by utilizing the electrochemical gradient under aerobic conditions or as central regulators of apoptosis by maintenance of transmembrane potential and release of apoptogenic proteins.[16,17]

The strong induction of apoptosis by PXA prompted us to examine mitochondrial function by analyzing the mitochondrial membrane potential (ΔΨm) upon PXA treatment. The accumulation of tetramethylrhodamine ethyl ester (TMRE) in mitochondria as surrogate for ΔΨm[18] was detected by flow cytometry or fluorescence microscopy. As shown in Figure 6, PXA induced rapid and concentration-dependent decreases in fluorescence intensity of TMRE (measured by flow cytometry) in both pairs of A2780 and J82 cells after 1 h or 2 h treatment (Figure 6A, B, C, D). IC_{50} values of PXA in ΔΨm breakdown (1 h or 2 h) were remarkably similar to IC_{50} values obtained by MTT (72 h, Table 1). Figure 6E and F show the concentration-dependent effect of 24 h treatment of PXA on ΔΨm in A2780 and A2780CisR, respectively.
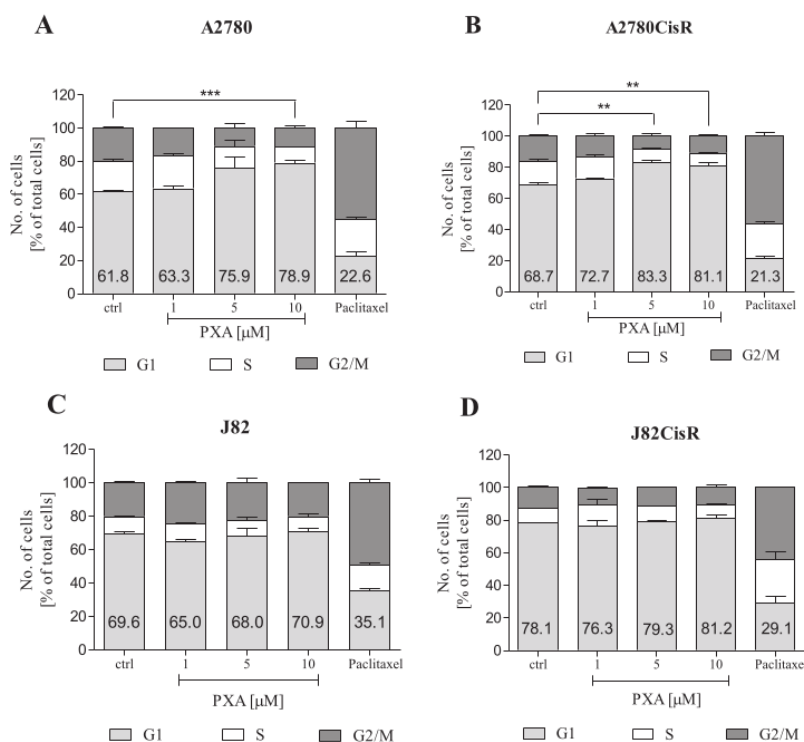
Figure 4. PXA induced cell cycle arrest is concentration and cell line dependent. After a 24 h incubation with the indicated concentrations, PXA was able to induce G1 cell cycle arrest in A2780 (A) and A2780CisR cells (B), but not in the J82 cell lines (C, D). Medium was used as control for untreated cells, paclitaxel as control for G2/M arrest. Data shown are the average ± SEM of three independent experiments. ***P < 0.001, **P < 0.01, *P < 0.05 in comparison to the untreated control.

Further, Figure 6E and F (right part, respectively) show the time-dependent effect of 1 μM PXA. 1 μM PXA for 1 h significantly reduced $\Delta\Psi$m to approx. 73%, and 2 h incubation reduced to approx. 50% of untreated control, whereas 24 h incubation reduced $\Delta\Psi$m to positive control (20 μM carbonyl cyanide m-chlorophenyl hydrazine, CCCP).[19] To confirm the approx. 3x lower potency of PXA in J82 and J82CisR compared to A2780 and A2780CisR cells (Figure 6A, B, C, D: IC$_{50}$ values for 2 h incubation were around 1 μM in A2780/A2780CisR and around 3 μM in J82/J82CisR), fluorescence imaging was additionally performed for 2 h incubation in J82 (Figure 6G) and J82CisR (Figure 6H). It was confirmed that 1 μM PXA had no effect (not significantly different from untreated control) whereas 5 and 10 μM PXA led to complete $\Delta\Psi$m breakdown (not significantly different from CCCP control). These results suggest that PXA is a compound targeting

mitochondria and inducing a rapid decrease of $\Delta\Psi$m in both A2780 and J82 cell lines as well as their cisplatin resistant subclones. Depolarized mitochondrial membrane potential may then trigger the intrinsic apoptotic pathway. These data are in full agreement with data recently published using lymphoma cells.[4]

2.5 PXA increases intracellular Ca^{2+} concentration

Rapid and strong breakdown of the mitochondrial membrane potential may be associated with Ca^{2+} release and increased cytoplasmic Ca^{2+} concentrations. This may in turn lead to the activation of Ca^{2+}-sensitive enzymes, e.g. involved in the apoptotic cascade or activation of caspases.[20] Thus, intracellular Ca^{2+} concentrations were determined in A2780 and A2780CisR in the presence and absence of 1 mM
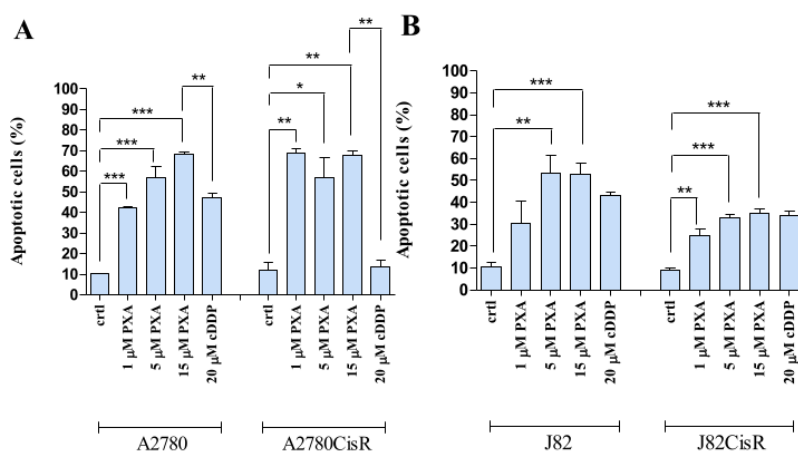
Figure 5. PXA mediates its antiproliferative effects via apoptosis. 24 h incubation with the indicated concentrations of PXA induced apoptosis in A2780 (A), A2780CisR (B), J82 (C), and J82CisR (D). As control, medium was used, and cisplatin served as positive control. Data are means ± SEM. ***P < 0.001, **P < 0.01, *P < 0.05, when compared with the untreated control group.
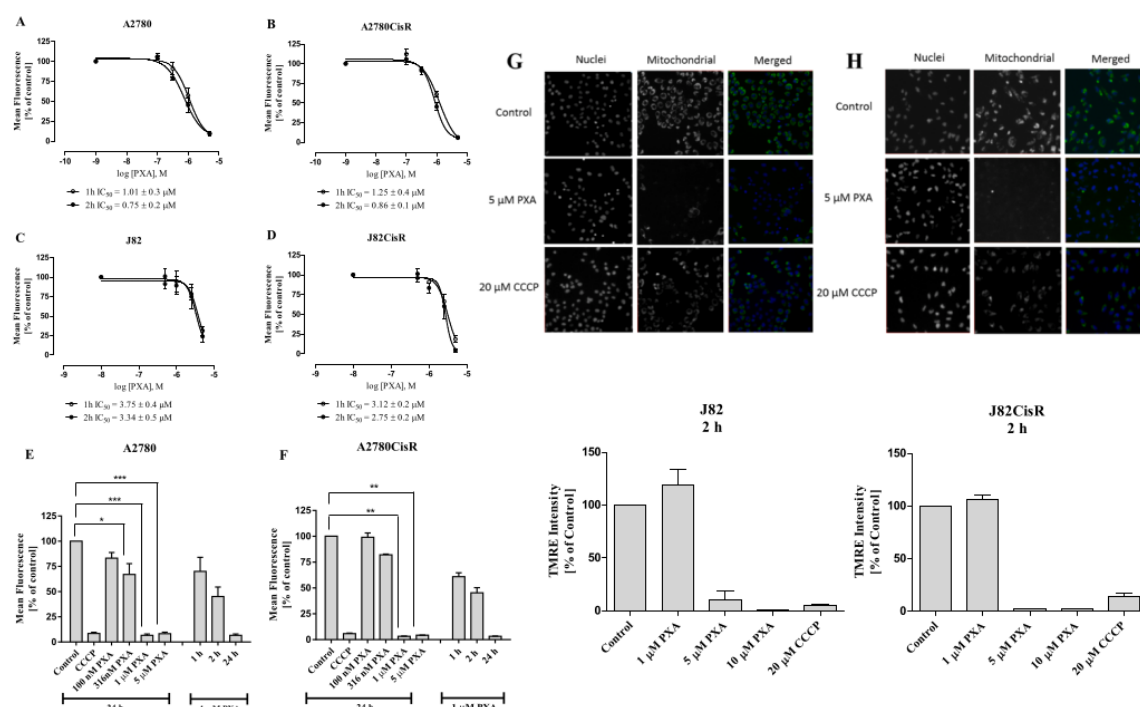
Figure 6. PXA depolarized mitochondrial membrane potential. A2780 (A), A2780CisR (B), J82 (C), and J82CisR (D) were treated for 1 h or 2 h with different concentrations of PXA before the mitochondrial potential was measured by flow cytometry. Medium was used as negative control and 20 μM CCCP was used as positive control. Further, A2780 (E) and A2780CisR cells (F) were treated with increasing concentrations of PXA for 24 h. In addition, Fig. 6E and F show the time-dependent depolarization of the membrane potential (analysis by flow cytometry) at 1 μM PXA. Furthermore, mitochondrial membrane potential was measured by fluorescence imaging in J82 (G) and J82CisR cells (H) after 2 h incubation. Data shown are mean ± SEM. ***$P < 0.001$, **$P < 0.01$, *$P < 0.05$ in comparison to the untreated control cells.

extracellular Ca^{2+} over 30 min after addition of PXA. 10 and 30 μM PXA led to a significant increase in intracellular Ca^{2+} in absence or presence of extracellular Ca^{2+} (Figure 7) whereas the Ca^{2+} increase induced by 1 μM PXA was only significant in the absence of extracellular Ca^{2+}. Mitochondrial membrane damage and increase in intracellular Ca^{2+} are thus hallmarks of the effects of PXA. Interestingly, Böhler et al. have reported that Ca^{2+} release upon PXA treatment is likely to be originated from the mitochondria (in lymphoma cells). It thus seems that mitochondrial damage by PXA results in Ca^{2+} release thereof and depolarization of the mitochondrial membrane potential.[4] The molecular target of PXA remains however elusive.

2.6 PXA leads to the activation of caspase 3/7 and reduces expression of anti-apoptotic proteins

The collapse of ΔΨm triggers the process of apoptosis soon after by activation of caspases that among others inactivate negative regulators of apoptosis such as Bcl-2.[21] Caspases are mainly divided into two subgroups known as "initiator caspases" and "executioner caspases" depending on their functions in apoptosis. Caspase 3 and 7, sharing high sequence similarities with each other, belong to the family of executioner caspases. The activation of these caspases is essential for the terminal phase of apoptosis.[22] Because of the finding that PXA results in the depolarization of ΔΨm, we tested the influence of PXA treatment on the activation of caspase 3 and 7 using fluorescence imaging. In untreated cells, basal activation of caspases 3/7 was 1.4%, 0.8%, 1.1%, and 0.5% in A2780, A2780CisR, J82, and J82CisR, respectively (Figure 8). 10 μM PXA (17x IC50 in A2780; 7x IC50 in A2780CisR) increased caspase 3/7 positive cells to 83% in A2780 and 71% in A2780CisR

whereas 100 μM cisplatin gave only 37% (A2780) and 12% (A2780CisR) even though the cisplatin concentration was relatively higher: 25x IC50 in A2780 and 8x IC50 in A2780CisR (Figure 8F). Similar data were obtained for J82 and J82CisR using 50 or 30 μM PXA, respectively (Figure 8G). Notably, the cisplatin-resistant cell line J82CisR was more sensitive to PXA as can be seen by 90% caspase 3/7 positive cells with 30 μM PXA whereas in J82 cells, the use of 50 μM PXA resulted in only 60% caspase 3/7 positive cells. These data are consistent with our findings described above that PXA is more potent in J82CisR in MTT assay (Table 1). Further, activation of caspase 3/7 was accompanied by nuclear condensation showing reduced size and increased intensity of nuclei (Figure 8A, B, C, D).

In addition to caspase 3/7 activation, we examined differences in the expression of pro- and antiapoptotic proteins after PXA treatment by means of a commercial proteome profiler in A2780 and A2780CisR cell lines (Figure 9). The proteome profiler confirmed an increase in cleaved caspase 3 upon PXA treatment. Additionally, PXA treatment reduced the expression of cIAP-1 (cellular inhibitor of apoptosis protein 1), a member of the IAP family, and of claspin, another anti-apoptotic protein involved in the checkpoint of the cell cycle. Taken together, these results demonstrate that PXA induces apoptosis after collapse of the mitochondrial membrane potential, activation of caspase 3/7 and by suppressing the expression of anti-apoptotic proteins.

2.7 PXA treatment does not rupture the plasma membrane

Disruption of the plasma membrane is a hallmark feature to distinguish between apoptotic and necrotic cell death. It is commonly accepted that cells undergoing apoptosis are phagocytized before
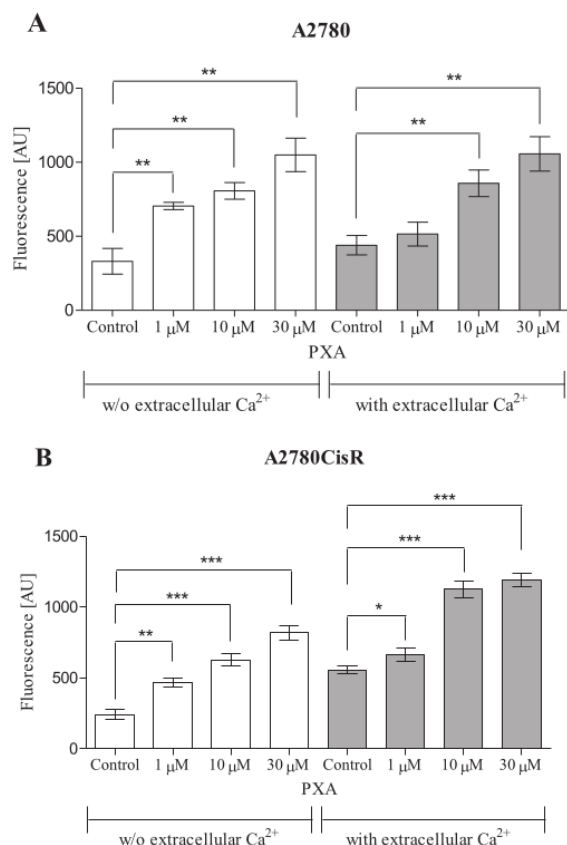
Figure 7. PXA increased concentration of intracellular Ca^{2+}. A2780 (A) and A2780CisR (B) were treated for 30 min with increasing concentrations of PXA while intracellular Ca^{2+} concentration was monitored. Data shown are mean ± SEM of three experiments. ***$P < 0.001$, **$P < 0.01$, *$P < 0.05$ in comparison to the untreated control cells.

membrane rupture and a release of intracellular components causing inflammation is prevented. However, a disruption of the cell membrane may occur in apoptotic cells due to secondary necrosis.[23] Therefore, we examined cell membrane integrity after PXA treatment. A2780 and A2780CisR cells were treated with different concentrations of PXA or cisplatin or triton-X-100 as control for 24 h, a time point which has shown an activation of caspase 3/7 and apoptosis induction. As Figure 10 shows, PXA had no effect on membrane integrity up to 10 μM. In contrast, the positive control triton X-100 showed 87% and 92% PI stained cells in A2780 and A2780CisR, respectively, indicating a rupture of the cell membrane. Given the fact that the number of PI stained cells did not raise with increasing concentrations of PXA, we suggest that PXA induces apoptosis but no membrane damage and no secondary necrosis.

2.8 PXA does not affect the generation of reactive oxidative species (ROS)

Many natural products are known to affect ROS levels, e.g. (poly)phenolic compounds. Oxidative stress may play a role in the generation and treatment of cancer cells.[24] We thus wanted to analyze if the tetrahydroxanthone derivative PXA has any impact on intracellular ROS levels. A2780 and A2780CisR cells were treated with PXA for 18 h, then labeled with H_2DCF-DA (2',7'-dichlorodihydrofluoresceine diacetate) treated with or without 250 μM H_2O_2 for 1 h, and then analyzed for ROS by flow cytometry (Figure 11). PXA had no effect on basal ROS

levels and showed only a slight, but no significant reduction of ROS induced by H_2O_2.

2.9 Potential of mean force computations indicate that PXA in neutral and singly deprotonated states can penetrate the inner mitochondrial membrane

Due to the lack of experimental pK_a values for PXA, we computed these for PXA in aqueous environment.[25,26] The pK_a values indicate that the hydroxyl groups in 8- and 8'-position are the most acidic functional groups ($pK_a = 5.1 \pm 1.1$, respectively). Thus, the computations do not reveal a mutual influence due to deprotonation of one hydroxyl group onto the pK_a value of the other group, which may be explained by the large separation between the two groups. Therefore, the doubly deprotonated species of PXA is predicted to be the predominant species under physiological conditions in aqueous solution. However, in a low dielectric medium such as a lipid bilayer membrane, pK_a values are known to increase,[27] which would shift the (de)protonation equilibrium to the side of the less charged species.

To address the question if differently charged PXA species can penetrate the inner mitochondrial membrane, which is a prerequisite for transferring protons across the membrane, we performed potential of mean force (PMF) computations of PXA penetration using umbrella sampling[28] and post-processing with the Weighted Histogram Analysis Method.[29] Prior to that, reference points of the sampling path were generated by steered molecular dynamics simulations, starting from the PXA species located at the membrane center and pulling it along the membrane normal (Figure 12A). Note that we paid close attention that the membrane composition in our simulations resembles that of the inner mitochondrial membrane in vivo.[30] As a reaction coordinate, the distance along the z axis between the membrane center and the center of mass of PXA was taken, with $z = \pm 19$ Å indicating the location of the polar head group/solvent interface (Supplementary Fig. 1A). The umbrella windows display considerable overlap regarding the frequency distribution of values for the reaction coordinate (Supplementary Fig. 2A, C, E). Furthermore, computing the PMFs with increasing sampling intervals show that the PMFs appear converged after 30–40 ns of sampling per window (Supplementary Fig. 2B, D, F). Accordingly, the statistical error was estimated by splitting the sampled data into equally sized chunks of 5 ns length, which exceeds the relaxation times in water or a membrane by at least two orders of magnitude. Computing the PMF for each chunk independently, a standard error of the mean of < 0.4 kcal mol^{-1} along the PMFs was obtained.

For both the uncharged and singly charged PXA, the global minima of the PMFs are located at $z = 13$ Å and ~ -2.8 kcal mol^{-1} (Figure 12B and C), revealing that a semi-immersed state of PXA within the membrane (state I, Figure 12E) is thermodynamically more favorable than a fully solvent-exposed state. In this state, the hydrophobic part of PXA is located towards the interior of the membrane, whereas the polar part is located close to the head group region, carrying a shell of water molecules. Performing unbiased MD simulations of 500 ns lengths as controls starting from PXA located at the membrane center confirm this finding in that the most frequently sampled distance of PXA from the center is at $z = 12.5$–13.0 Å (Supplementary Figure 1B, C). A small energy barrier of ~ 1.5 kcal mol^{-1} is observed at $z = 25$ Å, separating the semi-immersed state from the solvent-exposed one. Here, PXA is in proximity to the polar head groups of the lipids (state II, Figure 12E). The height of the energy barrier to pass the membrane is 3.8 and 6.4 kcal mol^{-1} with respect to the fully solvent-exposed state for PXA^0 and PXA^{-1}, respectively, and 6.7 and 9.2 kcal mol^{-1} with respect to state I, respectively. These barrier heights are markedly lower than those found for protein-free phosphatidylcholine, -ethanol, and -glycin lipid flip-flop in respective membranes.[31] Employing Eyring theory[32] at $T = 300$ K, kinetic rates of $1.4 \cdot 10^8$ to $9.9 \cdot 10^9$ s^{-1} are obtained, although obtaining a barrier height pertinent to kinetics via a PMF has been debated.[33] By contrast, the doubly charged species is most favorable in water, and the barrier height with respect to the fully solvent-exposed
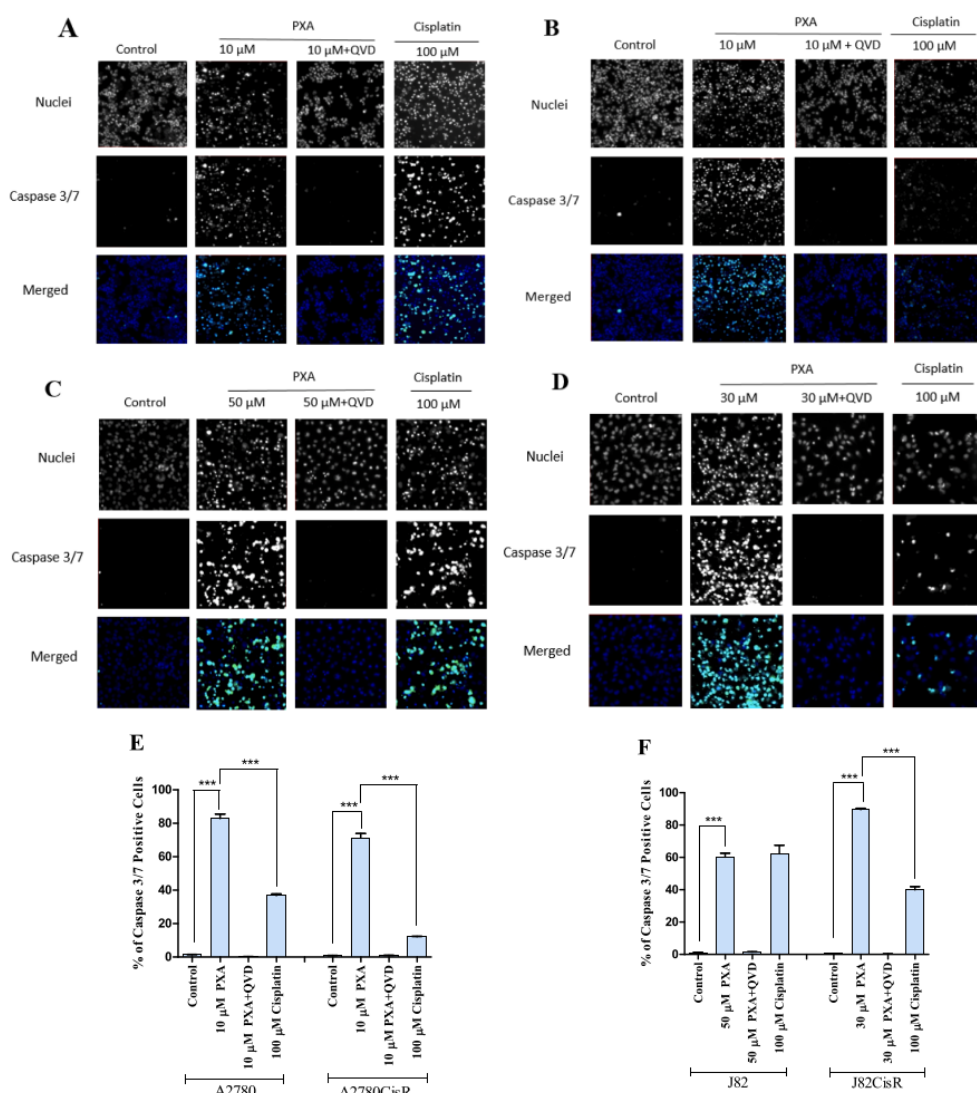
Figure 8. PXA-induced apoptosis is mediated via caspase3/7 activation. A2780 (A), A2780CisR (B), J82 (C), and J82CisR (D) were treated for 24 h with the indicated concentrations of PXA. Medium was used as control for untreated cells and cisplatin and staurosporine were used as positive control for caspase 3/7 activation. Cells were stained with Hoechst 33,342 (blue) for cell nuclei and CellEvent Caspase-3/7 green detection reagent for the activation of caspase 3/7. Quantification of caspase 3/7 positive cells of A2780, A2780CisR, J82, and J82CisR are displayed in (E) and (F). Data shown are mean ± SEM from three experiments. ***$P < 0.001$ in comparison to the untreated control cells. (For interpretation of the references to colour in this figure legend, the reader is referred to the web version of this article.)

state for passage through the membrane is 9.5 kcal mol^{-1} (Figure 12D), 1.5- to 2.5-fold higher than for PXA^0 and PXA^{-1}, leading to a 100-fold slower kinetic rate.

Taken together, our simulation results indicate that both the PXA^0 and PXA^{1-} species, but less so PXA^{2-}, show membrane partitioning and can penetrate the inner mitochondrial membrane with a high rate, similar to what can be estimated from membrane permeabilities of non-electrolyte compounds such as benzoic acid and codeine.[34] These properties of the differently protonated PXA species may contribute to the transfer of protons across the mitochondrial membrane: In our simulations, the membrane potential of the mitochondrial membrane was not considered, which would drive the passage of negatively charged deprotonated PXA towards the intermembrane space, where it can take

up a proton and penetrate back as neutral PXA across the membrane. Overall, these processes might allow PXA to act as a proton shuttle and dissipate the proton gradient along the inner mitochondrial membrane.

3 Conclusion

PXA is a strong inducer of mitochondrial membrane potential breakdown, subsequent caspase activation and apoptosis. Remarkably, the effect of PXA is equipotent (or slightly more potent) in cisplatin-resistant and cisplatin-sensitive cancer cell lines. Whereas the mode of action is still not fully understood, PXA leads to an increase in cytosolic Ca^{2+} concentration released from intracellular stores within a time scale that is comparable to the mitochondrial membrane potential
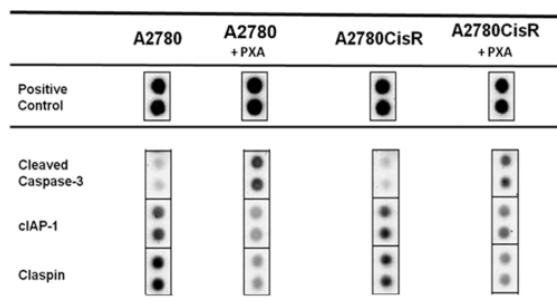
Figure 9. PXA rises the level of pro-apoptotic proteins and inhibits anti-apoptotic proteins. A2780 and A2780CisR cells were treated for 24 h with 5 μM PXA.

breakdown. These events then lead to caspase activation and apoptosis. Potential of mean force computations of PXA in an inner mitochondrial membrane environment suggest that PXA can act as a proton shuttle along the inner mitochondrial membrane and thus degrade the proton gradient and mitochondrial membrane potential. The remarkable effect of PXA in cisplatin-resistant cell lines (three digit nanomolar or low micromolar IC_{50} values) and previously shown selectivity for cancer over non-cancer cell lines[12] warrants further examination of PXA for the treatment of chemoresistant malignancies. Perspectively, mode of action studies need to be undertaken. This includes further studies of PXA on mitochondrial physiology (fusion, fission, potential) and a search for potential (sub)cellular binding proteins (e.g. by chemical modification of PXA to allow crosslinking of PXA with its cellular or subcellular (mitochondrial) binding partners followed by MS analysis). Further, the efficacy of PXA needs to be verified in in vivo xenograft models using chemoresistant cell lines such as those used in this study.

4. Experimental

4.1 Materials

Roswell Park Memorial Institute (RPMI) media 1640, Dulbecco's Modified Eagle Medium (DMEM), fetal bovine serum (FBS), penicillin/streptomycin (pen/strep) [10.000 U/ml; 10 mg/ml] and trypsin-EDTA (0.05% Trypsin, 0.02% EDTA in PBS) were purchased from PAN Biotech (Aidenbach, Germany). Cisplatin (cDDP), Pluronic® F-127 and Hoechst 33,342 were purchased from Sigma-Aldrich (Steinheim, Germany). Cisplatin was dissolved and subsequently diluted in 0.9% saline. 3-(4,5-dimethylthiazol-2-yl)-2,5-diphenyltetrazolium bromide (MTT) was purchased from Serva (Heidelberg, Germany) and was dissolved in PBS at a concentration of 5 mg/ml. Oregon Green® 488
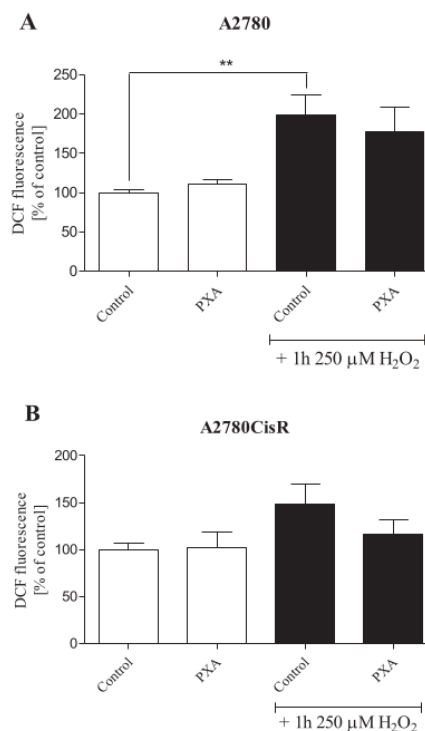
Figure 11. PXA does not affect the concentration of reactive oxidative species. A2780 (A) and A2780CisR (B) were treated for 18 h with a non-toxic concentration of PXA (IC_{10}: 316 nM). Then, cells were labeled with 10 μM H_2DCF-DA for 30 min, followed by 1 h treatment with or without 250 μM H_2O_2. Data shown are mean ± SEM of three independent experiments. **$P < 0.01$ in comparison to the untreated control cells.

BAPTA-1, AM was ordered from life technologies GmbH (Darmstadt, Germany). Propidium iodide was purchased from Santa Cruz Biotechnology (Heidelberg, Germany). Propidium iodide was dissolved in sterile filtered water. 0.9% NaCl, obtained from Fresenius Kabi (Bad Homburg, Germany) and supplemented with 0.01% sodium azide, was used as sheath fluid for flow cytometry analysis. The natural compound phomoxanthone A from fungus Phomopsis longicola was isolated in house (Institute of Pharmaceutical Biology and Biotechnology, Heinrich-Heine-University Duesseldorf, Germany). The compound was dissolved in DMSO and subsequently diluted in medium.
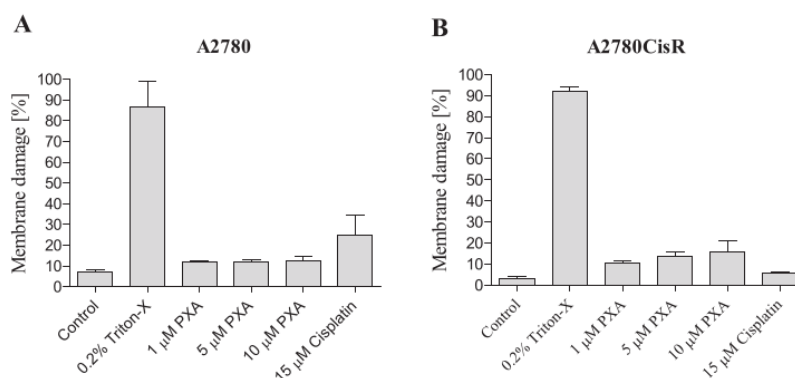
Figure 10. PXA does not damage the plasma membrane. A2780 (A) and A2780CisR (B) were treated for 24 h with different concentrations of PXA. Medium was used as negative control and 0.2% Triton-X was used as positive control. Data shown are mean ± SEM from three experiments.
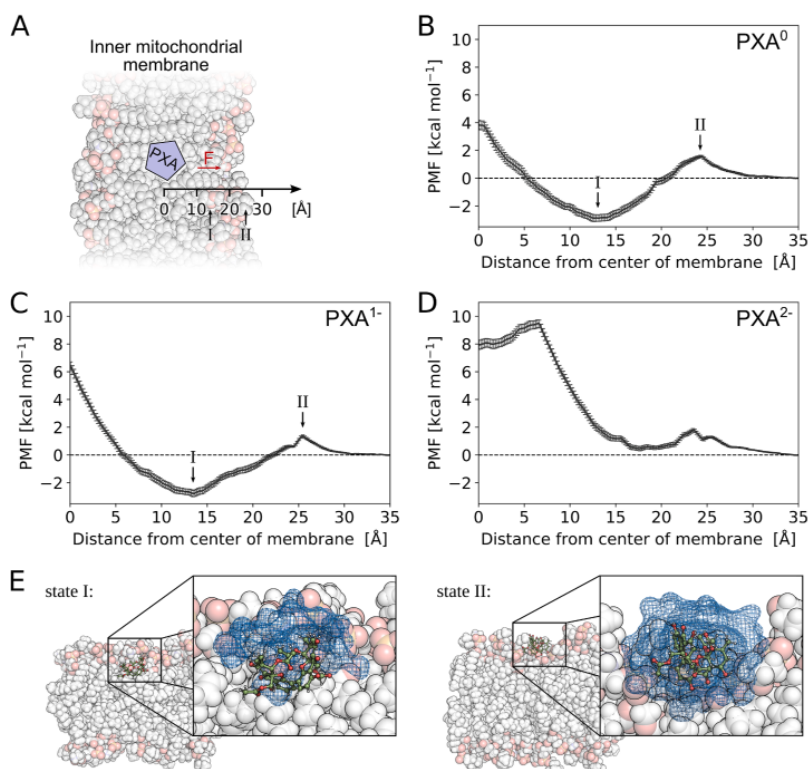
Figure 12. Ability of PXA to penetrate the inner mitochondrial membrane. Potential of mean force for the passage of PXA from the membrane center along the membrane normal to the outside (A) in the uncharged (B), singly (C) and doubly deprotonated (D) states. The PMF values were normalized to zero with respect to the state in the bulk solvent. Error bars indicate the SEM at the respective position. Interesting states in the potentials are marked with I and II, their location is indicated in panel A, and representative snapshots are given in (E), with water molecules solvating the solute displayed as blue meshes. (For interpretation of the references to colour in this figure legend, the reader is referred to the web version of this article.)

4.2 Cell lines

The human epithelial ovarian cancer cell line A2780 (ECACC, Salisbury, Wiltshire/UK), the human esophageal cancer cell line Kyse510 (German Collection of Microorganisms and Cell Cultures (DSMZ, Germany)) and the human myeloid leukemia cell line K562 (DSMZ) were cultivated in RPMI-1640 medium supplemented with 10% fetal bovine serum, 120 µg/ml streptomycin and 120 U/ml penicillin. The human tongue cancer cell line Cal27 and the human colon carcinoma cell line HCT116 were purchased from DSMZ. The urothelial bladder cancer cell line J82 was kindly provided by Prof. Wolfgang A. Schulz (Department of Urology, Medical Faculty, Heinrich Heine University). These cells were cultivated in DMEM supplemented with 10% fetal bovine serum, 120 µg/ml streptomycin and 120 U/ml penicillin. Additionally, the human triple negative breast carcinoma cell line MDA-MB-231 (ATCC, Manassas, USA) was used and cultivated in DMEM supplemented with 15% fetal bovine serum, 120 µg/ml streptomycin and 120 U/ml penicillin. The corresponding cisplatin-resistant (CisR) cell lines were generated by exposing the parental cell lines to weekly intermittent treatments with cisplatin in an IC_{50} concentration over a period of 24 till 30 weeks as previously described.[14] Cells were grown at 37 °C in a humidified atmosphere containing 5% CO_2. When cells reached a confluence of 80–90%, the cells were washed with 1x PBS and treated with Trypsin-EDTA before subculture.

4.3 MTT assay

MTT assays were performed as previously described.[15] Briefly, cells were seeded into 96 well plates (Sarstedt, Nümbrecht, Germany) and incubated overnight. Then, cells were exposed to increasing concentrations of test compound. After 72 h incubation, 25 µl of MTT solution (5 mg/ml) was added into each well and incubated for 15 min.

Thereafter, the mixture of medium and MTT solution was discarded and 75 µl of DMSO was added to dissolve formazan crystals. Absorbance of each well was measured at 544 nm (test wavelength) and 690 nm (background) using the BMG FLUOstar (BMG Labtechnologies Offenburg, Germany). Background was subtracted from the absorbance of each well.

4.4 Cell cycle analysis

Cell cycle was analysed using standard procedure as recently described.[35] Briefly, after exposing to various concentrations of PXA, cells were washed in ice-cold PBS and approximately 2 million cells were fixed in cold ethanol 70% and stored for at least 24 h at −20 °C. Then, fixed cells were washed with ice-cold PBS and incubated in staining solution (0.1% (v/v) Triton X-100 in PBS, 200 µg/ml DNAse-free RNAse A (Fermentas/Thermo Fisher Scientific, Waltham, MA, USA), 20 µg/ml propidium iodide) in the dark at 37 °C for 15 min. The DNA content was measured by flow cytometry with the CyFlow® space of Partec (Münster, Germany). The doublet discrimination mode was used.

4.5 Apoptosis assay

To determine apoptosis, nuclei were labeled with propidium iodide (PI). Each cell line was plated out in 24-well plates (approximately 100,000 cells per well) and after one day, cells were exposed to the respective treatments for 24 h. The caspase inhibitor Q-VD-OPh was added 1 h before apoptosis induction (20 µM). The plate was centrifuged and the supernatant was carefully removed. Cells were lysed in a hypotonic lysis buffer (sodium citrate tribasic dihydrate 0.1%, Triton X-100 0.1%, propidium iodide 100 µg/ml) and stored at 4 °C in the dark overnight. Sub-G1 fractions were detected by flow cytometry.

4.6 Analysis of mitochondrial membrane potential

Cells were seeded overnight before compound treatment. Shortly before compound treatment, the complete medium was replaced by FBS free medium to avoid cleavage of the TMRE ester (Biotrend Chemikalien GmbH, Köln, Germany). Treated cells were then stained with TMRE for 20 min and collected by trypsination. The cell suspension was centrifuged at 4° C and 8000 rpm for 4 min and the supernatant was then removed. The samples were stored on ice and protected from light until measurement. The cell pellet was resuspended in sheath fluid and the intensity of accumulated TMRE in each cell was determined using flow cytometry (CyFlow, Partec, Germany). For detection of mitochondrial membrane potential by ArrayScan XTI Live High Content Platform (Thermo Fisher Scientific Inc., USA), cells were labelled with TMRE and Hoechst 33,342 for 20 min after the compound treatment. Images were acquired using 10x magnification and data were analysed using HCS Studio Cellomics Scan (Thermo Fisher Scientific Inc., USA).

4.7 Calcium assay

Calcium assay was performed as previously described.[36] Briefly, cells were seeded into 96 well plates and incubated overnight. On the measurement day, medium was removed, and cells were washed with Krebs-HEPES buffer (KHB) twice. A mixture of Oregon Green BAPTA-1 AM (final concentration of 3 μM) and Pluronic F-127 (3 μl of 20% solution) was prepared in 2 ml of KHB, and 20 μl were added to each well. After 1 h incubation at 37 °C in the dark, the supernatant was removed and replaced by 180 μl pre-warmed KHB. Increasing concentrations of PXA were added (20 μl/well) and fluorescence intensity was measured at 544 nm for 30 min by a NOVOstar plate reader (BMG Labtechnologies Offenburg, Germany).

4.8 Caspase 3/7 activation test

The activity of caspase 3/7 after PXA treatment in A2780 and J82 cells was analysed by fluorescence image analysis. After cells were exposed to PXA for 24 h, medium was aspirated, and the cells were labelled with fluorescent staining solution containing CellEventTM Caspase-3/7 Green Detection Reagent (Invitrogen, Carlsbad, CA, USA) and Hoechst 33342. After 30 min incubation, images were acquired using ArrayScan XTI Live High Content Platform using excitation filters of 386 and 485 nm for Hoechst 33,342 and Caspase-3/7 Green Detection Reagent, respectively. The percentage of activated caspase 3/7 cells was calculated using HCS Studio Cellomics Scan.

4.9 Plasma membrane integrity test

Cells exposed to PXA for 24 h or triton X-100 for 20 min were trypsinized and collected by centrifugation at 4 °C and 266 rcf. The supernatant was removed, and the cell pellet was stained with 100 μg/ml propidium iodide. Samples were diluted with sheath fluid before measurement by flow cytometry. A sample treated with 0.2% Triton X-100 was used as positive control.

4.10 Reactive oxidative species

The measurement of reactive oxidative species was performed as follows: A2780 and A2780CisR were plated in 24-well plates (approximately 150,000 cells/well) (Sarstedt) and pre-incubated with growth medium overnight. Cells were exposed to PXA for 18 h. Cells were washed with PBS and then cultivated in phenolred-free RPMI-1640 (PAN) without FBS and antibiotics. Cells were then treated with 10 μM H2DCF-DA in the dark at 37 °C for 30 min. One aliquot of cells was analysed directly, the other aliquot was first treated with 250 μM H_2O_2 in the dark at 37 °C for 1 h and then analysed. Dichlorofluorescein

(DCF) fluorescence was detected by flow cytometry (CyFlow® space, Partec, Münster, Germany).

4.11 Analysis of apoptotic pathway proteins

The functional status of signal pathways was determined by human apoptosis array kit (Proteome ProfilerTM antibody array, biotechne, Germany) according to the manufactureŕs instructions. Relative levels of expression were measured with streptavidin-HRP and chemiluminescent detection reagents.

4.12 Statistical analysis

The statistical analysis was carried out with GraphPad Prism 6.0 (GraphPad Software Inc., San Diego, USA). Concentration-effect-curves were generated by nonlinear regression curve fitting using the 4-parameter logistic equation with variable hill slope. The IC_{50} is the concentration of the cytotoxic agent that led to a decrease of 50% of the recorded signal. pIC_{50} values are $-\log IC_{50}$. Assays were performed at least in three independent experiments each carried out in triplicates. Values shown are mean ± SEM. The two-tailed Studenŕs t-test was used and a p-value < 0.05 was considered as significant.

4.13 Preparation of the simulations

We used Maestro[37] to prepare the X-ray structure of PXA described in Rönsberg et al.[12] Using the program Epik[25–26], the protonation states at various pH values were evaluated. We generated structures for the uncharged (PXA^0), as well as the singly (PXA^{1-}) and doubly deprotonated (PXA^{2-}) molecule and optimized them with Gaussian09[38] at the B3LYP/6-311G(d) level of theory. Subsequently, atomic charges were calculated according to the RESP procedure[39] by a single point calculation at the HF/6-31G(d) level of theory.

For the setup of the membrane system, the PACKMOL-Memgen module (S. Schott, H. Gohlke, unpublished results) from AmberTools18 and tLEaP were used to generate a lipid bilayer system. LIPID17[40] parameters were used for the membrane lipids, while for the water phase TIP3P water[41] was used. The lipid composition was adjusted to resemble the inner mitochondrial membrane with DOPC, DOPE and DOPG as surrogates for cardiolipin in the ratios of 40:34:18.[30] One molecule of $PXA^{0/1-/2-}$ was placed in the center of the membrane, resulting in three individual systems. For the PXA species GAFF2[40] parameters were used. All following procedures were carried out on each of the systems.

4.14 Thermalization and density adjustment

Thermalization and density adjustment were carried out using pmemd from the Amber18 software package[42] with a time step of 2 fs. Langevin thermostat[43] and Berendsen barostat[44] were used for temperature and pressure control, respectively. For treatment of long-range electrostatic interactions the Particle Mesh Ewald method[45] was used with a cutoff of 8.0 Å. The SHAKE algorithm[46] was used to constrain bond lengths involving hydrogen atoms. Initial relaxation of the membrane, solvent, and both parts were carried out for 3,000 steps using the steepest decent algorithm, and further 2,000 steps with the conjugate gradient algorithm. Other components of the system were held fixed with positional restraints with a force constant of 5.0 kcal·mol^{-1}·Å^{-2}. Then, the system was heated to 300 K at a constant heating rate over 20 ps of NVT-MD and simulated for further 5 ps at 300 K. To adjust the system density, 1 ns of NPT-MD was performed.

From here on, the GPU version of pmemd[42,47] was used to further equilibrate the system for 50 ns. During all these steps, $PXA^{0/1-/2-}$ was held in the center of the membrane, using or distance restraints with a force constant of 5.0 kcal·mol^{-1}·Å^{-2}.

4.15 Steered molecular dynamics simulations, umbrella sampling, and PMF calculations

After equilibration, $PXA^{0/1-/2-}$ was gradually pulled out of the membrane into the solvent at a rate of 1 Å·ns^{-1} with a force constant of 2.5 kcal mol^{-1} Å^{-2}. The same MD settings as during the last step of the equilibration were applied. From the resulting trajectory, snapshots along the reaction coordinate with 1 Å spacing were extracted with CPPTRAJ[48]. These were used as reference points in umbrella sampling, further sampling each window for 100 ns while keeping $PXA^{0/1-/2-}$ restrained at its respective reaction coordinate value with a harmonic potential and a force constant of 2.5 kcal mol^{-1} Å^{-2}. The first 50 ns of the sampling were discarded as equilibration time. Reaction coordinate values from the last 50 ns of each window were extracted in 500 fs intervals and analyzed by weighted histogram analysis[49]. The error was estimated by performing the same calculation over ten individual windows of 5 ns each. Individual states were visually inspected and figures prepared with PyMOL[50]

4.16 Unbiased molecular dynamics simulations

In addition to the steered molecular dynamics simulations, we started unbiased simulations from the equilibrated structures. In these simulations the three protonation states of PXA were allowed to diffuse freely, from the initial position in the center of the membrane. For each of the systems 500 ns of NPT-MD were performed and analyzed with CPPTRAJ[48].

Acknowledgments

Appendix A. Supplementary data

Supplementary data to this article can be found online at https://doi.org/10.1016/j.bmc.2019.115044.

References

1. Dasari S, Tchounwou PB. Cisplatin in cancer therapy: molecular mechanisms of action. *Eur J Pharmacol.* 2014;740:364–378.
2. Siddik ZH. Cisplatin: mode of cytotoxic action and molecular basis of resistance. *Oncogene.* 2003;22(47):7265–7279.
3. Cannistra SA. Cancer of the ovary. *N Engl J Med.* 2004;351(24):2519–2529.
4. Bohler P, Stuhldreier F, Anand R, et al. The mycotoxin phomoxanthone A disturbs the form and function of the inner mitochondrial membrane. *Cell Death Dis.* 2018;9(3):286.
5. Galluzzi L, Senovilla L, Vitale I, et al. Molecular mechanisms of cisplatin resistance. *Oncogene.* 2012;31(15):1869–1883.
6. Renehan AG, Booth C, Potten CS. What is apoptosis, and why is it important? *BMJ.* 2001;322(7301):1536–1538.
7. Elmore S. Apoptosis: a review of programmed cell death. *Toxicol Pathol.* 2007;35(4):495–516.
8. Wajant H. The Fas signaling pathway: more than a paradigm. *Science.* 2002;296(5573):1635–1636.
9. Liu FT, Newland AC, Jia L. Bax conformational change is a crucial step for PUMA-mediated apoptosis in human leukemia. *Biochem Biophys Res Commun.* 2003;310(3):956–962.
10. Rogers C, Fernandes-Alnemri T, Mayes L, Alnemri D, Cingolani G, Alnemri ES.
11. Cleavage of DFNA5 by caspase-3 during apoptosis mediates progression to secondary necrotic/pyroptotic cell death. *Nat Commun.* 2017;8:14128.
11. Clark AM. Natural products as a resource for new drugs. *Pharm Res.* 1996;13(8):1133–1144.
12. Rönsberg D, Debbab A, Mandi A, et al. Pro-apoptotic and immunostimulatory tetrahydroxanthone dimers from the endophytic fungus Phomopsis longicolla. *J Org Chem.* 2013;78(24):12409–12425.
13. Frank M, Niemann H, Bohler P, et al. Phomoxanthone A-From Mangrove Forests to Anticancer Therapy. *Curr Med Chem.* 2015;22(30):3523–3532.
14. Gosepath EM, Eckstein N, Hamacher A, et al. Acquired cisplatin resistance in the head-neck cancer cell line Cal27 is associated with decreased DKK1 expression and can partially be reversed by overexpression of DKK1. *Int J Cancer.* 2008;123(9):2013–2019.
15. Engelke LH, Hamacher A, Proksch P, Kassack MU. Ellagic Acid and Resveratrol Prevent the Development of Cisplatin Resistance in the Epithelial Ovarian Cancer Cell Line A2780. *J Cancer.* 2016;7(4):353–363.
16. Green DR, Reed JC. Mitochondria and apoptosis. *Science.* 1998;281(5381):1309–1312.
17. Perry SW, Norman JP, Barbieri J, Brown EB, Gelbard HA. Mitochondrial membrane potential probes and the proton gradient: a practical usage guide. *Biotechniques.* 2011;50(2):98–115.
18. Griffiths EJ. Mitochondria–potential role in cell life and death. *Cardiovasc Res.* 2000;46(1):24–27.
19. Kane MS, Paris A, Codron P, et al. Current mechanistic insights into the CCCP-induced cell survival response. *Biochem Pharmacol.* 2018;148:100–110.
20. Hajnoczky G, Davies E, Madesh M. Calcium signaling and apoptosis. *Biochem Biophys Res Commun.* 2003;304(3):445–454.
21. Thornberry NA, Lazebnik Y. Caspases: enemies within. *Science.* 1998;281(5381):1312–1316.
22. Slee EA, Adrain C, Martin SJ. Executioner caspase-3, -6, and -7 perform distinct, non-redundant roles during the demolition phase of apoptosis. *J Biol Chem.* 2001;276(10):7320–7326.
23. Zhang Y, Chen X, Gueydan C, Han J. Plasma membrane changes during programmed cell deaths. *Cell Res.* 2018;28(1):9–21.
24. Rahal A, Kumar A, Singh V, et al. Oxidative stress, prooxidants, and antioxidants: the interplay. *Biomed Res Int.* 2014;2014:761264.
25. Shelley JC, Cholleti A, Frye LL, Greenwood JR, Timlin MR, Uchimaya M. Epik: a software program for pK a prediction and protonation state generation for drug-like molecules. *J Comput Aid Mol Des.* 2007;21(12):681–691.
26. Schrödinger Release 2018-1: Epik, Schrödinger, LLC: New York, NY, 2018.
27. Sarmini K, Kenndler E. Ionization constants of weak acids and bases in organic solvents. *J Biochem Bioph Methods.* 1999;38(2):123–137.
28. Torrie GM, Valleau JP. Nonphysical sampling distributions in Monte Carlo free-energy estimation: Umbrella sampling. *J Comput Phys.* 1977;23(2):187–199.
29. Kumar S, Rosenberg JM, Bouzida D, Swendsen RH, Kollman PA, THE,. weighted histogram analysis method for free-energy calculations on biomolecules. I. The method. *J Comput Chem.* 1992;13(8):1011–1021.
30. Horvath SE, Daum G. Lipids of mitochondria. *Prog Lipid Res.* 2013;52(4):590–614.
31. Allhusen JS, Conboy JC. The Ins and Outs of Lipid Flip-Flop. *Accounts Chem Res.* 2017;50(1):58–65.
32. Anglin TC, Cooper MP, Li H, Chandler K, Conboy JC. Free Energy and Entropy of Activation for Phospholipid Flip-Flop in Planar Supported Lipid Bilayers. *J Phys Chem B.* 2010;114(5):1903–1914.
33. Dellago C, Bolhuis PG, Csajka FS, Chandler D. Transition path sampling and the calculation of rate constants. *J Chem Phys.* 1998;108(5):1964–1977.
34. Lee CT, Comer J, Herndon C, et al. Simulation-Based Approaches for Determining Membrane Permeability of Small Compounds. *J Chem Inf Model.* 2016;56(4):721–733.
35. Darzynkiewicz Z. Nucleic Acid Analysis. In: Robinson JP, ed. *Current Protocols in Cytometry.* New York: J Wiley & Sons; 1997.
36. Kassack MU, Hofgen B, Lehmann J, Eckstein N, Quillan JM, Sadee W. Functional screening of G protein-coupled receptors by measuring intracellular calcium with a fluorescence microplate reader. *J Biomol Screen.* 2002;7(3):233–246.
37. Schrödinger Release 2018-1: Maestro, Schrödinger, LLC: New York, NY, 2018.
38. Frisch, M. J.; Trucks, G. W.; Schlegel, H. B.; Scuseria, G. E.; Robb, M. A.; Cheeseman, J. R.; Scalmani, G.; Barone, V.; Mennucci, B.; Petersson, G. A.; Nakatsuji, H.; Caricato, M.; Li, X.; Hratchian, H. P.; Izmaylov, A. F.; Bloino, J.; Zheng, G.; Sonnenberg, J. L.; Hada, M.; Ehara, M.; Toyota, K.; Fukuda, R.; Hasegawa, J.; Ishida, M.; Nakajima, T.; Honda, Y.; Kitao, O.; Nakai, H.; Vreven, T.; Montgomery Jr., J. A.; Peralta, J. E.; Ogliaro, F.; Bearpark, M.; Heyd, J. J.; Brothers, E.; Kudin, K. N.; Staroverov, V. N.; Kobayashi, R.; Normand, J.; Raghavachari, K.; Rendell, A.; Burant, J. C.; Iyengar, S. S.; Tomasi, J.; Cossi, M.; Rega, N.; Millam, J. M.; Klene, M.; Knox, J. E.; Cross, J. B.; Bakken, V.; Adamo, C.; Jaramillo, J.; Gomperts, R.; Stratmann, R. E.; Yazyev, O.; Austin, A. J.; Cammi, R.; Pomelli, C.; Ochterski, J. W.; Martin, R. L.; Morokuma, K.; Zakrzewski, V. G.; Voth, G. A.; Salvador, P.; Dannenberg, J. J.; Dapprich, S.; Daniels, A. D.; Farkas, O.; Foresman, J. B.; Ortiz, J. V.; Cioslowski, J.; Fox, D. J. Gaussian 09, Revision A.02, Gaussian, Inc.: Wallingford CT, 2009.
39. Bayly CI, Cieplak P, Cornell W, Kollman PA. A well-behaved electrostatic potential based method using charge restraints for deriving atomic charges: the RESP model. *J Phys Chem.* 1993;97(40):10269–10280.
40. Case DA, Betz RM, Cerutti DS, et al. *AMBER 2016.* San Francisco: University of California; 2016.
41. Jorgensen WL, Chandrasekhar J, Madura JD, Impey RW, Klein ML. Comparison of simple potential functions for simulating liquid water. *J Chem Phys.* 1983;79(2):926–935.
42. Case, D. A.; Ben-Shalom, I. Y.; Brozell, S. R.; Cerutti, D. S.; Cheatham III, T. E.;

Cruzeiro, V. W. D.; Darden, T. A.; Duke, R. E.; Ghoreishi, D.; Gilson, M. K.; Gohlke, H.; Goetz, A. W.; Greene, D.; R Harris; Homeyer, N.; Izadi, S.; Kovalenko, A.; Kurtzman, T.; Lee, T. S.; LeGrand, S.; Li, P.; Lin, C.; Liu, J.; Luchko, T.; Luo, R.; Mermelstein, D. J.; Merz, K. M.; Miao, Y.; Monard, G.; Nguyen, C.; Nguyen, H.; Omelyan, I.; Onufriev, A.; Pan, F.; Qi, R.; Roe, D. R.; Roitberg, A.; Sagui, C.; Schott-Verdugo, S.; Shen, J.; Simmerling, C. L.; Smith, J.; Salomon-Ferrer, R.; Swails, J.; Walker, R. C.; Wang, J.; Wei, H.; Wolf, R. M.; Wu, X.; Xiao, L.; York, D. M.; Kollman, P. A. AMBER 2018, University of California, San Francisco: 2018.

43. Pastor RW, Brooks BR, Szabo A. An Analysis of the Accuracy of Langevin and Molecular-Dynamics Algorithms. *Mol Phys.* 1988;65(6):1409–1419.

44. Berendsen HJC, Postma JPM, van Gunsteren WF, DiNola A, Haak JR. Molecular dynamics with coupling to an external bath. *J Chem Phys.* 1984;81(8):3684–3690.

45. Darden T, York D, Pedersen L. Particle Mesh Ewald - an N. Log(N) Method for Ewald Sums in Large Systems. *J Chem Phys.* 1993;98(12):10089–10092.

46. Ryckaert JP, Ciccotti G, Berendsen HJC. Numerical-Integration of Cartesian Equations of Motion of a System with Constraints - Molecular-Dynamics of N-Alkanes. *J Comput Phys.* 1977;23(3):327–341.

47. Le Grand S, Gotz AW, Walker RC. SPFP: Speed without compromise-A mixed precision model for GPU accelerated molecular dynamics simulations. *Comput Phys Commun.* 2013;184(2):374–380.

48. Roe DR, Cheatham TE. PTRAJ and CPPTRAJ: Software for Processing and Analysis of Molecular Dynamics Trajectory Data. *J Chem Theory Comput.* 2013;9(7):3084–3095.

49. Grossfield, A. WHAM: an implementation of the weighted histogram analysis method, version 2.0.9.1.

50. PyMOL: The PyMOL Molecular Graphics System, 2.1.0; Schrödinger, LLC.

Supplementary Data

The tetrahydroxanthone-dimer phomoxanthone A is a strong inducer of apoptosis in cisplatin-resistant solid cancer cells

Wang, C. [a], Engelke, L. [a], Bickel, D. [a], Hamacher, A. [a], Frank, M. [b], Proksch, P. [b], Gohlke, H. [a,c], and Kassack, M.U. [a]

[a] Institute of Pharmaceutical and Medicinal Chemistry, Heinrich Heine University Düsseldorf, Düsseldorf, Germany

[b] Institute of Pharmaceutical Biology and Biotechnology, Heinrich Heine Universität Düsseldorf, Düsseldorf, Germany

[c] John von Neumann Institute for Computing (NIC), Jülich Supercomputing Centre (JSC), Institute of Biological Information Processing (IBI-7: Structural Biochemistry) & Institute of Bio- and Geosciences (IBG-4: Bioinformatics), Forschungszentrum Jülich GmbH, Jülich, Germany

Supplementary Figure 1. Unbiased MD simulations confirm the location of minima in the PMF.
(**A**) Normalized electron density distribution of an unperturbed membrane used in the MD simulations, which shows the average location of the hydrophilic and hydrophobic components. Frequency distributions of PXA (colored bar plots) from unbiased MD simulations confirm the location of minima in the PMFs of PXA^0 (**B**), PXA^{1-} (**C**), and PXA^{2-} (**D**). The PMFs are identical to those in Figure 12. The frequency distributions were normalized for each simulation system separately; hence, they cannot be compared between simulation systems. The unbiased MD simulations were started with PXA located at the membrane center; thus, positions close to the center of the membrane may be oversampled, while the transition of a membrane-bound to a solvated state was not observed.
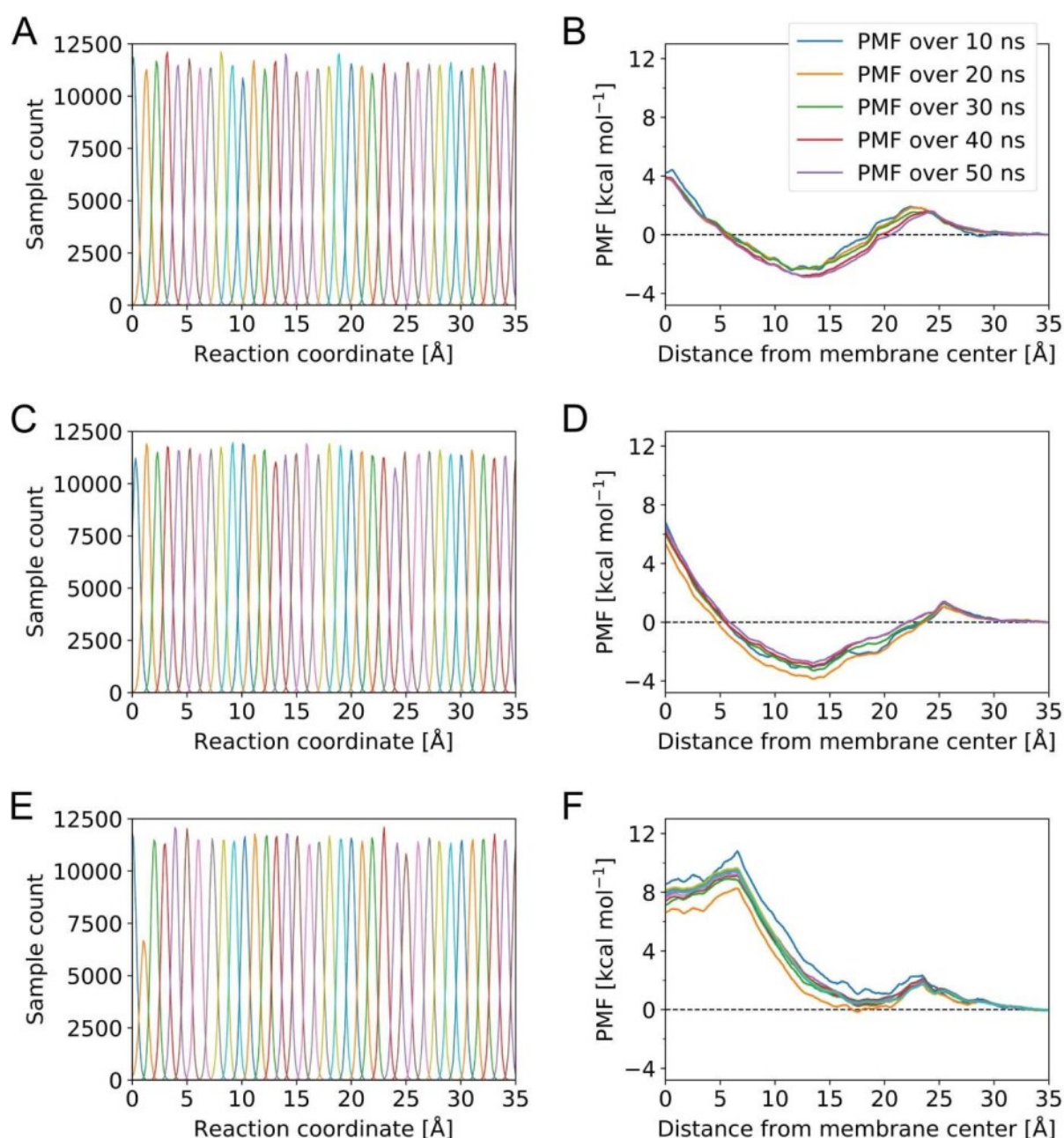
Supplementary Figure 2. Umbrella sampling simulations and convergence analysis of the potentials of mean force. The window-wise representation of the sampled data from the umbrella sampling simulations (PXA^0 **A**, PXA^{1-} **C**, PXA^{2-} **E**) shows good overlap of all windows for the range of sampled reaction coordinate values. The convergence of the potential of mean force is shown by calculating the free energy profiles from umbrella sampling simulations of increasing lengths (PXA^0 **B**, PXA^{1-} **D**, PXA^{2-} **F**). After 30 – 40 ns of sampling per window, the potentials of mean force appear converged.

Appendix

Publication III

Development of a first-in-class small molecule inhibitor of the C-terminal HSP90 dimerization

Bhatia, S. [a], Spanier, L. [b], Bickel, D. [b], Dienstbier, N. [a], Woloschin, V. [b], Vogt, M. [a], Pols, H. [b], Lungerich, B. [b], Reiners, J. [c], Aghaallaei, N. [d], Diedrich, D. [b], Frieg, B. [b,e], Schliehe-Diecks, J. [a], Bopp, B. [f], Lang, F. [a], Gopalswamy, M. [b], Loschwitz, J. [b], Bajohgli, B. [d], Skokowa, J. [d], Borkhardt, A. [a], Hauer, J. [g,h], Hansen, F.K. [i], Smits, S. [c,j], Jose, J. [f], Gohlke, H. [b,e], and Kurz, T. [b]

[a]   Department of Pediatric Oncology, Hematology and Clinical Immunology, Medical Faculty, Heinrich Heine University Düsseldorf, Düsseldorf, Germany

[b]   Institute for Pharmaceutical and Medicinal Chemistry, Heinrich Heine University Düsseldorf, Düsseldorf, Germany

[c]   Center for Structural Studies, Heinrich Heine University Düsseldorf, Düsseldorf, Germany

[d]   Department of Hematology, Oncology, Clinical Immunology and Rheumatology, University Hospital Tübingen, Germany

[e]   John von Neumann Institute for Computing (NIC), Jülich Supercomputing Centre (JSC), Institute of Biological Information Processing (IBI-7: Structural Biochemistry) & Institute of Bio- and Geosciences (IBG-4: Bioinformatics), Forschungszentrum Jülich GmbH, Jülich, Germany

[f]   Institute for Pharmaceutical and Medicinal Chemistry, PharmaCampus, Westphalian Wilhelms University, Münster, Germany

[g]   Department of Pediatrics, Pediatric Hematology and Oncology, University Hospital Carl Gustav Carus, Dresden, Germany

[h]   National Center for Tumor Diseases (NCT), Partner Site Dresden, Dresden, Germany

[i]   Pharmaceutical and Cell Biological Chemistry, Pharmaceutical Institute University of Bonn, Bonn, Germany

[j]   Institute of Biochemistry, Heinrich Heine University Düsseldorf, Düsseldorf, Germany

Development of a First-in-Class Small Molecule Inhibitor of the C-terminal Hsp90 Dimerization

Sanil Bhatia[1*], Lukas Spanier[2*], David Bickel[2], Niklas Dienstbier[1], Vitalij Woloschin[2], Melina Vogt[1],

Henrik Pols,[2] Beate Lungerich,[2] Jens Reiners[3], Narges Aghaallaei[4], Daniela Diedrich[2], Benedikt Frieg[2,5],

Julian Schliehe-Diecks[1], Bertan Bopp[6], Franziska Lang[1], Mohanraj Gopalswamy[2], Jennifer Loschwitz[2],

Baubak Bajohgli[4], Julia Skokowa[4], Arndt Borkhardt[1], Julia Hauer[7,8], Finn K. Hansen[9], Sander H.J.

Smits[3,10], Joachim Jose[6], Holger Gohlke[2, 5#] and Thomas Kurz[2#]

Affiliations:

1. Department of Pediatric Oncology, Hematology and Clinical Immunology, Medical Faculty, Heinrich Heine University Düsseldorf, Düsseldorf, Germany

2. Institute for Pharmaceutical and Medicinal Chemistry, Heinrich Heine University Düsseldorf, Düsseldorf, Germany

3. Center for Structural Studies, Heinrich Heine University Düsseldorf, Düsseldorf, Germany

4. Department of Hematology, Oncology, Clinical Immunology and Rheumatology, University Hospital Tübingen, Germany

5. John von Neumann Institute for Computing (NIC), Jülich Supercomputing Centre (JSC), Institute of Biological Information Processing (IBI-7: Structural Biochemistry) & Institute of Bio- and Geosciences (IBG-4: Bioinformatics), Forschungszentrum Jülich GmbH, Jülich, Germany

6. Institute for Pharmaceutical and Medicinal Chemistry, PharmaCampus, Westphalian Wilhelms University, Münster, Germany

7. Department of Pediatrics, Pediatric Hematology and Oncology, University Hospital Carl Gustav Carus, Dresden, Germany

8. National Center for Tumor Diseases (NCT), Partner Site Dresden, Dresden, Germany

9. Pharmaceutical and Cell Biological Chemistry, Pharmaceutical Institute University of Bonn, Bonn, Germany

10. Institute of Biochemistry, Heinrich Heine University Düsseldorf, Düsseldorf, Germany

* contributed equally to this work

shared senior authorship

Corresponding authors: (T.K.) Universitätsstr. 1, 40225 Düsseldorf, Germany, Phone: (+49) 211 81 14984, E-mail: thomas.kurz@uni-duesseldorf.de; (H.G.) Universitätsstr. 1, 40225 Düsseldorf, Germany, Phone: (+49) 211 81 13662, E-mail: gohlke@uni-duesseldorf.de; (S.B.) Moorenstraße 5, 40225 Düsseldorf, Germany, Phone (+49) 211 81 04896 Email, sanil.bhatia@med.uni-duesseldorf.de

Author ORCID: Benedikt Frieg: 0000-0002-7877-0262; Holger Gohlke: 0000-0001-8613-1447; David Bickel: 0000-0003-0332-8338; Sanil Bhatia: 0000-0001-6494-7744; Finn K. Hansen: 0000-0001-9765-5975 Thomas Kurz: 0000-0002-9474-4224; Sander Smits 0000-0003-0780-9251; Baubak Bajoghli: 0000-0002-7368-7523; Jennifer Loschwitz: 0000-0002-9066-1923

Keywords: protein-protein interaction, heat-shock protein, CML, BCR-ABL1, imatinib, Hsp90 inhibitor.

Abstract

Heat shock protein 90 (Hsp90) is a promising therapeutic target due to its involvement in stabilizing several aberrantly expressed oncoproteins. In cancerous cells, Hsp90 expression is elevated, thereby contributing in exerting anti-apoptotic effects, which is essential for the malignant transformation and progression of several tumor types. Most of the Hsp90 inhibitors (Hsp90i) under investigation target the ATP binding site in the N-terminal domain (NTD) of Hsp90. However, adverse effects, including induction of the pro-survival resistance mechanism (heat shock response or HSR) and associated dose-limiting toxicity, have so far precluded clinical approval of these Hsp90i. In contrast, modulators that interfere with the C-terminal domain (CTD) of Hsp90 do not inflict HSR and, thus, emerge as a promising alternative approach to target Hsp90. Since the CTD dimerization of Hsp90 is essential for its chaperone activity, interfering with this essential dimerization process by small-molecule protein-protein interaction (PPI) inhibitors is a promising strategy for anticancer drug research. We have developed the first-in-class small molecule inhibitor (**5b**) targeting the Hsp90 CTD dimerization interface, based on a tripyrimidonamide scaffold through structure-based molecular design, chemical synthesis, binding mode model prediction, assessment of the biochemical affinity and efficacy against therapy-resistant leukemia cells. **5b** reduces xenotransplantation of leukemia cells in zebrafish models and induces apoptosis in BCR-ABL1+ (T315I) tyrosine kinase inhibitors (TKIs) resistant leukemia cells, without inducing HSR.

Introduction

The heat shock protein (Hsp90) is an abundant, cytosolic molecular chaperone that modulates the folding, stabilization, and maturation of over 400 client proteins in eukaryotes.[1] It is involved in essential processes such as signal transduction, cell cycle progression, and transcription regulation.[1] In cancer cells, Hsp90 is overexpressed, involved in uncontrolled proliferation and anti-apoptotic effects, and, that way, essential for the malignant transformation and progression of several cancer types.[2] Thus, cancer cells are more dependent on Hsp90 activity than normal cells.[3,4] In various cancers, multiple signal transduction-promoting oncoproteins are clients of Hsp90.[5] Hence, inhibiting the activity of Hsp90 is a promising strategy for the development of anticancer therapy. Several Hsp90 inhibitors (Hsp90i) have been developed recently, however adverse effects including dose-limiting ocular and cardiac toxicity and poor patient stratification have precluded their clinical approval.[3] Most of the 19 Hsp90 inhibitors (Hsp90i) studied in clinical trials so far (except RTA 901) target the N-terminal ATP binding site (NTD) and are termed N-terminal inhibitors.[3,6-15] A common pitfall of Hsp90 NTD-targeting inhibitors is the induction of a pro-survival heat shock response (HSR).[3,6] The HSR is a stress response mechanism mediated by heat-shock factor 1 (HSF-1), which leads to the expression of other heat shock proteins (HSPs) including Hsp27, Hsp40 and Hsp70 as a rescue mechanism upon Hsp90 inhibition and eventually weakens cytotoxic effects of Hsp90i.[3,6,11-14] In addition, Hsp90 NTD-targeting inhibitors potentially inflict cytotoxicity through mechanisms that involve targets other than Hsp90, (off-target effects).[4,16] The off-target effect hypothesis is also supported by the drastic differences between cytotoxicity concentrations of Hsp90 NTD-targeting inhibitors vs. their binding affinity to Hsp90.[16] Furthermore, there are two major cytosolic isoforms of Hsp90 (Hsp90α and Hsp90β) expressed in humans. Hsp90α is an inducible isoform, overexpressed in several cancer types, whereas the Hsp90β isoform is expressed constitutively. Thus, targeting Hsp90 with isoform-specific inhibitors can afford a therapeutic window.[17,18] Most of the previously studied Hsp90i exhibit pan-inhibitory activity (i.e., targeting all isoforms). However, the Hsp90α and Hsp90β isoforms share a high degree of similarity (**SI Figure S21**), making it challenging to develop isoform-selective inhibitors.[18]

Hsp90 is a flexible homodimer, and each monomer consists of three major functional domains: N-terminal domain (NTD), middle domain, and C-terminal domain (CTD). Hsp90's activity depends on the binding and hydrolysis of ATP at the NTD and on its dimerization via the CTD.[2] The middle domain (MD) that connects the NTD and the CTD mediates the binding of clients and cochaperons. The CTD is connected to the MEEVD motif, which interacts with the subset of tetratricopeptide repeat (TPR) domain-containing cochaperones.[2] To our knowledge, inhibiting Hsp90 dimer formation by targeting the CTD dimerization interface constitutes a so far unexplored mode of action (MOA) of small-molecule Hsp90i. In contrast to Hsp90i targeting the N-terminal ATP binding site, C-terminal inhibitors do not generally induce HSR.[6,16,19-21] The most important classes of C-terminal inhibitors are: (1) inhibitors binding to the C-terminal ATP-binding site (e.g., novobiocin and analogs), (2) modulators of the Hsp90-CDC37 interaction (e.g., celastrol, induces HSR[22]), (3) modulators of the Hsp90-p23 interaction (e.g., gedunin), (4) modulators of the Hsp90-HOP interaction (e.g., LB76), and (5) aminoxyrone (AX), the first non-peptidic inhibitor of the C-terminal dimerization of Hsp90.[23]

Following a strategy recently introduced by us to identify PPI inhibitors,[24,25] we initially identified hot spot residues in the CTD dimerization interface that accounted for most of the binding affinity[26] and identified the first peptidic inhibitors shown to bind to the CTD of Hsp90.[27] Furthermore, we developed AX, the first peptidomimetic Hsp90 CTD dimerization inhibitor,[28] which is a promising lead candidate effective against BCR-ABL1+ TKI-resistant leukemic cells.[28] Based on these experiences, here, we report the rational design, chemical synthesis, binding mode model, biochemical affinity, and biological *in vitro* evaluation of the first-in-class small molecule inhibitor (**5b**) of Hsp90 CTD dimerization based on a tripyrimidonamide scaffold.

Results

Design of tripyrimidonamides as CTD Hsp90 inhibitors

Based on computational predictions and subsequent experimental validation, we identified the spatially clustered hot spot residues I688, Y689, I692, and L696 in the Hsp90 CTD interface, which are located on α-helix H5, form a functional epitope, and account for most of the protein dimerization energy.[26]

Furthermore, conformational analysis by 2D NMR and MD simulations revealed for the recently introduced tripyrimidonamide scaffold that it can act as a potential α-helix mimetic, mimicking side chains at positions *i*, *i*+4 (dimeric compound) or *i*, *i*+4, *i*+8 (trimeric compound). [29,30] This side chain pattern is concordant with the succession of the hot spot residues in the Hsp90 CTD interface.

Together, this provided the incentive for us to design and synthesize the tripyrimidonamide **5a,** which mimics the hot spots I688, I692, and L696. In compound **5a,** the side chain of V was used instead of I to avoid diasteromeres. **6,** which lacks the isopropyl side chain, was also designed to probe the influence of the absence of the third side chain in a tripyrimidonamide. Next, we aimed to design compounds that can also form polar interactions, as these should confer specificity of binding.[26] In addition, the binding to a well-defined cleft or groove in a PPI region has been described to yield a particularly effective PPI inhibitor.[26] The Y689 side chain of **7a** should be accommodated in an indentation in the binding epitope of helix H4' (**Figure 1**);[26] we also designed the homolog **7b** with a prolonged (4-hydroxy-phenyl)-ethyl side chain. Although both compounds mimic the three hot spots Y689, I692, L696, with the longer side chain in **7b**, we intended to accommodate for the apparent mismatch between the preferred side chain orientations in tripyrimidonamides and the side chain pattern of the hot spots (*i*, *i*+3, *i*+4). The side chain patterns of **5b** and **7a** are almost identical to that of the α-aminoxy-peptide AX, which was shown to bind to the CTD.[28]

Further analysis of the physicochemical properties of the CTD dimerization interface revealed a particular hydrophobic patch there (**Figure 1**). Interestingly, the 4-methoxy-benzyl side chain of **5b** should act as a (weak) hydrogen bond acceptor for S673' and T669' on helix H4', but at the same time decrease the side chain's hydrophilicity for a more favorable burial in the overall hydrophobic interface. To probe this with a larger substituent, we also designed the benzyloxy derivatives **5c** and **5d,** respectively, which are also precursors of **7a** and **7b**.

Synthesis of tripyrimidonamides

The monomeric building blocks **1** and **2a-e** were prepared according to our previously published protocol.[30] Subsequently, the designed tripyrimidonamides **5a-d** were synthesized using a modular approach. Briefly, a COMU-mediated amide coupling of the lithium carboxylate **2e** with

5-aminopyrimidone **1** afforded the benzoyl-protected dimer **3** in 75% yield. Deprotection of the benzoyl-group by treatment of **3** with sodium hydroxide in methanol at 80 °C afforded the unprotected dimer **4** (77% yield). Additional coupling reactions of **4** with the respective lithium salts **2a-d** in the presence of COMU furnished the tripyrimidonamides **5a-d** in 39-76% yield. Compound **6** with an *N*-unsubstituted N-terminal pyrimidone ring was synthesized by treating the corresponding 4-methoxybenzyl-substituted derivative **5b** with BBr$_3$ in DCM (Scheme 1). Finally, the trispyrimidonamides **7a** and **7b** with free phenolic groups were prepared by catalytic hydrogenation of their respective *O*-benzyl-protected precursors **5c** and **5d** (40 and 87% yield).
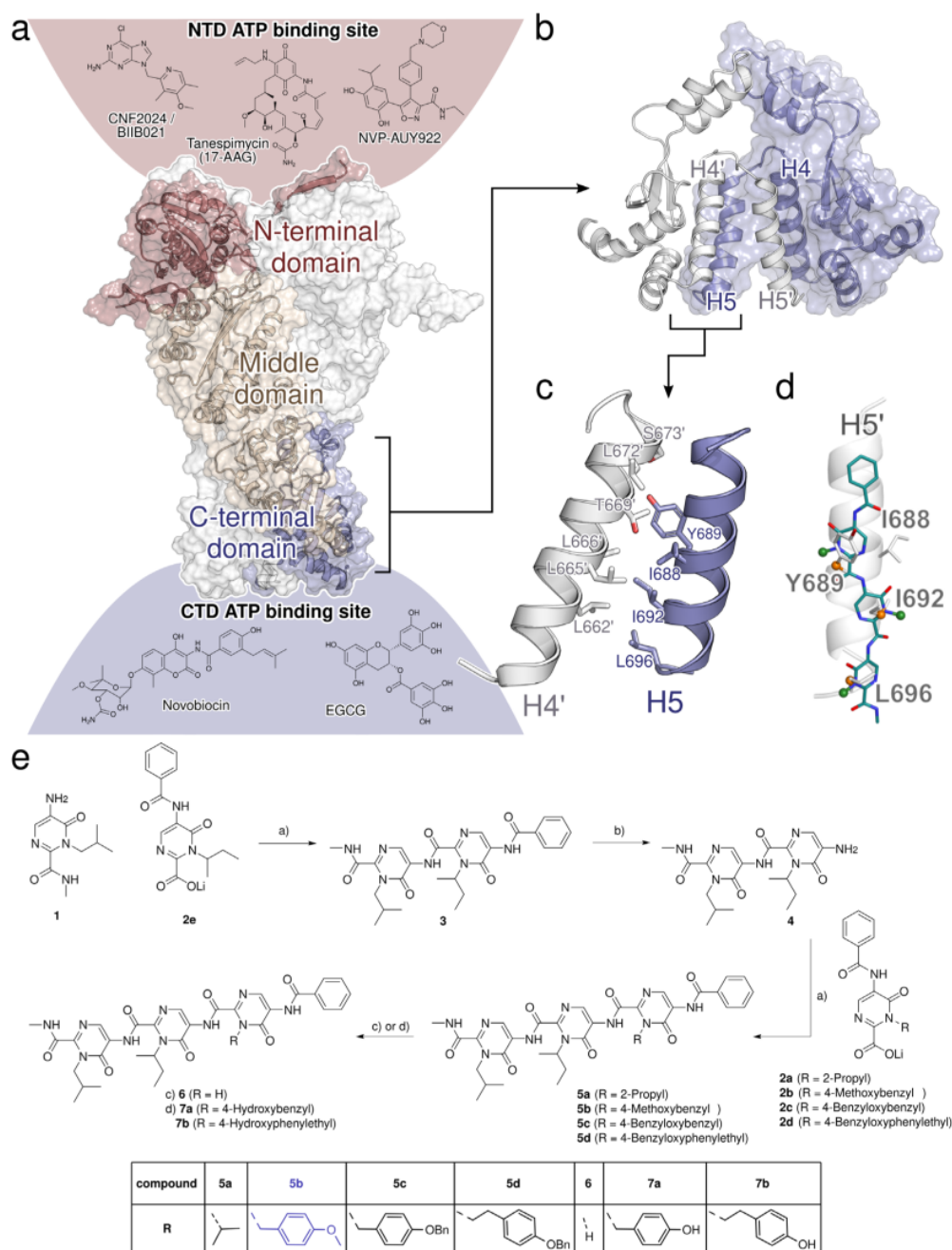
Figure 1: Rational design and synthesis of tripyrimidoneamides. a) Cryo-EM structure of the dimer of human Hsp90β (PDB ID 5FWK),[31] shown in surface and cartoon representation. For one of the Hsp90 monomers, the N-terminal domain (NTD) is colored in red, the middle domain in beige, and the C-terminal domain (CTD) in blue. Above and below the protein structure, the structures of Hsp90i and their potential binding sites (see ref. [32-36], color-coded according to the domains) are shown. **b)** Dimeric CTD of human Hsp90β with the two monomers in blue and white. Helices H4, H4', H5, and H5' of the CTDs form the dimerization interface. **c)** Residues forming the CTDs dimerization interface in human Hsp90α are primarily located on helices H4, H4', H5, and H5'.[26] **d)** Trispyrimidones can adopt conformations resembling the side chain orientation of an α-helix in i, $i+4$ and $i+7$ position.[30] **e)** Synthesis of tripyrimidoneamides: a) COMU, DMF, r. t., 18 h; b) NaOH, MeOH, 80 °C, 6 h; a) **2 a-d**, COMU, DMF, r. t., 18 h; c) **6** via **5b**, BBr₃, DCM, -78 °C, 1 h, r. t., 1 h; d) via **7a** via **5c** and **7b** via **5d**, H₂, Pd(C), MeOH, DCM, r. t., 1 h.

*Selection of **5b** as a lead candidate*

To evaluate the inhibition of Hsp90 dimerization, *E. coli* BL21 (DE3) pETSH-3 cells were used to display Hsp90α on their surface (**Figure 2a**).[27] Passenger-driven dimer formation of Hsp90α is facilitated through the motility of the β-barrel domain within the outer membrane of *E. coli*, as reported for other proteins.[37] To demonstrate the functionality of dimerized Hsp90 on the surface of *E. coli*, the transcription factor p53, a natural client protein of Hsp90, was labeled with fluorescein isothiocyanate (FITC) and added to cells displaying Hsp90 on their surface. Subsequent flow cytometer analysis revealed a high green fluorescence for cells displaying Hsp90, indicating dimerized and functional Hsp90 (**Figure 2b**). Compounds **5a**, **6**, and **7a** showed only weak inhibition of 3.27 %, 14.65 %, and 24.35 %, respectively. In contrast, **5b, 5c, 5d**, and **7b** showed moderate inhibition of 39.92 %, 41.83 %, 55.23 %, and 31.33 %, respectively (**Figure 2b**).

Later, the binding affinity of the compounds was determined with microscale thermophoresis (MST) measurements, using NT-647-labeled recombinant CTD of Hsp90α protein.[28] A nonlinear regression curve was fitted with the K_D formula, and, as expected, substances showing weak inhibition have high dissociation constants (**6**: 249 μM, **7a**: 286 μM; **Figure 2c, e**). The lowest K_D value was observed for **5b** with 3.42 μM (**Figure 2c, e**). Next, the in vitro cytotoxicity assessment of compounds **5a-d, 6, 7a**, and **7b** revealed **5b** as a promising candidate (with low IC_{50}: 1.8 ± 0.3 μM) in a BCR-ABL1+ tested leukemia cell line K562 (**Figure 2d, 2e**).

Based on the inhibition of Hsp90α CTD dimerization, low apparent K_D value for the Hsp90α CTD, and potent anti-leukemic activity, **5b** was selected for further detailed affinity and efficacy assessments.

Inhibitor	Inhibition (%) of Hsp90α dimerization at 50µM	Apparent K_D versus Hsp90α CTD	K562 (IC_{50} µM)
5a	3.27	47.2 ± 8.6	3.5 ± 0.1
5b	**39.9**	**3.4 ± 1.0**	**1.3 ± 0.3**
5c	41.8	14.9 ± 2.4	66.8 ± 13.0
5d	55.2	11.7 ± 1.0	97.9 ± 17.2
6	14.6	249 ±30.7	100.3 ± 25
7a	24.3	286 ± 19.5	60.8 ± 23.1
7b	31.3	86.4 ± 15	1.6 ± 0.1
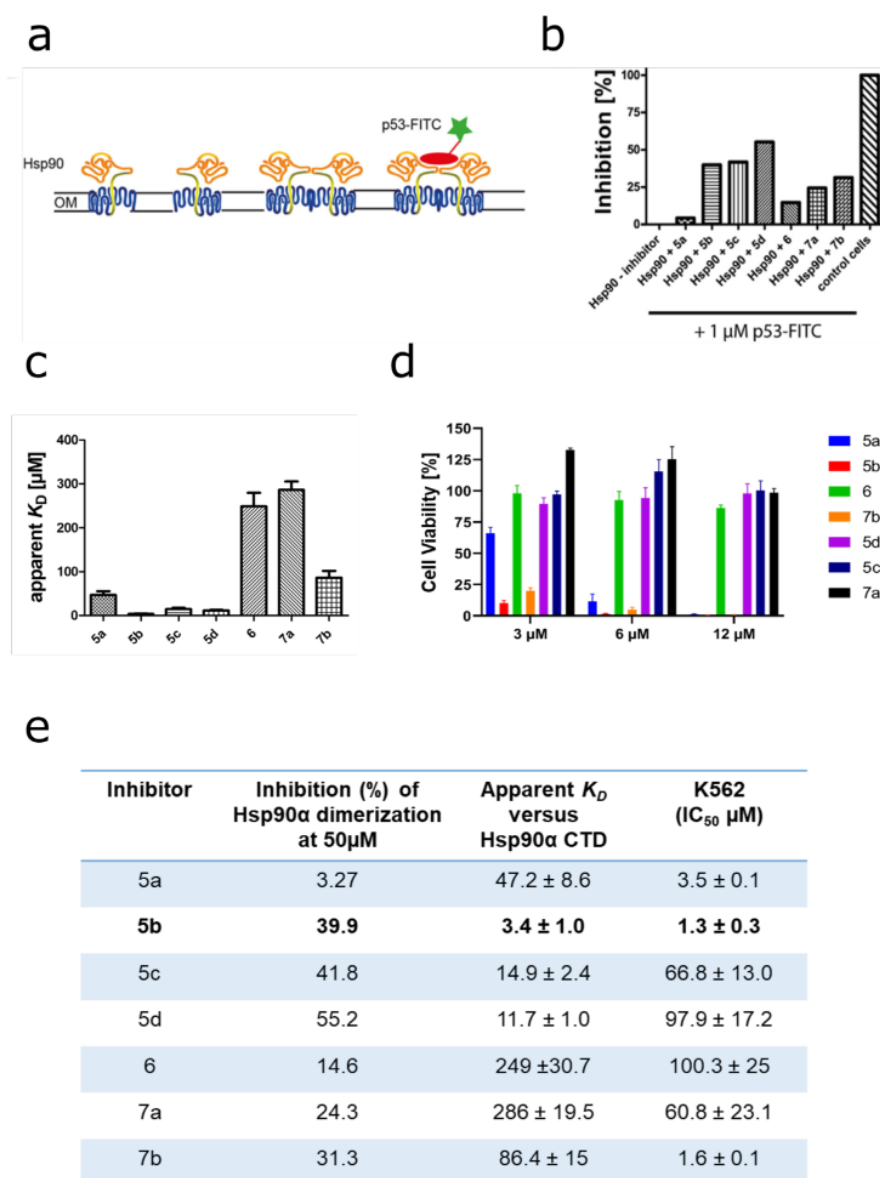
Figure 2: Selection of 5b as a lead candidate. a) Schematic view of the Hsp90 dimerization assay using Autodisplay. **b)** Flow cytometry measurements of the inhibition of dimerized Hsp90α displayed on *E. coli* cells.[28] *E. coli* BL21 (DE3) cells displaying Hsp90α incubated with 1 µM FITC-labeled p53 lead to a high cellular fluorescence indicating dimerization of Hsp90α. The value obtained was set as 0 % inhibition. In contrast, *E. coli* cells without displaying Hsp90α (control cells) show no cellular fluorescence. The value obtained here was set as 100 % inhibition. Preincubation of *E. coli* cells with surface-displayed Hsp90α with 50 µM of the respective substance leads to a lowered cellular fluorescence intensity indicating a lowered binding affinity of FITC-labeled p53 to surface-displayed Hsp90α. These values were set in relation to obtain the relative inhibition of dimerization. **c)** Apparent K_D values of purified CTD of Hsp90α and the respective substance measured via the MST method. A constant amount of 50 nM labeled CTD of Hsp90 was used, and three independent measurements were performed. The resulting mean values were determined and used in the K_D Fit formula. **d)** Cellular viability assessment of a leukemic cell line (K562) measured by incubating with the indicated inhibitors for 72 h, followed by viability measurement using ATP-based Celltitre Glo assay. **e)** Selection of **5b** as a lead candidate on the basis high inhibition of Hsp90α dimerization, low apparent K_D, and low IC_{50} (µM) in a tested leukemic cell line.

5b binds specifically to CTD of Hsp90α and blocks it cochaperone function

One of the major limitations of NTD-targeting inhibitors is their off-target activity.[4,16] Hence, it is important that the selected hit **5b** has a high degree of selectivity against its target, the CTD of Hsp90. To assess the selectivity of **5b**, biochemical cell-free and cellular assays were performed. First, we evaluated the affinity of **5b** against Hsp90 in a cell-free assay, where **5b** protected recombinant (full-length) Hsp90α protein in a dose-dependent fashion from degradation against thermolysin enzyme digestion, an assay commonly used to quantify drug affinity-responsive target stability (DARTS)[19,38] (**Figure 3a**). Next, we performed the cell-free thermal shift assay[39] to determine the potential binding affinity of **5b** to recombinant Hsp90α CTD and NTD protein. **5b** specifically destabilized the CTD of Hsp90α protein Hsp90 CTD (ΔTm: -8.45 $\pm$ 0.55 °C), whereas reference CTD targeting Hsp90i coumermycin A1 (CA1) stabilized Hsp90α CTD protein (**Figure 3b**, **SI Figure 22** and **SI Table 1**). NTD targeting Hsp90i Tanespimycin (TM) and PUH-71 served as positive (Hsp90α NTD) or negative control (Hsp90α CTD) in this assay. The thermostabilizing effect of **5b** to its target (total Hsp90) was also assessed in a cellular setup, termed cellular thermal shift assay (CETSA)[39-41], a biophysical method based on the ligand-induced thermal stabilization of the protein to directly probe the target engagement in the living cells (**SI Table 1, SI Figure 23**). The protein quantification for CETSA was performed using a digital western blotter for sensitive and quantitative evaluation of the ligand-protected intracellular Hsp90, whereas TM and PU-H71 served as controls. Next, the thermal stability of intracellular Hsp90 in an increasing concentration of **5b** (at a fixed temperature) was determined, a method termed isothermal dose-response fingerprint ITDRF$_{CETSA}$.[40] **5b** induced thermal stability of Hsp90 in a dose-dependent fashion, confirming its intracellular and specific target engagement (**Figure 3c**, **SI Table 1**).

Next, to assess the ability of **5b** to inhibit Hsp90 chaperone function, a cell-free luciferase-refolding assay[42-44] was performed using rabbit reticulocyte lysates as a source of Hsp90. Exposure of **5b** decreased the luciferase refolding capacity in a dose-dependent manner by blocking the chaperone function of Hsp90 (**Figure 3d**). The known Hsp90 NTD inhibitors geldanamycin (GM) and TM served as positive controls. Besides, to assess the specific effect of **5b** in obstructing Hsp90 CTD-interacting cochaperones, a time-resolved fluorescence resonance energy transfer (TR-FRET) assay was

conducted.[45] **5b** blocked the binding of PPID (or cyclophillin D, an Hsp90 CTD-interacting chaperone) to recombinant Hsp90α or Hsp90β CTD protein comparable to CA1 treatment, whereas PU-H71, TM, and GM served as negative controls (**Figure 3e, Table 1**). To rule out the possible interaction of **5b** with the NTD of Hsp90α, a fluorescence polarization (FP) competitive assay was carried out using FITC-labelled GM[42] (**Figure 3f**, **SI Table 1**). As expected, **5b** did not show any interaction with the NTD of Hsp90, whereas unlabeled Hsp90 NTD targeting inhibitors GM, Ganetespib (GP), TM, and PU-H71 served as positive controls.
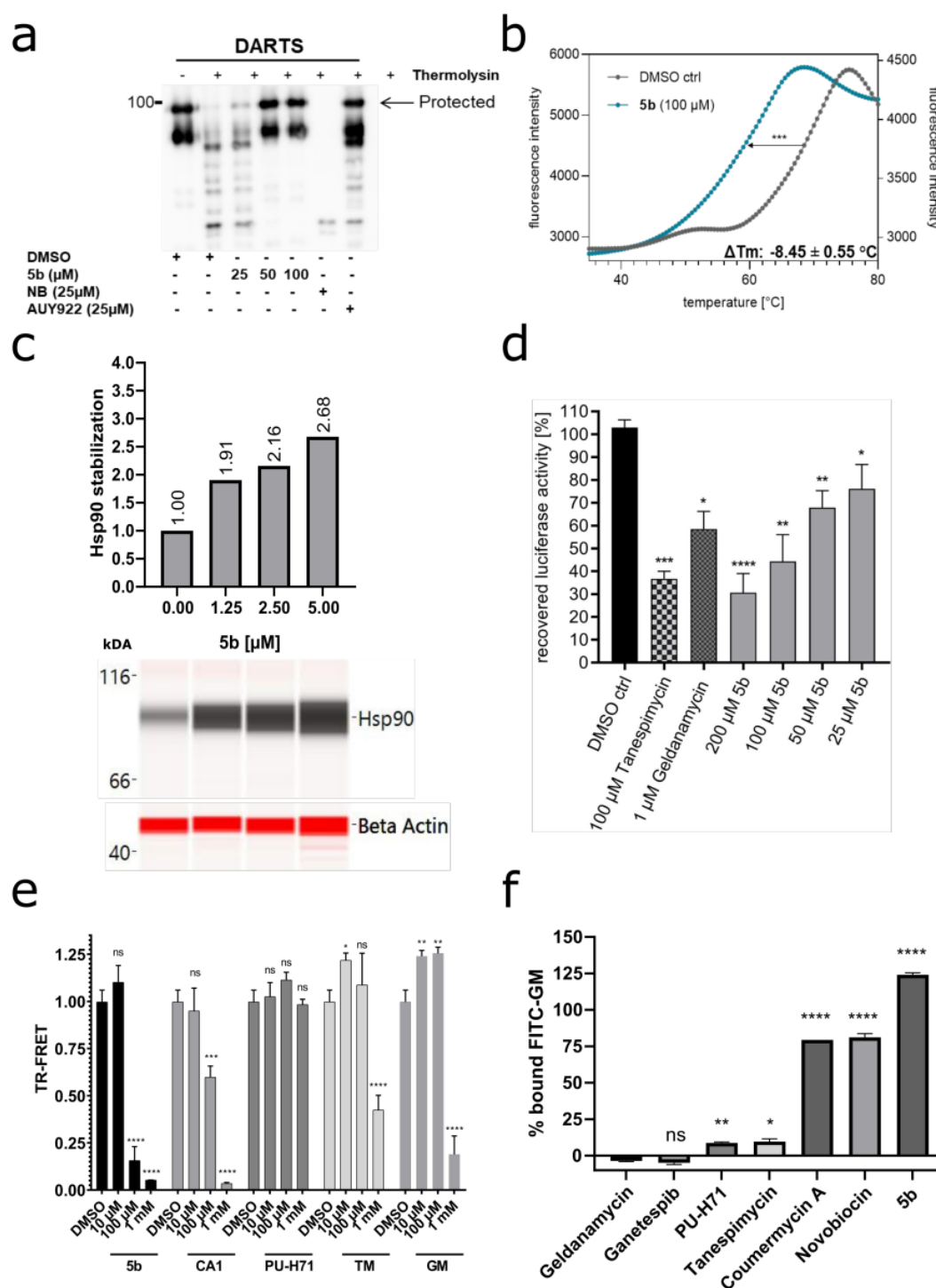
Figure 3: Specificity of 5b against Hsp90 CTD and its cochaperone function. a) Recombinant (full-length) Hsp90α (1 µg) was incubated with **5b** at indicated concentrations, followed by digestion with thermolysin. Treated protein samples were electrophoresed (SDS-PAGE) and immunoblotted with anti-Hsp90α for detecting protection of Hsp90α protein by **5b** (the upper band is protected from proteolysis). **b)** Cell-free thermal shift assay was performed by incubating recombinant Hsp90α CTD protein with **5b**, at an increasing temperature (up to 95 °C). Melting temperature (T_m) without inhibitors (DMSO) was used as a control. **c)** The dose-dependent intracellular (K562 cells) thermal stabilization (CETSA$_{ITDRF}$) of Hsp90 after **5b** incubation (24 h) at its increasing concentration (1.25 µM – 5 µM). **d) 5b** inhibits Hsp90α chaperone function, comparable to TM and GM, in cell-free luciferase refolding assay, where the incubation of the inhibitors prevented the rabbit reticulocyte lysate (a source of Hsp90) assisted refolding of denatured luciferase. **e)** Incubation of **5b** blocked the binding of Hsp90 CTD-interacting

cochaperone (PPID) in TR-FRET measurements. **f) 5b** did not reduce the amount of Hsp90-bound FITC-labelled GM and, therefore, does not compete for the GM binding pocket of full-length Hsp90α. Unlabelled GM, GP, PUH71, and TM served as positive controls and NB and CA1 as negative controls.

Binding mode prediction of 5b at Hsp90α

To provide structural insights how **5b** binds to the CTD of human Hsp90, we performed 40 independent molecular dynamics (MD) simulations of free diffusion of **5b** in the presence of truncated monomeric Hsp90α (aa 294-699), using the Amber 18 suite of molecular simulation programs[46] and the ff14SB[47] and a modified GAFF[30,48] force field for protein and ligand. Initially, we generated 40 individual starting configurations by randomly placing **5b** and the CTD structure, leaving at least 10 Å between atoms in **5b** and the CTD structure. After minimization, thermalization, and density adaptation, we performed MD simulations of 500 ns length, in which the **5b** molecule diffused freely. To counter the high flexibility of the C-terminal helix interface, we introduced positional restraints on the backbone atoms, adjusting the reference coordinates every 100 ns to allow for moderate protein movements.

From the trajectories, first, we extracted all frames where **5b** is bound to Hsp90 (no-fit RMSD of **5b** ≤ 1.5 Å to the previous frame after superimposing Hsp90). Mapping the probability density of occurrence of **5b** onto the surface of Hsp90 (**Figure 4a**) revealed two main binding regions: one in the C-terminal helix interface (**Figure 4a**, **green**), where binding occurred in 10 out of the 40 replicas, and another in a cleft between the CTD and middle domain (**Figure 4a**, **blue**), where binding occurred in 6 out of 40 replicas. In the latter case, an area of high density with the shape of **5b** is observed (**Figure 4a**, **light blue**), which resulted from a single trajectory. This indicates that the ligand was kinetically trapped in this one case, although the position is thermodynamically not favorable. By contrast, the densities in the C-terminal interface are more ambiguously shaped, indicating that, while binding there is favorable, the ligand can still explore multiple binding modes, which are also seen to interchange.

To further study these binding modes, we clustered the bound frames of **5b** mapped on the protein surface with respect to their RMSD after superimposing Hsp90. Among the binding modes were several that form interactions to the C-terminal helix interface, with **5b** positioned such that it mimics interactions formed by H5' in the dimer (**Figure 4c and d**). To corroborate that this binding mode is favorable, we computed the effective binding free energies by the MM-GB/SA approach for the trajectory that led to it. Already first transient interactions with the protein resulted in effective energies

down to ~-30 kcal mol^{-1}. The effective energies decreased further to ~-45 kcal mol^{-1} once the ligand bound in the C-terminal interface, thereby forming interactions with Hsp90 that remained stable even when the trajectory was extended to 1 μs, indicating that such poses are particularly favorable (**Figure 4b**). As to the magnitude of the effective energies, note that configurational entropy contributions were not considered, since estimating such contributions by normal mode analysis may introduce additional uncertainties.[49,50]

Overall, the probability density of bound **5b** poses, the proportion of replicas, and the results of the MM-GB/SA computations indicate that **5b** preferentially binds to the C-terminal helix interface, where it can adopt poses that mimic H5'.

*Comparison to **5b** binding at Hsp90β*

We then set out to study if there is an isoform specificity for the binding of **5b** because the helical interface regions differ in three positions: α: S641, β: P633; α: S658, β: A650; α: A685, β: S677 (**SI Figure 21**). Using the same setup as before, we performed MD simulations of free ligand diffusion around Hsp90β. The probability density of bound **5b** again revealed that the C-terminal helix interface is the most preferred region, followed by the cleft between the CTD and middle domain (**SI Figure 24**). Notably, no high density in this cleft was found now, in contrast to Hsp90α, confirming that the observation there resulted from kinetic trapping. Hence, despite the few sequence variations in the C-terminal helix interface between Hsp90α and Hsp90β, the same preferred binding region of **5b** was found in both cases.
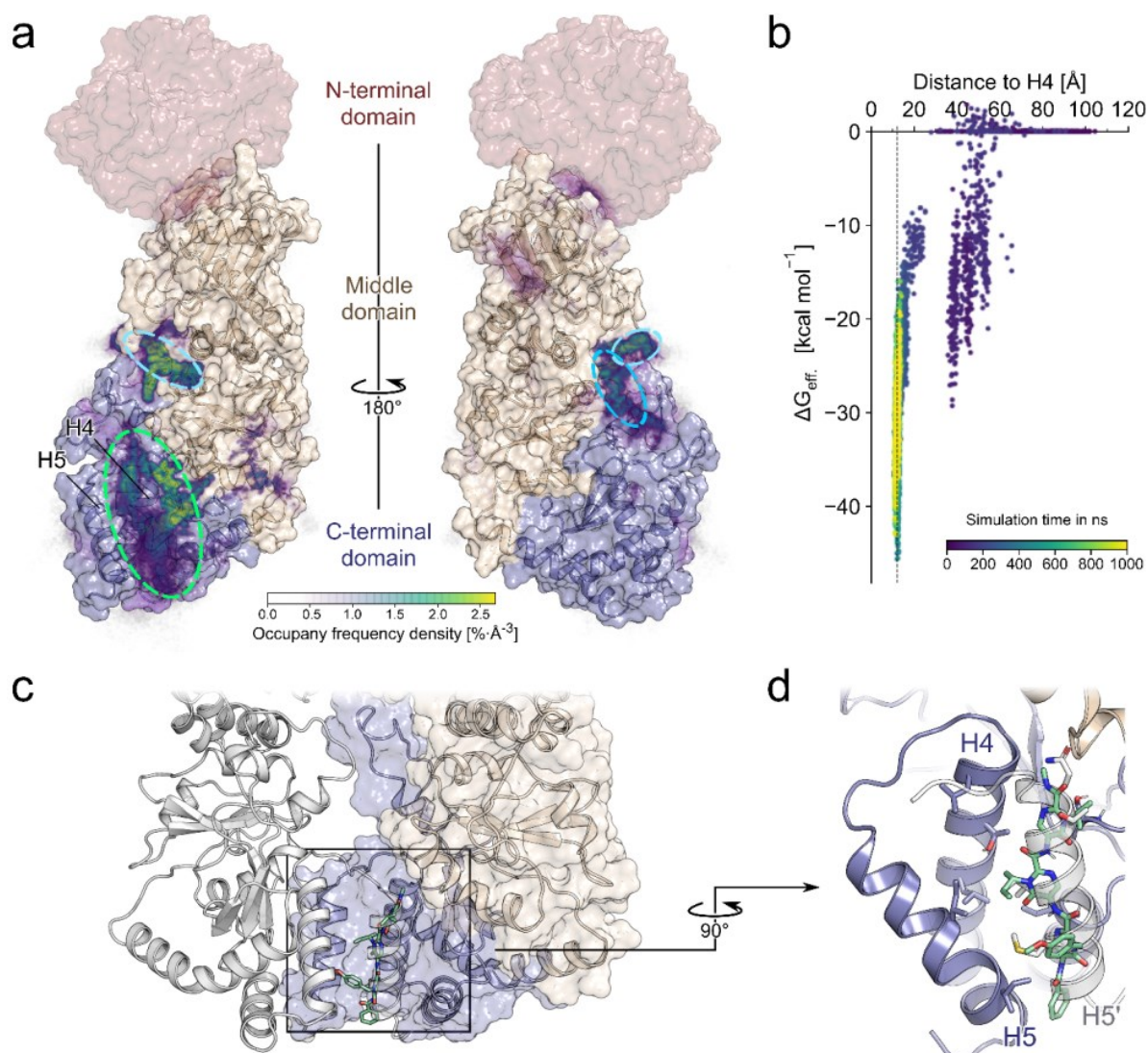
Figure 4: MD simulations of 5b diffusion and effective binding energy calculations to predict the binding mode.

a) The relative densities of the bound poses of **5b** after 500 ns are mapped on the Hsp90α monomer fragment used in the simulations (PDB ID 3q6m). The missing NTD is shown in red, based on the Hsp90β structure (PDB ID 5fwk). Particularly high densities are observed in the region between H4 and H5 (green circle). A second, less preferred site is in the cleft between the CTD and middle domain (blue circles). **b)** Effective binding energy calculations over a single trajectory that resulted in **5b** binding in the C-terminal helix interface as a function of the center-of-mass distance between **5b** and H4 and the simulation time (see color scale). The dashed line at 12.1 Å corresponds to the H4-H5' distance in the crystal structure of PDB ID 3q6m. **c)** Possible binding mode of **5b** in the helix interface, where **5b** mimics H5'. **d)** Blow-up of the possible binding mode of **5b** showing how its side chains mimic side chains of H5'.

5b interferes with Hsp90α CTD dimers and disrupts intracellular Hsp90 multiprotein complexes

CTD dimerization of Hsp90 is necessary for its function.[51,52] To study the effect of **5b** exposure on the dissociation of Hsp90 dimers in a cell-free assay, we used Hsp90α CTD protein after incubation with amine-reactive crosslinker BS[3], as previously described.[42,45] A dose-dependent reduction of Hsp90α

CTD dimers along with an increase in the high order oligomeric species was noticed upon incubation with **5b** (**Figure 5a**). Next, we performed small-angle X-ray scattering (SAXS) with the Hsp90α CTD protein, which was coupled to a size exclusion chromatography column (SEC-SAXS) at the ESRF beamline BM29 in Grenoble.[53,54] In the absence of **5b**, a clear dimeric profile of the Hsp90α CTD protein was visible on the chromatogram, with an additionally minor tetrameric species (**SI Figure 25**). We used the program CHROMIXS[55] to merge the frames containing the dimer from this SEC-SAXS profile. Buffer frames were then subtracted using PRIMUS.[56] From the SAXS data, a radius of gyration (*Rg*) of 3.23 nm was calculated, which describes the average particle dimension in solution. The *ab initio* model fit from DAMMIF[57] shows a χ^2 of 1.127, indicating good agreement with the experimental data (**Figure 5b and SI Table 2**). The corresponding dimeric envelope is highlighted in **Figure 5c**, superimposed with the calculated dimeric model of Hsp90α CTD. Further, we tested the effect of **5b** on the Hsp90 CTD dimer using SAXS (**Figure 5d**). Due to the low solubility of **5b**, we needed to measure the sample as an ensemble of species in solution. First, we tested Hsp90α CTD without **5b** on Xeuss 2.0 with Q-Xoom system and observed an increase of *Rg* to 3.40 nm. This increase is likely due to the small amount of tetramer in solution in the ensemble. Theoretically, the *Rg* of a tetrameric Hsp90α CTD species is 3.78 nm, using CRYSOL, indicating that even in batch mode SAXS measurements, the Hsp90α CTD protein is predominantly in a dimeric state. We added **5b** with an equimolar concentration to Hsp90α CTD protein, and the *Rg* value slightly increased from 3.40 nm to 3.46 nm. However, with an increasing concentration of **5b** to 1 mM, the *Rg* value increased to 4.11 nm. Compared to the theoretical *Rg* value of 3.78 nm for the tetramer, we observed that **5b** induces oligomerization of Hsp90α CTD to species even larger than the tetrameric form (**Figure 5e**). It is unclear, however, if the oligomers are formed from Hsp90α CTD monomers or dimers, as the single species could not be resolved in the ensemble measurement.

In a cellular context, Hsp90 acts in multiprotein complexes.[19] Therefore, interfering with Hsp90 function may lead to the disruption of these complexes. In a cellular assay, western blotting was performed under reducing (+dithiothreitol or +DTT) and non-reducing (-DTT) conditions after **5b** incubation of the K562 cells.[28] Similarly to AX,[28] **5b** inhibited the formation of Hsp90 higher-order multimeric species, in contrast to novobiocin (NB), but in concordance with AUY922 (**SI Figure 26**). Next, to study the effect

of **5b** exposure on Hsp90 native multiprotein complexes, blue native (BN) PAGE analysis was carried out with K562 cell lysates after **5b** incubation.[19,28] At cytotoxic concentrations of **5b**, Hsp90α and Hsp90β multiprotein complexes were disrupted, including monomers/dimers of Hsp40 and Hsp27; Hsp60 (primarily in mitochondria) multiprotein complexes, serving as a loading control, were not affected (**Figure 5e**).

Taken together, these results confirm that **5b** interferes with the Hsp90α CTD dimerization, induces oligomerization, and disrupts intracellular Hsp90 multiprotein complexes.

Basic physicochemical properties and microsomal stability of 5b

Next, we assessed the aqueous solubility, chemical stability, and *in vitro* metabolic stability of **5b**. The thermodynamic solubility of **5b** was determined in phosphate-buffered saline (PBS, 25 °C, pH 7.4) after 4 and 24 h incubation time (**Supplementary Note 2**). Ondansetron was used as a reference compound with high solubility of 95 μM. The thermodynamic solubility of **5b** was low, ranging from 4 μM after 4 h to 8 μM after 24 h (n = 2).

To study the chemical stability of **5b** at physiological pH, the compound was dissolved in a mixture of Tween20/ethanol/phosphate buffer pH 7.5 (7/3/90) and monitored over 24 h (**Supplementary Note 2**). After 24 h, almost no decomposition was detected (0.7 % drug decomposition, n = 2). The chemical stability of **5b** at acidic pH was determined by dissolving **5b** in a mixture of Tween20/ethanol/phosphate buffer pH 2 (7/3/90) and monitoring over 24 h. After 24 h, only slight decomposition was detected (1.3 % drug decomposition, n = 2).

Metabolic stability screening of **5b** in human liver microsomes revealed 91 % stability after a 40 min incubation at 37 C (**Supplementary Note 2**). Propanolol, a reference drug with medium to high metabolic stability, showed 74 % of the parent compound remaining, and therefore demonstrated slightly decreased stability compared with **5b**.[13] Calculated results for the intrinsic clearance suggest that **5b** (6 μL/min/mg) is a low-clearance compound with estimated long half-life (n = 2).
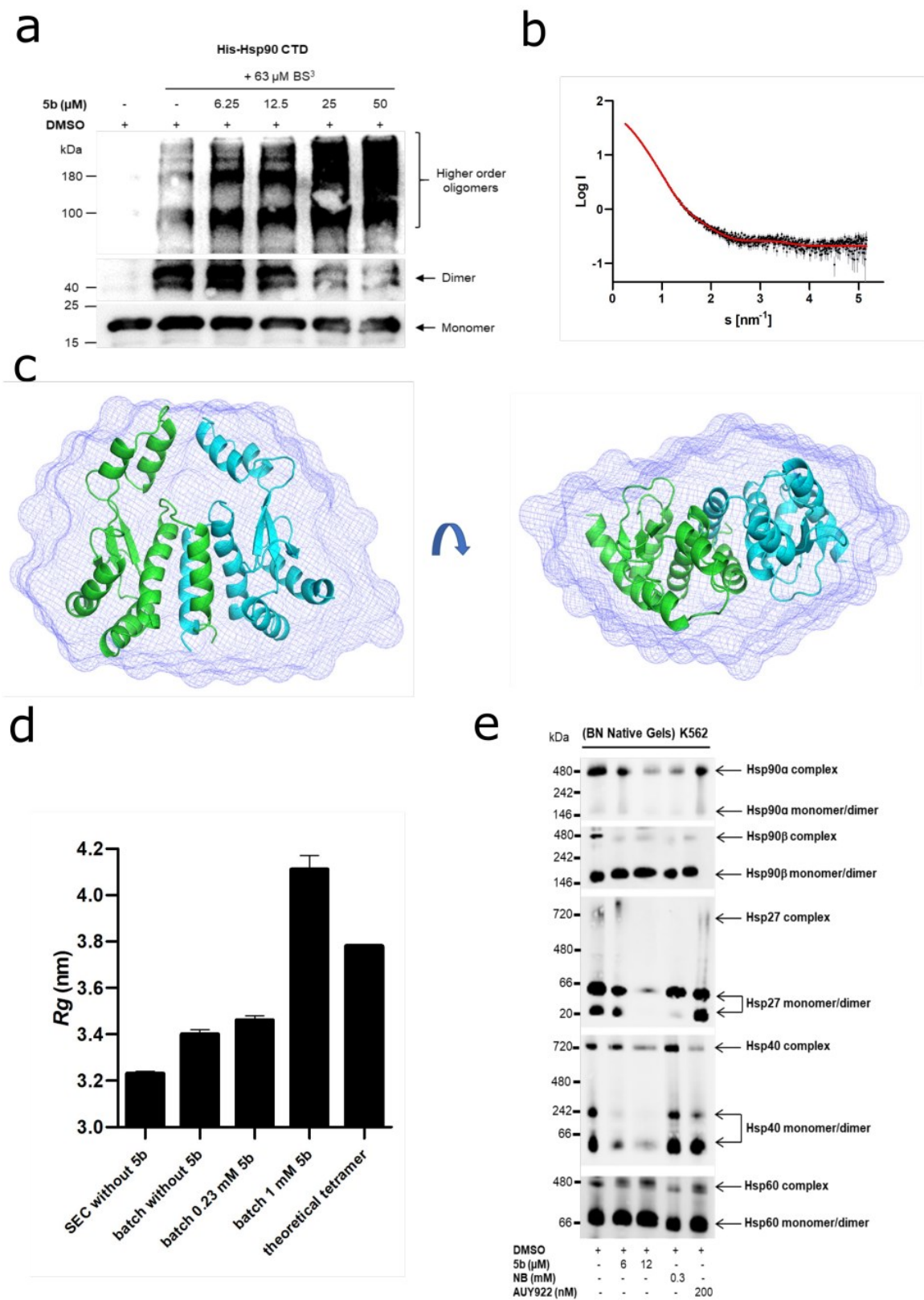
Figure 5: Effect of 5b on Hsp90 oligomeric species and CTD-mediated dimerization. a) Recombinant Hsp90α CTD was incubated with 63 μM BS^3 crosslinker, with (at indicated concentration) or without **5b**, followed by immunoblotting with anti-Hsp90 (AC88) antibody. **b)** Scattering data of Hsp90α CTD is shown in black dots, with grey error bars. The ab-initio DAMMIF model fit is shown as a red line. The intensity is displayed as a function of momentum transfer s. **c)** The volumetric envelope, calculated from the scattering data using DAMMIF [57], is shown as a blue surface. The monomers of the predicted Hsp90 CTD dimer model are shown in green and cyan. Superimposing was done using SUPCOMB.[57] **d)** The Radius of gyration (*Rg*) of the different Hsp90α CTD protein samples was calculated using the Guinier approximation.[58] The theoretical *Rg* of the tetramer was calculated using CRYSOL based on the structure PDB ID 3q6m.[59] **e)** Native Hsp90 complexes in K-562 (24h administration of **5b**) was identified by running Blue Native (BN) gels followed by immunoblotting analysis. The cytotoxic concentration of **5b** resulted in the potent disruption of Hsp90α, Hsp90β, Hsp40, and Hsp27 complexes and monomers/dimers. AUY922 exposure elevated the expression of HSR associated protein complexes and monomers/dimers (Hsp40 and Hsp27), whereas Hsp60 served as loading controls.

5b is effective against resistant leukemia cells and in the zebrafish xenotransplantation model

Elevated Hsp90 expression is reported in several resistant leukemia subtypes such as BCR-ABL1$^+$ CML/BCP-ALL, FLT3-ITD-driven AML, and Ph-like BCP-ALL.[60-63] Besides that, client proteins of Hsp90 include several kinases (e.g., AKT, BCR-ABL1, BRAF, EGFR2, HER2, and JAK1/2), growth and steroid receptors, and apoptotic factors (e.g., BCL-2 and mutant p53), which are often aberrantly regulated in several malignancies.[2,64] Therefore, we determined the efficacy of **5b** on therapy-resistant cell lines obtained from different leukemia subtypes (B-ALL, T-ALL, CML, and AML), including imatinib (IM), multi TKI-resistant and bortezomib (BTZ)-resistant leukemic cell lines.[28] Average IC$_{50}$ values of **5b** in these cell lines were determined using ATP-based viability assay and plotted in a clustered heat map, indicating the superior efficacy against BCR-ABL1+ and AML leukemic cell lines, when compared to T-ALL cell lines (**Figure 6a**).

As previously performed with AX[28], we next determined the destabilizing effect of **5b** on BCR-ABL1 expression and associated downstream signaling. In K562 cells, 48 h exposure of **5b** down-regulated the phospho-BCR-ABL1 and total-BCR-ABL1 levels, as well as the related downstream signaling pathways, as evaluated by immunoblot analysis (**Figure 6b**). **5b** additionally reduced the expression of client proteins associated with Hsp90 chaperone activity, involving Akt, Stat5, and c-Myc (**Figure 6b**). In contrast to AUY922, the exposure of **5b** on the K562 cells did not induce the expression of Hsp70, Hsp40, and Hsp27 involved in HSR (**Figure 6c**). Exposure of **5b** to the leukemic cell lines (K562, KCL22 and HL60) inhibited their proliferation (**SI Figure 27**) and induced apoptosis in a caspase 3/7 enzyme-dependent assay, with induction of approximately two- to eight-fold increase of apoptotic cells, in accordance to the reference Hsp90 CTD-targeting inhibitor, novobiocin (NB) (**SI Figure 28**).

Besides, **5b** facilitated early differentiation measured by expression of differentiation markers involving CD14 vs. CD11b in HL60 cells, and CD133 vs. CD11b in Mutz-2 cells (**SI Figure 29**). In this line, 48 h exposure of **5b** to K562 cells significantly reduced the colony-forming capacity (**SI Figure 30**). To further evaluate the efficacy of **5b** on leukemic cells, we used the zebrafish xenotransplantation model[65] (**Figure 6d**). MOLT-4 cells were transplanted into zebrafish embryos at 32 hours post-fertilization (hpf). At this stage, the adaptive immune system is not yet developed, therefore, human cells can be tolerated by the host. The transparency of zebrafish embryos also enabled us to monitor the distribution of human cells, which were stained with a vital fluorescent dye. Xenotransplanted embryos were treated with AUY922 (500 nM) and **5b** (500 nM) for 48 h, whereas DMSO was used as a negative control. No toxicity of drugs at the given concentration was noticed on the development of xenotransplanted embryos. We then determined the number of MOLT4 cells in each treated group using flow cytometry. Compared to the DMSO-treated group, the number of transplanted cells was significantly reduced in AUY922- and **5b**-treated embryos.

To conclude, this data confirms the anti-leukemic effect of **5b** without inducing HSR.

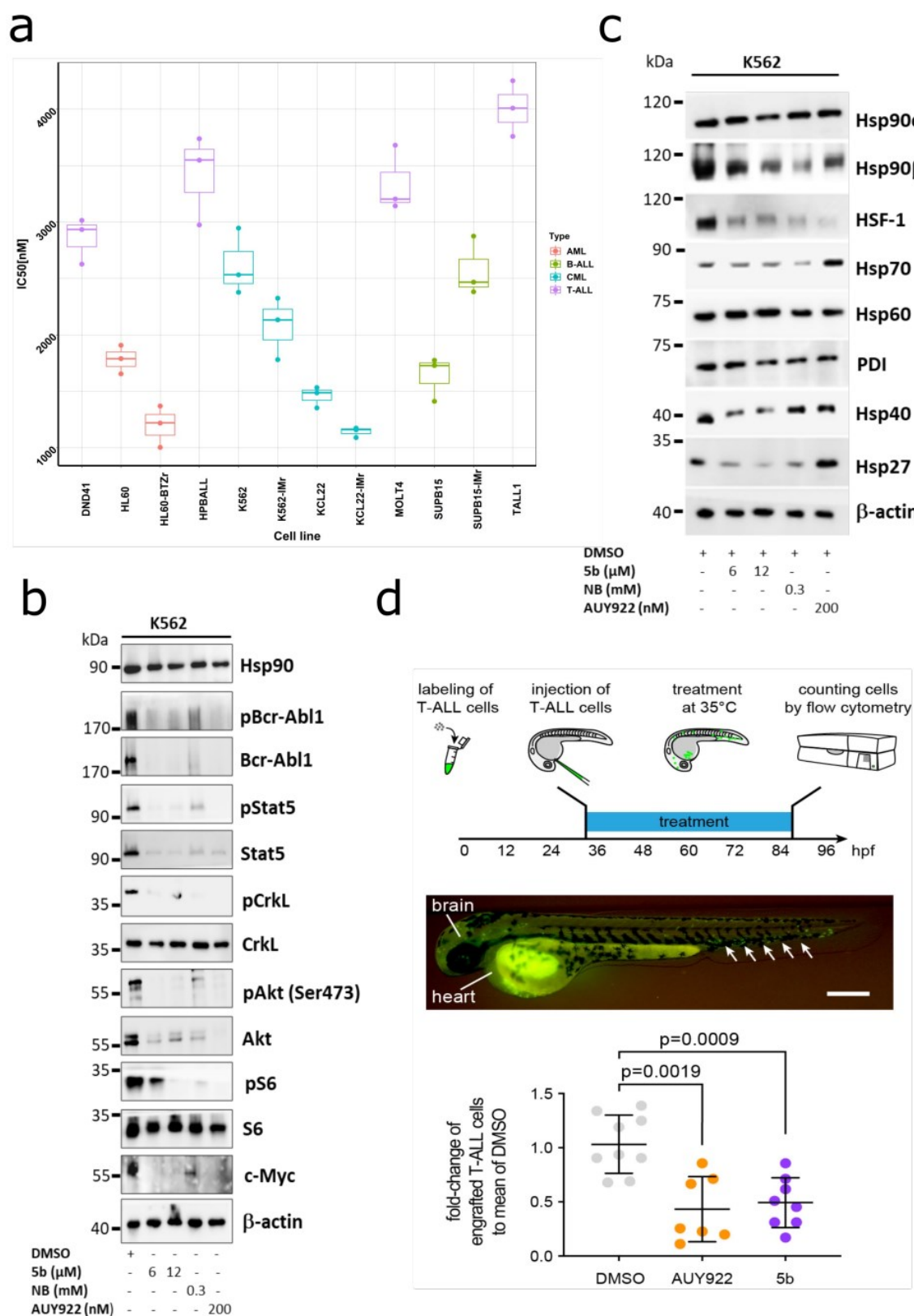**Figure 6: 5b is effective against human leukemic cell lines without inducing any HSR. a)** Comparative cytotoxicity assessment of different sub-groups of leukemic cell lines (K562, KCL22, SUPB15, HL60, MOLT4, DND41, TALL1 and HPBALL), imatinib-resistant cell lines (K562-IMr, KCL22-IMr, SUPB15-IMr), and bortezomib-resistant cell line (HL60-BTZr), after 72 h exposure to **5b**. The IC$_{50}$ data was plotted as a clustered

heat map, followed by unsupervised hierarchical clustering. The vertical axis of the dendrogram exemplifies the dissimilarity between clusters, whereas the color of the individual cell is related to its position along a log IC_{50} (µM) gradient. **b)** Treatment of K562 cells with **5b** and respective controls (AUY922 and NB) for 48 h resulted in the downregulation of BCR-ABL1+ and subsequently downstream signaling pathways including phosphorylated and unphosphorylated Stat5a, Crkl, Akt, S6 (mTOR), and cMyc. **c)** K562 cells were treated with the indicated (cytotoxic) concentration of **5b**, NB, and AUY922 for 48 h, and later protein lysates were subjected to immunoblot analysis. As expected, **5b** and NB did not induce expression of Hsp70, Hsp40, and Hsp27, whereas AUY922 leads to HSR induction. Hsp60 (primarily present in mitochondria) and PDI (endoplasmic reticulum) served as a control. **d)** Upper panel describes the experimental rationale. (Middle panel) A representative image of xenotransplanted zebrafish embryo at 32 hpf. Scale bar, 250µm. Note human T-ALL cells (green) were distributed in the yolk, brain, and hematopoietic tissue (arrows). (Lower panel) Fold-change of labeled cells normalized to the average percentage of labeled cells in the DMSO-treated group. Each dot represents three embryos pooled as one biological sample. Data are mean ± standard deviation. The *p*-values were calculated with the Mann-Whitney test.

5b acts on TKI-resistant BCR-ABL1+ leukemic cells

The integration of specific tyrosine kinase inhibitors (TKI) such as imatinib (Gleevec) into polychemotherapy treatment protocols has significantly improved the response rate in BCR-ABL1+ leukemia patients (initial remission went from 35% to 88%).[66] However, stable remission cannot be sustained in many cases as the leukemic cells pursue several escape mechanisms against TKI treatment; one of them is the occurrence of mutations in the ABL1 kinase domain. Especially, in the BCR-ABL1[T315I] mutant, only ponatinib (TKI) is effective[67], albeit with severe cardiovascular side effects.[68] As Hsp90 facilitates the correct folding of several oncogenic newly synthesized or denatured proteins, among them BCR-ABL1,[69-71] therefore targeting Hsp90 with small molecule inhibitors would destabilize BCR-ABL1 and can serve as a therapeutic target.[3,10] We, therefore, next tested the efficiency of **5b** in a murine BA/F3 cell line stably expressing clinically relevant mutants (BCR-ABL1[T315I], BCR-ABL1[E255K], and BCR-ABL1[M351T]) with prominent TKI resistance profiles.[28] As expected, similar to K562 cells, exposure of **5b** significantly reduced proliferation (**Figure 7a**) and induced apoptosis (**Figure 7b**) at 6 and 12 µM, comparable to NB (at 0.3 mM) in BA/F3 cells expressing BCR-ABL1[T315I, E255K, or M351T] mutants. Additionally, after the application of **5b**, BCR-ABL1 oncoprotein was destabilized, and downstream signaling pathways (Akt and Stat5) were blocked with increasing concentrations of **5b**, comparable to the human leukemic cell lines (**Figure 7c**). Furthermore, 24 h exposure of **5b** on BCR-ABL1[T315I, E255K or M351T] mutants-expressing BA/F3 cells significantly inhibited the colony formation ability (**Figure 7d**). In addition, in our generated human BCR-ABL1+ IM-resistant cell line models (K562-IMr and KCL22-IMr),[28] **5b** did not differentiate in inducing apoptosis between IM-resistant vs. IM-sensitive clones, proposing a superior effect of **5b** in human IM-resistant BCR-

ABL1-positive cells (**Figure 7e and SI Figure 31**). Encouraged by these results, we next tested **5b** on three primary CML^{CD34+} IM-resistant patient samples in the range of cytotoxic concentration (5-10 µM) obtained from leukemic cell lines. Similar to BCR-ABL1+ leukemic cell lines, the exposure of **5b** reduced the proliferation, induced apoptosis, and reduced the colony-forming ability of CML^{CD34+} IM-resistant patient cells and also revealed a potent combinatorial inhibitory effect when used in combination with IM (**Figure 7f – 7h**).
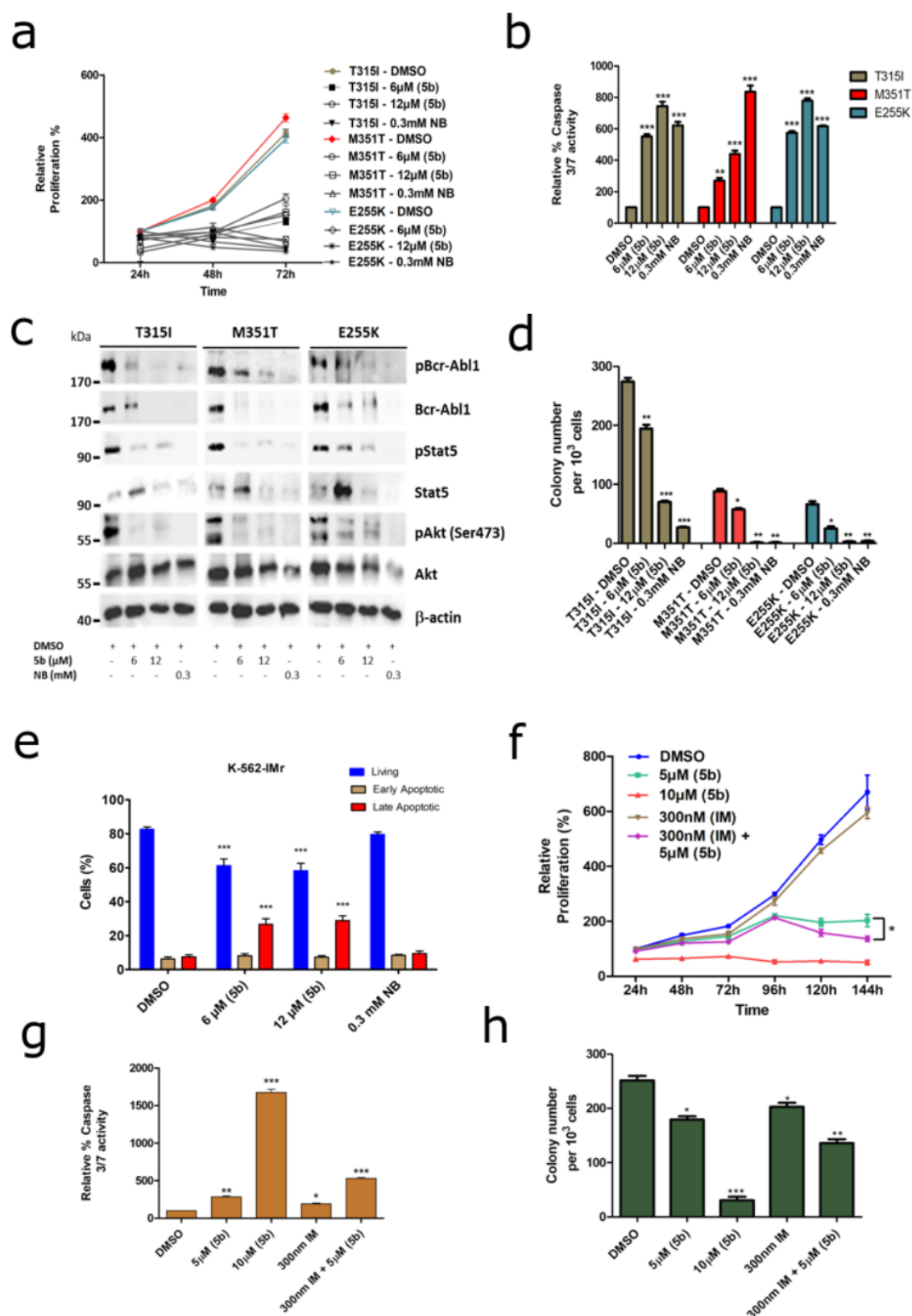
Figure 7: 5b as a potent inhibitor against TKI-resistant BCR-ABL1 mutant and a primary patient sample. **a)** BA/F3 cells expressing BCR-ABL1 mutants (T315I, M351T & E255K) were treated with the indicated concentration of **5b**, and later the viable cells were counted after every 24 h interval for 3 days. **b)** Apoptosis induction of the same cells after 48 h incubation of the compounds at indicated concentration, determined by Caspase 3/7 dependent Glo assay. **c)** Exposure of **5b** to these cells destabilizes BCR-ABL1 and subsequently its

associated downstream signaling pathways. **d)** BA/F3 BCR-ABL1 mutant-expressing cells were seeded in methylcellulose-based semisolid medium, after 24 h treatment with **5b**. Colonies were counted after 14 days. **e)** K562-IMr cells were treated with the indicated concentration of **5b** for 48 h, later dually stained with annexin V/PI, and subsequently measured by FACS. **f)** Primary CML[CD34+] patient cells were treated with the indicated concentration of **5b** or IM alone or in combination, and later the viable cells were counted after every 24 h interval for 6 days. **g)** Apoptosis induction in primary CML[CD34+] patient cells after exposure of **5b** or IB alone or in combination. **g)** Primary CML[CD34+] patient cells were seeded in methylcellulose medium after 24 h treatment with **5b**, IM alone or both in combination. Colonies were counted after 14 days. Columns depict the mean of three independent experiments ($n = 3$).

Discussion

The CTD of Hsp90 contains several binding areas: the C-terminal ATP binding site, the MEEVD motif at the end of the CTD, and the primary dimerization interface of Hsp90.[23] The C-terminal ATP binding site is only available upon occupation of the N-terminal ATP binding pocket and binds purine and pyrimidine nucleotides, while the N-terminal ATP binding site (NTD) is more specific for adenine derivatives.[72] The MEEVD motif binds the TRP-domain of cochaperones such as Hop and immunophilins, which is formed by a four-helix bundle and is crucial for Hsp90 dimerization.[2] Protein-protein interactions in the interface of the four-helix bundle maintain the dimeric state of Hsp90.[51]

In this study, we present the development of the first-in-class small-molecule inhibitor of Hsp90, **5b**, which was rationally designed to target the C-terminal dimerization interface. Based on our prior hotspot prediction[26] and the prototype compound AX[28], we successfully performed a scaffold-hopping from the aminoxy peptide-backbone towards more drug-like tripyrimidones. **5b** mimics α-helical side-chains that form hotspot residues located on H5 in the dimerization interface. To independently predict the binding site and mode of **5b**, we performed extensive MD simulations, in which the inhibitor was allowed to diffuse freely around an MD-CTD construct of Hsp90α, similar to our analysis on AX binding[28] and related studies.[73-75] The results revealed the C-terminal dimerization interface as the most likely binding region of **5b**, which was confirmed by effective binding energy computations, corroborating the hypothesis underlying the design of **5b**. Following the high sequence-identity in the interface region, similar results were obtained for Hsp90β, suggesting that **5b** does not exhibit isoform specificity.

Next, the selective binding of **5b** to Hsp90 was validated in a variety of biochemical and cellular assays, including DARTS, thermal and isothermal shift assays, whereas intracellular Hsp90 engagement and

disruption of Hsp90 multiprotein complexes were established via CETSA and ITDRF$_{CETSA}$ assays, and immunoblotting under reducing conditions (+/- DTT) and non-denaturing (BN-PAGE) conditions. Moreover, a crosslinker and auto display dimerization assay, as well as SEC-SAXS measurements, repeatedly confirmed the destabilization of Hsp90α CTD dimers upon **5b** incubation, whereas no unspecific binding of **5b** was reported on the Hsp90α NTD protein in an FP-based competitive assay. However, during SAXS measurements, which were performed on an ensemble of species in solution, we were unable to determine whether **5b**-induced oligomers originated from Hsp90α CTD monomeric or dimeric species. In addition, **5b** blocks the chaperone function of Hsp90, as determined by TR-FRET assay and in cell-free luciferase refolding assay. Markedly, even though there are differences in the inhibitory concentrations against tested leukemia cells between **5b** (IC$_{50}$ in submicromolar range) and reference Hsp90 NTD control inhibitors (IC$_{50}$ in subnanomolar range), a comparative selectivity profile (in cell-free or cell-based biochemical assays) toward Hsp90 was observed between **5b** and Hsp90 NTD reference inhibitors. This data indicate that the conventional Hsp90 NTD inhibitors induce cellular inhibitory effects through their off-target activity, besides targeting Hsp90.[4,16]

Moreover, **5b** exhibited potent *in vitro* anticancer activity against a broad spectrum of therapy-resistant leukemia cell lines (including TKI and proteasome inhibitor-resistant) and primary TKI-resistant (BCR-ABL1+) leukemia patient cells. **5b** significantly reduced the leukemia burden in the zebrafish xenotransplantation model and induced apoptosis in TKI-resistant BCR-ABL1[T315I, E255K or M351T] mutant cells by destabilizing the BCR-ABL1 expression and, thereby, hampering related downstream signaling cascades without HSR induction. These data collectively established **5b** as a first-in-class small-molecule inhibitor that targets the C-terminal dimerization interface.

Conclusion

Through structure-based molecular design, chemical synthesis, molecular simulations-based prediction of the binding mode, and evaluation of biochemical affinity, we have developed the first low-molecular weight compound interfering with the Hsp90 CTD dimerization. The C-terminal Hsp90 inhibitor **5b** contains a tripyrimidonamide scaffold and is active against therapy-resistant leukemia cells as well as

in a zebrafish xenotransplantation model without exhibiting the pro-survival resistance mechanism HSR.

Methods

Chemical synthesis: See **Supplementary Note 1** for general methods, synthetic protocols, compound characterization, and spectral data (**SI Figure 1 - 20**).

Expression and purification of recombinant Hsp90: Human Hsp90α CTD (563-732 amino acids) recombinant protein purification was performed as previously described.[26] Human Hsp90α NTD (amino acids 9-236; Addgene #22481) protein was expressed in E. coli BL21-DE3 cells.[76] BL21-DE3 expression strains were grown overnight and used to inoculate LB medium at 37 °C supplemented with 100 μg/mL ampicillin to an (OD_{600} = 0.5-0.8), followed by overnight induction of protein expression with 0.5 mM Isopropyl β-D-1-thiogalactopyranoside (IPTG) at 25 °C. After induction, cells were harvested by centrifugation at 5000 × g and lysed using B-PER bacterial protein extraction reagent (ThermoFisher Scientific, Wesel, Germany). GST-tagged Hsp90 CTD and NTD proteins were affinity purified spin columns (ThermoFisher Scientific) and eluted using glutathione elution buffer. Protein aliquots were made and supplemented with 5% glycerol and stored at −80 °C.

Microscale thermophoresis (MST): The labeling of the CTD of Hsp90 (Hsp90 CTD) was described before.[26,28] For determination of the apparent K_D value of Hsp90 CTD and the respective inhibitor, 10 μl of 50 nM labeled Hsp90 CTD in PBS containing 0.5 % BSA and 0.1 %Tween-20 were mixed with 10 μl of the respective inhibitor in different concentrations ranging from 15 nM to 500 μM and incubated for 15 min at RT in the dark. Thermophoresis of each mixture was induced at 1475 nm ± 15 nm and measured using the Monolith NT.115 (NanoTemper Technologies GmbH, München, Germany)[77]. The measurement was repeated three times independently for each sample and each measurement was performed at 25 °C for 25 s at 70 % LED power and 40 % infrared laser power. The resulting fluorescence values were plotted against the concentration of the titrant and the apparent K_D was calculated using the KD Fit formula Y = E + (A - E) / 2 * (T + x + K_D - sqrt((T + x + K_D)^2 − 4 * T *

x)) by GraphPad Prism software (GraphPad Software, Inc. La Jolla, USA). T, the concentration value for the labeled Hsp90 CTD, was set to 50 nM.

Autodisplay dimerization assay: *E. coli* strain BL21 (DE3) [B, F⁻, *dcm, ompT, lon, hsdS* (rB⁻mB⁻), *gal*, λ(DE3)] pETSH-3 Hsp90 encoding CtxB signal peptide, AIDA-I autotransporter and Hsp90 was used for the surface display of Hsp90.[27,28] *E. coli* strain BL21 (DE3)[B, F⁻, *dcm, ompT, lon, hsdS* (rB⁻mB⁻), *gal*, λ(DE3)] pETSH-3 SDH08 encoding CtxB signal peptide, AIDA-I autotransporter and sorbitol dehydrogenase was used as control[37]. Recombinant bacteria were routinely grown at 37 °C in lysogeny broth (LB) containing carbenicillin (100 µg/ml). Cells were grown to the mid log phase (OD$_{600}$ = 0.5) and the protein expression was induced by adding 1 mM IPTG for 16 h at 30 °C. Cells were then washed three times and suspended in PBS to an OD$_{600}$ = 0.35 in a final volume of 100 µl. Prior to p53-FITC incubation at a final concentration of 1 µM for 1 hour at RT in the dark, cells were incubated for 15 minutes either with or without inhibitor. Subsequently, cells were washed three times with PBS containing 0.1 % Tween-20 to avoid unspecific binding. The cellular fluorescence was measured with a FACS Aria III (BD, Heidelberg, Germany), using 488 nm as excitation wavelength, 530 nm for detection and the mean fluorescence value of at least 50,000 events for each measurement was determined.

Drugs affinity responsive target stability (DARTS): DARTS assay was performed to assess protease protection of Hsp90 protein from thermolysin digestion after incubation of Hsp90i, as described previously.[19,28] Briefly, 1 µg of recombinant Hsp90α was incubated on ice for 15 min with 25, 50 & 100 µM of **5b,** NB, AUY922 and DMSO. After incubation the samples were treated with thermolysin (1:50 of protein) for 5 min. The reaction was halted by addition of 50 mM EDTA and later examined by immunoblot analysis.

Luciferase refolding assay: Luciferase refolding assay was performed using recombinant firefly luciferase from *Photinus pyralis* (Sigma-Aldrich, St. Louis, MO, USA; 10x10^{10} Units/mg), which was diluted (1:100) in denaturation buffer (25 mM Tricine, pH 7.8, 8 mM MgSO4, 0.1 mM EDTA, 1% Triton X-100, 10% glycerol, and 10 mg/mL BSA) at 38°C for 8 min.[42-44,78] Rabbit reticulocyte lysate (Promega, Madison, WI, USA) was diluted 1:1 by the addition of cold mix buffer (100 mM Tris, pH 7.7, 75 mM Mg(OAc)2, 375 mM KCl, and 15 mM ATP), creatine phosphate (10 mM) and creatine

phosphokinase (16 U/mL) and was pre-incubated at 30°C with the respective inhibitors and controls for 1h. Afterwards, 1µL denatured luciferase or active luciferase (as a control) was added to 20 µL rabbit reticulocyte mixture. As a control, denatured or active luciferase was incubated without reticulocyte lysate in buffer containing 20 mM Tris, pH 7.5, 150 mM NaCl, 1 % haemoglobin and 4 % BSA. At desired time points, 1.5 µL samples were removed and added to 40 µL assay buffer (25 mM Tricine, pH 7.8, 8 mM MgSO4, 0.1 mM EDTA, 33 µM DTT, 0.5 mM ATP, and 0.5 mM luciferin) and luminescence was read using a Spark® microplate reader (Tecan). Percent luciferase refolding was determined using luminescence of DMSO at 120 min as 100% and comparing all samples to this value.

Thermal shift assay: CTD or NTD of r-Hsp90α (5 µM) protein and the indicated concentrations of the inhibitors were mixed together in the assay buffer (1X PBS, pH = 7.5) and were incubated for 2h. Then, 6X SYPRO Orange dye (Sigma-Aldrich) was added to the mixture (20 µl), which binds to the exposed hydrophobic residues of unfolded protein (during thermal exposure) and thereby showing an increase fluorescence.[39,79] 96-well polymerase chain reaction (PCR) plates, and a PCR system (BioRad, CFX Connect™ Real-time system) were used to heat the samples from room temperature to 95 °C in increments of 0.5 °C for 10 seconds, with excitation wavelength at 470 nm and emission wavelength at 570 nm. For determination of protein melting temperature values (Tm), melting curve for each data set was analysed by GraphPad Prism 8.0.2 and fitted with the sigmoidal Boltzmann fit. Melting temperatures without the inhibitors were used as control.

Isothermal shift assay was performed following similar procedure as with thermal shift assay. However, increasing indicated concentrations of the inhibitors (98 nM – 200 µM) were used, which was incubated with either C-terminal or N-terminal of Hsp90 (5 µM) in the assay buffer (1X PBS, pH = 7.5) for 2 h. The samples were heated to 46°C after adding 6X SYPRO Orange dye (Sigma-Aldrich). Percent unfolding was calculated by normalizing to 100 % unfolding and comparison to vehicle control (DMSO).

Cellular thermal shift assay (CETSA): CETSA assay was performed as described previously,[39-41] with minor modifications. K562 cells were incubated with the indicated inhibitors (or DMSO) for 24h. Cells were harvested by centrifugation (400 x g for 5 min at RT) and washed three times with PBS. The pellets were dissolved in PBS and later equally divided into 200 µL-PCR tubes. Solutions were heated at the

indicated temperature gradient for 3 min (T-Gradient Cycler, Biometra). Aliquots were then snap-freeze in liquid nitrogen and thawed at 25°C in a thermal cycler (GeneAMP PCR System2700, Applied Biosystems) three times, followed by centrifugation at 10000 x g for 20 min at 4°C. The supernatants were harvested and protein levels were measured by quantitative simple western immunoassay (JESS, BioTechne, MN, USA). Protein levels represented by the area under the curve of the electropherograms were normalized to the lowest temperature set as 0% degradation. ΔT_m for compounds were determined by plotting normalized data using sigmoid dose curve and nonlinear regression (GraphPad Prism 8.0.2).

Isothermal dose-dependent fingerprint (ITDRF) CETSA: Based on the previously determined IC50 values, K562 cells were treated with the indicated dilution range of inhibitor for 24h. Then, cells were harvested by centrifugation (400 x g for 5 min at RT) and washed three times with PBS. The pellets were dissolved in 200 μL PBS and transferred into PCR tubes (Eppendorf). Results of prior CETSA runs were utilized to determine the optimal melting temperature of 54.1°C for Hsp90. Samples were heated once at 54.1°C for 3 min (T-Gradient Cycler, Biometra) and then snap-frozen in liquid nitrogen and thawed at 25°C in a thermal cycler (GeneAMP PCR System2700, Applied Biosystems) three times, followed by centrifugation at 10000 x g for 20 min at 4°C. The supernatants were harvested and protein levels were measured by quantitative simple western immunoassay (JESS, BioTechne, MN, USA). Protein levels are calculated by the area under the curve of the electropherograms.

Simple western immunoassay: Fluorescent (5X) master mix, DTT and biotinylated ladder were prepared as per manufacturer's instruction (BioTechne). Lysates were diluted with 0.1x sample buffer and mixed 5:1 with fluorescent 5x master mix to obtain a target sample concentration of 0.40 μg/μl per well. Samples were then denatured for 5 min at 95°C in a PCR cycler (GeneAMP PCR System2700, Applied Biosystems). The assay plate was loaded as per manufacture's instruction and centrifuged for 5 min at 1000 x g at RT. The immunoassay was performed using a 12-230 kDA separation module with 25 cartridges (SM-W004, BioTechne). Lysates were separated 25 min at 375 volt, blocked for 5 min with antibody diluent 2, 30 min incubated with primary antibody and 30 min incubated with secondary antibody, subsequently. Primary antibody multiplex mix consisted of 1:100 anti-Hsp90 (#4877S, Cell Signaling Technology, Danvers, MA, USA) and 1:50 anti-β-actin (#MAB8929, R&D) diluted in

Antibody Diluent 2. Signals were detected using an anti-rabbit detection module of JESS (DM-001, BioTechne), multiplexed with an anti-mouse secondary NIR antibody (#043-821, BioTechne).

Time-resolved fluorescence resonance energy transfer (TR-FRET): The evaluation of the Hsp90 binding affinity to PPID (Cyclophilin D) was performed using the Hsp90 CTD TR-FRET assay kit (#50289, BPS Bioscience, San Diego, CA, USA). Terbium (Tb) labeled donor and dye-labeled acceptor were diluted 100-fold in (1X) Hsp90 assay buffer 2. 10 µL diluted tb-labeled donor and 10 µl diluted dye-labeled acceptor were mixed with 4 µL (indicated concentration) inhibitor, 10 µL of 3 ng/µl PPID-GST-tag (BPS Bioscience) and 6 µL of 2 ng/µl biotin labeled CTD of Hsp90 (BPS Biosciences). For the positive control, the inhibitor was substituted for DMSO and for the negative control PPID-GST-tag was substituted for 1X Hsp90 assay buffer. Samples were incubated for 2 hours at RT protected from light and measured with a microplate-reader (SPARK10M, Tecan). Fluorescence was measured using a time resolved reading mode with two subsequent measurement: First measurement was performed using 340 nm / 620 nm (excitation/emission) wavelength with a lag time of 60 µs and integration time of 500 µs. Second measurement was performed using 340 nm / 665 nm (excitation/emission) wavelength with a lag time of 60 µs and integration time of 500 µs. Data analysis is performed using the TR-FRET ratio (665 nm emission / 620 nm emission). The TR-FRET ratios are normalized to % activity by setting the negative control as zero percent activity and the positive control as one hundred percent activity [(FRET$_{sample}$ − FRET$_{neg}$)/(FRET$_{pos}$ − FRET$_{neg}$) * 100%].

Fluorescence polarization (FP) measurements: The evaluation of the binding affinity of compounds towards the ATP pocket of Hsp90 NTD was determined by a competitive binding assay against FITC-labeled geldanamycin (GM) using the Hsp90 NTD assay kit (#50293, BPS Bioscience).[42] The inhibitor sample wells were filled with 15 µl 5X Hsp90 assay buffer, 5 µL 40 mM DTT, 5 µL 2 mg/ml BSA, 40 µL H$_2$O, 5 µL FITC-labeled GM (100 nM) and 10 µL inhibitor (at indicated concentration). The reaction was initiated by adding 20 µl Hsp90 (17 ng/µl) and incubation at room temperature for 3 hours with slow shaking. Background wells (master mix only); negative controls (FITC-labeled GM, buffer and DMSO) and positive controls (FITC-labeled GM, buffer, DMSO, Hsp90) were also included within the assay plate. Fluorescence was measured at 470 nm excitation wavelength and 525 nm emission wavelength in a microtiter-plate reader (Infinite M1000pro by Tecan). Polarization was calculated using

$(I_{II} - G(I⊥)/ (I_{II} + G(I⊥)))*1000$ and a g-factor of 1,187. The percentage of Hsp90-bound FITC labelled GM was calculated using $P_{norm} = (P_{Inhibitor}-P_{neg}) / (P_{pos} − P_{neg})*100$.

Molecular dynamics (MD) simulations: The structures of Hsp90α and β (PDB IDs 3q6m and 5fwk respectively) were prepared using Schrödinger Maestro[80]. For each of the isoforms, 40 individual MD simulations were performed. Initial random placement of **5b** and solvation in TIP3P water[81] was done using PACKMOL[82], neutralizing the system by the addition of sodium ions. ff14SB was used as force field for the protein and a modified GAFF version 1.5 for **5b**.[26,48] All simulations were carried out using the Amber18 software package.[46] To treat long-range electrostatics, the particle mesh Ewald method[83] was used with a cutoff of 9.0 Å for equilibration and 10.0 Å for production. The SHAKE algorithm[84] and hydrogen mass repartitioning[85] were used to allow for simulation steps of 2 fs in the equilibration and 4 fs in the production.

Initially, the systems were energy-minimized using the steepest descent (500 steps) and conjugate gradient (2000 steps) methods and placing positional restraints with a force constant of 5 kcal mol^{-1} Å^{-2} on all protein atoms; the restraints were reduced in a second energy minimization to a force constant of 1 kcal mol^{-1} Å^{-2} (for 2000 steps of steepest descent followed by 8000 steps of conjugate gradient), and removed in a third one (for 1000 steps of steepest descent followed by 4000 steps of conjugate gradient). Placing positional restraints with a force constant of 1 kcal mol^{-1} Å^{-2} on the backbone atoms, first, the system was heated to 100 K in 50 ps of NVT MD and further heated to 300 K in 5 ps of NPT MD. Further 65 ps of NPT MD were performed for density equilibration, still applying the backbone restraints. Afterward, over the course of further 300 ps of NPT MD, the backbone restraints were gradually reduced to a force constant of 0.2 kcal mol^{-1} Å^{-2}.

After the thermalization, 500 ns of NPT MD simulations were carried out with positional restraints with a force constant of 0.1 kcal mol^{-1} Å^{-2} on the backbone atoms. The Langevin thermostat with a collision frequency of 1 ps^{-1} and the Monte Carlo barostat with a pressure relaxation time of 1 ps were used. The reference coordinates for these restraints were readjusted every 100 ns to allow for moderate protein flexibility. For Hsp90α, these simulations were later extended to 1 µs. The trajectories were postprocessed and analyzed with CPPTRAJ[86], and results were visualized with PyMol[76].

MM-GB/SA computations: Effective binding energies were computed over one MD trajectory that resulted in binding of **5b** in the CTD dimerization interface and led to a binding mode in which **5b** mimics H5'. In the computations, the single trajectory approach was used, where complex, protein, and ligand configurations were extracted from the complex trajectory.[87] After removing water molecules and counterions, gas-phase energies (van der Waals and electrostatic contributions) were evaluated on every frame sampled at an interval of 200 ps using MMPBSA.py [88]; the polar contribution to the solvation free energy was calculated using the "OBC II" generalized Born model[89], together with mbondi2 radii and a dielectric constant of 1 for the solute and 80 for the solvent. The ionic strength was set to 150 mM of a 1:1 salt. The non-polar contribution to the solvation free energy was calculated as a function of the solvent-accessible surface area using 0.0050 kcal mol^{-1} Å^{-2} as surface tension. No absolute binding free energies can be derived from this approach since configurational entropy contributions are not considered here to reduce the uncertainty in the computations.[49,50]. However, the sum of gas-phase energies and solvation free energies, the effective energy, is suitable to estimate relative differences in binding free energies for differential binding poses.[28]

WB & Blue-native gels: Cells were treated with the indicated concentration of the compound or vehicle (DMSO) for 48 hours. Immunoblot analysis was performed by following standard protocol using antibodies: anti-Hsp90 (#4877), anti-Hsp70 (4872), anti-Hsp40 (#4871), anti-Hsp27 (#2402), anti-HSF-1 (4356), anti-Hsp60 (#12165), anti-PDI (#2446), anti-Hsp90α (#8165), anti-Hsp90β (#5087), anti-c-Abl (#2862), anti-phospho-c-Abl (#2865), anti-Stat5 (#9363), anti-phospho-Stat5 (#9351), anti-CrkL (#3182), anti-phospho-Crkl (#3181), anti-Akt (#2920), anti-phospho-Akt (#4060) , anti-S6 ribosomal protein (#2217), anti-phospho-S6 ribosomal protein (#4858), anti-c-Myc (#13987) from Cell Signaling Technology and anti-β-actin (Sigma-Aldrich). Blue-native (BN) gels were performed following manufacturer's instructions (Invitrogen) and performed previously.[28] Briefly, lysates were generated from K562 cell line after 48 h treatment with inhibitors (at indicated concentration) using NativePAGE Sample Prep kit (Invitrogen) by 2-3 freezing thawing cycles followed by centrifugation at 20,000 x g for 25-30 min at 4°C.

Dimerization assay: Hsp90 CTD dimerization was evaluated using an amine-reactive chemical cross-linker bis(sulfosuccinimidyl) suberate (BS^3) (Pierce). [42,45] Hsp90α CTD protein (2 μM) was diluted in

Na$_2$HPO$_4$ (25 mM; pH 7.4) and treated with different concentrations of the inhibitor to make a final volume of 25 μL. The reaction mixture was incubated at RT for 1 h. The amine-reactive crosslinker BS^3 was added to a final concentration of 63 μM and the samples were incubated for 1 h at RT. Crosslinking was quenched by the addition of SDS sample buffer and subsequent heating for 5 min at 95 °C. Samples were run in 12% SDS-PAGE gels followed by western blotting. Blots were probed with anti-Hsp90 (AC88, Abcam) antibody.

SEC-SAXS: We collected the SEC-SAXS data on beamline BM29 at the ESRF Grenoble [53,54]. The BM29 beamline was equipped with a PILATUS 2M detector (Dectris) at a fixed distance of 2.827 m. The measurement of Hsp90 CTD (18 mg/ml) was performed at 20°C on a Superdex 200 increase 3.2/300 column (Buffer 50 mM TRIS pH 7.5, 100 mM NaCl) with a flowrate of 0.075 ml/min, collecting one frame each two seconds. Data were scaled to absolute intensity against water. Further, we have collected SAXS data on our Xeuss 2.0 Q-Xoom sytem from Xenocs, equipped with a PILATUS 3 R 300K detector (Dectris) and a GENIX 3D CU Ultra Low Divergence x-ray beam delivery system. The chosen sample to detector distance for the experiment was 0.55 m, results in an achievable q-range of 0.10 - 6 nm^{-1}. All measurements were performed at 20°C with protein concentrations of 9.7 and 10.8 mg/mL. Compound 5b was added and incubated for 30 min at 20 °C. Samples were injected in the Low Noise Flow Cell (Xenocs) via autosampler. For each sample, 18 frames with an exposer time of ten minutes were collected. Data were scaled to absolute intensity against water. All used programs for data processing were part of the ATSAS Software package (Version 3.0.3) [90]. Primary data reduction was performed with the programs CHROMIXS and PRIMUS [55,56]. With the Guinier approximation [58], we determine the forward scattering $I(0)$ and the radius of gyration (R_g). The program GNOM [91] was used to estimate the maximum particle dimension (D_{max}) with the pair-distribution function $p(r)$. Low resolution *ab initio* models were calculated with DAMMIF [57]. Superimposing of the predicted model was done with the program SUPCOMB [92].

Physicochemical properties of 5b (See **Supplementary Note 2** for more details):
Aqueous solubility of 5b
The aqueous thermodynamic solubility of **5b** was determined in phosphate-buffered-saline (PBS, pH 7.4) after 4 and 24 h incubation time at 25°C. Ondansetron was used as reference compound with high

solubility of 95 μM. The thermodynamic solubility of **5b** was ranging from 4 μM after 4 h to 8 μM after 24 h (n = 2). For detailed information see Bienta, Enamie Biological Services study reports.

Chemical stability of 5b

Drug decomposition was determined by high-performance liquid chromatography (HPLC, Method 1). *Instrument*: Knauer HPLC system in combination with a Knauer UV Detector Azura UVD 2.1L. *Column*: KNAUER Eurospher II 100-5 C18, 150x4 mm *Mobile phase* 1: linear gradient (90−0%) of water with 0.1 % trifluoroacetic acid. *Mobile phase* 2: linear gradient (10–100%) of acetonitrile with 0.1 % of trifluoroacetic acid. *Run time*: 20 min, followed by an isocratic elution with 100% acetonitrile for 10 min. *Flow rate*: 1 mL/min. *Detection*: 254 nm.

5b was dissolved in a mixture of Tween20/ethanol/phosphate buffer pH 7,4 (7/3/90) and the stability monitored over a period of 24 h at 37°C. After 24h, almost no decomposition was detected (0.7 % drug decomposition, *n* = 2).

The stability of **5b** at acidic pH was determined by dissolving **5b** in a mixture of Tween20/ethanol/phosphate buffer pH 2 (7/3/90) and the stability monitored over a period of 24 h at 37°C. After 24h, only slight decomposition was detected (1.3 % drug decomposition, *n* = 2).

In vitro metabolic stability of 5b in human liver microsomes

The metabolic stability screening of **5b** in human liver microsomes revealed **91 %** stability after a 40 min incubation at 37°C. Propanolol, a reference drug with medium to high metabolic stability showed 74 % of the parent compound remaining, and therefore demonstrated slightly decreased stability compared with **5b**. Calculated results for the intrinsic clearance suggest that **5b** (6 μL/min/mg) is a low clearance compound with an estimated long half-life (n=2). For detailed information see Bienta, Enamie Biological Services study reports.

Cell culture: K562, KCL22, SUPB15 (BCR-ABL1+ CML/BCP-ALL), HL-60 (AML), DND41, HPBALL, TALL1 and MOLT4 (T-ALL) leukemic cell lines (DSMZ, Braunschweig, Germany) were cultured in RPMI1640 GlutaMAX (ThermoFisher Scinetific) supplemented with 10-20% FCS (Sigma-Aldrich, St. Louis, MO, USA) and penicillin/streptomycin (Invitrogen, Carlsbad, CA, USA), and maintained at 37°C with 5% CO_2. Normal BA/F3 and BA/F3 cells expressing BCR-ABL1 mutants (T315I, M351T & E255K) (murine pro B cell line) were cultured in RPMI1640 GlutaMAX (10% FCS) supplemented with or without IL-3 (10ng/ml) respectively. BA/F3 cells expressing BCR-ABL1 mutants were resistant against imatinib (IM) until ~10 μM.[28] IM resistant BCR-ABL1+ K562 (K562-IMr), KCL22 (KCL22-IMr) and SUPB15 (SUPB15-IMr) were generated by gradual increase (1-2.5 μM) in

the concentration of IM (Sigma-Aldrich, St. Louis, MO, USA) over a period of 3 months.[28,93] Bortezomib (BTZ) resistant clones (80 nM) of HL60 (HL60-BTZr) was established following similar protocol as described to pick IM resistant clones. Primary patient derived CML^CD34+ blast cells were cultured in mononuclear cell medium (PromoCell, Heidelberg, Germany).

Hsp90 CTD/NTD targeting reference inhibitors: Coumermycin A1 (CA1) and novobiocin (NB) were purchased from Sigma-Aldrich, and Hsp90 NTD targeting reference control inhibitors: geldanamycin (GM), tanespimycin (TM), PUH-71 were purchased from Selleckchem.

Viability assay: Cells were seeded in white 96-well plate (Corning, NY, USA) with increasing concentration (50 nM – 25 μM) of inhibitors and respective controls for 48 h. Cell viability was monitored using Celltitre Glo luminescent assay (based on the ATP quantification), following manufacturer's guidelines (Promega).[28] IC_{50} for compounds were determined by plotting raw data (normalized to controls) using sigmoid dose curve and nonlinear regression (GraphPad Prism).

Proliferation assay: Cell proliferation was examined after treatment with the compounds at their indicated concentration with trypan exclusion method using automated cell counter (Vi-CELL™ XR - Beckman Coulter, Fullerton, CA), after every 24 h interval.

Annexin V staining: For evaluating apoptosis, 48 h inhibitor treated cells were stained with Annexin V and propidium iodide (PI), following supplier's guidelines (Invitrogen, Carlsbad, CA) and later the stained cells were subjected to FACS (Cytoflex, Beckman Coulter).

Caspase 3/7 Glo assay: Cells were incubated with the respective inhibitors or control for 48 h and later enzymatic activity of caspase 3/7 was examined (SPARK10M, Tecan) by using caspase 3/7 dependent Glo assay (absorbance at 405 nm), following manufacturer's instructions (Promega).[28]

Zebrafish: Zebrafish wild-type TE strain were maintained according to standard protocols and handled in accordance with European Union animal protection directive 2010/63/EU and the local government (Tierschutzgesetz §11, Abs. 1, Nr. 1, husbandry permit 35/9185.46/Uni TÜ). All experiments described in this study were conducted on embryos younger than 5 days post-fertilization (dpf) – prior to the legal onset of animal life.

Xenotransplantation in zebrafish embryos: Xenotransplantation experiment was performed as described previously.[65] Briefly, MOLT-4 cells were labeled with Vybrant™ CFDA SE Cell Tracer Kit (Invitrogen) following the manufacturer's instructions, and then were suspended in PBS at a density of 1×10^8 cells/ml. Approximately 1 nl cell suspension (around 200 cells) was injected into the perivitelline space of embryos at 32 hpf. Injected embryos were first incubated at 28°C for one hour. Only embryos with good engraftment were selected for treatment with DMSO (control group), AUY922 (500 nM) or 5b (500 nM) for 48 hours at 35°C. This temperature enables the maintenance of embryos with grafted cells without compromising zebrafish development. Drug-treated embryos were dissociated by passing through a 40-µm cell strainer (Greiner Bio-One) and then analyzed using a BD LSR II flow cytometer. Fold change of engrafted MOLT4 cells was calculated to mean of DMSO-treated embryos. GraphPad Prism software (version 7) was used for graphing and statistical analysis.

Differentiation assay: FACS measurements were performed after incubating the respective inhibitors at indicated concentration for 48h by using fluorochrome coupled monoclonal antibodies (mAbs) along with matched isotype controls: anti-CD11b (Bear1; Beckman Coulter), anti-CD14 (RMO52; Beckman Coulter), anti-CD133 (AC133; MiltenyiBiotec, Gladbach, Germany).[38]

Colony forming unit (CFU) assay: CFU assay was performed by plating inhibitor treated cells (48 h) in methylcellulose medium (Methocult H4100 - StemCell Technologies, Vancouver, BC, Canada) supplemented with 50 ng/ml SCF, 10 ng/ml IL-3, 10 ng/ml GM-CSF (Peprotech, Hamburg, Germany) and 3 U/ml erythropoietin (ebiosciences, San Diego, USA).[38] Colonies were counted after 14 days (n=3).

Significance analyses of normally distributed data with variance similar between groups used paired, two-tailed Student's t-test: *, $p < 0.05$; **, $p < 0.005$; ***, $p < 0.001$.

Author Contributions:

Funding Sources:

Notes:

Acknowledgments:

138

Abbreviations:

TLC, thin-layer chromatography; MOA mode of action; MD molecular dynamics; MM-GB/SA molecular mechanics generalized Born surface area; NTD N-terminal domain; MD Middle domain; CTD C-terminal domain; PPIs, protein-protein interactions; HSR, Heat shock resposne.

References

1   Sanchez, J., Carter, T. R., Cohen, M. S. & Blagg, B. S. Old and New Approaches to Target the Hsp90 Chaperone. *Current cancer drug targets*, doi:10.2174/1568009619666191202101330 (2019).

2   Schopf, F. H., Biebl, M. M. & Buchner, J. The HSP90 chaperone machinery. *Nature reviews. Molecular cell biology* **18**, 345-360, doi:10.1038/nrm.2017.20 (2017).

3   Butler, L. M., Ferraldeschi, R., Armstrong, H. K., Centenera, M. M. & Workman, P. Maximizing the therapeutic potential of HSP90 inhibitors. *Molecular cancer research : MCR* **13**, 1445-1451, doi:10.1158/1541-7786.MCR-15-0234 (2015).

4   Wang, Y., Koay, Y. C. & McAlpine, S. R. How Selective are Hsp90 Inhibitors for Cancer Cells over Normal Cells? *ChemMedChem* **12**, 353-357, doi:10.1002/cmdc.201600595 (2017).

5   Wu, J. *et al.* Heat Shock Proteins and Cancer. *Trends Pharmacol Sci* **38**, 226-256, doi:10.1016/j.tips.2016.11.009 (2017).

6   Wang, Y. & McAlpine, S. R. Heat-shock protein 90 inhibitors: will they ever succeed as chemotherapeutics? *Future Med Chem* **7**, 87-90, doi:10.4155/fmc.14.154 (2015).

7   Hsu, H. S. *et al.* Chemoresistance of lung cancer stemlike cells depends on activation of Hsp27. *Cancer* **117**, 1516-1528, doi:10.1002/cncr.25599 (2011).

8   Gandhi, N. *et al.* Novel Hsp90 inhibitor NVP-AUY922 radiosensitizes prostate cancer cells. *Cancer biology & therapy* **14**, 347-356, doi:10.4161/cbt.23626 (2013).

9   Modi, S. *et al.* A multicenter trial evaluating retaspimycin HCL (IPI-504) plus trastuzumab in patients with advanced or metastatic HER2-positive breast cancer. *Breast cancer research and treatment* **139**, 107-113, doi:10.1007/s10549-013-2510-5 (2013).

10   Wang, M. *et al.* Development of Heat Shock Protein (Hsp90) Inhibitors To Combat Resistance to Tyrosine Kinase Inhibitors through Hsp90-Kinase Interactions. *J Med Chem*, doi:10.1021/acs.jmedchem.5b01106 (2016).

11   Bagatell, R. *et al.* Induction of a heat shock factor 1-dependent stress response alters the cytotoxic activity of hsp90-binding agents. *Clin Cancer Res* **6**, 3312-3318 (2000).

12   McCollum, A. K., Teneyck, C. J., Sauer, B. M., Toft, D. O. & Erlichman, C. Up-regulation of heat shock protein 27 induces resistance to 17-allylamino-demethoxygeldanamycin through a glutathione-mediated mechanism. *Cancer research* **66**, 10967-10975, doi:10.1158/0008-5472.CAN-06-1629 (2006).

13   Guo, F. *et al.* Abrogation of heat shock protein 70 induction as a strategy to increase antileukemia activity of heat shock protein 90 inhibitor 17-allylamino-demethoxy geldanamycin. *Cancer research* **65**, 10536-10544, doi:10.1158/0008-5472.CAN-05-1799 (2005).

14   Maloney, A. *et al.* Gene and protein expression profiling of human ovarian cancer cells treated with the heat shock protein 90 inhibitor 17-allylamino-17-demethoxygeldanamycin. *Cancer research* **67**, 3239-3253, doi:10.1158/0008-5472.CAN-06-2968 (2007).

15   Hall, J. A., Forsberg, L. K. & Blagg, B. S. Alternative approaches to Hsp90 modulation for the treatment of cancer. *Future Med Chem* **6**, 1587-1605, doi:10.4155/fmc.14.89 (2014).

16   Wang, Y. & McAlpine, S. R. N-terminal and C-terminal modulation of Hsp90 produce dissimilar phenotypes. *Chemical communications* **51**, 1410-1413, doi:10.1039/c4cc07284g (2015).

17   Li, L., Wang, L., You, Q. D. & Xu, X. L. Heat Shock Protein 90 Inhibitors: An Update on Achievements, Challenges, and Future Directions. *J Med Chem* **63**, 1798-1822, doi:10.1021/acs.jmedchem.9b00940 (2020).

18   Khandelwal, A. *et al.* Structure-guided design of an Hsp90beta N-terminal isoform-selective inhibitor. *Nat Commun* **9**, 425, doi:10.1038/s41467-017-02013-1 (2018).

19   Eskew, J. D. *et al.* Development and characterization of a novel C-terminal inhibitor of Hsp90 in androgen dependent and independent prostate cancer cells. *BMC Cancer* **11**, 468, doi:10.1186/1471-2407-11-468 (2011).

20   Koay, Y. C. *et al.* Chemically accessible hsp90 inhibitor that does not induce a heat shock response. *ACS medicinal chemistry letters* **5**, 771-776, doi:10.1021/ml500114p (2014).

21   Sellers, R. P. *et al.* Design and synthesis of Hsp90 inhibitors: exploring the SAR of Sansalvamide A derivatives. *Bioorganic & medicinal chemistry* **18**, 6822-6856, doi:10.1016/j.bmc.2010.07.042 (2010).

22   Westerheide, S. D. *et al.* Celastrols as inducers of the heat shock response and cytoprotection. *J Biol Chem* **279**, 56053-56060, doi:10.1074/jbc.M409267200 (2004).

23   Bickel, D. & Gohlke, H. C-terminal modulators of heat shock protein of 90kDa (HSP90): State of development and modes of action. *Bioorganic & medicinal chemistry* **27**, 115080, doi:10.1016/j.bmc.2019.115080 (2019).

24   Metz, A. *et al.* Hot spots and transient pockets: predicting the determinants of small-molecule binding to a protein-protein interface. *J Chem Inf Model* **52**, 120-133, doi:10.1021/ci200322s (2012).

25   Metz, A., Schanda, J., Grez, M., Wichmann, C. & Gohlke, H. From determinants of RUNX1/ETO tetramerization to small-molecule protein-protein interaction inhibitors targeting acute myeloid leukemia. *J Chem Inf Model* **53**, 2197-2202, doi:10.1021/ci400332e (2013).

26   Ciglia, E. *et al.* Resolving hot spots in the C-terminal dimerization domain that determine the stability of the molecular chaperone Hsp90. *PloS one* **9**, e96031, doi:10.1371/journal.pone.0096031 (2014).

27   Bopp, B. *et al.* Design and biological testing of peptidic dimerization inhibitors of human Hsp90 that target the C-terminal domain. *Biochimica et biophysica acta* **1860**, 1043-1055, doi:10.1016/j.bbagen.2016.01.005 (2016).

28   Bhatia, S. *et al.* Targeting HSP90 dimerization via the C terminus is effective in imatinib-resistant CML and lacks the heat shock response. *Blood* **132**, 307-320, doi:10.1182/blood-2017-10-810986 (2018).

29   Krieger, V. *et al.* alpha-Aminoxy Peptoids: A Unique Peptoid Backbone with a Preference for cis-Amide Bonds. *Chemistry* **23**, 3699-3707, doi:10.1002/chem.201605100 (2017).

30   Spanier, L. *et al.* Design, synthesis, and conformational analysis of trispyrimidonamides as alpha-helix mimetics. *The Journal of organic chemistry* **79**, 1582-1593, doi:10.1021/jo402353z (2014).

31   Verba, K. A. *et al.* Atomic structure of Hsp90-Cdc37-Cdk4 reveals that Hsp90 traps and stabilizes an unfolded kinase. *Science* **352**, 1542-1547, doi:10.1126/science.aaf5023 (2016).

32   Marcu, M. G., Chadli, A., Bouhouche, I., Catelli, M. & Neckers, L. M. The heat shock protein 90 antagonist novobiocin interacts with a previously unrecognized ATP-binding domain in the carboxyl terminus of the chaperone. *J Biol Chem* **275**, 37181-37186, doi:DOI 10.1074/jbc.M003701200 (2000).

33   Eccles, S. A. *et al.* NVP-AUY922: A novel heat shock protein 90 inhibitor active against xenograft tumor growth, angiogenesis, and metastasis. *Cancer research* **68**, 2850-2860, doi:10.1158/0008-5472.Can-07-5256 (2008).

34   Yin, Z. Y., Henry, E. C. & Gasiewicz, T. A. (-)-Epigallocatechin-3-gallate Is a Novel Hsp90 Inhibitor. *Biochemistry-Us* **48**, 336-345, doi:10.1021/bi801637q (2009).

35   Lundgren, K. *et al.* BIIB021, an orally available, fully synthetic small-molecule inhibitor of the heat shock protein Hsp90. *Mol Cancer Ther* **8**, 921-929, doi:10.1158/1535-7163.MCT-08-0758 (2009).

36   Pacey, S. *et al.* A Phase II trial of 17-allylamino, 17-demethoxygeldanamycin (17-AAG, tanespimycin) in patients with metastatic melanoma. *Invest New Drugs* **30**, 341-349, doi:10.1007/s10637-010-9493-4 (2012).

37   Jose, J. & von Schwichow, S. Autodisplay of active sorbitol dehydrogenase (SDH) yields a whole cell biocatalyst for the synthesis of rare sugars. *Chembiochem* **5**, 491-499, doi:10.1002/cbic.200300774 (2004).

38   Bhatia, S. *et al.* Control of AC133/CD133 and impact on human hematopoietic progenitor cells through nucleolin. *Leukemia* **29**, 2208-2220, doi:10.1038/leu.2015.146 (2015).

39   Wang, L. *et al.* Discovery and Optimization of Small Molecules Targeting the Protein-Protein Interaction of Heat Shock Protein 90 (Hsp90) and Cell Division Cycle 37 as Orally Active Inhibitors for the Treatment of Colorectal Cancer. *Journal of medicinal chemistry* **63**, 1281-1297, doi:10.1021/acs.jmedchem.9b01659 (2020).

40   Liang, C. *et al.* Design and synthesis of N-(5-chloro-2,4-dihydroxybenzoyl)-(R)-1,2,3,4-tetrahydroisoquinoline-3-carboxamid es as novel Hsp90 inhibitors. *European journal of medicinal chemistry* **121**, 272-282, doi:10.1016/j.ejmech.2016.05.033 (2016).

41   Jafari, R. *et al.* The cellular thermal shift assay for evaluating drug target interactions in cells. *Nat Protoc* **9**, 2100-2122, doi:10.1038/nprot.2014.138 (2014).

42   Goode, K. M. *et al.* Targeting the Hsp90 C-terminal domain to induce allosteric inhibition and selective client downregulation. *Biochimica et biophysica acta. General subjects* **1861**, 1992-2006, doi:10.1016/j.bbagen.2017.05.006 (2017).

43   McConnell, J. R., Alexander, L. A. & McAlpine, S. R. A heat shock protein 90 inhibitor that modulates the immunophilins and regulates hormone receptors without inducing the heat shock response. *Bioorg Med Chem Lett* **24**, 661-666, doi:10.1016/j.bmcl.2013.11.059 (2014).

44   Galam, L. *et al.* High-throughput assay for the identification of Hsp90 inhibitors based on Hsp90-dependent refolding of firefly luciferase. *Bioorganic & medicinal chemistry* **15**, 1939-1946, doi:10.1016/j.bmc.2007.01.004 (2007).

45   Allan, R. K., Mok, D., Ward, B. K. & Ratajczak, T. Modulation of chaperone function and cochaperone interaction by novobiocin in the C-terminal domain of Hsp90: evidence that coumarin antibiotics disrupt Hsp90 dimerization. *J Biol Chem* **281**, 7161-7171, doi:10.1074/jbc.M512406200 (2006).

46   AMBER 2018 (University of California, San Francisco, 2018).

47   James, A. M. *et al.* ff14SB: Improving the accuracy of protein side chain and backbone parameters from ff99SB. *Journal of Chemical Theory and Computation* **11**, 3696-3713 (2015).

48   Wang, J., Wolf, R. M., Caldwell, J. W., Kollman, P. A. & Case, D. A. Development and testing of a general amber force field. *J Comput Chem* **25**, 1157-1174, doi:10.1002/jcc.20035 (2004).

49   Sun, H. Y. *et al.* Assessing the performance of MM/PBSA and MM/GBSA methods. 7. Entropy effects on the performance of end-point binding free energy calculation approaches. *Phys Chem Chem Phys* **20**, 14450-14460, doi:10.1039/c7cp07623a (2018).

50   Gohlke, H. & Case, D. A. Converging free energy estimates: MM-PB(GB)SA studies on the protein-protein complex Ras-Raf. *Journal of Computational Chemistry* **25**, 238-250, doi:10.1002/jcc.10379 (2004).

51   Pearl, L. H. & Prodromou, C. Structure and mechanism of the Hsp90 molecular chaperone machinery. *Annual review of biochemistry* **75**, 271-294, doi:10.1146/annurev.biochem.75.103004.142738 (2006).

52   Wayne, N. & Bolon, D. N. Dimerization of Hsp90 is required for in vivo function. Design and analysis of monomers and dimers. *J Biol Chem* **282**, 35386-35395, doi:10.1074/jbc.M703844200 (2007).

53   Pernot, P. *et al.* New beamline dedicated to solution scattering from biological macromolecules at the ESRF. *Journal of Physics: Conference Series* **247**, 012009 (2010).

54   Pernot, P. *et al.* Upgraded ESRF BM29 beamline for SAXS on macromolecules in solution. *J Synchrotron Radiat* **20**, 660-664, doi:10.1107/S0909049513010431 (2013).

55   Panjkovich, A. & Svergun, D. I. CHROMIXS: automatic and interactive analysis of chromatography-coupled small angle X-ray scattering data. *Bioinformatics*, doi:10.1093/bioinformatics/btx846 (2017).

56   Konarev, P. V., Volkov, V. V., Sokolova, A. V., Koch, M. H. J. & Svergun, D. I. PRIMUS: a Windows PC-based system for small-angle scattering data analysis. *J Appl Crystallogr* **36**, 1277-1282, doi:10.1107/S0021889803012779 (2003).

57   Franke, D. & Svergun, D. I. DAMMIF, a program for rapid ab-initio shape determination in small-angle scattering. *J Appl Crystallogr* **42**, 342-346, doi:10.1107/S0021889809000338 (2009).

58   Guinier, A. Diffraction of x-rays of very small angles-application to the study of ultramicroscopic phenomenon. *Annales de Physique* **12**, 161-237 (1939).

59   Svergun, D., Barberato, C. & Koch, M. H. J. CRYSOL - A program to evaluate x-ray solution scattering of biological macromolecules from atomic coordinates. *J Appl Crystallogr* **28**, 768-773, doi:Doi 10.1107/S0021889895007047 (1995).

60   Mahalingam, D. *et al.* Targeting HSP90 for cancer therapy. *British journal of cancer* **100**, 1523-1529, doi:10.1038/sj.bjc.6605066 (2009).

61   Khajapeer, K. V. & Baskaran, R. Hsp90 Inhibitors for the Treatment of Chronic Myeloid Leukemia. *Leukemia research and treatment* **2015**, 757694, doi:10.1155/2015/757694 (2015).

62   Lazenby, M., Hills, R., Burnett, A. K. & Zabkiewicz, J. The HSP90 inhibitor ganetespib: A potential effective agent for Acute Myeloid Leukemia in combination with cytarabine. *Leukemia research* **39**, 617-624, doi:10.1016/j.leukres.2015.03.016 (2015).

63   Miyata, Y., Nakamoto, H. & Neckers, L. The therapeutic target Hsp90 and cancer hallmarks. *Current pharmaceutical design* **19**, 347-365 (2013).

64   Lu, X., Xiao, L., Wang, L. & Ruden, D. M. Hsp90 inhibitors and drug resistance in cancer: the potential benefits of combination therapies of Hsp90 inhibitors and other anti-cancer drugs. *Biochemical pharmacology* **83**, 995-1004, doi:10.1016/j.bcp.2011.11.011 (2012).

65   Morishima, T. *et al.* LMO2 activation by deacetylation is indispensable for hematopoiesis and T-ALL leukemogenesis. *Blood* **134**, 1159-1175, doi:10.1182/blood.2019000095 (2019).

66   Schultz, K. R. *et al.* Improved early event-free survival with imatinib in Philadelphia chromosome-positive acute lymphoblastic leukemia: a children's oncology group study. *Journal of clinical oncology : official journal of the American Society of Clinical Oncology* **27**, 5175-5181, doi:10.1200/JCO.2008.21.2514 (2009).

67   Gibbons, D. L. *et al.* Molecular dynamics reveal BCR-ABL1 polymutants as a unique mechanism of resistance to PAN-BCR-ABL1 kinase inhibitor therapy. *Proceedings of the National Academy of Sciences of the United States of America* **111**, 3550-3555, doi:10.1073/pnas.1321173111 (2014).

68   Ariad suspends ponatinib sales. *Cancer discovery* **4**, 6-7, doi:10.1158/2159-8290.CD-NB2013-163 (2014).

69   Blagosklonny, M. V., Toretsky, J. & Neckers, L. Geldanamycin selectively destabilizes and conformationally alters mutated p53. *Oncogene* **11**, 933-939 (1995).

70   Chavany, C. *et al.* p185erbB2 binds to GRP94 in vivo. Dissociation of the p185erbB2/GRP94 heterocomplex by benzoquinone ansamycins precedes depletion of p185erbB2. *J Biol Chem* **271**, 4974-4977 (1996).

71   Stepanova, L., Leng, X., Parker, S. B. & Harper, J. W. Mammalian p50Cdc37 is a protein kinase-targeting subunit of Hsp90 that binds and stabilizes Cdk4. *Genes & development* **10**, 1491-1502 (1996).

72   Soti, C., Racz, A. & Csermely, P. A Nucleotide-dependent molecular switch controls ATP binding at the C-terminal domain of Hsp90. N-terminal nucleotide binding unmasks a C-terminal binding pocket. *J Biol Chem* **277**, 7066-7075, doi:10.1074/jbc.M105568200 (2002).

73   Frieg, B., Gremer, L., Heise, H., Willbold, D. & Gohlke, H. Binding modes of thioflavin T and Congo red to the fibril structure of amyloid-beta(1-42). *Chemical communications* **56**, 7589-7592, doi:10.1039/d0cc01161d (2020).

74   Milic, D. *et al.* Recognition motif and mechanism of ripening inhibitory peptides in plant hormone receptor ETR1. *Sci Rep* **8**, 3890, doi:10.1038/s41598-018-21952-3 (2018).

75   Gohlke, H. *et al.* Binding region of alanopine dehydrogenase predicted by unbiased molecular dynamics simulations of ligand diffusion. *J Chem Inf Model* **53**, 2493-2498, doi:10.1021/ci400370y (2013).

76   Fontana, J. *et al.* Domain mapping studies reveal that the M domain of hsp90 serves as a molecular scaffold to regulate Akt-dependent phosphorylation of endothelial nitric oxide synthase and NO release. *Circ Res* **90**, 866-873, doi:10.1161/01.res.0000016837.26733.be (2002).

77   Seidel, S. A. *et al.* Microscale thermophoresis quantifies biomolecular interactions under previously challenging conditions. *Methods* **59**, 301-315, doi:10.1016/j.ymeth.2012.12.005 (2013).

78   Thulasiraman, V. & Matts, R. L. Luciferase renaturation assays of chaperones and chaperone antagonists. *Methods Mol Biol* **102**, 129-141, doi:10.1385/0-89603-520-4:129 (1998).

79   Lo, M. C. *et al.* Evaluation of fluorescence-based thermal shift assays for hit identification in drug discovery. *Anal Biochem* **332**, 153-159, doi:10.1016/j.ab.2004.04.031 (2004).

80   Schrödinger Release 2018-1: Maestro (Schrödinger, LLC, New York, NY, 2018).

81   Jorgensen, W. L., Chandrasekhar, J., Madura, J. D., Impey, R. W. & Klein, M. L. Comparison of Simple Potential Functions for Simulating Liquid Water. *J Chem Phys* **79**, 926-935, doi:Doi 10.1063/1.445869 (1983).

82   Martinez, L., Andrade, R., Birgin, E. G. & Martinez, J. M. PACKMOL: A Package for Building Initial Configurations for Molecular Dynamics Simulations. *Journal of Computational Chemistry* **30**, 2157-2164, doi:10.1002/jcc.21224 (2009).

83   Darden, T., York, D. & Pedersen, L. Particle Mesh Ewald - an N.Log(N) Method for Ewald Sums in Large Systems. *J Chem Phys* **98**, 10089-10092, doi:Doi 10.1063/1.464397 (1993).

84   Ryckaert, J. P., Ciccotti, G. & Berendsen, H. J. C. Numerical-Integration of Cartesian Equations of Motion of a System with Constraints - Molecular-Dynamics of N-Alkanes. *J Comput Phys* **23**, 327-341, doi:Doi 10.1016/0021-9991(77)90098-5 (1977).

144

85   Hopkins, C. W., Le Grand, S., Walker, R. C. & Roitberg, A. E. Long-Time-Step Molecular Dynamics through Hydrogen Mass Repartitioning. *J Chem Theory Comput* **11**, 1864-1874, doi:10.1021/ct5010406 (2015).

86   Roe, D. R. & Cheatham, T. E. PTRAJ and CPPTRAJ: Software for processing and analysis of molecular. *Dynamics Trajectory Data* **9** (2013).

87   Homeyer, N. & Gohlke, H. Free Energy Calculations by the Molecular Mechanics Poisson-Boltzmann Surface Area Method. *Mol Inform* **31**, 114-122, doi:10.1002/minf.201100135 (2012).

88   Miller, B. R., 3rd *et al.* MMPBSA.py: An Efficient Program for End-State Free Energy Calculations. *J Chem Theory Comput* **8**, 3314-3321, doi:10.1021/ct300418h (2012).

89   Onufriev, A., Bashford, D. & Case, D. A. Exploring protein native states and large-scale conformational changes with a modified generalized born model. *Proteins* **55**, 383-394, doi:10.1002/prot.20033 (2004).

90   Manalastas-Cantos, K. *et al.* ATSAS 3.0: expanded functionality and new tools for small-angle scattering data analysis. *J Appl Crystallogr* **54**, doi:doi:10.1107/S1600576720013412 (2021).

91   Svergun, D. I. Determination of the Regularization Parameter in Indirect-Transform Methods Using Perceptual Criteria. *J Appl Crystallogr* **25**, 495-503, doi:Doi 10.1107/S0021889892001663 (1992).

92   Kozin, M. B. & Svergun, D. I. Automated matching of high- and low-resolution structural models. *J Appl Crystallogr* **34**, 33-41, doi:Doi 10.1107/S0021889800014126 (2001).

93   Mahon, F. X. *et al.* Selection and characterization of BCR-ABL positive cell lines with differential sensitivity to the tyrosine kinase inhibitor STI571: diverse mechanisms of resistance. *Blood* **96**, 1070-1079 (2000).

Table of Content:
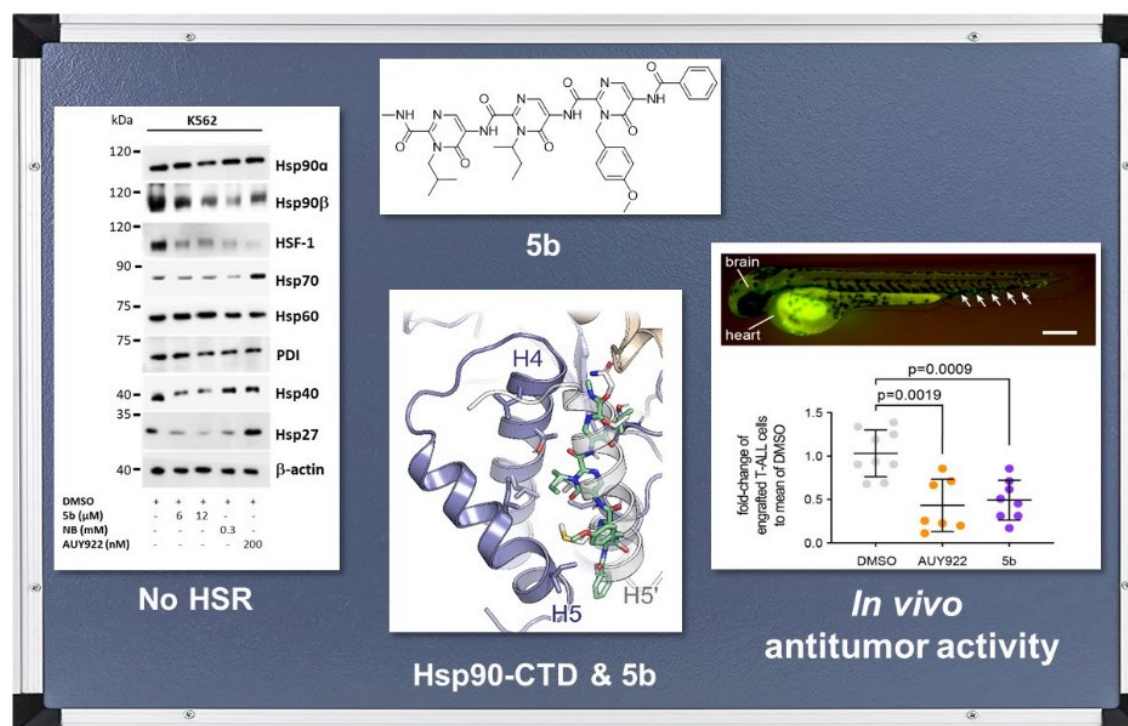
Supplementary Note 1

Sanil Bhatia[1*], Lukas Spanier[2*], David Bickel[2], Niklas Dienstbier[1], Vitalij Woloschin[2], Melina Vogt[1], Henrik Pols,[2] Beate Lungerich,[2] Jens Reiners[3], Narges Aghaallaei[4], Daniela Diedrich[2], Benedikt Frieg[2,5], Julian Schliehe-Diecks[1], Bertan Bopp[6], Franziska Lang[1], Mohan Gopalswamy[2], Jennifer Loschwitz[2], Baubak Bajohgli[4], Julia Skokowa[4], Arndt Borkhardt[1], Julia Hauer[7,8], Finn K. Hansen[9], Sander H.J. Smits[3,10], Joachim Jose[6], Holger Gohlke[2, 5#] and Thomas Kurz[2#]

Affiliations:

1. Department of Pediatric Oncology, Hematology and Clinical Immunology, Medical Faculty, Heinrich Heine University Düsseldorf, Düsseldorf, Germany

2. Institute for Pharmaceutical and Medicinal Chemistry, Heinrich Heine University Düsseldorf, Düsseldorf, Germany

3. Center for Structural Studies, Heinrich Heine University Düsseldorf, Düsseldorf, Germany

4. Department of Hematology, Oncology, Clinical Immunology and Rheumatology, University Hospital Tübingen, Germany

5. John von Neumann Institute for Computing (NIC), Jülich Supercomputing Centre (JSC), Institute of Biological Information Processing (IBI-7: Structural Biochemistry) & Institute of Bio- and Geosciences (IBG-4: Bioinformatics), Forschungszentrum Jülich GmbH, Jülich, Germany

6. Institute for Pharmaceutical and Medicinal Chemistry, PharmaCampus, Westphalian Wilhelms University, Münster, Germany

7. Department of Pediatrics, Pediatric Hematology and Oncology, University Hospital Carl Gustav Carus, Dresden, Germany

8. National Center for Tumor Diseases (NCT), Partner Site Dresden, Dresden, Germany

9. Pharmaceutical and Cell Biological Chemistry, Pharmaceutical Institute University of Bonn, Bonn, Germany

10. Institute of Biochemistry, Heinrich Heine University Düsseldorf, Düsseldorf, Germany

* contributed equally to this work

shared senior authorship

Corresponding authors: (T.K.) Universitätsstr. 1, 40225 Düsseldorf, Germany, Phone: (+49) 211 81 14984, E-mail: thomas.kurz@uni-duesseldorf.de; (H.G.) Universitätsstr. 1, 40225 Düsseldorf, Germany, Phone: (+49) 211 81 13662, E-mail: gohlke@uni-dueseldorf.de; (S.B.) Moorenstraße 5, 40225 Düsseldorf, Germany, Phone (+49) 211 81 04896 Email, sanil.bhatia@med.uni-duesseldorf.de

Author ORCID: Benedikt Frieg: 0000-0002-7877-0262; Holger Gohlke: 0000-0001-8613-1447; David Bickel: 0000-0003-0332-8338; Sanil Bhatia: 0000-0001-6494-7744; Finn K. Hansen: 0000-0001-9765-5975 Thomas Kurz: 0000-0002-9474-4224; Sander Smits 0000-0003-0780-9251; Baubak Bajoghli: 0000-0002-7368-7523; Jennifer Loschwitz: 0000-0002-9066-1923

Keywords: protein-protein interaction, heat-shock protein, CML, BCR-ABL1, imatinib, Hsp90 inhibitor.

1

Synthesis

All solvents and chemicals were used as purchased without further purification. The progress of all reactions was monitored on silica gel plates (with fluorescence indicator UV254) using the solvent system stated. Flash column chromatography was carried out using CombiFlash® 200 (Teledyne Isco) and prepacked RediSep® (NP) silica cartridges. Melting points (Mp) were taken in open capillaries and are uncorrected. [1]H and ^{13}C spectra were recorded on Avance™ DRX-500 (Bruker) ([1]H 500 MHz; [13]C 126 MHz) and Avance™ III–600 (Bruker) ([1]H 600 MHz; [13]C 151 MHz) spectrometers, respectively, using DMSO-d_6 or Chlorodorm-d as solvents. Chemical shifts are given in parts million (ppm), (δ relative to residual solvent peak for ^{1}H and ^{13}C or to external standard tetramethylsilane). Elemental analysis (CHN) was performed with a Perkin Elmer PE 2400 CHN Elemental Analyzer. Azlactone **I** was prepared as reported by MATOS et al. and crystallized from isopropyl alcohol.[1] Amidine hydrochlorides **IIa** and **IIb** were prepared following a literature procedure by MARTINU et al. with the minor modification using 0.6 equiv. of the corresponding amine hydrochloride.[2] The preparation of the pyrimidone monomers **1**, **2a**, **2b**, **2e**, dimers **3**, **4** and tripyrimidonamide **5a** was previously reported by us.[3]

*Synthesis of pyrimidone monomers **III - IV***
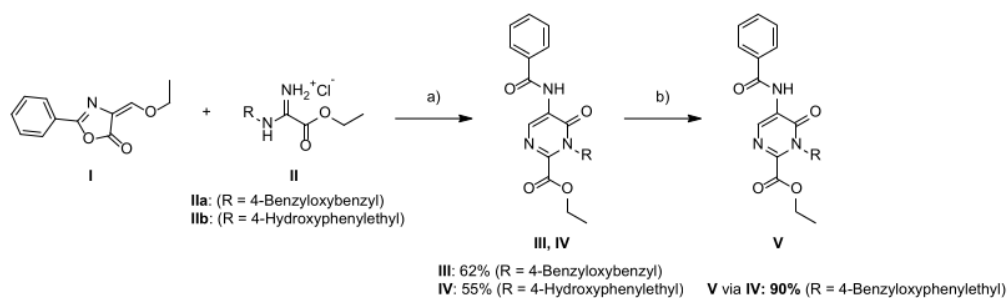
Supplementary scheme 1. Synthesis of the pyrimidones **III-V**: a) NEt$_3$, acetonitrile, reflux, 6 h; b) K$_2$CO$_3$, KI, benzyl bromide, acetonitrile, 60°C, 3h.

*General procedure for the synthesis of pyrimidone monomers **III** and **IV**.*

A mixture of 4-ethoxymethylene-2-phenyl-2-oxazolin-5-one **I** (0.217 g, 1 mmol), the respective amidine hydrochloride **IIa** or **IIb** (1 mmol) and triethylamine (0.101 g, 1 mmol) in dry acetonitrile (5 mL) was heated under a nitrogen atmosphere for 6 h. The solvent was removed under reduced pressure, and aqueous citric acid (10 wt %, 3 mL) was added. The mixture was extracted with ethyl acetate (3 × 30 mL), the combined organic layers were dried over anhydrous sodium sulfate, filtered and concentrated under vacuum. The crude products were purified by flash column chromatography (gradient: 10:90 → 30:70 ethyl acetate : n-hexane) to yield monomeres **III** and **IV**.

2

Pyrimidone monomer III

$C_{28}H_{25}N_3O_5$
483,52 g/mol
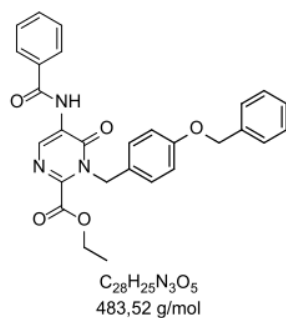
Yield: 62% (299 mg, 0.62 mmol), yellow crystalline solid.

Mp: 109 °C (dichloromethane).

¹H NMR (600 MHz, DMSO-d_6) δ 9.58 (s, 1H), 8.81 (d, J = 3.9, 1H), 8.18 – 7.85 (m, 2H), 7.71 – 7.60 (m, 1H), 7.55 (t, J = 7.7, 2H), 7.43 (d, J = 7.4, 2H), 7.38 (t, J = 7.5, 2H), 7.32 (t, J = 7.3, 1H), 7.17 (d, J = 8.7, 2H), 7.01 – 6.95 (m, 2H), 5.30 (s, 2H), 5.03 (d, J = 73.9, 2H), 4.28 (q, J = 7.1, 2H), 1.36 – 1.07 (t, 3H).

¹³C NMR (151 MHz, DMSO-d_6) δ 165.48, 160.44, 157.83, 156.77, 144.72, 136.95, 133.14, 132.35, 128.84, 128.67, 128.39, 127.79, 127.69, 127.63, 127.58, 127.56, 114.83, 69.14, 62.91, 47.52, 13.53.

CHN: Calculated [%]: C, 69.55; H, 5.21; N, 8.69 Found [%]: C, 69.60; H, 5.41; N, 8.53.
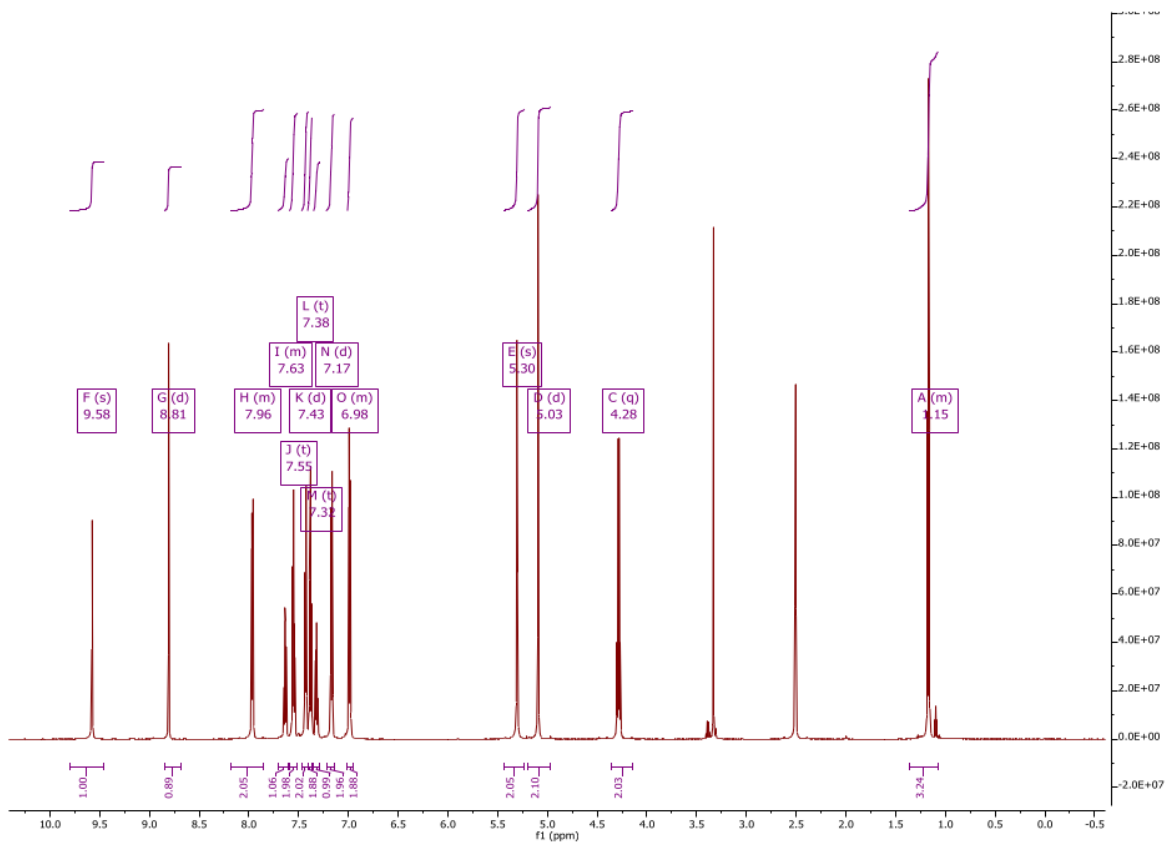
Supplementary Figure 1. ¹H-NMR (600 MHz, DMSO- d_6) of **III** at room temperature.

3
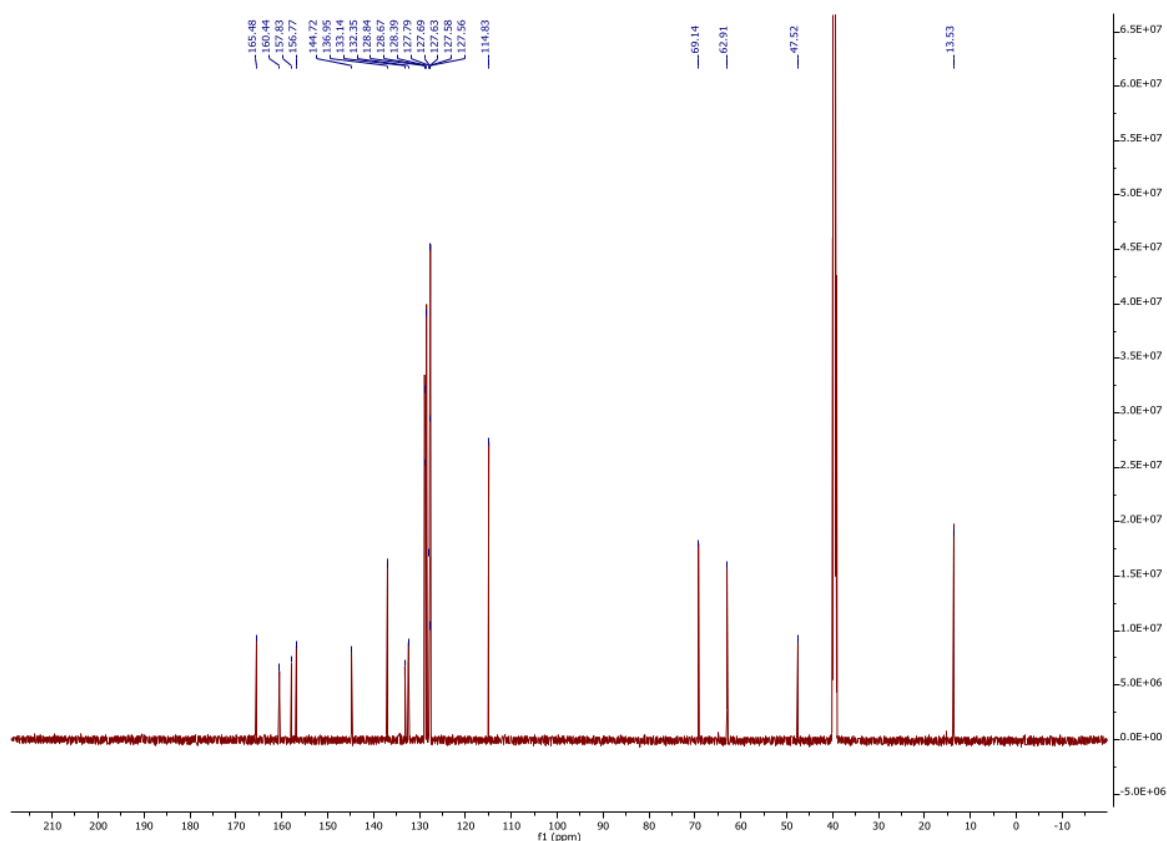
Supplementary Figure 2. ^{13}C-NMR (151 MHz, DMSO-d_6) of **III** at room temperature.

Pyrimidone monomer IV

C$_{22}$H$_{21}$N$_3$O$_5$
407,43 g/mol
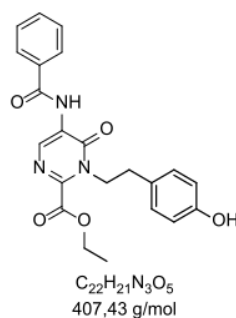
Yield: 55% (224 mg, 0.55 mmol), yellow crystalline solid.

Mp: 191 °C (dichloromethane).

^{1}H NMR (500 MHz, DMSO-d_6) δ 9.57 (s, 1H), 9.30 (s, 1H), 8.79 (s, 1H), 7.98 (d, J = 8.4, 2H), 7.65 (t, J = 7.3, 1H), 7.57 (t, J = 7.6, 2H), 6.95 (d, J = 8.3, 2H), 6.70 (d, J = 8.4, 2H), 4.35 – 4.23 (m, 5H), 3.33 (s, 1H), 2.92 – 2.84 (m, 2H), 2.54 – 2.49 (m, 2H), 1.30 (t, J = 7.1, 3H).

^{13}C NMR (126 MHz, DMSO-d_6) δ 165.39, 160.34, 156.61, 156.12, 144.14, 136.51, 133.10, 132.32, 129.56, 128.65, 127.56, 127.43, 127.28, 115.39, 62.88, 47.49, 32.92, 13.56.

CHN: Calculated [%]: C, 64.86; H, 5.20 N, 10.31 Found [%]: C 64.71; H, 5.22; N, 10.25.

4

Supplementary Figure 3. ^{1}H-NMR (500 MHz, DMSO-d$_6$) of **IV** at room temperature.

Supplementary Figure 4. ^{13}C-NMR (126 MHz, DMSO-d$_6$) of **IV** at room temperature.

5
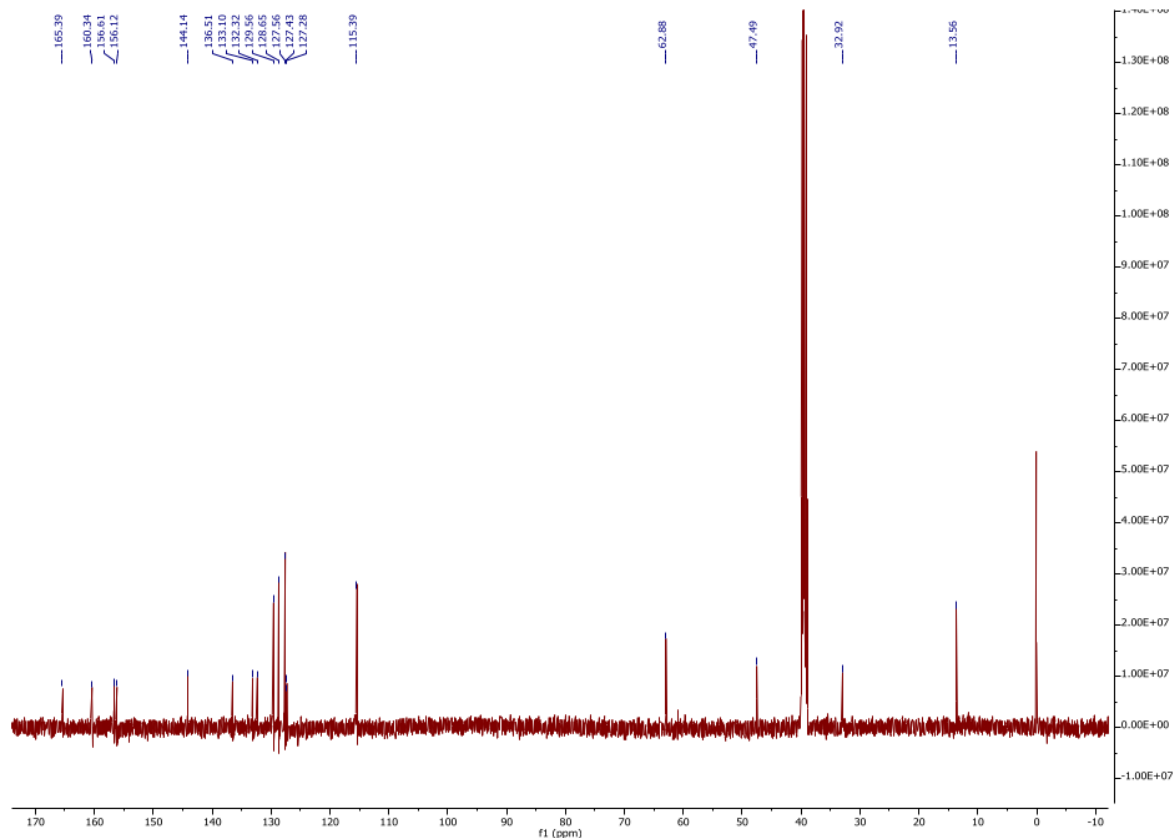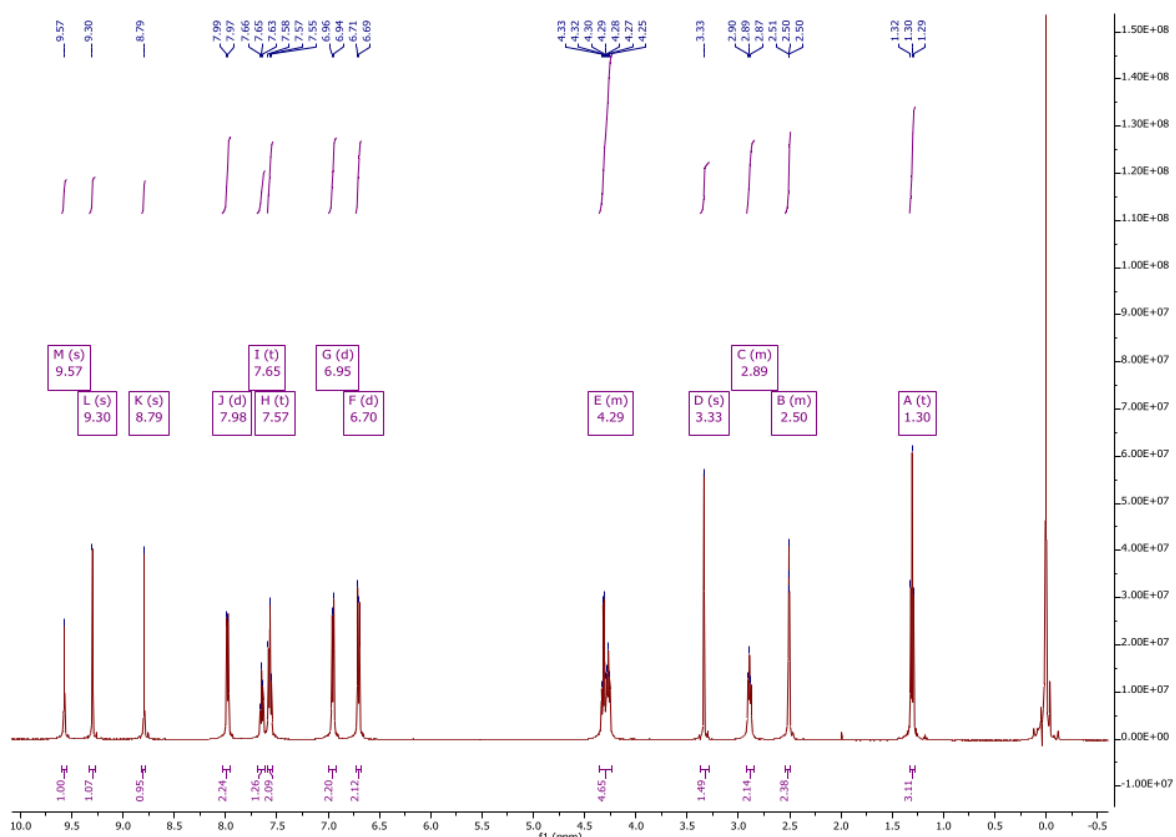
Procedure for the synthesis of pyrimidone monomer V

To a suspension of **IV** (0.407 g, 1.0 mmol), potassium carbonate (0.207 g, 1.5 mmol) and potassium iodide (0.166 g) in acetonitrile (2 mL) benzyl bromide (0.342 g, 2.0 mmol) was added dropwise under stirring. The suspension was stirred at 60 °C for 3 h under an argon atmosphere. Subsequently dichloromethane (10 mL) and water (10 mL) was added and the stirring was continued until a phase separation was observed. The organic phase was separated and dried over sodium sulfate. After filtration the solvent was removed under reduced pressure and the resulting oil was treated with diethyl ether to initiate crystallization. The solid was separated by filtration and purified by recrystallization from dichloromethane.

Pyrimidone monomer V

$C_{29}H_{27}N_3O_5$
497,55 g/mol
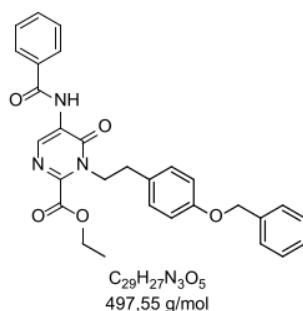
Yield: 90% (403 mg, 0.81 mmol), yellow crystalline solid.

Mp: 83 °C (dichloromethane).

^{1}H NMR (600 MHz, chloroform-*d*) δ 9.20 (s, 1H), 8.98 (s, 1H), 7.94 (m, 2H), 7.59 (d, *J* = 7.4, 1H), 7.52 (t, *J* = 7.7, 2H), 7.40 (m, 4H), 7.33 (d, *J* = 7.2, 1H), 7.13 (d, *J* = 8.6, 2H), 6.93 (m, 2H), 5.05 (s, 2H), 4.47 (m, 2H), 4.38 (q, *J* = 7.2, 2H), 3.04 (m, 2H), 1.41 (t, *J* = 7.2, 3H).

^{13}C NMR (151 MHz, chloroform-*d*) δ 165.63, 160.63, 157.90, 157.40, 142.76, 136.94, 134.73, 133.34, 132.63, 130.05, 129.49, 128.96, 128.61, 128.05, 128.01, 127.48, 127.36, 115.19, 70.02, 63.42, 47.89, 33.99, 13.96.

CHN: Calculated [%]: C, 70.01; H, 5.47; N, 8.45 Found [%]: C, 69.89; H, 5.44; N, 8.56.

6
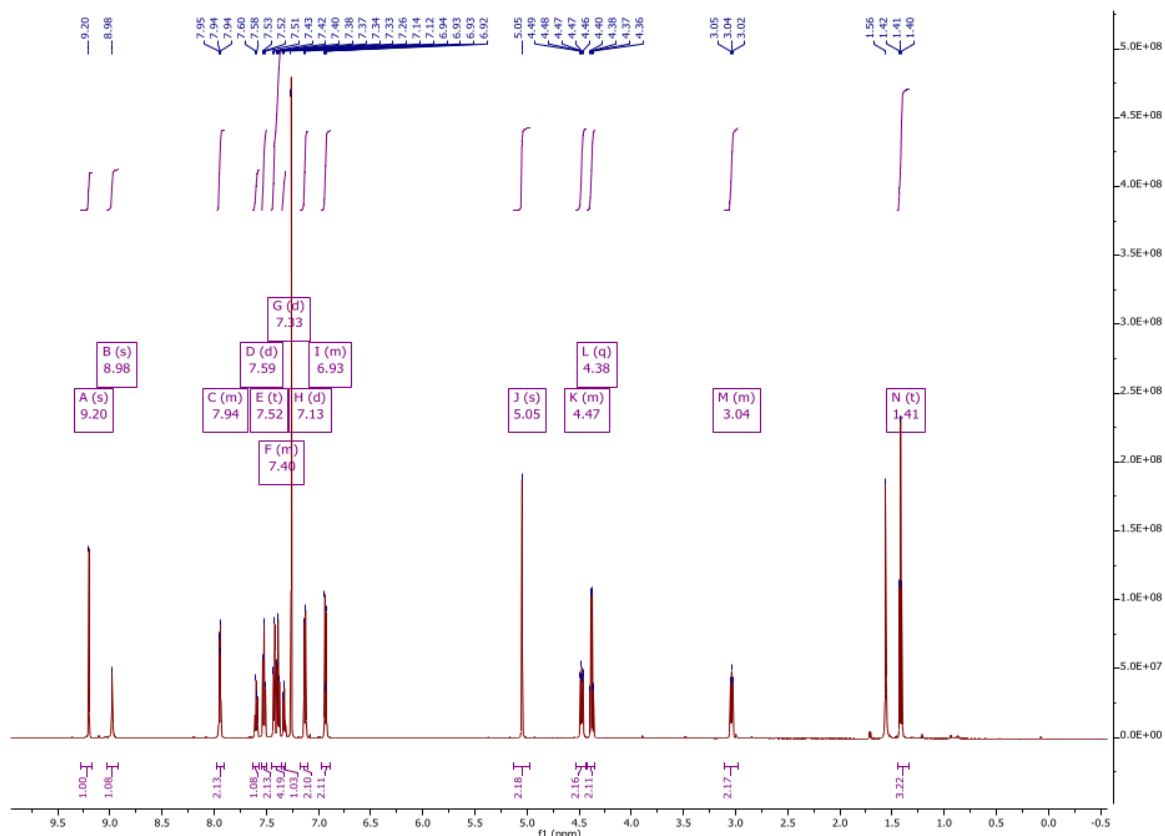
Supplementary Figure 5. ^{1}H-NMR (500 MHz, Chloroform-d) of **V** at room temperature.
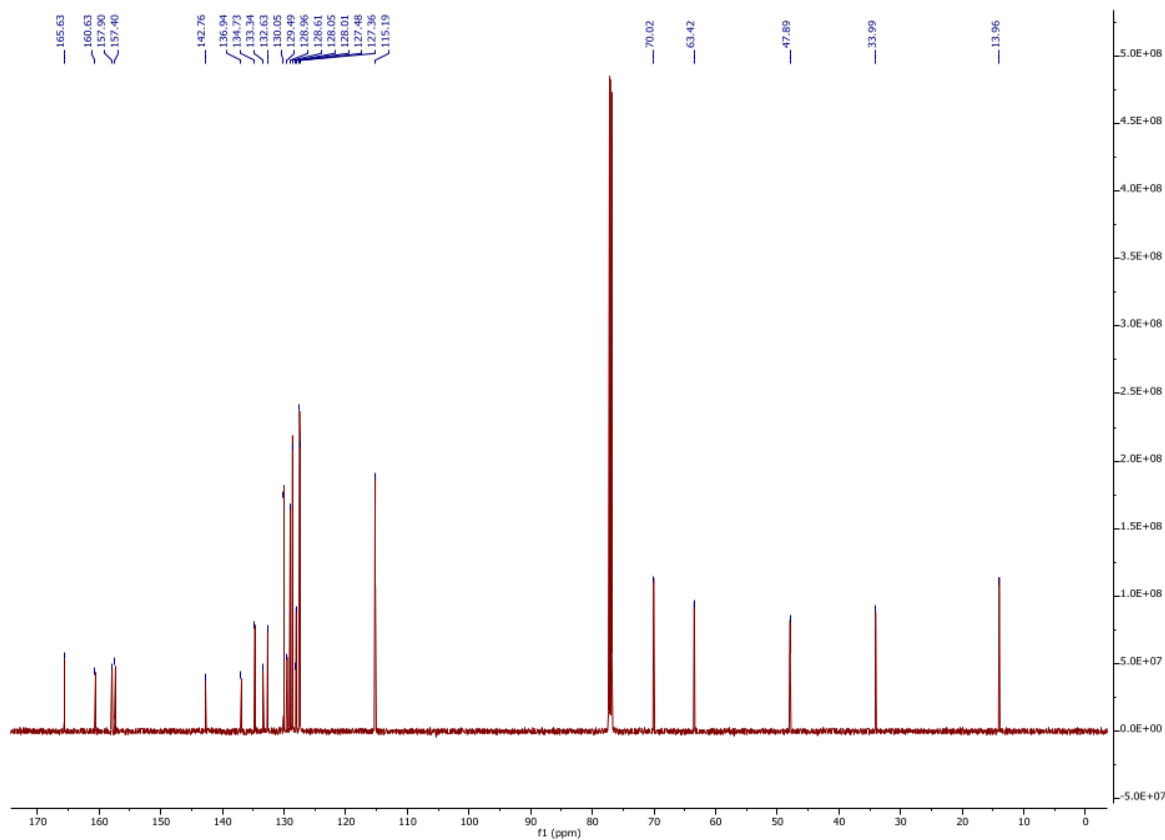
Supplementary Figure 6. ^{13}C-NMR (151 MHz, Chloroform-d) of **V** at room temperature.

7

Synthesis of dimeric pyrimidonamides (3 ,4)[3] and tripyrimidonamides (5a[3]-5d)
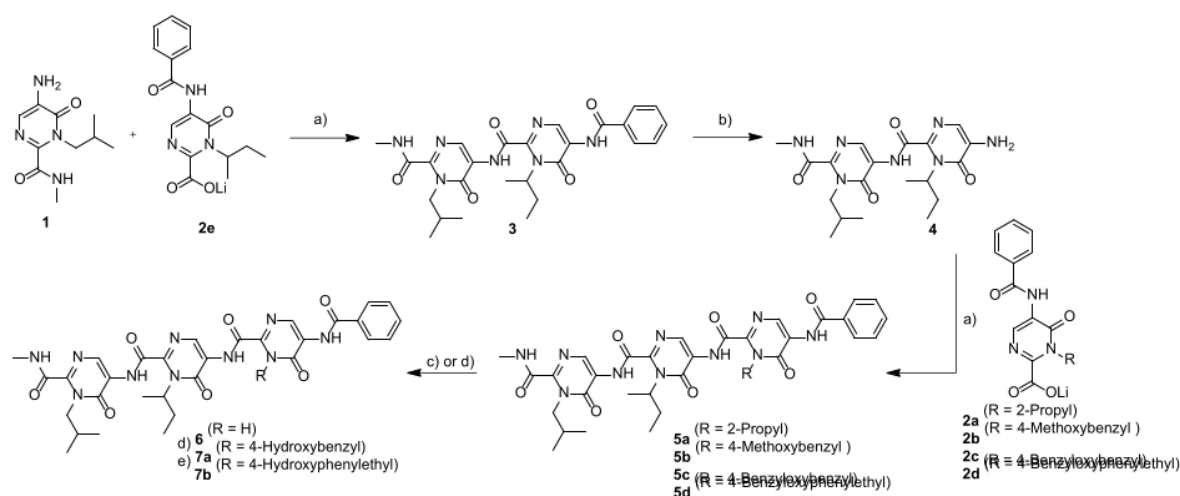
Supplementary scheme 2. Synthesis of tripyrimidon amides: a) COMU, DMF, r. t., 18 h; b) NaOH, MeOH, 80 °C, 6 h; c) via **5b**, BBr₃, DCM, -78 °C, 1 h, r. t., 1 h; d) via **5c** and **5d**, H₂, Pd(C), MeOH, DCM, r. t., 1 h.

General procedure for synthesis the dimeric 5 aminopyrimidonamide (4) [3]

A mixture of the dipyrimidonamide **3** (1 mmol, obtained from monomer **1** and lithium carboxylate **2e** according to[3]) and sodium hydroxide (0.12 g, 3 mmol) in methanol 3 mL) was heated for 6 h. The solvent was removed under reduced pressure, water (5 mL) was added, and the aqueous layer was extracted with ethyl acetate (3 × 15 mL). The combined organic layers were dried over sodium sulfate, filtered and concentrated under reduced pressure. The crude residue was purified by flash column chromatography (gradient: 30:70 → 100:0 ethyl acetate:*n*-hexane) to yield **4** (77%).

General procedure for synthesis of tripyrimidonamides (5a-5d)

The preparation tripyrimidonamide **5a** was previously reported.[3]

The appropriate ethyl 5-benzamido-6-oxo1,6-dihydropyrimidine-2-carboxylate (**III, V**, 1.5 equiv.) and lithium hydroxide hydrate (1.5 equiv) were dissolved in methanol and stirred for 12 h at room temperature. The solvent was removed under vacuum using an ice cooled water bath. The resulting yellow oil was treated with dry diethyl ether to initiate crystallisation. The precipitate was filtrated off, dried under vacuum to obtain the novel lithium carboxylates **2c, 2d**.

Next, the respective lithium carboxylate (1 mmol, **2a-2d**) was transferred into a two-neck round-bottom flask containing the dimeric 5 aminopyrimidonamide **4** (1 mmol.) and COMU (1.8 equiv.). The mixture was dissolved in dry DMF (1 mL per mmol) and stirred for 18 h under nitrogen atmosphere at ambient temperature. Dichloromethane (40 mL) was added, and the organic layer was washed with saturated sodium bicarbonate solution (10 mL), 10% aqueous citric acid solution (10 mL) and brine (10 mL). After drying over sodium sulfate the organic layer was concentrated in vacuum. The residue was crystallized by treatment with dry diethyl ether and the respective tripyrimidoneamide (**5a-5d**) recrystallized from dichloromethane or *n*-hexane/ethyl acetate 1:1, respectively.

Tripyrimidonamide 5a
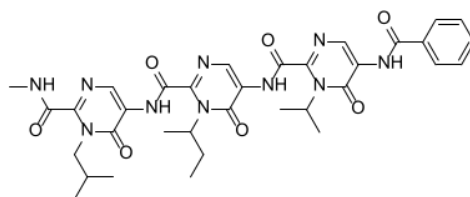
$C_{34}H_{40}N_{10}O_7$
700,76 g/mol

Yield: 65% (455 mg, 0.65 mmol), yellow crystalline solid.

Mp: 257 °C (dichloromethane).

^{1}H NMR (600 MHz, chloroform-*d*) δ 10.17 (s, 1H), 10.05 (s, 1H), 9.09 (s, 1H), 9.03 (s, 1H), 8.95 (s, 1H), 8.93 (s, 1H), 7.96 – 7.91 (m, 2H), 7.69 (q, *J* = 4.5 Hz, 1H), 7.58 (t, *J* = 7.4 Hz, 1H), 7.50 (t, *J* = 7.7 Hz, 2H), 5.49 (hept, *J* = 6.6 Hz, 1H), 5.18 (h, *J* = 6.8 Hz, 1H), 4.67 (d, *J* = 7.3 Hz, 2H), 2.98 (d, *J* = 5.1 Hz, 3H), 2.29 (dp, *J* = 7.5, 15.2 Hz, 1H), 2.10 (hept, *J* = 7.1 Hz, 1H), 1.99 (dp, *J* = 7.3, 14.5 Hz, 1H), 1.70 (d, *J* = 6.8 Hz, 9H), 0.92 (dd, *J* = 1.6, 6.7 Hz, 6H), 0.85 (t, *J* = 7.4 Hz, 3H).

^{13}C NMR (151 MHz, Chloroform-*d*) δ 165.70, 161.04, 158.93, 158.87, 158.46, 158.01, 157.89, 145.14, 144.94, 143.52, 134.44, 133.69, 133.48, 132.98, 132.71, 129.04, 129.02, 128.15, 127.48, 127.05, 60.35, 54.22, 51.15, 28.92, 26.75, 26.00, 19.94, 19.83, 17.98, 11.50.

CHN: Calculated [%]: C, 58.28; H, 5.75; N, 19.99 Found [%]: C, 58.17; H, 5.80; N, 19.85.
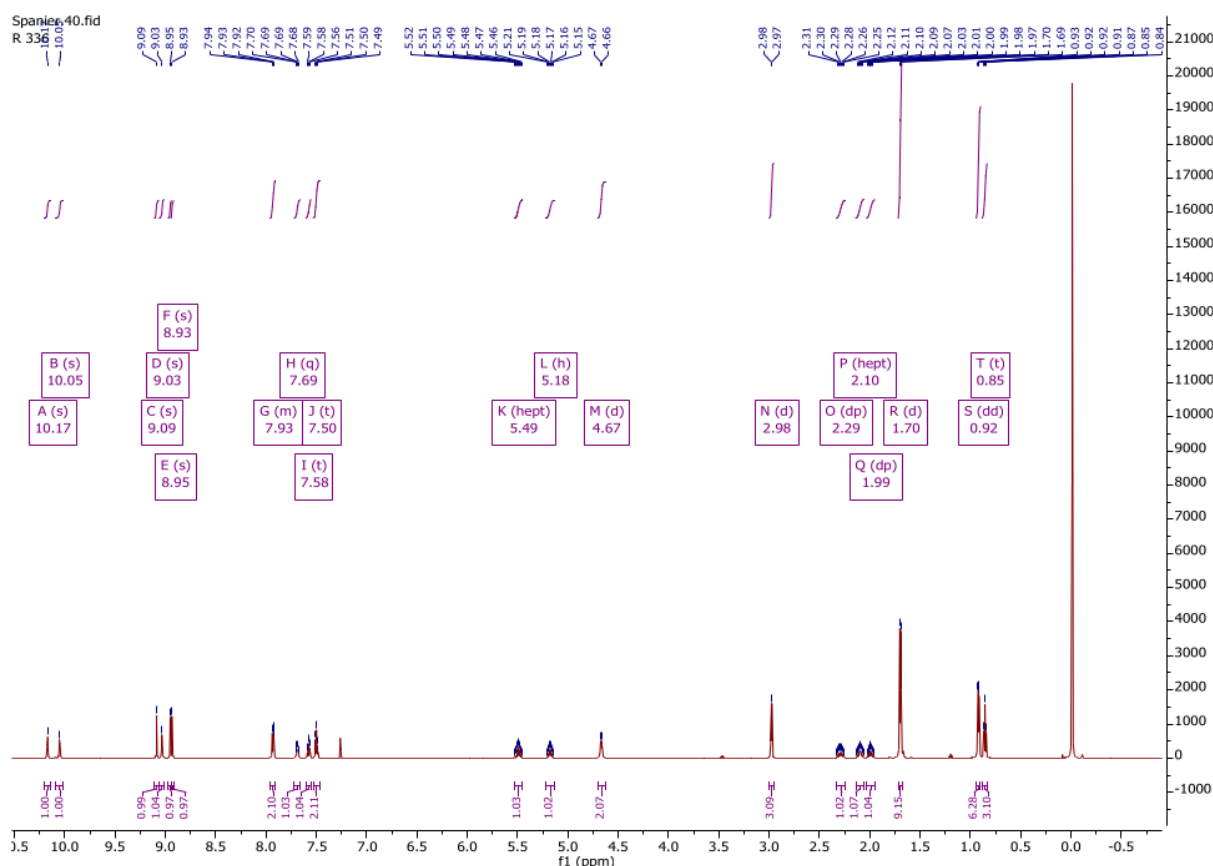

Supplementary Figure 7. ^{1}H-NMR (600 MHz, , Chloroform-d) of **5a** at room temperature.

9
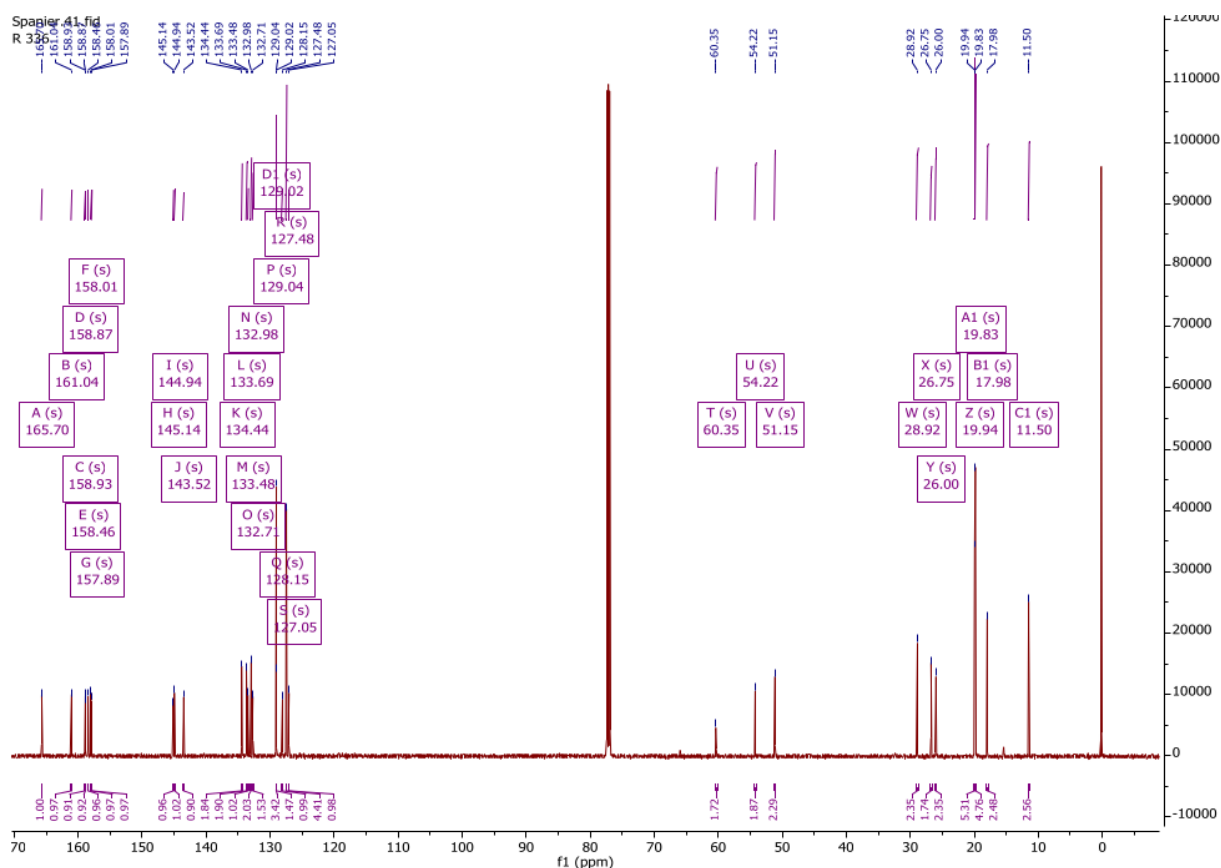
Supplementary Figure 8. ^{13}C-NMR (151 MHz, Chloroform-d) of **5a** at room temperature.

Tripyrimidonamide 5b
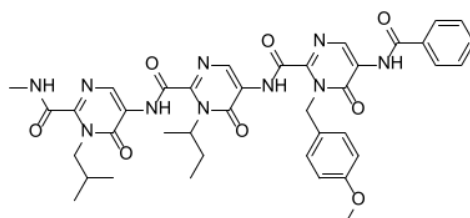
C$_{39}$H$_{42}$N$_{10}$O$_8$
778,83 g/mol

Yield: 39% (152 mg, 0.19 mmol), yellow solid.

Mp: 264 °C (dichloromethane).

^{1}H NMR (600 MHz, chloroform-d) δ 10.48 (s, 1H), 10.09 (s, 1H), 9.18 (s, 1H), 9.02 (s, 1H), 8.98 (s, 1H), 8.93 (s, 1H), 7.95 – 7.86 (m, 2H), 7.69 (d, J = 5.0 Hz, 1H), 7.58 (t, J = 7.4 Hz, 1H), 7.50 (t, J = 7.7 Hz, 2H), 7.32 (d, J = 8.8 Hz, 2H), 6.82 (d, J = 8.8 Hz, 2H), 6.00 (s, 2H), 5.28 – 5.09 (m, 1H), 4.67 (d, J = 7.4 Hz, 2H), 3.75 (s, 3H), 2.98 (d, J = 5.1 Hz, 3H), 2.37 – 2.23 (m, 1H), 2.10 (dp, J = 6.9, 13.9 Hz, 1H), 1.98 (td, J = 7.3, 14.4 Hz, 1H), 1.69 (t, J = 9.4 Hz, 3H), 0.92 (dd, J = 1.3, 6.7 Hz, 6H), 0.85 (t, J = 7.4 Hz, 3H).

^{13}C NMR (151 MHz, chloroform-d) δ 165.65, 160.93, 159.28, 158.80, 158.27, 158.23, 157.90, 157.74, 144.92, 144.80, 141.33, 134.25, 133.58, 133.41, 133.24, 132.66, 129.73, 128.94, 128.68, 128.22, 127.95, 127.38, 126.93, 114.02, 60.14, 55.23, 51.02, 47.33, 28.81, 26.62, 25.86, 19.82, 17.84, 11.36.

10

CHN: Calculated [%]: C, 60.15; H, 5.44; N, 17.98 Found [%]: C, 60.15; H, 5.42; N, 17.98.
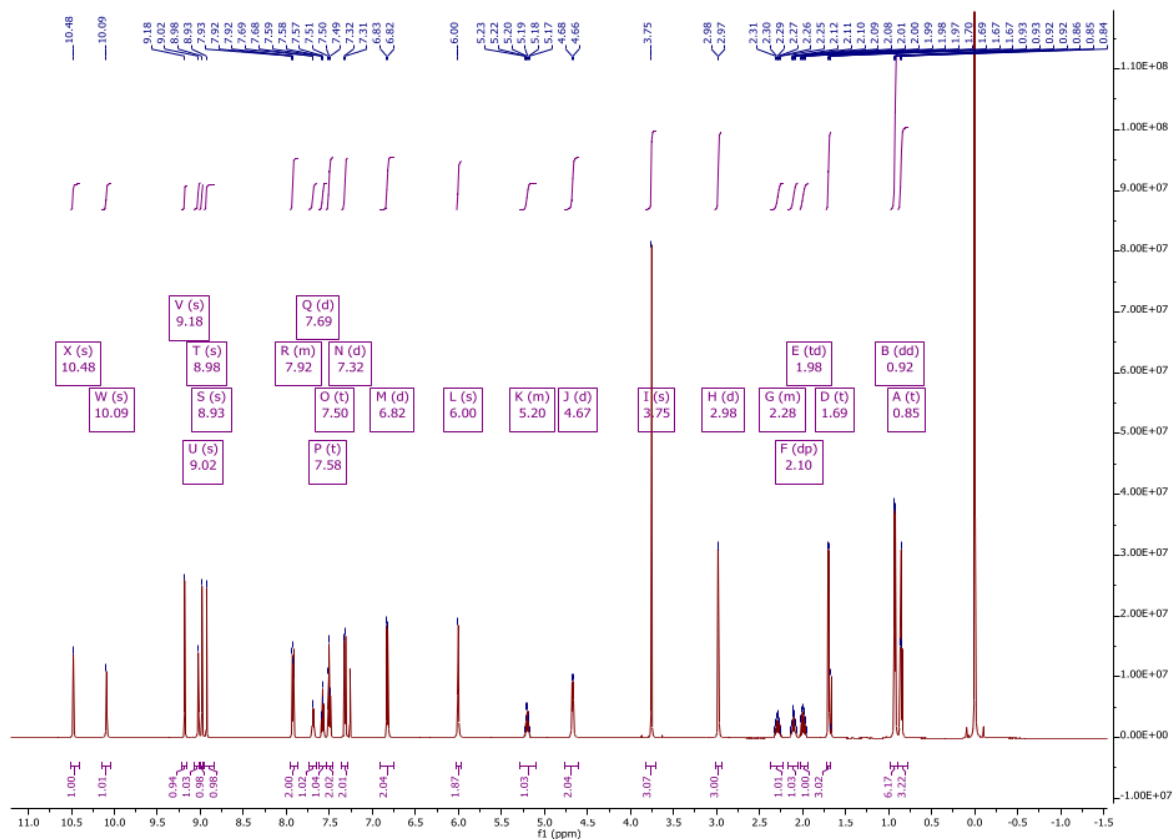
Supplementary Figure 9. ^{1}H-NMR (600 MHz, , Chloroform-d) of **5b** at room temperature.
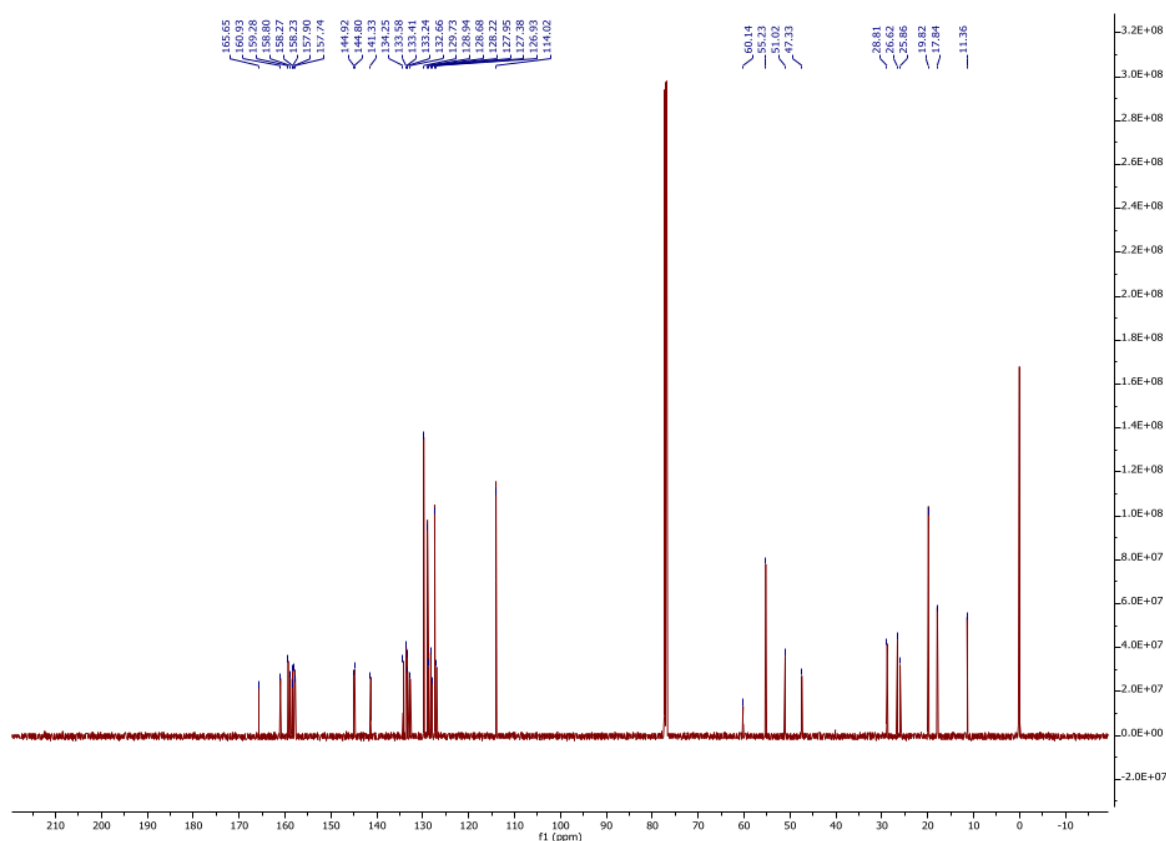
Supplementary Figure 10. ^{13}C-NMR (151 MHz, Chloroform-d) of **5b** at room temperature.

5c
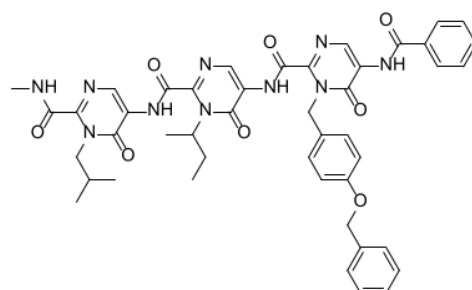
$C_{45}H_{46}N_{10}O_8$
854.93 g/mol

Yield: 71% (455 mg, 0.53 mmol), yellow solid.

Mp: 258 °C (dichloromethane).

^{1}H NMR (600 MHz, chloroform-*d*) δ 10.51 (s, 1H), 10.10 (s, 1H), 9.19 (s, 1H), 9.03 (s, 1H), 8.99 (s, 1H), 8.94 (s, 1H), 7.93 (d, *J* = 7.2 Hz, 2H), 7.67 (q, *J* = 4.2 Hz, 1H), 7.59 (t, *J* = 7.4 Hz, 1H), 7.51 (t, *J* = 7.7 Hz, 2H), 7.42 – 7.27 (m, 7H), 6.91 (d, *J* = 8.7 Hz, 2H), 6.01 (s, 2H), 5.20 (h, *J* = 6.8 Hz, 1H), 5.02 (s, 2H), 4.68 (d, *J* = 7.3 Hz, 2H), 2.98 (d, *J* = 5.1 Hz, 3H), 2.29 (dp, *J* = 7.5, 15.2 Hz, 1H), 2.16 – 2.05 (m, 1H), 2.00 (dp, *J* = 7.4, 14.5 Hz, 1H), 1.70 (d, *J* = 6.7 Hz, 3H), 0.93 (d, *J* = 6.8 Hz, 6H), 0.86 (t, *J* = 7.4 Hz, 3H).

^{13}C NMR (151 MHz, chloroform-*d*) δ 165.81, 161.05, 158.94, 158.64, 158.40, 158.38, 158.05, 157.90, 145.06, 144.91, 141.42, 136.96, 134.39, 133.75, 133.56, 133.38, 132.81, 129.88, 129.08, 128.83,

12

128.71, 128.62, 128.11, 128.09, 127.58, 127.52, 127.08, 115.08, 70.13, 60.29, 51.17, 47.49, 28.97, 26.77, 26.01, 19.96, 18.00, 11.52.

CHN: Calculated [%]: C, 63.22; H, 5.42; N, 16.38 Found [%]: C, 63.23; H, 5.50; N, 16.14.
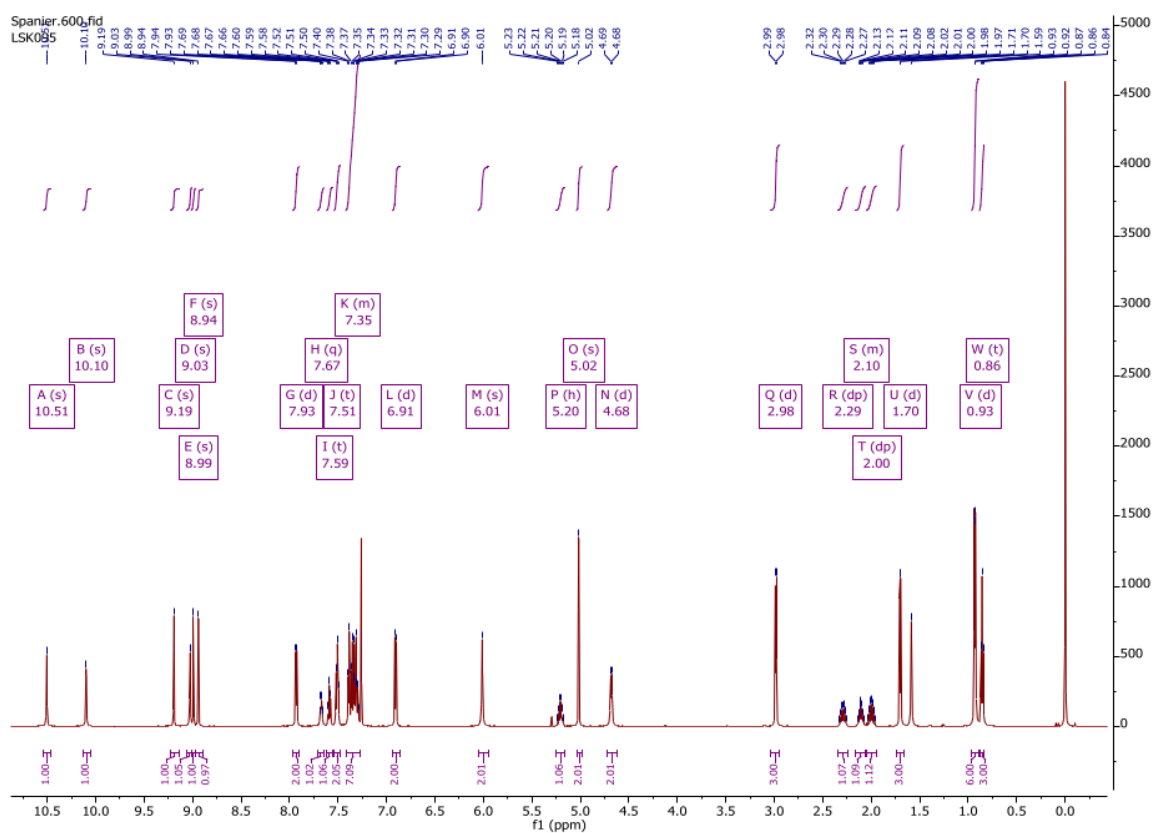
Supplementary Figure 11. ^{1}H-NMR (600 MHz, , Chloroform-d) of **5c** at room temperature.
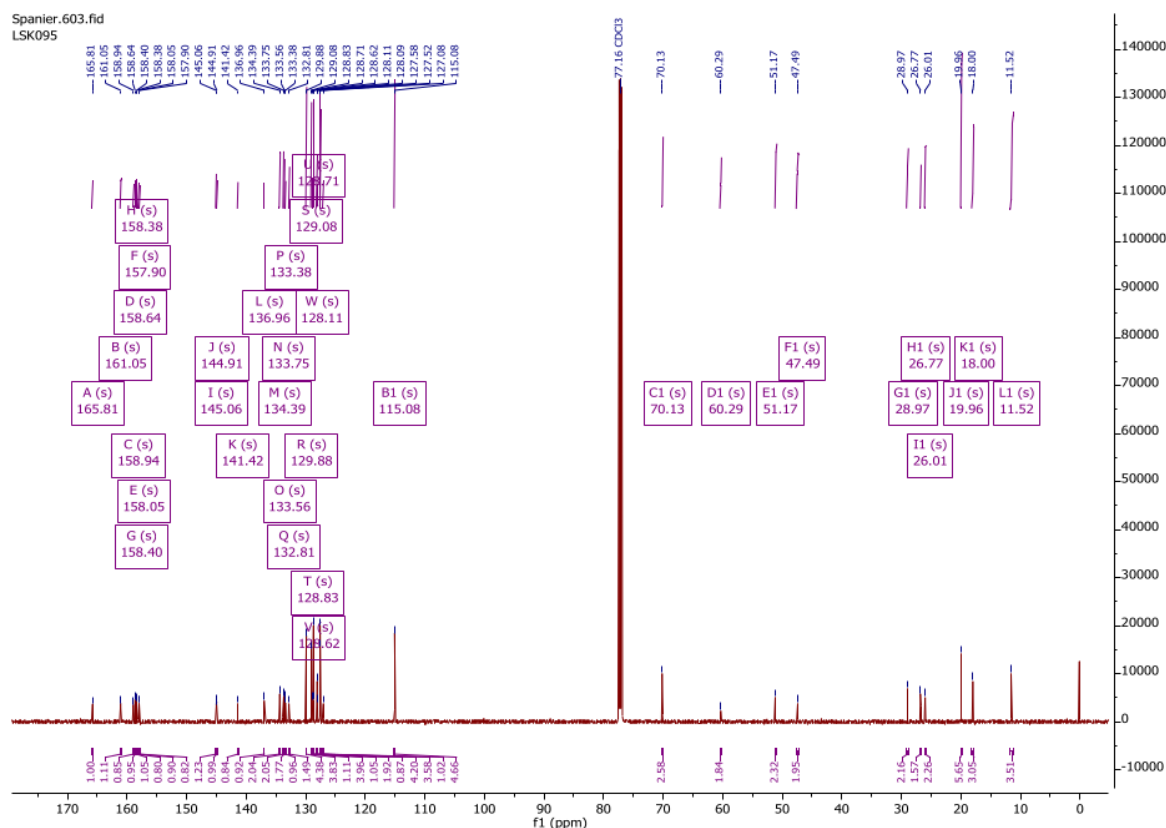
Supplementary Figure 12. ^{13}C-NMR (151 MHz, Chloroform-d) of **5c** at room temperature.

5d

$C_{46}H_{48}N_{10}O_8$
868,95 g/mol
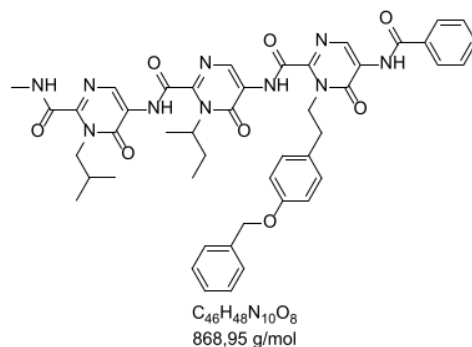
Yield: 76% (330 mg, 0.38 mmol), yellow solid.

Mp: 253 °C (dichloromethane).

^{1}H NMR (600 MHz, chloroform-d) δ 10.32 (s, 1H), 10.17 (s, 1H), 9.18 (s, 1H), 9.04 (s, 1H), 9.00 (s, 1H), 8.94 (s, 1H), 7.95 (d, J = 7.3 Hz, 2H), 7.68 (q, J = 4.7 Hz, 1H), 7.60 (t, J = 7.4 Hz, 1H), 7.52 (t, J = 7.7 Hz, 2H), 7.41 (d, J = 7.2 Hz, 2H), 7.36 (t, J = 7.5 Hz, 2H), 7.30 (t, J = 7.2 Hz, 1H), 7.22 (d, J = 8.5 Hz, 2H), 6.92 (d, J = 8.6 Hz, 2H), 5.23 (h, J = 6.8 Hz, 1H), 5.03 (s, 2H), 4.93 – 4.87 (m, 2H), 4.69 (d, J = 7.4 Hz, 2H), 3.07 – 3.03 (m, 2H), 2.99 (d, J = 5.1 Hz, 3H), 2.27 (dp, J = 7.5, 15.2 Hz, 1H), 2.12 (dp, J = 6.9, 13.9 Hz, 1H), 1.99 (dp, J = 7.4, 14.6 Hz, 1H), 1.68 (d, J = 6.7 Hz, 3H), 0.96 – 0.92 (m, 6H), 0.84 (t, J = 7.4 Hz, 3H).

^{13}C NMR (151 MHz, chloroform-d) δ 165.79, 161.05, 158.89, 158.22, 158.08, 158.05, 157.95, 157.83, 144.90, 144.88, 141.85, 137.17, 134.32, 133.63, 133.61, 133.41, 132.81, 130.40, 129.92, 129.10,

14

128.67, 128.52, 128.08, 128.00, 127.51, 127.49, 127.08, 115.20, 70.10, 60.19, 51.18, 47.33, 34.47, 28.97, 26.77, 26.04, 19.97, 17.97, 11.50.

CHN: Calculated C, 63.58; H, 5.57; N, 16.2 Found [%]: C, 63.6; H, 5.58; N, 15.84.


Supplementary Figure 13. ^{1}H-NMR (600 MHz, , Chloroform-d) of **5d** at room temperature.

Supplementary Figure 14. ^{13}C-NMR (151 MHz, Chloroform-d) of **5d** at room temperature.

Procedure for the synthesis of 6

A solution of **5b** (85 mg, 0.109 mmol) in dry dichloromethane was cooled to -78 °C using an acetone dry ice bath under an argon atmosphere. Subsequently a 1 M BBr$_3$ solution in dichloromethane (0.218 mmol, 0.22 ml) was added dropwise to the solution of **5b**. The reaction mixture was stirred at -78 °C for 1 h. After warming to r. t. the stirring was continued for 1 h. The reaction was quenched by adding water (2 ml). After phase seperation the aqueous layer was extracted using dichloromethane (2 x 10 ml) and the combined organic layers were dried over sodium sulfate. After filtration, the solvent was removed under reduced pressure and the resulting solid was recrystallized from dichloromethane to yield the expected tripyrimidonamide.

Tripyrimidonamide 6

$C_{31}H_{34}N_{10}O_7$
658,68 g/mol

16
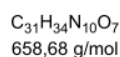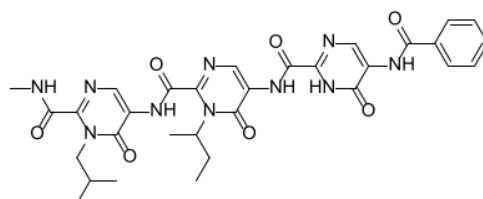
Yield: 65% (30 mg, 0.046 mmol), yellow crystalline solid.

Mp: 253 °C (dichloromethane).

^{1}H NMR (600 MHz, DMSO-d_6/TFA-d) δ 10.73 (s, 1H), 10.19 (s, 1H), 9.46 (s, 1H), 8.89 (s, 1H), 8.83 (s, 1H), 8.80 (s, 1H), 7.96 (d, J = 7.0 Hz, 2H), 7.63 (t, J = 7.4 Hz, 1H), 7.55 (t, J = 7.6 Hz, 2H), 4.35 (dd, J = 7.4, 11.7 Hz, 1H), 4.15 (d, J = 7.4 Hz, 2H), 2.19 (tt, J = 7.7, 15.4 Hz, 1H), 2.02 (dt, J = 6.7, 13.7 Hz, 1H), 1.91 (tt, J = 8.1, 15.0 Hz, 1H), 1.57 (d, J = 6.7 Hz, 3H), 0.85 – 0.79 (m, 9H).

^{13}C NMR (151 MHz, DMSO-d_6/TFA-d) δ 152.46, 146.24, 138.13, 133.02, 131.03, 58.37, 32.11, 30.02, 29.40, 22.01, 19.75, 13.24.

CHN: Calculated [%]: C, 56.53; H, 5.20; N, 21.27 Found [%]: C, 56.28; H, 5.19; N, 21.06.
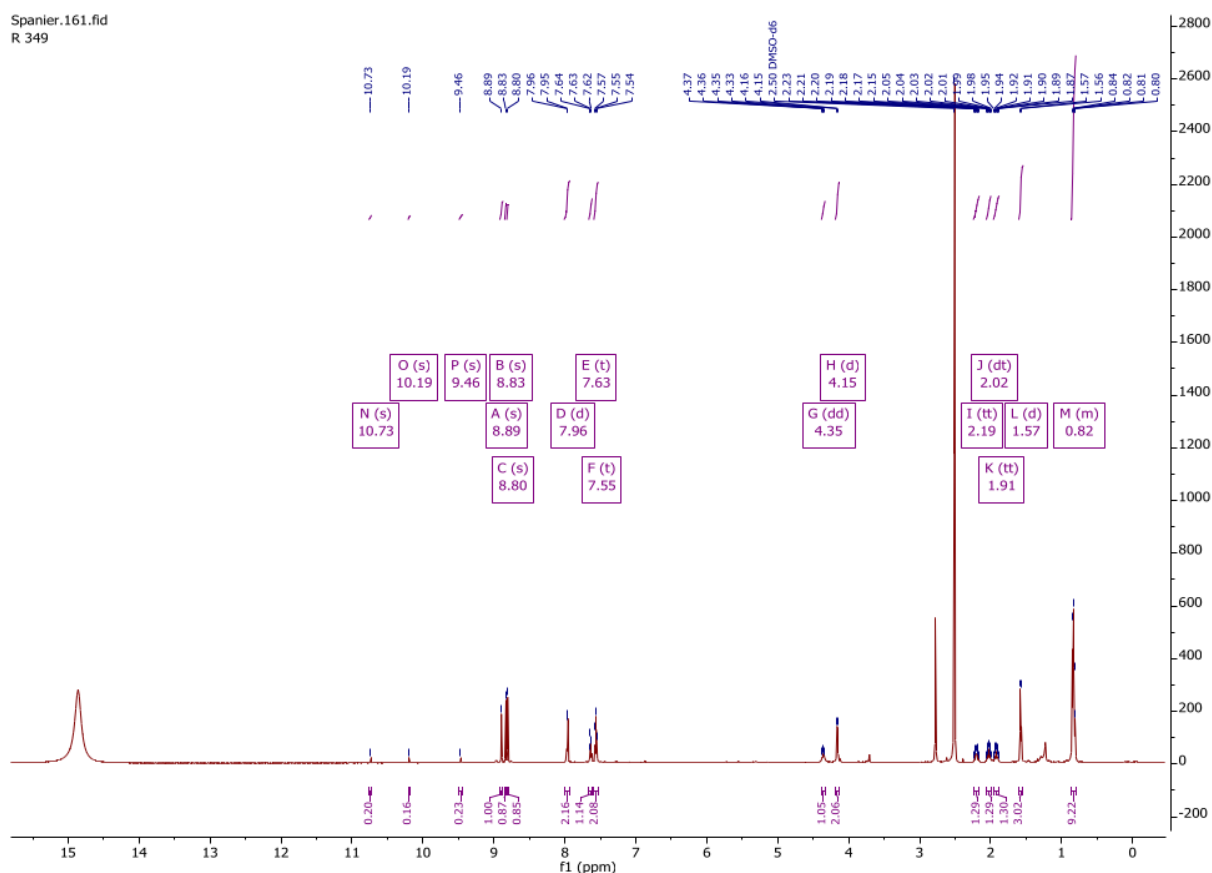
Supplementary Figure 15. ^{1}H-NMR (600 MHz, DMSO-d$_6$/TFA-d) of **6**[1] at room temperature.

---

[1] Amide protons display weak signals at 9,46 ppm, 10,19 ppm and 10,73 ppm due to a hydrogen deuterium exchange between **6** and TFA-d.

17
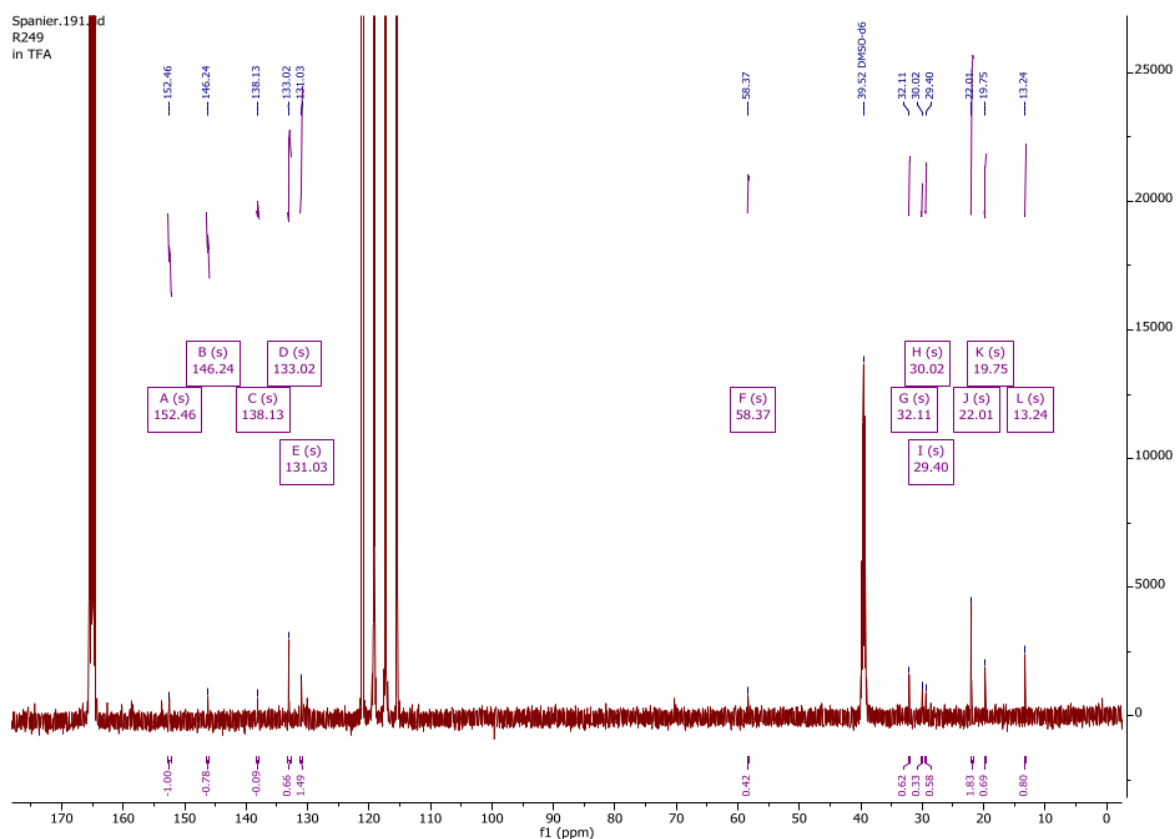
Supplementary Figure 16. ^{13}C-NMR (151 MHz, DMSO-d$_6$/TFA-d) of **6**[2] at room temperature.

General procedure for the synthesis of 7a and 7b

The respective benzyl protected tripyrimidonamides **5c** or **5d** (0.25 mmol) and palladium on carbon (10 mg, 10% wt. loading) were suspended in a mixture of dichloromethane and methanol 2:1 (3 ml). The reaction vessel was evacuated and backfilled with hydrogen gas three times. After stirring the reaction mixture at r.t. for 3 h the suspension was filtered through celite and the solvent was removed under reduced pressure. The respective solid (**7a, 7b**) was purified by recrystallization from dichloromethane.

Tripyrimidonamide 7a

$C_{38}H_{40}N_{10}O_8$
764,80 g/mol

---
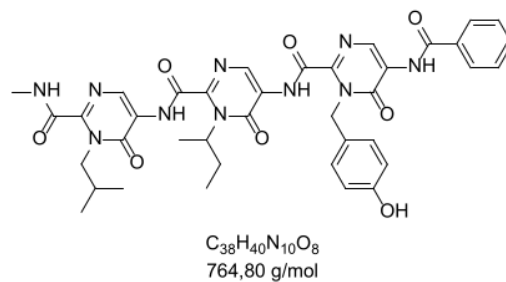
[2] Not all carbon signals were detected.

18

164

Yield: 40% (11 mg, 0.015 mmol), yellow solid.

Mp: 226 °C (dichloromethane).

¹H NMR (600 MHz, chloroform-*d*) δ 10.49 (s, 1H), 10.10 (s, 1H), 9.20 (s, 1H), 9.03 (s, 1H), 8.99 (s, 1H), 8.93 (d, *J* = 11.8 Hz, 1H), 7.94 (d, *J* = 7.4 Hz, 2H), 7.67 (d, *J* = 4.9 Hz, 1H), 7.59 (t, *J* = 7.4 Hz, 1H), 7.51 (t, *J* = 7.7 Hz, 2H), 7.28 (d, *J* = 8.6 Hz, 2H), 6.76 (d, *J* = 8.6 Hz, 2H), 6.00 (s, 2H), 5.20 (dd, *J* = 7.0, 14.5 Hz, 1H), 4.91 (s, 1H), 4.68 (d, *J* = 7.3 Hz, 2H), 2.98 (t, *J* = 6.1 Hz, 3H), 2.35 – 2.25 (m, 1H), 2.16 – 2.06 (m, 1H), 1.99 (dd, *J* = 7.1, 14.1 Hz, 1H), 1.69 (t, *J* = 9.3 Hz, 3H), 0.92 (t, *J* = 7.2 Hz, 6H), 0.84 (dt, *J* = 7.4, 15.0 Hz, 4H).

¹³C NMR (151 MHz, chloroform-*d*) δ 165.74, 160.94, 158.81, 158.26, 157.93, 157.76, 155.53, 144.93, 144.80, 141.34, 134.33, 133.63, 133.51, 132.70, 129.94, 129.74, 128.95, 128.67, 128.58, 128.22, 127.94, 127.39, 126.94, 115.51, 60.16, 51.06, 47.35, 28.82, 26.64, 25.87, 19.81, 17.84, 11.37.

CHN: Calculated [%]: C, 56.53; H, 5.20; N, 21.27 Found [%]: C, 56.28; H, 5.19; N, 21.06.
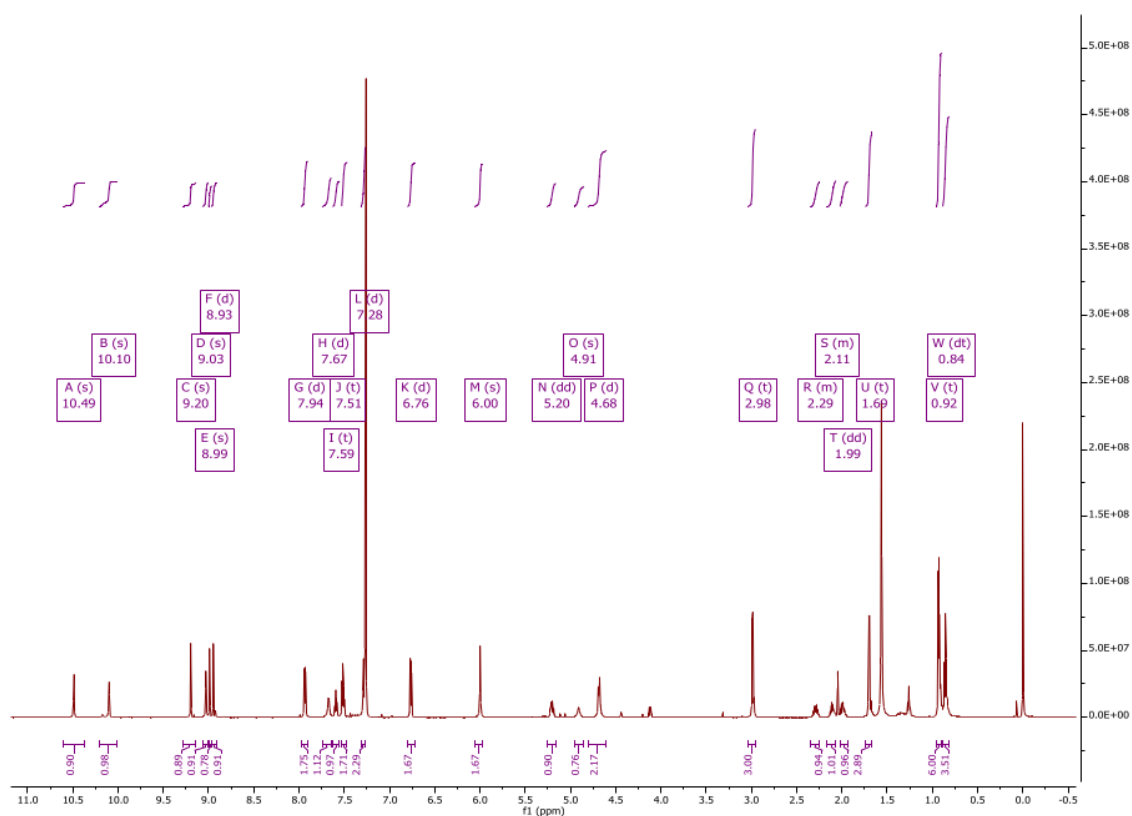

Supplementary Figure 17. ¹H-NMR (600 MHz, Chloroform-d) of **7a** at room temperature.

19
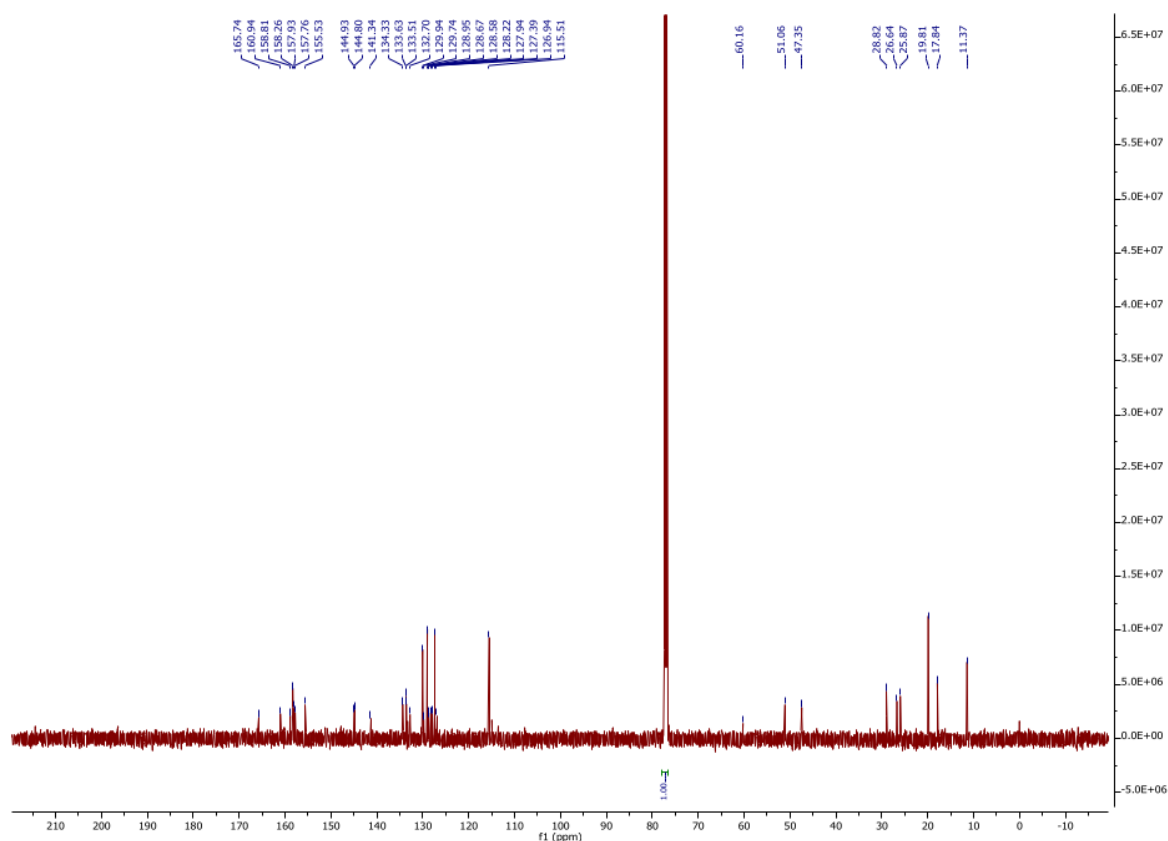
Supplementary Figure 18. ^{13}C-NMR (151 MHz, Chloroform-d) of **7a** at room temperature.
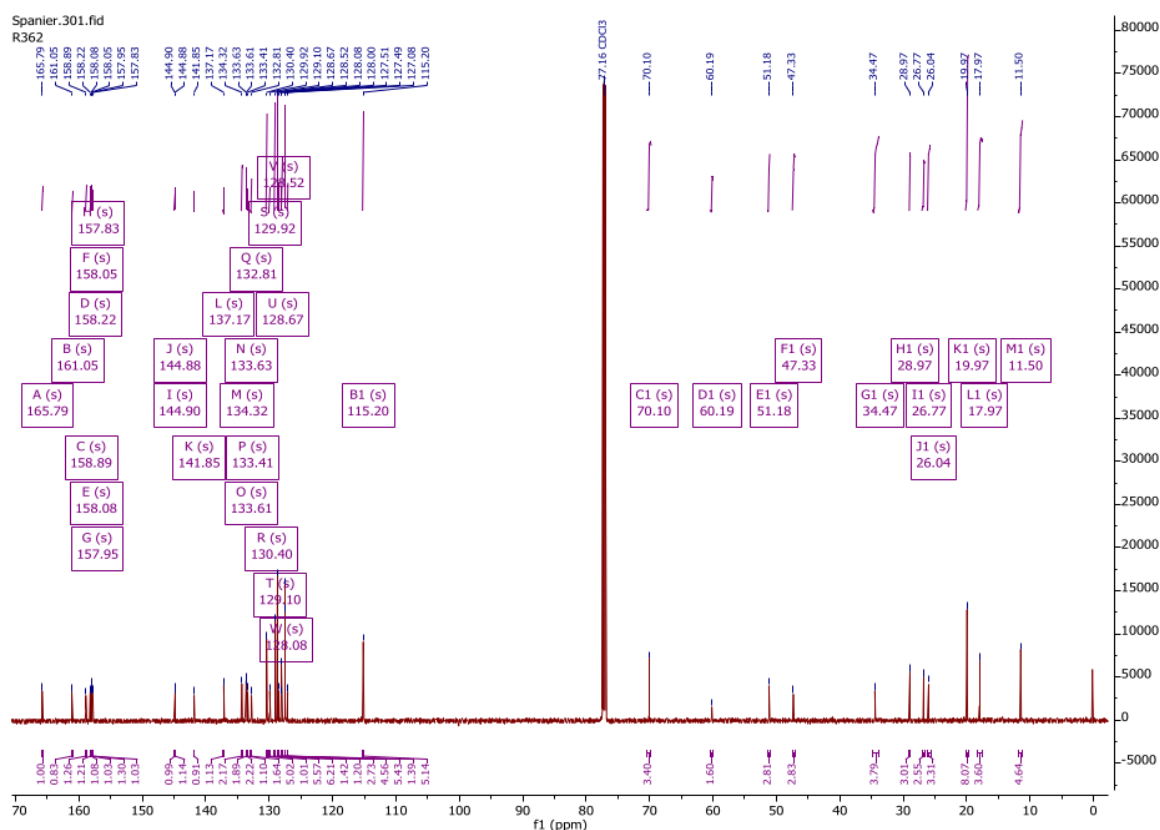
Tripyrimidoneamide 7b

C$_{39}$H$_{42}$N$_{10}$O$_8$
778,83 g/mol
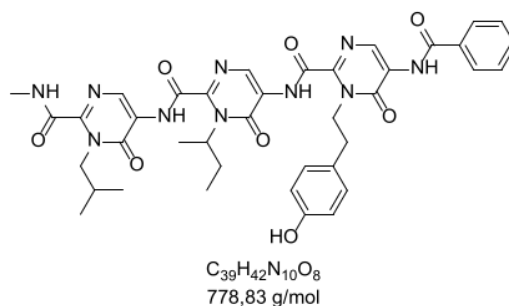
Yield: 87% (81 mg, 0.10 mmol), yellow solid.

Mp: 256 °C (dichloromethane).

^{1}H NMR (600 MHz, DMSO-d_6) δ 10.76 (s, 1H), 10.32 (s, 1H), 9.62 (s, 1H), 9.24 (s, 1H), 8.99 (q, J = 4.6 Hz, 1H), 8.86 (s, 1H), 8.81 (s, 1H), 8.79 (s, 1H), 8.00 (d, J = 7.3 Hz, 2H), 7.66 (t, J = 7.4 Hz, 1H), 7.58 (t, J = 7.6 Hz, 2H), 7.04 (d, J = 8.4 Hz, 2H), 6.69 (d, J = 8.4 Hz, 2H), 4.53 – 4.43 (m, 2H), 4.35 (d, J = 6.2 Hz, 1H), 4.16 (d, J = 7.4 Hz, 2H), 3.04 – 2.84 (m, 2H), 2.79 (d, J = 4.7 Hz, 3H), 2.27 – 2.11 (m, 1H), 2.03 (td, J = 6.9, 13.8 Hz, 1H), 1.92 (dt, J = 7.2, 14.1 Hz, 1H), 1.58 (d, J = 6.7 Hz, 3H), 0.84 (dd, J = 7.2, 16.2 Hz, 9H).

^{13}C NMR (151 MHz, DMSO) δ 165.49, 161.52, 160.41, 158.79, 157.14, 156.78, 156.60, 156.12, 148.69, 148.25, 144.96, 137.13, 136.04, 135.39, 133.16, 132.40, 129.67, 128.72, 127.73, 127.66, 127.36, 126.39, 125.81, 115.35, 50.66, 47.02, 33.41, 27.67, 25.86, 25.36, 19.71, 17.07, 11.01.

20

HCN: Calculated [%]: C, 60.15; H, 5.44; N, 17.98 Found [%]: C, 59.93; H, 5.46; N, 17.91.
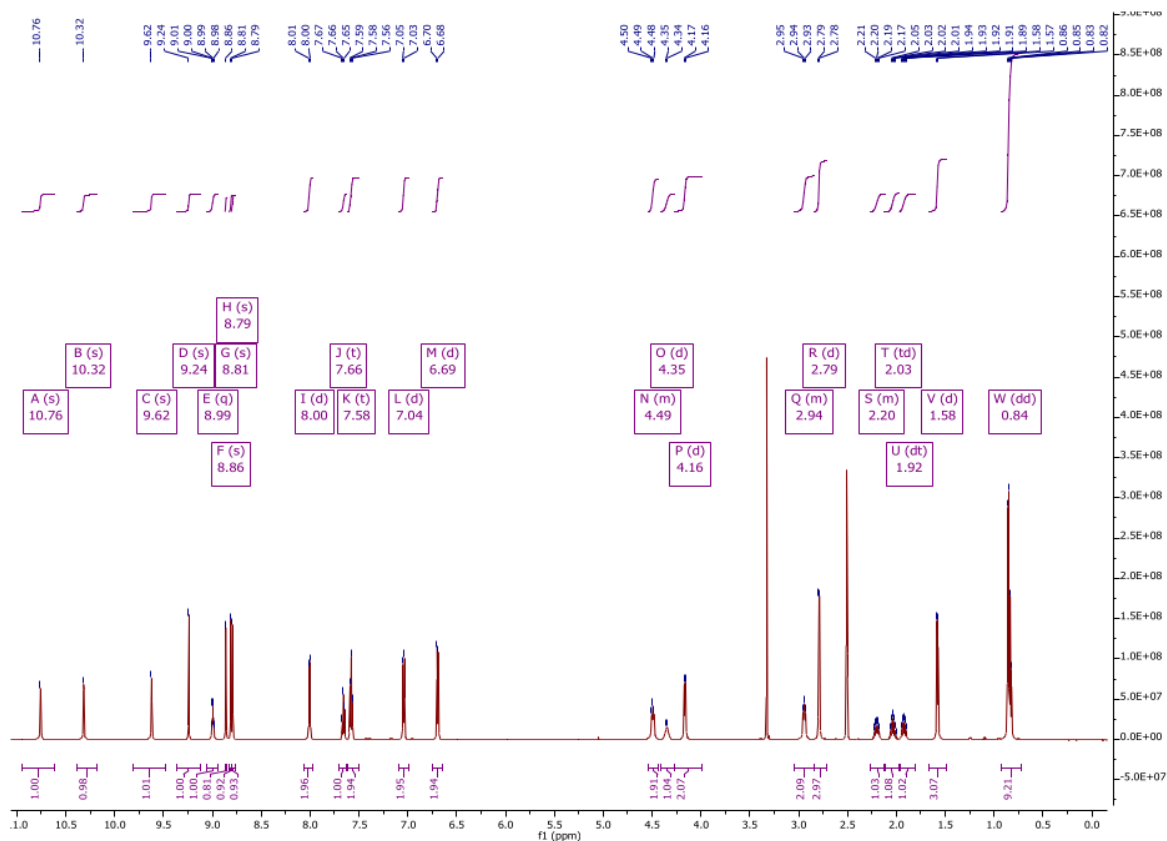
Supplementary Figure 19. ^{1}H-NMR (600 MHz, DMSO-d$_6$) of **7b** at room temperature.
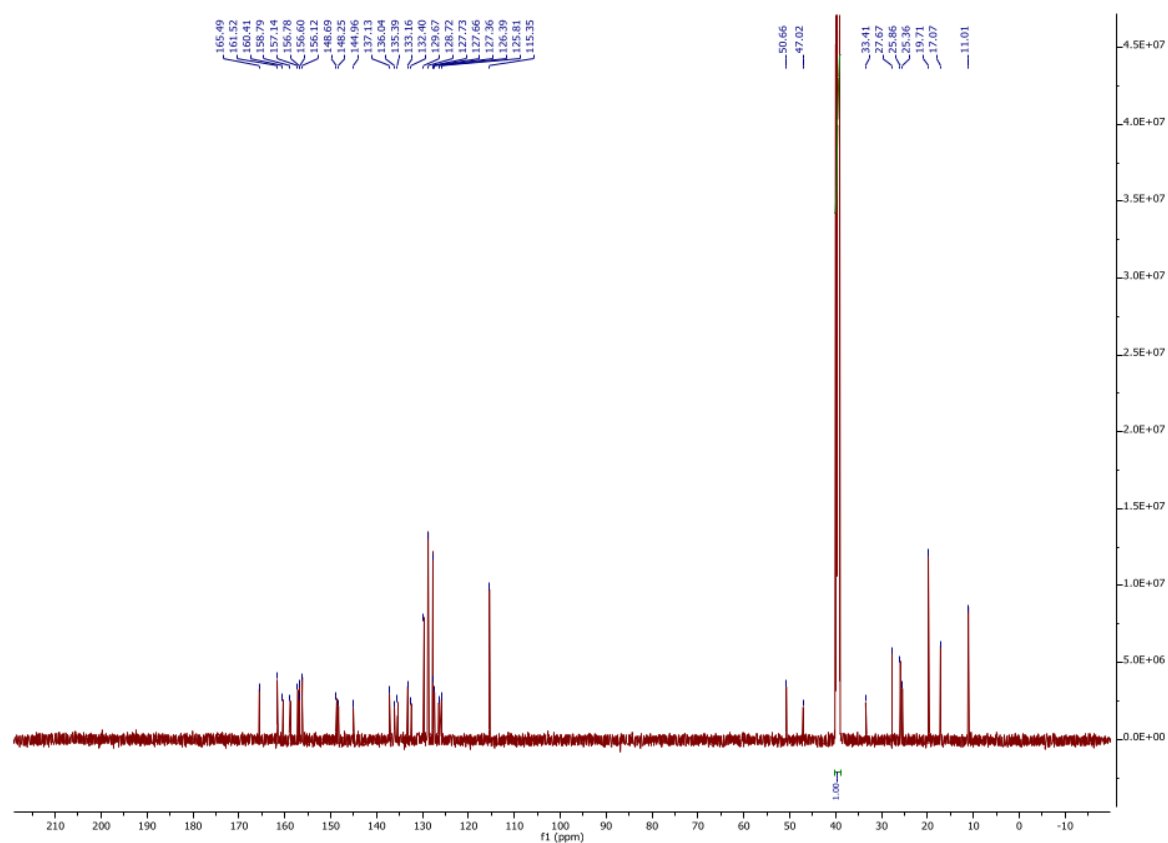
Supplementary Figure 20. ^{13}C-NMR (151 MHz, DMSO-d$_6$) of **7b** at room temperature.

22
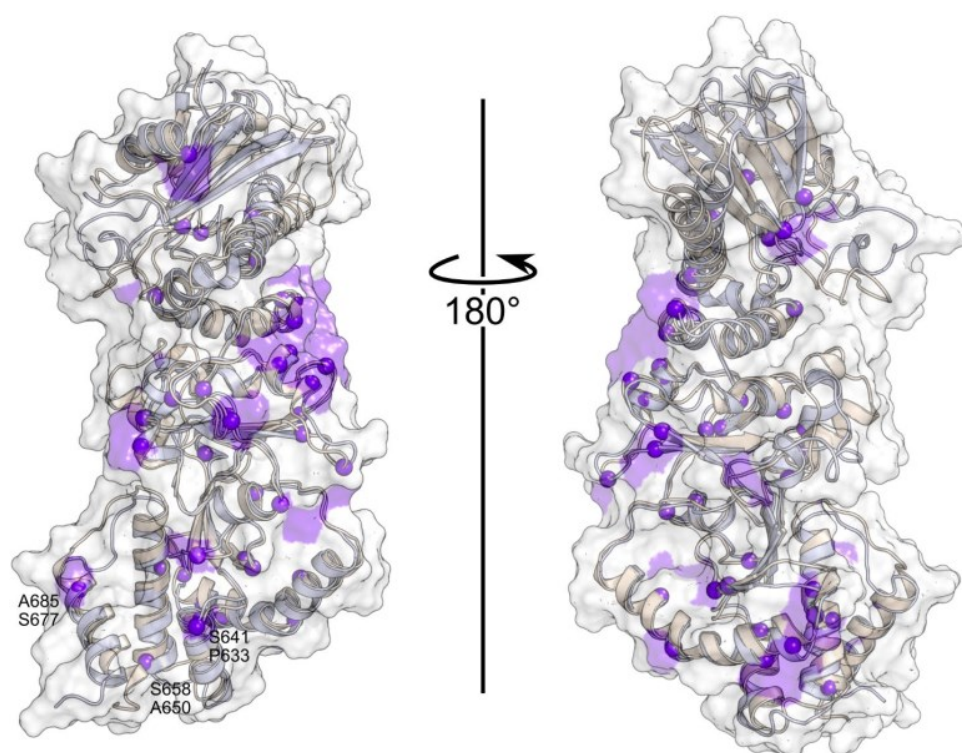
Supplementary Figure 21: Comparison of Hsp90α and Hsp90β. Overlay of the simulated MD-CTD part of Hsp90α (PDB ID 3q6m) and Hsp90β (PDB ID 5fwk). The isoforms share over 85% sequence identity and are structurally very similar, as shown in the backbone superposition (α: orange; β: blue). Non-identical residues are indicated by purple spheres and labeled in the CTDs' dimerization interface.

23
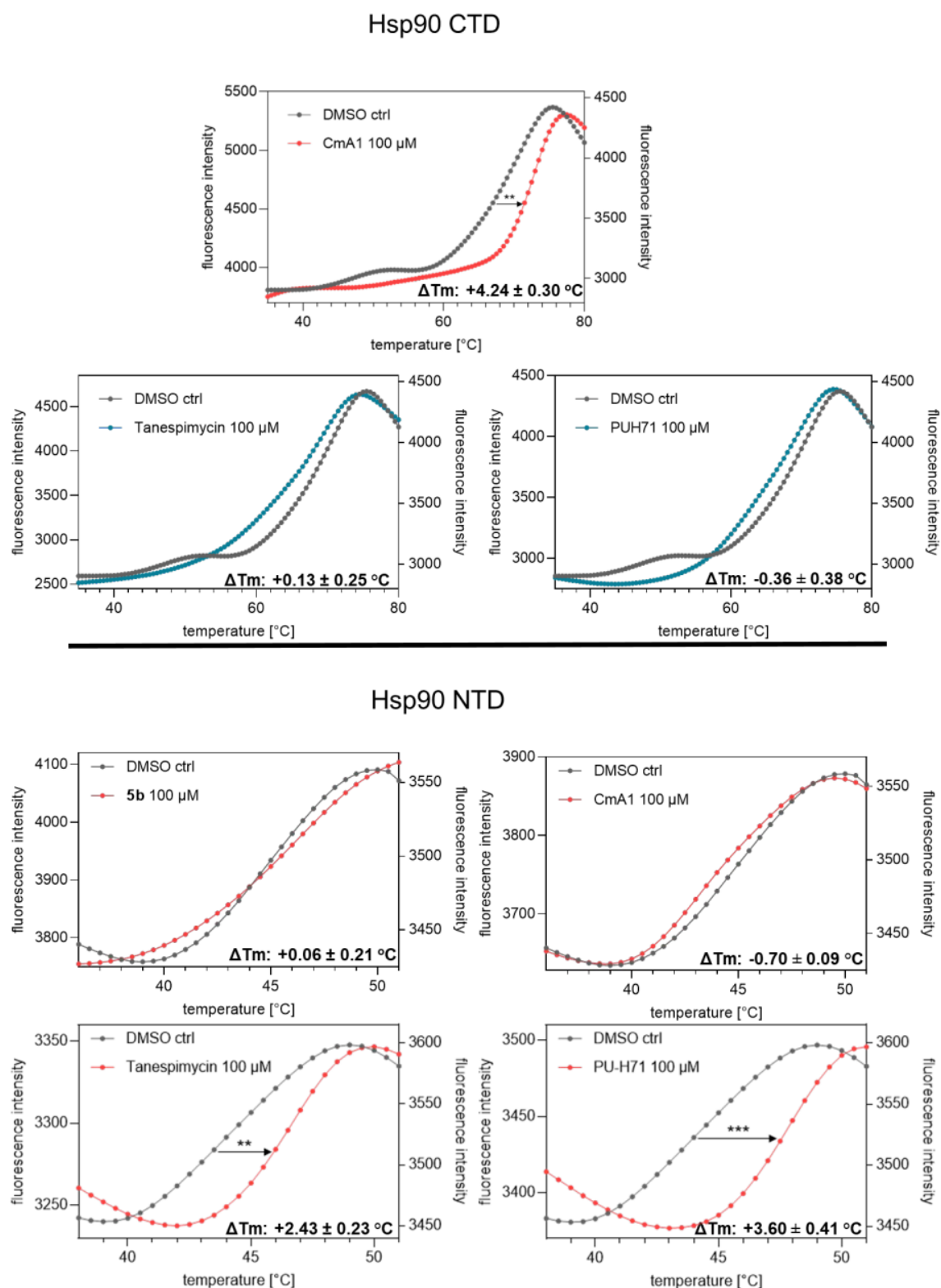
Supplementary Figure 22: Cell-free thermal shift assay was performed by incubating recombinant Hsp90α CTD (upper panel) and Hsp90α NTD (lower panel) recombinant protein with CmA1, Tanespimycin or **5b** (100µM) at an increasing temperature (up to 95 °C). Melting temperature (Tm) without inhibitors (DMSO) was used as a control.

24

170
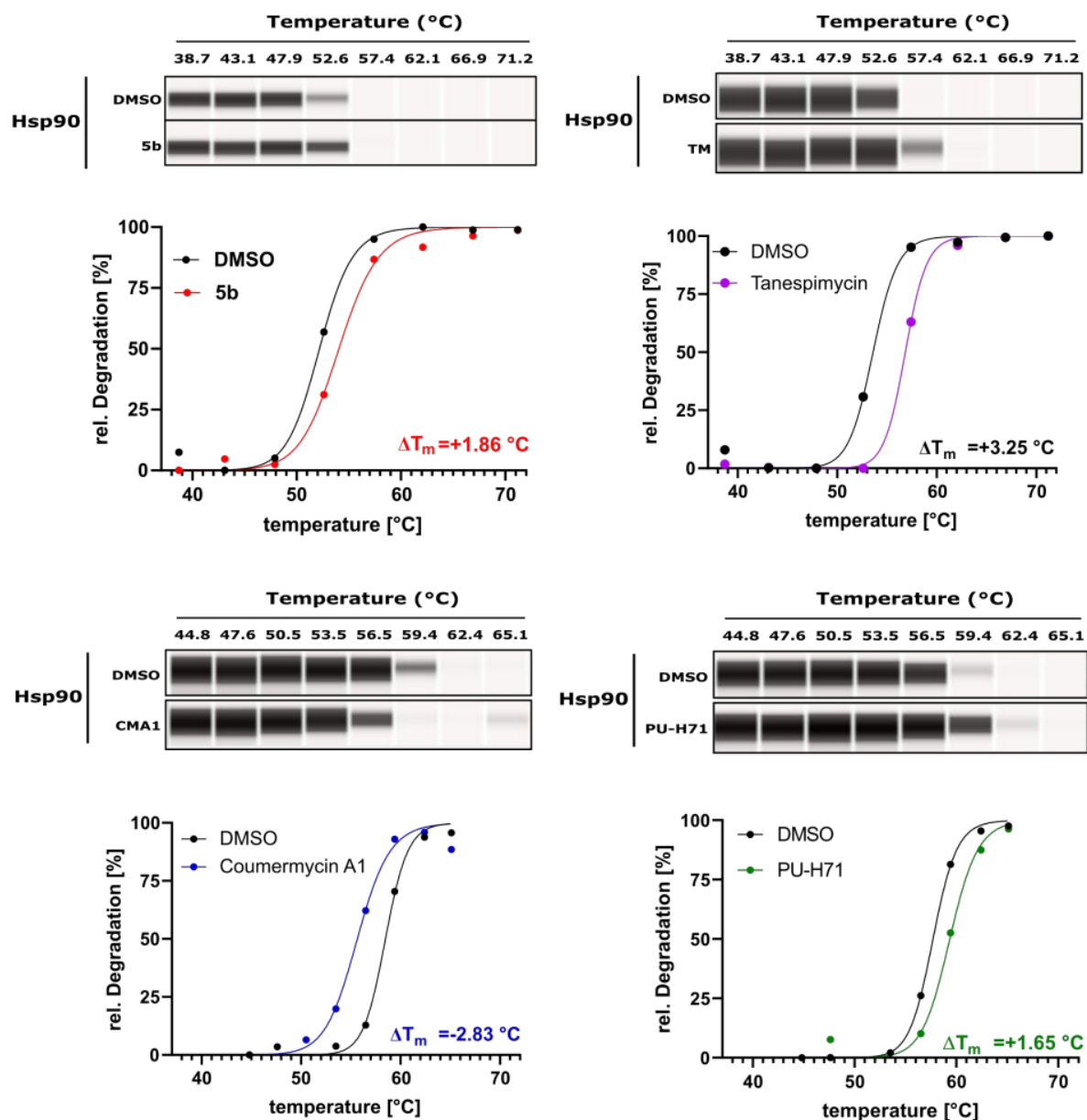
Supplementary Figure 23: The temperature-dependent intracellular thermal stabilization of t-Hsp90 protein after **5b** incubation with K562 cells for 24 h, at its increasing temperatures. Treated samples were measured by quantitative simple western immunoassay. Protein levels represented by the area under the curve of the electropherograms were normalized to the lowest temperature set as 0% degradation. ΔTm for compounds were determined by plotting normalized data using a sigmoid dose curve and non-linear regression.

25

Supplementary Table 1. Comparison of **5b** with the reference Hsp90 CTD and NTD inhibitors in thermal shift assay (Cell-free and cellular), time-resolved fluorescence resonance energy transfer (TR-FRET) assay with labeled PPID (Hsp90-CTD interacting chaperone), fluorescence polarization with FITC-labelled geldanamycin and cell-free recombinant luciferase refolding assay.

Assay	Targeting	Thermal Shift ΔTm [°C] HSP90			TR-FRET HSP90 CTD inhibition %		FP inhibition %	Cell free r-Luciferase refolding Inhibition %
Compound	Domain/Isoform	HSP90α CTD	HSP90α NTD	Cellular	HSP90α	HSP90β	HSP90α NTD	
	[conc.]	[100 μM]	[100 μM]		[1 mM]	[1 mM]	[10 μM]	[100 μM]
5b	Experimental HSP90 CTD	-8.45 ± 0.55	+0.06 ± 0.21	+1.86	92.95 ± 2.96 %	94.76 ± 0.03 %	no inhibition	60%
Coumermycin A1	Reference HSP90 CTD	+4.24 ± 0.30	-0.70 ± 0.09	-2.83	94.99 ± 0.86 %	96.54 ± 0.40 %	20.61 ± 0.44 %	-
Tanespimycin (17-AAG)	Reference HSP90 NTD	+0.13 ± 0.25	+2.43 ± 0.23	+3.25	no Inhibition	57.62 ± 5.53%	90.36 ± 1.39 %	63%
PU-H71	Reference HSP90 NTD	-0.36 ± 0.38	+3.60 ± 0.41	+1.65	no Inhibition	no inhibition	91.23 ± 0.62 %	-

26
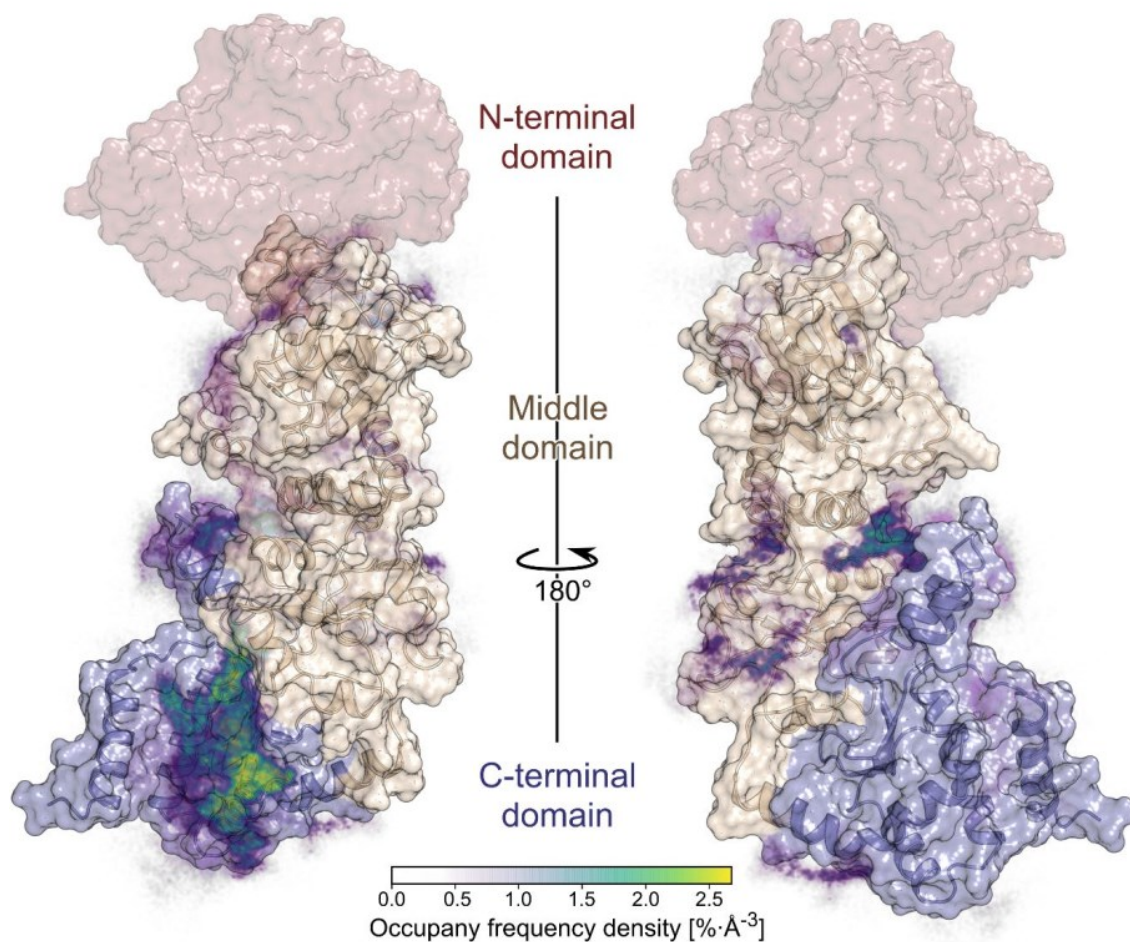
Supplementary Figure 24: MD simulations of 5b with Hsp90β. The relative densities of the bound poses of **5b** after 500 ns are mapped onto the Hsp90β monomer fragment used in the simulations (PDB ID 5fwk). The missing NTD is shown in red. Particularly high densities are observed in the region between H4 and H5, as in our simulation results for the α isoform (see Fig. 4). The less preferred site in the cleft between the CTD and MD is also observed but with lower density.

27
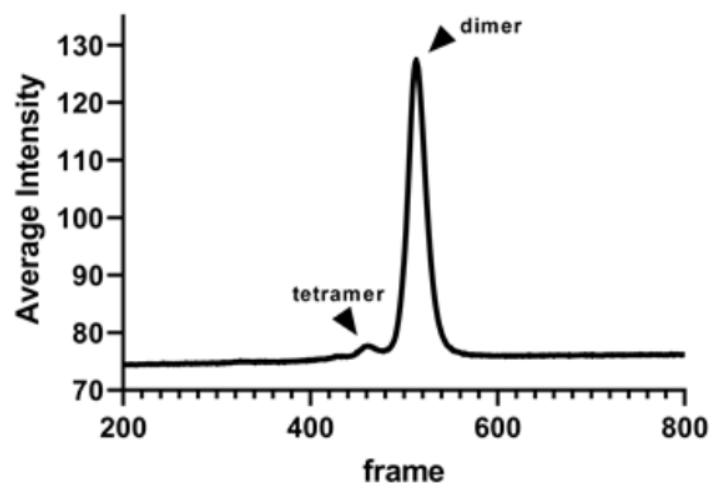
Supplementary Figure 25: SEC-SAXS elution profile of Hsp90 CTD. Shown is the average intensity of the different frames of the SEC-SAXS elution profile, performed with a Superdex 200 increase 3.2/300 column. The chromatogram was created using CHROMIXS [1]. The arrows indicate the dimer and the tetramer species within the profile. Frames of the corresponding dimer peak and the buffer were merged with CHROMIXS [1].

Supplementary Table 2. Overall SAXS data of Hsp90α CTD

SAXS Device	BM29, ESRF Grenoble[2,3]	Xenocs Xeuss 2.0 with Q-Xoom		
Data collection parameters				
Detector	PILATUS 2 M	PILATUS 3 R 300K windowless		
Detector distance (m)	2.827	0.550		
Beam size	200 µm x 200 µm	0.8 mm x 0.8 mm		
Wavelength (nm)	0.099	0.154		
Sample environment	Quartz capillary, 1 mm ø	Low Noise Flow Cell, 1 mm ø		
s range (nm^{-1})[‡]	0.025–6.0	0.10 – 6.0		
Exposure time per frame (s)	2	600		
Sample	**Hsp90 CTD**			
Mode of measurement	SEC-SAXS	batch		
Temperature (°C)	20	20		
Protein concentration (mg/ml)	18	10.8	9.7	9.7
SEC-Column	Superdex 200 increase 3.2/300	-	-	-
Injection volume (µl)	100	50	50	50
Substrate	without	without	LSK82 230 µM	LSK82 1 mM
Structural parameters				
$I(0)$ from $P(r)$	46.78	0.04	0.04	0.05
R_g (real-space from) (nm)	3.29	3.46	3.46	4.11
$I(0)$ from Guinier fit	46.98	0.04	0.04	0.05
s-range for Guinier fit (nm^{-1})	0.170–0.349	0.117–0.350	0.169–0.374	0.216–0.304
R_g (from Guinier fit) (nm)	3.23	3.40	3.46	4.11
points from Guinier fit	19 - 54	4 - 44	14 - 49	24 - 39
D_{max} (nm)	12.21	11.34	11.71	14.83
POROD volume estimate (nm^3)	92.15	103.32	102.28	116.82
Molecular mass (kDa)				
From $I(0)$	46.78	60.93	60.93	70.62
From Qp [4]	55.86	67.08	66.40	79.44
From MoW2 [5]	46.91	58.58	56.80	61.60
From Vc [6]	51.75	62.03	60.67	65.60
Bayesian Inference [7]	49.76	63.86	62.35	74.33
From POROD	56.97	64.58	63.93	73.01
From sequence	42.66 (dimer) 85.32 (tetramer)			
Structure Evaluation				
DAMMIF fit χ^2	1.127	-	-	-
Ambimeter score	0.845	-	-	-
Software				
ATSAS Software Version [8]	3.0.3			
Primary data reduction	CHROMIX [1] / PRIMUS [9]			
Data processing	GNOM [10]			
Ab initio modelling	DAMMIF [11]			
Averaging & superimposing	DAMAVER [12] / SUPCOMB [13]			
Structure evaluation	AMBIMETER [14]			
Model visualization	PyMOL [15]			

[‡]$s = 4\pi\sin(\theta)/\lambda$, 2θ – scattering angle, λ – Xray-wavelength, n.d. not determined

29
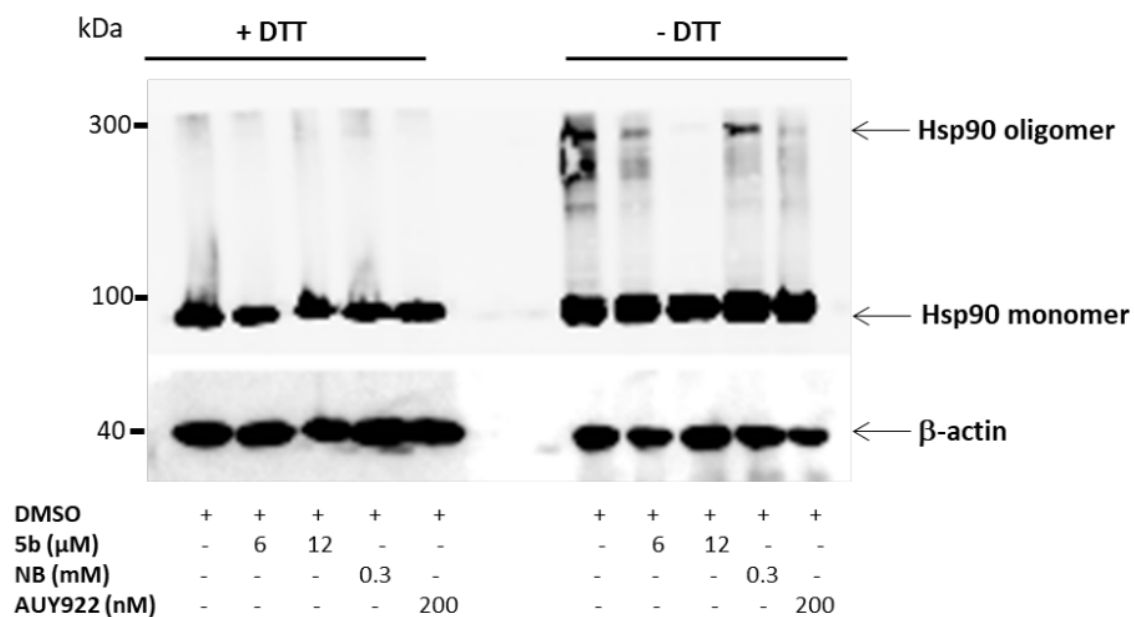
Supplementary Figure 26: After treating K562 cells with **5b**, NB, or AUY922 for 24 h, lysates were generated with or without reducing conditions (DTT) and were subjected to immunoblot analysis using Hsp90 antibody. An additional oligomeric Hsp90 band appeared in lysates without DTT in control (DMSO), however, the expression of Hsp90 oligomer was abolished after treatment with 5b.

30
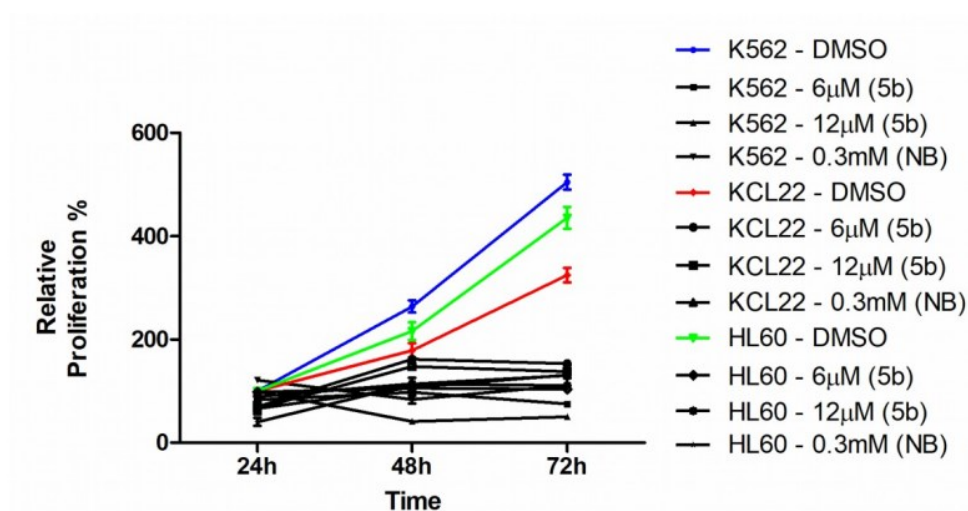
Supplementary Figure 27. K562, KCL22, and HL60 cell lines were treated with the indicated concentration of **5b** and later viable cells were counted at 24h, 48h, and 72h time periods (n=3).

31
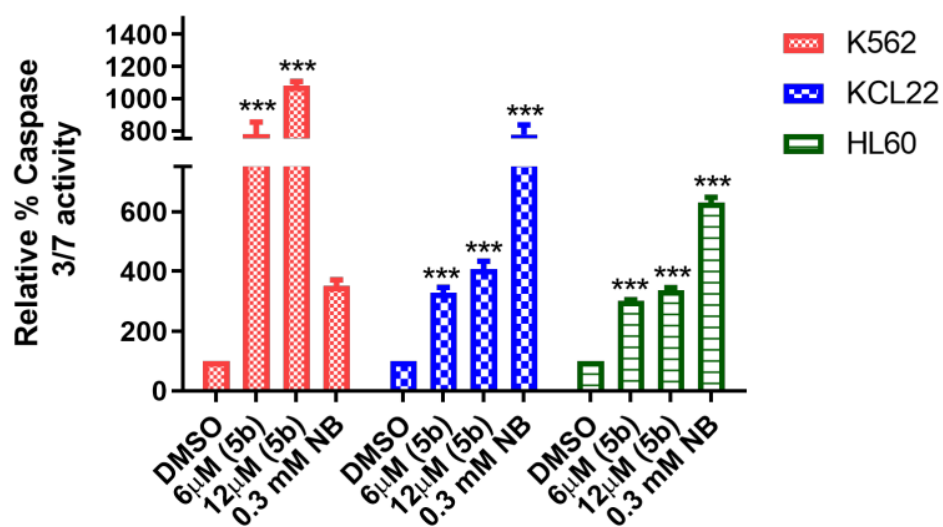
Supplementary Figure 28. K562, KCL22, and HL60 were treated with **5b** for 48 h. Apoptosis induction was examined using Caspase 3/7 enzyme-dependent glo assay. Columns depict the mean of three independent experiments ($n = 3$).

32
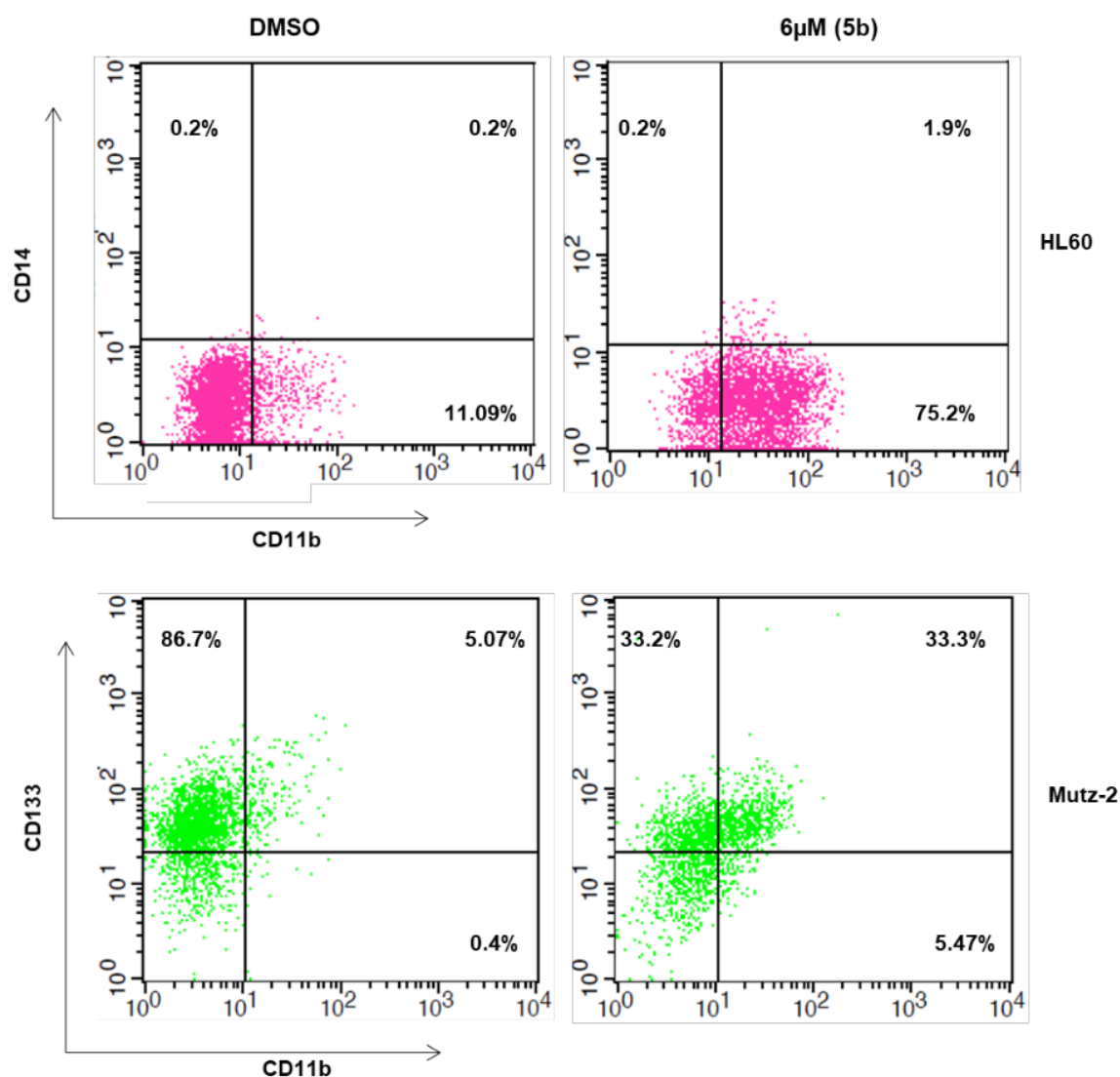
Supplementary Figure 29. HL60 & Mutz-2 cells were treated with **5b** (6μM) for 48 h and were subjected to FACS after staining with CD11b, CD14 & CD133, CD11b antibodies, respectively. Representative diagram show bivariate FACS analysis of CD14 versus CD11b in HL-60 & CD133 versus CD11b in Mutz-2 cells (n=3).

33
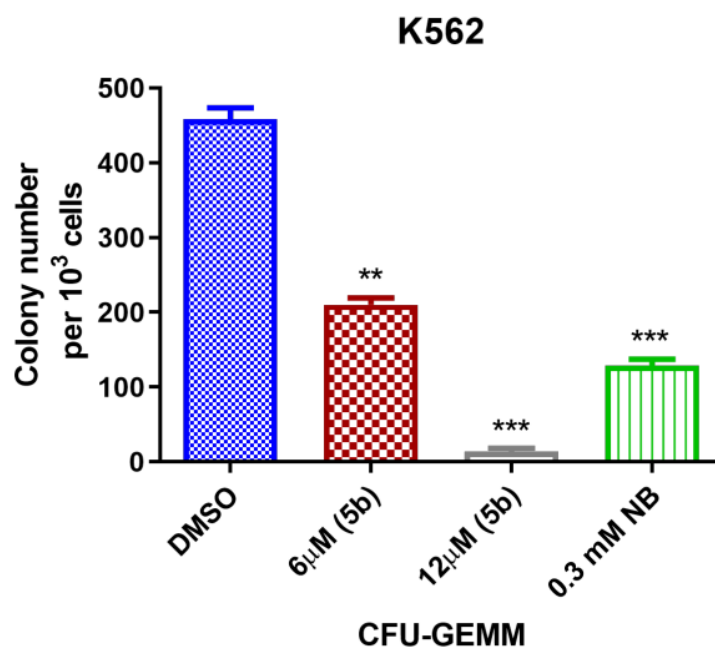
Supplementary Figure 30. K562 cells were seeded in methylcellulose medium after treatment with **5b** for 24h. Colonies were counted after 14 days. Columns depict the mean of three independent experiments (n = 3).
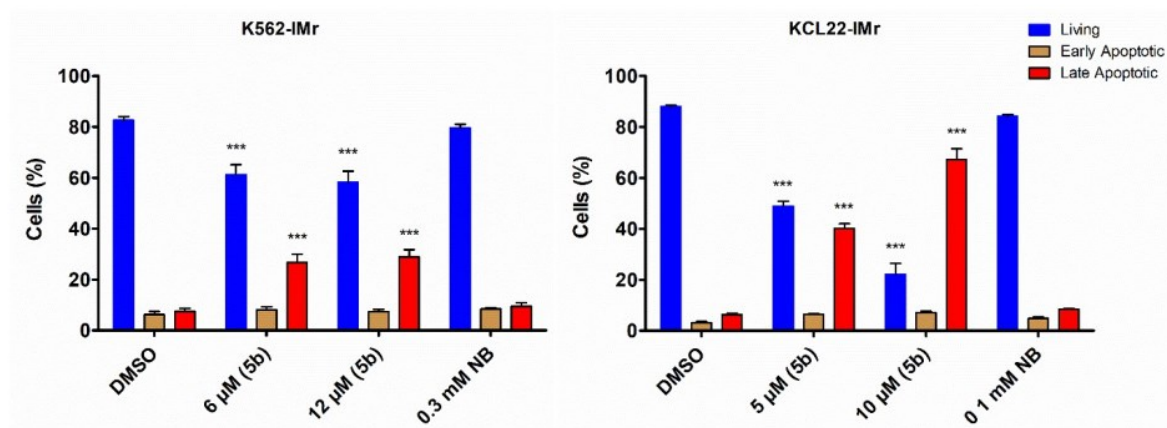
Supplementary Figure 31. Annexin V/PI staining of K562-IMr and KCL22-IMr after 24 h, 48 h, and 72 h treatment with **5b** and Novobiocin (NB) at indicated doses, based on the determined IC50 determination (n=3). Based on the co-appearance of annexin V/PI staining, the cells were separated in late and early apoptotic stages.

35

Supplemental References

1 Panjkovich, A. & Svergun, D. I. CHROMIXS: automatic and interactive analysis of chromatography-coupled small angle X-ray scattering data. *Bioinformatics*, doi:10.1093/bioinformatics/btx846 (2017).

2 Pernot, P. *et al.* Upgraded ESRF BM29 beamline for SAXS on macromolecules in solution. *J Synchrotron Radiat* **20**, 660-664, doi:10.1107/S0909049513010431 (2013).

3 Pernot, P. *et al.* New beamline dedicated to solution scattering from biological macromolecules at the ESRF. *Journal of Physics: Conference Series* **247**, 012009 (2010).

4 Porod, G. Die Röntgenkleinwinkelstreuung Von Dichtgepackten Kolloiden Systemen - 1 Teil. *Kolloid Z Z Polym* **124**, 83-114, doi:Doi 10.1007/Bf01512792 (1951).

5 Fischer, H., Neto, M. D., Napolitano, H. B., Polikarpov, I. & Craievich, A. F. Determination of the molecular weight of proteins in solution from a single small-angle X-ray scattering measurement on a relative scale. *J Appl Crystallogr* **43**, 101-109, doi:10.1107/S0021889809043076 (2010).

6 Rambo, R. P. & Tainer, J. A. Accurate assessment of mass, models and resolution by small-angle scattering. *Nature* **496**, 477-481, doi:10.1038/nature12070 (2013).

7 Hajizadeh, N. R., Franke, D., Jeffries, C. M. & Svergun, D. I. Consensus Bayesian assessment of protein molecular mass from solution X-ray scattering data. *Sci Rep* **8**, 7204, doi:10.1038/s41598-018-25355-2 (2018).

8 Manalastas-Cantos, K. *et al.* ATSAS 3.0: expanded functionality and new tools for small-angle scattering data analysis. *J Appl Crystallogr* **54**, doi:doi:10.1107/S1600576720013412 (2021).

9 Konarev, P. V., Volkov, V. V., Sokolova, A. V., Koch, M. H. J. & Svergun, D. I. PRIMUS: a Windows PC-based system for small-angle scattering data analysis. *J Appl Crystallogr* **36**, 1277-1282, doi:10.1107/S0021889803012779 (2003).

10 Svergun, D. I. Determination of the Regularization Parameter in Indirect-Transform Methods Using Perceptual Criteria. *J Appl Crystallogr* **25**, 495-503, doi:Doi 10.1107/S0021889892001663 (1992).

11 Franke, D. & Svergun, D. I. DAMMIF, a program for rapid ab-initio shape determination in small-angle scattering. *J Appl Crystallogr* **42**, 342-346, doi:10.1107/S0021889809000338 (2009).

12 Volkov, V. V. & Svergun, D. I. Uniqueness of ab initio shape determination in small-angle scattering. *J Appl Crystallogr* **36**, 860-864, doi:doi:10.1107/S0021889803000268 (2003).

13 Kozin, M. B. & Svergun, D. I. Automated matching of high- and low-resolution structural models. *J Appl Crystallogr* **34**, 33-41, doi:Doi 10.1107/S0021889800014126 (2001).

14 Petoukhov, M. V. & Svergun, D. I. Ambiguity assessment of small-angle scattering curves from monodisperse systems. *Acta Crystallogr D Biol Crystallogr* **71**, 1051-1058, doi:10.1107/S1399004715002576 (2015).

15 PyMOL. The PyMOL Molecular Graphics System, Version 2.0 Schrödinger, LLC. (2015).

Supplementary Note 2

Sanil Bhatia[1*], Lukas Spanier[2*], David Bickel[2], Niklas Dienstbier[1], Vitalij Woloschin[2], Melina Vogt[1], Henrik Pols,[2] Beate Lungerich,[2] Jens Reiners[3], Narges Aghaallaei[4], Daniela Diedrich[2], Benedikt Frieg[2,5], Julian Schliehe-Diecks[1], Bertan Bopp[6], Franziska Lang[1], Mohan Gopalswamy[2], Jennifer Loschwitz[2], Baubak Bajohgli[4], Julia Skokowa[4], Arndt Borkhardt[1], Julia Hauer[7,8], Finn K. Hansen[9], Sander H.J. Smits[3,10], Joachim Jose[6], Holger Gohlke[2, 5#] and Thomas Kurz[2#]

Affiliations:

1. Department of Pediatric Oncology, Hematology and Clinical Immunology, Medical Faculty, Heinrich Heine University Düsseldorf, Düsseldorf, Germany

2. Institute for Pharmaceutical and Medicinal Chemistry, Heinrich Heine University Düsseldorf, Düsseldorf, Germany

3. Center for Structural Studies, Heinrich Heine University Düsseldorf, Düsseldorf, Germany

4. Department of Hematology, Oncology, Clinical Immunology and Rheumatology, University Hospital Tübingen, Germany

5. John von Neumann Institute for Computing (NIC), Jülich Supercomputing Centre (JSC), Institute of Biological Information Processing (IBI-7: Structural Biochemistry) & Institute of Bio- and Geosciences (IBG-4: Bioinformatics), Forschungszentrum Jülich GmbH, Jülich, Germany

6. Institute for Pharmaceutical and Medicinal Chemistry, PharmaCampus, Westphalian Wilhelms University, Münster, Germany

7. Department of Pediatrics, Pediatric Hematology and Oncology, University Hospital Carl Gustav Carus, Dresden, Germany

8. National Center for Tumor Diseases (NCT), Partner Site Dresden, Dresden, Germany

9. Pharmaceutical and Cell Biological Chemistry, Pharmaceutical Institute University of Bonn, Bonn, Germany

10. Institute of Biochemistry, Heinrich Heine University Düsseldorf, Düsseldorf, Germany

* contributed equally to this work

\# shared senior authorship

 # Corresponding authors: (T.K.) Universitätsstr. 1, 40225 Düsseldorf, Germany, Phone: (+49) 211 81 14984, E-mail: thomas.kurz@uni-duesseldorf.de; (H.G.) Universitätsstr. 1, 40225 Düsseldorf, Germany, Phone: (+49) 211 81 13662, E-mail: gohlke@uni-dueseldorf.de; (S.B.) Moorenstraße 5, 40225 Düsseldorf, Germany, Phone (+49) 211 81 04896 Email, sanil.bhatia@med.uni-duesseldorf.de

Author ORCID: Benedikt Frieg: 0000-0002-7877-0262; Holger Gohlke: 0000-0001-8613-1447; David Bickel: 0000-0003-0332-8338; Sanil Bhatia: 0000-0001-6494-7744; Finn K. Hansen: 0000-0001-9765-5975 Thomas Kurz: 0000-0002-9474-4224; Sander Smits 0000-0003-0780-9251; Baubak Bajoghli: 0000-0002-7368-7523; Jennifer Loschwitz: 0000-0002-9066-1923

Keywords: protein-protein interaction, heat-shock protein, CML, BCR-ABL1, imatinib, Hsp90 inhibitor.

1. Analysis of Aqueous Solubility (Thermodynamic Solubility): 5b (LSK82)

Study Objective

The test articles (**5b** or **LSK82**) and reference compound (Ondansetron) were assessed for thermodynamic solubility in phosphate-buffered saline, pH 7.4.

Materials

1.   Reagents and consumables
Phosphate buffered saline, pH 7.4 (Sigma-Aldrich, USA; Cat #P3813)
Acetonitrile Chromasolv, gradient grade, for HPLC, ≥99.9% (Sigma-Aldrich, USA; Cat #34851)
Ondansetron base powder (Enamine, Ukraine, Cat # EN300-117273)
DMSO (Sigma-Aldrich, USA; Cat # 34869)
Costar 96 Well Assay Blocks (Corning, USA; Cat # 3958)
UV-Star® 96 Well Microplate (Greiner Bio-One, Germany; Ca t #655801)
Matrix Disposable pipette tips (ThermoScientific, USA; Cat ## 8041, 7622, 7321)
Flex-Tubes Microcentrifuge Tubes, 1.5ml (Eppendorf, Germany; Cat # 22364111)
MultiScreen HTS 96 Well Filter Plates (Millipore, Ireland; Cat # MSGVS2210)

2.   Equipment

Water purification system Millipore Milli-Q Gradient A10 (Millipore, France)
Thermomixer R Block, 1.5 ml (Eppendorf, Germany; Cat # 5355)
Matrix Multichannel Electronic Pipette 2-125 µL, 5-250 µL, 15-1250 µL (Thermo Scientific, USA; Cat ## 2011, 2012, 2004)
SpectraMax Plus Microplate Reader (Molecular Devices, USA; Product # 02196)
Multi-Well Plate Vacuum Manifold (Pall Corporation, USA; Product # 5014)
Vacuum pump (Millipore, USA; Model # XX5500000)

3.   Analytical System
The measurements were performed using Spectra Max Plus reader in UV-Vis mode. Acquisition and analysis of the data were performed using SoftMax Pro v.5.4 (Molecular Devices) and Excel 2010 data analysis software.

Methods

The thermodynamic solubility assay was performed according to Enamine's aqueous solubility SOP. Briefly, the dry powder forms of the test compounds were mixed with phosphate-buffered saline pH 7.4 to the theoretical concentration of 4 mM and further allowed to equilibrate at 25°C on a thermostatic shaker. After 4 and 24 hours shaking, incubation mixtures were filtered through HTS filter plates using a vacuum manifold. The filtrates of test compounds were diluted 2-fold with acetonitrile with 4% DMSO before measuring.

In parallel, compounds dilutions in 50% acetonitrile/buffer (pure acetonitrile for **LSK82**) were prepared to the theoretical concentrations of 0 µM (blank), 10 µM, 25 µM, 50 µM, 100 µM and 200 µM with 2% final DMSO to generate calibration curves. Ondansetron was used as a reference compound to control proper assay performance. 150 µl of samples was transferred to 96-well plate and measured in 200-550 nm range with 5 nm step.

The concentrations of compounds in PBS are calculated using a dedicated Microsoft Excel calculation script. Proper absorbance wavelengths for calculations are selected for each compound manually based on absorbance maximums (absolute absorbance unit values for the minimum and maximum concentration points within $0 - 3$ OD range). Each of the final datasets is additionally visually evaluated by the operator and goodness of fit ($R2$) is calculated for each calibration curve. The effective range of this assay is approximately 2-400 µM and the compounds returning values close to the upper limit of the range may have higher actual solubility (e.g.5'-deoxy-5-fluorouridine). This method is not suitable for liquid (at 25°C) substances (were not present among the tested compounds).

Results

The solubility data of the test and reference compounds are listed in the table below. The calibration curves are shown in the Appendix. Please note that thermodynamic solubility determined in the conditions of this test depends strongly upon the properties of the solid material used (particular crystal/amorphous form). Hydrophobic, poorly soluble compounds may sometimes have extremely slow kinetics of dissolution resulting in very low solubility values, as opposed to the data from "kinetic solubility" testing, which is usually more relevant for early stages of drug discovery phase.

Table 1. Solubility of compounds in PBS, pH 7.4

Compound ID	Time Point	PBS solubility, pH 7.4, µM			SE
		Incubation 1	**Incubation 2**	**Mean**	
Ondansetron	4h	95	95	95	0.0
	24h	96	93	95	1.6
5b (LSK82)	4h	5	5	5	0.0
	24h	7	9	8	1.0

*Goodness of fit (R2) in all titration curves as well as the variations between repeat measurements indicates high quality of the experimental data in the current batch of the test articles.
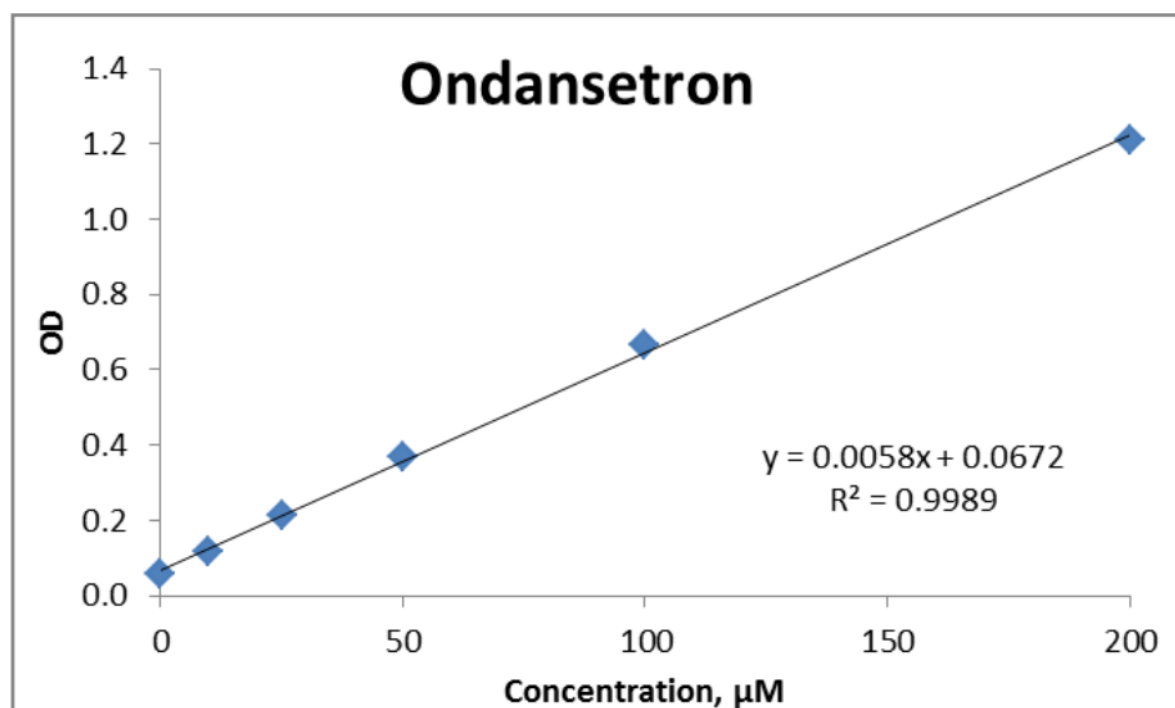
Figure 1. Calibration curve for **Ondansetron**
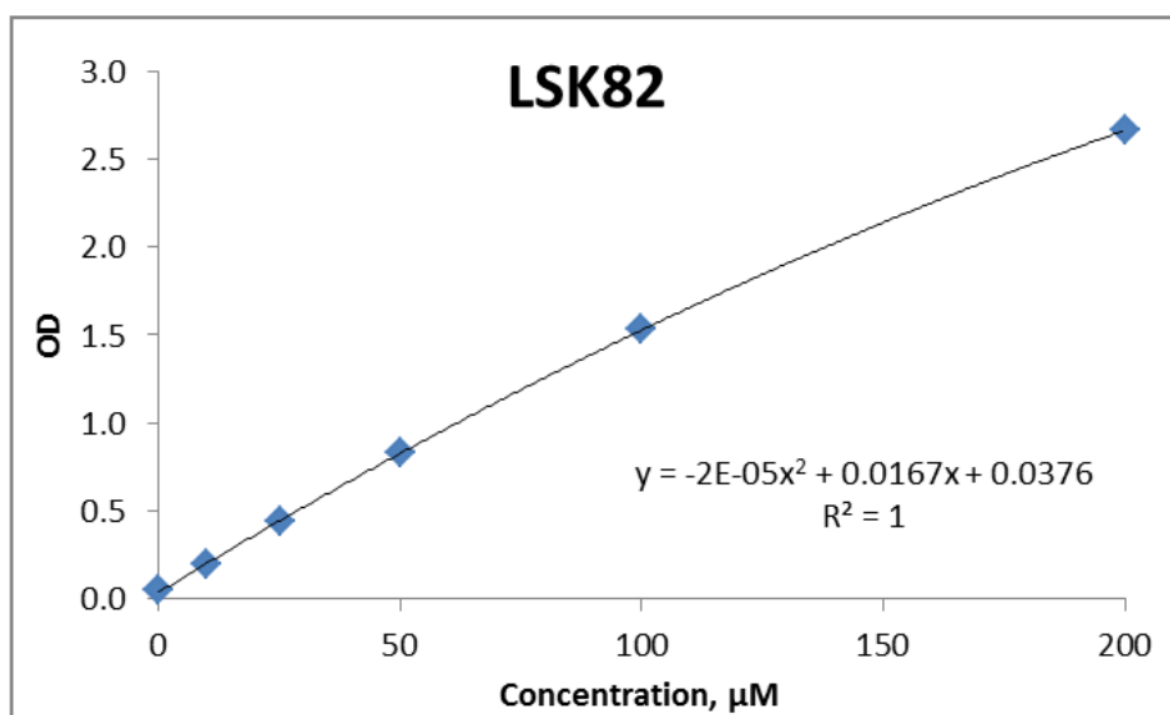
Figure 2. Calibration curve for **5b** (**LSK82**)

2. Assessment of Metabolic Stability in Human Liver Microsomes: 5b (LSK82)

Study Objective

The objective of this study was to determine metabolic stability of **5b (LSK82)** and reference compounds (Propranolol and Diclofenac) in human liver microsomes at five time points over 40 minutes using HPLC-MS. Metabolic stability is defined as the percentage of parent compound lost over time in the presence of a metabolically active test system.

Materials

Reagents and consumables

DMSO (Sigma-Aldrich, 34869 - Chromasolv Plus, for HPLC, ≥99.7%)

Acetonitrile (Sigma-Aldrich, 34851 - Chromasolv Plus, for HPLC, ≥99.9%)

Potassium phosphate monobasic (Helicon, Am-O781-0.5)

Potassium phosphate dibasic (Helicon, Am-O705-0.5)

Magnesium chloride hexahydrate (Helicon, Am-O288-0.1)

Human Liver Microsomes: pooled, mixed gender (XenoTech, H0630/lot N#1810003)

Glucose-6-phosphate dehydrogenase from baker's yeast, type XV (Sigma-Aldrich, G6378)

Glucose-6-phosphate sodium salt (Sigma-Aldrich, G7879)

β-Nicotinamide adeninedinucleotide-2'-phosphate reduced, tetrasodium salt

(Sigma Aldrich N1630-100 MG)

Formic acid (Sigma-Aldrich, 94318)

(+,-) Propranolol hydrochloride (Sigma-Aldrich, P0884)

Diclofenac, 96% purity (Enamine, # EN300-119509)

Phenomenex Luna® C18 HPLC column, 2.1x50 mm, 5 μm (Cat #5291-126)

1.1 ml microtubes in microracks, pipettor tips (Thermo Scientific).

Equipment

Gradient HPLC system (Shimadzu)

Triple quadrapole mass-detector API 3000 with TurboIonSpray Ion Source (AB Sciex, Canada)

Nitrogen generator N2-04-L1466, nitrogen purity 99%+ (Whatman)

Environmental Incubator Shaker G24; Digital Refrigerated Incubator/Shaker Innova 4330 (New Brunswick Scientific)

Water purification system Millipore Milli-Q Gradient A10 (Millipore, France)

Multichannel pipettors 5-250 μL, 2-125 μL, 15-1250 μL (Thermo Scientific)

Analytical System

All measurements were performed using Shimadzu Prominence HPLC system including vacuum degasser, gradient pumps, reverse phase column, column oven and autosampler. The HPLC system was coupled with tandem mass spectrometer API 3000 (PE Sciex). The both positive and negative ion modes of the TurboIonSpray ion source were used. Acquisition and analysis of the data were performed using Analyst 1.5.2 software (PE Sciex).

Methods

Microsomal incubations were carried out in 96-well plates in 5 aliquots of 40 μL each (one for each time point). Liver microsomal incubation medium comprised of phosphate buffer (100 mM, pH 7.4), MgCl2 (3.3 mM), NADPH (3 mM), glucose-6-phosphate (5.3 mM), glucose-6-phosphate dehydrogenase (0.64 units/ml) with 0.42 mg of liver microsomal protein per ml. In the control reactions the NADPH-cofactor system was substituted with phosphate buffer. Test compounds (2 μM, final solvent concentration 1.6 %) were incubated with microsomes at 37 °C, shaking at 100 rpm. Each reaction was performed in duplicates. Five time points over 40 minutes were analyzed. The reactions were stopped by adding 5 volumes of 90% acetonitrile-water to incubation aliquots, followed by protein sedimentation by centrifuging at 5500 rpm for 3 minutes. Each reaction was performed in duplicates. Supernatants were analyzed using the HPLC system coupled with tandem mass spectrometer. The elimination constant (kel), half-life (t1/2) and intrinsic clearance (Clint) were determined in plot of ln(AUC) versus time, using linear regression analysis:[1]

$$k_{el} = -slope$$

$$t_{1/2} = \frac{0.693}{k}$$
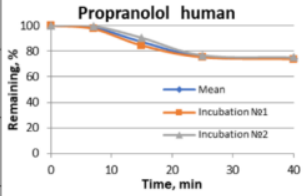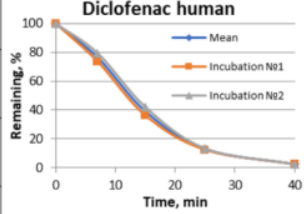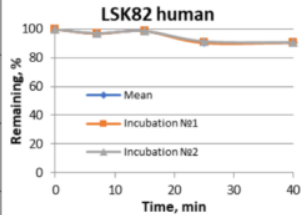
$$Cl_{int} = \frac{0.693}{t_{1/2}} \times \frac{\mu l_{incubation}}{mg_{microsomes}}$$

[1] In order to indicate the quality of the linear regression analysis, the R (correlation coefficient) values are provided. In some cases, the last time point is excluded from the calculations to ensure acceptable logarithmic linearity of decay.

Results

Human microsomal stability data for reference and test compounds is provided in the table below.

Table 1. Human microsomal stability

| Compound ID | Time, min | Analyte Peak Area | | Analyte Peak Area, Mean of 2 | % Remaining, Mean of 2 | R | kel, min-1 | $t_{1/2}$, min | C_{lint}, µl/min/mg | % Remaining without cofactor, Mean of 2 |
		Inc. 1	Inc. 2							
1	2	3	4	5	6	7	8	9	10	11
Propranolol human	0	9.98E+04	9.84E+04	9.91E+04	100	0.947	0.008	82.5	20	100
	7	9.73E+04	9.80E+04	9.77E+04	99					
	15	8.42E+04	8.89E+04	8.66E+04	87					
	25	7.50E+04	7.55E+04	7.53E+04	76					
	40	7.36E+04	7.40E+04	7.38E+04	74					103
Diclofenac human	0	2.24E+05	2.09E+05	2.17E+05	100	0.991	0.096	7.2	231	100
	7	1.65E+05	1.66E+05	1.66E+05	76					
	15	8.10E+04	8.79E+04	8.45E+04	39					
	25	2.78E+04	2.80E+04	2.79E+04	13					
	40	5.27E+03	5.34E+03	5.31E+03	2					95
5b (LSK82)	0	8.48E+04	8.48E+04	8.48E+04	100	0.894*	0.003*	261.2*	6*	100
	7	8.22E+04	8.24E+04	8.23E+04	97					
	15	8.37E+04	8.37E+04	8.37E+04	99					
	25	7.67E+04	7.75E+04	7.71E+04	91					
	40	7.68E+04	7.68E+04	7.68E+04	91					96

*Parameter should be considered as approximate due to the high stability of the compound

Interpretation of microsomal stability assay data

The test compounds can be classified in terms of their microsomal stability into low, medium and high clearance groups. The intrinsic clearance classification bands for mouse, rat, and human species are calculated according to the well stirred model equation:[1]

$$CL_{int} = \frac{CLH}{fu \times (1-E)}$$

where CLH is a hepatic clearance (mL/min/kg), CLH = E x QH
QH = liver blood flow (mL/min/kg)[2]
E = extraction ratio, assumed at 0.3 for low clearance and at 0.7 for high clearance compounds
fu = fraction unbound in plasma, assumed at 1.

The CLint classification values were calculated for mouse, rat, and human species using the literature data on liver weight[3] and microsomal protein concentration[3,4] and are represented in the following table.

The intrinsic clearance groups for classification of test compounds

Classification group	Intrinsic clearance (µL/min/mg protein)		
	Mouse	Rat	Human
Low clearance	<8.6	<13	<8.8
High clearance	>48	>72	>48

[1]. Houston J.B., Utility of in vitro drug metabolism data in predicting in vivo metabolic clearance, Biochemical Pharmacology, 1994, 47, 1469-1479.

[2]. Davies B. and Morris T., Physiological parameters in laboratory animals and humans, Pharmaceutical Research, 1993, 10, 1093-1095.

[3]. Barter Z.E., et al., Scaling factors for the extrapolation of in vivo metabolic drug clearance from in vitro data: reaching a consensus on values of human microsomal protein and hepatocellularity per gram of liver, Current Drug Metabolism, 2007, 8, 33-45.

[4]. Iwatsubo T., et al., Prediction of species differences (rats, dogs, humans) in the in vivo metabolic clearance of YM796 by the liver from in vitro data, Journal of Pharmacology and Experimental Therapeutics, 1997, 283, 462-469.

Publication IV

Biophysical and pharmacokinetic characterization of a small-molecule inhibitor of RUNX1/ETO tetramerization with anti-leukemic effects

Gopalswamy, M. [a], Kröger, T. [a], Bickel, D. [a], Frieg, B. [b], Akter, S. [a], Schott-Verdugo, S. [a,b,c], Viegas, A. [d], Pauly, T. [d], Mayer, M. [e], Przibilla, J. [e], Reiners, J. [f], Nagel-Steger, L. [d], Smits, S. [f], Groth, G. [g], Etzkorn, M. [d], and Gohlke, H. [a,b,c]

[a] Institute for Pharmaceutical and Medicinal Chemistry, Heinrich Heine University Düsseldorf, Düsseldorf, Germany

[b] Institute of Biological Information Processing (IBI-7: Structural Biochemistry), Forschungszentrum Jülich GmbH, Jülich, Germany

[c] John von Neumann Institute for Computing (NIC), Jülich Supercomputing Centre (JSC), and Institute of Bio- and Geosciences (IBG-4: Bioinformatics), Jülich, Germany

[d] Institute for Physical Biology, Heinrich Heine University Düsseldorf, Düsseldorf, Germany

[e] Pharmacelsus GmbH, Saarbrücken, Germany

[f] Institute of Biochemistry, Heinrich Heine University Düsseldorf, Düsseldorf, Germany

[g] Institute of Biochemical Plant Physiology, Heinrich Heine University Düsseldorf, Düsseldorf, Germany

Biophysical and pharmacokinetic characterization of a small-molecule inhibitor of RUNX1/ETO tetramerization with anti-leukemic effects

Mohanraj Gopalswamy[a], Tobias Kroeger[a], David Bickel[a], Benedikt Frieg[b], Shahina Akter[a], Stephan Schott-Verdugo[a,b,c], Aldino Viegas[d,§], Thomas Pauly[b,d], Manuela Mayer[e], Julia Przibilla[e], Jens Reiners[f], Luitgard Nagel-Steger[b,d], Sander H.J. Smits[f], Georg Groth[g], Manuel Etzkorn[d,h], and Holger Gohlke[a,b,c*]

[a] Institute for Pharmaceutical and Medicinal Chemistry, Heinrich Heine University Düsseldorf, Universitätsstr. 1, 40225 Düsseldorf, Germany

[b] Institute of Biological Information Processing (IBI-7: Structural Biochemistry), Forschungszentrum Jülich GmbH, Wilhelm-Johnen-Str., 52425 Jülich, Germany

[c] John von Neumann Institute for Computing (NIC), Jülich Supercomputing Centre (JSC), and Institute of Bio- and Geosciences (IBG-4: Bioinformatics), Forschungszentrum Jülich GmbH, Wilhelm-Johnen-Str., 52425 Jülich, Germany

[d] Institute for Physical Biology, Heinrich Heine University Düsseldorf, Universitätsstr. 1, 40225 Düsseldorf, Germany

[e] Pharmacelsus GmbH, Science Park 2, 66123 Saarbrücken, Germany

[f] Institute of Biochemistry and Center for Structural Studies, Heinrich Heine University Düsseldorf, Universitätsstr. 1, 40225 Düsseldorf, Germany

[g] Institute of Biochemical Plant Physiology, Heinrich Heine University Düsseldorf, Universitätsstr. 1, 40225 Düsseldorf, Germany

[h] Jülich Center for Structural Biology (JuStruct), Forschungszentrum Jülich GmbH, Wilhelm-Johnen-Str., 52425 Jülich, Germany

Running title: Characterization of ligand binding to NHR2

§ Current address: UCIBIO, Chemistry Department, Faculty of Sciences and Technology, NOVA University of Lisbon, 2829-516, Caparica, Portugal

*Address: Universitätsstr. 1, 40225 Düsseldorf, Germany.
Phone: (+49) 211 81 13662; Fax: (+49) 211 81 13847
E-mail: gohlke@uni-duesseldorf.de and h.gohlke@fz-juelich.de

Abstract

Acute myeloid leukemia (AML) is a malignant disease of immature myeloid cells and the most prevalent acute leukemia among adults. The oncogenic homo-tetrameric fusion protein RUNX1/ETO results from the chromosomal translocation t(8;21) and is found in AML patients. The nervy homology region 2 (NHR2) domain of ETO mediates tetramerization; this oligomerization is essential for oncogenic activity. Previously, we identified the first-in-class small-molecule inhibitor of NHR2 tetramer formation, **7.44**, which was shown to specifically interfere with NHR2, restore gene expression down-regulated by RUNX1/ETO, inhibit the proliferation of RUNX1/ETO-depending SKNO-1 cells, and reduce the RUNX1/ETO-related tumor growth in a mouse model. However, no biophysical and structural characterization of **7.44** binding to the NHR2 domain has been reported. Likewise, the compound has not been characterized as to physicochemical, pharmacokinetic, and toxicological properties. Here, we characterize the interaction between the NHR2 domain of RUNX1/ETO and **7.44** by biophysical assays and show that **7.44** interferes with NHR2 tetramer stability and leads to an increase in the dimer population of NHR2. The affinity of **7.44** with respect to binding to NHR2 is $K_{lig} = 3.95 \pm 1.28$ μM. By NMR spectroscopy combined with molecular dynamics simulations, we show that **7.44** binds with both heteroaromatic moieties to NHR2 and interacts with or leads to conformational changes in the N-termini of the NHR2 tetramer. Finally, we demonstrate that **7.44** has favorable physicochemical, pharmacokinetic, and toxicological properties. Together with biochemical, cellular, and in vivo assessments, the results reveal **7.44** as a lead for further optimization towards targeted therapy of t(8;21) AML.

Introduction

RUNX1/ETO is an oncogenic homotetrameric fusion protein found in t(8;21)-dependent acute myeloid leukemia (AML) patients [1]. This form of AML is characterized by an achieved complete remission for ~50% to 75% of patients [2], a relapse-free survival rate of ~20% to 30% [2], and a 5-year overall survival rate of ~50% [3]. Because no targeted treatment of t(8;21)-dependent AML is available at the moment, the discovery of new therapeutic targets with the potential to improve the overall survival rate is of utmost importance [4]. RUNX1/ETO is composed by the DNA-binding Runt-domain [5], the product of the RUNX1 gene, and by four nervy homology regions (NHR1-4), the product of the ETO gene (**Figure 1A**) [6]. The NHR2 domain is responsible for the tetramerization of RUNX1/ETO [7]. Furthermore, the NHR3- and NHR4-deleted versions of RUNX1/ETO and other short variants rapidly induce leukemia in a mouse bone marrow transplantation model [8]. Recently, the specificity of the NHR2 domain was displayed by replacing the NHR2 domain from full-length RUNX1/ETO with a structurally similar BCR tetramerization domain resulting in a loss of CD34+ progenitor cell expansion [9]. Thus, the NHR2-mediated tetramerization is necessary for the onset and maintenance of t(8;21)-dependent AML [10]. Hence, the disruption of RUNX1/ETO tetramerization is a promising strategy to fight AML.

Previous studies identified five hot spots residues, W498, W502, D533, E536, and W540 (**Figure 1B and C**), as essential for the tetramerization NHR2 [11]. By mutating the hot spots to alanine, resulting in what has been termed M5 variant, we demonstrated that RUNX1/ETO-dimers, in contrast to tetramers, do not block myeloid differentiation and fail to induce AML in mice [10]. Thus, the hot spot residues of NHR2 represented a target for developing inhibitors of RUNX1/ETO tetramerization and a molecular intervention in t(8;21)-dependent AML that had not yet been addressed. An 18-mer peptide containing the hot spot residues inhibited the tetramerization of NHR2 with an IC_{50} of 250 μM (BS^3 cross-linking assay) and 390 μM (ELISA) [11]. Although this example shows that inhibiting NHR2 tetramerization on a molecular level is possible, the 18-mer has unfavorable pharmacological properties. Therefore, exploiting the pattern of a subset of the hot spots (D533, E536, and W540) as a query for virtual screening, we identified the first-in-class small-molecule inhibitor of NHR2 tetramer formation, **7.44 (Figure 1D)** [11]. **7.44** was shown to specifically interfere with NHR2, restore gene expression down-regulated by RUNX1/ETO, inhibit the proliferation of RUNX1/ETO-depending SKNO-1 cells, and reduce the RUNX1/ETO-related tumor growth in a mouse model [12]. These findings, together with other favorable properties of **7.44** [11], such as low

molecular weight, a high ligand efficiency, and a non-complex chemical structure, suggest that **7.44** could serve as a lead structure to guide the development of structurally related compounds with increased binding affinity, improved bioavailability, and enhanced anti-leukemic effects to inhibit RUNX1/ETO oncogenic function in t(8;21) AML. However, biophysical and structural characterization of **7.44** binding to the NHR2 domain has not been done yet. Likewise, the compound has not yet been characterized as to physicochemical, pharmacokinetic, and toxicological properties.

In this study, we established biophysical assays based on differential scanning fluorimetry (also termed thermal shift assay (TSA)) and microscale thermophoresis (MST) to determine the binding affinity of **7.44** to NHR2 and show that the dissociation constant of **7.44** from the NHR2 dimer, K_{lig}, is 3.95 ± 1.28 μM. We also suggest how **7.44** interferes with NHR2 tetramer stability based on integrative modeling using saturation transfer difference NMR (STD-NMR) and multidimensional NMR experiments as well as molecular dynamics (MD) simulations of free ligand diffusion. These studies indicate that **7.44** binds at the NHR2 termini and reveal moieties of **7.44** important for binding. Finally, we report favorable physicochemical, pharmacokinetic, and toxicological properties of **7.44**. These results are a significant step towards understanding how **7.44** inhibits NHR2 tetramerization at the molecular level and should aid in the development of improved inhibitors of NHR2 tetramerization.
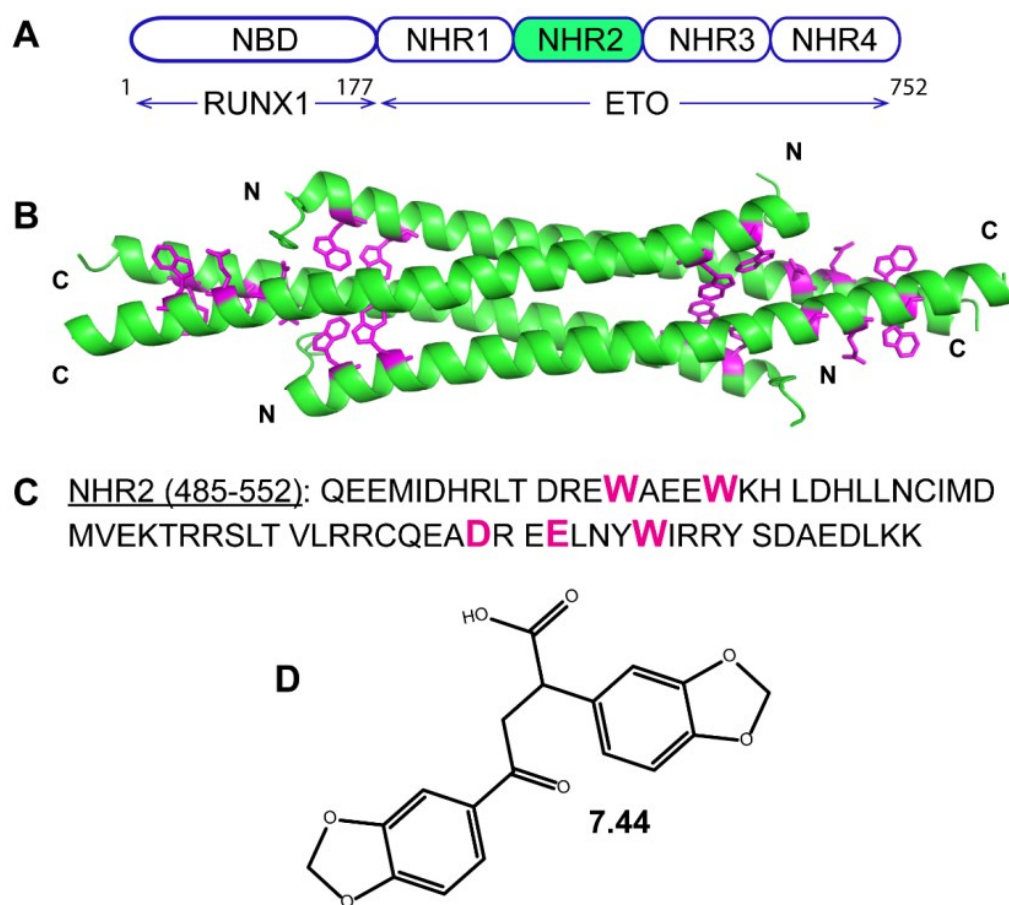
Figure 1. Schematic representation of RUNX1/ETO tetramerization. A) Depiction of the chimeric RUNX1/ETO fusion protein containing the nucleotide-binding domain (NBD) and four *nervy homology regions* (NHR). The NHR2 domain (marked in green) mediates homo-tetramerization. B) X-ray crystal structure (PDB ID 1WQ6) of the NHR2 domain. C) Amino acid sequence of the NHR2 domain. In B) and C) predicted hot spot residues [11] are highlighted in magenta. D) Molecular structure of **7.44**.

Materials & Methods

Cloning, expression, and purification

Codon-optimized synthetic DNA (Genscript Biotech) of the NHR2 domain (residues 485-552 of human RUNX1/ETO) or M5 variant (five residues of the NHR2 domain W498, W502, D533, E536, and W540 were mutated to alanine) was cloned into expression vector pETSUMO in *E. coli* Rosetta (DE3)pLysS (Invitrogen).

The NHR2 domain or M5 variant was expressed as a SUMO (small ubiquitin-related modifier) fusion protein. The transformed *E. coli* was transferred into dYT-medium (10 g yeast extract, 5 g NaCl, and 16 g tryptone or peptone), containing kanamycin and chloramphenicol, and incubated at 37 °C until an OD_{600} of ~1 was reached. The expression was induced by adding isopropyl-1-thio-β-D-galactopyranoside to 1 mM final concentration. The expression was continued overnight at 25 °C. The cells were harvested by centrifugation and disrupted via sonification.

The same purification protocol for the SUMO fusion protein was used as mentioned earlier [13]. In brief, the fusion protein was purified by nickel affinity chromatography (cell lysis buffer- 50 mM sodium phosphate, 300 mM sodium chloride, 10 mM imidazole, pH 8) on a HisTrap column (elusion buffer- 50 mM sodium phosphate, 300 mM sodium chloride, 500 mM imidazole, pH 8) and the 6His-SUMO tag removed by incubation with the SUMO protease (1:100 ratio) 50–150 μg/ml followed by affinity chromatography [14]. Cleaved products were further purified by S-75 size exclusion chromatography (SEC buffer- 50 mM sodium phosphate, 50 mM sodium chloride, 1 mM DTT, pH 8) (GE Healthcare Life Sciences) .The purity of the protein was inspected using a 15% SDS PAGE (**Figure S1**). Isotope labeling of NHR2 was achieved in ~98% D_2O-containing M9 media supplemented with ^{13}C-glucose and ^{15}N-NH$_4$Cl as sole carbon and nitrogen sources, respectively. The labeled protein was purified with the same protocol as the unlabeled one. The M5 variant was purified with the same protocol as the NHR2 domain except for the SEC step: After SUMO cleavage, the M5 variant was precipitating; thus, high salt was used for the SEC step (SEC buffer- 50 mM sodium phosphate, 300 mM sodium chloride, 1 mM DTT, pH 8). The concentration of NHR2 was determined (at 280 nm) using the molar extinction coefficient of 19480 M^{-1} cm^{-1} with molecular weight of 8547 Da, and 2980 M^{-1} cm^{-1} and 8100 Da for the M5 variant, respectively, calculated using the online server ProtParam.

Inhibitor compound 7.44

The compound **7.44 (Figure 1D)** was kindly provided by the Developmental Therapeutics program, National Cancer Institute, USA (NCI code 162496). The **7.44** molecule was dissolved in DMSO-d_6 as a 100 or 150 mM stock solution and stored at -20 °C for future use. The purity of the compound was shown to be >90% by LC-MS (**Figure S2**) and NMR techniques (**Figure 4A)**, and it was used without further purification.

Size exclusion chromatography

Size exclusion chromatography (SEC) was performed with a Superdex 75 Increase 10/300 GL (GE Healthcare Life Sciences) column connected to ÄKTApure (Cytiva Life Sciences). Column efficiency was tested as described by the company [15]. The sample was prepared with 30 µM of NHR2 alone and in complex with a 1:1, 1:2, and 1:5 molar stoichiometric ratio of **7.44**, prepared in 50 mM sodium phosphate, 300 mM sodium chloride, 0.5 mM tris(2-carboxyethyl)phosphine, 3% (v/v) DMSO, pH 7.5 with a total volume of 250 µl, and filled into a 1 ml sample loop operated at a flow rate of 0.7 ml/min. The column was equilibrated with the same buffer as the sample buffer. Samples were incubated at 37 °C for 2 hours and then incubated overnight at room temperature before the experiment.

Differential scanning fluorimetry

The method was applied as described in Kroeger *et al.*[16]. In short, the fluorescent dye SYPRO Orange interacts with hydrophobic surfaces of denatured proteins. This interaction changes the quantum yield of the dye [17, 18]. The fluorescence was measured with the real-time thermo-cycler qTOWER 2.0 (Analytik Jena AG, Germany). Here, 0.2 mg/ml NHR2 containing a His-tag were mixed with SYPRO Orange (1:1000) and **7.44** with concentrations ranging from 143 µM to 5.72 mM. The fluorescence signal was measured at the starting temperature (25 °C). The temperature was then increased by 1 °C/min up to 100 °C. With every increase in temperature, the fluorescence was measured. Every measurement was performed at least eight times independently.

Circular dichroism spectroscopy

Far-UV circular dichroism (CD) spectra, used to investigate the thermal unfolding of NHR2 and the NHR2-**7.44** complex, were obtained using a JASCO Model J-815 CD spectrometer (Jasco, Japan) equipped with a temperature-controlled cell holder using a quartz cell with a 1-mm path length. The sample of 12.5 µM NHR2 for the apo form and, in addition, 200 µM of **7.44** for the complex was diluted in 10 mM sodium phosphate, 10 mM sodium chloride, 0.5 mM tris(2-carboxyethyl)phosphine, <1% (v/v) DMSO pH 6.5. The spectra were collected from

the wavelength of 190–250 nm for apo NHR2 and 213-250 nm for the complex sample with accumulations of 20 scans at a speed of 200 nm min^{-1} at 25 °C. The thermal denaturation was recorded at the spectral minima of 222 nm by increasing the temperature from 25 °C to 95 °C in 1 °C increments with a slope of 1 °Cmin^{-1}. CD curves were plotted using the Origin software (OriginLab Corporation, USA).

Microscale thermophoresis

Prior to the MST experiments, purified NHR2 protein was labeled either with the dye Alexa Fluor® 488 (NHS Ester Protein Labeling kit, ThermoFisher Scientific, USA) or Monolith NT^{TM} (Protein Labeling Kit Blue-NHS, NanoTemper GmbH, Germany). The labeling was achieved by incubating 115 µM of protein and 350 µM of dye (465 µl reaction volume) for 1 h at room temperature, followed by 35 min at 30 °C in a buffer consisting of 20 mM sodium phosphate, 50 mM sodium chloride, pH 8.0 (MST buffer). The dye-labeled protein was purified using a PD-10 column containing Sephadex G-25 Medium (GE Healthcare Life Sciences) and then centrifuged at 50000 rpm for 30 min. The concentrations and the efficiency of the labeling were determined as indicated in the manual.

To determine the constant of dissociation of the NHR2 tetramer into dimers (K_{tet}, **Eq. S1a**), 10 µl of 100 nM labeled NHR2 in MST-buffer (included with the capillary set from NanoTemper) was mixed with 10 µl unlabeled NHR2 with concentrations ranging from 10.3 nM to 337.5 µM, and the mixtures were incubated in the dark for 30 minutes.

To determine the EC_{50} of **7.44** binding to NHR2 protein, 100 nM of labeled NHR2 was mixed with **7.44** to concentrations ranging from 122 nM to 4 mM to the final volume of 50 µl (serial 1:1 dilution) in MST buffer containing 10% (v/v) DMSO. The samples were incubated overnight in the dark before the experiment. Each dilution was filled into Monolith NT.115 standard treated capillaries (NanoTemper Technologies GmbH). Thermophoresis was measured using a Monolith NT.115 instrument, with an excitation power of 50% for 30 s and MST power of 40% at an ambient temperature of 24 °C. Triplicates of the same dilution were measured. Microscale thermophoresis results were analyzed by the MO affinity analysis software (NanoTemper Technologies GmbH)

The data was analyzed and the K_{tet} (**Eq. 1**) or EC_{50} (**Eq. 2**) calculated using the MO affinity analysis software (NanoTemper, Germany), considering a 1:1 model.

$$f(c) = [\text{unbound}] + \frac{[\text{bound}] - [\text{unbound}]}{2 * \left(FluoConc + c + K_{\text{tet}} - \sqrt{(FluoConc + c + K_{\text{tet}})^2 - 4 * FluoConc * c}\right)} \quad \text{Eq. 1}$$

Here, $f(c)$ is the fluorescence intensity, [*unbound*] is the concentration of unbound labeled and unlabeled NHR2, [*bound*] is the concentration of bound labeled and unlabeled NHR2, *FluoConc* is the concentration of labeled NHR2, c is the concentration of unlabeled NHR2.

$$f(c) = [\text{unbound}] + \left(\frac{[\text{bound}] - [\text{unbound}]}{1 + \left(\left(\frac{EC50}{c}\right)^n\right)}\right) \quad \text{Eq. 2}$$

Here, $f(c)$ is the fluorescence intensity, [*unbound*] is the concentration of unbound labeled NHR2, [*bound*] is the concentration of bound labeled NHR2, c is the concentration of **7.44**, n is the Hill coefficient. For **7.44** binding to NHR2, an additional 1:2 model included in the PALMIST software was considered to assess the MST data [19, 20]; this model takes into account the symmetry of an NHR2 dimer, which would allow binding of two **7.44** per dimer. The dissociation constant of **7.44** from an NHR2 dimer, K_{lig}, was finally calculated using **Eqs. S1 to S12** by solving the equation systems with SymPy [21] and estimating the error with functions from Hans Dembinski [22].

NMR spectroscopy

NMR experiments were performed at 298 K or 308 K on Bruker Avance III HD spectrometers operating at 600 MHz, 700 MHz, or 750 MHz, equipped with 5 mm triple resonance TCI (^{1}H, ^{13}C, ^{15}N) cryoprobes and shielded z-gradients. Data was processed on NMRPipe [23] and analyzed by NMRView [24] software or TopSpin 3.2 (Bruker BioSpin). Sodium 2,2-dimethyl-2-silapentane-5-sulfonate (DSS) was used for chemical shift referencing.

Assignment of ligand 7.44

For the assignment of the ^{1}H resonances of ligand **7.44,** we prepared a solution of 2 mM of the ligand in 20 mM sodium phosphate buffer, pH 7.4, containing 100 mM sodium chloride and 10% (v/v) D_2O at 298 K. The assignment of the protons of the ligand was achieved by the analysis of the 1D ^{1}H and 2D ^{1}H,[1]H-TOCSY spectra and aided by ^{1}H chemical shift prediction as performed by the ChemNMR package, contained within the software ChemDraw (PerkinElmer). The 2D ^{1}H,[1]H-TOCSY spectrum was acquired with 8 transients in a matrix with 2k data points in F2 and 256 increments in F1 with a relaxation delay of 1.0 s. "The obtained chemical shifts of ligand **7.44** were as follows: δH2''= 6.09 ppm (*s*); δH4''= 7.41 ppm ($J = 1.7$ Hz, d); δH3a= 3.66 ppm ($J = 8.4$; 17.5 Hz, dd); δH3b= 3.36 ppm ($J = 7.3$; 17.5 Hz, dd); δH2=

3.96 ppm (J = 7.7 Hz, t); δH4'= 6.89 ppm (J = 1.4 Hz, d); δH2'= 5.95 ppm (*s*); δH6' and 7'=
6.86 – 6.81 ppm (*overlapped*); δH6"= 7.65 ppm (J = 6.8; 10.1 Hz, dd); δH7"= 6.98 ppm (J =
8.4 Hz, d).

pKa value determination of 7.44

For the pKa value determination, 23 samples of 200 μM concentration of **7.44** were prepared
from the pH range of 2 to 13 (pH of 0.5 steps) in 50 mM sodium phosphate, 100 mM sodium
chloride, 10% (v/v) DMSO-d_6. 1D ^{1}H-NMR experiments were performed using 256 scans for
each sample. ^{1}H chemical shift values were extracted for the reporter protons using TopSpin
3.2 (Bruker BioSpin). The pKa was calculated using the chemical shifts of the protonated and
unprotonated forms and their corresponding mole fraction values applying the Henderson-
Hasselbalch equation as explained by Gift *et al.* [25]. The data were processed and plotted with
the Origin software (OriginLab Corporation, USA).

Saturation transfer difference NMR

For the STD-NMR experiments, two samples were prepared in 20 mM sodium phosphate,
50 mM sodium chloride, 0.5 mM tris(2-carboxyethyl)phosphine, 5% (v/v) DMSO$_{d6}$, pH 6.5,
and 10% (v/v) D$_2$O, in which the ^{13}C, ^{15}N-NHR2 concentration was 50 μM and the ligand
concentration was either 0 or 5000 μM for the reference and mixture, respectively. The STD-
NMR spectra were acquired at 308 K with 512 scans. Selective saturation of protein resonances
(on-resonance spectrum) was performed by irradiating at 0.6 ppm for a total saturation time of
2 s. For the reference spectrum (off-resonance), the samples were irradiated at -30 ppm. To
obtain an STD effect, the subtraction was performed internally via phase cycling after every
scan to minimize artifacts arising from temperature and magnet instability [26]. Proper control
experiments were performed with the reference sample to optimize the frequency for protein
saturation and off-resonance irradiation, to ensure that the ligand signals were not affected.

The STD effect was calculated using $(I_0 − I_{STD})/I_0$, in which $(I_0 − I_{STD})$ is the peak intensity in
the STD spectrum and I_0 is the peak intensity in the off-resonance spectrum. The STD intensity
of the largest STD effect was set to 100% as a reference, and the relative intensities were
determined [27]. The binding epitope is created by the comparison of the STD intensity relative
to the reference one, and this relative intensity value is described by the STD amplification
factor (A_{STD}).

Assignment of uniformly ^{2}H, ^{13}C, ^{15}N-labeled NHR2 and interaction with 7.44

For 3D NMR experiments, 325 μM of uniformly ^{2}H, ^{13}C, ^{15}N-labelled NHR2 in NMR buffer (20 mM sodium phosphate, 50 mM sodium chloride, 0.5 mM tris(2-carboxyethyl)phosphine, 10% (v/v) D_2O, pH 6.5) was transferred into a 5 mm Shigemi tube (Sigma-Aldrich), and the experiments were performed at 308 K. Sequence-specific assignments were carried out using standard TROSY-based triple resonance experiments (HNCO, HN(CO)CA, HNCACB, HN(CO)CACB, ^{1}H,^{15}N-NOESY-HSQC, ^{1}H,^{15}N-TROSY-HSQC) [28, 29].

For the interaction experiments, two NMR samples, 47 μM of ^{2}H, ^{13}C, ^{15}N-labelled NHR2 alone or in complex with 2 mM of **7.44**, were prepared in NMR buffer, which in addition contained 10% (v/v) DMSO$_{d6}$, with a total volume of 200 μl and transferred into 3 mm NMR tubes.^{1}H-^{15}N-TROSY-HSQC experiment was performed using 216 scans per increment (about 19 hours) for both the samples at 353 K [28, 29].

In vitro **pharmacokinetics and toxicology prediction**

The ADME property data was generated by Pharmacelsus GmbH, Saarbrücken, Germany. The methods of the six assays, aqueous solubility, plasma protein binding, plasma stability, hepatocyte clearance measurements, chemical stability, and Cytochrome P450 (CYP) inhibition, are described in detail in the Supporting Information. Further pharmacokinetic parameters were computed using the QikProp-Schrödinger suite (Release 2021-2) [30]. A computational toxicology assessment was performed using the toxicology modeling tools DEREK Nexus® (Derek Nexus: 6.0.1, Nexus: 2.2.2) [31] and SARAH Nexus® (Sarah Model - 2.0 Sarah Nexus: 3.0) [32] from Lhasa Limited, Leeds, UK.

Molecular dynamics simulations

To investigate interactions between **7.44** and NHR2 in full atomic detail, we performed unbiased molecular dynamics (MD) simulations of **7.44** binding to NHR2. We used the tetrameric crystal structure of NHR2 (PDB ID 1WQ6); hereafter, we follow the residue numbering of the whole fusion protein RUNX1/ETO [1]. The protein structure was prepared using Maestro [33] for pH 7.4 to mimic physiological conditions. All titratable residues are present in the ionic state, except for histidines, which were assigned to the HID state. The initial 3D structure of **7.44** was prepared according to the 2D structural formula in **Figure 1D** and using the *S*-configuration. The initial 3D structure was geometry optimized at the HF/6-31G* level of theory using Gaussian 09 [34]. The optimized 3D structure was used for subsequent binding simulations. To do so, we randomly placed the tetrameric NHR2 structure, two **7.44**

molecules, and sodium ions using PACKMOL [35]. The systems were solvated with the TIP3P solvent model, also using PACKMOL [35]. All relevant system files for subsequent simulations were generated using LEaP of Amber17 [36]. That way, we prepared a set of 35 independent initial configurations for MD simulations of **7.44** binding to NHR2. We applied the Amber ff14SB force field [37] for the protein and the GAFF force field [38] for **7.44**. Missing atomic partial charges of **7.44** were derived according to the restraint electrostatic potential (RESP) fit procedure [39, 40]. Ion parameters were taken from reference [41].

Details of the minimization, thermalization, and equilibration protocol are reported in ref. [42], which was successfully applied to study ligand binding processes [43, 44]. In short, the solvated systems were subjected to three rounds of energy minimization to eliminate bad contacts. Subsequently, systems were heated to 300 K, and the pressure was adapted such that a density of 1 g cm^{-3} was obtained. During thermalization and density adaptation, we kept the solute fixed by positional restraints of 1 kcal mol^{-1} Å^{-2}, which were gradually removed. Subsequently, the systems were subjected to unbiased production simulations of 1000 ns length each to study **7.44** binding to NHR2 at a **7.44** concentration of ~1.2 mM. During these simulations, all molecules were allowed to diffuse freely without any artificial guiding force. All minimization, equilibration, and production simulations were performed with the pmemd.cuda module [45, 46] of Amber17 [36]. During production simulations, we set the time step for the integration of Newton's equations of motion to 4 fs following the hydrogen mass repartitioning strategy [47]. Coordinates were stored into a trajectory file every 200 ps.

To identify epitopes on the NHR2 tetramer, where **7.44** preferentially binds, we computed occurrence propensities of heavy atoms of **7.44** around the tetramer structure (using the grid command in cpptraj and a grid spacing of 0.5 Å). For this, only frames were considered where any heavy atom of **7.44** is within 4 Å of any heavy atom of NHR2.

To observe how **7.44** interacts with the NHR2 tetramer, we first recorded for the whole trajectory, with which residues the ligand interacts (distance between heavy atoms < 4 Å). This constitutes for each frame a 244 bits vector. For further analysis, we only considered frames where the ligand interacts with at least five residues. After accounting for the internal symmetry of NHR2 by orienting all frames to a standard orientation, we applied a hierarchical clustering approach as implemented in scipy, using the Jaccard distance as a metric and a distance cutoff between cluster centroids of 0.3. The three most populated clusters from this approach correspond to the areas of highest propensity shown in **Figure 5**.

Details about the setup and performance of MD simulations for calculating the PAMPA permeability of **7.44** in its protonated and deprotonated form can be found in the Supplemental Notes.

Results

Expression, purification, and oligomer state of the NHR2 domain and the M5 variant

The NHR2 domain was overexpressed and purified, and the resulting material yielded homogeneous, monodisperse species in solution. The sample was homogenous as analyzed by size exclusion chromatography (SEC) (**Figure 2A**), SDS-PAGE (**Figure S1**), and dynamic light scattering (DLS) (**Figure S3**). The oligomeric state of purified NHR2 was assessed by analytical ultracentrifugation (AUC) (**Figure S4**). The sedimentation profiles of NHR2 show a single major species with a sedimentation coefficient (*S* value) of 3.07, which corresponds to the molecular weight of 37.3 kDa. This value is in agreement with the calculated molecular weight of an NHR2 tetramer of 34.2 kDa. The weight percent contribution of the tetramer in 35 µM of NHR2 is 94% as obtained by integration of the continuous sedimentation coefficient distribution function. To check the function of the purified NHR2, we performed isothermal titration calorimetry (ITC) with the HEB fragment of E proteins (HEB (176-200)). The NHR2 domain has been shown to interact with the HEB fragment [48]. The resulting isotherm (**Figure S5**) yielded a binding enthalpy $\Delta H = -15 \pm 6$ kcal/mol and a dissociation constant $K_D = 30 \pm 4$ µM, and this K_D value is in the same range as previously reported [48].

The SEC profile of NHR2 showed peaks that likely correspond to higher-order oligomer (a), tetramer (b), and dimer (c) (black in **Figure 2A**). Integration of peaks (b) and (c) reveals a relative abundance of 92% for the tetramer and 8% for the dimer, similar to the AUC data. These data are consistent with previously published sedimentation results [7, 10]. Earlier it was shown that the M5 variant forms a dimer but not a tetramer [10]. This finding is concordant with the crystal structure of NHR2 (PDB ID 1WQ6) [7], which reveals a four-helix bundle formed by four amphipathic α-helices, consisting of a symmetric dimer of dimers, where monomers in a dimer are oriented in a head-to-tail orientation. The M5 variant was overexpressed, purified, and characterized by SEC (**Figure 2A**), SDS-PAGE (**Figure S1**), and AUC (**Figure S4**). The SEC profile of the M5 variant showed higher-order oligomers (a), a potential contribution of tetramers (b), and dimer (c) (cyan in **Figure 2A**). The high intensity of elution peak (a) is concordant with the increased instability of the variant, which shows a higher tendency to form oligomers. AUC data of the M5 variant showed a slightly greater molecular weight compared to the theoretical one. Therefore, to confirm the dimeric state of the M5 variant, we performed AUC for the SUMO-M5 fusion protein, where we observed a measured molecular weight of 43.4 kDa, which agrees very well with the theoretical one of 43.9 kDa for the dimer (**Figure S4**).

Influence of 7.44 on the NHR2 tetramer stability

Next, we analyzed the stability of the NHR2 tetramer in the presence of **7.44** by SEC, differential scanning fluorimetry (DSF), and CD spectroscopy [16, 49]. The SEC chromatograms indicate that increasing **7.44** concentrations lead to an increase in the relative ratio of NHR2 dimer to tetramer in the sample (**Figure 2B**). **7.44** alone, measured as a control, does not show any absorbance (**Figure 2B**). Peak (c) of the dimer species increases with increasing **7.44** concentration, most probably due to a shift in the equilibrium from the tetramer to the dimer, indicating that **7.44** interferes with NHR2 tetramer stability. The decrease in the height of peak (b) of the tetramer species is not monotonic. Note, however, that the peak heights are inversely mirrored by those of peak (a) of higher-order oligomers. Due to the involvement of higher-order oligomers and the possibility that the absorption characteristics of **7.44** change when interacting with NHR2, which may contribute to the height of peak (c), we refrained from analyzing this data quantitatively.

In DSF, the thermally induced protein unfolding is monitored by the binding of the fluorescent dye SYPRO Orange [50] to the hydrophobic core of a protein that becomes exposed upon unfolding, leading to a related increase in fluorescence emission. The temperature at the midpoint of the unfolding transition is defined as the melting temperature (T_m) of the protein [47]. Usually, interference of a ligand with a protein results in a shift in T_m of the protein compared to the native state [49] and monophasic melting [51]. However, we previously showed that the melting points of the NHR2 dimer and NHR2 tetramer are ~55 °C and ~85 °C, respectively [10]. Inhibition of NHR2 tetramer formation by **7.44** should alter the proportions of the two species in a dose-dependent manner towards the dimer [11], as also suggested by the SEC results. In such cases, rather than a monophasic melting at an intermediate melting temperature, a biphasic melting can occur, with NHR2 appearing to melt at the melting temperatures of the dimer and the tetramer [51]. Over a concentration range of **7.44** of a factor of ~100, melting occurs at 84-85 °C (**Figure 2C, Figure S7**), suggesting that this melting point relates to the tetramer species. The height of the fluorescence peak associated with this melting decreases with increasing **7.44** concentration (**Figure 2C**), indicating that the NHR2 tetramer concentration in the equilibrium declines. As to the melting of the dimer species at ~55 °C, an increase in the fluorescence signal at that temperature with increasing **7.44** concentration is observed, indicating that the NHR2 dimer concentration in the equilibrium rises. However, no clear melting points can be detected, because of an overlay with a strong and, with increasing temperature decreasing, fluorescence signal that has its maximum at ~30 °C. The fluorescence signal at that temperature also roughly increases with **7.44** concentration. This fluorescence

signal may be explained in that dimeric NHR2 exposes its hydrophobic protein-protein interface [10] to which SYPRO Orange can bind; a temperature increase disfavors SYPRO Orange binding, which leads to a decrease in fluorescence [16]. Although these results demonstrate that **7.44** interferes with NHR2 tetramer stability and leads to a decline in NHR2 tetramer concentration with increasing **7.44** concentration, a quantitative analysis of this data is compromised due to the lack of a clear melting point at ~55 °C [51].

We also examined the thermal stability of NHR2 in the absence and presence of **7.44** by CD spectroscopy. The minima at negative ellipticity values at 208 nm and 222 nm wavelength indicate the presence of an α-helical structure in NHR2 in the absence of **7.44** (**Figure S6**), as expected from the crystal structure [7]. Upon addition of **7.44**, the ellipticity curve followed the same trend as for free NHR2, demonstrating that the α-helical structure is retained in the presence of **7.44** (**Figure S6**); likewise, the dimeric M5 variant also retained the α-helical structure [10]. Note that due to the high voltage in the detector caused by the presence of DMSO in the buffer, the spectrum was recorded only from 213 nm to 250 nm wavelength. Therefore, the impact on the thermal stability of NHR2 by **7.44** was monitored at 222 nm wavelength (**Figure 2D**). Both *apo* NHR2 and NHR2 in the presence of **7.44** exhibited a cooperative biphasic melting (**Figure 2D**). The melting point (T_m) of the first transition is ~48 °C, indicative of melting of the dimer, and the second T_m is ~88 °C, indicative of melting of the tetramer [10, 51]. The T_m of the tetramer is similar to the result from DSF (see above) and previous CD experiments [10]. For the dimeric M5 variant, a melting point of 60 °C was reported, associated with a broad transition between the folded and unfolded state [10]. The first phase transition is more pronounced in the presence of **7.44**, indicating a higher population of dimers due to the interference of **7.44** with NHR2. In addition, the second phase transition of NHR2 in the presence of **7.44** occurs at a lower temperature and is broader, suggesting a less tight association between the NHR2 a-helices.

To conclude, these results demonstrate that **7.44** interferes with NHR2 tetramer stability. Furthermore, the increase in the dimer population upon the addition of **7.44** indicates that **7.44** fosters a tetramer-to-dimer transition of NHR2.
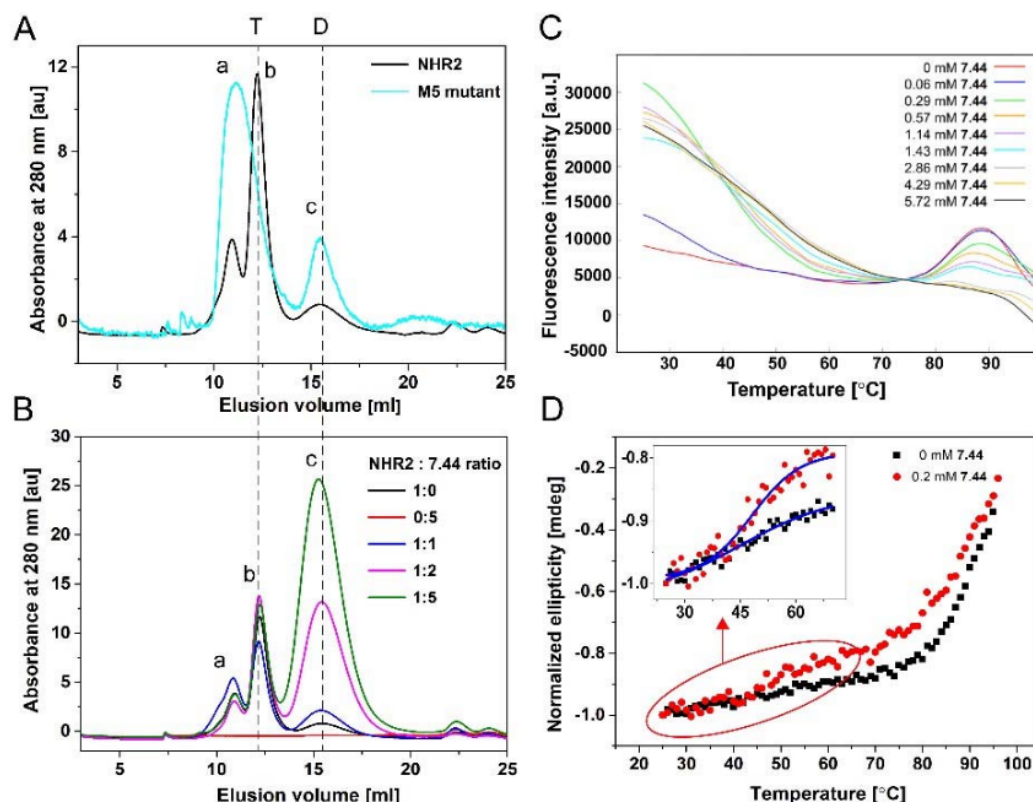
Figure 2. Stability of the NHR2 tetramer with and without 7.44 studied by size exclusion chromatography, DSF, and CD spectroscopy. A) Elution profiles of purified proteins of the NHR2 domain (black) and M5 variant (cyan) from size exclusion chromatography (SEC) obtained at 280 nm absorbance: Higher-order oligomers (a), tetramer (b), and dimer (c). The integration of peaks (b) and (c) of the NHR2 domain yields 92% of the tetramer and 8% of the dimer. **B)** Elution profiles of 30 μM of apo NHR2 (black), 150 μM of **7.44**, and NHR2:**7.44** with molar ratios of 1:1 (blue), 1:2 (magenta), and 1:5 (green) obtained from SEC at 280 nm. Samples were incubated at 37 °C for 2 hours and then incubated overnight at room temperature prior to the experiment. **C)** Fluorescence intensity in the presence of **7.44** at different concentrations; for better visualization, the curves were shifted along the y-axis to match them at the point between the two melting points of dimer and tetramer. **D)** Thermal denaturation of apo NHR2 (black) and NHR2 in the presence of **7.44** (red) monitored by CD spectroscopy at 222 nm wavelength. The CD data was normalized with respect to the highest ellipticity value for better comparison.

Dissociation constants of the NHR2 tetramer and of 7.44 with respect to the NHR2 dimer

For determining the dissociation constant of **7.44** binding to NHR2, K_{lig} (**Eq. S1b**), the tetramer-to-dimer equilibrium upstream of the ligand binding needs to be considered (**Eq. 4**), characterized by the dissociation constant K_{tet} (**Eq. S1a**). For that, we assume that tetrameric NHR2 (T) is in equilibrium with its dimer (D) and that **7.44** (L) binds to D after dissociation of T, leading to **Eq. 4**. Because of the large distance between the anticipated binding sites at the hot spot regions (**Figure 1C**), we furthermore assume that K_{lig} of the first and second ligand binding events are identical.

$$T \overset{K_{tet}}{\rightleftharpoons} D \overset{K_{lig}}{\rightleftharpoons} DL \overset{K_{lig}}{\rightleftharpoons} DLL \qquad\qquad \text{Eq. 4}$$

We determined K_{lig} by microscale thermophoresis (MST) measurements as a function of K_{tet} and EC_{50} of **7.44** binding to NHR2 according to equations S1-S12 [52, 53]. MST is based on measuring the directed movements of molecules along a generated temperature difference (thermophoresis). The movements depend on the combined impact of size, charge, and solvation shell of the molecules. For determining K_{tet} and EC_{50}, a constant concentration of fluorescently labeled NHR2 was measured in the presence of varying concentrations of the titrants, unlabeled NHR2 or **7.44**, respectively. With increasing concentration of the titrant, the fraction of labeled NHR2 that forms a complex with the titrant will increase.

To determine K_{tet}, unlabeled NHR2 was titrated to 50 nM of labeled NHR2 in 16 concentrations ranging from 10.3 nM to 337.5 μM. MST was recorded for each sample, and a non-linear regression curve was fit with the K_D Fit equation (**Eq. 1**) (**Figure 3A**). The inflection point of the curve revealed K_{tet} = 11.3 ± 1.81 μM. Next, we titrated 16 concentrations ranging from 122 nM to 4 mM of **7.44** to 100 nM of labeled NHR2. Based on the calculated K_{tet}, more than 99% of the protein is in a dimeric state at this NHR2 concentration. This calculation was confirmed by a microfluidic diffusional sizing experiment, where 100 nM of dye-labeled NHR2 showed only dimer size, according to the measured hydrodynamic radius of 2.22 nm, with a calculated molecular weight of 16.74 kDa (**Figure S8**). After overnight incubation of the samples, MST was recorded for each sample (**Figure S9**). To obtain K_{lig}, the MST data was analyzed in two independent ways. First, the resulting binding data was fit to a non-linear regression curve to obtain the EC_{50} value (**Eq. 2**) (**Figure 3B**). The inflection point of the curve revealed an EC_{50} of 2.5 ± 0.8 μM (**Table 1**), demonstrating binding of **7.44** to NHR2 and suggesting a slow dissociation kinetic [19]. The range of Hill coefficients n = 1.0-1.5 obtained from the fits reveals no or only weakly cooperative binding of **7.44** to NHR2. A control experiment was performed using the same concentrations of **7.44** together with the labeling dye, but without NHR2. A K_{lig} = 3.95 ± 1.28 μM was subsequently computed using **Eqs. S11 and S12**. A simulation of the species distribution using K_{lig} and K_{tet} shows how both constants result in a EC_{50} of 2.5 μM, which was used as a parameter to calculate K_{lig} (**Figure S11**). As the majority of NHR2 is in a dimeric state during the MST experiments and assuming that the MST signal is dominated by the formation of DL (**Eq. 4**), one can expect that $EC_{50} \approx K_{lig}$; these values are in the range of 2 μM to 4 μM and similar within experimental uncertainties. Second, as a further control, K_{lig} was obtained from MST data by considering a 1:2 binding model, assuming that two **7.44** can bind to the symmetric NHR2 dimer, as implemented in the PALMIST software [19, 20]. This yielded K_{lig} = 2 μM, 68.3% CI [0,6] μM **(Figure S10)**, in the same range as K_{lig} and EC_{50} above, although with high uncertainty (see **Figure S10** for details).

To conclude, to our knowledge for the first time, the equilibrium constant for the dissociation of the NHR2 tetramer to NHR2 dimers and K_{lig} for **7.44** binding to the NHR2 dimer were determined.
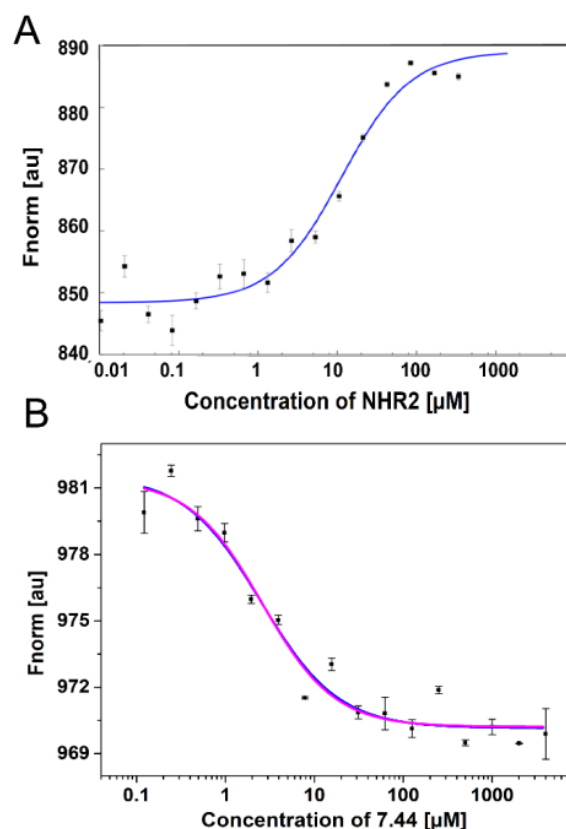
Figure 3. 7.44 binding to NHR2 detected with MST. A) Titration of unlabeled NHR2 to a constant concentration of labeled NHR2 induces a change in thermophoresis. $K_{tet} = 11.3 \pm 1.81$ µM was calculated using **Eq. 1**. **B)** Titration of **7.44** to a constant concentration of labeled NHR2 induces a change in thermophoresis. EC_{50} was calculated by fitting the data points to **Eq. 2**. The fitted values are shown in **Table 1**. The range of Hill coefficients $n = 1$-1.5 was obtained from the fits. Error bars denote the standard error in the mean and were calculated from technical triplicate.

Table 1. Binding characteristics of **7.44** binding to NHR2 from MST experiments.[a]

Analysis method	EC_{50}[b]
Thermophoresis	2.6 ± 0.8
Thermophoresis with T-jump	2.5 ± 0.8
T-jump	2.1 ± 0.7

[a] EC_{50} was calculated using **Eq. 2**.

[b] In µM.

Epitope mapping of 7.44 via STD-NMR

In order to understand how **7.44** interacts with NHR2, we used saturation transfer difference-NMR (STD-NMR) [26, 27] to identify which atoms of **7.44** come close to the protein when the

complex is formed (ligand epitope mapping). A typical STD-NMR experiment relies on the ligand exchange between the bound and free states. The difference between a spectrum without saturation of protein resonances (reference spectrum) and a saturated one yields the STD spectrum, in which it is possible to identify i) if the ligand binds to the protein (there are signals in the STD-NMR spectrum), ii) which protons of the ligand are involved in binding (only these are visible), and iii) which protons of the ligand are closer to the protein upon binding (by comparing the relative signal intensities) [26, 27].

The reference ^{1}H spectrum of **7.44** and the corresponding STD-NMR spectrum, acquired in the presence of 100-fold molar excess of **7.44**, are shown in **Figure 4A** and **B**. All **7.44** protons show a signal in the STD-NMR spectrum, which is a clear indication that **7.44** binds to NHR2, in accordance with MST data. Different protons receive differential amounts of saturation (see color scale in **Figure 4B**), which allows mapping the epitope of the ligand. Proton H7′′ shows the highest saturation and was thus set to 100%, indicating its closest proximity to the protein. Other protons of the two ring systems show relative intensities between 64% and 97%, suggesting that **7.44** binds with both ring systems to NHR2. Protons H2 and H3, which are in the connecting alkyl chain, show the lowest detectable intensities of 48% and 20%, respectively. Protons more than 5 Å away from the protein normally do not appear in the STD-NMR spectrum.

To conclude, the STD-NMR data revealed that **7.44** interacts with NHR2 via both heteroaromatic moieties.
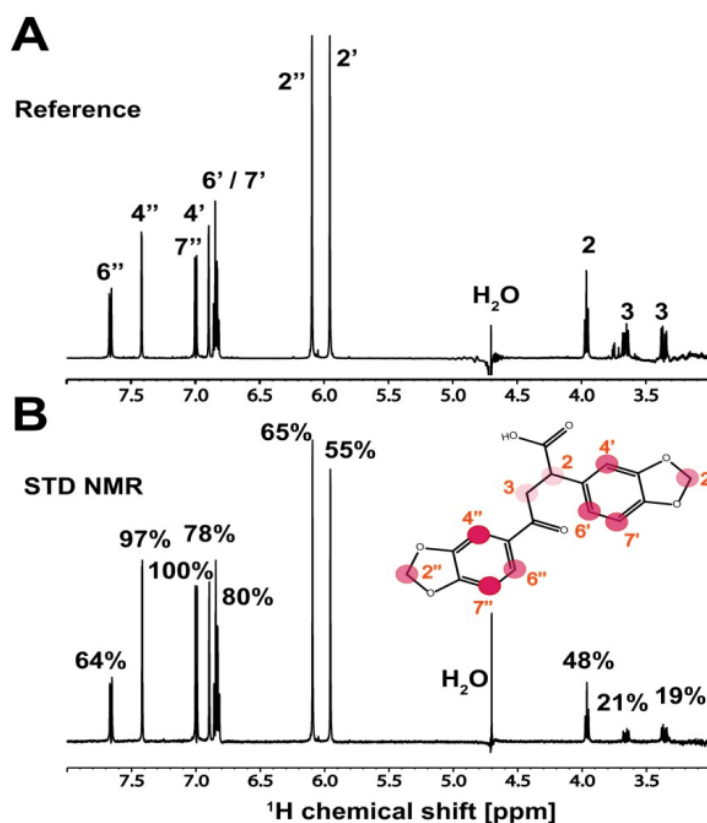
Figure 4. ¹H STD-NMR experiment of 7.44 binding to NHR2.
A) Reference spectrum of **7.44**. Assignment of the individual peaks is indicated (see **7.44** structure in the bottom panel). **B)** ¹H STD-NMR spectrum of ligand **7.44** in the presence of NHR2. Relative intensities are indicated on top of the corresponding peaks and mapped onto the structure of **7.44**. The circles are colored by the relative intensity of the protons, which is correlated with the proximity to the protein: red – 100% (the closest), lighter red– 97% to 64%, fade red – 48% to 19%. The proton numbering is indicated by the red numbers. Data was acquired at 600 MHz and 298K, with a 100-fold molar excess of **7.44**.

The presence of 7.44 induces CSPs in the NHR2 N-terminus including the predicted tryptophan hot spot residues

Next, we proceeded to study the interaction of **7.44** with NHR2 from the protein side. We started by assigning the backbone resonance peaks of NHR2. We used a 325 μM sample of uniformly [²H, ¹³C, ¹⁵N]-labeled NHR2 and followed a standard triple-resonance-based approach [28, 29]. The NHR2 concentration in these experiments was about 30-times higher than K_{tet}, shifting the equilibrium to the tetramer side. The solution NMR experiments of the tetrameric NHR2 protein were challenging due to the size and shape of the molecule [54]. The four inter-twined α-helices of 68 amino acids each led to a rod-like shape of 102 Å length (**Figure 1B**). This extended conformation results in a large rotational diffusion anisotropy, causing a poor signal-to-noise ratio and only subtle peaks to be detected in the triple resonance experiments. Furthermore, the chemical shift dispersion of the backbone amide protons is limited to values between 7.5 ppm

and 8.5 ppm. Albeit 61 backbone amide peaks were observed in the ^{1}H-^{15}N TROSY-HSQC spectrum (**Figure S12**), only 32% of these could be assigned sequence-specifically due to the low dispersion and low sensitivity in more complex (3D) experiments. The complexity of performing NMR experiments on coiled-coil assemblies is reflected in the PDB database where no solution NMR structure of a tetramer has been deposited (until October 2021) with a monomer size > 65 amino acids [54]. The number of amide cross-correlations in the ^{1}H-^{15}N TROSY-HSQC spectrum of ^{2}H, ^{13}C, ^{15}N-labeled NHR2 (**Figure 5A**) is consistent with a single conformation, indicating that NHR2 forms a symmetric homotetramer in solution. No additional amide peaks were found after three weeks of storing the NMR sample at 35 °C, indicating that no alternative oligomeric structure formed over this time. The N-terminal residues from Q485 to D495, T519, and the C-terminal residues from Y544 to K552 residues were unambiguously assigned (**Figure 5A**). These regions are most important for evaluating 7.44 binding according to our binding mode model [11].

To investigate the interaction of **7.44** with NHR2, NMR samples of ^{2}H, ^{13}C, ^{15}N-labeled NHR2 (47 µM) in the absence and presence of **7.44** (2 mM) were prepared in 10 % (v/v) DMSO, and ^{1}H-^{15}N TROSY-HSQC spectra were measured at 60 °C for 19h. **Figure 5A** shows the superposition of the spectra. Considerable chemical shift perturbations (CSPs) occur for the N-terminal residues Q485 to L493 (colored in blue in **Figure 5B**); no CSPs were found for residues at the C-terminus. Unassigned peaks also showed CSPs. In addition, the protons at the indole nitrogen of tryptophan residues (Wsc) also displayed minor CSP (insert in **Figure 5A**).

The most affected residues are H491 and R492 (**Figure 5A, B, D**). R492 is likely important for tetramerization as it forms a salt bridge with D533 and a solvent-exposed salt bridge with E536 that, in turn, interacts by a charge-assisted hydrogen bond with the indole NH of W540 [11]. Hence, the CSP suggest that **7.44** interferes with these interactions. Even though the backbone chemical shift assignments are also missing for the other two hotspot tryptophane residues (W498, W502; NHR2 contains three tryptophans in total), weak CSP of tryptophan side chains (Wsc) suggest that at least one (or even two) hotspot residue(s) is (are) involved in binding or experience a change in the environment (insert in **Figure 5A**). No signals for a third Wsc were observed, likely due to signal overlap or a low signal-to-noise ratio.

To conclude, CSP of NHR2 residues in the presence of **7.44** indicate interactions or conformational changes, particularly involving R492 in the N-termini, which is associated with three hotspot residues. At least one or two tryptophan side chains are involved; all three tryptophans of NHR2 were predicted as hot spots [11].

Figure 5. TROSY-HSQC NMR experiments of ²H, ¹⁵N, ¹³C-labeled NHR2 in the absence and presence of 7.44. A) 2D ¹H-¹⁵N TROSY-HSQC spectra of 47 μM of apo NHR2 (blue) and in complex with 2 mM of **7.44** (red). Both spectra were recorded at 60 °C on a 750 MHz spectrometer for about 19 hours each and illustrate the changes in amide proton and nitrogen chemical shifts induced in NHR2 upon binding of **7.44**. 32% of amide signals from the N- (light blue; residues Q485 to D495, T519) and C- (light green; residues Y544 to K552) terminus were unambiguously assigned (depicted above the spectra); these residues are labeled with a single-letter code (see also panel B for the location). Note that the first five (QEEMI) and last four (DLKK) amino acids were also assigned but are not shown in the crystal structure. **B)** Chemical shift perturbations (CSPs) of residues Q485 to L493 (blue) upon addition of **7.44** mapped onto the NHR2 crystal structure (PDB ID 1WQ6). Residue R492, which shows the highest CSP, is associated with three hotspot residues (see text). **C)** Occurrence propensities of **7.44** interacting with the NHR2 tetramer from MD simulations; the densities are mapped around the NHR2 crystal structure (PDB ID 1WQ6). Assigned residues at the termini showing CSP are colored in black. The side chains of the previously identified hotspots are shown as sticks in the figure. The preferred binding epitopes with the highest densities are labeled as **I**, **II**, and **III**. Identical binding epitopes due to the internal symmetry of the NHR2 tetramer are labeled identically. Here, ligands binding to epitope **I** and **II** form interactions with the hotspots W502 and W540, respectively. **D)** Representative binding pose of **7.44** in epitope **I**. The 1,3-benzodioxole moiety inserts in between the helices, close to the hotspot residue W502. Identical binding poses are observed for all epitopes **I**.

Prediction of molecular interaction patterns of 7.44

To predict how **7.44** elicits its effect on NHR2 on a molecular level, we performed a series of MD simulations of free diffusion of **7.44** around the tetramer. We focused on the tetramer to mimic the situation in the NMR experiments where no NHR2 dimer was detectable. In these simulations, no biasing force was applied to any of the molecules. We observed multiple events of **7.44** binding to and unbinding from the NHR2 tetramer on visual inspection of the MD trajectories. By calculating occurrence propensities of **7.44** when the compound is in contact (distance between non-hydrogen atoms of **7.44** and NHR2 < 4 Å) with the NHR2 tetramer, distinct epitopes where **7.44** preferably forms contacts with the NHR2 tetramer emerge (**Figure 5B**). Due to the internal symmetry of the NHR2 tetramer, there are up to four identical locations for each epitope. Among these, epitope **I**, located between helices A and B of one dimer, is the most populated one. Here, **7.44** inserts its 1,3-benzodioxole moiety between the helices to form interactions with W502 (**Figure 5C**). In epitope **II**, only moderately less populated, the ligand intercalates between the helices A and A' of the opposing dimers with its 1,3-benzodioxole moiety in the vicinity of W540. In epitope **III**, the ligand mostly forms interactions with the N-terminal part of NHR2, which was resolved as an unstructured loop in the crystal structure.

To conclude, the highly populated epitopes **I** and **II** suggest that at least one of the 1,3-benzodioxoles forms interactions with one of two buried tryptophan residues in the tetramer complex that had been identified as hot spots before [11].

pKa value determination of 7.44 by NMR

7.44 contains a single acidic group. To determine its pKa value, NMR spectra are collected for a pH range from 2 to 13 using 200 μM of **7.44**. As the pH of the solution is changed, the position of the proton peaks in the ^{1}H NMR spectrum shift (**Figure 6A**). Sodium 2,2-dimethyl-2-silapentane-5-sulfonate (DSS) was used for chemical shift referencing and calibrated to a zero ppm value in each case. Using the assignment of **7.44** (**Figure 4A**), we identified H2 and H3 as reporter protons, which are close to the acidic group and displayed pronounced chemical shift changes over the pH titration. Then the pKa was calculated by using the chemical shifts of the protonated and unprotonated forms at the respective pH and fitting to the Henderson-Hasselbalch equation [25] (**Figure 6B**). This yielded pKa = 3.99 ± 0.01 and 3.93 ± 0.01 of the carboxylic group as indicated by proton H2 and H3, respectively.
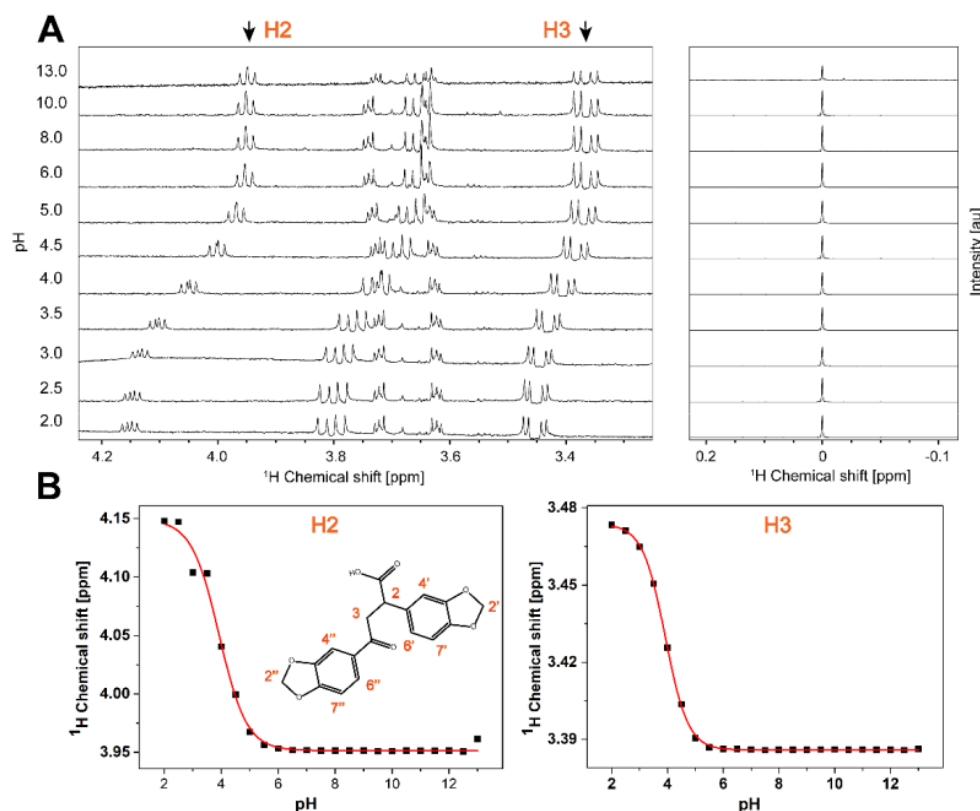
Figure 6. Determination of the pKa value for 7.44 by ¹H NMR. A) ¹H NMR spectra of 200 μM of **7.44** measured from pH 2 to 13 at 298 K at 600 MHz. Sodium 2,2-dimethyl-2-silapentane-5-sulfonate (DSS) was used for chemical shift referencing and calibrated to a zero ppm value. **B)** Titration curves obtained from the ¹H chemical shifts of the protons H2 and H3 as a function of pH. The pKa values were calculated using the Henderson-Hasselbalch equation [25], yielding a pKa value of 3.99 ± 0.01 and 3.93 ± 0.01 of the carboxylic group as indicated by proton H2 and H3, respectively.

Physicochemical, *in vitro* pharmacokinetic, and toxicological properties of 7.44

Next, we assessed physicochemical, *in vitro* pharmacokinetic, and toxicological properties of **7.44** (**Table 2, 3**). (1) *Kinetic solubility in PBS*. The aqueous solubility was determined in phosphate-buffered saline (PBS) containing 1% DMSO at pH 7.4 and yielded 177 ± 8 μM (60 μg/ml) for **7.44**. To achieve oral absorption, a compound with medium intestinal permeability and a projected human potency of 1 mg/kg needs a minimum aqueous solubility of 52 μg/ml [55]. (2) *Plasma protein binding*. Plasma protein binding was determined by the ultrafiltration procedure. This assay involves the separation of the free fraction from the bound fraction by a semi-permeable membrane with a high mass cutoff of 30 kDa. **7.44** showed a high (bound fraction: 98.4%) binding to plasma proteins from a mouse. Plasma protein binding influences the distribution of drugs in body tissues, and compounds with > 99% plasma protein binding are limited in terms of the amount of free compound that are available to act on the targeted tissue [56]. (3) *Plasma stability*. No degradation was observed for **7.44** when incubated in

mouse plasma up to 4 h at 37 °C. Hence, plasma enzymes will not significantly alter the bioavailability of the compound. (4) *Hepatocyte stability.* Metabolic conversion of **7.44** was monitored by the disappearance of the compound in the presence and absence of hepatocytes from mouse. After 120 min of incubation time, 73.8% of **7.44** remained, demonstrating a half-life time > 120 min. An intrinsic clearance rate (C_{Lint}) of 2.5 µl / min / million cells for **7.44** was obtained, indicating high hepatocyte stability. (5) *Chemical stability in PBS.* Chemical stability of **7.44** in PBS buffer at pH 7.4 was assessed for 4 h. No degradation was observed, suggesting that the compound is stable under physiological conditions for at least 4 h. (6) *Cytochrome P450 (CYP) inhibition.* Inhibition assays were performed for seven CYP isoforms at two different concentrations (1 µM and 10 µM, **Figure 7**). For **7.44**, there is a potential risk to inhibit CYP2B6, 2C9, 2C19, and 3A4 as indicated by a dose-dependent effect and inhibition > 50% at 10 µM. For the other tested enzymes CYP1A2, 2C8, and 2D6, the potential is considered low (inhibition < 25% at 10 µM resulting in estimated IC_{50} values of < 10 µM). (7) *Permeability prediction (PAMPA).* We predicted **7.44**'s permeability through a PAMPA membrane from molecular simulations and configurational free energy computations applying experimental data from nine reference compounds for calibration (**Figure 8A, Table S10**), as done before (see Supporting Information) [57]. The computed P_{eff} is 1.51×10^{-6} cm sec^{-1} for deprotonated (negatively charged) **7.44** and 8.51×10^{-6} cm sec^{-1} for the protonated (neutral) form (**Figure 8B**, **Table S11**, **Table 3**). This classifies **7.44** as low to medium (P_{eff} = 0.7×10^{-6} - 2.1×10^{-6} cm sec^{-1}) and highly permeable (P_{eff} > 4.7×10^{-6} cm sec^{-1}) [58]. (8) *Prediction of further pharmacokinetic properties.* Using Qikprop from the Schrödinger software suite [30], we predicted the central nervous system activity, the brain-blood partition coefficient, and the IC_{50} value for blockage of HERG K^{+} channels (**Table 3**). The results classify **7.44** as almost central nervous system-inactive and predict no blockage of HERG K^{+} channels. Furthermore, no violations of Lipinski's rule of five [59] or Jorgensen's rule of three [60], for judging oral bioavailability, were found. Finally, no property of **7.44** computed by Qikprop falls outside the 95% range of similar values for known drugs. (9) *Toxicology prediction.* We predicted toxicological properties of **7.44** using the softwares DEREK Nexus [31] for a variety of endpoints and SARAH Nexus [32] for mutagenicity predictions (**Table 3**). No toxicophores were identified in **7.44**, and the compound is predicted to be inactive with respect to bacterial mutagenicity.

To conclude, **7.44** has favorable physicochemical and ADME properties with high aqueous solubility, high stability in buffer and plasma, and a low hepatic intrinsic clearance *in vitro*.

There is a slight potential for CYP-related drug-drug interaction that has to be further investigated.

Table 2. Physicochemical and *in vitro* pharmacokinetic properties of **7.44**.

No.	Description	Value
1	Kinetic solubility (99% PBS, 1% DMSO)	177 ± 8 μM
2	Plasma protein binding (mouse plasma, 60 min)	$98.4 \pm 0.2\%$
3	Plasma stability (mouse plasma, 0-240 min)	No degradation
4	Hepatocyte stability (mouse hepatocytes)	2.5 μl/min/million cells
5	Chemical stability in PBS (0-4 h)	No degradation
6	Cytochrome P450 inhibition (at 1 μM and 10 μM concentration)	**See Figure 7**

Table 3. Predicted pharmakokinetic [a] and toxicological [b] properties of **7.44**.

No.	Description	Value
7	Permeability (PAMPA), deprotonated **7.44**	1.51×10^{-6} cm sec^{-1}
	Permeability (PAMPA), protonated **7.44**	8.51×10^{-6} cm sec^{-1}
8	CNS	-1
	QPlogBB	-0.75
	QPlogHERG	-2.73
	Rule of 5	0
	Rule of 3	0
	#stars	0
9	Toxicology alert count	0
	Bacterial mutagenicity	Inactive

[a] The pharmacokinetic properties were predicted as described in the text (PAMPA permeability) or with the Qikprop module of the Schrödinger software suite. CNS: The predicted central nervous system activity (–2 (inactive) to +2 (active)). QPlogBB: The predicted brain-blood partition coefficient for oral drugs (recommended range: -3.0 to 1.2). QPlogHERG: The predicted IC$_{50}$ value for blockage of HERG K$^+$ channels ($\geq$ -5 recommended). Rule Of 5: Number of violations of Lipinski's rule of five (recommended £ 4). Rule Of 3: Number of violations of Jorgensen's rule of three (recommended £ 2). #stars: The number of properties falling outside the 95% range of similar values for known drugs (0 (good) to 5 (bad)).
[b] The toxicological properties were predicted with DEREK Nexus and SARAH Nexus. Toxicology alert count: Number of predicted toxicophores. Bacterial mutagenicity: Predicted bacterial mutagenicity *in vitro*.
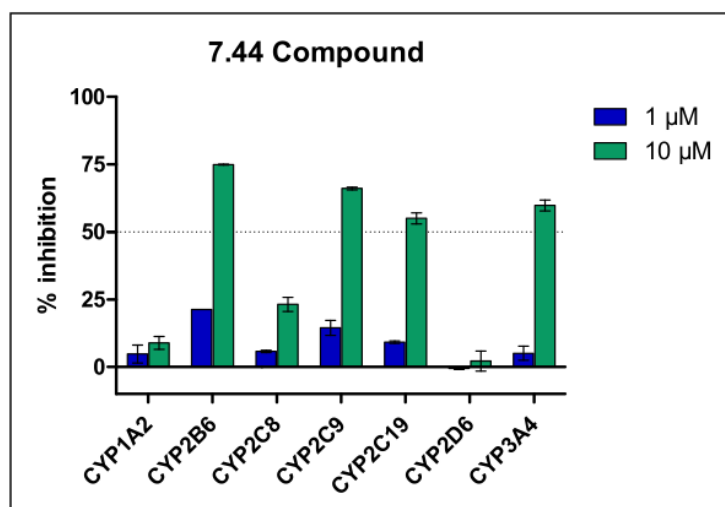
Figure 7. Cytochrome P450 (CYP) inhibition assay for 7.44. The inhibition assays were performed for seven CYP enzymes at two different concentrations, 1 µM (blue) and 10 µM (green). **7.44** showed a potential to inhibit CYP2B6, 2C9, 2C19, and 3A4. For the other tested enzymes, CYP1A2, 2C8, and 2D6, the potential is regarded low (with estimated IC_{50} values > 10 µM).
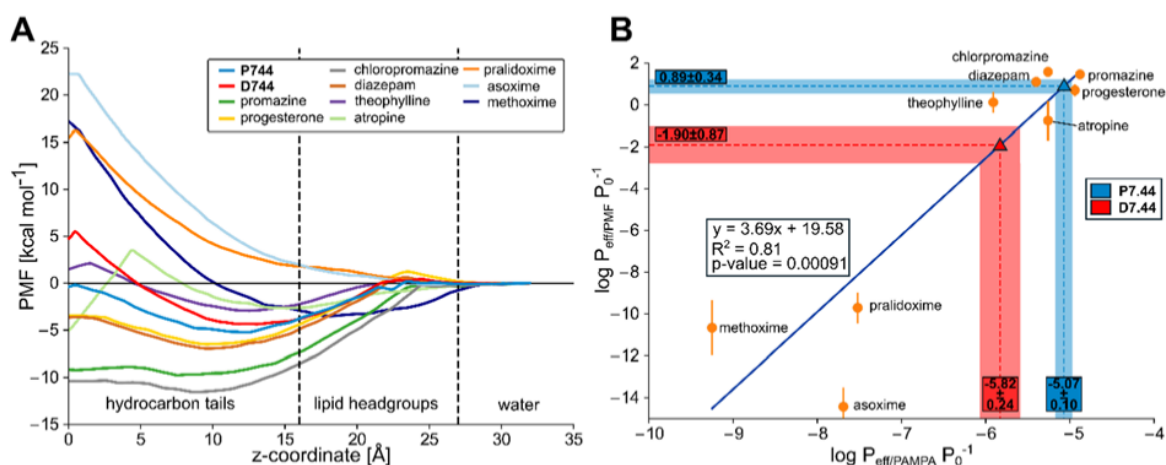
Figure 8. A) Potential of mean force (PMF) of permeation of **7.44** in a protonated (P7.44, blue) and deprotonated (D7.44, red) form, and nine calibration molecules. As a reaction coordinate, the distance to the center of a DOPC membrane bilayer was used, setting the profile in the water phase to zero. Molecules with a higher permeability (like progesterone or promazine) display favorable free energy in the membrane center, while those that are impermeable (like the oximes) display a high energy barrier in the membrane center. **B)** Calibration curve between the calculated permeabilities obtained from MD simulations and the experimental values obtained from PAMPA experiments from [58]. In blue (P7.44) and red (D7.44) are the results obtained from the simulations (y-axis, 0.89 ± 0.34 and -1.90 ± 0.87 for P7.44 and D7.44, respectively), and the corresponding predictions obtained from the calibration curve (-5.07 ± 0.10 and -5.82 ± 0.24, respectively), indicating that **7.44** is highly permeable in its protonated state and low to medium permeable in its deprotonated state. P_{eff} is the effective permeability, and P_0 is the unit factor corresponding to 1 cm sec⁻¹.

Discussion

In this study, we characterized the interaction between the NHR2 domain of RUNX1/ETO, the product of t(8;21) chromosomal translocation that has an oncogenic function in t(8;21) acute myeloid leukemia [6, 10], and the first-in-class molecule to interfere with RUNX1/ETO tetramerization, **7.44**, for targeting acute myeloid leukemia [11, 12]. We established biophysical assays based on DSF and MST to show that **7.44** interferes with NHR2 tetramer stability and increases the dimer population of NHR2, indicating that **7.44** fosters a tetramer-to-dimer transition of NHR2. We also determined the affinity of **7.44** for binding to NHR2; the dissociation constant of **7.44** from the NHR2 dimer, K_{lig}, is 3.95 ± 1.28 μM. Furthermore, by NMR spectroscopy, we show that **7.44** binds with both heteroaromatic moieties to NHR2 and interacts with or leads to conformational changes in the N-termini of the NHR2 tetramer. Combined with MD simulations of free ligand diffusion, we suggest that at least one of the 1,3-benzodioxoles of **7.44** forms interactions with one of two buried tryptophan residues in the tetramer complex that had been identified as hot spots before. Finally, we demonstrate that the pKa of **7.44** is ~3.9 and that the compound has favorable physicochemical, pharmacokinetic, and toxicological properties.

That **7.44** interacts with the NHR2 domain and interferes with NHR2 tetramer stability was shown in five independent biophysical experiments. First, SEC revealed that the amount of dimeric NHR2 increases with increasing **7.44** concentration, most probably due to a shift in the equilibrium from the tetramer to the dimer. Second, DSF revealed typical curves [16, 61, 62] (**Figure 2A**) applying protein concentrations in commonly used ranges [49, 61, 63, 64]. With increasing **7.44** concentration, the results show decreased fluorescence intensities at the previously determined melting point of the NHR2 tetramer at ~85°C [10] and generally increasing fluorescence intensities at the previously determined melting point of the NHR2 dimer at ~55°C [10]. Third, examining the thermal stability of NHR2 in the absence and presence of **7.44** by CD spectroscopy revealed a cooperative biphasic melting in both cases, with the phase transition at the temperature of dimer melting becoming more pronounced in the presence of **7.44**. These findings demonstrate that **7.44** alters the proportions of the two NHR2 species in a dose-dependent manner towards the dimer and, thus, provide biophysical evidence for the destabilization of NHR2 tetramerization by **7.44**.

Fourth, we quantified the dissociation constant of the NHR2 tetramer into NHR2 dimers (K_{tet}) and the dissociation constant of **7.44** with respect to the NHR2 dimer (K_{lig}) using MST, exploiting that the measured molecular movements along a temperature gradient depend on the size, charge, and solvation shell of the molecules [65]. With increasing concentrations, binding

of nonfluorescent NHR2 to dye-labeled one resulted in increased fluorescence intensity, whereas binding of **7.44** decreases the fluorescence intensity. From the data, K_{tet} = 11.3 ± 1.81 µM was obtained. **7.44** titration data analyzed by three independent modes yielded an EC_{50} of 2.5 ± 0.8 µM. As all three analysis modes resulted in very similar EC_{50} values, a slow dissociation kinetic of the complex is suggested [19]. According to the obtained Hill coefficients, the binding of **7.44** to NHR2 is not or weakly cooperative, in line with our previous results [11]. In the extreme case of strict binding cooperativity, the Hill coefficient reflects the number of ligand binding sites on a protein [66]; n = 1.0-1.5 then indicates a stoichiometry of about one **7.44** molecule per NHR2 monomer. From these results, K_{lig} = 3.95 ± 1.28 µM was computed, assuming that **7.44** binds in a 2:1 stoichiometry to the NHR2 dimer and that K_{lig} of the first and second ligand-binding event are identical. The assumptions are further supported in that **7.44** shifts the equilibrium from the tetramer to the dimer, the NHR2 dimer is C_2-symmetric, and the binding sites of the two ligands do not overlap (see below). The K_{lig} of **7.44** is comparable to K_D or K_i of marketed PPIM or compounds subjected to clinical trials [67], such as pentamidine [68], gossypol [69], or sulindac [70].

Fifth, we used STD-NMR to map the **7.44** epitope binding to NHR2. Multiple protons across **7.44** showed a signal in the STD-NMR spectrum, clearly indicating that **7.44** binds to NHR2, but that not all protons receive the same amount of saturation, indicating that **7.44** interacts with both heteroaromatic moieties with NHR2. These results agree well with the structural model of the **7.44** epitope proposed by us [11] and suggest that modifications at the carboxy group, e.g., a bioisosteric replacement [71] or fluorescent tagging to study in-cell properties [72], should not grossly impact the affinity.

Using multidimensional solution NMR spectroscopy, we further characterized the interaction between **7.44** and NHR2. Observing a good solution NMR spectrum of a coiled-coil domain like NHR2 is highly challenging [54] as the size (34 kDa), rod-like shape (~100 Å length), poor dispersion of the α-helical protein, and large rotational diffusion anisotropy cause poor signal-to-noise ratios in the multiple-resonance spectra [48, 54]. This issue was circumvented by using TROSY-based NMR experiments measured at high temperature on uniformly ^{2}H, ^{13}C, ^{15}N-labeled NHR2 protein. The ^{1}H-^{15}N TROSY-HSQC spectrum shows one set of peaks for each amino acid of the NHR2 domain, as expected for the highly symmetric homotetramer as shown by X-ray crystallography [48] and the high prevalence of the NHR2 tetramer according to our AUC, SEC, and DLS results. We succeeded in assigning 32% of the backbone amide signals, which are located in the termini of NHR2. Unassigned residues are located in the middle of the coiled-coil region, which is the most rigid NHR2 part.

The interaction of NHR2 with **7.44** was measured via a ^{1}H-^{15}N TROSY-HSQC spectrum. Pronounced CSP backbone amide resonances (**Figure 5**) indicated binding of **7.44** to NHR2 and/or conformational changes induced by the ligand. CSP were found in the N-terminus (Q485 to L493) and for some unassigned amino acids of the middle region. No CSP were found for the assigned C-terminal residues (Y544 to K552). The C-termini do not form helical interfaces in the tetramer according to the X-ray structure [48]. Of the most affected residues, R492 forms a salt bridge with D533 and a solvent-exposed salt bridge with E536, which interacts with the indole NH of W540 via a charge-assisted hydrogen bond. Notably, residues D533, E536, and W540 were the template motif with which **7.44** was identified by virtual screening and which **7.44** is thought to mimic as a tetramerization inhibitor [11]. The CSP results support this model. Furthermore, CSP of tryptophan side chains indicate the involvement of at least one, if not two, tryptophans in the **7.44** effect.

Next, we performed unbiased MD simulations of free **7.44** diffusion around the NHR2 tetramer to obtain structural information on the binding of the ligand in the context of the oncogenic tetramer, mimicking the situation in the NMR experiments. Such MD simulations have been used previously successfully to identify binding modes of small-molecules at proteins by us [43, 73] and others [74, 75] and complement the NHR2 epitope mapping by NMR by providing information at the atomistic level. Throughout the simulations, the tetramer remained largely structurally invariant (**Figure S13**). Of the three epitopes where **7.44** preferably forms contacts with the NHR2 tetramer, epitopes I and II represent poses in which **7.44** intercalates between the helices of the NHR2 tetramer, once between helices of one dimer and once between helices of two dimers. In either case, **7.44** interacts with at least one of its 1,3-benzodioxoles with tryptophan residues identified as hot spots [11], which may explain the observed STD-NMR results and tryptophan side chain CSP. Although no dissociation of the NHR2 tetramer was observed during our simulation times, in line with the determined K_{tet}, particularly the intercalation between two helices of two dimers, targeting W540, might represent an early step in the separation of the dimers. Note that this is concordant with our previously proposed binding model for **7.44** at the NHR2 dimer [11, 12]. Still, we could not obtain an (experimentally validated) binding mode of **7.44** at the NHR2 dimer - probably because, on the one hand, the NHR2 dimer population in the NMR experiments was too low ([NHR2] = 4 x K_{tet}), which shifted the equilibrium to the tetramer side. On the other hand, detecting the precise NHR2 binding mode was hampered because the NHR2 dimer shows marked structural changes at the termini in MD simulations, which makes obtaining converged results for **7.44** binding cumbersome.

Finally, we assessed six physicochemical and *in vitro* pharmacokinetic properties and the pKa of **7.44** experimentally and further pharmacokinetic and toxicological properties computationally, which are key properties in early drug discovery [76]. In all cases, **7.44** shows favorable properties, suggesting that **7.44** is suitably orally bioavailable. Together with its low molecular weight, high ligand efficiency, and non-complex chemical structure [11], this distinguishes **7.44** from other recent first-in-class peptidomimetic protein interaction inhibitors [43].

In summary, we biophysically characterized the interaction between the NHR2 domain of RUNX1/ETO and **7.44** and assessed **7.44**'s physicochemical, *in vitro* pharmacokinetic, and toxicological properties. The results, together with previous biochemical, cellular, and *in vivo* [12] assessments, reveal **7.44** as a lead for further optimization of structurally related compounds with increased binding affinity and enhanced anti-leukemic effects to inhibit RUNX1/ETO oncogenic function in t(8;21) AML.

Supporting information

Supplemental notes for the cloning, expression, and purification of 6His-NHR2, determination of K_{tet} and K_{lig} from MST experiments, and permeability estimation from molecular dynamics simulations. Supplemental **Tables S1-S11**. Supplemental **Figures S1 – S13**.

Acknowledgments

References

1. Miyoshi, H., et al., *The t(8;21) translocation in acute myeloid leukemia results in production of an AML1-MTG8 fusion transcript.* EMBO J, 1993. **12**(7): p. 2715-21.

2. Tallman, M.S., D.G. Gilliland, and J.M. Rowe, *Drug therapy for acute myeloid leukemia.* Blood, 2005. **106**(4): p. 1154-63.

3. Marcucci, G., et al., *Prognostic factors and outcome of core binding factor acute myeloid leukemia patients with t(8;21) differ from those of patients with inv(16): a Cancer and Leukemia Group B study.* J Clin Oncol, 2005. **23**(24): p. 5705-17.

4. Arora, R., S. Sawney, and D. Saluja, *Potential Therapeutic Approaches for the Treatment of Acute Myeloid Leukemia with AML1-ETO Translocation.* Curr Cancer Drug Targets, 2016. **16**(3): p. 215-25.

5. De Braekeleer, E., C. Ferec, and M. De Braekeleer, *RUNX1 translocations in malignant hemopathies.* Anticancer Res, 2009. **29**(4): p. 1031-7.

6. Wichmann, C., et al., *Targeting the oligomerization domain of ETO interferes with RUNX1/ETO oncogenic activity in t(8;21)-positive leukemic cells.* Cancer Res, 2007. **67**(5): p. 2280-9.

7. Liu, Y., et al., *The tetramer structure of the Nervy homology two domain, NHR2, is critical for AML1/ETO's activity.* Cancer Cell, 2006. **9**(4): p. 249-60.

8. Kohrs, N., et al., *MiR144/451 Expression Is Repressed by RUNX1 During Megakaryopoiesis and Disturbed by RUNX1/ETO.* PLoS Genet, 2016. **12**(3): p. e1005946.

9. Chen-Wichmann, L., et al., *Compatibility of RUNX1/ETO fusion protein modules driving CD34+ human progenitor cell expansion.* Oncogene, 2019. **38**(2): p. 261-272.

10. Wichmann, C., et al., *Dimer-tetramer transition controls RUNX1/ETO leukemogenic activity.* Blood, 2010. **116**(4): p. 603-13.

11. Metz, A., et al., *From determinants of RUNX1/ETO tetramerization to small-molecule protein-protein interaction inhibitors targeting acute myeloid leukemia.* J Chem Inf Model, 2013. **53**(9): p. 2197-202.

12. Schanda, J., et al., *Suppression of RUNX1/ETO oncogenic activity by a small molecule inhibitor of tetramerization.* Haematologica, 2017. **102**(5): p. e170-e174.

13. Gopalswamy, M., et al., *Structural characterization of amyloid fibrils from the human parathyroid hormone.* Biochim Biophys Acta, 2015. **1854**(4): p. 249-57.

14. Mossessova, E. and C.D. Lima, *Ulp1-SUMO crystal structure and genetic analysis reveal conserved interactions and a regulatory element essential for cell growth in yeast.* Mol Cell, 2000. **5**(5): p. 865-76.

15. Hagel, L., *Gel filtration: size exclusion chromatography.* Methods Biochem Anal, 2011. **54**: p. 51-91.

16. Kroeger, T., et al., *EDTA aggregates induce SYPRO orange-based fluorescence in thermal shift assay.* PLoS One, 2017. **12**(5): p. e0177024.

17. Forneris, F., et al., *ThermoFAD, a Thermofluor-adapted flavin ad hoc detection system for protein folding and ligand binding.* FEBS J, 2009. **276**(10): p. 2833-40.

18. Joubert, M.K., et al., *Classification and characterization of therapeutic antibody aggregates.* J Biol Chem, 2011. **286**(28): p. 25118-33.

19. Scheuermann, T.H., et al., *On the acquisition and analysis of microscale thermophoresis data.* Anal Biochem, 2016. **496**: p. 79-93.

20. Tso, S.C., et al., *Using two-site binding models to analyze microscale thermophoresis data.* Anal Biochem, 2018. **540-541**: p. 64-75.

21. Meurer A, S.C., Paprocki M, Čertík O, Kirpichev SB, Rocklin M, Kumar A, Ivanov S, Moore JK, Singh S, Rathnayake T, Vig S, Granger BE, Muller RP, Bonazzi F, Gupta H, Vats S, Johansson F, Pedregosa F, Curry MJ, Terrel AR, Roučka Š, Saboo A, Fernando I, Kulal S, Cimrman R, Scopatz A, *SymPy: symbolic computing in Python.* PeerJ Computer Science, 2017. **3:e103**.

22. Dembinski, H., *Error propagation with Sympy.* https://github.com/HDembinski/essays/blob/master/error_propagation_with_sympy.ipynb.

23.   Delaglio, F., et al., *NMRPipe: a multidimensional spectral processing system based on UNIX pipes.* J Biomol NMR, 1995. **6**(3): p. 277-93.

24.   Johnson, B.A. and R.A. Blevins, *NMR View: A computer program for the visualization and analysis of NMR data.* J Biomol NMR, 1994. **4**(5): p. 603-14.

25.   Gift, A.D., S.M. Stewart, and P.K. Bokashanga, *Experimental Determination of pK(a) Values by Use of NMR Chemical Shifts, Revisited.* Journal of Chemical Education, 2012. **89**(11): p. 1458-1460.

26.   Mayer, M. and B. Meyer, *Group epitope mapping by saturation transfer difference NMR to identify segments of a ligand in direct contact with a protein receptor.* Journal of the American Chemical Society, 2001. **123**(25): p. 6108-6117.

27.   Viegas, A., et al., *Saturation-Transfer Difference (STD) NMR: A Simple and Fast Method for Ligand Screening and Characterization of Protein Binding.* Journal of Chemical Education, 2011. **88**(7): p. 990-994.

28.   Salzmann, M., et al., *TROSY in triple-resonance experiments: New perspectives for sequential NMR assignment of large proteins.* Proceedings of the National Academy of Sciences of the United States of America, 1998. **95**(23): p. 13585-13590.

29.   Sattler, M., J. Schleucher, and C. Griesinger, *Heteronuclear multidimensional NMR experiments for the structure determination of proteins in solution employing pulsed field gradients.* Progress in Nuclear Magnetic Resonance Spectroscopy, 1999. **34**(2): p. 93-158.

30.   QikProp, *Schrödinger Release 2021-3.* Schrödinger, LLC, New York, NY. (http://gohom.win/ManualHom/Schrodinger/Schrodinger_2012_docs/qikprop/qikprop_user_manual.pdf), 2021.

31.   Greene, N., et al., *Knowledge-based expert systems for toxicity and metabolism prediction: DEREK, StAR and METEOR.* SAR QSAR Environ Res, 1999. **10**(2-3): p. 299-314.

32.   Barber, C., et al., *Evaluation of a statistics-based Ames mutagenicity QSAR model and interpretation of the results obtained.* Regul Toxicol Pharmacol, 2016. **76**: p. 7-20.

33.   Maestro-Schrödinger, *Schrödinger Release 2018-2: Maestro.* 2018, Schrödinger, LLC: New York, NY.

34.   Frisch, M.J., et al., *Gaussian 16 Rev. B.01.* 2016: Wallingford, CT.

35.   Martinez, L., et al., *PACKMOL: a package for building initial configurations for molecular dynamics simulations.* J Comput Chem, 2009. **30**(13): p. 2157-64.

36.   Case, D., et al., *Amber 2017, University of California, San Francisco.* 2017.

37.   Maier, J.A., et al., *ff14SB: Improving the Accuracy of Protein Side Chain and Backbone Parameters from ff99SB.* J Chem Theory Comput, 2015. **11**(8): p. 3696-713.

38.   Wang, J., et al., *Development and testing of a general amber force field.* J Comput Chem, 2004. **25**(9): p. 1157-74.

39.   Bayly, C.I., et al., *A well-behaved electrostatic potential based method using charge restraints for deriving atomic charges: the RESP model.* The Journal of Physical Chemistry, 1993. **97**(40): p. 10269-10280.

40.   Cornell, W.D., et al., *Application of Resp Charges to Calculate Conformational Energies, Hydrogen-Bond Energies, and Free-Energies of Solvation.* Journal of the American Chemical Society, 1993. **115**(21): p. 9620-9631.

41.   Joung, I.S. and T.E. Cheatham, 3rd, *Determination of alkali and halide monovalent ion parameters for use in explicitly solvated biomolecular simulations.* J Phys Chem B, 2008. **112**(30): p. 9020-41.

42.   Frieg, B., et al., *Molecular Mechanisms of Glutamine Synthetase Mutations that Lead to Clinically Relevant Pathologies.* PLoS Comput Biol, 2016. **12**(2): p. e1004693.

43.   Bhatia, S., et al., *Targeting HSP90 dimerization via the C-terminus is effective in imatinib resistant CML and lacks heat shock response induction.* Blood, 2018: p. blood-2017-10-810986.

44.   Frieg, B., D. Haussinger, and H. Gohlke, *Towards Restoring Catalytic Activity of Glutamine Synthetase With a Clinically Relevant Mutation.*

45.   Darden, T., D. York, and L. Pedersen, *Particle mesh Ewald: An N·log (N) method for Ewald sums in large systems.* The Journal of chemical physics, 1993. **98**(12): p. 10089-10092.

46.   Salomon-Ferrer, R., et al., *Routine Microsecond Molecular Dynamics Simulations with AMBER on GPUs. 2. Explicit Solvent Particle Mesh Ewald.* Journal of Chemical Theory and Computation, 2013. **9**(9): p. 3878-3888.

47.   Hopkins, C.W., et al., *Long-Time-Step Molecular Dynamics through Hydrogen Mass Repartitioning.* J Chem Theory Comput, 2015. **11**(4): p. 1864-74.

48.   Sun, X.J., et al., *A stable transcription factor complex nucleated by oligomeric AML1-ETO controls leukaemogenesis.* Nature, 2013. **500**(7460): p. 93-7.

49.   Ciglia, E., et al., *Resolving hot spots in the C-terminal dimerization domain that determine the stability of the molecular chaperone Hsp90.* PLoS One, 2014. **9**(4): p. e96031.

50.   Steinberg, T.H., et al., *SYPRO orange and SYPRO red protein gel stains: one-step fluorescent staining of denaturing gels for detection of nanogram levels of protein.* Anal Biochem, 1996. **239**(2): p. 223-37.

51.   Vivoli, M., et al., *Determination of protein-ligand interactions using differential scanning fluorimetry.* J Vis Exp, 2014(91): p. 51809.

52.   Bopp, B., et al., *Design and biological testing of peptidic dimerization inhibitors of human Hsp90 that target the C-terminal domain.* Biochim Biophys Acta, 2016. **1860**(6): p. 1043-55.

53.   Metz, A., *Predicting and Exploiting the Determinants of Protein/Protein Interactions to Identify Low-Molecular Inhibitors of RUNX1-ETO Tetramerization (PhD Thesis).* 2014, Düsseldorf: Heinrich Heine Universität.

54.   Zheng, T., et al., *Probing coiled-coil assembly by paramagnetic NMR spectroscopy.* Org Biomol Chem, 2015. **13**(4): p. 1159-68.

55.   Lipinski, C.A., *Drug-like properties and the causes of poor solubility and poor permeability.* Journal of Pharmacological and Toxicological Methods, 2000. **44**(1): p. 235-249.

56.   Mu, Y., et al., *From fighting depression to conquering tumors: a novel tricyclic thiazepine compound as a tubulin polymerization inhibitor.* Cell Death & Disease, 2016. **7**.

57.   Wan, H., *What ADME tests should be conducted for preclinical studies?* ADMET and DMPK, 2013. **1**(3): p. 19-28.

58.   Bennion, B.J., et al., *Predicting a Drug's Membrane Permeability: A Computational Model Validated With in Vitro Permeability Assay Data.* J Phys Chem B, 2017. **121**(20): p. 5228-5237.

59.   Benet, L.Z., et al., *BDDCS, the Rule of 5 and drugability.* Adv Drug Deliv Rev, 2016. **101**: p. 89-98.

60.   Lionta, E., et al., *Structure-based virtual screening for drug discovery: principles, applications and recent advances.* Curr Top Med Chem, 2014. **14**(16): p. 1923-38.

61.   Pantoliano, M.W., et al., *High-density miniaturized thermal shift assays as a general strategy for drug discovery.* J Biomol Screen, 2001. **6**(6): p. 429-40.

62.   Wan, K.F., et al., *Differential scanning fluorimetry as secondary screening platform for small molecule inhibitors of Bcl-XL.* Cell Cycle, 2009. **8**(23): p. 3943-52.

63.   DeSantis, K., et al., *Use of differential scanning fluorimetry as a high-throughput assay to identify nuclear receptor ligands.* Nucl Recept Signal, 2012. **10**: p. e002.

64.   Rice, L.B., et al., *Structural and Regulatory Changes in PBP4 Trigger Decreased beta-Lactam Susceptibility in Enterococcus faecalis.* MBio, 2018. **9**(2).

65.   Jerabek-Willemsen, M., et al., *Molecular interaction studies using microscale thermophoresis.* Assay Drug Dev Technol, 2011. **9**(4): p. 342-53.

66.   Schott-Verdugo, S., et al., *Structural Model of the ETR1 Ethylene Receptor Transmembrane Sensor Domain.* Sci Rep, 2019. **9**(1): p. 8869.

67.   Metz, A., E. Ciglia, and H. Gohlke, *Modulating protein-protein interactions: from structural determinants of binding to druggability prediction to application.* Curr Pharm Des, 2012. **18**(30): p. 4630-47.

68.   Markowitz, J., et al., *Identification and characterization of small molecule inhibitors of the calcium-dependent S100B-p53 tumor suppressor interaction.* J Med Chem, 2004. **47**(21): p. 5085-93.

69.   Kitada, S., et al., *Discovery, characterization, and structure-activity relationships studies of proapoptotic polyphenols targeting B-cell lymphocyte/leukemia-2 proteins.* J Med Chem, 2003. **46**(20): p. 4259-64.

70.   Lee, H.J., et al., *Sulindac inhibits canonical Wnt signaling by blocking the PDZ domain of the protein Dishevelled.* Angew Chem Int Ed Engl, 2009. **48**(35): p. 6448-52.

71.   Lassalas, P., et al., *Structure Property Relationships of Carboxylic Acid Isosteres.* J Med Chem, 2016. **59**(7): p. 3183-203.

72.   Raudszus, R., et al., *Fluorescent analogs of peptoid-based HDAC inhibitors: Synthesis, biological activity and cellular uptake kinetics.* Bioorg Med Chem, 2019. **27**(19): p. 115039.

73.   Gohlke, H., et al., *Binding region of alanopine dehydrogenase predicted by unbiased molecular dynamics simulations of ligand diffusion.* J Chem Inf Model, 2013. **53**(10): p. 2493-8.

74.   Buch, I., T. Giorgino, and G. De Fabritiis, *Complete reconstruction of an enzyme-inhibitor binding process by molecular dynamics simulations.* Proc Natl Acad Sci U S A, 2011. **108**(25): p. 10184-9.

75.   Dror, R.O., et al., *Pathway and mechanism of drug binding to G-protein-coupled receptors.* Proc Natl Acad Sci U S A, 2011. **108**(32): p. 13118-23.

76.   Hughes, J.P., et al., *Principles of early drug discovery.* Br J Pharmacol, 2011. **162**(6): p. 1239-49.

Supporting Information

Biophysical and pharmacokinetic characterization of a small-molecule inhibitor of RUNX1/ETO tetramerization with anti-leukemic effects

Mohanraj Gopalswamy[a], Tobias Kroeger[a], David Bickel[a], Benedikt Frieg[b], Shahina Akter[a], Stephan Schott-Verdugo[a,b,c], Aldino Viegas[d], Thomas Pauly[b,d], Manuela Mayer[e], Julia Przibilla[e], Jens Reiners[f], Luitgard Nagel-Steger[b,d], Sander H.J. Smits[f], Georg Groth[g], Manuel Etzkorn[d,h], and Holger Gohlke[a,b,c*]

[a] Institute for Pharmaceutical and Medicinal Chemistry, Heinrich Heine University Düsseldorf, Universitätsstr. 1, 40225 Düsseldorf, Germany

[b] Institute of Biological Information Processing (IBI-7: Structural Biochemistry), Forschungszentrum Jülich GmbH, Wilhelm-Johnen-Str., 52425 Jülich, Germany

[c] John von Neumann Institute for Computing (NIC), Jülich Supercomputing Centre (JSC), and Institute of Bio- and Geosciences (IBG-4: Bioinformatics), Forschungszentrum Jülich GmbH, Wilhelm-Johnen-Str., 52425 Jülich, Germany

[d] Institute for Physical Biology, Heinrich Heine University Düsseldorf, Universitätsstr. 1, 40225 Düsseldorf, Germany

[e] Pharmacelsus GmbH, Science Park 2, 66123 Saarbrücken, Germany

[f] Institute of Biochemistry and Center for Structural Studies, Heinrich Heine University Düsseldorf, Universitätsstr. 1, 40225 Düsseldorf, Germany

[g] Institute of Biochemical Plant Physiology, Heinrich Heine University Düsseldorf, Universitätsstr. 1, 40225 Düsseldorf, Germany

[h] Jülich Center for Structural Biology (JuStruct), Forschungszentrum Jülich GmbH, Wilhelm-Johnen-Str., 52425 Jülich, Germany

Table of content

Supplemental Notes

List of abbreviations

ACN   acetonitrile

AMMC   3-[2-(*N*,*N*-diethyl-*N*-methylamino)-ethyl]-7-methoxy-4-methyl-coumarin

BFC   7-benzyloxy-trifluoromethyl coumarin

CEC   3-cyano-7-ethoxycoumarin

CYP   cytochrome P450

Da   daltons

DBF   dibenzylfluorescein

DMSO   dimethyl sulfoxide

EFC   7-ethoxy-4-trifluoromethyl-coumarin

ESI   electro spray ionization

F   fluorescein

FA   formic acid

FF   furafylline

G6PDH   glucose-6-phosphate dehydrogenase

H-ESI   heated electrospray ionization (ion source type)

HEPES   4-(2-hydroxyethyl) piperazine-1-ethanesulfonic acid

HFBA   heptafluorobutyric acid

HPLC   high-performance liquid chromatography

HRMS   high-resolution mass spectrometry

IC_{50} concentration inhibiting an enzymatic reaction by 50%

ISTD   internal standard

KTZ   ketoconazole

LC   liquid chromatography

m/z   mass-to-charge ratio

MeOH   methanol

MFC   7-methoxy-4-trifluoromethyl coumarin

MS   mass spectrometry

MS-SIM   mass spectrometry-single ion monitoring

MW   molecular weight

N   normality

NaOH   sodium hydroxide

3

PBS	phosphate-buffered saline (without Ca^{2+} and Mg^{2+})
PPB	plasma protein binding
pH	potential hydrogen
QCT	quercetin
QND	quinidine
Q-TOF	quadrupole time-of-flight
RFU	relative fluorescence unit
RT	room temperature or retention time
RV	recovery
S	seconds
SFZ	sulfaphenazole
S/N	signal-to-noise ratio
TCP	tranylcypromine
Tris HCl	tris(hydroxymethyl)-amino-methan hydrochlorid
v/v	volume per volume
v	volts
w/v	weight per volume
WME	William's medium E

4

Cloning, expression, and purification of 6His-NHR2

Synthetic DNA corresponding to the coding region of residues 498-548 of RUNX1/ETO was cloned into expression vector pET19b in *E. coli* BL21 (DE3). A cysteine-free version of the NHR2 sequence was used where both cysteines were replaced by serines to comply with the construct used in previous studies [1, 2].

A His-tag was added to the N-terminus to allow for purification of NHR2 via immobilized metal ion affinity chromatography (IMAC). The transformed *E. coli* was transferred into LB-medium (5 g yeast extract, 5 g NaCl, and 10 g tryptone or peptone), containing ampicillin, and incubated at 37 °C until an OD_{600} of ~1 was reached. The expression was induced by adding (per liter LB-medium) 1 ml 1 M isopropyl-1-thio-β-D-galactopyranoside. The expression was continued for ~4 h at 37 °C. The cells were harvested by centrifugation and disrupted via sonification. The target protein was purified using IMAC, and the purity of the protein was inspected using a 15% SDS gel (Figure S1)

Determination of K_{tet} and K_{lig} from MST experiments

The EC_{50} value determined by MST in this study as well as the EC_{50} values determined by BS^3 cross-linking assay and ELISA previously [3] are composites of the dissociation constant of the NHR2 tetramer (K_{tet}) and the dissociation constant of **7.44** to the NHR2 dimer (K_{lig}). As the NHR2 tetramer (T) is in equilibrium with its dimeric form (D), the ligand (L) can only bind to the NHR2 dimer (D) after dissociation of T. Given the symmetry of an NHR2 dimer, a second ligand can bind to the DL complex, resulting in a DLL complex (see eq. 4 in the main text). The respective equilibrium constants are defined as:

$$K_{tet} = [D]^2 / [T] \tag{S1a}$$

and

$$K_{lig} = [D] \cdot [L] / [DL]. \tag{S1b}$$

K_{lig} could not be determined directly. Instead, K_{lig} was determined as a function of EC_{50} and K_{tet} according to the following equations [4, 5]. The following derivation was taken from ref. [6] and has been applied in a related context in ref. [4].

In the absence of L, the concentration of unbound NHR2 dimer D is $[D]_0$, and the concentration of the NHR2 tetramer T is $[T]_0$. The total concentration of NHR2 dimer $[D]_{tot}$ is (eq. S2):

5

$$[D]_{tot} = 2\,[T]_0 + [D]_0 \tag{S2}$$

Substituting eq. S2 into eq. S1a and solving the obtained equation with respect to [D]$_0$ leads to eq. S3:

$$[D]_0 = -\frac{K_{tet}}{4} + \sqrt{\left(\frac{K_{tet}}{4}\right)^2 + \frac{K_{tet}[D]_{tot}}{2}} \tag{S3}$$

Substituting eq. S3 into eq. S2 and rearranging leads to eq. S4, allowing the calculation of the maximal NHR2 tetramer concentration [T]$_0$ as a function of K_{tet} and [D]$_{tot}$.

$$[T]_0 = \frac{[D]_{tot} + \frac{K_{tet}}{4} - \sqrt{\left(\frac{K_{tet}}{4}\right)^2 + \frac{K_{tet}[D]_{tot}}{2}}}{2} \tag{S4}$$

In the presence of a total ligand concentration of $[L]_{tot} = EC_{50}$, the total NHR2 dimer concentration [D]$_{tot}$ is defined by eq. S5:

$$[D]_{tot} = 2[T]_{50} + [D]_{50} + [DL]_{50} + [DLL]_{50} \tag{S5}$$

in which [T]$_{50}$, [D]$_{50}$, [DL]$_{50}$, and [DLL]$_{50}$ are the concentrations of the respective molecular species at $[L]_{tot} = EC_{50}$.

MST experiments in the presence of **7.44** were performed at an NHR2 concentration where >99% of NHR2 is in a dimeric arrangement. Neglecting the tetramer and assuming that the majority of the MST signal change comes from the D to DL equilibrium, [D]$_{50}$ is half of the maximal dimer concentration [D]$_0$ at [L] = 0 (eq. S6).

$$[D]_{50} = \frac{[D]_0}{2} \tag{S6}$$

The concentration of the unbound NHR2 tetramer [T]$_{50}$ is obtained by substituting eq. S6 into eq. S1a (eq. S7):

$$[T]_{50} = \frac{[D]_{50}^2}{K_{tet}} = \frac{[D]_0^2}{4K_{tet}} \tag{S7}$$

Based on the definition of the dissociation constant of the **7.44**-bound complexes K_{lig}, the concentrations of the ligand-bound complexes are given by eq. S8 and eq. S9

6

$$[DL]_{50}=\frac{[D]_{50}[L]_{50}}{K_{lig}} \tag{S8}$$

$$[DLL]_{50}=\frac{[D]_{50}[L]_{50}^2}{K_{lig}^2} \tag{S9}$$

if one assumes that the dissociation constants for both ligand binding events are equal, in agreement with the remote ligand binding sites and our model (eq. 4) that depends on the pre-dissociation of T. $[L]_{50}$ is the concentration of the unbound PPIM at EC_{50}.

Substituting eq. S8 and eq. S9 into eq. S5 and solving the resulting quadratic equation with respect to K_{lig} leads to eq. S10. The negative solution of eq. S10 has no physical meaning because of $K_{lig} \geq 0$ and was omitted.

$$K_{lig}= \frac{-[D]_{50}[L]_{50}}{2(2[T]_{50}+[D]_{50}-[D]_{tot})}+\frac{1}{2}\sqrt{\left(\frac{[D]_{50}[L]_{50}}{(2[T]_{50}+[D]_{50}-[D]_{tot})}\right)^2-\frac{4[D]_{50}[L]_{50}^2}{(2[T]_{50}+[D]_{50}-[D]_{tot})}} \tag{S10}$$

According to eq. S6 and eq. S7, the terms $[D]_{50}$ and $[T]_{50}$ in eq. S10 are constants for given $[D]_0$ and K_{tet}. Thus, eq. S10 is a function of $[L]_{50}$, which remains to be defined.

For $[L]_{tot} = EC_{50}$, the total ligand concentration $[L]_{tot}$ is defined by eq. S11.

$$[L]_{tot}=EC_{50}=[L]_{50}+[DL]_{50}+2[DLL]_{50} \tag{S11}$$

Substituting eq. S8 and eq. S9 into eq. S11 and solving the resulting quadratic equation with respect to $[L]_{50}$ leads to eq. S12. The negative solution of eq. S12 has no physical meaning because of $[L]_{50} \geq 0$ and was omitted.

$$[L]_{50}= -\frac{\left(\frac{[D]_{50}}{K_{lig}}+1\right)}{4\frac{[D]_{50}}{K_{lig}^2}}+\sqrt{\left(\frac{\left(\frac{[D]_{50}}{K_{lig}}+1\right)}{4\frac{[D]_{50}}{K_{lig}^2}}\right)^2+\frac{EC_{50}}{2\frac{[D]_{50}}{K_{lig}^2}}} \tag{S12}$$

According to eq. S7, $[D]_{50}$ in eq. S12 is constant for given $[D]_0$. Finally, solving the system of eq. S10 and eq. S12 allows calculating K_{lig} for given $[D]_{tot}$, K_{tet}, and EC_{50}. For this purpose, $[D]_{tot}$ is the total concentration of NHR2 dimer in the assay.

In vitro **ADME investigations of compound 7.44**

The materials and methods of the six assays, aqueous solubility, plasma protein binding (PPB), plasma stability, hepatocyte clearance measurements, chemical stability, and cytochrome P450 (CYP) inhibition, are described in detail below [7-12].

Materials

In the assays described herein, the materials were used as shown in **Table S1**.

Table S1. Details of materials.

Material	Catalog ID	Supplier	Lot
Internal standards			
Diazepam	D0899	Sigma-Aldrich	105F0451
Diclofenac	D6899	Sigma-Aldrich	BCBN3367V
Griseofulvin	PHR1534	Sigma-Aldrich	LRAB4111
Solubility			
PBS (pH 7.4)	P04-36500	PAN Biotech	1516119
PPB			
Mouse plasma (CD-1, male, pooled, Li-heparin)	MSEPLLIHP-M	Biotrend	MSE308232
Warfarin	45706	Sigma-Aldrich	SZBF197XV
Plasma stability			
Mouse plasma (CD-1, male, pooled, Li-heparin)	MSEPLLIHP-M	Biotrend	MSE308232
Propantheline	P8891	Sigma-Aldrich	110M1921
Chemical stability			
PBS (pH 7.4)	P04-36500	PAN Biotech	1560119
Omeprazole	O104	Sigma-Aldrich	BCBQ8476V
Hepatocyte stability			
7-Ethoxycoumarin	E1379	Sigma-Aldrich	MKBN6201V
1 M HEPES solution	P05-01100	PAN Biotech	2190518
In vitro GRO HT medium	Z99019	IVT Bioreclamation	C11020A
L-glutamine	P04-80100	PAN Biotech	4140319
Primary mouse hepatocytes[a]	M005052	IVT Bioreclamation	MHD
Williams Medium E	P04-29510	PAN Biotech	2861019
CYP inhibition using HITS™ kits			
Furafylline	F124	Sigma-Aldrich	59790
Tranylcypromine[b]	P8511	Sigma-Aldrich	MKBW0574V
Quercetin dihydrate	0020-05-95	Sigma-Aldrich	HWI00580-2
Sulfaphenazole	S0758	Sigma-Aldrich	63530
Quinidine HCl monohydrate	Q0750	Sigma-Aldrich	SLSS3542V
Ketoconazole	K1003	Sigma-Aldrich	SLCC4160

8

G6PDH	G5885	Sigma-Aldrich	096K8605
CYP1A2/CEC kit	459500	Corning	5239001
CYP2B6/EFC kit	459220	Sigma-Aldrich	4296001
CYP2C8/DBF kit	459320	Corning	4300001
CYP2C9/MFC kit	459300	Corning	535003
CYP2C19/CEC kit	459400	Corning	5313006
CYP2D6/AMMC kit	459200	Corning	5162021
CYP3A4/BFC kit	459100	Corning	6102001

[a] cryopreserved, strain ICR/CD-1, male, pooled

[a] *trans*-2-phenylcyclopropyl-aminehydrochloride

Buffers / media / solvents

In the assays described herein, solvents were used as shown in **Table S2**.

Table S2. Solvents

Material	Catalog ID	Supplier
Acetonitrile (ACN)	34851-PPB	Honeywell
Deionised water (H_2O)	NANOpure DIamond Life Science Water purification system	
Dimethylsulfoxide (DMSO)	4720.2-PPB	Carl Roth
Ethanol (EtOH)	32205	Honeywell
Methanol (MeOH)	34885	Honeywell

Further buffers were used in the assays:

Solubility in aqueous solutions:

Ready to use PBS, pH 7.4, as described in **Table S1** was used.

Hepatocyte stability assay:

InvitroGRO HT Medium: Ready-to-use medium for thawing of cells was applied.

Incubation medium: WME supplemented with 25 mM HEPES and 2 mM L-glutamine

Description of key quantitative analytical equipment

LC-MS: Surveyor MS Plus HPLC (Thermo Electron) HPLC system connected to a TSQ Quantum Discovery Max (Thermo Electron) triple quadrupole mass spectrometer equipped with an electrospray (ESI) (Thermo Fisher Scientific, USA); connected to a PC running the standard software Xcalibur 2.0.7. It is used for solubility, PPB, and plasma stability assays.

9

LC-MS: 1260 Infinity II BioInert Quarternary U-HPLC pump, 1260 Inifinity II BioIntert Multisampler, 1260 Inifinity II BioIntert Column Compartment and 1260 Inifinity II Diode Array Detector (Agilent, Germany) connected to a QTOF X500B (SCIEX, Canada) mass spectrometer, data handling with the standard software SCIEX OS (Version 1.5 and higher). It is used for chemical stability and hepatocytes stability assays.

Fluorimeter: Wallac Victor 1420 Multilabel Counter, Perkin Elmer.

Methods

Preparation of test solutions

In **Table S3**, the concentrations of the test and reference item stock solutions in their respective solvents are displayed. By default, working solutions of test and reference items were diluted from the stock solutions in an appropriate solvent to obtain working solutions of 100-fold (solubility), 50-fold (PPB, plasma stability, chemical stability), and 200-fold (hepatocyte stability) higher strength than the final incubation concentrations and the respective final organic solvent content (**see next section**).

Table S3. Stock and working solutions of test and reference items

Item	Stock solution		Working solution solvent
	(mM)	Solvent	
7.44 compound	20	DMSO	DMSO (Solubility, Hepatocyte stability) 25% DMSO in H_2O (PPB, Plasma stability, Chemical stability)
Propantheline (Plasma stability)	10	H_2O	H_2O
Omeprazole (Chemical stability)	10	DMSO	25% DMSO in H_2O
7-Ethoxycoumarin (Hepatocyte stability)	10	ACN	ACN

Test concentration selection

The test item **7.44** compound was dissolved in DMSO at 20 mM. The cut-off concentration of test item **7.44** in the **solubility assay** was 200 µM with a final solvent content of 1% DMSO. **For PPB assay**, the test item was tested at final concentrations of 10 µM in the presence of 0.5% DMSO. Reference item warfarin was tested at a standardized final concentration of 10 µM in the presence of 1% ACN.

For plasma stability assay, working solutions of the test and reference item were diluted from the stock solutions in the appropriate solvent (**Table S3**) to reach working solutions of 50-fold higher strength than the final intended incubation concentrations of the compounds. Test item and propantheline (reference item for low plasma stability) were tested at a final concentration of 10 µM. The final solvent content in the test item incubations was 0.5% DMSO, while in the propantheline incubations, no organic solvent was added.

For chemical stability assay, working solutions of the test and reference items were diluted from the stock solutions in the appropriate solvent (**Table S3**) to reach working solutions of 50-fold higher strength than the final intended incubation concentrations of the compounds. Test item and Omeprazole (reference item for low chemical stability) were tested at a final concentration of 10 µM. The final solvent content in the test item incubations was 0.5% DMSO.

For the hepatic stability assay, working solutions of the test and reference items were diluted from the stock solutions in the appropriate solvent (**Table S3**) to reach working solutions of a 200-fold higher strength than the intended final concentrations. In a second step, working solutions were further diluted in incubation medium to reach 10-fold concentrated starting solutions. The final test concentrations were 5 µM with a solvent content of 0.5% DMSO or 1% ACN in all test item and reference item incubations, respectively.

For CYP inhibition assay, the test item was tested at final concentrations of 1 µM and 10 µM, and reference items were tested at eight appropriate concentrations. Stock solutions of test items were diluted in DMSO to prepare a 200-fold concentrated working solution for CYP2B6, or stock solutions were diluted in NADPH-cofactor-mix (all other CYPs) to reach concentrations 20-fold higher than the requested final test concentration of 10 µM and 1 µM, respectively. The final organic solvent content was 0.5 % DMSO for CYP2B6 or 0.2% DMSO for all other tested CYP isoforms, respectively. Stock solutions of the reference items were diluted 50-fold in the first well of a row for CYP1A2, CYP2C9, CYP2C19, CYP2D6, and CYP3A4, 100-fold for CYP2C8, 200-fold for CYP2B6, followed by a serial 1:3 dilution in the 96-well plates containing cofactor mix to obtain the respective eight test concentrations. The final solvent content in the incubations was 2% ACN for CYP1A2, CYP2C9, CYP2C19, CYP2D6, CYP3A4 and 1% ACN for CYP2C8 and 0.5% ACN for CYP2B6.

Preparation of calibration standards of test and reference items
By default, working solution of the test and reference items were prepared for each calibration level. The calibration standards were ranged from 0.02 µM to 300 µM for the solubility assay,

11

from 0.001 µM to 20 µM for the PPB assay, from 0.05 µM to 20 µM for the plasma stability and chemical stability assays, and from 0.005 µM to 10 µM for the hepatocytes stability assay by appropriate dilution of the corresponding stock solution with the corresponding solvent by serial dilution.

Solubility

Calibration standards for the solubility assay were prepared by spiking 198 µL of the respective buffer (PBS buffer (pH 7.4)) with 2 µL of the corresponding working solution. The final standard solutions contained 1% DMSO.

PPB

For the PPB assay calibration standards were prepared by spiking 73.5 µL mouse plasma with 1.5 µL of the corresponding working solution. To avoid unspecific test item metabolism in calibration standards, protein was inactivated by addition of 150 µL ACN containing the internal standards (Diazepam, 1 µM, Griseofulvin, 1 µM, and Diclofenac, 10 µM) prior to addition of working solutions. The final standard solutions contained 1% DMSO (test item) or 1% ACN (reference item).

Plasma stability and Chemical stability

Calibration standards for plasma stability and chemical stability assays were prepared by spiking 147 µL mouse plasma or PBS buffer, respectively with 3 µL of the corresponding working solution. Plasma was inactivated by addition of 300 µL ACN containing the internal standards (Diazepam, 1 µM, Griseofulvin, 1 µM, and Diclofenac, 10 µM) before addition of working solutions to avoid unspecific metabolism in calibration standards. The final standard solutions contained 0.5% DMSO.

Hepatocyte stability assay

Calibration standards were prepared by mixing the appropriate volumes of incubation medium (196 µL) and the corresponding working solution (4 µL). The final standard solutions contained 2% DMSO or 1% ACN for test item and reference item, respectively.

Calibration solutions were processed for precipitation (ACN containing the internal standards) and quantitative bioanalysis as described in **Sample preparation section**.

12

Assay procedures

7.44 compound was prepared as 20 mM stock solution in DMSO and further diluted in 25% DMSO/H$_2$0 or assay matrix if applicable.

Kinetic solubility in PBS

2.5 µl of the compound **7.44** stock solution was mixed with 247.5 µl of PBS (pH 7.4), resulting in a cut-off concentration of 200 µM and a final solvent content of 1% DMSO. The test solutions (triplicates) were put on a filter plate and were shaken protected from light at 300 rpm at room temperature for 1.5 hours, followed by centrifugation at 500 x g for 3 minutes. 200 µl of the filtrate were mixed with 100 µl ACN containing the ISTD as described in **Sample preparation section**.

PPB

Plasma protein binding was performed according to the modified ultrafiltration procedure described by Taylor and Harker[12]. Test and reference item stock solutions were diluted in 25% DMSO/H$_2$O or ACN, respectively (see **Preparation of test solutions section**) to give a working solution of 50-fold higher strength than the intended final test concentration. The plasma was prewarmed for 30 min at 37°C. The incubation solutions were prepared by adding 1.5 µL of the 50-fold concentrated working solution to 73.5 µL of plasma and vortexed for 2 min, resulting in a final incubation concentration of 10 µM for the test items (0.5% DMSO final solvent concentration) and of 10 µM for the reference item warfarin in the presence of 1% ACN. The assay was performed with plasma from CD-1 mice (**Materials section**). Plasma samples (with test or reference item) as well as the control plasma samples (without test or reference item) were incubated at 37°C for 60 min in the dark.

After incubation, the plasma samples (with test or reference item) were added to sample reservoirs of Microcon® centrifugal filter units (Ultracel-YM30, MWCO 30000 Da; Millipore, USA) For each unit loaded with plasma sample, a partner ultrafiltration unit was loaded with control plasma. All ultrafiltration units were centrifuged (6,500 x g for 12 minutes, room temperature). The sample reservoirs containing plasma retentate were then inverted and placed on the filtrate collection tubes of the partner ultrafiltration unit. The ultrafiltration units were centrifuged a second time (700 x g for 20 seconds), such that the retentate was mixed with the filtrate of the partner sample. As a result, two reconstituted plasma samples were produced, one representing drug in the filtrate and one representing drug in the retentate. The reconstituted samples were processed for sample preparation as described below.

13

In parallel, stability control plasma samples (with test or reference item) were prepared and incubated for 0 or 60 min, respectively. After incubation, stability control plasma samples were processed for sample preparation as described below to determine the post-incubation test item concentration.

All experimental incubations containing the test items were run in duplicate (n = 2). Warfarin was used as high-binding positive control (n = 3).

Plasma Stability and Chemical Stability

The test item stock solution was diluted in 25% DMSO/H$_2$O to prepare a working solution of 50-fold higher strength than the intended incubation concentration and kept protected from light. The incubation solutions were prepared by adding 3 µL of this 50-fold concentrated working solution to 147 µL of pre-incubated assay matrix (i.e. PBS (pH 7.4) or plasma pre-warmed to 37°C for chemical stability and plasma stability assays, respectively) resulting in an incubation concentration of 10 µM. Sampling time points were (0, 30, 60, 120, and 240 minutes) for plasma stability assay and (0 and 240 minutes) for chemical stability assay. Per time point, two replicates were conducted. The final solvent concentration was 0.5% DMSO for the test items. The plasma stability and chemical stability assays were performed using plasma from CD-1 mice and PBS buffer (pH 7.4), respectively.

Propantheline, a hydroxyethyl-diisopropylmethyl-ammonium xanthene-9-carboxylate, is cleared from plasma rapidly by the release of the hydroxyl-ethyl-diisopropylmethylammonium moiety catalyzed by esterases and was included as positive control (n = 2) in the experiment. These results were used as marker for comparison of test item reactivity in plasma.

For the positive control propantheline, samples were removed after 0 and 120 minutes of incubation with mouse plasma. Samples were stopped by addition of ACN containing ISTDs and processed.

Omeprazole is chemically unstable and easily degradable in buffer, so it was included as positive control (n = 2) in the experiment. Samples were removed after 0 and 240 minutes of incubation of omeprazole samples with PBS buffer. The reaction was stopped by addition of ACN containing ISTDs and processed as described in **Sample preparation section**.

Hepatocyte stability

Working solutions of the test and reference items were diluted from the stock solutions in the appropriate solvent (**Table S3**) to reach working solutions of a 200-fold higher strength than

14

the intended final concentrations. In a second step, working solutions were further diluted in incubation medium to reach 10-fold concentrated starting solutions. The final test concentrations were 5 µM with a solvent content of 0.5% DMSO or 1% ACN in all test item and reference item incubations, respectively. **7.44** compound was dissolved 20 mM in DMSO and 25% DMSO/H$_2$O. Primary hepatocytes from CD-1 mice (pooled, male) were thawed according to the instructions of the manufacturer. The incubation samples were composed of 0.2 x 10^6 cells/well in 225 µL incubation medium and 25 µL test item solution (50 µM in incubation medium), resulting in a final start concentration of 5 µM. Samples were taken from the suspension cultures after 0, 15, 30, 60, and 120 minutes of incubation and processed for LC-MS analysis as described in **Sample preparation section**.

Positive control incubations were performed using 7-ethoxycoumarin as substrate. Metabolic turnover rates were measured at 0 and 120 minutes of incubation. Aliquotes were taken from the incubations for sample preparation and analysis. Hepatocyte enzyme activity was assessed in terms of 7-ethoxycoumarin turnover, i.e., loss of 7-ethoxycoumarin.

Negative controls were performed to observe non-metabolic degradation processes; i.e. test item concentrations remaining stable over the investigated time suggests that a decrease of the parent compound is mainly due to metabolism. Negative control incubations were performed in line with all experiments using incubation medium with test and reference item in the absence of hepatocytes. Samples were taken from the incubations at 0 and 120 minutes and processed as described below (in **Sample preparation section**).

CYP inhibition using HTS^{TM} kits
Assays were performed in black 96-well plates according to the manufacturer's instructions (BD Gentest/Corning, P450 High Throughput Inhibitor Screening Kits). The final concentrations of the reagents required for the individual CYP isozymes are given in **Table S4**. Shortcuts given in the table are shown below.

For determination of reference item IC$_{50}$ values, twelve wells in one row including solvent control (100% enzyme activity, no inhibition) and negative controls (NC, blank values) were used for inhibition curve for each reference item. All reactions were performed in duplicates. The source of NADPH in these enzyme assays was a NADPH-regenerating system: glucose-6-phosphate-dehydrogenase converts NADP$^+$ to NADPH in the presence of glucose-6-phosphate.

Cofactor mix, containing the NADP$^+$-regenerating system, was prepared according to the manual and was filled in the plate to well 1 for determination of IC$_{50}$ values of reference items

15

or to each test item well. Cofactor/solvent mix was prepared according to the manual and was filled in the plate from well 2 to well 12 of the reference items, and in solvent control as well as in NC wells for test items. The working solutions of the test items were added to each test well.

For reference items, working solutions were diluted 50-fold in the first well of a row for CYP1A2, CYP2C9, CYP2C19, CYP2D6, and CYP3A4, 100-fold for CYP2C8 or 200-fold for CYP2B6, followed by a serial 1:3 dilution from well 1 to 8. Wells 9 and 10 did not contain inhibitor (solvent control, 100% enzyme activity, no inhibition). For the test items, the cofactor mix-containing working solutions were diluted 1:10 (v/v) in the respective wells. All wells contained final organic solvent concentrations as given in **Test concentration selection** section.

Table S4. Final concentrations in P450 inhibition screening according to the manufacturer[a]

Isoenzyme	CYP1A2	CYP2B6	CYP2C8	CYP2C9
Substrate	CEC,	EFC	DBF	MFC
Substrate concentration	5 µM	2.5 µM	1 µM	75 µM
Metabolite formed	CHC	HFC	F	HFC
NADP+	1.3 mM	1.3 mM	1.3 mM	1.3 mM
Glucose-6-phosphate	3.3 mM	3.3 mM	3.3 mM	3.3 mM
MgCl2 x 6H2O	3.3 mM	3.3 mM	3.3 mM	3.3 mM
Glucose-6-phosphate-dehydrogenase	0.4 U/mL	0.4 U/ml	0.4 U/ml	0.4 U/ml
Phosphate buffer, pH 7.4	100 mM	100 mM	50 mM	25 mM
Enzyme	2.5 pmol/ml	5 pmol/ml	20 pmol/ml	5 pmol/ml
Reference inhibitor, highest concentration	FF 100 µM	TCP 5 µM	QCT 20 µM	SFZ 10 µM
Isoenzyme	CYP2C19	CYP2D6	CYP3A4	
Substrate	CEC	AMMC	BFC	
Substrate concentration	25 µM	1.5 µM	50 µM	
Metabolite formed	CHC	AHMC	HFC	
NADP+	1.3 mM	8.2 µM	1.3 mM	
Glucose-6-phosphate	3.3 mM	0.41 mM	3.3 mM	
MgCl2 x 6H2O	3.3 mM	0.41 mM	3.3 mM	
Glucose-6-phosphate-dehydrogenase	0.4 U/ml	0.4 U/ml	0.4 U/ml	
Phosphate buffer, pH 7.4	50 mM	100 mM	200 mM	
Enzyme	2.5 pmol/ml	7.5 pmol/ml	5 pmol/ml	
Reference inhibitor, highest concentration	TCP 100 µM	QND 0.5 µM	KTZ 5 µM	

16

[a]AHMC = 3-[2-(*N*,*N*-diethylamino)ethyl]-7-hydroxy-4-methylcoumarin AMMC = 3-[2-(*N*,*N*-diethyl-*N*-methylamino)ethyl]-7-methoxy-4-methylcoumarin, BFC = 7-benzyloxy-trifluoromethyl coumarin, C = coumarin, CEC = 3-cyano-7-ethoxycoumarin CHC = 3-cyano-7-hydroxycoumarin, DBF = dibenzylfuorescein, DDTC = diethyldithiocarbamic acid, EFC = 7-ethoxy-4-trifluoromethylcoumarin, F = fluorescein, FF = furafyllin, HC= 7-hydroxycoumarin, HFC = 7-hydroxytrifluoromethyl coumarin, KTZ = ketoconazole, MFC = 7-methoxy-4-trifluoromethyl coumarin, QCT = quercetin, QND = quinidine, SFZ = sulfaphenazole, TCP = tranylcypromine.

After 10 minutes of pre-incubation at 37°C, the reactions were started by addition of pre-warmed enzyme/substrate mix. Incubations with a final volume of 200 µl per well were performed for 15 minutes (CYP1A2), 30 minutes (CYP2B6, CYP2C19, CYP2D6, CYP3A4 – BFC substrate), 40 minutes (CYP2C8) or 45 minutes (CYP2C9) at 37°C. The reaction was stopped as described below (in **Sample preparation**).

Test item was tested for auto-fluorescence, which might interfere with the measurement of the fluorescent metabolite. For this purpose, a solution, replacing cofactor-mix and enzyme/substrate-mix was prepared by mixing appropriate volumes of assay buffer, control protein, and water (auto-fluorescence control mix, AFC). An aliquot of AFC mix was removed and spiked with the respective solvent at the concentration suitable for the individual isoenzyme. 90 µl of the AFC/solvent mix was filled in the plate for all test item wells.

10 µl of the test item working solutions, concentrated as described in **Test concentration selection** section, were added to each AFC well in duplicate for each test concentration (1 µM and 10 µM). The plate was incubated for 10 min at 37°C, imitating the pre-incubation step of test item in cofactor mix. At the end of the pre-incubation, 100 µl of AFC mix was added to each well. Incubations with a final volume of 200 µl per well were performed as described above.

The fluorescence was measured using a Wallac Victor fluorescence plate reader, and the wavelengths for excitation and emission were shown in **Table S8**.

Sample preparation

As ISTDs for LC-MS analysis, compounds were chosen from the Pharmacelsus pool known to be suitable for ACN precipitation. Injection volumes of all measurements are listed in **Table S5**.

17

Kinetic solubility in PBS

The sample solution preparation was performed by mixing the 0.5-fold volume of ACN containing the internal standards (1 µM Diazepam, 1 µM Griseofulvin, and 10 µM Diclofenac) with the sample (i.e., filtrate) or calibration standard solution. After vigorously shaking (10 seconds), the samples were centrifuged (2200 x g) for 5 minutes at room temperature. Aliquots (70 µL) of the particle-free supernatants were transferred to 200 µl sample vials and subsequently subjected to LC-MS/MS.

PPB

The sample and standard preparation for the PPB assay were performed by mixing 150 µl of ACN containing the internal standards (1 µM Diazepam, 1 µM Griseofulvin, and 10 µM Diclofenac) with 75 µl sample or calibration standard solutions. After vigorously shaking (10 seconds), the samples were centrifuged (6,800 x g) for 5 minutes at room temperature. Particle-free supernatants were diluted with an equal volume of H_2O to reduce the organic solvent content of the samples to 33% and subsequently subjected to LC-MS analysis.

Plasma Stability and Chemical Stability

Isolation of the compounds was performed by addition of 300 µl ACN containing the internal standards (1 µM Diazepam, 1 µM Griseofulvin, and 10 µM Diclofenac) to 150 µl samples and calibration standard solutions. After shaking (10 seconds) and sonication (10 seconds), the samples were centrifuged (2200 x g) at room temperature for 10 min. Aliquots (80 µl) of the particle-free supernatants were diluted with an equal volume of PBS buffer to reduce the organic solvent content to 33%. The resulting samples were transferred to a 96-well plate and subsequently subjected to LC-MS/MS.

Hepatocyte stability

Metabolic stability samples from hepatocyte incubations were stopped by addition of 200 µl ACN containing the internal standards (1 µM Diazepam, 1 µM Griseofulvin, and 10 µM Diclofenac) to 200 µL sample or calibration standards. Samples were shaken vigorously (10 seconds) then centrifuged (4800 x g, room temperature, 5 minutes). Aliquots of the particle-free supernatants (100 µL) were diluted with an equal volume of H_2O to reduce the organic solvent content of the samples to 25%. The resulting sample was transferred to autosampler vials and subsequently subjected to LC-MS analysis.

CYP inhibition using HTS^{TM} kits

For CYP2C8, the reaction was stopped by addition of 75 µl 2N NaOH. Before analysis, samples were further incubated at 37°C for 2 h to increase the signal-to-noise ratio.

The reactions of all other CYP isoforms were stopped by the addition of 75 µl/well stop solution containing 60% ACN and 40% 0.1 M Tris, pH 9.0. To wells 11 and 12, the stop solution was added prior to the addition of enzyme/substrate mix to serve as blanks for background fluorescence.

Table S5. Injection volumes.

Analyte	Injection volume (µl)
Solubility	
7.44 compound	20
PPB	
7.44 compound	10
Plasma stability	
7.44 compound	9
Propantheline	3
Chemical stability	
7.44 compound	15
Omeprazole	15
Hepatocyte stability	
7.44 compound	15

Key instruments

Liquid chromatography – mass spectrometry (LC-MS)

For quantitative analysis of test and reference items, LC-MS systems as described in **Description of key quantitative analytical equipment** section were used. The pump flow rate was set to 600 µL/min and the analytes were separated on a Kinetex Phenyl-Hexyl analytical column, 2.6 µm, 50 x 2.1 mm (Phenomenex, Germany) with a corresponding pre-column using the gradients as presented in **Table S6**.

For solubility, PPB, and plasma stability measurements applying the triple quadrupole technology, full scan mass spectra were acquired in the positive mode using syringe pump infusion to identify the protonated quasimolecular ions $[M+H]^+$. Auto-tuning was carried out for maximizing ion abundance followed by the identification of characteristic fragment ions using a generic parameter set: ESI ion-transfer-capillary temperature 350°C, capillary voltage 3.8 kV, collision gas 0.8 mbar argon, sheath gas, ion sweep gas, and auxiliary gas pressure were

19

40, 2, and 10 (arbitrary units). Ions with the highest S/N ratio were used to quantify the item in the selected reaction monitoring mode (SRM) and as qualifier, respectively.

For chemical and hepatocytes stability measurements applying the Q-TOF technology, a generic tune MS method was used and the system was calibrated every five samples. The MS was operated in the positive full scan polarity mode (TOF start mass 250 Da; TOF stop mass 700 Da). The accurate mass of the monitoring ions ± 2 mDa was used for test item and internal standard peak integration. Full MS-TOF was applied with the m/Z ranges and mass resolutions of the Q-TOF set to ''high''. Further analyzer settings were as follows: curtain gas 35, ion source gas1 50, ion source gas2 50, temperature 450°C, accumulation time 0.25 s, declustering potential 80.

Table S6. HPLC gradients (LC-MS/MS analysis)

7.44 compound		**Solubility / PPB / Plasma Stability**					
[min]		0.00	0.10	0.40	1.70	1.80	2.50
Mobile phase	A (%)[a]	0	0	97	97	0	0
	B (%)[b]	100	100	3	3	100	100
Propantheline		**Plasma Stability**					
[min]		0.00	0.10	0.40	1.70	1.80	2.50
Mobile phase	A (%)[a]	5	5	97	97	5	5
	B (%)[a]	95	95	3	3	95	95
7.44 compound / Omeprazole		**Chemical Stability & Hepatocyte Stability**					
[min]		0.00	0.10	0.40	2.70	2.80	5.50
Mobile phase	A (%)[a]	5	5	97	97	5	5
	B (%)[a]	95	95	3	3	95	95

[a] A: ACN / 0.1% (v:v) FA.

[b] B: H_2O / 0.1% (v:v)FA.

Table S7 gives an overview of the MS and chromatography parameters used for the analytes and the internal standard (ISTD).

Table S7. MS and chromatographic parameters (LC-MS/MS)

Triple quadrupole, ESI positive						
Compound	Molecular weight	[M+H]+ (m/z)	Monitoring ion (m/z)	Scan time (s)	Collision energy (V)	RT (min)
7.44 compound	342.3	343	149	0.010	15	1.13
Griseofulvin (ISTD)	352.80	353	215	0.010	25	1.26
Warfarin	308.33	309	251	0.100	15	1.31

20

Propantheline	448.39	368	181	0.015	35	0.95
Diazepam (ISTD)	284.7	285	193	0.015	20	1.19
LC-HRMS (QTOF)						
Compound	Molecular weight	[M+H]$^+$ (m/z)	Scan time (s)		Collision energy (V)	RT (min)
7.44 compound	342.3	343.085	0.557		10	2.10
Omeprazole	345.4	346.122	0.557		10	1.85
Diclofenac (ISTD)	296.1	296.0239				2. 09

Fluorescence plate reader - Wallac Victor (Perkin Elmer)

The fluorescent metabolites were detected using a Wallac Victor[3] fluorescence plate reader. The wavelengths for excitation and emission of the individual fluorescent metabolites depending on the substrates are given in **Table S8**. The final concentrations of the reagents required for the individual CYP isozymes are given. Shortcuts given in the tables are shown below.

Table S8. Excitation and emission wavelengths in P450 screening[a]

Isoenzyme	CYP1A2	CYP2B6	CYP2C8	CYP2C9
Metabolite	CHC	HFC	F	HFC
Excitation	405 nm	405 nm	485	405 nm
Emission	460 nm	535 nm	545	535 nm

Isoenzyme	CYP2C19	CYP2D6	CYP3A4
Metabolite	CHC	AHMC	HFC
Excitation	405 nm	380 nm	405 nm
Emission	460 nm	460 nm	535 nm

[a]AHMC= 3-[2-(*N*,*N*-diethylamino)ethyl]-7-hydroxy-4-methylcoumarin, CHC = 3-cyano-7-hydroxycoumarin, F = fluorescein, HFC = 7-hydroxytrifluoromethyl coumarin

Data analysis

Solubility in aqueous buffer

The aqueous solubility (µM) of the compound was calculated using the following equation:

$$\text{Compound solubility [µM]} = \text{concentration in buffer supernatant [µM]} \qquad \text{S14}$$

PPB

The test item concentration in the 60 minutes stability control sample was compared to the non-incubated negative control sample concentration (= 100%) to proove test item plasma stability.

21

The percentage of compound bound to plasma proteins (% PPB) was calculated using the following equations:

(B) PPB referring to plasma filtrate:

$$\text{PPB } [\%] = 100 - \frac{(\text{test item concentration}_{\text{plasma filtrate}} / RV)}{\text{mean test item concentration}_{\text{incubated plasma}}} * 100 \qquad \text{S15}$$

Results are expressed as mean PPB value calculated from plasma filtrate. In addition, the concentration of test item was corrected for the specific test item recovery (RV):

$$RV = \frac{(\text{concentration }_{\text{plasma filtrate}} [nM] + \text{concentration }_{\text{plasma retentate}} [nM])}{\text{mean concentration }_{\text{incubated plasma}} [nM]} \qquad \text{S16}$$

Plasma stability and Chemical stability

The amount of test item in the plasma stability samples and buffer (chemical stability) were expressed as percentage of remaining compound compared to time point zero (=100%). The depletion of test item was presented.

Half-life ($t_{1/2}$) estimates for the test item were determined using the rate of parent disappearance and following equation:

$$t_{1/2} = \frac{\ln 2}{-k} \qquad \text{S17}$$

$t_{1/2}$ = half life [min]

k = slope from the linear regression of log [test compound] versus time plot [1/min]

Hepatocyte stability

The amount of compound in the samples was expressed as percentage of remaining compound compared to time point zero (=100%). These percentages were plotted against the corresponding time points. *In vitro* intrinsic clearance (CL_{int}) and half-life ($t_{1/2}$) estimates were determined using the rate of precursor disappearance and following equation, based on the well-stirred liver model:

22

$$t_{1/2} = \frac{\ln 2}{-k}$$
S18

$t_{1/2}$ = half life [min]

k = slope from the linear regression of log [test compound] versus time plot [1/min]

$$CL_{int} = (-k) * V * f_u$$
S19

CL_{int} = *in vitro* intrinsic clearance [μl/min/10^6 cells]

k = slope from the linear regression of log [test compound] versus time plot [1/min]

V = ratio of incubation volume and cell number

f_u = unbound fraction in the blood

As f_u is not known for the tested compound, the calculation was performed with f_u =1.

CL_{int} was used to calculate *in vivo* intrinsic clearance (CL_{int} *in vivo*) based on S21. Scaling parameters are given in **Table S9.**

$$CL_{int} \, in \, vivo = CL_{int} * w_{liver} * cd$$
S20

CL_{int} *in vivo* = in vivo intrinsic clearance [ml/min/kg]

CL_{int} = *in vitro* intrinsic clearance [ml/min/10^6 cells]

w_{liver} = liver weight [g/kg]

cd = liver cell density [10^6 hepatocytes / g liver]

Hepatic clearance (CL_{hep}) was calculated as follows:

$$CL_{hep} = \frac{CL_{int} \, in \, vivo * Q}{CL_{int} \, in \, vivo + Q}$$
S21

CL_{hep} = hepatic clearance [ml/min/kg]
CL_{int} *in vivo* = *in vivo* intrinsic clearance [ml/min/kg]
Q = blood flow [ml/min/kg]

Table S9. Scaling parameters for inter-species comparison

Species	Liver weight/ body weight [g/kg]	Liver blood flow [ml/min/kg]	Liver cell density [10^6 hepatocytes / g liver]
Mouse (CD-1)	87.5	90	135

23

CYP inhibition using HTS^{TM} kits

Mean blank values (NC) were subtracted from the sample values to obtain the net fluorescence signals. For each inhibitor concentration, the percent inhibition was calculated relative to the wells without inhibitor (PC, no inhibition).

The resulting fluorescence signals of those compounds, for which auto-fluorescence has been detected, were corrected as follows. The mean values of the resulting auto-fluorescent signals of each test concentration (mean of three wells) were subtracted from the corresponding assay wells. The resulting corrected fluorescent signal was corrected by the blank value (NC).

24

Permeability estimation from molecular dynamics simulations

System setup

To compute the permeability of **7.44**, a total of nine molecules with previously experimentally determined PAMPA measurements were selected as control compounds: progesterone, chlorpromazine, promazine, atropine, diazepam, theophylline, pralidoxime (2-PAM), asoxime (HI-6), and methoxime (MMB4). This set of molecules has been previously used to estimate permeabilities from MD simulations and free energy computations [13]. In all cases, atom types and their corresponding parameters were obtained from the AMBER GAFF2 force field [14], using antechamber. The restrained electrostatic potential (RESP) method was used to assign the charges from HF/6-31G calculations performed in Gaussian 09 [15]. Each simulation system was packed using PACKMOL-Memgen [16] to obtain a bilayer of 75x75 $Å^2$, resulting in ~165 1,2-dioleoyl-*sn*-glycero-3-phosphocholine (DOPC) molecules, 6585 TIP3P water molecules [17], and one ligand, in total ~43000 atoms. K^+ ions were added to neutralize the system when negatively charged compounds were simulated.

Molecular dynamics simulations

All MD simulations were performed using AMBER20 [14]. The minimization of the systems was performed using the MPI implementation of PMEMD [18]. 5000 cycles of steepest descent were followed in the first step of minimization by conjugate gradient minimization for a total of 10000 cycles. Only water molecules (and ions, if included) were minimized initially, using harmonic restraints of 25 kcal mol^{-1} A^{-2} on the rest of the system. In the second minimization step, the harmonic restraints were decreased to 5 kcal mol^{-1} A^{-2}, while in the third and fourth steps of minimization, the restraints were applied only on the ligand. The fifth minimization step was performed without restraints. The minimized systems were then heated from 0 to 100 K for 5 ps in the NVT ensemble. The temperature was controlled using Langevin dynamics with a coupling constant of 1 ps^{-1}, SHAKE, and a time step of 2 fs in all cases [19]. Further heating to 300 K was performed under NPT conditions, using the Berendsen barostat with semiisotropic pressure scaling along the membrane plane for 115 ps. The simulations were further relaxed under the same conditions until 5 ns were obtained.

To calculate the permeabilities of the selected compounds, simulations were setup as previously demonstrated with the AMBER suite [14, 20]. In brief, simulations were carried out for each molecule, pulling for 32 ns at 300 K with a force constant of 1.1 kcal mol^{-1} A^{-2} and a pulling speed of 1 Å ns^{-1} along the membrane normal (z-axis). A total of 33 umbrella windows were extracted, covering 0 to 32 Å with respect to the membrane center along the z-axis. In umbrella

25

sampling simulations, each extracted structure was simulated for 100 ns, maintaining as a reaction coordinate the distance to the membrane center along the z-axis in the umbrella window with a force constant of 2.5 kcal mol^{-1} Å^{-2}. The initial 50 ns of each simulation were considered as equilibration time, with the last 50 ns of each simulation being used for further analysis.

Permeation potential of mean force and permeability calculations

From the distance distributions obtained from the umbrella sampling simulations, PMF profiles were calculated using the weighted histogram analysis method (WHAM) [21], assigning the value of the probed molecule in bulk water to zero (**Figure 8A**). To calculate the membrane permeability (P, eq. S24), the diffusion along the membrane normal (z-axis) ($D(z)$, eq. S22), was calculated for each window as described by Hummer [22], implemented by Lee, Comer [23], and adapted by Dickson [20]:

$$D\left(z = (z)\right) = \frac{var(z)}{\tau_z} \tag{S22}$$

where τ_z corresponds to the characteristic time of the z-position autocorrelation in the given window. The diffusion $D(z)$ together with the free energy profile ($\Delta G(z)$) were used to obtain the resistivity (R) along the z-axis (eq. S23) and integrated to obtain the effective permeability P_{eff} [23] (eq. S24):

$$R(z) = \frac{e^{\beta(\Delta G(z))}}{D(z)} \tag{S23}$$

$$P_{eff} = \frac{1}{R} = \frac{1}{\int_0^z R(z)\,dz} \tag{S24}$$

where β is the inverse of the Boltzmann constant times the absolute temperature, and the range 0 to z covers the width of the whole membrane [13, 24]. Errors of the calculated permeabilities were estimated by performing the calculations in ten slices of 5 ns from the total 50 ns used for the analysis.

From the computed permeability data of our simulations and the experimentally determined PAMPA data of the reference molecules by Bennion *et al.* [13] (log $P_{eff/PMF}$ P_0^{-1} and log $P_{eff/PAMPA}$ P_0^{-1}, respectively, **Table S10**), a linear regression was computed (Figure 8B). The calculated permeability rates (log $P_{eff/PMF}$ P_0^{-1}) of **7.44** in a protonated and deprotonated state were used to predict the experimental values (log $P_{eff/PAMPA}$ P_0^{-1}) from the linear regression (**Table S11**).

26

Table S10. Permeability data of reference compounds

Compound	log $P_{eff/PMF} P_0^{-1}$ [a]	log $P_{eff/PAMPA} P_0^{-1}$ [b]
progesterone	0.70±0.28	-4.94
theophylline	0.12±0.50	-5.91
pralidoxime (P2-PAM)	-9.71± 0.74	-7.52
atropine	-0.75±0.94	-5.26
chlorpromazine	1.58±0.18	-5.26
diazepam	1.10±0.16	-5.40
asoxime (HI-6)	-14.43±0.91	-11.16
methoxime (MMB4)	-10.67±0.87	-9.25
promazine	1.46±0.17	-4.88

[a] $P_{eff/PMF}$, effective permeability in cm sec^{-1} calculated from free energy calculations (eq. S24). P_0, unit factor corresponding to 1 cm sec^{-1}. Errors correspond to the standard deviation obtained from calculating the permeability when dividing 50 ns into ten independent 5 ns simulation slices.

[b] $P_{eff/PAMPA}$, effective permeability in cm sec^{-1} obtained from PAMPA assays Bennion, Be [13]. P_0, unit factor corresponding to 1 cm sec^{-1}.

Table S11. Permeability data of **7.44**.

Compound	log $P_{eff/PMF} P_0^{-1}$ [a]	log $P_{eff/PAMPA} P_0^{-1}$ [b]	P_{eff} [cm sec^{-1}]
P7.44[c]	0.89±0.34	-5.07±0.10	8.51 x 10^{-6}
D7.44[d]	-1.90±0.87	-5.82±0.24	1.51 x 10^{-6}

[a] $P_{eff/PMF}$, effective permeability in cm sec^{-1} calculated from free energy calculations (eq. S24). P_0, normalization factor corresponding to 1 cm sec^{-1}. Errors correspond to the standard deviation obtained from calculating the permeability from dividing 50 ns into ten independent 5 ns simulation slices.

[b] $P_{eff/PAMPA}$, effective permeability in cm sec^{-1} calculated from the linear regression obtained from compounds in Table S10. P_0, normalization factor corresponding to 1 cm sec^{-1}.

27

[c] P7.44: **7.44** in the protonated (neutral) state;

[d] D7.44: **7.44** in the deprotonated (negatively charged) state.
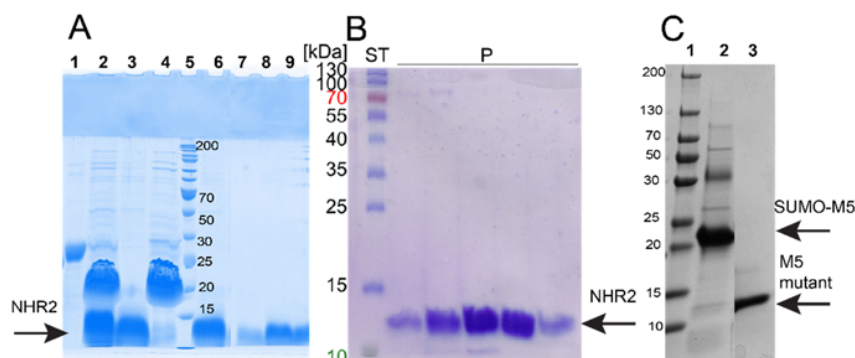
28

Supplemental Figures

Figure S1. SDS-PAGE of the NHR2 and M5 mutant purification. The fractions from the elution step of the IMAC were analyzed using a 15% polyacrylamide gel. **A)** The purification of NHR2 from SUMO fusion protein. Lane numbers from left: 1- SUMO-NHR2 fusion protein from IMAC, 2- SUMO cleavage reaction, 3- NHR2 from a flowthrough from reverse IMAC, 4- SUMO elution from reverse IMAC, 5- PageRuler™ Marker, 6 to 9- SEC elution (8.5 kDa). **B)** Purification of 6His-NHR2. The protein bands correspond to the molecular weight of the NHR2 monomer (11.3 kDa). ST: 5 µl protein standard (PageRuler™ Prestained Protein Ladder; Thermo Scientific), P: fractions from the purification. **C)** The purification of M5 mutant from SUMO fusion protein. Lane numbers from left: 1-PageRuler™ Marker, 2- SUMO-M5 fusion protein from IMAC, 3- SEC elution (8.1 kDa).
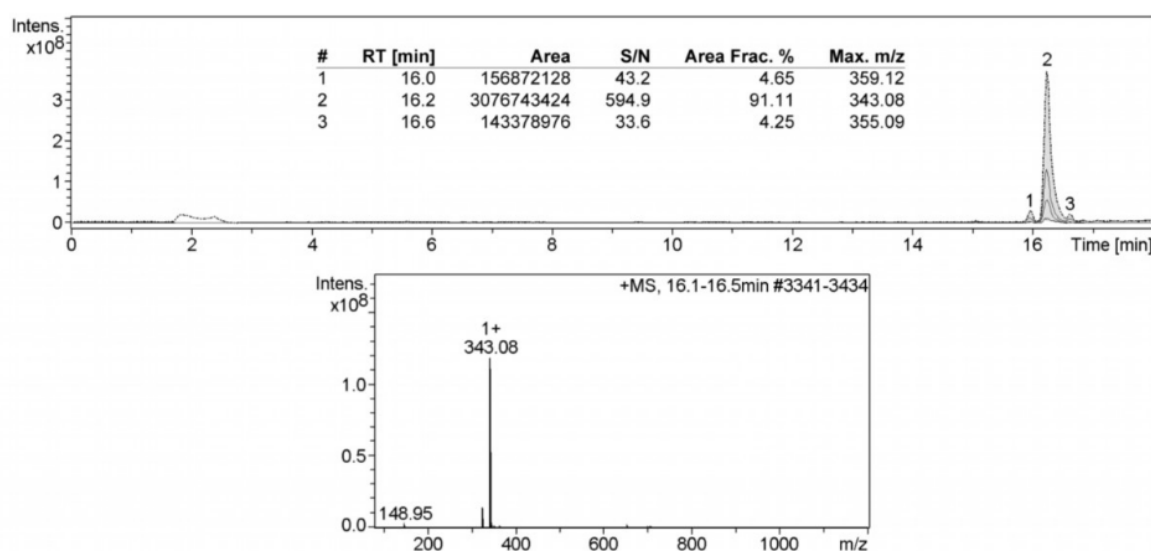
Figure S2. LC-MS analysis of 7.44. Ethanol-dissolved **7.44** (1 mg/mL) was used for LC-MS (amaZon speed ETD - Ion Trap, Bruker) analyses. The ionizations were generated by ESI. The upper panel is the chromatographic separation of **7.44** performed on a C18 reversed-phase analytical column. The most abundant compound **7.44** (peak 2) and lower amounts of other compounds (peak 1 and 3) were detected, and the respective masses are given as an insert. The lower panel is the MS data of **7.44** eluted from peak 2. The analyses of samples were carried out after three transitions for the sample. The first transition was for quantification and the second and third for verification.
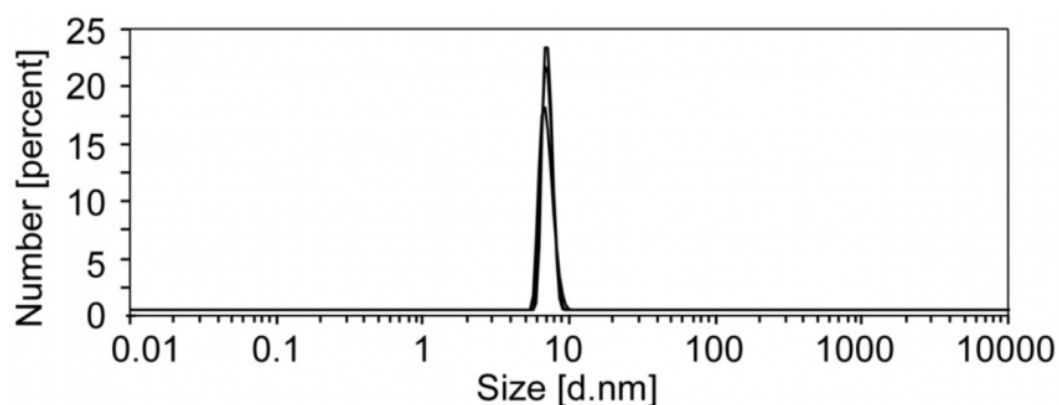
29

Figure S3. Graph of the size distribution by number of NHR2 obtained from dynamic light scattering (DLS) measurements. DLS experiments were performed at 298 K with a Zetasizer Nano S (Malvern Panalytical) light scattering instrument. The measurements were carried out with 53 μM and 25 μM of NHR2 protein in 20 mM sodium phosphate, 50 mM sodium chloride, 0.5 mM tris(2-carboxyethyl)phosphine, 10% (v/v) DMSO, pH 6.5. The plot of the size distribution versus the number shows a homogeneous distribution of the NHR2 sample with the average hydrodynamic radius of 6.939 nm.

30
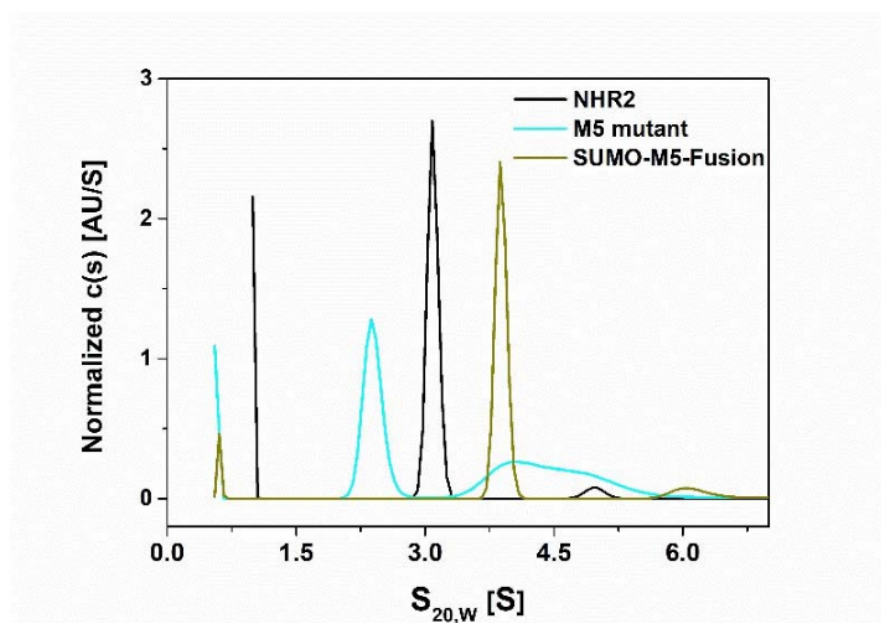
Figure S4. Analysis of NHR2 oligomerization by analytical ultracentrifugation. Sedimentation velocity concentration profiles of 13 μM of NHR2, 88 μM of M5 mutant, and 88 μM fusion protein of SUMO M5 mutant were obtained with a Beckman Coulter XL-I instrument in aluminum-filled double sector cells at 20°C and 50,000 RPM in 20 mM sodium phosphate, 50 mM sodium chloride, 0.5 mM tris(2-carboxyethyl)phosphine, pH 6.5. Samples were measured at 280 nm. The sedimentation profiles were fit to finite element solutions of the Lamm equation using a model of a continuous distribution of discrete, noninteracting species with the program SEDFIT [25]. The measured sedimentation coefficient (S) values were 3.07, 2.28, 3.89 for NHR2, M5 mutant, and SUMO-M5 fusion protein, respectively. The measured molecular weights were 37.3 kDa, 28.0 kDa, and 43.4 kDa, and the theoretically calculated molecular weights are 34.2 kDa (tetramer), 17.1 kDa (dimer), and 43.9 kDa (dimer) for NHR2, M5 mutant, and SUMO-M5 fusion protein, respectively. The measured molecular weight of the M5 mutant is higher than the calculated molecular weight. Hence, to clarify the size of the dimer, the SUMO-M5 fusion protein was measured, and the expected molecular weight of the dimer was obtained. The molecular weight and sedimentation coefficient of the predominant species were determined using a continuous distribution model (c(s)) [26]. A weight percent contribution of 94% of the majority species (tetramer) was obtained for 35 μM of NHR2 by integration of a continuous sedimentation coefficient distribution function. Then, the same 35 μM concentration of NHR2 was used for the SEC study (see main text about SEC and Figure 2A).
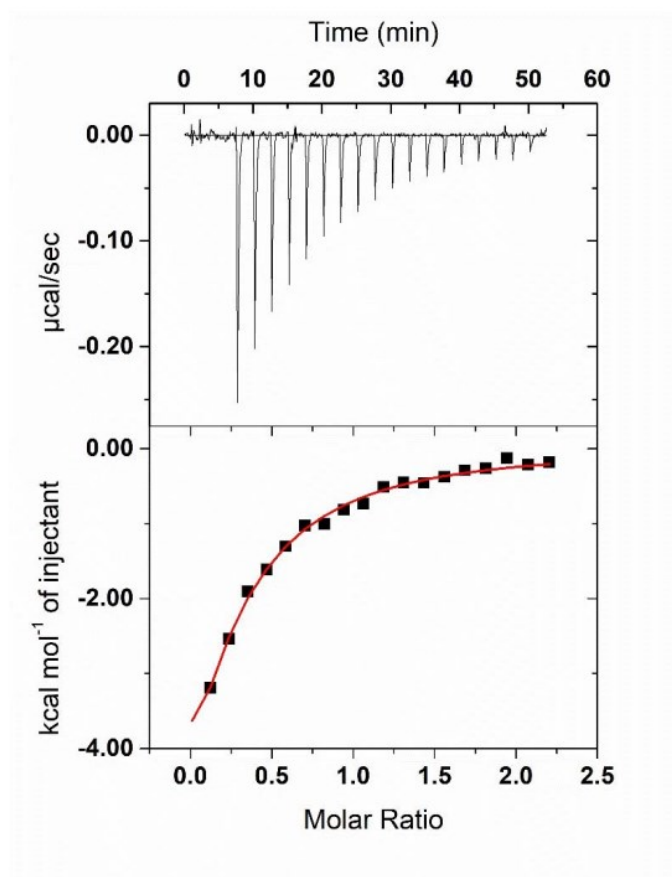
Figure S5. NHR2 interaction with E proteins (HEB (176-200)) by isothermal titration calorimetry (ITC). Titration of 600 µM HEB (176-200) peptide into a 53 µM NHR2 solution and resulting heat change are shown in the upper panel. The integrated data were fitted to a one-site binding model (lower panel) to yield $K_D = 30 \pm 4$ µM and $\Delta H = -15 \pm 6$ kcal mol^{-1}. ITC measurements were performed at 25°C using a MicroCal ITC200 (Malvern Instruments Ltd., United Kingdom) calorimeter. Buffer conditions were 50 mM sodium phosphate, 50 mM sodium chloride pH 8. Data were fitted using Origin Software package (OriginLab, Northampton, MA) provided by Malvern company.
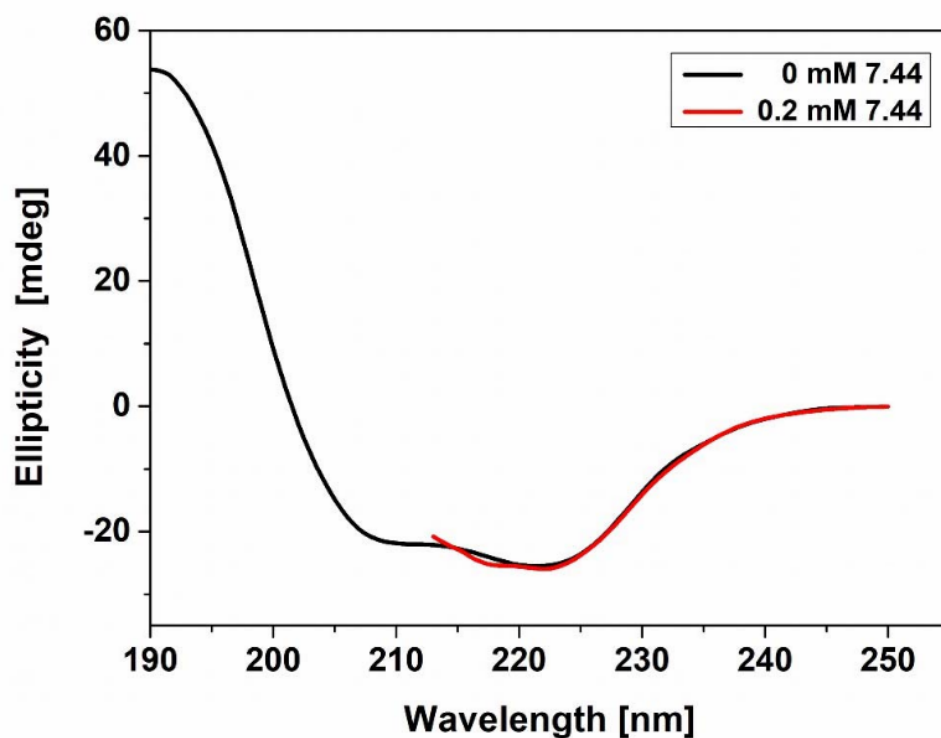
32

Figure S6. CD spectrum of NHR2 apo and in complex with 7.44. CD spectra were measured at 25 °C for the sample of 12.5 µM NHR2 for the apo state (black) and in complex with 200 µM of **7.44** (red). The samples were diluted in 10 mM sodium phosphate, 10 mM sodium chloride, 0.5 mM tris(2-carboxyethyl)phosphine, <1% (v/v) DMSO pH 6.5. Due to the scattering (high voltage in CD) of DMSO in the complex sample, the spectrum was measured from 213 nm to 250 nm, whereas the apo protein was measured from 190-250 nm.
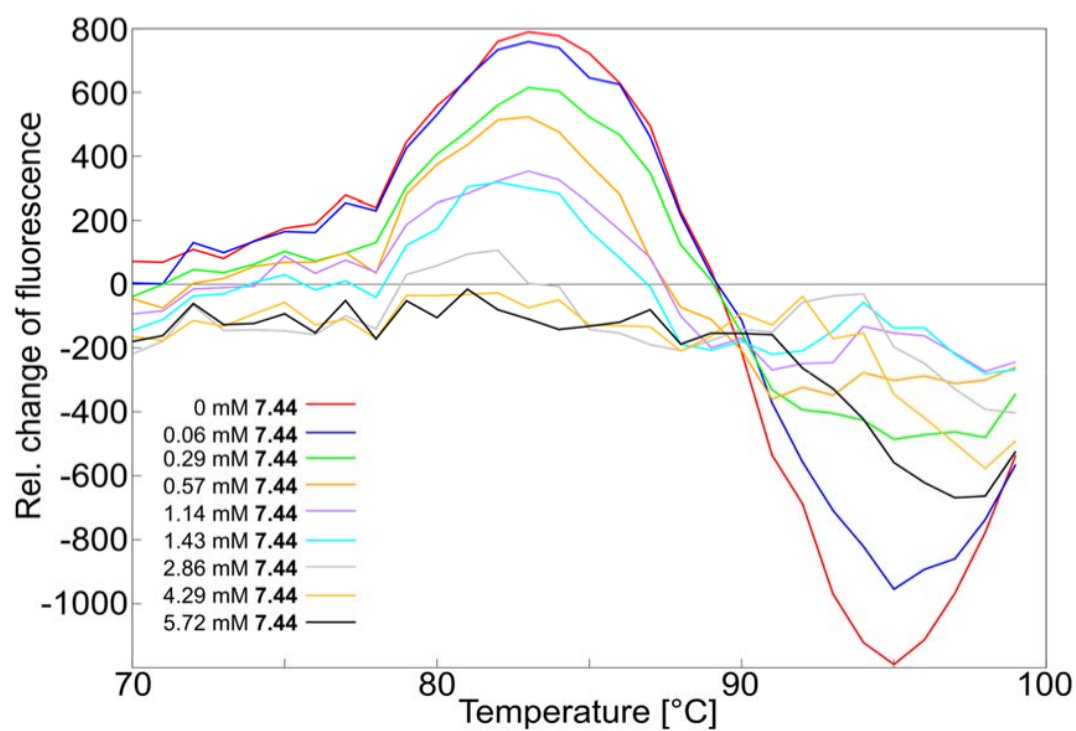
33

Figure S7. Differential scanning fluorimetry. dF/dT was calculated for nine samples containing a constant concentration of NHR2 and a varying concentration (provided in the legend) of **7.44**.
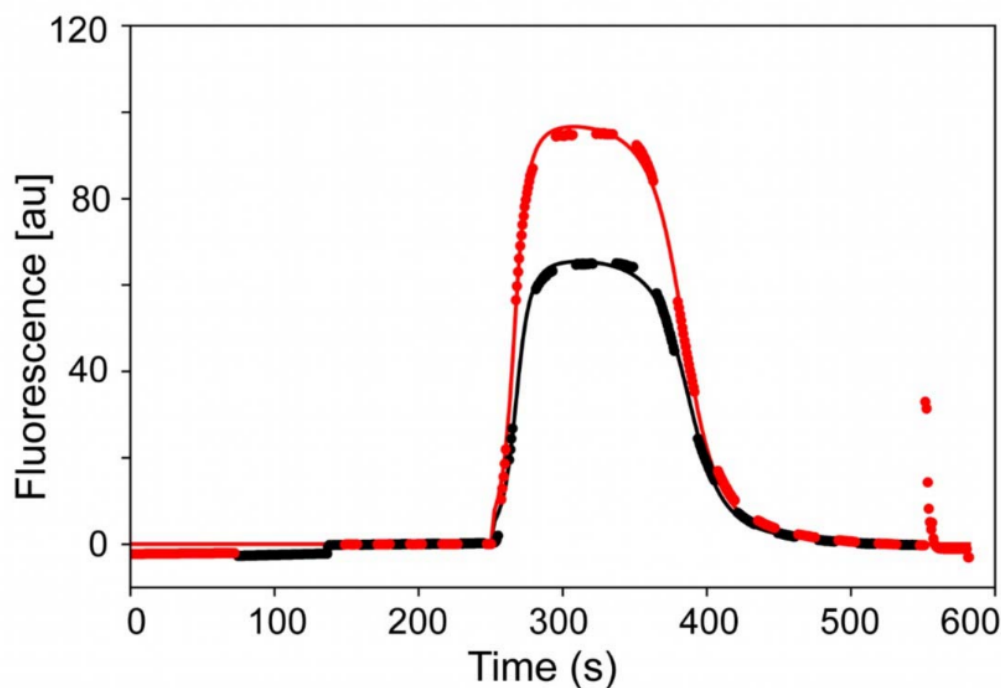
Figure S8. Measurement of the hydrodynamic radius of fluorescently labeled NHR2 by using microfluidic diffusional sizing method. Hydrodynamic radius was measured for 100 nM concentration of Alexa 488 dye-labeled NHR2 sample in 50 mM sodium phosphate, 50 mM sodium chloride pH 8, with microfluidic diffusional sizing using the Fluidity One-W instrument (Fluidic Analytics Ltd) at 25 °C. Fluorescence emission intensity at ~520 nm of labeled NHR2 after injection into a microfluidic laminar flow chamber and separation into two detection channels corresponding to diffused (black) and undiffused fluorophores (red). The measured hydrodynamic radius was 2.22 nm, which corresponds to the molecular weight of 16.72 kDa (NHR2-dimer) calculated by the software supplied with the machine [27]. Experiments were performed as triplicates.
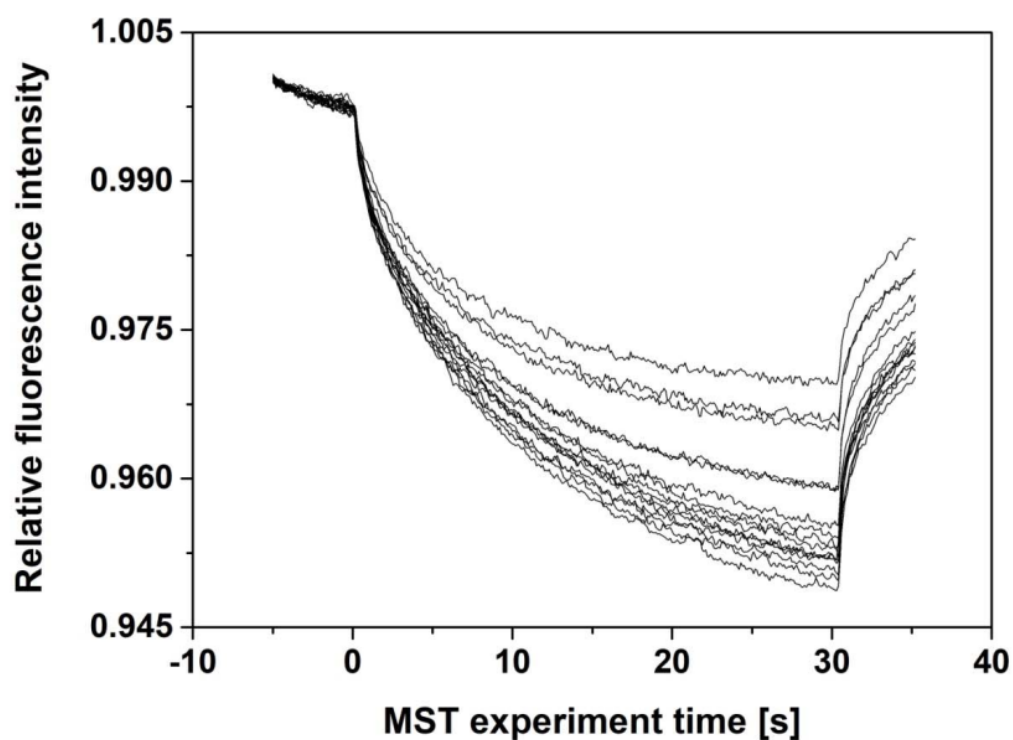
Figure S9. **MST traces of 7.44 binding to NHR2.** 100 nM of labeled NHR2 was mixed with **7.44** to concentrations ranging from 122 nM to 4 mM to the final volume of 50 μl (serial 1:1 dilution) in 20 mM sodium phosphate, 50 mM sodium chloride, pH 8.0, 10% (v/v) DMSO. The samples were incubated overnight in the dark prior to the experiment. Thermophoresis was measured using a Monolith NT.115 instrument, using an excitation power of 50% for 30 s and MST power of 40% at an ambient temperature of 24 °C. Microscale thermophoresis results were analyzed by MO affinity analysis software (NanoTemper Technologies GmbH).
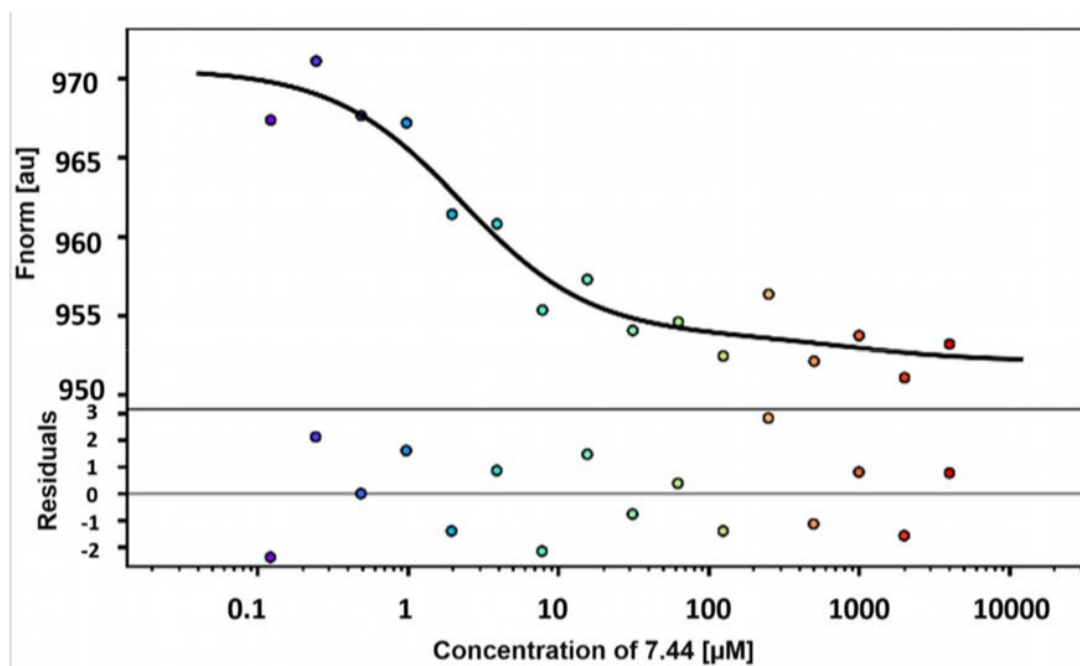
Figure S10. MST studies of 7.44 binding to NHR2. Titration of **7.44** to a constant concentration of dye-labeled NHR2 induces a change in thermophoresis. Data were fitted to a 1:2 binding model, assuming a 2-fold symmetry in the NHR2 dimer using the PALMIST software [28, 29]. The fitting results in $K_{lig} = 2$ µM, 68.3% CI [0, 6] µM. The broad confidence interval is a result of too few data points to clearly resolve a second binding step due to the insolubility of **7.44** at higher concentrations.
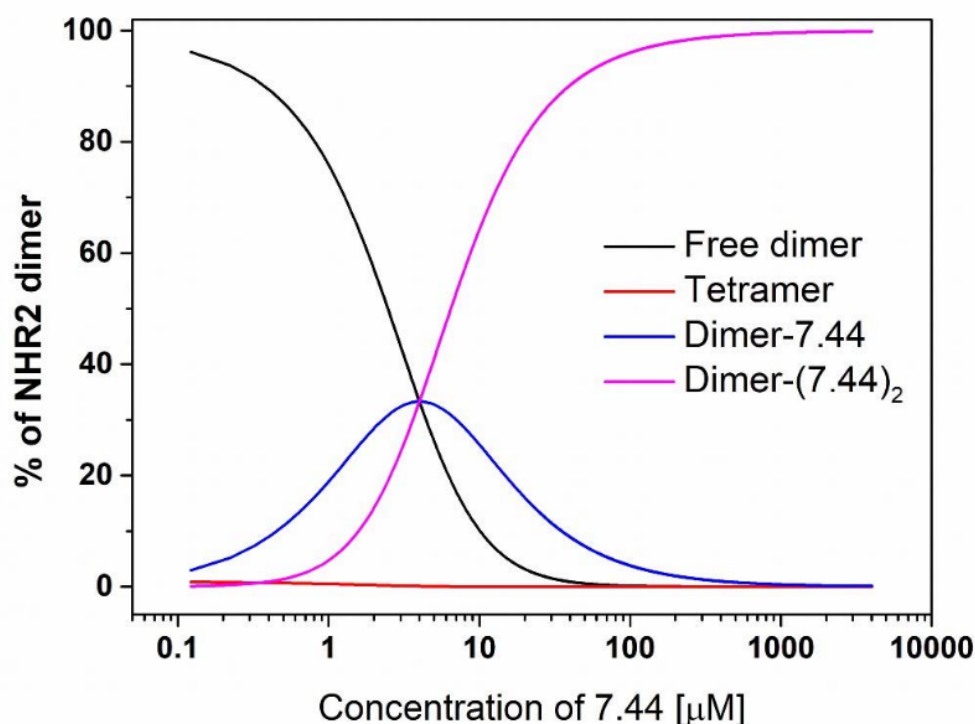
37

Figure S11. Simulated species distributions of the NHR2 / 7.44 equilibrium (eq. 4 in the main text). The distributions for NHR2 tetramer and dimer as well as singly and doubly **7.44**-bound dimer were obtained from the determined K_{tet} and K_{lig} using HySS2009 [30]. In the absence of **7.44**, > 99% of NHR2 is in a dimer configuration under the experimental conditions of the MST experiments. Increasing the **7.44** concentration reduces the amount of free NHR2, including the NHR2 tetramer. For calculating K_{lig} according to eqs. S11 and S12, it was assumed that the majority of the MST signal change is attributable to the dimer, yielding that, at $EC_{50} = 2.5$ µM of **7.44** (eq. 3 in the main text), the amount of free NHR2 dimer in the absence of **7.44** is reduced by half. This is retrieved back from the simulation.

38

NHR2 (485-552) : [485]QEEMIDHRLT DREWAEEWKH LDHLLNCIMD
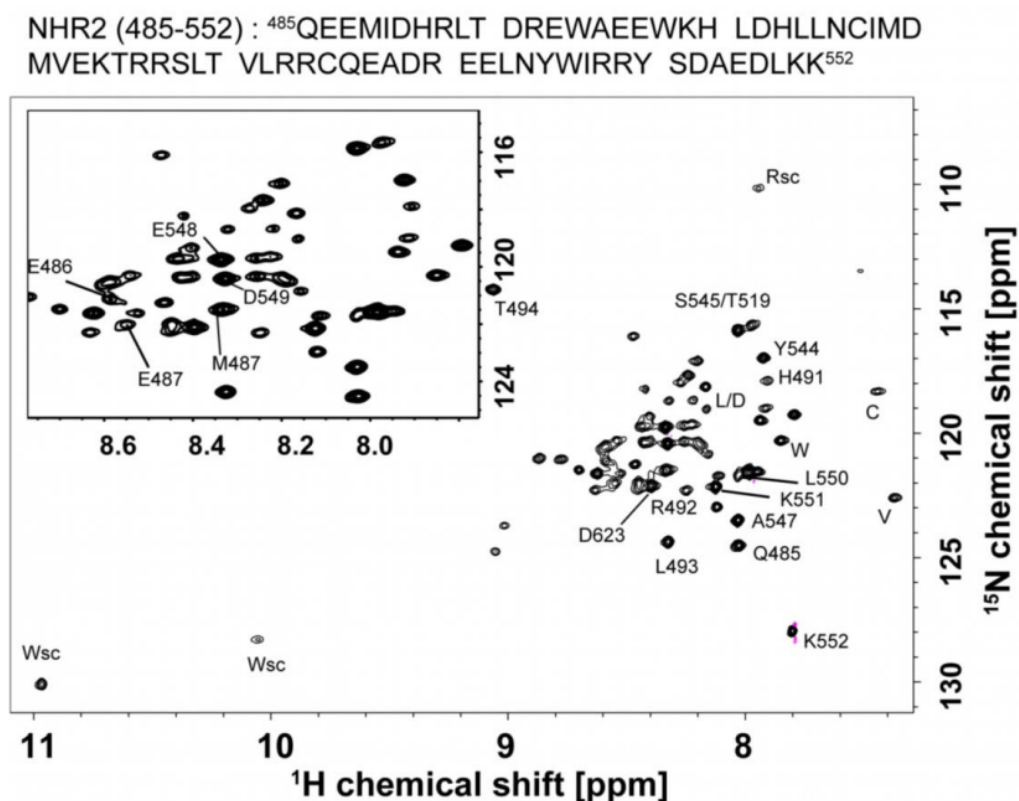MVEKTRRSLT VLRRCQEADR EELNYWIRRY SDAEDLKK[552]

Figure S12. 2D ¹H-¹⁵N TROSY-HSQC spectrum of 47 µ M of uniformly ²H, ¹⁵N, ¹³C-labeled NHR2. The amino acid sequence of NHR2 is depicted at the top of the spectrum. The spectrum was recorded at 60 °C on a 750 MHz spectrometer for about 19 hours. The assignments were done by 3D NMR experiments with 325 µM of ²H, ¹³C, ¹⁵N-NHR2 in 20 mM sodium phosphate, 50 mM sodium chloride, 0.5 mM tris(2-carboxyethyl)phosphine, 10% (v/v) D₂O, pH 6.5 in a Shigemi tube and at 308 K. 32% of the amide signals were unambiguously assigned and labeled in the spectrum. The assignments were hindered by missing signals in the 3D spectra, which is due to the coiled-coil nature of the protein.
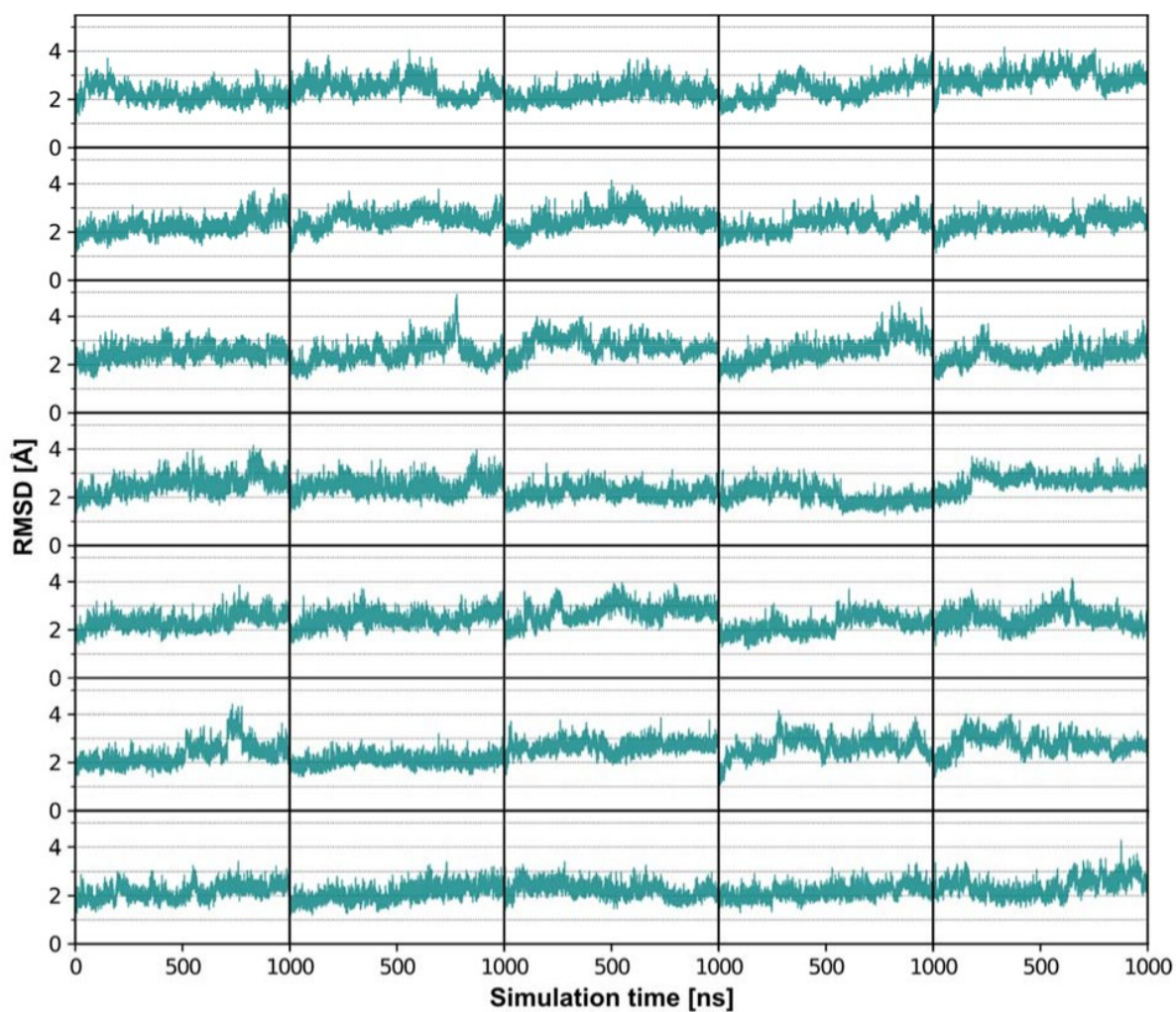
39

Figure S13. Structural variability of the NHR2 tetramer in the molecular dynamics simulations. The C$_\alpha$-RMSD of the NHR2 tetramer during the simulations with respect to the crystal structure is shown (PDB ID: 1wq6). Occasional higher RMSD values up to 5 Å correspond to motions of the dynamic termini, while the core structure of the tetramer remains stable.

40

Supplemental References

1. Bartel, Y., M. Grez, and C. Wichmann, *Interference with RUNX1/ETO leukemogenic function by cell-penetrating peptides targeting the NHR2 oligomerization domain.* Biomed Res Int, 2013. **2013**: p. 297692.
2. Becker, Y., *Inhibierung der leukämischen Funktion des Fusionsproteins AML1/ETO durch Interferenz mit der Oligomerisierungsdomäne.* 2011.
3. Metz, A., et al., *From determinants of RUNX1/ETO tetramerization to small-molecule protein-protein interaction inhibitors targeting acute myeloid leukemia.* J Chem Inf Model, 2013. **53**(9): p. 2197-202.
4. Bopp, B., et al., *Design and biological testing of peptidic dimerization inhibitors of human Hsp90 that target the C-terminal domain.* Biochim Biophys Acta, 2016. **1860**(6): p. 1043-55.
5. Metz, A., *Predicting and Exploiting the Determinants of Protein/Protein Interactions to Identify Low-Molecular Inhibitors of RUNX1-ETO Tetramerization (PhD Thesis).* 2014, Düsseldorf: Heinrich Heine Universität.
6. Metz, A., *Predicting and Exploiting the Determinants of Protein/Protein Interactions to Identify Low-Molecular Inhibitors of RUNX1-ETO Tetramerization.* 2004, Düsseldorf: Heinrich Heine University Düsseldorf.
7. Lipinski, C.A., *Drug-like properties and the causes of poor solubility and poor permeability.* Journal of Pharmacological and Toxicological Methods, 2000. **44**(1): p. 235-249.
8. McGinnity, D.F., et al., *Evaluation of fresh and cryopreserved hepatocytes as in vitro drug metabolism tools for the prediction of metabolic clearance.* Drug Metab Dispos, 2004. **32**(11): p. 1247-53.
9. Obach, R.S., *Prediction of human clearance of twenty-nine drugs from hepatic microsomal intrinsic clearance data: An examination of in vitro half-life approach and nonspecific binding to microsomes.* Drug Metab Dispos, 1999. **27**(11): p. 1350-9.
10. Onofrey, T., Kazan, G., *MultiScreen Solubility Filter Plate.* Millipore Corporation, Life Science Division, Danvers, MA: p. www.millipore.com.
11. Riley, R.J., D.F. McGinnity, and R.P. Austin, *A unified model for predicting human hepatic, metabolic clearance from in vitro intrinsic clearance data in hepatocytes and microsomes.* Drug Metab Dispos, 2005. **33**(9): p. 1304-11.
12. Taylor, S. and A. Harker, *Modification of the ultrafiltration technique to overcome solubility and non-specific binding challenges associated with the measurement of plasma protein binding of corticosteroids.* J Pharm Biomed Anal, 2006. **41**(1): p. 299-303.
13. Bennion, B.J., et al., *Predicting a Drug's Membrane Permeability: A Computational Model Validated With in Vitro Permeability Assay Data.* J Phys Chem B, 2017. **121**(20): p. 5228-5237.
14. D.A. Case, K.B., I.Y. Ben-Shalom, S.R. Brozell, D.S. Cerutti, T.E. Cheatham, III, V.W.D. Cruzeiro, T.A. Darden, R.E. Duke, G. Giambasu, M.K. Gilson, H. Gohlke, A.W. Goetz, R. Harris, S. Izadi, S.A. Izmailov, K. Kasavajhala, A. Kovalenko, R. Krasny, T. Kurtzman, T.S. Lee, S. LeGrand, P. Li, C. Lin, J. Liu, T. Luchko, R. Luo, V. Man, K.M. Merz, Y. Miao, O. Mikhailovskii, G. Monard, H. Nguyen, A. Onufriev, F.Pan, S. Pantano, R. Qi, D.R. Roe, A. Roitberg, C. Sagui, S. Schott-Verdugo, J. Shen, C.L. Simmerling, N.R.Skrynnikov, J. Smith, J. Swails, R.C. Walker, J. Wang, L. Wilson, R.M. Wolf, X. Wu, Y. Xiong, Y. Xue, D.M. York and P.A. Kollman, *AMBER 2020; University of California, San Francisco, CA https://ambermd.org/AmberMD.php.* 2020. **2020 oct 5**.
15. Cornell, W.D., et al., *Application of Resp Charges to Calculate Conformational Energies, Hydrogen-Bond Energies, and Free-Energies of Solvation.* Journal of the American Chemical Society, 1993. **115**(21): p. 9620-9631.
16. Schott-Verdugo, S. and H. Gohlke, *PACKMOL-Memgen: A Simple-To-Use, Generalized Workflow for Membrane-Protein-Lipid-Bilayer System Building.* Journal of Chemical Information and Modeling, 2019. **59**(6): p. 2522-2528.
17. Price, D.J. and C.L. Brooks, *A modified TIP3P water potential for simulation with Ewald summation.* Journal of Chemical Physics, 2004. **121**(20): p. 10096-10103.

18. Le Grand, S., A.W. Gotz, and R.C. Walker, *SPFP: Speed without compromise-A mixed precision model for GPU accelerated molecular dynamics simulations.* Computer Physics Communications, 2013. **184**(2): p. 374-380.

19. Miyamoto, S. and P.A. Kollman, *Settle - an Analytical Version of the Shake and Rattle Algorithm for Rigid Water Models.* Journal of Computational Chemistry, 1992. **13**(8): p. 952-962.

20. Dickson, C.J., *AMBER-Umbrella_COM_restraint_tutorial.* https://github.com/callumjd/AMBER-Umbrella_COM_restraint_tutorial, 2020. **2020 oct 08**.

21. Kumar, S., et al., *The Weighted Histogram Analysis Method for Free-Energy Calculations on Biomolecules .1. The Method.* Journal of Computational Chemistry, 1992. **13**(8): p. 1011-1021.

22. Hummer, G., *Position-dependent diffusion coefficients and free energies from Bayesian analysis of equilibrium and replica molecular dynamics simulations.* New Journal of Physics, 2005. **7**: p. 34-34.

23. Lee, C.T., et al., *Simulation-Based Approaches for Determining Membrane Permeability of Small Compounds.* Journal of Chemical Information and Modeling, 2016. **56**(4): p. 721-733.

24. Carpenter, T.S., et al., *A Method to Predict Blood-Brain Barrier Permeability of Drug-Like Compounds Using Molecular Dynamics Simulations.* Biophysical Journal, 2014. **107**(3): p. 630-641.

25. Schuck, P., *Size-distribution analysis of macromolecules by sedimentation velocity ultracentrifugation and lamm equation modeling.* Biophys J, 2000. **78**(3): p. 1606-19.

26. Liu, Y., et al., *The tetramer structure of the Nervy homology two domain, NHR2, is critical for AML1/ETO's activity.* Cancer Cell, 2006. **9**(4): p. 249-60.

27. Arosio, P., et al., *Microfluidic Diffusion Analysis of the Sizes and Interactions of Proteins under Native Solution Conditions.* ACS Nano, 2016. **10**(1): p. 333-41.

28. Scheuermann, T.H., et al., *On the acquisition and analysis of microscale thermophoresis data.* Anal Biochem, 2016. **496**: p. 79-93.

29. Tso, S.C., et al., *Using two-site binding models to analyze microscale thermophoresis data.* Anal Biochem, 2018. **540-541**: p. 64-75.

30. Alderighi, L., et al., *Hyperquad simulation and speciation (HySS): a utility program for the investigation of equilibria involving soluble and partially soluble species.* Coordination Chemistry Reviews, 1999. **184**: p. 311-318.